UNIVERSITY OF SOUTHAMPTON

Faculty of Natural and Environmental Sciences
Ocean and Earth Science

Faculty of Engineering and the Environment
Civil, Maritime, and Environmental Engineering

Southampton Marine and Maritime Institute

Coherent Turbulence Structures and Sediment Resuspension in the Coastal Benthic Boundary Layer

by

Hachem Kassem

Thesis for the degree of Doctor of Philosophy

Graduate School of the National Oceanography Centre, Southampton

September 2016

Abstract

This work addresses the complex interactions between bed-generated coherent turbulence structures and suspended non-cohesive sediment in wave-dominated environments and under combined wave-current flows. Coherent structures are intermittent, connected fluid masses with a defined spatial extent and life-span and characterised by vorticity; and define entrainment and momentum exchanges in turbulent flows. Prototype-scale experimental observations of flow, bedforms and suspensions are presented; focusing on the structural, spatial and temporal dynamics of these motions and their role in sediment entrainment. Two scenarios are considered: (a) shoaling (and breaking) erosive and accretive waves in the nearshore of a sandy barrier beach (spilling and plunging breakers); and (b) collinear steady currents aligned with, and opposing the direction of wave propagation over a rippled, sandy bed.

Measurements collected in the nearshore of a prototype-scale sandy barrier beach show intermittent momentum exchanges characterised by large wave-induced coherent structures within the benthic boundary layer, corresponding to the mean flow properties. These structures can be described by a 3D bursting sequence which plays a significant role in moving and maintaining sediment in suspension. The temporal variability of these events dictates the net onshore and offshore transport. Periods associated with a succession of powerful turbulent events cause powerful suspension clouds across multiple frequency scales. The bulk of suspension is attributed to wave-induced fluctuations of low frequencies. These modulate smaller, rapidly decaying high-frequency turbulence extending outside the boundary layer. As larger structures persist for a considerable amount of time, suspensions near the bed are amplified before decaying as the supply of momentum ceases. Outside the boundary layer, momentum transfer via turbulent fluctuations maintains the suspensions until their energy is depleted.

In combined wave-current flows, the current plays a significant role in dictating the prevalence of specific turbulent motions within a bursting sequence. The current-aligned structures contribute significantly to the stress, and display characteristics of wall-attached eddies formed by the pairing of counter-rotating vortices. In aligned wave-current flows, the flow is characterised by a local balance between turbulent production and dissipation, and displays the 'universal' inertial cascade of energy in the outer flow, while just outside the combined boundary layer a superposition of eddies is observed, often linked to intermittent coherent turbulent structures at an intermediate range between energy production and dissipation. When the current opposes the direction of wave propagation, stress-bearing coherent structures break rapidly as they are ejected higher in the water column. Suspended clouds through vortex shedding thus cease rapidly in opposing flows, compared to more continuous sediment transport in aligned flow.

Both studies indicate that bed-induced coherent turbulence structures play a significant role in the entrainment and transport of suspended sediment in flows typically encountered in the coastal environment. Suspension clouds induced be vortex shedding are maintained by the continuous supply of momentum through vortex clusters; and transport is described by the advection of these particles through net currents. A complex feedback is then imparted by the suspended particles on these structures. This merits a re-evaluation of coastal sediment transport models, and a shift towards a stochastic description of the problem.

Table of Contents

List of Figures

List of Tables

List of Appendices

Academic Thesis: Declaration of Authorship

I, Hachem Kassem, declare that this thesis and the work presented in it are my own and has been generated by me as the result of my own original research.

Coherent Turbulence Structures and Sediment Resuspension in the Coastal Benthic Boundary Layer

I confirm that:

1. This work was done wholly or mainly while in candidature for a research degree at this University;

2. Where any part of this thesis has previously been submitted for a degree or any other qualification at this University or any other institution, this has been clearly stated;

3. Where I have consulted the published work of others, this is always clearly attributed;

4. Where I have quoted from the work of others, the source is always given. With the exception of such quotations, this thesis is entirely my own work;

5. I have acknowledged all main sources of help;

6. Where the thesis is based on work done by myself jointly with others, I have made clear exactly what was done by others and what I have contributed myself;

7. Either none of this work has been published before submission, or parts of this work have been published as: [please list references below]:

Signed: Hachem Kassem

Date: 24/01/2017

Acknowledgements

'And they'll build systems dark and deep
And systems broad and high
But two on three will never agree
About the reason why'
Peter Pindar – The Three Wise Men of Gotham

Legend has it that Albert Einstein warned his son, Hans, having glanced through some papers he was reading for his engineering exams, of the incomprehensible complexity of sediment dynamics. Little did I know, when I started my Masters, that this warning, shared enthusiastically by Prof Carl Amos in his first lecture on the subject, will haunt me for the rest of my life. I was captivated by this professor and the subject he was preaching, and his constant 'we don't really know!'. Sooner than I thought, I embarked, foolishly perhaps, on answering some of these unknowns. My sanity would be tested to the extremes, and without the following people, I would have never survived.

First and foremost, I offer my most sincere gratitude to Dr Charlie Thompson, whose outstanding support, expert guidance, and sharp wit kept me in line and kept the target undimmed all the way. As my first supervisor, Charlie often had the unenvied task of having to deal with me, and my other supervisors, a task she masterfully handled. She has been an exceptional mentor, a continuous source of encouragement, an astute critic, a most reliable supporter and an endlessly patient advisor. To be Charlie's first PhD student (as a first supervisor) is a badge of honour I will most proudly uphold. I thank her for never giving up on me, and to her I am forever indebted.

My gratitude also extends to Prof Carl Amos for his invaluable advice and relentless enthusiasm that kept the flame going, even when nothing else seemed to be. Carl's support was most crucial in keeping my morale high and my wits sharp(-ish). Our scientific conversations were often thought-provoking, incentivised me to widen my horizons or sharpen my questions and often revealed perspectives that never crossed my mind. Our arguments over coffee, be it sports, politics, philosophy or turbulence lead to many

cherished breaks and many great memories. Carl facilitated most of my field trips to Venice, Sardinia, and Quebec, yet none of these data featured in the thesis and he has been such a sport about it. Carl, 'the legend' as ECE students like to call him, has been such an inspiration, and to him, I owe everything.

I am also most thankful to Prof Ian Townend, for his invaluable advice, continued support, and often different perspective on things. Ian repeatedly engaged me in complex conversations, made me re-evaluate my approach to problem solving and think outside of the norms; and ensured whatever I said was put in the right context. Many thanks go to him for convincing HR Wallingford to be my industrial sponsor, and facilitating the use of the Fast Flow Facility; and I apologise for not including any modelling in this work!

I thank Prof Robert Nicholls for his supervision, help, and advice; and for supporting my PhD though the Faculty of Engineering and the Environment. Thanks are also extended to Dr Justin Dix for chairing my panel meetings and directing my studies, for smoothing so many hurdles along the way, and for containing my supervisors endless discussions; making sure we were all on track. Dr Aggelos Dimakopolous has also been immensely helpful with discussions and advice on modelling turbulence.

This PhD was funded jointly by the Graduate School of the National Oceanography Centre, Southampton (Ocean and Earth Science); the Faculty of Engineering and the Environment, the Southampton Marine and Maritime Institute, and HR Wallingford ltd. Special thanks are due to Mary Smith from GSNOCS, and Sue Smith from SMMI for administering my progress, and offering help and advice when needed. The data reported in Chapter 5 were collected as part of the EU-funded Barrier Dynamics Experiment II (HYDRALAB IV Contract no. 261520 by the European Community Seventh's Framework Programme). Many thanks go to Dr Charlie Thompson for offering me the chance to participate in this experiment, and to every member of the huge team which made it a great experience, especially Prof Gerd Masselink. The data reported in Chapter 6 were collected in the HR Wallingford Fast Flow Facility, and funded by HR Wallingford ltd. Special

thanks are due to Prof Richard Whitehouse for presenting this opportunity, and to Dr David Todd and Elizabeth Chellew for all their invaluable help.

Furthermore, to Amani, Alanoud, Sara, Ibrahim, Said, Joul, Anas, Robert, Saikiran, Amy, Julien, Mario, Angeliki, Eleni, Katerina, Christos, Himar, Guisseppe, to all members of the Coastal group, the GSNOCS cohort, the wider NOCS community and the Student Union Lebanese Society, I offer my kindest regards for keeping me motivated, for offering plenty of coffee breaks and discussions, for great moral support, and many sweet desserts. Without you, my life would have been miserable, and I would have certainly finished my thesis much earlier. Many thanks are also due to my aunt and cousins in London for being my home away from home. To Kifah and Eyad, who were there every step of the way and picked me up whenever I fell down, I am forever indebted.

Finally, my heartfelt gratitude is due to my family for their insurmountable sacrifices that got me here. You have been a blessing, continuously supporting and motivating me and offering me beyond anything I ever needed, especially most sought after moral boosts in my darkest hours. You have been ceaselessly patient, have endured so much along the way so I feel least inconvenienced, and put your lives on hold so I can get on with mine. You make me want to be the better me, and your most-cherished prayers have guarded me along the way. To you, my everything, I dedicate this humble piece of work.

Hachem Kassem

List of Symbols and Abbreviations

Subscripts, superscripts and indices

x, y, z	spatial dimensions, along mean flow (x-axis), across flow (y-axis), vertical (z-axis)
$_{1, 2, 3}$	subscripts pertaining to 1st, 2nd, and 3rd component in space
$_{i, j, k}$	subscripts pertaining to 1st, 2nd, and 3rd component in space
$_{i}$	Instantaneous property; *e.g.* U_i
$_{c}$	Current related property; *e.g.* δ_c
$_{w}$	Wave related property; *e.g.* δ_w
$_{c,w}$; $_{w,c}$	Combined wave-current related property; *e.g.* $\delta_{c,w}$
$_{T}$	Turbulence property, *e.g.* ν_T, u_T
$_{0}$	Near-bed or near wall property/ pipe centre-line; *e.g.* U_0, A_0
$_{\delta}$	Property at the edge of boundary layer full thickness; *e.g.* U_δ
$_{\infty}$	Freestream property; *e.g.* U_∞
$'$	Fluctuating property; *e.g.* u', v', w'
$^{+}$	Wall-units; *e.g.* z^+, u^+
*	Friction (shear) related property; *e.g.* u^*
$_{cr}$	Critical value (threshold)
$_{max}$	Property magnitude at its maximum; *e.g.* U_{max}, τ_{max}
$_{m}$	Mean magnitude of a property; *e.g.* τ_m; δ_m
$_{s}$	Property pertaining to sediment; *e.g.* ρ_s , w_s
$_{s}$	Suspension-related ; *e.g.* θ_s
$_{50}$	Median value of a statistical distribution
$_{35}$, $_{65}$ $_{85}$, $_{90}$,	Subscripts denoting the percentage of components smaller than that value in a statistical distribution
$_{100}$	Property measured at a height of 100 cm above bed, *e.g.* U_{100}
$_{k_s}$	Subscript pertaining to property at level of physical (grain-equivalent) roughness; *e.g.* Re_{w,k_s}

Dimensional Units:

Symbol	Definition	SI unit
[L]	Spatial dimension (characteristic length scale)	Metres (m)
[T]	Time dimension (characteristic time scale)	Seconds (s)
[M]	Mass dimension	Grams (g)

Latin symbols

Symbol	Definition	Dimension	SI unit
a	scale of the wavelet (dilation)	[ ]	
a_0	Wavelet scale at octave zero	[ ]	
a_r	Empirical coefficient	[ ]	
b	position (translation) of a wavelet	[ ]	
b_0	Abscissa of wavelet scale at octave zero	[ ]	

b_{ij}	Anisotropy in non-linear RANS model		
c	Concentration	[M/L^3]	g/m^3
c	Constant of proportionality	[ ]	
d	Displacement height	[L]	m
d	Full water depth	[L]	m
d_0	Wave near bed orbital diameter	[L]	m
f_c	Current only friction factor	[ ]	
f_w	Wave friction factor	[ ]	
f_{wr}	Wave friction factor in rough flow	[ ]	
$f_{c,w}, f_{w,c}$	Combined wave current friction factor	[ ]	
$f(t)$	Signal (time-series)	[ ]	
g	Gravitational acceleration	[L/T^2]	m/s^2
h	Still water depth	[L]	m
k	Wave number	[L^{-1}]	m^{-1}
k	Turbulent kinetic energy (per unit)	[L^2/T^2]	m^2/s^2
k_ℓ	Wavenumber for eddy scale of the size ℓ	[L^{-1}]	m^{-1}
k_s	Projection (height) of the roughness element; Nikuradse-equivalent physical roughness	[L]	m
k^*	non-dimensional wave-number at height of measurement	[ ]	
k_ψ	Wave vector modulated by a Gaussian envelop of unit width	[ ]	
$l, l_m,$	Mixing length	[L]	m
ℓ	Length scale of an eddy	[L]	m
n	Number of grain detachments	[ ]	
p	Pressure	[M/L.T^2]	N/m^2
$\overline{q}^2$	Turbulent intensity	[L^2/T^2]	m^2/s^2
rms	Root mean squared	[ ]	
s	Relative density (specific gravity)	[ ]	
s	Dilation scale	[ ]	
t	Time (at an instance)	[T]	s
t_0	Starting time	[T]	s
u	Streamwise (along mean flow) velocity component	[L/T]	m/s
v	Number of degrees of freedom	[ ]	
v	Crosswise (transverse) velocity component	[L/T]	m/s
w	Vertical velocity component	[L/T]	m/s
w_s	particle settling (fall) velocity in still water	[L/T]	
$x(t)$	A continuous signal in time	[ ]	
z_0	Reference height, hydrodynamic roughness length	[L]	m
z	Elevation above the bed	[L]	m
z	Height of a measurement above bed	[L]	m
z_a	Reference height above the bed	[L]	m

z^+	wall units (non-dimensional wall distance of wall-bounded flow	[ ]	

A	area	[L^2]	m^2
A_w	wave orbital amplitude (semi-orbital excursion)	[L]	m
$A_{0,cw}$	Current-modified, near bed orbital amplitude	[L]	m
B	Constant of integration		
C	Sediment (mass) concentration	[M/L^3]	g/m^3
C_a	Reference sediment concentration	[M/L^3]	g/m^3
C_D	Coefficient of drag	[ ]	
C_{D_r}	Rough turbulent current drag coefficient	[ ]	
$C_{D,m,r}$	Mean drag coefficient for rough turbulent combined wave-current flow	[ ]	
C_H^i	Concentration of data points within each quadrant (i) with a threshold H	[ ]	
C_K	Kolmogorov's constant	[ ]	
$C_{\varepsilon 1}$	Eddy viscosity model constant		
$C_{\varepsilon 2}$	Eddy viscosity model constant		
D	Dissipation by turbulent transport and viscous diffusion	[L^2/T^3]	m^2/s^3
D^*	Dimensionless grain diamter	[ ]	
E	Turbulent kinetic energy spectrum	[L^2/T]	m^2/s
E	Ejection type motion (Q2)		
F_r	Froude's number	[ ]	
F_s	Sampling frequency	[T^{-1}]	Hz
H	Wave height	[L]	m
H_s	Significant wave height (statistical)	[L]	m
H_{m0}	Significant wave height computed spectrally (4 times zeroth-order moment)	[L]	m
H	Hyperbolic hole size (threshold) in a quadrant plot	[ ]	
II	Inward interaction type motion (Q3)		
K_s	Eddy diffusivity in the nearshore	[L^2/T]	m^2/s
M_{ww}	integral of the 3D wave-number space	[ ]	
N	Number of sampled data points	[ ]	
N	Temporal rate of transport	[ ]	
OI	Outward interaction type motion (Q1)		
P	Pressure field	[M/L.T^2]	N/m^2
P	Rate of shear production	[L^2/T^3]	m^2/s^3
Q1	1st quadrant motion (equivalent to Outward Interaction in xy)		

Q2	2nd quadrant motion (equivalent to Ejection in xy)		
Q3	3rd quadrant motion (equivalent to Inward Interaction in xy)		
Q4	4th quadrant motion (equivalent to Sweep in xy)		
R	Pipe radius	[L]	m
R	Hydraulic radius	[L]	m
R	The Rouse exponent	[ ]	
$R_b^2(a)$	Wavelet coherence	[ ]	
Re	Reynolds' number	[ ]	
R_{ij}	pressure rate-of-strain tensor	[ ]	
R	Rouse exponent	[ ]	
S	Sweep type motion (Q4)		
S	Cross-wavelet smoothing operator	[ ]	
$S(k)$	Spectral energy distribution in wave-number space	[L^3/T]	m^2/s
S_{ij}	rate of strain tensor	[ ]	
S_*	Dimensionless sediment factor	[ ]	
T	Wave period	[T]	s
T_p	Peak wave period	[T]	s
T	Time (overall)	[T]	s
$T_{ij}^{(n)}$	Tensor base	[ ]	
T_{kij}	Reynolds stress flux	[L^2/T^2]	m^2/s
U	Characteristic velocity	[L/T]	m/s
U	Three-dimensional velocity field	[L/T]	m/s
U_{orb}	Wave orbital velocity	[L/T]	m/s
$U_{orb,cw}$	Wave orbital velocity modified by non-linear wave-current interactions	[L/T]	m/s
W	Mean rotation	[L]	rd
$W_b^{XY}(a)$	Cross-spectrum of wavelet transform of signals X and Y scaled by a and translated by b	[ ]	
$X(f)$	Fourier transform of a function		
$Z_v(p)$	confidence level associated with the probability p with v degrees of freedom		
C_a	Reference sediment concentration	[M/L^3]	g/m^3
C_z	mass/ volumetric sediment concentrations at height z	[M/L^3] or [L^3/L^3]	
C_μ	2-equation eddy-viscosity model constant		
$C_{\varepsilon 1}$	Eddy viscosity model constant		
$C_{\varepsilon 2}$	Eddy viscosity model constant		

Greek symbols

Symbol	Definition	Dimension	SI unit
α	Non-dimensional scaling factor	[ ]	
α	Kolmogorov's constant	[ ]	
a_{ij}	anisotropy of Reynolds stress	[ ]	
α_n'	tensorial expansion coefficient	[ ]	
α_{sv}	attenuation coefficients pertaining to viscous dissipation due to relative motion between particles and the fluid	[ ]	
α_w	attenuation coefficient for viscous dissipation due to freshwater fluid motion under the oscillating pressure	[ ]	
β	Stoke's parameter	[ ]	
δ	Boundary layer thickness	[L]	m
δ_{ij}	Kronecker's delta	[ ]	
ε	Yalin's incipient motion statistical criterion		
ε	Rate of turbulence/shear dissipation	[L^2/T^3]	m^2/s^3
ε_s	Eddy diffusivity (sediment mixing coefficient)	[L^2/T]	m^2/s
η	the scalar invariance of strain	[ ]	
η_r	Height of a ripple (bedform)	[L]	m
θ	Relative tilt between sensor and flow	[ ]	rd
θ_{cr}	Sheilds' entrainment function	[ ]	
κ	von Kármán's constant	[ ]	
λ	Universal despiking threshold	[ ]	
λ_r	Wavelength of a ripple (bedform)	[L]	m
μ	coefficient of dynamic viscosity	[M/LT]	$Pa.s$
ν	coefficient of kinematic viscosity	[L^2/T]	m^2/s ; st
ν	Effective viscosity	[M/LT]	$Pa.s$
ν_T	Turbulent eddy viscosity (Boussinesq's turbulent coefficient)	[L^2/s]	m^2/s
ξ	Surf-similarity parameter (Irribaren Number)		
ρ	Fluid density	[M/L^3]	g/m^3
ρ_s	Sediment density	[M/L^3]	g/m^3
σ	Standard deviation		
σ	Sediment sorting		
σ_{ij}	Viscous stress tensor		
$\sigma_{u,v,w}^2$	3D wave-dominated verlocity variance		
σ_ε	Eddy viscosity model constant		
τ	Reynolds' (deviatoric) stress tensor	[$M/L.T^2$]	N/m^2
τ	Translation scale of a wavelet		
χ	Ratio between shear-normalised particle settling rate and non-dimensional grain diameter	[ ]	
ω	Angular frequency		rd/s

ω	Specific dissipation rate (per unit k)	[ ]	
Δt	Time lag	[T]	s
Π	Cole's wake factor	[ ]	
ψ ; $\psi(t)$	Mother wavelet		
$\psi_{b,a}(t)$	Daughter wavelets translated by b and dialted by a from the mother wavelet		
ψ^*	complex conjugate of ψ		
$\hat{\psi}$	Fourier transform of ψ		
Λ	Scaling factor of cone of influence	[ ]	
Ξ	Yalin's entrainment parameter	[ ]	
$\Phi^i_{\mathrm{H,j}}$	Binary criterion for data point identification in a quadrant analysis with threshold H		
ϕ ; ϕ_{cw}	Relative angle between the wave and current direction		$°$; rd
ψ	Departure from spherical spreading		
ψ ; $\psi(t)$	Mother wavelet		
$\psi_{b,a}(t)$	Daughter wavelets translated by b and dialted by a from the mother wavelet		
ψ^*	complex conjugate of ψ		
$\hat{\psi}$	Fourier transform of ψ		

Operators

$\langle\ \rangle$	Ensemble-averaged
$\overline{}$	Time averaged (mean)
$\widehat{}$	Wave-averaged
$\widehat{}$	Fourier transformed
$\sim$	Periodic component
*	Complex conjugate
$\partial\ /\ \partial$	Partial derivative
$d\ /d$	Full derivative
∇^2	Laplace operator
Φ , Φ_0, Φ_1	a function of
f, f_1, f'	a function of
§	Sections of the main text
| |	Absolute value
ln	Natural logarithm
log	Logarithm to the base 10
CO	Co-spectrum

Acronyms and abbreviations

ABS	Acoustic backscatter system
ADE	Advection-diffusion equation
ADV	Acoustic Doppler velocimetre
ASM	algebraic stress models
CFD	Computational fluid dynamics
coi	Cone of influence
CWT	Continuous wavelet transform
DNS	Direct numerical simulation
DES	Detached eddy simulation
DIA	Direct Interaction Approximation
DSM	differential second-moment (Reynolds' stress) models
EDQNM	Eddy damped quasi-normal Markovian
FFT	Fast Fourier Transform
LES	Large eddy simulation
PT	Pressure transducer
PIV	Particle image velocimetry
RANS	Reynolds averaged Navier Stokes equation
rms	Root mean squared
SIS	Sediment imaging sonar
SRPS	Sediment ripple profiling system
SSS	Sector scanning sonar
SSC	Suspended sediment concentration
TFM	Test Field models
3D	Three-dimensional
SNR	Signal-to-noise ratio
TKE	Turbulent kinetic energy
WT	Wavelet transform
XWT	Cross wavelet transform

At any moment, there exists a narrow layer between trivial and impossible where mathematical discoveries are made. Therefore, an applied problem is either solved trivially or not solved at all. It is an altogether different story if an applied problem is found to fit (or made to fit!) the new formalism interesting for a mathematician.

A.N. Kolmogorov, diary, 1943.

Chapter 1.

Introduction

> "It is not meaningful to talk about the properties of turbulent flow independently of the physical situation in which it arises… Perhaps there is no 'real turbulence problem', but a large number of turbulent flows and our problem is the self-imposed and possibly impossible task of fitting many phenomena into the Procrustean bed of a universal turbulence theory." Saffman (1978)

1.1 Prologue

Nature, with "scant regard for the desires of the mathematician" as Ames (1965) so eloquently put, is essentially non-linear – that is to say, "the mathematical models believed best to approximate her are non-linear". True to form, the flow of fluids in the natural environment from the smallest streams to the bewildering scale of the cosmos is non-linear, displaying complex, dynamic spatial structures (Goldenfeld and Kadanoff, 1999; Davidson, 2004). The evolution and deformation of these structures is associated with turbulence, and can be strongly influenced by shear and proximity to boundaries (Hinze, 1959; Davidson et al., 2013). Understanding and predicting how such flows behave remain a formidable challenge, and one of the most notorious problems in classical physics (Holmes et al., 1996; Kellay, 2011).

Simply put, turbulence refers to irregular fluid motion exhibiting random/ disordered spatial and temporal variations in flow quantities (*e.g.* velocity, pressure, temperature); and is induced by a fluid moving past a solid surface (friction-induced "wall turbulence") or past another stream of fluid, otherwise known as "free" turbulence (Hinze, 1959). Turbulence is characterised by high values of the Reynolds number (Re), a dimensionless parameter of flow representing the ratio of inertial to viscous forces, for given velocity and length scales (Reynolds, 1883; Schlichting, 1955). Turbulent flows possess an

increased ability to transfer momentum, thus exerting greater forces on rigid bodies in contact with the fluid, manifest by increased drag of wall-bounded flows (Lozano-Duran et al., 2012). Turbulence also enhances a flow's capacity to transfer heat, soluble admixtures, and suspended particles, to propagate chemical reactions (particularly combustion), and to scatter or alter sound and electromagnetic waves. Beyond its vast technological applications and importance in understanding natural phenomena, turbulence is of great interest as an example of nonlinear mechanical systems with very large numbers of degrees of freedom (Monin et al., 1971; Kaneda and Morishita, 2013). In other words, while flow conditions may be identical, they will result in largely different motions such that predicting them in full detail becomes a rather difficult challenge. Nonetheless, the ultimate quest in the study of turbulent fluid flows is to obtain a tractable quantitative theory or model which can be applied and used to calculate relevant flow quantities (Pope, 2000), be it for engineering applications, or natural sciences.

1.2 Turbulence and sediment dynamics

In coastal and estuarine settings, turbulence plays a fundamental role in bed-load and suspended sediment transport; both governed by shear stresses at the bed and within the benthic boundary layer (BBL) (Hunt, 1954; Bagnold, 1966; Soulsby, 1983; Dyer and Soulsby, 1988). Defining the physical processes which dictate the resuspension of sediments in coastal and estuarine settings is fundamental for accurate predictions of bed morphology evolution (van Rijn et al., 2007), and has profound implications for the biogeochemical processes that shape their local ecology (Thompson et al., 2011). It is also a prerequisite to quantifying erosion and deposition trends, and hence guiding engineering applications such as beach nourishment, defence schemes against erosion and flooding, maintenance of marine infrastructure and waterways, and aggregate dredging. Turbulence resides at the micro-scale (fifth order; seconds to days and up to 10's of metres or sub-grid scales) within a coastal-tract cascade system, often classified as the 'noisy end' of the spectrum of drivers of coastal morphological change (Larson and Kraus, 1995; Cowell et al., 2003). Nonetheless, it is acknowledged that the

cumulative effect of such sub-grid scale phenomena dictates the mobilisation of sediment which is eventually manifest by changes in coastal morphology; however inconvenient this may be from a modelling perspective.

Fluid flows in the coastal zone are often characterised by the simultaneous presence of both waves and currents, extending towards the bed in shallow waters and resulting in complex dynamic interactions with direct implications for sediment transport studies (Grant and Madsen, 1979). The mobilisation of sediments in the nearshore and at the shoreface is dominated by wave-induced bed shear stresses in moderate and stormy conditions (Thompson et al., 2012). The vertical structure of sediment flux components on the shoreface and in the inner surf zone, as well as the dynamics of sediment transport under shoaling waves in the nearshore, are both considered to be insufficiently understood (van Rijn et al., 2013). Moreover, where both currents and waves are present, the problem is further complicated by the different timescales between the uniform shear of the (steady) current, and the oscillating nature of the wave orbital motion (unsteady).

There is a genuine need for better, robust models of suspended sediment transport in the coastal zone (Aagaard and Jensen, 2013). A plethora of practical (engineering) and theoretical models currently exists to describe sediment suspension, designed specifically for wave-only, current-only or combined wave current flows. Such models employ differing formulations to parametrise turbulence and display large disparities in results, particularly for rippled beds. Davies et al. (2002) showed divergences up to a factor of 2 – 10 times the measured concentrations in the bottom 1 m of flow, in a host of research and practical (engineering) models covering a range of wave and current conditions, bed morphology, turbulence schemes, and fluid-sediment interaction. Earlier studies have shown that most models where waves (symmetric or asymmetric; regular or irregular, alone or superimposed on a current) do no provide a good description of the time-dependent sediment suspension, mainly due to the strong non-linearity in stress and inadequacy of employed turbulence models (Soulsby et al., 1993; Davies et al., 1997; Malarkey and Davies, 1998; 2012). Such uncertainty may have huge cost

implications when predicting, for example, the volume of beach recharge material needed in a nourishment project (Mason, T., 2016, pers. comm.). Accurate predictions of sediment transport remain limited by insufficient understanding of the hydrodynamics and physical processes the contribute to the mobilisation and suspension of bed material in the coastal zone (Aagaard and Jensen, 2013).

In a vision paper on future research needs in coastal dynamics, van Rijn et al. (2013) highlighted the pressing need for research to support such models, focusing in particular on sand transport in the shoreface (non–breaking waves), surf and swash zones; employing field and controlled laboratory experiments. This requires prioritising research with reference to coherent flow structures and the intermittent stirring of sediments by breaking and shoaling waves, and the time-history effects of suspended sediments under irregular wave conditions (*ibid.*). Understanding the spatial and temporal behaviour of sediment suspension events in relation to turbulent fluctuations, both in structural form and in temporal distribution, is an important step towards providing a more satisfactory conceptual model for describing suspended sediment transport.

1.3 Turbulence: order and chaos

Turbulence is characterised by apparently disordered and unpredictable vorticity at a multitude of scales, varying spatially and temporally in three dimensions (Hinze, 1959; Tennekes and Lumley, 1972; Davidson, 2004; Jimenez, 2012). While most of the turbulent energy resides at large scales, most of the degrees of freedom (potential independent variations) reside in the small scales, making such motions important from a practical perspective as well as the theoretical (Kaneda and Morishita, 2013). Classically, turbulence studies advocated a 'phenomenology of cascades', arguing that the enormous number of excited degrees of freedom dictates that turbulence can only be described statistically, in large ensembles under macroscopically identical external conditions (Monin et al., 1971). As such, one can only try to model the evolution of averaged flow quantities.

Nonetheless, the unrelenting scientific quest for order among chaos has shown that turbulence is also characterised by remarkably organised and sharply defined flow patterns of irregular yet repetitive nature, perceived as 'coherent', or – perhaps 'deterministic' (Kline et al., 1967; Kim et al., 1971; Offen and Kline, 1975; Hussain, 1986; Fiedler, 1988; Holmes et al., 1996; Schoppa and Hussain, 2002). Such complex motions vary in intensity, wane and wax in coherence, and interact nonlinearly with one another and with the prevailing flow and nearby boundaries (Hunt et al., 2010; Marusic et al., 2010b; Lozano-Duran et al., 2012; Davidson et al., 2013). The vast wealth of studies into the problem generally considers two main issues, the structural features of turbulence in the boundary layer, and the momentum/energy transfer mechanism resolved in both space and time; employing numerical simulations, flow visualisation and experimental measurements. The role of vortex structures is seen as pivotal, while a statistical approach is needed to deal with the irregularity of turbulent flow at all scales (Davidson et al., 2011).

1.4 Coherent flow structures and sediment dynamics

The suspension of sediment is essentially an extremely complex case of fluid-particle interaction, and a large number of studies have attempted to describe or solve this problem theoretically, experimentally and/or numerically (Zhu et al., 2013). A complete mathematical description of the problem necessitates elaborate models, accounting for both fluid–sediment and sediment–sediment interactions and these are riddled with difficulties in theoretical formulations and computational requirements, and thus, they tend to rely on empiricism (Zhang et al., 2011). Laboratory and field measurements and flow/ transport visualisation are thus often the first step towards understanding this complex problem.

The onset of movement and ensuing transport of sediments, both as bedload and in suspension, are dictated by bed (bottom) shear stress, which represents the frictional force exerted by the flow per unit area of the bed (Soulsby and Clarke, 2005). The bed shear stress depends upon the turbulence structure at the boundary, and is influenced by the presence of

bedforms and the properties of the (entrained) sediment (McLean et al., 1999; Maddux et al., 2003; Singh and Foufoula-Georgiou, 2013). Interchangeably, the mobilisation of sediment, once stress exceeds the threshold for incipient motion (cf. §3.2), may result in different bedform configurations, potentially altering the flow characteristics and stress generation/dissipation. Therefore, the dynamic and interdependent feedback between bed morphology, mobile sediments, and flow hydrodynamics need to be considered (Bagnold, 1951; Amos and Collins, 1978; Thorne and Hanes, 2002; Bolaños et al., 2012; van Rijn et al., 2013).

The role played by bed–generated coherent eddy structures in entraining and transporting sediment particles is widely acknowledged, yet the exact mechanism is still unclear (Dey et al., 2012; Ji et al., 2013). Coherent turbulence structures have been defined, albeit reluctantly, as "connected turbulent fluid masses with instantaneously phase-correlated vorticity over their spatial extent" (Hussain, 1983; 1986). In other words, turbulence is characterised by an organised component of large-scale vorticity, which is spatially coherent at any given instant, underlying the random and chaotic three-dimensional vorticity typical of turbulent flows. In that sense, a coherent structure can be identified through the intermittent transfer of momentum marked by velocity fluctuations within a 'bursting' sequence in the boundary layer (Heathershaw, 1974). The turbulent bursting process is a critical mechanism in production of turbulent kinetic energy, and refers either to violent intermittent eruptions of fluid away from the wall implying a local instability, or describes localised ejections of fluid due to the passage of vortices which persist for longer times than ejections (Robinson, 1991). These motions involve ejections of low speed near-bed fluid away from the boundary, or sweeping of faster fluids down towards the bed.

Fiedler (1988) added several criteria to the aforementioned definition, namely; composite scales, recurrent patterns (lifespan longer than the passage time of the structure), high organisation and quasi-periodic appearance. Thus, besides the "conventional" bursting events which describe the intermittent, energetic process resulting from the passage of near-wall

vortices as perceived by passive markers and/or visualisation studies (Schoppa and Hussain, 2002); one may identify vortices induced by wave breaking (Aagaard and Hughes, 2010), or by flow separation from vortex ripples upon reversal in an oscillatory flow, *i.e.* vortex entrainment/shedding (Amoudry et al., 2013). These intermittent, structural features of the flow arising near smooth and rough boundaries are directly linked to relatively organised sediment 'streaks' with corresponding scales (Grass, 1971; Grass et al., 1991; Smith, 1996). Nonetheless, no accurate mechanism has been described for the interaction between these vortical structures and the sediment, beyond the conceptual model of 'spinning-wheel' vortices scooping up sediment along the surface of rolling grain ripples put forward by Bagnold and Taylor (1946) and modelled by Hansen et al. (1994). The latter's work was restricted to a Lagrangian cloud of sediment within a discrete vortex (fluid in a cell concept), treated from a time-averaged perspective. Similarly, Williams et al. (2007) reported numerical and experimental results of sediment suspension by vortex pairs, modelled by assuming no initial interaction between independently released vortices and sediment particles. More recently, studies are focusing on the structural features of turbulence and their role in sediment entrainment (Hardy et al., 2010; Grigoriadis et al., 2013; Keylock et al., 2014). What these studies lack is often a clear resolution of the correlations between the varied temporal and spatial scales of turbulent structures, and the corresponding observed suspensions. Furthermore, almost all of these studies are restricted to current only or wave-only flows; and very little is known about the characteristics of coherent motions in combined wave-current flows (Hare et al., 2014). Even less is known about their dynamics in space and time; a major shortcoming for process-based modelling of sediment transport in the coastal zone.

1.5 Aim and Objectives

This thesis investigates the complex interactions between bed-generated coherent turbulence structures and suspended non-cohesive sediment transport in (non-breaking) wave-dominated environments and under combined wave-current flows. The overarching aim is to quantify, through

prototype-scale experimental observations, the spatial and temporal scales of coherent turbulence structures, and provide a conceptual model of entrainment and suspension of sand in wave-induced, and combined wave-current benthic boundary layers. To this end, a number of objectives are identified through the following questions:

- What structural features of flow (type of coherent motion) dominate the production of Reynolds stresses in irregular oscillatory flow over rippled beds?
- What temporal and spatial relationships govern the interaction between wave-generated boundary layer turbulence and event driven sediment suspension; to what extent these co-vary; and how do suspended particles affect vorticity dynamics under shoaling waves?
- Can we quantify the dynamics of coherent flow structures in combined flows in space and time, and how do these vary between currents aligned with and opposed to the direction of wave propagation? What implications does this have on sediment resuspension in the coastal zone?

1.6 Structure of the thesis

To address these questions, results from two prototype scale experiments are presented and discussed. Chapters 2 provides an extensive review of turbulence and boundary layer theory, coherent turbulence structures and vorticity dynamics, as well as limitations of and approaches to modelling turbulence. Chapter 3 addresses the fundamental processes governing coastal sediment transport, with focus on the role of turbulence in stress production and sediment transport. This is primarily tailored towards non-cohesive sediment dynamics (sands) under oscillatory flows over rough (rippled) beds and to combined wave-current flows. A suite of tools for analysing the temporal, spatial and spectral properties of turbulence stresses and sediment transport through acoustically measured high frequency velocity and backscatter is introduced in Chapter 4. Subsequently 5 introduces the Barrier Dynamics Experiment II, a large scale experimental project studying sandy

barrier beach dynamics under irregular waves. This chapter focuses on identification of structural features of turbulence within and outside the wave-induced benthic boundary layer, drawing on the difference between waves that cause erosion or accretion of a barrier beach. The spatial and temporal relationships between wave induced structures and sediment resuspension are also assessed, and the scale of covariance determined through wavelet and coherence analysis is investigated. Chapter 6 presents the results of another prototype scale experiment on wave current interactions conducted in the HR Wallingford Fast Flow Facility. This chapter focuses on the hydrodynamics of turbulence in the near bed region, and assesses trends, structural features, and energy spectra of Reynolds stresses to describe the spatial and temporal evolution of coherent structural features with currents aligned with, and opposing the direction of wave propagation. These are also linked to event driven sediment resuspension/transport given prevailing bed configurations. A brief discussion to summarise the above results into a conceptual model for sediment suspension by coherent structures is presented in chapter 7, together with the conclusions and limitations of the present work, and suggestions to extend the study in the future.

[This page is intentionally blank]

Chapter 2.

Turbulence and the Benthic Boundary Layer

"It remains to call attention to the chief outstanding difficulty of our subject" Lamb (1932) - *Hydrodynamics*

2.1 Turbulent Fluid Flows

2.1.1 Turbulent behaviour and flow regimes

Turbulence is the predominant and most complicated form of fluid motion (Bradshaw, 1971). Original definitions, such as that attributed to Taylor, refer to irregular motion of fluids over solid surfaces or neighbouring fluid streams (Von Kármán, 1937). However, Hinze (1959) argues that for a better definition, one must stipulate that such irregularity pertains to random variations of flow quantities with space and time coordinates, such that "statistically distinct values can be discerned". This implies that while turbulent flows are irregular and thus it is impossible to describe the motion in all details spatially and temporally; it is possible to describe the flow quantities such as velocity, pressure, temperature, *etc*., using the laws of probability, and indicate distinct average values of these. This view underpins all approaches to describing the motion of viscous fluids by averaging the equations of motion following Reynolds (1895). It also forms the basis for statistical and spectral descriptions of turbulent flows advocated by Taylor (1935; 1938) and Kolmogorov (1941a, b; 1991a, b). Collectively, such a view became known as the 'classical' school in turbulence theory, following development of alternative schools advocating structural approaches and renormalisation groups. The classical school argues that the enormous number of excited degrees of freedom can only be described statistically, in large ensembles under identical large-scale external conditions (Monin and

Yaglom, 1971). Besides irregularity, which calls for a stochastic approach in dealing with the problem rather than a deterministic one, turbulent flows are characterised by non-linearity in all three dimensions, whereby small perturbations may grow spontaneously, rendering the flow unstable (Tennekes and Lumley, 1972). These instabilities are related to complex interactions between viscosity and inertia, and the onset of turbulence is dependent upon the relative magnitudes of viscous and inertial forces.

2.1.2 Reynolds number and the transition to turbulence

The onset of turbulence is defined as the point at which viscous forces are no longer sufficient to dampen any irregularities within a moving fluid (Reynolds, 1883). The dimensionless ratio between inertial forces pertaining to the mean flow velocity, and the viscous forces pertaining to molecular interactions, is known as the Reynolds number, Re, defined by:

$$Re = \frac{U.L}{\nu} \qquad \text{(Eq. 2.1)}$$

where L is a characteristic length scale [L]; U is the characteristic velocity [L/T] pertaining to that length scale, and ν is the coefficient of kinematic viscosity [L^2/T]. Effectively, by choosing suitable velocity and length scales, critical values of Reynolds number can be used to define the transition from laminar (sinuous) to turbulent fluid motion. For instance, in conduit flows (pipes), where the concept was originally investigated by Osbourne Reynolds, an Re = 2000 – 4000 delimits the transition from laminar to turbulent flows (Reynolds, 1883). Meanwhile in open channels, replacing the characteristic length (pipe diameter) with the hydraulic radius, R, yields a transition threshold value of 500 (Chow, 1959).

When the Reynolds number of a flow exceeds its corresponding critical value, instabilities within the flow reach a disordered, chaotic state whereby fluid particles no longer follow straight streamlined trajectories as in laminar flow. As a result, the flow develops vorticity, manifest by three-dimensional eddy

structures of varying sizes. The nonlinearity within the flow also induces vortex stretching, which transfers energy over decreasing scales of motion until it reaches those small enough to be confined by the diffusive action of molecular viscosity, where energy is ultimately dissipated as heat (Tennekes and Lumley, 1972).

The transition between laminar and turbulent flow remains poorly understood since it was first described in Reynolds (1883) seminal paper. Several factors are known to influence this transition, including surface roughness, curvature of the boundary, temperature, free stream turbulence, Reynolds number, pressure gradients, and injection/suction of fluid at the boundary (Dhawan and Narasimha, 1958; Williams et al., 1969). The process is intermittent in both space and time (Korinna and Bruno, 2012), and represents an interplay between 'bunches' of flow perturbations, their transient growth, and ensuing nonlinear mixing (Gebhardt and Grossmann, 1994; Grossmann, 2000). Direct numerical simulation results of Zaki (2013) show an initial penetration of low-frequency disturbances induced by the free-stream flow into the region affected by wall friction (the boundary layer, cf. §2.2); streaks of varying scales get amplified as a consequence, then either get lifted in slow-speed streaks near the edge of the boundary layer (outer instability) or appear as near wall turbulent spots/ wave-packets (inner instability). This presupposes the existence of a steady 'base' flow upon which perturbations are superimposed, and sets out a basis for a structural description of the boundary layer; leading eventually to coherent structures educed through seemingly chaotic turbulent fluctuations within the flow.

The transition problem can also be described in relation to the conditions of optimal energy growth given initial conditions, external forcing, and internal perturbations (Schmid, 2007). This fits in neatly with a parallel switch by theoretical mathematicians to treat the problem as a dynamical system problem; namely through 'non-modal stability theory' (Obrist and Schmid, 2003; Fransson et al., 2004; Chomaz, 2005). This approach incorporates stochastic influences within the flow, and accounts for time-dependency (both short and longer terms), spatially varied configurations, and complex

underlying geometries (Schmid, 2007); and highlights the role of coherent turbulence structures extracted by statistical analysis of velocity correlations decomposed into three orthogonal planes (Manneville, 2015). Indeed, observations of coherent structures in turbulent flows in the late 1960's have shifted our view of turbulence from a purely random process to one where deterministic, structural features play an important role in defining flow behaviour (Smith, 1996). The existence of such organised vortex structures near a boundary results in regions of high and low momentum; these in turn can be directly linked to classical structural descriptions of wall-bounded flows (Venditti et al., 2013). The subsequent section provides a review of the classical structure of turbulent wall-bounded flows, then an overview of coherent turbulence structures and their role in momentum exchanges near the boundary.

2.2 The boundary layer

2.2.1 The boundary layer in canonical flows

When a real fluid (a fluid where viscous effects cannot be neglected) flows past a solid boundary (wall), it adheres to the surface such that the relative velocity between the fluid and the wall is zero. This implies that the motion is retarded in the vicinity of the wall due to frictional forces (Schlichting, 1955). A layer thus exists whereby the relative velocity profile increases with distance from zero at the wall (known as the condition of no-slip) to the full upstream velocity pertaining to the external 'frictionless' flow (one that can be essentially described as irrotational (Stokes, 1880; Lamb, 1932)). The region of flow affected by friction at the boundary is known as the boundary layer (whose thickness is denoted by δ [L]); a concept introduced by Prandtl in the 1904 as the 'transition layer' (Tani, 1977) and developed further by his students at Göttingen, including Blasius and von Kármán (Anderson Jr, 2005; Bodenschatz and Eckert, 2011). These early studies focussed on what we now call canonical flows, including flat-plate zero-pressure-gradient boundary layers, and fully developed open channel and pipe (or closed conduit) flows (Marusic and Adrian, 2013).

2.2.2 Classical scaling and boundary layer structure

The transition from zero to freestream velocity in the direction normal to the wall necessitates shearing action between fluid layers, resulting in strong shear stress at the boundary that weakens with increasing distance (Middleton and Southard, 1984). This view of the boundary layer structure is concerned with the variations of mean velocity, and as such subscribes to the classical school of turbulence theory (statistical fluid mechanics). Soulsby (1983) favours defining the boundary layer as the region where turbulent energy (cf. § 2.4.1.2) and shear stresses are non-zero, rather than using velocity profiles. Smith et al. (1991) also warn against classifying flow structure near the wall based upon the shape of the mean velocity profile rather than dynamical features of turbulence, particularly when the dynamics are essentially Lagrangian near the boundary (*i.e.* better treated through the passage of individual fluid parcels in space and time).

Whether velocity or turbulence arguments are used, the boundary layer is often viewed as comprising of two principal, partially overlapping regions, an 'inner' region (also [near] wall region) where viscosity is important, and an 'outer' one where inertia dominates (Schlichting, 1955). This is commonly referred to as classical scaling. The total, wall-normal shear stress, τ_{xz}, is the sum of the viscous stress, defined by Newton's law of viscosity, $\rho\nu.\partial\langle U\rangle/\partial z$; and the inertia-induced Reynolds stress, defined by the velocity covariance in the vertical plane $-\rho\langle u.w\rangle$ (cf. § 2.3.2):

$$\tau_{xz} = \rho\nu.\frac{\partial\langle U\rangle}{\partial z} - \rho\langle u.w\rangle \qquad (Eq.\,2.2)$$

where ρ is the fluid density [M/L^3]; ν is the kinematic viscosity [L^2/T]; U is the mean flow velocity [L/T]; u and w are the streamwise and vertical (wall-normal) components of the velocity field, respectively, and the angular brackets $\langle\ \ \rangle$ represent a time-average.

A thinner region ($z/\delta < 0.1$) in the immediate vicinity of the boundary is characterised by a large velocity gradient normal to the wall, such that while

viscosity might be small, the resulting shear stress is large given that the viscous stress, $\tau_{xz,visc}$, is directly proportional to the velocity gradient (Pope, 2000). Outside this region, turbulence dominates and the flow can be treated as essentially inviscid. Within the inner layer, a small excess of turbulent energy production over dissipation contributes to energy within the outer region (Townsend, 1951; Townsend, 1956). Townsend proposed a model whereby the interaction between these two layers occurs in two ways: (i) mean flow energy is transferred from the outer to the inner region at a rate controlled by the Reynolds stress gradient, and (ii) by vertical diffusion of energy (with both turbulent intensity ($\overline{q}^2$) and pressure (p) components) in the opposite direction (Figure 2.1).

The two regions can be subdivided into several constituent sub-layers, often based upon inner region/viscous scales of length and velocity. The velocity scale often used is the wall shear velocity (also friction/turbulent velocity), which denotes wall shear stress in velocity dimensions [L/T];

$$u_\tau = u_0^* = \sqrt{\frac{\tau_0}{\rho}} \qquad (Eq\ 2.3)$$

where $u_\tau = u_0^*$ in this particular formulation is the local friction velocity at the wall (equivalent wall shear stress in velocity units [L/T]); and $\tau_0 = \tau_w$ is the wall shear stress [M/L.T^2] at $z = 0$. Similarly, the viscous length scale is defined by:

$$\delta_v = \nu \sqrt{\frac{\rho}{\tau_0}} = \frac{\nu}{u_0^*} \qquad (Eq.\ 2.4)$$

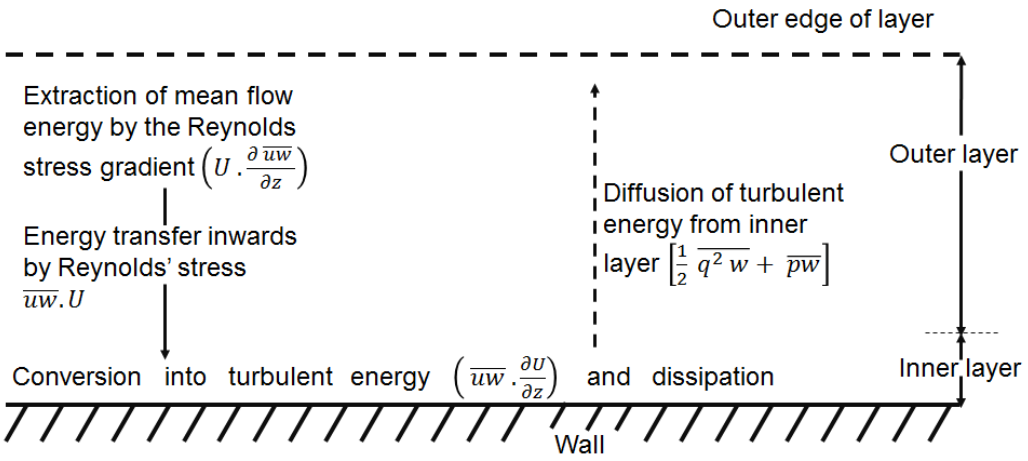

Figure 2.1 Townsend's model for energy flow between the inner and outer regions in a boundary layer (after Townsend, 1956).

The merit of this scaling is that the corresponding Reynold's number, $Re = u^*.\delta_v/\nu$ equates to unity, hence providing a clear distinction between the viscous dominated and inertia dominated regions of the flow (Figure 2.2). It follows that a friction Reynolds number (ratio of boundary length to viscous length scales) can be defined as $Re_\tau = Re^* = \delta/\delta_v$. The distance from the wall can be measured in terms of viscous lengths, otherwise known as wall units, denoted with a "+" superscript, which take the form of a local Reynolds number, thus demonstrating the relative importance of viscous and turbulent processes locally (Pope, 2000):

$$z^+ = \frac{z}{\delta_v} = \frac{u^*.z}{\nu} \qquad (Eq.2.5)$$

Similarly, this scaling is evident in the mean velocity profile at high Reynolds numbers, or the velocity gradient, which can be shown by pure dimensional analysis to be a function of z^+ and Re_τ, given $Re_\tau = \delta/\delta_v = \left({}^{z}/_{\delta_v}\right) \div \left({}^{z}/_{\delta}\right)$:

$$\frac{d\langle U\rangle}{dz} = \frac{u^*}{z}\,\Phi\left(\frac{z}{\delta_v}, \frac{z}{\delta}\right) \qquad (Eq.2.6)$$

Prandtl proposed in 1925 that as $z/\delta \to 0$; equation (2.6) tends asymptotically to a function of z/δ_v ; such that (Pope, 2000; Davidson, 2004):

$$\frac{d\langle U\rangle}{dz} = \frac{u^*}{z}.\Phi_1\left(\frac{z}{\delta_v}\right), \qquad for\frac{z}{\delta} \ll 1 \qquad (Eq.2.7)$$

Whereby the function Φ takes on a specific form, Φ_1 , close to the bed:

$$\lim_{z/\delta\to 0} \Phi\left(\frac{z}{\delta_v}, \frac{z}{\delta}\right) = \Phi_1\left(\frac{z}{\delta_v}\right) \qquad (Eq.2.8)$$

In wall units; this takes the form:

$$\frac{du^+}{dz^+} = \frac{1}{z^+}.\Phi_1(z^+) \qquad (Eq.2.9)$$

By integrating equation (Eq. 2.9) it can be shown that $u^+ = u/u^*$ is a function of only z^+ at high Reynolds numbers (beyond transitional); with plentiful experimental evidence supporting universality of this relationship in wall bounded flows, known as the Law of the Wall:

$$u^+ = f\,(z^+) \qquad (Eq.2.10)$$

Subsequently, it is rather common to delimit four constituent sublayers within the boundary layer in a flow of a given Reynolds number, classically defined as follows:

The **viscous sub-layer**: this is the layer in the direct vicinity of the wall where the viscous shear stress dominates the turbulent shear stress, and where the shear is particularly high due to the sharp vertical gradient in mean velocity. This layer is occasionally misnamed the laminar sublayer, owing to limited thickness which forces streamlines to be parallel (the original definition of sinuous motion proposed by Reynolds). However, this sublayer does experience random fluctuations in velocity, and hence it is not strictly laminar, despite the molecular diffusion dominating the turbulent flux of momentum. Nonetheless, these fluctuations, which are often parallel to the boundary, can induce significant variations in stress, with implications for the transport of scalars within the flow (Middleton and Southard, 1984). The viscous sublayer

is most commonly delimited by wall units $z^+ < 5$ and $u^+ = z^+$. However, some authors delimit the viscous sublayer by $z^+ < 11.6$ based on roughness arguments, with $z^+ < 5$ defining the extent of the 'laminar' part of it (Sleath, 1984; Paphitis and Collins, 2001).

The **buffer-layer**: just outside the viscous sub-layer, the mean velocity gradient is still rather high, yet the flow is markedly turbulent, and both viscous and turbulent shear stresses are significant. It is often delimited between $5 < z^+ < 30$, and a velocity scale that is a linear function of the length scale, $u^+ = f_1(z^+)$. High-energy small-scale turbulence is generated in this sub-layer due to the strongly sheared flow where the generation of turbulent kinetic energy (by conversion from mean-flow energy into longitudinal streaks and streamwise vortices (Jiménez, 2004)); as well as dissipation are both at their peaks, albeit dependent on the value of flow Reynolds number (Willmarth and Lu, 1972; Wei and Willmarth, 1989; Hutchins and Marusic, 2007; Hutchins et al., 2009) .

The **log-layer** (inertial sub-layer), also called the **overlap region**, often assumed to extend up to 10-20% of the full boundary thickness, is dominated by turbulent Reynolds stresses, given $z^+ \cong 0.1\ (\delta/\delta_v) = 0.1.Re \gg 1$. These exchanges of momentum work against the mean velocity gradient extracting energy from the flow and generating large-scale eddies. The velocity profile in this region follows a logarithmic distribution (hence log-layer) and the stress, as a result, is often assumed constant. The eddies, nonetheless, 'cascade' their energy down through smaller and smaller scales via vortex pairing, intensifying vorticity (Willmarth, 1975). In this layer, insignificant viscosity reduces $\Phi_1(z^+)$ to a constant value; given by:

$$\Phi_1(z^+) = \frac{1}{\kappa}, \text{ for } \frac{z}{\delta} \ll 1 \text{ and } z^+ \gg 1 \qquad (Eq.2.11)$$

This relationship can also be derived from self-similarity arguments between the local and global Reynolds numbers outside the small viscous sublayer, in

thermally neutral bounded flows at high Reynolds numbers (Barenblatt and Monin, 1979).

It follows that the mean velocity gradient can be written as:

$$\frac{du^+}{dz^+} = \frac{1}{\kappa\, z^+} \qquad (Eq.\,2.12)$$

Or by integration;

$$u^+ = \frac{1}{\kappa}\ln z^+ + B \qquad (Eq.\,2.13)$$

where B is a constant of integration, related to wall condition (*e.g.* roughness, cf §2.2.2). In fully expanded form; this becomes:

$$\frac{u_z}{u^*} = \frac{1}{\kappa}\ln\left(\frac{u^*.z}{\nu}\right) + B \qquad (Eq.\,2.14)$$

This equation is known as the logarithmic law of the velocity profile for a clear fluid near a wall (log-law), attributed to von Kármán-Prandtl. The parameter κ is the von Kármán's constant, often given the value of ~ 0.40 (Schlichting, 1955). Figure 2.2 reproduces a full representation of the law of the wall in the inner part of a smooth, turbulent boundary layer, based on measurements from a range of mean-flow Reynolds numbers and flow geometries; presented in Middleton and Southard (1984). The viscous dominated region is defined by $u^+ = z^+$; whereas the inertia dominated region is given by Equation 2.14; whereby the slope represents von Kármán's constant and the intercept, derived experimentally, is equal to 5.1 for a smooth boundary outside the viscous and buffer layers (the latter of which is not particularly evident here). For a rough boundary; the intercept is often given the value of 8.5 over granular walls (*ibid.*).

Prandtl also showed the logarithmic relationship from mixing length arguments. Prandtl introduced the concept of a mixing length, $l = \kappa.z$, denoting the average transverse distance in the region of flow over which a small fluid mass is carried by the turbulent mixing process, at a height z above

the bed (Prandtl, 1925; 1926). He argued that the difference between the original average velocity of the particle and that of the region into which it comes must be proportional to the magnitude of the velocity fluctuations (denoted by the prime $'$ symbol), involved in the lateral exchange in momentum caused by an eddy (Rouse, 1937). As such, the effective shear stress is given by:

$$\tau = \rho\,|u'|\,l.\frac{d\bar{u}}{dz} \qquad (Eq.2.15)$$

which yields $u^* = l.(du/dz)$; the integral of which, in the vertical, is the more commonly used version of the logarithmic law of the wall; given by:

$$\overline{u} = \frac{u^*}{\kappa}\ln\left(\frac{z}{z_0}\right) \qquad (Eq.2.16)$$

where z_0 is the height at which the velocity profile falls to zero for a logarithmic distribution. Yalin (1972) suggests that if the fluid were not clear, this distribution can be logarithmic only if the vertical gradient of suspended particle concentration, dC/dz = 0, such that κ < 0.4. However, there is no consensus on the matter, with experimental results supporting (*e.g.* Castro-Orgaz et al. (2012); Gust (1984)); or contradicting (*e.g.* Coleman (1981; 1986)); the view that κ depends on concentration.

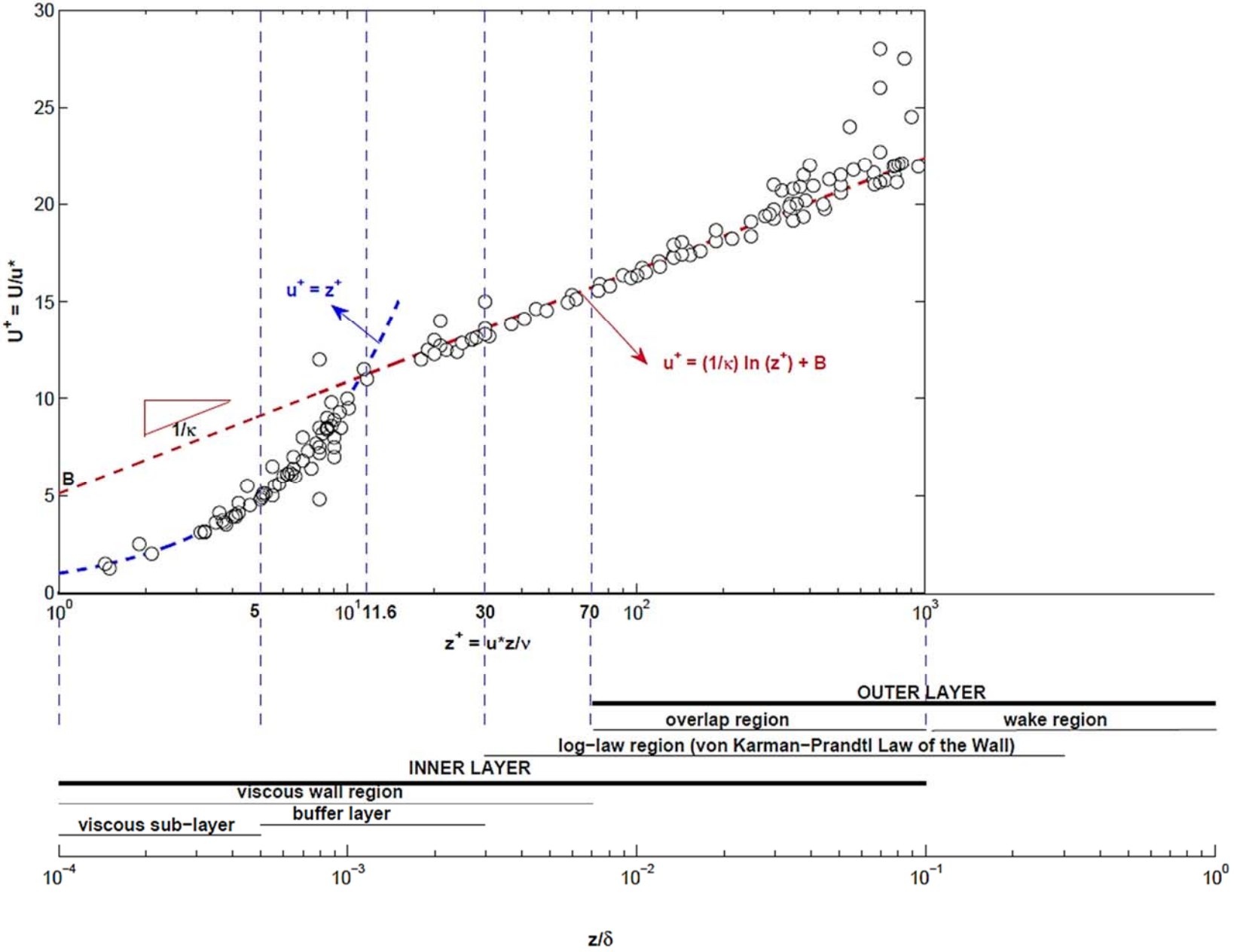
U+ = U/u*
u+ = z+
u+ = (1/κ) ln (z+) + B
1/κ
B
z+ = u*z/ν
OUTER LAYER
overlap region
wake region
log−law region (von Karman−Prandtl Law of the Wall)
INNER LAYER
viscous wall region
buffer layer
viscous sub−layer
z/δ

Figure 2.2 The law of the wall, represented as a semi-log plot of measured, dimensionless velocity, u^+, ratio of local time-averaged velocity to shear velocity, against dimensionless height above bed (z^+, wall unit) for the inner layer of a smooth turbulent boundary layer (modified from Middleton and Southard (1984). Boundary layer zones defined following Pope (2000)).

The **wake layer/core flow**: further away from the boundary, outside the log-layer, the velocity distribution no longer follows a logarithmic profile. In this region, which occupies most of the flow, viscosity is assumed to have no role in the mean relative and turbulent energy containing motions, and hence Φ tends asymptotically to a function Φ_0 of z/δ for large values of z^+:

$$\lim_{z/\delta_v \to \infty} \Phi\left(\frac{z}{\delta_v}, \frac{z}{\delta}\right) = \Phi_0\left(\frac{z}{\delta}\right) \qquad (Eq.\,2.17)$$

By substituting this relation into equation Eq. 2.6, the Velocity-Defect Law was derived by von Kármán for flow between parallel walls (von Kármán, 1930):

$$\frac{U_0 - \langle U \rangle}{u^*} = f'\left(\frac{z}{\delta}\right) \qquad (Eq.\,2.18)$$

This relationship describes the difference between the mean velocity $\langle U \rangle$ and the centre-line velocity U_0 (centre of the flow) such that the defect (normalised by u^*) is solely a function of z/δ, yet without a universal formulation. The log-law can be derived by applying both equations Eq. 2.7 and Eq. 2.12 in the overlap region at high Reynolds numbers. Yalin (1972) suggests that the universal law for velocity distribution for fully developed flow over a flat wall (zero-pressure gradient) is given by :

$$\frac{U_{max} - \langle U \rangle}{u^*} = -\frac{1}{\kappa}.\ln\left(\frac{z}{\delta}\right) \qquad (Eq.\,2.19)$$

where the velocity is maximum, $u = U_{max}$ at $z = \delta$. This expression indicates universality in the sense that the 'dimensionless velocity deficit' (left hand side) varies with dimensionless position above the wall, in the same fashion for any stage of a two-dimensional turbulent fluid flow for any geometry and roughness, independent of density, viscosity, bed shear stress and turbulent kinetic energy (in the right hand side of Equation 2.14), and is a 'good approximation' otherwise. The log-law and the defect law can also be derived by dimensional analysis (Millikan, 1939), and have been extensively supported by empirical evidence (Fernholz and Finleyt, 1996). Ludwieg and Tillmann

(1949) have shown that both the log-law and the velocity-defect law still apply to boundary layers with positive/adverse pressure gradients (Clauser, 1954), and ample experimental evidence supports these laws for smooth and rough surfaces. Clauser (1954) has demonstrated that while the velocity profile in the outer layer is nearly universal, the vertical distribution deviates more considerably in the transitions between the inner, log and outer layers. This deviation was shown by Coles (1956) to have a wake-like shape relative to the free steam, and as such, it is common practice to combine the two into Cole's law of the wake:

$$u^+ = f(z^+) + \Pi\, g\left(\frac{z}{\delta}\right) \qquad (Eq.\ 2.20)$$

where Π is Cole's wake factor (which varies with upstream distance and elevation) and g is gravitational acceleration [L/T^2]. Nonetheless, the logarithmic law of the wall (Equation 2.11), which can encompass this variation within the B parameter, still enjoys immense support as an alternative to multi-layered formulations. In fact, it is often seen as superior to alternative formulations, including 'power laws', with ample experimental evidence providing consistent and accurate description of mean flow properties (Monkewitz et al., 2008; Marusic et al., 2013).

It is rather remarkable that such complex processes can be reduced into a velocity profile that can be described by relatively simple formulae. The logarithmic law of the wall has fallen under criticism, particularly in relation to the Reynolds number influence within the wake sub-region (*e.g*. Barenblatt and Monin, 1979; Barenblatt, 1993). One of the underlying assumptions of the log-law is that the Reynolds stress profiles are independent of the Reynolds number in the inner layer (Pope, 2000) which contradicts experimental observations (Wei and Willmarth, 1989; Gad-el-Hak and Bandyopadhyay, 1994). The latter study showed that at the same z^+ near the wall, power spectra of streamwise fluctuations scaled with the inner variables over most of the energy-containing frequency range yet the vertical fluctuations did not. They attributed this primarily to increased stretching along the stream, as well

as to geometry effects from the side walls of the channel. Similarly, Wosnik et al. (2000) argue that there exists a 'mesolayer' at the bottom of the overlap layer (bounded between 30< z+ <300) where no scale separation necessarily exists between energy production and dissipation ranges while inertia dominates. This implies that both the Reynolds stress and the mean flow depend upon the Reynolds number despite the fact that the viscosity terms are negligible within the equations of motion. Fernholz and Finleyt (1996) suggest that any Reynolds number dependence is often hidden in the scatter of measurements in experimental work. Figure 2.3 illustrates, as an example, the variation of boundary layer structure (classical scaling) as a function of the Reynolds number.

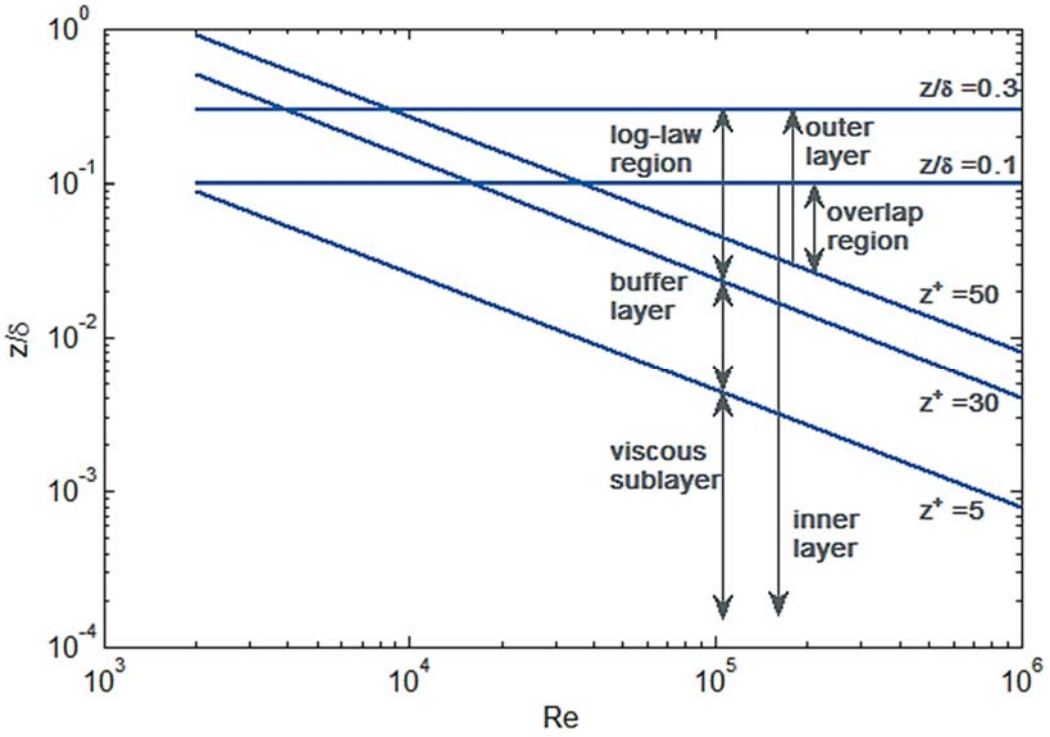

Figure 2.3 Inner and outer regions and sub-layers of the boundary layer in a turbulent channel flow, as a function of the flow Reynolds number, Re, in open channels; after Pope (2000).

2.2.3 Wall roughness and flow regimes

While most of the original boundary layer theory work assumed a smooth wall, considerable work has been dedicated to assess their applicability for flows over rough surfaces. Systematic assessment of roughness is often hindered by the difficulty arising from the potentially infinite number of geometric forms and shapes of protrusions. Schlichting (1955) postulates that for a wall of identical protrusions, for example, the drag will be a function of the density of these elements (*i.e.* number per unit area) and how they are distributed, as well as their shape and height. The review by Hopf (1923) showed that, for pipes and channels, roughness due to tightly spaced elements (*e.g.* coarse sand glued onto a pipe wall) can induce 'skin friction' that is proportional to the squared velocity (*i.e.*, independent of the Reynolds number). In this case, roughness can be expressed singularly by the term 'relative roughness', the ratio between the height of protrusion and the hydraulic radius. Conversely, roughness due to more 'gentle', scarcely distributed protrusions is a function of both the Reynolds number and relative roughness. Nikuradse (1933) represented wall roughness protrusions by cementing sand grains of defined sizes, as closely as possible, into the inner walls of circular pipes, to study resistance as a function of relative roughness and Reynolds number (Figure 2.4). He showed that the form of the velocity profile is more directly dependant on relative roughness, defined as k_s/R; where k_s is the projection (height) of the roughness element and R is the pipe radius; rather than on the Reynolds number, particularly in flows of high Reynolds number. Friction is only a function of the Reynolds number in laminar flows. By incorporating the logarithmic law of the wall (Equation 2.11) into this argument; the following equation can be written (Nikuradse, 1933; Schlichting, 1955; Yalin, 1972):

$$\frac{u}{u^*} = \frac{1}{\kappa}\ln\left(\frac{u^*.k_s}{\nu}\right) + B \qquad (Eq.\,2.21)$$

whereby u^*k_s/ν is an equivalent of the roughness element (grain) Reynolds number (Re^* *or* k_s^*), which dictates the relation between the wall roughness

elements, and the thickness of the viscous sublayer, δ_v; manifest within the integration parameter B. Therefore, three regimes of flow can be discerned, illustrated in Figures 2.4 and 2.5, as follows:

- **Hydraulically smooth**: the protrusion of the roughness elements, k_s, is small enough that they are fully contained within the viscous sublayer, δ_v. Here the friction related coefficient, B, is a function of the Reynolds number only. This region is delimited by a roughness grain Reynolds number between: $0 \leq u^*.k_s/\nu \leq 5$.
- **Transitional**: the protrusions extend outside the 'laminar' sublayer ($z^+ < 5$), yet are still partly contained within the upper limit of the viscous sublayer ($z^+ < 11.6$). In this regime, delimited by grain Reynolds number $5 \leq u^*.k_s/\nu \leq \sim 70$; the resistance is a function of both the relative roughness, and the Reynolds number.
- **Hydraulically rough (completely turbulent)**: the height of the roughness elements exceeds the thickness of the now incoherent viscous sublayer as these protrusions perturb and instigate irregularities into the buffer layer. Defined by $u^*.k_s/\nu \geq 70$, this regime is only a function of the relative roughness.

It is important, however, to note that in the above framework for describing flow over rough walls pertains to what is commonly referred to as k-type roughness, characterised by roughness geometry, namely average height and shape of protrusion, and density of distribution, as opposed to d-type (groove-like) roughness which was first noted by (Perry et al., 1969). In this case, it is common to identify an equivalent sand roughness, the k_s parameter, which represents the size of uniform sand-grains that would produce identical wall shear stress as the actual roughness under the same flow conditions (Hinze, 1959). For flow of loose boundaries (*e.g.* bed with mobile sediment); the value of k_s is often related to diameter of the largest grains of the (plane) bed, or some statistical description of the particle size distribution (*e.g.* $D_{65}, D_{50}, D_{84}, D_{90}$; where the subscript denotes the percentage of mass comprised of smaller particles in the sample) with no regard to gradation, shape or flow conditions (e.g. Einstein and El-Samni, 1949; Engelund and Hansen, 1967; Ackers and

White, 1973; Sleath, 1984; Nielsen, 1992). van Rijn (1982) reviewed a number of these relationships and showed a variability of about 1-10 D_{90} that is independent of the sediment transport stage for mobile plane beds. He also demonstrated a dependency on bedform height and steepness where mobile bedforms were present, and numerous alternative empirical equations are present in the literature and used.

In the k-type roughness, the skin friction has a direct effect on the mean flow velocity and at high Reynolds number, once the smallest eddies shed by the protrusions are of comparable size, the viscous effects are no longer enough to supress these perturbations (Allen et al., 2007). The effect of wall roughness is thus expressed as a vertical shift in the mean velocity distribution for a smooth wall, with this shift dependent on the type and magnitude of the roughness (hence hydraulic roughness, z_0). For large values, the flow becomes fully rough, and the friction is independent of the Reynolds number; with 'form drag' on the roughness elements being a principle mechanism of friction, and the wall shear stress can be described as a quadratic function of velocity (Sternberg, 1968; Yalin, 1972; Allen et al., 2007). Bradshaw (2000) thus raises the challenging point of whether a critical roughness height or a Reynolds number exist to denote the onset of roughness effects in a flow, suggesting that Nikuradse's work is a very special case where roughness was uniform and Reynolds numbers within the transitional regime. On the other hand, the poorly-understood d-type roughness is characterised by indentations and grooves at the wall, the studies of which, while limited in scope, indicate the possibility of perturbing the buffer layer without affecting the outer flow (Jiménez, 2004).

Another 'conceptual' form of roughness is given by the parameter z_0 in the logarithmic law of the wall (Equation 2.16), which denotes the height at which the velocity profile is zero for a logarithmic distribution. This term is often referred to as the hydrodynamic bed roughness, and represents the bulk influence of the physical roughness elements on the mean flow. The value of z_0 often falls within the viscous sublayer where technically the flow velocity distribution deviates from the log-law description. It is often assumed that the hydrodynamic roughness is directly proportional to the physical roughness

height in fully rough flow, or the equivalent sand-grain in densely-packed uniform elements (Middleton and Southard, 1984). The two are often related such that $z_0 = k_s/30$, based on the work of Nikuradse (1933); and this relation is commonly used for the derivation of (time-varying) bed shear stress (Soulsby, 1997). Heathershaw (1981) collated various authors' measurements of z_0 based on the logarithmic profile for different seabed bottom types in the field, and this was extended by Soulsby (1983). They found that mixtures of grain sizes have relatively small values of z_0, albeit highly varied, as the finer grains tend to fill in the spaces between the coarser roughness elements. Where ripples are present, the value of z_0 is higher than a comparable flat bed due to form drag (pressure field effect over the bed geometry), extending to heights that even exceed the ripple wavelength. A further complexity arises when sediment is mobilised into suspension affecting the velocity profile and hence the value of z_0 derived from field measurements (Smith and McLean, 1977; Dyer, 1980). Finally, where the roughness elements are large obstacles (*e.g.* a vegetation canopy), the corresponding displacement in the velocity profile is distinguished from the hydrodynamic roughness as a 'zero-displacement height', d, equivalent to the level that would be obtained by flattening the roughness elements into a smooth surface (Schlichting, 1936; Pasquill, 1950; Takeda, 1966; Jackson, 1981):

$$\frac{\overline{u}}{u^*} = \frac{1}{\kappa}\ln\left(\frac{z-d}{z_0}\right) \qquad (Eq.\,2.21)$$

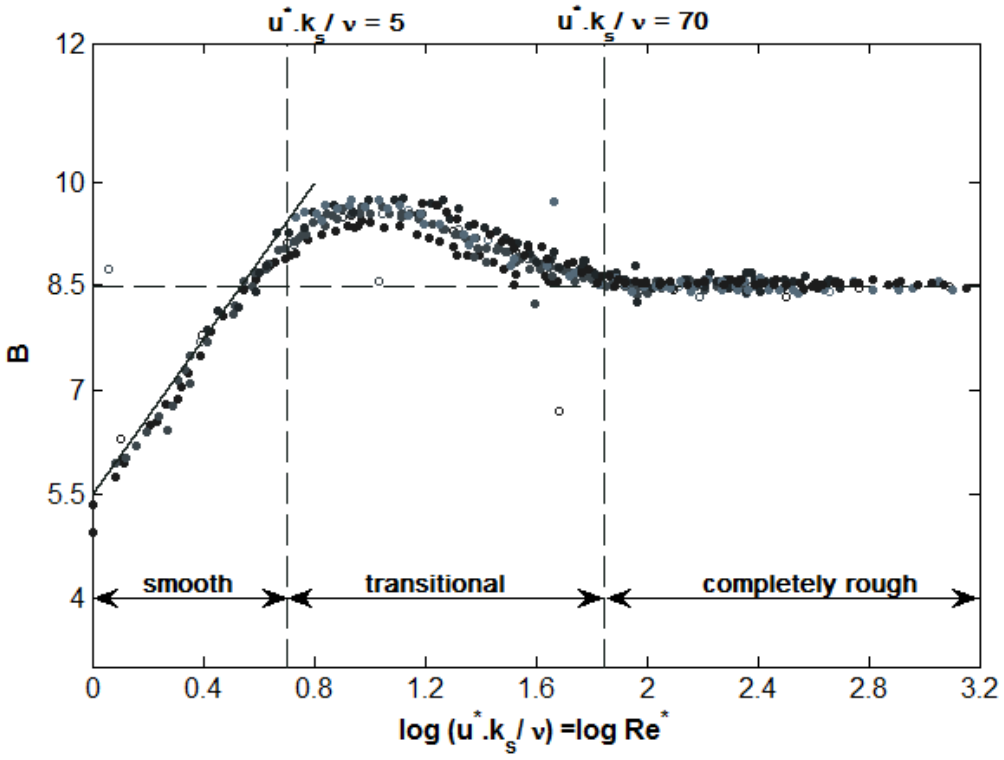

Figure 2.4 Variation of integration constant B with roughness Reynolds number Re^* for hydraulically smooth and rough walls; after Nikuradse (1933).

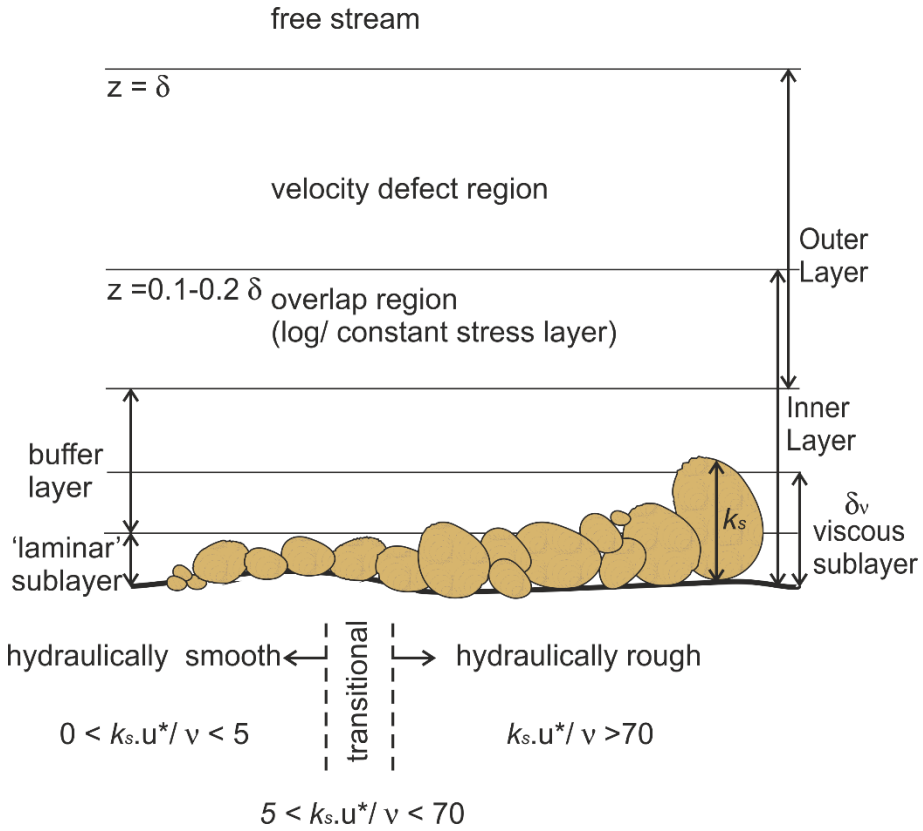

Figure 2.5 Schematic representation (not to scale) of smooth and rough boundary conditions and wall roughness height; after Tomlinson (1993).

2.2.4 Unsteady boundary layers in oscillatory and combined flows

So far, the discussion of boundary layers has been restricted to those where the flow is steady, resulting in uniform, time-invariant shear across the wall boundary layer. Oscillatory turbulent boundary layers, such as those encountered in offshore and coastal environments due to surface gravity waves, differ from classical layers described above in that they are unsteady. The main issue to contend with when dealing with oscillatory or combined flows in the coastal zone is the different time scales between what is essentially a steady, slowly-varying current (tidal or density driven); and the unsteady oscillatory motion of waves (Grant and Madsen, 1979). With steady currents (uniform shear), it is common to assume that a fully developed boundary layer occupies most of the depth of flow (*e.g.* in a tidal setting); whereas the short time scales of orbital motion imply an oscillatory boundary layer confined to the vicinity of the wall (or sea bed). Hence, oscillatory flows are characterised by a very thin layer of high shear near the bed, outside of which the flow can often be considered as potential flow (irrotational velocity field) for non-breaking waves, where various wave theories can be applied (Svendsen, 2006).

The structure of the wave boundary layer, where the velocity profile is also directly linked to friction at the bed, differs from uniformly sheared flow due to phase differences between the bed stress and ambient velocity (Kajuira, 1968). A further level of complexity arises from the variety of wave theories available to describe the wave-induced flow outside the boundary layer, as well as wave transformations, asymmetry, and non-linear interactions leading to wave-induced currents, including boundary layer streaming and return flows (Longuet-Higgins, 1953; Svendsen, 2006). This is particularly important as water waves in the environment tend to fall along a spectrum of superimposed waves at various stages of generation, propagation and dissipation. As such, most wave theories are often simplifications of reality; and founded upon a number of assumptions including homogeneous and incompressible fluid (water) that is inviscid and lacks surface tension; flowing in an essentially 2D, quiescent (purely oscillatory) fashion of constant form over a horizontal and impermeable seabed (Tomlinson, 1993).

In simplest terms, assuming the (incompressible) flow varies in a sinusoidal fashion parallel to a plane wall, (*i.e.* first order approximation or Airy waves with zero net flow within a single wave period, T), then the ambient velocity varies in time, t, and may be described as follows:

$$U_t = U_\infty . \sin(\omega t) \qquad (Eq. 2.22)$$

where $\omega = 2\pi/T$ is the angular frequency, and U_∞ is the amplitude of the free stream (ambient) oscillation velocity derived from a chosen wave theory outside the boundary layer (Justesen, 1988). The amplitude of the local velocity oscillates around the free stream; implying that the velocity defect is akin to a dampened wave that propagates away from the boundary (Nielsen, 1992). The wave-induced boundary layer thickness, δ_w, is defined by Jonsson (1966b) as the distance from the wall over which velocities deviate significantly from the maximum free-stream. Flows within this boundary depend upon the ambient velocity, the wave orbital amplitude (semi-orbital excursion, $A_w = U_\infty/\omega$), the (Nikuradse-equivalent) wall roughness, k_s ; and, for low Reynolds numbers; the fluid viscosity in the viscous sub-layer (Svendsen, 2006). Thus, several characteristic Reynolds numbers in oscillatory flows can be defined, depending on the chosen length scale (Justesen, 1988): (a) a wave-induced freestream (amplitude) Reynolds number, Re_w; (b) a wave-induced boundary layer thickness Reynolds number, $Re_{w,\delta}$, and (c) a wave roughness Reynolds number, Re_{w,k_s}:

$$Re_w = \frac{U_\infty . A_{w,\delta}}{\nu} \qquad (Eq. 2.23)$$

$$Re_{w,\delta} = \frac{U_\infty . \delta}{\nu} \qquad (Eq. 2.24)$$

$$Re_{w,k_s} = \frac{U_\infty k_s}{\nu} \qquad (Eq. 2.25)$$

For low Reynolds numbers, flow over a rough boundary can be laminar, following its outline or relief. In this case, the thickness of the laminar oscillatory boundary layer, δ_w, is proportional to $1/\beta$ where $\beta = \sqrt{\omega/2\,\nu}$ is known as Stoke's parameter (Justesen, 1988). The thickness of the boundary layer is considered maximum in phase with the maximum ambient horizontal velocity. As the roughness and/or maximum orbital velocity increase(s), the wave-induced boundary layer becomes thinner, and the associated Reynolds number increases until a critical stage whereupon the flow separates behind individual roughness elements into vortices ejected into the flow at half cycles (Sleath, 1984). This, while not strictly turbulence, is true for both smooth and rough beds, and is often viewed as the start of transitional flow for practical reasons, although there is no consensus on this definition due to the range of different experimental approaches employed (*ibid.*). The majority of such laboratory studies are concerned with the dynamics of sediment transport, either using oscillating beds or oscillating fluid over a stationary bed. Nonetheless, a more quantitative definition for the onset of fully developed turbulence has been suggested whereby the horizontal and vertical turbulence intensities reach a fixed proportion (80 - 90%) of their fully developed values, independent of the Reynolds number (Sleath, 1988). As such, by equating the equivalent grain roughness to the median grain diameter, $k_s = D_{50}$, Sleath suggests an empirical threshold for transition in coarse-grained sediments given by:

$$Re_{w,k_s=D_{50}} = 5770.\left(\frac{A_{w,0}}{D_{50}}\right)^{0.45} \qquad (Eq.\,2.26)$$

Jonsson (1966b) introduced the wave friction factor, f_w, to link the wall shear stress to the free stream velocity; such that:

$$\tau_{o,w} = \frac{1}{2}\,\rho\, f_w\, U_\infty^2 \qquad (Eq.\,2.27)$$

where $\tau_{o,w}$ is the maximum value of time-varying bed shear stress. Similar to canonical flows presented earlier, the friction factor is solely dependent on the boundary layer Reynolds number in laminar flows; otherwise, three flow regimes can be discerned:(i) hydraulically smooth roughness regime, where relative roughness is buried within the viscous sublayer, (ii) transitional; and (iii) rough turbulent flow where the friction factor is solely a function of the relative roughness at the bed, defined as A_w/k_s . In laminar flows, the wave friction factor can be determined analytically; as a function of the wave-induced freestream Reynolds number (Nielsen, 1992):

$$f_w = \frac{2}{\sqrt{Re_w}} \qquad (Eq.\ 2.28)$$

Conversely, for fully turbulent rough flows, a considerable number of empirical relationships attempt to describe the wave friction factor as a function of the relative roughness, some of which are summarised in Table 2.1.

In combined wave-current flows, the contributions of the uniform shear due to steady current, and time-varying shear due to the oscillating flow interact in a complex, non-linear fashion (Grant and Madsen, 1986). Bijker (1966) proposed that the waves and current induced stresses could be considered independently averaged over a single wave cycle, then added, demonstrating that the waves increase the shear stress compared to a steady current. In fact, the bed shear stress under combined flows is often enhanced beyond the simple summation of wave-only and current-only stresses (Soulsby, 1997). Studies of combined flows often resort to assuming, questionably, that the steady current does not vary with height above the bed; and, even more problematically, that the combined wave-current friction factor is constant in time (Sleath, 1984).

Table 2.2 Some empirical formulations of wave friction factor for fully rough turbulent flow.

Jonsson (1966b): $f_w = 0.04\left(\frac{A_w}{k_s}\right)$ for $\left(\frac{A_w}{k_s}\right) > 50;\ k_s = 2.5\ D_{50}$	$(Eq. 2.29)$
Swart (1974): $\ln\ f_w = -5.977 + 5.213\ \left(\frac{A_w}{k_s}\right)^{-0.194}$ for all $\left(\frac{A_w}{k_s}\right)$	$(Eq. 2.30)$
Kamphuis (1975): $f_w = 0.4\ \left(\frac{A_w}{k_s}\right)^{-0.75}$ for $\left(\frac{A_w}{k_s}\right) < 50$	$(Eq. 2.31)$
Vongvisessomjai (1985): $f_w = 0.287\ \left(\frac{A_w}{k_s}\right)^{-2/3}$ for $\left(\frac{A_w}{k_s}\right) > 1$; oscillating fluid $f_w = 0.082\ \left(\frac{A_w}{k_s}\right)^{-1/2}$ for all values of $\left(\frac{A_w}{k_s}\right)$; oscillating bed	$(Eq. 2.32)$ $(Eq. 2.33)$
Nielsen (1992): $f_w = \exp\left[5.5\left(\frac{k_s}{A_w}\right)^{0.2} - 6.3\right];\ k_s = D_{90}$	$(Eq. 2.34)$
Soulsby (1997): $f_w = 1.39\ \left(\frac{A_w}{z_0}\right)^{-0.52}$; where $z_0 = \frac{k_s}{30}$; for all $\left(\frac{A_w}{k_s}\right)$	$(Eq. 2.35)$

A rough approximation for the combined wave current friction factor, $f_{c,w}$, defined in terms of the wave-only, f_w , and current only, f_c , friction factors was suggested by Jonsson (1966a); given by:

$$f_{c,w} = \frac{U_\infty\ f_w + \overline{U} f_c}{U_\infty + \overline{U}} \qquad (Eq. 2.36)$$

where $f_c = \ 2\ \tau_0/\rho\ \overline{U}^2$; $\overline{U}$ is the steady current, and U_∞ the wave-induced freestream velocity. Grant and Madsen (1979) defined the combined wave-current friction factor, $f_{c,w}$, in terms of the combined wave-current shear velocity , u^*_{cw}, using the maximum near-bottom wave orbital velocity derived from linear wave theory, $u_{0,max}$; and the mean steady current above the bed, $\overline{U}$; accounting for the relative angle between the wave and current direction, ϕ_c:

$$|u^*_{cw}| = \left(\frac{1}{2}\ f_{c,w}\ \alpha\ \right)^2 . |\overline{U}| \qquad (Eq. 2.37)$$

whereby $u_{cw}^{*} = \sqrt{\frac{|\tau_c + \tau_{w,max}|}{\rho}}$; and $(Eq. 2.38)$

$$\alpha = 1 + \left(\frac{|\overline{U}|}{|\overline{u_{0,max}}|}\right)^2 + 2\left(\frac{|\overline{U}|}{|u_{0,max}|}\right)\cos\phi_c \quad (Eq. 2.39)$$

Kemp and Simons (1982) attempted to assess the discrepancy between measured combined stresses and those predicted by linear superposition for flows over smooth and rough boundaries. Their measurements were taken within the viscous-dominated wave boundary layer near the bed, and the logarithmic layer in the turbulent flow at regular phases of the wave cycle. They showed that the current boundary layer is often reduced in thickness due to the superimposed waves for both rough and smooth walls; and that the maximum bed shear stress within the wave dominated part was twice that measured in the log-layer. They also showed that the addition of the individual wave and current stresses linearly only varied by around 10-20% from the measured combined stress within the viscous dominated region of the flow. Soulsby et al. (1993) compared a number of wave-current interaction models; showing variations of up to 30% in the estimated maximum bed shear stress (Figure 2.6). Most such models, developed for rough beds, require iterative solutions or numerical discretisation, making them excessively time-consuming. Explicit algebraic models, such as Antunes Do Carmo et al. (2003) and Soulsby and Clarke (2005), developed for smooth beds, and with differing amounts of non-linearlity (Malarkey and Davies, 2012) have shown close agreement with experimental data, and variations of the order of 20% when extended to rough beds. All such models, however, attempt to describe the turbulent stresses in a statistical sense, resulting in time-averaged mean and maximum estimates, with no account for the instantaneous exchanges of momentum, while visualisation studies show that stress varies intermittently both in space, across a wave phase and through time series (Carstensen et al., 2010; Sumer et al., 2010); thus leaning towards a structural description of boundary layers focussing on coherent turbulent structures within the flow.

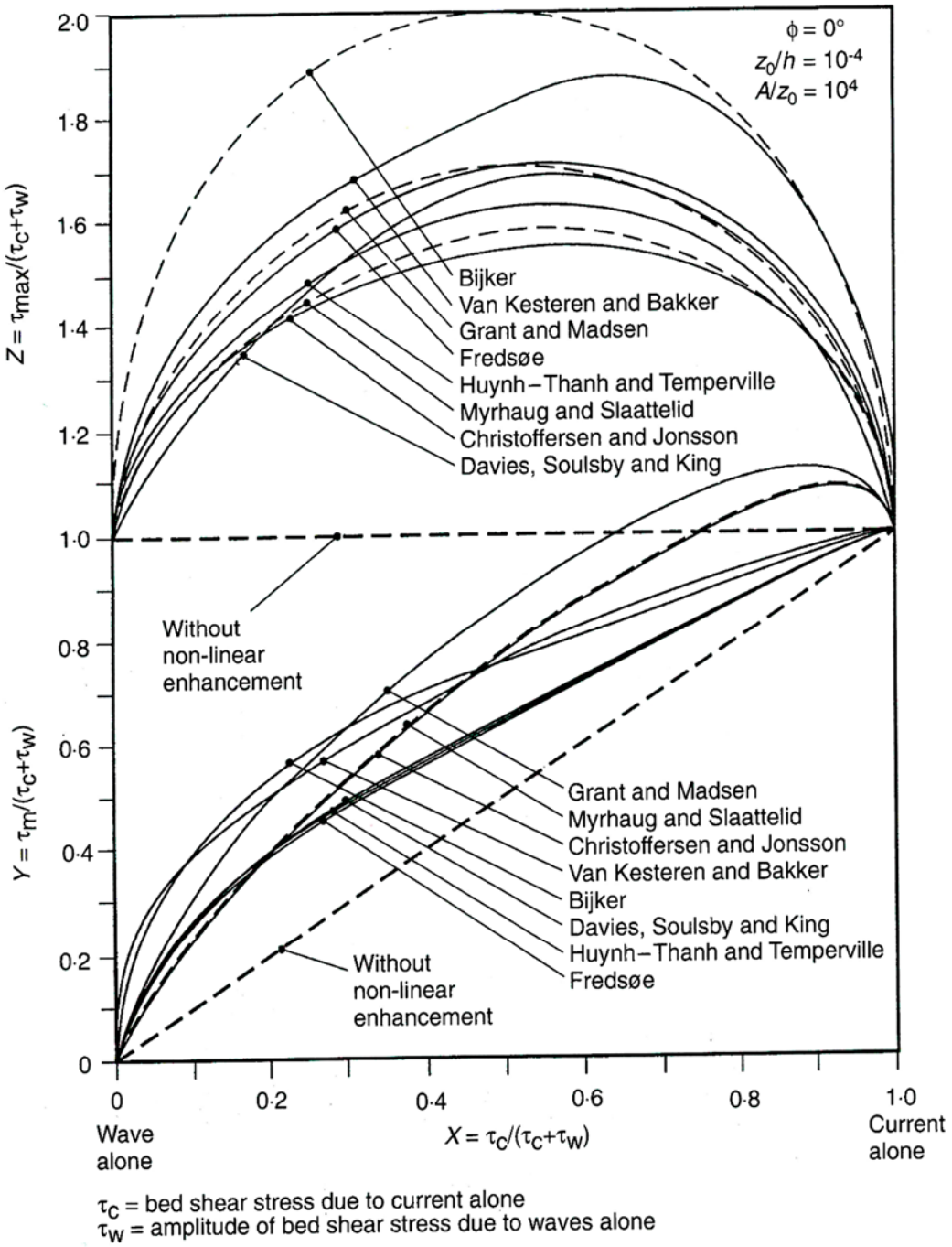

Figure 2.6 Comparison by Soulsby et al. (1993) of eight models for estimating mean and maximum bed shear stress for combined wave and current flows (after Soulsby, 1997). The models listed are: (Bijker (1966); Fredsøe (1984); van Kesteren and Bakker (1984); Christoffersen and Jonsson (1985); Davies et al. (1988); Myrhaug and Slaattelid (1989); Huyng-Thanh and Temperville (1990)). τ_m is mean bed shear stress over the wave cycle; τ_{max} is the maximum value of bed shear stress during the wave cycle.

2.3 Modelling Turbulence

2.3.1 The Reynolds averaged Navier-Stokes equations

The transfer of momentum by the fluctuating velocity field in turbulent fluid flows gives rise to Reynolds stresses (Novak et al., 2010), often modelled with eddy viscosity in a similar way the momentum transfer by molecular diffusion is modelled with molecular viscosity (Kundu et al., 2008). These Reynolds stresses involve interactions between large-scale structures of turbulence and small-scale eddies, and modellers would choose to avoid the expense of computing these sub-grid small-scale motions where possible (Gunzburger et al., 2010).

It is generally accepted that the Navier-Stokes equations (NSE) contain a full description of turbulence in viscous incompressible flows (Antunes do Carmo, 2012). In fact, it has been recently argued that they do provide an increasingly good approximation, together with the continuum assumption, over an increasing range of turbulence spatial scales associated with higher Reynolds numbers (Moser, 2006). By decomposing the velocity (U_i) and pressure (P) fields into their mean ($\overline{U_i}$, $\overline{P}$) and the fluctuating components (u_i', p) about that mean, the Reynolds-averaged Navier-Stokes (RANS) equations are obtained from conservation laws of mass and momentum (Pope, 2000).

$$\frac{DU_i}{Dt} = -\frac{1}{\rho}\nabla p + \nu\nabla^2 U \qquad (Eq.\,2.40)$$

where, the pressure $p = P + \rho g z$; ν is kinematic viscosity, and ∇^2 is the Laplace operator; ρ is fluid density, g is gravitational acceleration, and z is vertical coordinate. Where combined wave-current flows are involved, the velocity field (in each dimension) is often decomposed into steady ($\overline{u}$, $\overline{v}$, $\overline{w}$), random (u', v', w') and periodic components ($\tilde{u}, \tilde{v}, \tilde{w}$).

In tensor form, RANS equations can be written as (Gatski and Rumsey, 2002):

$$\frac{DU_i}{Dt} = -\frac{1}{\rho}\frac{\partial P}{\partial x_i} + \frac{\partial \sigma_{ij}}{\partial x_j} - \frac{\partial \tau_{ij}}{\partial x_j} \qquad (Eq.\,2.41)$$

where τ_{ij} is the (deviatoric) Reynolds stress tensor, defined as:

$$\tau_{ij} = -P\delta_{ij} + \mu\left(\frac{\partial U_i}{\partial x_j} + \frac{\partial U_j}{\partial x_i}\right) \qquad (Eq.\,2.42)$$

with, δ_{ij} being Kronecker delta, μ the coefficient of dynamic viscosity, and σ_{ij} is the viscous stress tensor, which, for an incompressible Newtonian fluid, is given by:

$$\sigma_{ij} = 2\nu_T S_{ij} \qquad (Eq.\,2.43)$$

where, ν_T is (turbulent) eddy viscosity, and S_{ij} is rate of strain tensor;

$$S_{ij} = \frac{1}{2}\left(\frac{\partial U_i}{\partial x_j} + \frac{\partial U_j}{\partial x_i}\right) \qquad (Eq.\,2.44)$$

2.3.2 Reynolds stresses and eddy viscosity

By applying the aforementioned Reynolds decomposition;

$$U_i = \overline{u_i} + u_i' + \widetilde{u_i} \qquad (Eq.\,2.45)$$

and taking the mean of the momentum equation above, the Reynolds equations can be written as:

$$\frac{\bar{D}U_j}{\bar{D}t} = \nu\nabla^2 \bar{U_j} - \frac{\partial\left(\overline{u_i u_j}\right)}{\partial x_i} - \frac{1}{\rho}\frac{\partial \bar{P}}{\partial x_j} \qquad (Eq.\,2.45)$$

This can be rewritten as the general form of the momentum conservation equation:

$$\frac{\bar{D}U_j}{\bar{D}t} = \frac{\partial}{\partial x_i}\left[\mu\left(\frac{\partial \bar{U}_\iota}{\partial x_j} + \frac{\partial \bar{U}_J}{\partial x_i}\right) - \bar{P}\,\delta_{ij} - \rho\overline{u_\iota\, u_J}\right] \qquad (Eq.\,2.45)$$

The terms within the square brackets represent the viscous stress; the isotropic stress $-\bar{P}\,\delta_{ij}$ from the mean pressure field; and the apparent stress arising from the fluctuating velocity field, $-\rho\overline{u_\iota\, u_j}$, respectively. The non-linear term in the above equation (*i.e.*, the velocity covariance or second moment) is referred to as the Reynolds stress $\left(\tau_{ij} = -\rho\overline{u_\iota\, u_j}\right)$.

The three components of the Reynolds equations and the continuity equation are needed to describe a general three-dimensional flow. However, these four equations contain more than 4 unknowns (velocity field, U, in 3 dimensions, and pressure, P; in addition to the Reynolds stresses), hence forming an unclosed system (Pope, 2000). The infamous turbulence closure problem seeks to solve this by determining the Reynolds stresses. Ironically, this is a simple, deterministic unclosed equation governing the flow field, which behaves randomly yet appears to have well-behaved and reproducible statistical properties (Davidson, 2004).

Perhaps the earliest attempt at closing the RANS equations, and the most widely used closure since then, was that presented by Joseph Boussinesq to the French Academy of Sciences in 1872 and reported later in 1877 (Boussinesq, 1877). For turbulent flows, Boussinesq proposed, intuitively through a temporal average of the transport equations, that the tensor, we now call Reynolds stresses, of the components of the 'mean actions exerted through fixed planes' on an element of fluid could be approximated as proportional to the element's deformation rate, analogous to molecular momentum transfer (Schmitt, 2007; De Lemos, 2012). According to this hypothesis, the so-called turbulent-viscosity hypothesis or Boussinesq approximation, a coefficient of viscosity which depends mainly on the mean agitation produced. Therefore, Reynolds stresses can be defined as:

$$\overline{u_\iota\, u_j} = \frac{2}{3}k\,\delta_{ij} - \nu_T\left(\frac{\partial \bar{U}_\iota}{\partial x_j} + \frac{\partial \bar{U}_J}{\partial x_i}\right) \qquad (Eq.\,2.46)$$

where k is the kinetic energy (it follows that, in equation 2.42; $P = \frac{2}{3}k$, through a Taylor's series expansion of the mean actions exerted, akin to kinetic theory).

For simple shear flows, this equation reduces to (Tennekes and Lumley, 1972):

$$\overline{u_\iota u_J} = -\nu_T \cdot \frac{\partial \overline{U}}{\partial y} \qquad (Eq. 2.47)$$

An intrinsic assumption in the definition given by Boussinesq is that the anisotropy of Reynolds stress, a_{ij}, is defined by the mean velocity gradient, $\frac{\partial \overline{U_i}}{\partial x_j}$.

$$a_{ij} = \overline{u_\iota u_J} - \frac{2}{3}k\,\delta_{ij} = -\nu_T \left(\frac{\partial \overline{U}_\iota}{\partial x_j} + \frac{\partial \overline{U}_J}{\partial x_i}\right) \qquad (Eq. 2.48)$$

That is equivalent to

$$a_{ij} = -2\nu_T \overline{S_{\iota J}} \qquad (Eq. 2.49)$$

This, obviously, is the analogy to the relationship of viscous stress in a Newtonian fluid; the Reynolds stress anisotropy is determined by the mean rate of strain locally. Although this intrinsic assumption has been proven incorrect by some laboratory work (*e.g.* in rapid axisymmetric contractions where turbulence is subjected to rapid distortions (Sreenivasan and Narasimha, 1978; Lee, 1989)); there is a multitude of flows where it is more reasonable. In mixing layers, round jets, channel flows, and the boundary layer, turbulence characteristics and mean velocity gradients change relatively slowly (after the mean flow). It follows that the local mean velocity gradients characterise the history of mean distortion in these simple turbulent shear flows (Pope, 2000). Hence, the balance of Reynolds stress is dominated by local processes such as production and dissipation of kinetic energy, and pressure-rate of strain tensor, and thus equation (2.47) becomes more reasonable. Similarly, it can be argued from timescale and level-of-anisotropy perspective, that the specific assumption that the Reynolds stress anisotropy is linearly

related to the mean rate-of-strain tensor via the eddy viscosity holds true for simple shear flows (*ibid.*).

Therefore, if Boussinesq's approximation were to be accepted as a valid hypothesis, then the problem becomes that of specifying the eddy viscosity term in the RANS equations. This is reasonable, as explained above, for a variety of simple shear flows which are important in nature and a number of engineering applications. A plethora of formulations have been proposed for linear eddy viscosity, ranging from "simple" algebraic to complex differential models, as well as non-linear models which do not necessarily conform to the Boussinesq approximation. Within such framework, a hierarchy of closure schemes exist, ranging from zero-equation algebraic models to half-equation, one- and two-equation models, and a good yet concise review of these is given in Gatski and Rumsey (2002). A brief review of closure schemes is presented in Appendix 1.

Despite the important achievements in mathematical modelling of turbulence, and the practical utility of such models, there remains a variety of issues yet to be resolved, simply due to lack of understanding of the underlying physics and the need to employ far more complicated formulations and numerical schemes (Hanjalić, 1994). Complicating factors include, but are not restricted to, three-dimensionality of the velocity field, its time dependence and randomness, unsteadiness and periodicity, multiplicity of time and length scales which is directly dependent on the Reynolds number and boundary geometry, straining of eddies (Kolmogorov's kinetic energy cascade, cf. §2.4.1.2), viscosity in wall proximity, nonlinearity and non-locality of the convective term and more so in the pressure-gradient term, as well as other specific issues such as flow separation and reversal, buoyancy and rotation, *etc.* (Rogallo and Moin, 1984; Hanjalić, 1994; Pope, 2000; Coleman and Sandberg, 2010).

The challenge presented by the turbulent closure problem is such that Rotta expressly warned "a really universal turbulence model is a dream and will be a dream possibly for ever" (Rotta, 1986); while Bradshaw famously noted that turbulence was "probably the invention of the Devil on the seventh day of

creation (when the Good Lord wasn't looking)" in his article titled: The chief outstanding difficulty of our subject (Bradshaw, 1994). Progress in experimental study of turbulence has proven to be less difficult, however, and numerical simulations have proven a valuable means of providing insight into the problem. In simulating turbulent flows, the time-dependent velocity field (representing approximately the velocity field $U(x,t)$, is solved for; as opposed to solving for some mean quantity such as $\langle U \rangle$; $\langle u_i u_j \rangle$ or diffusivity. The common approaches include Large Eddy Simulation (LES), Direct Numerical Simulation (DNS), and more recently, Detached Eddy Simulation (DES). In the meantime, experimental and visualisation techniques are employed to study turbulent flows, particularly at scales not currently feasibly attainable through numerical modelling, including high-Reynolds numbers flows typical of natural processes such as geophysical and environmental flow over rough and loose boundaries.

2.4 Coherent turbulence structures in the benthic boundary layer

2.4.1 Order and chaos in the turbulent boundary layer

2.4.1.1 Scaling from a momentum perspective

Designating a multi-layered structure to the boundary layer, for both steady and unsteady flows over smooth or rough walls, has so far been concerned with the behaviour of the mean velocity profile, following the classical scaling approach employed traditionally. Nonetheless, the limits for each of the sublayers identified, the viscous, buffer, logarithmic and wake layers, are not universally defined. Wei et al. (2005) have presented an alternative four layer structure for canonical flows by assessing the changing balance of the mean momentum equations governing the mean velocity through advection and gradients in viscous and Reynolds shear stresses (cf. section §2.3). They identified a thin sublayer, defined for $0 \leq z^+ \leq 3$; where pressure/advection and viscous forces dominate the momentum balance equation. This is overlain by a Reynolds number dependent region whereby the viscous and Reynolds stress gradients balance out as they are of nearly equal magnitudes yet

opposing signs (hence, the 'stress gradient balance' layer). This region, ranging between $3 \leq z^+ \leq 1.6\sqrt{\delta^+}$; extends to the traditional logarithmic layer in classical scaling (based on mean velocity profile). The third sublayer is a 'meso viscous/advection balance' layer whereby viscous forces balance out with the advective force or pressure forces in zero-pressure boundary layers, or channel flows, respectively. The gradient of the Reynolds stress passes through zero at the centre of this meso-layer, which encompasses flow between $1.6\sqrt{\delta^+} < z^+ < 2.6\sqrt{\delta^+}$. Finally, the fourth layer is an 'inertial/advection balance' layer with negligible viscous effects (*ibid.*).

2.4.1.2 Statistical turbulence and order among chaos

The above scaling raises an interesting alternative view for the boundary layer structure, based upon momentum exchanges within the flow. As mentioned in section §2.1.2; the transition to turbulence is concerned with inner and outer instabilities, which map to the two layered structure in Townsend's model (section §2.2.2). These correspond to the classical inner/outer zones of a boundary layer. Townsend's 'big eddy' hypothesis postulated a double structure with big eddies in equilibrium while turbulent energy is contained with the stochastic substructure (Townsend, 1956). This perhaps was an early attempt at driving the statistical description of seemingly chaotic turbulent fluctuations towards a more deterministic one. The quest for order among chaos was thus driven by observations of turbulent motion within the boundary layer.

The advancement of flow visualisation techniques since the late 1960's has informed the study of boundary layers in terms of structural, stress-bearing features within the flow, often termed coherent flow/turbulence structures. This highlights the problem of structure versus statistics which lies at the heart of turbulence theory since Richardson's cascade which depicted turbulence as an assembly of interacting swirls and eddies exchanging energy. In this sense, inertia drives vortex stretching thus rapidly breaking up the largest eddies, created by instabilities in the mean flow, cascading into ever smaller vortices (Tennekes and Lumley, 1972). This culminates in dissipation of energy through

viscosity, and the process is commonly referred to as the "energy cascade". Kolmogorov's Theory (1941; K41) quantified this cascade, assuming that at very high but not infinite Reynolds numbers, all small-scale statistical properties are uniquely and universally determined by the integral length scale, the mean energy dissipation rate and the viscosity (Frisch, 1995). In other words, the central assumption of the K41 theory is the self-similarity of the random velocity field at inertial-range scales. Kolmogorov postulated such similarity, and derived the well-known $k^{-5/3}$law, where k is the wavenumber, for the energy spectrum in Fourier Space, which has also been observed experimentally (cf. §4.2.2.2). The idea itself was previously realised by Taylor, who argued that for a statistically steady state, where large eddies are supplied at a given rate and their energy fully disappearing due to viscosity, a definite spectrum would exist (Sreenivasan, 2011). Nonetheless, Landau's famously cryptic remarks in 1944 objected to the universality of small-scale turbulence structure, pointing out the intermittent nature of viscous dissipation, and hence its dependence on the large scale, where geometry differs from one flow to another (Frisch, 1995; Davidson, 2004). Landau foresaw that a suitably defined local average of the energy flux is important for the statistics of the "turbulence signature/structure function" (which identifies whether turbulence is composed of swirling blobs of fluid or vortex rings, *i.e.* energy distribution across different eddy sizes), not the globally averaged dissipation (Davidson, 2004). Another issue lies in the spotty nature of the small-scale vorticity field, which differs from that at the large scale as a consequence of vortex stretching, teasing vorticity into finer and finer filaments rather than being caused by inhomogeneities due to large-scale chaotic vorticity attempting to initiate or maintain turbulence (Davidson, 2004). However, Landau reconciles that Kolmogorov's K41 is an asymptotic theory, shown to work well in the limit of very high Reynolds numbers, with a possibility that inertial-range intermittency may possess certain universal statistical features.

While no universally accepted theory for turbulence exits, attempts at reconciling the two approaches, statistical vs. coherent turbulence, emphasise that the statistical/spectral description of turbulence is a manifestation of the

emergence, growth and decay of coherent flow structures (Venditti et al., 2013). This leads to an alternative structural description of the boundary layer, focusing on the role of these turbulent structures in defining the mean flow behaviour. This is often welcomed as a somewhat 'quasi-deterministic' attempt at understanding what are presumably chaotic turbulent flows; due to the self-organisation and quasi-periodicity of these coherent motions. Adrian and Marusic (2012) refer to this as 'neo-classical' scaling.

2.4.2 Coherent turbulence structures

2.4.2.1 Intermittency and coherence in turbulent flows

The quest for order among the otherwise chaotic nature of turbulence came into fruition with an increased interest in visualising turbulence in the 1960s, following on from Prandtl's (1925) mixing length theory. The first idea was Townsends "big eddy" hypothesis in 1956, which postulated a double structure with big eddies in equilibrium while the turbulent energy is contained within the stochastic substructure (Townsend, 1956). However, the notion of coherent structures was brought onto prominence by the dye, hot-wire and hydrogen-bubble observations and quantitative velocity measurements carried out in the late 1960's and early 1970's, which reported surprisingly well-organised intermittent motions in the boundary layer, which were self-dependent in both space and time (Kline et al., 1967; Kim et al., 1971). Such motions lead to low-speed streaks within the viscous sub-layer, which would interact with the outer portions of flow through a process of gradual 'lift up', sudden oscillation, bursting and ejection (Offen and Kline, 1974; Offen and Kline, 1975). These parcels of low-momentum fluid ejected from the viscous sub-layer or the interstices of roughness elements, result in significant, positive contributions to Reynolds stresses and hence momentum transport, potentially across the entire thickness of the boundary layer (Grass, 1971).

The intermittent transfer of momentum by coherent structures is manifest by velocity fluctuations, and is linked to short–term variations in near–wall stresses (Heathershaw, 1974; Laufer, 1975). This is reflected in the turbulent "bursting" process (Kline et al., 1967; Offen and Kline, 1974; 1975), which is a

critical mechanism for production of turbulent kinetic energy (Schoppa and Hussain, 2002; Dey et al., 2012). Turbulent bursting may be explained by the advection of spatially distributed vortices and structural features past a fixed point of measurement (Robinson, 1991), although this may not detect how such vortices evolve in time (Schoppa and Hussain, 2002). The term 'bursting" could refer either to violent intermittent eruptions of fluid away from the wall implying a local instability, or to describe localised ejections of fluid due to the passage of tilted quasi–streamwise vortices which persist for longer times than ejections (Robinson, 1991).

There is no clear criteria delimiting what constitutes or characterises a coherent turbulent structure, however, and several definitions have been proposed. Falco (1977) identified the so-called 'typical eddies' whose motion produced a significant proportion of the Reynolds stress compared to the surrounding fluid. Cantwell (1981) identified bursts, sweeps, streaks, typical eddies, streamwise and transverse vortices and large eddies as being coherent structures as they are produced regularly and can be mathematically described by space and time correlations. A more discriminating definition, proposed by Hussain (1986), describes them as "connected turbulent fluid masses with instantaneously phase-correlated vorticity over their spatial extent". In other words, turbulence is characterised by a component of large-scale vorticity, which is spatially coherent at any given instant, underlying the random three-dimensional vorticity typical of turbulent flows. These structures are also characterised by composite scales (as large as the lateral flow dimension), recurrent patterns (lifespan longer than passage time of structure), high organisation and quasi-periodic (stochastically intermittent) appearance (Fiedler, 1988). Robinson (1991) characterised vortices as the most coherent of turbulent motions, which he defined as

"three-dimensional regions over which at least one fundamental flow variable (velocity component, density, temperature, *etc*.) exhibits significant correlation with itself or with another variable over a range of space and/or time that is significantly longer than the smallest local scales of the flow".

Adrian (2007), however, suggests that spatial coherence is not sufficient on its own to define a coherent motion as all fluid motions are spatially coherent due to the continuity equation. Therefore, he suggests that only motions that survive long enough to be visible within a flow visualisation movie and/or which contribute significantly to the time-averaged statistics of flow can be considered 'organised' structures. A major issue with most of the earlier definitions is that there are other motions within the flow which have both space and time coherence, and yet can be properties of the mean flow rather than turbulence. More recently, Adrian and Marusic (2012) proposed a definition whereby coherent structures are defined as recurrent, persistent motions which have a significant role in characterising mean flow, and determining stress and other statistical properties of the flow. They further note that

"It suffices to think of coherent structures as building blocks of flows that are recognizable, despite randomness, by their common topological patterns, and that occur over and over again."

The study of coherent structures in turbulence has advanced considerably in recent years, largely due to advances in particle image velocimetry (PIV) and direct numerical simulations (DNS). This has brought about deeper insight into the development of these spatially coherent, stress-bearing structures which play an important role in transport problems in turbulent boundary layers, particularly in the near-wall region (Marusic et al., 2010b). Sustaining wall-turbulence must be related to the time-dependent interactions of these structures (Panton, 2001), and a number of scenarios has been proposed to describe them. Prominently, one view concentrates on the regeneration mechanisms of hair-pin vortex structures into packets, in line with Townsend's attached eddy hypothesis (Adrian, 2007), while an alternative identifies a transient streak growth mechanism principally in the inner-region, considered to be more frequent and energetic (Schoppa and Hussain, 2002).

2.4.2.2 Coherent structures and boundary layer scaling

A large number of studies attempt to describe the relationship between coherent turbulence structures and the wall-normal structure of the turbulent boundary layer (cf. Robinson, 1991; Adrian, 2013; Jimenez and Kawahara, 2013). Fluid motion near the wall is characterised by regions of high and low momentum, with large scale, counter-rotating vortices shed from the roughness elements that dominate the structure of the boundary layer from both hydrodynamically smooth and rough beds (Venditti et al., 2013). The region below $z^+ \approx 100$ is dominated by coherent streaks of streamwise velocity, caused by advection of the mean velocity gradient through vortices, as well as quasi-streamwise vortices resulting from the instability of these streaks (Jimenez and Kawahara, 2013). Streaks represent an array of sinuous, alternating jets imposed on the mean sheared flow; whereas the vortices are tilted away from the wall. Very large scale motions (VLSM), or superstructures, mainly feature within the logarithmic layer at high Reynolds number, yet their influence is felt at the wall, with small fluctuations within that larger motions, akin to Townsend's model (Marusic et al., 2010a). These authors represent superstructures as elongated, counter-rotating streamwise structures that occupy the inner layer, namely the viscous, [buffer] and part of the log layer (Figure 2.7).

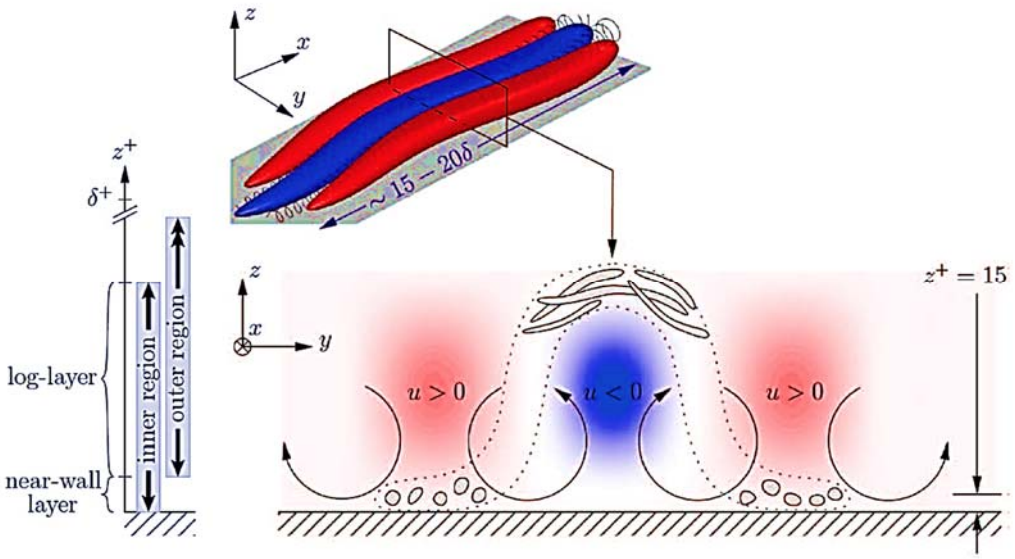

Figure 2.7 schematic of Very large scale organised motions and their interactions within the turbulent boundary layer (modified from Marusic et al. (2010a))

Robinson (1991) suggests that the viscous sublayer, buffer, log and wake regions are characterised by coherent motions of different structural features, while asserting that the buffer layer is the most important in terms of generation and dissipation of energy. Strong shear within the buffer layer leads to the generation of turbulent kinetic energy by converting the mean flow energy into longitudinal streaks and streamwise vortices. In this sublayer, production and dissipation of energy are at their peak (Hutchins and Marusic, 2007). Most of the energy generated at a given distance from the wall gets dissipated locally (Hoyas and Jiménez, 2008).

While much research has focussed on visualising coherent turbulence structures, experimentally or through numerical simulation, a number of issues still remain far from clear. Firstly, there is no clear definition, nor a clear topological description of these motions, particularly in geophysical/environmental fluid flows often with very high Reynolds numbers. In such environments, where the bed is loose and often permeable, the interaction between the bed, suspended particles, and these motions is an area that requires significant research (Venditti et al., 2013). Studies which attempt

this often fall short of describing the feedback between transported sediment and these coherent structures (Shugar et al., 2010; Mohajeri et al., 2016), or more conveniently assume little or no feedback. As such, recent investigations have focused in the evolution and form of coherent structures from roughness elements or bedforms, particularly in gravel streams (Shvidchenko and Pender, 2001; Hardy et al., 2010; Franca and Lemmin, 2015; Hardy et al., 2016). The role of bed generated coherent structures in sediment entrainment and transport is widely acknowledged, yet the exact mechanism is still unclear (Dey et al., 2012; Ji et al., 2013). van Rijn et al. (2013) recently highlighted the need for experimental research into the role of coherent turbulence structures in sediment transport to inform process-based modelling as a major research need in a vision paper on future research needs in coastal sediment dynamics. For practical applications, time-averaged or wave-averaged formulations of eddy viscosity are often employed in numerical models to predict boundary layer structure and empirical formulae are used to predict and mode and rate of sediment transport. Yet, with turbulence research extending beyond classical scaling towards a more 'deterministic' description of coherent structures, and more accurate modelling of sediment transport will need to shift towards an intermittently stochastic description of the problem, accounting for the momentum exchanges imparted by these flow structures entraining sediment particles and vice-versa. Chapter 3 reviews the current state-of-the-art understanding of the role played by coherent turbulence structures in mobilising and transporting sediment; highlighting the well-established utility of statistical descriptions of turbulence is studying sediment transport (averaged values), and the need for an improved understanding of the dynamic interactions between coherent turbulence structures and mobile beds required for more accurate, process-based models of transport.

Chapter 3.

Coastal Sediment Dynamics

> "'… this area of research [drag reduction] has quite a lot in common with studies of alleged paranormal phenomena, such as precognition, telepathy , ghosts, messages from the underworld, and so on" McComb (1990) - *The Physics of Fluid Turbulence*.

3.1 Sediment transport in the coastal zone

In coastal and estuarine settings, turbulence plays a fundamental role transporting sediments as bed load or in suspension; both governed by shear stresses at the bed and within the benthic boundary layer (Hunt, 1954; Bagnold, 1966; Soulsby, 1983; Dyer and Soulsby, 1988). Bed load (also referred to as 'surface creep/ traction') refers to the proportion of the total load of local sediment moving in relatively continuous contact with the bed, either rolling, sliding or in saltation (jumping) due to the effective bed shear stress (Fredsøe and Deigaard, 1992). In this case, the weight of the moving grains is borne by grain-to-grain collisions or solid-transmitted stresses (Bagnold, 1954; Bagnold, 1956). Suspension, on the other hand, refers to the part of the total sediment transport load moving without continuous contact with the bed, agitated and maintained within the flow by turbulent eddies. While there is no distinctive line between these two modes of transport (rather a gradual transition), this distinction is practical from a modelling perspective. Strictly speaking, the total load also incorporates an additional component, known as the wash load, representing the advection of very fine suspended particles that are not represented locally at the bed.

A sound understanding of the physical processes that govern the transport of sediment in coastal environments is fundamental to define and accurately predict the dynamic behaviour of such systems, their morphological evolution, and their biogeochemistry (including nutrient exchanges and contaminant

transport); and thus their ecological and economical service (Thompson et al., 2011; Aagaard and Jensen, 2013). It is also a prerequisite to quantifying sediment erosion or deposition trends in beaches, estuaries, water ways and coastal management cells. Hence, it has profound implications for a host of engineering applications including beach nourishment, coastal protection, maintenance of harbours and waterways, and aggregate dredging, as well as the integrity of coastal defences and offshore structures, cables and pipelines against erosion and scour (Soulsby, 1997). While other processes may have a significant contribution to the mobilisation and/or transport of sediment in the coastal zone, including gravity, Aeolian (wind) processes, bioturbation, and anthropogenic activities; this work is concerned with the transport of abiotic, non-cohesive sediments (primarily sand) due to overlying fluid flow. The initiation of sediment motion (threshold of motion) depends upon local flow characteristics, as well as the nature and position of individual grains and the bulk properties of the bed.

3.2 The threshold of incipient motion

3.2.1 The balance of forces on a stationary grain

A stationary, non-deformable cohesionless grain on the seabed is set in motion once the balance between the drag, uplift and gravitational forces acting on it is disturbed; *i.e.* when the driving forces (horizontal shear and vertical uplift) exceed the stabilising forces (friction and gravity) as shown in Figure 3.1(a). The velocity at which this happens is called the critical flow velocity, or the threshold for incipient motion. The horizontal shear stress (drag) is induced by skin friction on the surface of the grain, and form drag due to pressure differences upstream and downstream of the grain owing to flow separation (Fredsøe and Deigaard, 1992). The drag is a function of the boundary layer Reynolds number for hydraulically smooth beds, and independent of it for high Reynolds number, turbulent rough flows (Middleton and Southard, 1984). The vertical lift force is in part due to the curvature of the streamlines which cause a local decrease in pressure (below the hydrostatic) at the top of the grains and partly due to flow separation (Figure 3.1(b)). A thorough analysis of these forces is given in Raudkivi (1976) for unidirectional flows and in Nielsen

(1979) for wave-induced motion. Whether a given particle moves once the combined lift and drag forces exceed those holding it in position will depend on the configuration of said particle within the bed, including bed slope and geometry, particle shape, sorting and packing and thus its pivoting angle, exposure, orientation, and its degree of armouring (Miller et al., 1977; Dyer, 1986; Evans and Hardisty, 1989; Carling et al., 1992; Wallbridge et al., 1999). A number of intrinsic sediment properties are essential in defining how a sediment particle will respond to flow conditions, including particle size (often defined by the median grain diameter, D_{50}; and statistics of the grain size distribution), the particle's mineralogy and composition (hence its density ρ_s and specific weight, $s = \rho_s/\rho$); as well as the particle shape which dictates its settling velocity. The settling (also fall/terminal) velocity, w_s, is related to the relative balance between fluid drag forces and gravity, and thus depends on the fluid properties too, including viscosity and temperature.

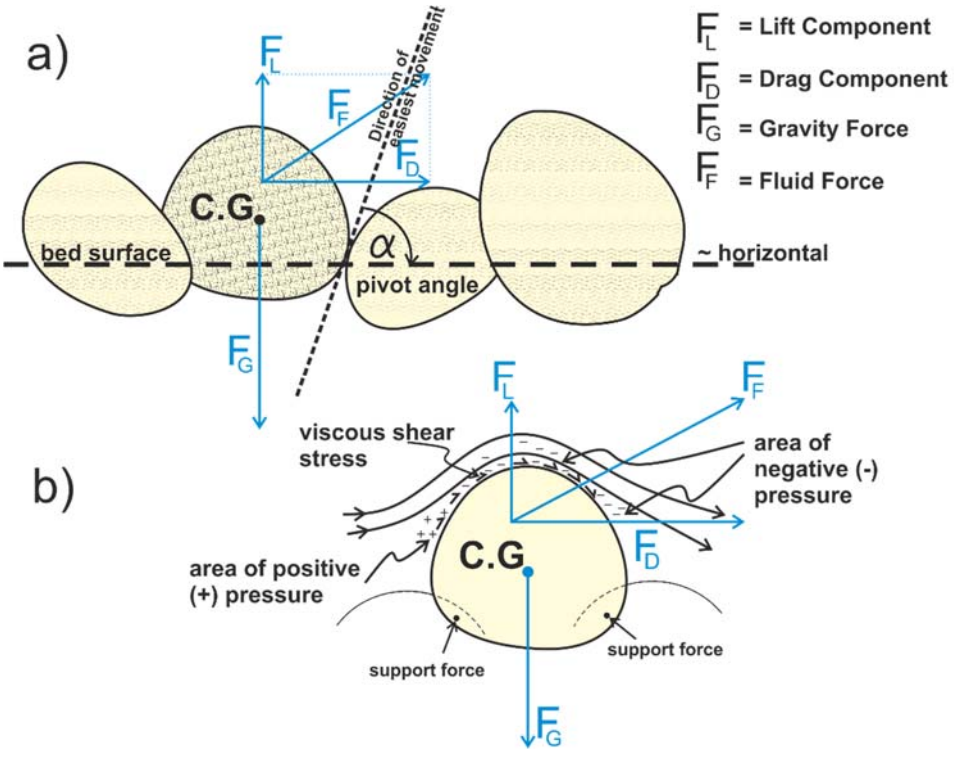

Figure 3.1 (a) Schematic of the balance of forces acting on an individual cohesionless grain resting on a horizontal bed of similar sediment; (b) illustration of pressure gradient due to curving streamlines over a grain resulting in the uplift force. C.G. is the centre of gravity of the grain. Adapted from Middleton and Southard (1984).

3.2.2 Deterministic versus stochastic definitions of threshold

Most studies of the threshold for incipient motion have attempted to define a relationship between certain sediment characteristics and a critical bed shear stress (or shear velocity); or alternatively between some dimensionless parameters representing the sediment and flow properties (Paphitis, 2001). However, the variety of factors influencing how a particular grain of sediment responds to a destabilising fluid force imply an inherent inadequacy of the deterministic approach, with most attempts having focussed on empirical observations. Such studies are often marred by a lack of unified definition for the threshold of motion, and reconciling the results often adds to the scatter in established empirical threshold curves (Miller et al., 1977; Paphitis, 2001). The threshold of motion has been defined as the tractive force required to move a sediment layer (du Boys, 1879); or the stress required for the dislodging of, and beginning of movement of an arbitrary number of uniform grains from the uppermost (bed surface) layer of sediment (Kramer, 1935). Kramer proposed four levels of sediment movement: (i) 'none'; (ii) 'weak', with several of the smallest particles in isolated spots moving in countable numbers; (iii) 'medium', where grains of mean diameter move all over the bed in considerable numbers that they cannot be counted yet do not alter the bed configuration; and (iv) 'general' where grains, including the largest, move in sufficient numbers to alter the bed, with a significant amount of material transported.

The benchmark study on incipient motion was presented in Shields (1936) doctoral thesis. Starting from dimensional similarity arguments and using laboratory work, Shields postulated the most important parameters to determine incipient motion include the bed shear stress, τ_0; relative particle density (specific or immersed weight; described by ratio of sediment particle density, ρ_s to fluid density, ρ), gravitational acceleration, g; the grain diameter (D_{50}), and the fluid kinematic viscosity, ν. Shields thus combined these into a dimensionless factor, the Sheilds' entrainment function θ_{cr}:

$$\theta_{cr} = \frac{\tau_0}{(\rho_s - \rho) g\, D_{50}} \qquad \text{(Eq. 3.1)}$$

Shields demonstrated that the entrainment function varies with the grain Reynolds number, Re^*, which represents the ratio between boundary roughness and thickness of the viscous sublayer. He thus presented the threshold for incipient motion as a narrow curve above which particles are set in motion (Figure 3.2), based on his and previously published data of Casey (1935), Kramer (1935), and the US Waterways Experiment Station (USWES, 1933). While Shields defined the threshold for uniform grains based on flume observations in the sense of Kramer's weak to general movement, subject to being in a state of 'constancy', he is often referred to as having defined the threshold as the extrapolated value of bed shear stress for which the sediment flux is zero (Miller et al., 1977; Lavelle and Mofjeld, 1987; Dey and Papanicolaou, 2008; Dey, 2011). This confusion stems from Shields' vague discussion about extrapolating zero bed load from measured rates of transport for sand mixtures, and there is no clear indication of the approach he used to present his results (Buffington, 1999; 2000). A large number of attempts to extends Shields' data have followed, resulting in a plethora of modified threshold curves, and spanning a wide range of particle sizes, and going into the suspension mode of transport (Miller et al., 1977; van Rijn, 1993; Paphitis, 2001; van Rijn, 2007a). Alternative formulations have been proposed to avoid the use of shear stress/ shear velocity terms on both axes (Vanoni, 1964; Yalin, 1972). Neill and Yalin (1969) and Yalin (1972) presented another modification to Shields' diagram, by combining θ_{cr} and Re^* into a single Yalin's parameter, Ξ, such that the shear (friction) velocity is no longer on both axes:

$$\sqrt{\Xi} = \frac{Re^*}{\sqrt{\theta_{cr}}} = \left[\frac{(\rho_s - \rho) g\, D_{50}^3}{\rho\, \nu^3}\right]^{0.5} \qquad \text{(Eq. 3.2)}$$

where ν is the kinematic viscosity of the fluid, and D_{50} is the median grain diameter. From statistical arguments, they presented a quantitative incipient motion criterion, ε , to define the number of grain detachments, n, in time t over a given area A, where the lower limit is set to $\varepsilon = 1.0 .\times 10^{-6}$:

$$\varepsilon = \frac{n}{At} \cdot \sqrt{\frac{\rho D_{50}^5}{(\rho_s - \rho)g}} \qquad \text{(Eq. 3.3)}$$

Figure 3.2 shows an extended Shield's diagram, compiled by (Paphitis, 2001), including data from 29 published experimental works (in rectangular flumes) on cohesionless, uniform/well-sorted natural and artificial grains of near quartz densities, in uniform steady flow. Paphitis (2001) demonstrated that a given particle size can be displaced by different critical shear stresses in repeated experiments. This implies that the occurrence of entrainment events is distributed across a range, and thus is better described stochastically.

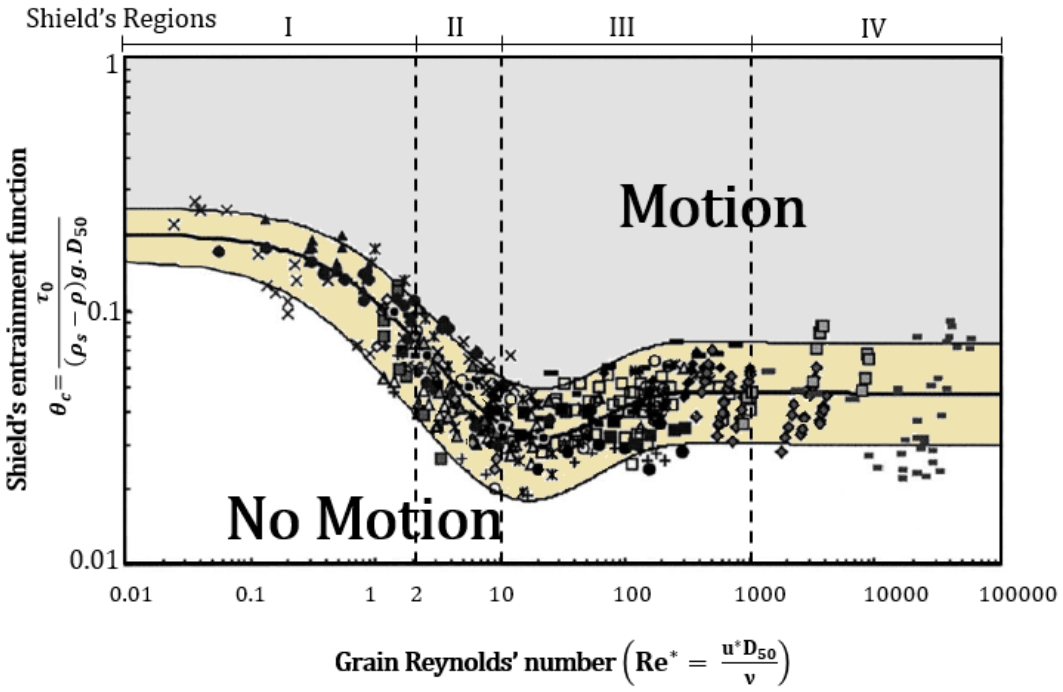

Figure 3.2 Shields' diagram extended by Paphitis (2001); with threshold for incipient motion of cohesionless grains in uniform flow, defined as Shields' entrainment function as a function of the grain Reynolds number. The envelop defines the lowest (incipient motion of discrete particles) and highest (the onset of mass sediment transport); with the bold curve representing the mean threshold. Shields' identified 4 regions: (I) $Re^* < 2$; θ_C decreases progressively from a maximum, as Re^* increases; (II) $2 < Re^* < 10$; negative slope with u^* is assumed independent of grain size which are submerged within the viscous sublayer (hence hydraulically smooth); (III), $10 < Re^* < 1000$; the envelop approaches a minimum; and (IV) where $Re^* > 1000$; with θ_c independent of Re^* (Modified from Paphitis, 2001).

Lavelle and Mofjeld (1987) also argued against the use of a deterministic approach to establish the critical threshold of sediment transport using a time-averaged shear stress/ velocity; favouring the stochastic approaches which advocate that instantaneous stresses in the turbulent flow move individual particles (Einstein, 1936; 1950; Yalin, 1972). Turbulent eddies can influence entrainment either through increasing drag induced by: (i) a passing eddy which moves a particle (impulse force); (ii) lowering the local pressure such that particles (even sheltered ones) can be ejected by hydrostatic pressure, or (iii) by moving entrained particles directly into suspension (Raudkivi, 1976). Several investigators have in fact demonstrated that some sediment movement is possible for any non-zero current velocity, due to an instantaneous stress that could far exceed the mean shear stress (Kalinske, 1947; Paintal, 1971). Even Shields remarked that particle size, shape and relative positions are distributed properties for which the critical shear stress cannot be sharply defined (Shields, 1936). When assessing the detachment of an individual stationary grain from its position within the bed, several authors assume that it is entirely due to the uplift force exceeding particle weight (Einstein, 1936; 1950; Yalin, 1972). As such, when mass movement of sediment is considered, both fluctuating and non-fluctuating lift forces can be recognised, and the detachment of a grain is described by a probability of occurrence at any instance, taking into account its geometry (size, shape, position within the bed). Einstein (1950) asserted that the probability of a given grain moving depends upon its geometry and near bed flow but not its history, hence it occurs only when the instantaneous lift exceeds the particle weight. Therefore, the probability can be defined as the fraction of the total time during which the local flow at a given location can induce a sufficiently large lift force to dislodge the particle. By decomposing the instantaneous velocity above a cohesionless grain into the sum of the time-mean and turbulent fluctuations, Christensen (1965) argued that a better description of the instantaneous bed shear stress can be attained with a frequency distribution of the fluctuating velocity component rather than a fluctuating lift force. This probability increases as the time interval considered increases due to the increase in number of fluctuating events (Yalin, 1972). Grass (1970) represented these fluctuations through a

series of stress-distribution curves where measured fluctuations were both due to turbulence and grain geometry that varies as the grain moves from one position to another. Through high-speed imaging and fluid marking, Grass determined fluctuations in shear stress within the viscous sublayer due to overlying turbulence, and the variations in local, instantaneous bed shear stress at which sediment grains were observed to move. The distributions of instantaneous, local bed shear stress needed to move a group of particles on the bed surface can then be compared through time to the statistical distribution of instantaneous local shear stress acting on a given area of the bed with comparable particle size. Where the two distributions overlap, a number of particles which can move are thus set in motion; otherwise the flow is never strong enough to move any particles (*ibid.*).

3.2.3 The threshold of motion in oscillatory and combined flows

Studies of incipient motion under unsteady wave and combined wave-current flows have had far less attention than in the case of steady, unidirectional flows, and commonly, Shields' or Yalin's criteria are applied (*e.g.* Hammond and Collins, 1979). This is usually done under the assumption that once the oscillating motion exceeds the threshold as defined in an open channel, the particles will be entrained, with no regard to the greater stresses exerted by accelerating/decelerating motion compared to the mean current (Komar and Miller, 1973). Bagnold and Taylor (1946) studied the beginning of grain movement on a smooth bed oscillating within a still water tank (no apparent turbulence), and established an empirical threshold as the critical angular speed related to the near bed amplitude and the period of oscillation. Komar and Miller (1973) pointed out that Bagnold and Taylor's results were obtained in laminar conditions, and presented a threshold criterion for medium to fine sands in laminar conditions under waves with orbital diameter, d_0, given by:

$$\frac{\rho\, u_{w,cr}^2}{(\rho_s - \rho)\, g\, D_{50}} = 0.30 \left(\frac{d_0}{D_{50}}\right)^{0.5} \qquad \text{(Eq. 3.4)}$$

For coarse grain sediment, they presented an empirical threshold curve relating d_0/d_{50} to the dimensionless ratio between acceleration and effective

gravity forces acting on a grain, given by $\rho\, u_w/(\rho_s - \rho)g\, T$; where u_w is a wave-induced near bed velocity, and d_0 is the near bed orbital diameter (= $2.A_{w,0}$, *i.e.* twice the near bed orbital amplitude, $A_{w,0}$). Madsen and Grant (1975), however, argued that Bagnold's & Taylor's (1946) data were in agreement with Shields' curve as long as the critical shear stress is calculated with a wave friction factor calculated following Jonsson (1966b). Equation 3.4, was later revised so that the empirical coefficient on the right hand side was set to 0.21 for grains with $d_{50} < 500\ \mu m$ (Komar and Miller, 1975). Madsen and Grant (1976) later presented [yet another] modified Shields' diagram to be used for oscillatory (unsteady) flows, by replacing the grain Reynolds number with a dimensionless factor, S_* , for a sediment of relative density (specific gravity, $s = \rho_s/\rho$):

$$S_* = \frac{D_{50}}{4\,\nu}.\sqrt{(s-1)gD_{50}} \qquad \text{(Eq. 3.5)}$$

Sleath (1984) presented a list of 26 alternative equations for the threshold of motion under waves. However, whilst noting that approaches such as Komar and Miller's (1973, 1975) or Madsen and Grant (1975, 1976) may be 'superficially attractive', he raised a concern regarding the use of wave friction factors for unsteady flows at ranges where data is particularly lacking. Sleath (1984) noted that the relation between drag and lift forces in oscillatory flows differs from that in steady flows as the shear stress is augmented by an additional horizontal force induced by the pressure gradient within the fluid acting on the grains.

Defining a threshold of motion in combined wave-current flows is even more complex than that of steady or unsteady forces by currents or waves on a grain, and the number of governing parameters increases further due to non-linear wave-current interactions. Hammond and Collins (1979) conducted threshold experiments in combined waves and currents on an oscillating bed. Using Yalin's criterion for unidirectional flow, they showed that the combined threshold velocity is dependent on both grain size (directly proportional) and wave periods (inversely proportional), attributed to near-bed stress

fluctuations (turbulent bursting) acting in a forward/ reverse manner. The latter finding agrees with earlier studies which found reduced sediment transport or reverse in direction in some cases with currents superimposed on oscillating beds (George and Sleath, 1979). Voulgaris et al. (1995) suggested that the wave-period dependency can be resolved through non-linear interaction models for long period waves (whilst admitting such models are not satisfactory), and linear addition of individual wave and current components at short periods. Lee-Young and Sleath (1989) studied initial motion with currents perpendicular to the direction of oscillation; suggesting that a vector addition of the wave and current components (assuming no nonlinear interaction) provides a reasonable representation of threshold conditions. Comparisons between flume based studies and field observations often show considerable differences in the values of threshold, attributed to the greater bed roughness, 'relict' nature of ripples, and wider wave spectra in the field (Komar and Miller, 1975).

Field observations by Amos et al. (1988) were collected near Sable Island Bank to examine the applicability of flume derived thresholds for sand motion to the storm dominated Canadian continental shelf. The site was dominated by combined wave-current flows with wave crests generally orthogonal to peak tidal currents, and eight distinctive types of bedforms were observed for well-defined combinations of near-bed orbital velocities and mean current speeds. The current-only bed shear stress, $\overline{\tau}_{0,c}$ was defined using the Quadratic stress law, with a constant drag coefficient, $C_D = 2\ f_c$, using velocity measured 100 cm above the bed (U_{100}):

$$\overline{\tau}_{0,c} = \rho . C_D\ U_{100}^2 \qquad \text{(Eq. 3.6)}$$

Active ripples, usually indicative of bedload, were observed in flow conditions below the threshold of sand transport, defined as the wave Shields' parameter with wave-induced bed shear stress given by equation 2.27; with the Jonsson (1966b) friction factor. This was found to be applicable for high wave Reynolds number, otherwise a combined threshold was needed. In the latter case, a combined wave-current friction factor given by Grant and Madsen (1979),

modified to account for the relative angle between the direction of the mean current and that of the wave propagations:

$$\hat{\tau}_{0,w} = \frac{1}{2} f_w \rho U_\infty^2 \qquad \text{(Eq. 3.7)}$$

Based on their observations, Amos et al. (1988) suggested a Shield's type threshold, defined by:

$$[\theta_w + \theta_c]_{critical} = \frac{\overline{\tau}_{0,c} + \hat{\tau}_{0,w}}{\rho(s-1)g \, . D_{50}} = 0.04 \qquad \text{(Eq. 3.8)}$$

3.3 The threshold for sediment suspension

The movement of sediment along the bed is the predominant form of transport at low rates. As bedload intensifies, collisions between particles become more important, and particles experience short-lived, water-borne jumps from the bed (saltation) due to the impulse forces or ballistic momentum (Middleton and Southard, 1984). Saltation represents a transition from traction bedload towards suspension within the water column as a result of turbulence associated with the total bed shear stress (Madsen and Wood, 2002). The entrainment of a sediment particle into suspension is often described through pick-up functions integrated into the bedload theory, such as those presented by Einstein (1950) and Yalin (1972). However, van Rijn (1984a) found both such relations to be rather poor; favouring formulations that incorporate an excess bed shear stress term such as that of Fernandez Luque and Van Beek (1976).

Bagnold (1966) argued that solid particles can only remain in suspension if some turbulent eddies had an upward, vertical velocity component, w'_{up} exceeding the particle's settling (fall) velocity, w_s. Bagnold thus defined the threshold for suspension at some critical value of the ratio $w'_{up}/w_s < 1$; and full suspension at a higher value, to account for the variability of w'_{up} of different eddies within the flow. Similarly, the settling velocity can be replaced by an effective settling rate for heterogeneous suspensions. By defining $\overline{w}'_{up} \cong$

$w_s \cong 0.8\, u^*$; a statistical approximation that $rms(w'_{up}) = 1.25\sqrt{\tau_0/\rho}$ (following Lane and Kalinske (1941)) yields a Shields-like threshold criterion for suspension of uniform, quartz-density grains in clear water, given by:

$$\theta_s = 0.64.\frac{w_s^2}{\rho D_{50}(s-1)} \qquad \text{(Eq. 3.9)}$$

This approach relating the upward velocity component to the particle settling rate has been suggested by a number of authors, and the ratio of w'_{up}/w_s has been referred to as the moveability number (Collins and Rigler 1982) or the inverse Rouse number (Lee et al., 2004). The exact value of the ratio w_s/u^* for suspension to be maintained has been contested in the literature (Engelund, 1965; Komar and Clemens, 1986; Samaga et al., 1986; Amos et al., 2010). According to van Rijn (1984b), the ratio w_s/u^* depends on the dimensionless grain diameter, D^*;

$$D^* = \left[\frac{g\,(\rho_s - \rho)}{\rho\nu^2}\right]^{\frac{1}{3}}.D_{50} \qquad \text{(Eq. 3.10)}$$

and thus is not universal. By defining the relationship of w_s/u^* and D^* as:

$$\frac{w_s}{u^*} = \frac{D^*}{\chi} \qquad \text{(Eq. 3.11)}$$

van Rijn (1993) shows that the threshold for suspension (Shield criterion) can be rewritten to incorporate both w_s/u^* and D^*:

$$\theta_s = \frac{\chi^2}{D^{*2}}.\frac{w_s^2}{\rho D_{50}(s-1)} \qquad \text{(Eq. 3.12)}$$

Based on experimental results, van Rijn (1984b) suggests $\chi = 4$ for $1 \leq D^* \leq 10$. For $D^* \geq 10$; the ratio w_s/u^* is assumed constant. Alternative limits have been presented in (van Rijn, 1993; NiÑo et al., 2003; Amos et al., 2010). Bose and Dey (2013), on the other hand, presented probabilistic Shield's curves for entrainment into suspension; which vary as a function of both the grain Reynolds number and the Rouse number, a parameter often used in modelling the vertical distribution of suspended sediments (cf. §3.5.2).

3.4 Coherent flow structures and sediment suspension

3.4.1 Sediment entrainment and coherent structures

While classical descriptions of Shields'-type criteria for the thresholds of motion and suspension are still widely accepted and used, there remains no consensus as to what actually destabilises the balance of forces acting on a grain at rest and mobilises it. As such, expressions of threshold are often attributed to stresses or flow velocities (instantaneous or time-averaged, local or spatially averaged), velocity gradients, fluid acceleration, pressure forces and pressure gradients, rate of energy transfer/stream power; shear instabilities, vortex structures, and ejections and sweeps of a bursting sequence, all of which have their advocates and opponents (Coleman and Nikora, 2008). Variations in bed shear stress associated with velocity fluctuations are clear manifestations of intermittent momentum transfer within the near-bed fluid due to coherent turbulence structures (Laufer, 1975). Such motions are characterised by violent eruptions of fluid, resulting in the production of turbulent kinetic energy; a mechanism knowing as 'bursting' (Offen and Kline, 1974; Offen and Kline, 1975).

The role played by bed–generated coherent bursting structures in entraining and transporting sediment particles is widely acknowledged, yet the exact mechanism is still unclear (Dey et al., 2012; Ji et al., 2013). Observations by Sutherland (1967) reported a tendency for bed grains to move in a series of short, intermittent bursts confined to small areas. Many grains would move simultaneously during each burst before motion subsides until another burst takes place, and with increased flow velocities, the motions became more violent and eventually projected as suspensions. For flat beds, Sutherland observed a constant frequency at which these bursts occur, whereas over developed bedforms, intermittent motions occurred first in the troughs and stagnation points with several grains moving simultaneously in no specific direction. Greater velocities brought more grains into suspension, with particular agitation near the trough, and sediment clouds being lifted occasionally over short durations. Sutherland's observations describe two fundamental features of a bursting sequence, (i) the 'sweep' whereby

downward inrushes of fast-moving fluid induce significant shear stresses and high velocities just above the grain particles; and (ii) the burst/ejection, in which the slower, near-bed fluid moves higher away from the bed with high stresses yet slow localised velocities (Dyer, 1986). Ejections thus promote the movement of sediment into suspension due to the increase in upward velocity fluctuation, whereas sweeps are effective at moving sediments along the bed (*ibid.)*. The particle remains suspended by the ejection until the latter breaks up, and as the settling rate exceeds that upward fluctuation in velocity, the particle falls. During the descent, the particle could be caught by another bursting motion, and hence is maintained in suspension. The bursting process within coherent turbulence structures is often considered a plausible mechanism in light of Bagnold's argument that suspension of a particle can be maintained only when upwards velocity fluctuations exceed the downward motion (Bagnold, 1966). Jackson (1976) argued that strong upward flow in a burst provides the vertical anisotropy in turbulence needed to suspend sediment, hence promoting entrainment of more and coarser sediment than traction alone. Similarly, the contribution to entrainment associated with pressure fluctuations may also be of importance. Offen and Kline (1975) proposed that the rise of a particle into suspension is strongly affected by the passage of a bursting structure above it; as it imposes a temporary, local adverse pressure gradient. Amir et al. (2014) demonstrated a link between regions of positive and negative high-amplitude pressure fluctuations attributed to the passage and dynamics of coherent structures; affecting the mean bed shear stress and thus supporting their role in particle entrainment and transport. Furthermore, Diplas et al. (2008) demonstrated that the so-called 'impulse', representing the product of the magnitude of instantaneous fluctuating forces induced by flow structures and the duration in which they are imparted on a grain, is a better criterion for describing sediment entrainment. Many studies since Sutherland's early work have confirmed the intermittent nature of sediment resuspension linked to the bursting phenomenon (Sutherland, 1967; Gordon, 1975; Jackson, 1976; Sumer and Oguz, 1978; Sumer and Deigaard, 1981; Soulsby, 1983; Bedford et al., 1987; Kawanisi and Yokosi, 1993; Soulsby et al., 1994; Kawanisi and Yokosi, 1997;

Nikora and Goring, 2002; Cellino and Lemmin, 2004; Yuan et al., 2009; Dey et al., 2012; Liu et al., 2012; Grigoriadis et al., 2013).

3.4.2 Coherent structures and intermittent resuspension in unsteady flows

The vast majority of studies into coherent turbulent structures are concerned with steady boundary layers. Fishler and Brodkey (1991) used flow visualisation to establish the existence of coherent turbulence structures for transitional and fully turbulent oscillatory flows, as a series of deterministic events occurring randomly in space, but only during decelerating flow. They postulated several events, namely local deceleration, acceleration, excitation-transverse vortex, ejection and sweep with the local deceleration, excitation and ejection events mobilising large amounts of tracer particles. Sarpkaya (1993) used laser-induced fluorescence to trace the emergence and evolution of coherent structures within an oscillating, unsteady boundary layer, showing a multitude of structural forms occurring from low Reynolds number all the way up to fully turbulent flow. These unevenly spaced streaks were generated towards the end of the decelerating phase and disappeared during the accelerating phase at low Reynolds numbers. As the wave Reynolds number increased, these motions merged into more clearly defined structures, with intense bursting. However, only a few hairpin structures were observed as their short-lived emergence was prematurely terminated by flow reversal. Carstensen et al. (2010) observed two types of coherent structures in oscillatory and combined oscillatory-current flow boundary layers within transitional flow regimes, namely vortex tubes and turbulent spots. The former may cause insignificant variations in bed shear stress whereas the latter features bursts with violent oscillations, causing spikes within the bed shear stress signals, with significant implications for transport.

Nielsen (1992) argued that the most important flow structure in connection with suspended sediments is that of a vortex with a horizontal axis as these vortices are able to trap sand grains and carry them along considerable distances, as opposed to the orbital wave motion which has no trapping ability. Nonetheless, a number of flow structures in unsteady flows are often associated

with the entrainment and suspension of sediment particles. Nadaoka et al. (1988) described large, three-dimensional, obliquely-descending eddies in the surf zone that would lift considerable amounts of sediment into suspension, forming clouds ejecting from the bed, advecting horizontally, and settling down. These turbulent coherent structures induced by wave breaking can inject surface-generated turbulence into the seabed, arriving as downward bursts associated with counter-rotating vortices (Ting, 2008). Numerical simulations of these structures under breaking solitary waves conducted by Zhou et al. (2014) suggest that significant suspension of sediment occurs at the location where such motions impinge on the seabed, albeit with some time lag. At the centre of the impinging region, intense downward velocity fluctuations supress suspension, yet as this is accompanied by an uprush in the adjacent regions, sediment shoots higher into the water column in clouds. The suspension of sediment by downward injected turbulence from breaking waves is supported by ample evidence from field measurements (Grasso and Ruessink, 2012; Aagaard and Jensen, 2013). Aagaard and Hughes (2010) showed that plunging breaker waves are much more efficient at suspending sediment than surface bores. The intermittent, coherent vortex structures impinging on the bed results in significant increase in the local, instantaneous bed shear stresses; and are several orders of magnitude more efficient than shoaling waves. Large vertical accelerations and pressure differentials under the plunging breakers mobilise and lift large amounts of sediment into the water column. As the sediment concentration is in phase with the wave crest, sediments get advected landwards. Sumer et al. (2013) also observed coherent vortices generated by plunging, regular waves in the lab, which they attributed to shear layer instability. This refers to instabilities within a shear layer formed between the onshore-directed crest and the offshore-directed rundown being concentrated in more defined vortices. These vortices were shown to significantly enhance the bed shear stress, and amplify the corresponding turbulent fluctuations significantly; as well as cause large, upward-directed pressure gradients, further contributing to suspended sediment plumes.

Another commonly identified form of coherent structures associated with sediment resuspension is vortex shedding. The process of vortex shedding from bedforms in wave dominated flows was first reported by Bagnold and Taylor (1946) and has particularly enjoyed wide exposure in the scientific literature. Bagnold and Taylor (1946) investigated the interaction between shallow water waves and sandy bottoms, describing two mechanisms of formation: rolling-grain and vortex ripples. In vortex type ripples, a full grown vortex begins to over-run the ripple, scooping sand grains from the trough, and shooting upwards, parallel to the surface of the slope, like a spinning wheel, before resting at the ripple crest. As flow reverses over these steep two-dimensional bedforms, the benthic boundary layer can separate from the bed, trapping sediments and ejecting them higher into the flow (O'Hara Murray et al., 2011). This is in essence a repeatable and hence coherent, convective entrainment process (Nielsen, 1992) that is observed in both regular (at half cycle) and irregular wave conditions (Thorne et al., 2003; O'Hara Murray et al., 2012). Localised ejections of vortices can interact with advecting or preceding motions, often laden with sediment, and thus maximum concentrations tend to form above the ripple troughs where the horizontal velocity peaks, whereas maximum concentrations at the crest lag due to the advection of coherent suspension events (Villard and Osborne, 2002). The more energetic suspension events could persist several wave cycles particularly where small waves are followed by larger ones. For combined waves and currents, Fredsøe et al. (1999) demonstrated that the periodic shedding of coherent structures from vortex ripples dominates the turbulence structure near the bed, and hence persists almost unchanged. Furthermore, the formation of these vortices depends on the bed material, the ripple size and wave characteristics. In high frequency waves one vortex is formed and the flow reverses before another one could be formed, and at low frequencies, it may fully decay after shedding, before another vortex forms (Williams et al., 2007). Where vortex pairs may develop, sediments may be violently ejected much higher (several orders of a ripple height) than classically described, reaching distances that exceed ripple height by over an order of magnitude. Subsequently, sediment particles can be entrained within the accelerating (jet-like) fluid formed between the two

vortices, shooting at speeds exceeding those of the vortex pair, until the gravitational forces are enough to induce settling (*ibid.*). For very high concentrations, particle-particle interactions may modify the settling rates; and feedback by the suspended material on the turbulence structures may no longer be negligible.

3.5 The suspended sediment transport problem from a modelling perspective

The complexity of the interactions between suspended sediment particles and the carrying fluid in turbulent flows, as well as amongst particles themselves, has seen the development of various theoretical, numerical and experimental frameworks to tackle the problem (Zhu et al., 2013). Numerical models of sediment transport often used to guide engineering applications employ coupled models for waves, currents, sediment transport and changes in bed level. As such, they are often based on some numerical integration of the Reynolds-averaged Navier Stokes (RANS) equations for conservation of mass (continuity) and momentum of the fluid (cf. Appendix 1); and the advection-diffusion equations to describe the vertical distribution of suspended sediment concentrations, together with some empirical formulae to estimate bed-load transport (Vittori, 2003; van Rijn et al., 2007). The RANS equations are usually closed by the Boussinesq hypothesis and the eddy viscosity and diffusivity are computed by means of algebraic relationships or differential equations. Most of the bed-load equations are derived from laboratory experiments with regular, non-breaking waves; while suspended sediment profiles are often described in a wave-averaged sense, with no explicit account for intra-wave phenomena such as turbulent bursting. The evolution of the bed is often derived from a simple mass balance, given by the Exner Equations (Exner, 1920; Exner, 1925; Paola and Voller, 2005); usually assuming that the erosion from the bed is equal to the entrainment rate under equilibrium conditions (Amoudry and Souza, 2011; Villaret et al., 2013).

3.5.1 Modelling suspended sediment

The traditional approach to modelling the suspension of sediments is founded upon the passive scalar hypothesis (Chauchat and Guillou, 2008), whereby no interaction between sediment particles and other, concurrent transport processes (*e.g.* thermal) within the fluid flow is assumed (Combest et al., 2011) nor does the concentration of the scalar (sediment) affect the dynamics of the fluid motion itself (Warhaft, 2000). Under such a framework, these 'single-phase' models employ the gradient-diffusion hypothesis which states that the settling of the grains towards to bed by gravity would be balanced by upwards diffusions induced by vertical turbulent motions in the boundary layer (Nielsen, 1992; Zhang et al., 2011). According to this hypothesis, the conserved scalar (*e.g.* sediment) flux is aligned with the mean scalar gradient (in magnitude and direction) through a positive scalar – the turbulent diffusivity (Pope, 2000). The implication of this assumption is that the horizontal velocity of the sediment is equal to that of the fluid, and the difference in true density between solid particles and surrounding fluids is accounted for only in the vertical via a settling velocity term. In other words, sediment transport in suspension is described by the balance between the downward settling of sediment particles due to gravity versus the upward mixing of sediment by turbulent motions. Similarly, the relative velocity between a non-cohesive particle and the surrounding fluid in waves is also assumed to be equal to the settling rate of the particle in still water; such that fluid accelerations due to the wave motion are considered negligible compared to the acceleration due to gravity (Nakato et al., 1977; Nielsen, 1992). Molecular and turbulent diffusivities, in analogy to Fourier's law of heat conduction, and Fick's law of molecular diffusion, are combined into an "effective diffusivity" used in the conservation equations. In the vertical dimension (z), the advection diffusion equation (ADE) for describing the volumetric concentration $C(z,t)$ of suspended sediment at a given height (z) at a time, t, is:

$$\frac{\partial C(z,t)}{\partial t} = \frac{\partial}{\partial z}\left(w_s . C(z,t) + \varepsilon_{s,z} . \frac{\partial C(z,t)}{\partial z} \right) \qquad \text{(Eq. 3.13)}$$

where w_s represents the particle settling velocity, and $\varepsilon_{s,z}$ denotes the vertical component of sediment mixing coefficient (eddy diffusivity), a measure of the turbulent diffusivity (Chen et al., 2013; van Rijn et al., 2013). In a time-averaged sense, van Rijn et al. (2007) used $\varepsilon_{s,cw}$ to represent combined wave-current diffusivity, giving Equation 3.12 for combined flows at equilibrium as:

$$c.w_s + \varepsilon_{s,cw}\frac{dc}{dz} = 0 \qquad \text{(Eq. 3.14)}$$

The diffusivity term, in line with the passive scalar hypothesis, is often related to the eddy (turbulent) viscosity, ν_T, of the flow, a measure of deformation (strain) of the fluid element relative to the applied momentum (Reynolds stress), in analogy to molecular transfer, as proposed by Boussinesq (Boussinesq, 1877; Schmitt, 2007). The ratio of turbulent diffusivity of momentum (*i.e.* eddy viscosity, ν_T) to the turbulent diffusivity of particulates/sediment grains (sediment diffusivity) is known as the Prandtl number (Pope, 2000), or the Schmidt number (Amoudry et al., 2005; Absi, 2010; Buscombe and Conley, 2012), or collectively the Prandtl-Schmidt number (Hassan and Ribberink, 2010). Despite both eddy and sediment diffusivities varying considerably, the ratio is often taken as a constant value. This relationship between ν_T and ε_s holds true if the source of a vertical suspension "plume" is the ground (bed) level (Robins and Fackrell, 1979). Nonetheless, the fact that a proportional relationship given by Prandtl-Schmidt number between eddy viscosity and sediment diffusivity certainly implies that particles do not necessarily follow the turbulent fluid motions. Yet, this ratio is commonly assumed to be unity for steady uniform flows (Li and Davies, 2001; Hassan and Ribberink, 2010); although its value has been shown to depend upon particle sizes (Nielsen, 1992), vertical decay of velocity (Nielsen and Teakle, 2004) and concentration (Amoudry et al., 2005), selective suspension (Lee, 2008), and vortex entrainment (van Rijn, 2007b; Amoudry et al., 2013). This disparity has been the foundation for the argument in favour of a convection-diffusion approach for oscillatory flows (Nielsen, 1992; van Rijn, 2007b). Hence, solving advection-diffusion equation is predicated on how the diffusivity term (ε_s), and thus how the eddy viscosity is described/ closed. This

highlights a major issue in modelling sediment suspension, whereby the feedback imparted by the suspended particles on the flow is completely neglected. Attempts at reconciling intermittent sediment entrainment by coherent structures and classical models of suspended sediment transport thus need to address the time-dependent relationship between eddy viscosity (pertaining to the flow) and eddy diffusivity (pertaining to the sediment).

3.5.2 The classical model: The Rouse profile of suspended sediment

Perhaps the most classical model within the ADE framework is that proposed by Hunter Rouse (1937). Rouse argued that if the mean components of streamwise ($u_i = u$), crosswise ($u_j = v$) and vertical ($u_k = w$) velocity (U) (following a Reynolds decomposition) do not vary in either space or time, then the turbulent flow may be considered steady and uniform (Rouse, 1937). Substituting these in the original RANS equations leads to an expression equivalent to the Newtonian equilibrium of force by mass-acceleration. By introducing "Boussinesq's turbulent coefficient", or eddy viscosity, Rouse describes the effective shear of momentum transport in the vertical as a shear stress in the form:

$$\overline{\tau_{xz}} = \overline{u_i\, u_k} = -\nu_T \,.\frac{\partial \overline{U}}{\partial z} \qquad \text{(Eq. 3.15)}$$

where $\overline{u_i\, u_j}$ is the time-averaged velocity covariance of two orthogonal velocity components (second moment or Reynolds stress, τ_{xz}) in the vertical plane, and ν_T is the eddy viscosity term which describes the turbulent diffusivity of momentum. The above equation holds true only for simple shear flows, where the Reynolds stress anisotropy is linearly related to the mean rate-of-strain tensor via the eddy viscosity (Pope, 2000). Rouse thus closes the equations by using a one-equation model (cf. Appendix 2 for full derivation); whereby a mixing length, l [L], denotes the average distance in the logarithmic part of the flow over which a small fluid mass is carried by turbulent mixing processes, following Prandtl (1925). Rouse (1937) thus argued that the difference between the original velocity of the particle and that of the region to which it comes must be proportional to the magnitude of the velocity fluctuations

involved in that transverse motion, thus defining the effective shear stress (whilst ignoring molecular viscosity) as:

$$\overline{\tau_{xz}} = \rho\ |w'|\ l\frac{dw}{dz} \qquad \text{(Eq. 3.16)}$$

By comparison, he therefore defines the 'kinematic turbulence factor' (*i.e.* the turbulent eddy viscosity), as:

$$v_T = \ |w_z'| \times l. \qquad \text{(Eq. 3.17)}$$

Rouse suggested that the problem of suspended load (or temperature, or salinity) in a stream can be tackled similarly, in a convective manner. Using the settling velocity of a given particle size, w_s, the temporal rate of transport of concentration per unit area must equate the number of particles per unit volume multiplied by their rate of fall.

Thus, by simplifying the RANS equations for two dimensional, uniform flow; and applying boundary conditions whereby shear stress at the bed is given by the energy slope equation, and zero stress at the water surface (Raudkivi, 1976); all that remains is to describe the vertical distribution of eddy viscosity. Rouse thus opted for a parabolic distribution, in line with the logarithmic velocity distribution, showing the concentration to vary in a parabolic fashion in the water column, extending from a near bed reference height, c_a, to the full water depth, d, in the fashion now commonly referred to as a Roussian distribution of suspended sediment:

$$C_z = C_a.\left[\frac{z_a}{z}.\frac{(d-z)}{(d-z_a)}\right]^{\frac{w_s}{\kappa u^*}} \qquad \text{(Eq. 3.18)}$$

whereby C_z and C_a are the mass/volumetric sediment concentrations [M/L^3 or L^3/L^3] at heights z and z_a above the bed, κ is von Kármán's constant, and u^* is the shear velocity. The exponent $w_s\ /\kappa u^* = R$ is known as the Rouse exponent.

The above relation indicates that the relative sediment distribution (for a given particle size and hence a particular settling velocity, w_s) is a function of relative depth only, and can only extend to a given arbitrary depth such that the concentration at that depth does not affect the fluid-mixture density nor the velocity distribution (hence the notion of a reference concentration, C_a at the reference height z_a). The vertical distribution of suspended sediments can only be computed for rough turbulent flows where a log-law is valid, and provided the log-layer extends to the free surface. A major disadvantage here is that the profile assumes the concentration is zero at the surface (Raudkivi, 1976). Einstein (1950) emphasised that the suspended load theory only determines the local distribution of sediment and not the absolute amount of suspended sediment in transport. The concentration at the lower edge of suspension in equilibrium conditions is extended down to the bed layer, to account for the fact that this theory only describes locally-derived bed sediments. It follows that the problem is thus reduced to one of determining the concentration at the upper boundary of the bed layer, defined as the weight of solids per unit volume of the water sediment mixture. Einstein assumed that this bed layer is only two diameters thick, and as such, the concentration within the bed layer must be constant (*ibid.*). Quantifying the reference concentration or specifying the height at which it can be defined (*i.e.* specifying the lower boundary condition of the problem, or the reference concertation, C_a, at the reference height, z_a) is a rather contentious problem, particularly as the upper limit of the bedload cannot be strictly defined and arbitrarily chosen limits are commonly used, based on bed grain properties, degree of packing, bed porosity and density, availability of local sediment at the bed, the Shields' entrainment parameter, and existing skin friction and bedform configuration (van Rijn, 1984b; Nielsen, 1986; Drake and Cacchione, 1989; Garcia and Parker, 1991; Green and Black, 1999; Agrawal and Traykovski, 2001; Lee et al., 2004).

While still enjoying unparalleled utility in modelling suspended sediment transport, the Rouse profile can be scrutinised as it seems that the validity of nearly all of its underlying assumptions has been questioned in the literature, not least of which is the use of the mixing length hypothesis. At the very heart

of the problem lies the turbulence closure problem, whereby resorting to a one-equation closure model through specifying a particular vertical structure of eddy viscosity dictates the vertical distribution profile of suspended particles. As such, many eddy viscosity closures have been applied to model the vertical distribution of suspended sediments within the RANS – ADE framework. Nielsen and Teakle (2004) presented a finite mixing-length model to both momentum and sediment profiles in the 'constant stress layer'; which described differential diffusion, and thus described the upward-convex concentration profiles of fine sediment above wave ripples, and the upward concave profile of coarse sediment concentrations. A similar model was also presented by Absi (2010). Camenen and Larson (2008) estimated sediment diffusivity by assuming a linear combination of mixing due to breaking wave and energy dissipation in the bottom boundary layer due to the mean current, wave, or combination of both, and a reference concentration that varies with Shields' parameter, yielding satisfactory predictions within a tidal inlet. Huang et al. (2008) modified the Rouse-equation to account for a stochastic behaviour of the vertical diffusion flux. Bose and Dey (2009) proposed a two-parameter sediment diffusivity defined by a depth modification factor and the reciprocal to the Prandtl-Schmidt number. Cheng et al. (2013) showed that this type of parametrisation yields improved predictions of suspended sediment concentration. Amoudry et al. (2013) suggested that a constant (height invariant) sediment diffusivity coupled with a Shields-number-dependent reference concentration was sufficient to describe the vertical distribution of wave-averaged suspended sediment concentrations above steep ripples under waves in 2D RANS models. Besides the plethora of profile realisations; it is crucial to consider the time-dependent variability of a particular eddy viscosity profile; particularly when dealing with unsteady flow. More recently, a new class of so-called fractional dispersion models have been proposed to describe the transport of sediment in turbulent flows, at the heart of which lies the stochastic approach introduced in the seminal work of Einstein (1950). These models consider both the random variations in time of a given sediment motion (particle residence time and memory) besides the randomness of the path itself (Ganti et al., 2009; Ganti et al., 2011), to account for non-local hydraulic effects

at a distance (Meerschaert et al., 1999; Benson et al., 2000; Meerschaert et al., 2002; Baeumer et al., 2005; Yong et al., 2006; Baeumer and Meerschaert, 2007; Wheatcraft and Meerschaert, 2008; Schumer et al., 2009). This highlights a shift towards process-based modelling of sediment entrainment and suspension, at the heart of which lies a recognition of the intermittency of the problem due to coherent turbulence structures; and an appreciation for the need to account for the non-linear interactions and feedback between these motions and the entrained sediment.

3.5.3 Interactions between coherent structures and suspended sediment

Describing the suspension of sediment accurately is intrinsically linked to an accurate description of the turbulent fluid flow inducing it. Nonetheless, the feedback imparted by the suspended particles on the flow may have significant implications on the maintenance of suspension and on subsequent suspension events. A crucial assumption of the ADE framework is that particles are passive scalars, obeying a linear relation to the turbulent motions. This particularly is a contentious issue as these suspension events display characteristics rather remarkably different from those of the advecting velocity field. Warhaft (2000) reviewed the existing experimental literature and concluded there exist many departures from the expected behaviour given by the classical theory. The author lists the existence of an exponential tail in the scalar signal while the velocity is Gaussian; a strong intermittency within the inertial sub-range at low Reynolds numbers which is absent in the velocity field; a clear contrast between the scalar and velocity spectra; and anisotropy in the inertial range (defying the fundamental notion of local isotropy in turbulence theory) and in the dissipation and inertial scales (*ibid.)*. He also reports, inconclusively, a particular dependency on Schmidt's number, and that at high Schmidt and Reynolds numbers, velocity dissipates at scales smaller than the scalar (sediment) fluctuations. This is inconsistent with Batchelor's prediction for turbulence cascades, displaying two dissipation scales, both Kolmogorov and Batchelor's wave numbers (Tennekes and Lumley, 1972). This disparity has been the foundation for the argument in favour of a convection-diffusion approach for oscillatory flows, which employs a convective distribution

function and accounts for time dependency and can explain sediment 'boils' under breaking waves (Nielsen, 1992; Duy and Shibayama, 1997; van Rijn, 2007b).

Further complications are introduced by the feedback mechanism whereby sediments put into suspension by the mean flow (and associated turbulent fluctuations in 3 dimensions) would then alter the structure of the boundary layer through turbulence damping and stress reduction (Gust, 1984). Drag reduction is often associated with cohesive sediments (Gust, 1976; Gust and Walger, 1976; Cloutier et al., 2006; Thompson et al., 2006); yet accurate calculation of suspended sediment profiles must account for density stratification and the effect of sediment mixtures (McLean, 1992). Smith and McLean (1977) described damping due to sediment concentration-gradient-induced stratification over sand waves, with reduction of eddy diffusivity. This has implications for particle settling and shear stress, particularly in regions where a density gradient exists such as vortex-entrained sediment, and thus these interactions cannot be neglected. Tooby et al. (1977) conducted experimental and theoretical investigations into the interaction between a particle and an idealised turbulent eddy core. Their experiments shows that particles followed nearly closed, spiralling orbits and thus remained in suspension for long times within the fluid even when the flow velocity opposed the particle's own motion. They suggested that for particles to remain suspended, the interaction with coherent flow structures is such that the fluid within an eddy core preferentially opposes that of the particles. Therefore, the time-averaged velocity affecting the particles in suspension differs from that of the space-averaged velocity of the fluid.

By relaxing the assumptions underpinning the advection–diffusion equation (ADE) governing the behaviour of single particles, the stochastic framework given by the fractional advection – dispersion equations treats the problem from a non–local perspective (collective behaviour of particle transport). This attempts to describe particle motion with memory in time based on particle residence time distribution, and account for variation in the flow field over the entire spatial domain (Schumer et al., 2009). This approach has been motivated

by a need to describe the non–local effect of sediment suspension due to turbulent bursting, which may sweep particles from the water column or eject them upwards resulting in a diverse pattern of dispersion over larger distances than those described classically (Chen et al., 2013). It provides a means of utilising the traditional ADE–based equations (such as the Rouse profile model), modified by a fractional derivative, without the passive scalar constraints.

An alternative class of models attempts to resolve the problem from a multi–phase perspective, accounting for differences in velocities between sediment particles and the surrounding fluid, and interactions between sediment particles and the fluid, inspired by similar approaches in chemical, biological and mechanical engineering. This formulates the problem either as a two–phase system of particulate solids and the fluid (Crowe et al., 1996; Greimann et al., 1999; Amoudry et al., 2005; Chauchat and Guillou, 2008; Amoudry and Liu, 2009; Nguyen et al., 2009; Chauchat et al., 2013), or as a combined phase/mixture treating the particle–laden viscous flow as a single fluid (Armanini and Di Silvio, 1988; Phillips et al., 1992; Charru and Mouilleron-Arnauld, 2002; Charru and Hinche, 2006; Mukhopadhyay et al., 2009; Ouriemi et al., 2009; Penko et al., 2011; 2013). In the former, the conservation equations of mass and momentum are derived for each of the phases by averaging the local instantaneous equations in space, time, or both; and introducing interfacial terms for momentum, stress and turbulence correlations (Chauchat and Guillou, 2008). In the latter, the momentum equations for the fluid–sediment continuum are combined, while parameterising inter– and intra– phase interactions such as effective viscosity, hindered settling, shear–induced diffusion, *etc.* (Penko et al., 2013). The coupling can be two–way for dilute suspensions, accounting only for fluid–sediment interaction; or a four way coupling for dense suspensions adding the effects of particle–particle interactions (Elghobashi, 1991; Balachandar and Eaton, 2010).

3.6 Concluding remarks

Despite the unceasing efforts of practicing scientists and engineers, and our ever increasing computational prowess, perhaps a really universal turbulence model may never be realised notwithstanding the emergence of some nearly universal features (Rotta, 1986; Bradshaw, 1994; Lu et al., 2010). The multiplicity of scales, both in time and space, of the eddies which define vorticity in the flow, and how these distort and vary in response to external fluctuations along the thinly sheared layers of flow are important processes to consider, in order to understand how entrainment and fluid transport occur (Hunt et al., 2010). A statistical approach is needed to describe averaged flow quantities, and hence time-averaged sediment transport erosion and deposition from and towards the bed, and advection of the suspended plume, and yet a structural understanding of coherent flow structures is necessary for better description of sediment entrainment and accurate estimates of intermittent sediment dynamics. With increasing strides in modelling turbulence and sediment suspensions, there remains no clear resolution of the scale of interaction between these structures and suspended particles, and the feedback imparted by particles on the dynamics of turbulent motions in space and time. Therefore, shedding light into the spatial and temporal relationship between the vertical structure of turbulence in the bottom boundary layer and the ensuing suspension of sediments is be of immense practical relevance, were sediment grains to be considered passive scalars or to have a direct influence on the flow structure itself. This characterises a trend towards deterministic process–based models of sediment transport, compared to the more traditional parameterised engineering formulae incorporated into (behavioural) morphological models at larger scales (Amoudry and Souza, 2011; van Rijn et al., 2013). While process–based models may require long computational times and be restricted to specific flow conditions, they can resolve the vertical (and occasionally horizontal) structure of time–dependent velocity and sediment concentration. The pressing need for research focusing on sand transport processes in shoreface (non–breaking waves), surf and swash zones employing field and controlled laboratory experiments, supporting process–based

modelling, was recently highlighted in a vision paper on future research needs in coastal sediment dynamics (van Rijn et al., 2013).

Advanced visualisation and data analysis techniques reveal complex interactions between passing coherent energetic structures and sediments in suspension, such as particle response to turbulent fluctuations in the frequency domain (Liu et al., 2012), and modifications of the mean velocity profile by the dispersed sediments (Ji et al., 2013). Increasingly, sediment suspension models are starting to account for turbulent bursting, generally by implementing entrainment functions that theoretically account for the average time and space scales of these motions (Cao, 1997; Wu and Yang (2004)), Wu and Jiang (2007). Considerable recent work is focussing on the structural form of these features of flow, and their role in fluid and sediment entrainment, bed shear stress generation, energy transfer and velocity asymmetry; and the influence of the space-time structure of the flow, with emphasis on oscillatory flows, and different bed roughnesses (Okamoto et al., 2007; Carstensen et al., 2010; Hardy et al., 2010; Adrian and Marusic, 2012; Carstensen et al. (2012); Grigoriadis et al., 2013; Hare et al., 2014). In order to accurately model suspension events, it is necessary to understand the mechanisms through which large-scale turbulent vortex structures are generated, their highly-non-linear dynamics; and the processes that leads to their breakdown and dissipation (Vittori, 2003). Moreover, most studies are often restricted to steady flows (current-only) or oscillatory flows; and very little is known about the characteristics and dynamics of coherent structures in combined wave current flows which often characterise fluid motion in the coastal zone. This work attempts to further investigate the complex interaction between bed-generated coherent turbulence structures and suspended non-cohesive sediment transport in unsteady boundary layers, under (non-breaking) wave-dominated and combined wave-current flows at prototype scale, focussing on statistical and spectral characteristics of these vortices, and the space-time dynamics of coherent structures and vortex-entrained suspensions.

Chapter 4.

Quantifying the Dynamics of Coherent Structures

> " Vether it's worth goin' so much, to learn so little, as the charity-boy said ven he got to the end of the alphabet, is a matter o' taste " Charles Dickens (1836) - *The Posthumous Papers of the Pickwick Club*

4.1 Introduction

The dynamics of coastal sediment transport are extremely complex, not least due to the unclosed turbulence problem (cf. Chapter 2, §2.3), but also due to the highly non-linear interactions between flow (waves and/or currents), sediment and the seabed. This, coupled with limitations in computational resources needed to fully resolve the problem in all its temporal and spatial scales at high Reynolds numbers typical of the problem, has resulted in a heavy reliance on experimental laboratory and field research. Prototype scale experiments provide controlled reproduction of fluid and sediment behaviour as observed in the field with minimal scaling artefacts. To achieve the objectives of this thesis, results from two prototype-scale experiments are reported, with high-frequency measurements of velocity (and turbulence), bed morphology and suspended sediments. The first experiment focuses on coherent structures and wave-induced suspensions under irregular erosive and accretive waves in the nearshore. The second experiment focuses on the space- time dynamics of coherent structures under combined wave-current flows, with currents aligned and opposed to the direction of wave propagation. The details of each experiment are presented in the chapters 5 and 6, respectively. This chapter describes some of the tools applied to quantify the flow and turbulent properties, educe coherent structures, and describe the interaction (space-time dynamics) between coherent turbulent structures and suspended sediments over mobile bedforms.

4.2 Measuring turbulent structures

Coherent turbulence structures are relatively obvious in visualisation studies, yet quantitative assessment of their dynamics within the benthic boundary layer remains quite challenging. With volumetric/tomographic measurements of the flow velocity in the field still limited to small scale flume experiments (the technology is just starting to emerge for field-deployable particle image velocimetry), pointwise (single or profile) measurements using acoustic or optical techniques are the predominant tool for characterising turbulence in the field; and inferring the structural attributes of organised features within the flow. At high turbidity, the quality of optical transmission deteriorates rapidly, and as such acoustic instruments are often deployed in highly energetic settings where sediment is likely to be in suspension at high concentrations. In particular, acoustic Doppler velocimeters (ADVs) have become the instrument of choice for laboratory and field, high-frequency measurements of velocity and its fluctuating components in three dimensions (Goring and Nikora, 2002).

ADVs operate using the Doppler shift principle, whereby velocity is calculated as a function of the phase lag between two acoustic pulses of different durations, transmitted with some time lag; and then backscattered, due to particulates within the flow, inside a small sampling volume situated at a small distance from the probe head (MacVicar et al., 2007). This ensures that the measurements are relatively non-intrusive; away from the direct effect of the probe. Nonetheless, raw ADV measurements in highly dynamic settings are often prone to electronic contamination related to the ability of the electronic circuit to resolve phase differences between pulses (Voulgaris and Trowbridge, 1998) and acoustic (Doppler) noise influence aliasing the return signal (Nikora and Goring, 1998). ADV measurements under shoaling and breaking waves in the nearshore and surf zones are also susceptible to spikes due to entrained air bubbles within the flow (Goring and Nikora, 2002). Further sources of errors include lack of submergence under wave troughs, biofouling and blockage (*e.g.* by floating kelp), and insufficient distance between the sampling volume and an accreting sea floor (Elgar et al., 2005), while estimates of stress may be sensitive to sensor misalignment (Soulsby and Humphery, 1990; Elgar et al.,

2001). Nevertheless, the inherent zero-drift, and highly accurate velocity measurements make ADVs suitable for mean flow measurement, as well as accurately estimating turbulent properties including Reynolds stresses, eddy statistics, production and dissipation of energy; and a number of techniques have been identified for detection, quality control, and correction of corrupt measurements (Nikora and Goring, 1998; Trowbridge and Elgar, 2001; Goring and Nikora, 2002; Elgar et al., 2005; Feddersen and Williams, 2007; Mori et al., 2007; Feddersen, 2010; Feddersen, 2012a; Spydell et al., 2014).

4.2.1 Extracting turbulent components from ADV measurements

Accurate estimates of velocity and turbulence using an acoustic Doppler velocimeter require that the strength of the received backscatter signal amplitude exceeds the background (system) noise. A typical ADV measures the three-dimensional flow field, giving streamwise (u; along-flow), cross–wise (v; across-flow, horizontally orthogonal to u); and vertical (w; wall-normal) components of instantaneous velocity, respectively, and reports the corresponding signal-to-noise ratios (SNR) and beam correlation coefficients within the small, cylindrical sampling volume; often considered as single point measurements. Beam correlations account for successive returns from different scatterers within the flow (Cabrera et al., 1987). Measurement ensembles are thus chosen, often arbitrarily, such that a compromise is reached whereby a high quality time series with few exceptional low SNR values (following manufacturer's recommendation) is retained, whereas time-series with corrupted sections are often rejected. The size of statistical fluctuations is almost proportional to the square root of the sampling frequency. Thus, for quality control purposes, Elgar et al. (2005) suggest a correlation threshold based on the instrument sampling frequency (F_s) , given by:

$$Correlation\ threshold = 0.3 + 0.4\sqrt{\frac{F_s}{25}} \qquad \text{(Eq. 4.1)}$$

Measurements where the correlation value falls below the threshold are removed, and replaced by some means of interpolation (Thompson et al., 2012). Subsequently, it is important to ensure no sequence of bad data exceeds the time scales of turbulent fluctuations, so as to avoid an artificially synthesised data set, and as such, interpolated gaps are often limited to within 1- 2 seconds (Elgar et al., 2001). The effects of sensor misalignment with the mean flow direction can be corrected geometrically, by rotating the 3D axis of measurements to eliminate horizontal velocity 'leaks' into estimates of the vertical velocity component, and vice-versa due to relative tilt, θ (rd), between observed and true velocity directions in the main (streamwise-vertical) plane of motion (X-Z), following (Elgar et al., 2005):

$$w_{observed} = w_{true}\cos(\theta) + u_{true}\sin(\theta) \qquad \text{(Eq. 4.2)}$$

$$u_{observed} = u_{true}\cos(\theta) + w_{true}\sin(\theta) \qquad \text{(Eq. 4.3)}$$

The angle (θ) can be calculated from the cross-spectra (CO) of the observed velocities according to linear wave theory in shallow water waves:

$$\tan(\theta) = \frac{CO(u_{observed}w_{observed})}{CO(u_{observed}u_{observed})} \qquad \text{(Eq. 4.4)}$$

A similar operation can be applied in the transverse planes (X-Z and Y-Z) to remove contamination of the streamwise and vertical components by horizontal transverse fluctuations.

Following the pre-processing of ADV measurements to ensure quality and robustness, turbulence can be extracted from the flow using a Reynolds decomposition of the time series; as the variation (fluctuation) of the instantaneous flow field about the time-averaged flow. Superimposed currents can be removed by de-trending (removing linear trends) while a wave-signal can be extracted by applying a moving average as a low pass filter, before removing it from the original waveform to obtain high–frequency turbulence (Thompson et al., 2012). This is essentially an all–zero filter, also known as a finite-duration impulse response (FIR) filter (Yong and Parker, 1983); that is a

zero–phase, digital filter which ensures zero–phase distortion by processing the input data both in forward and reverse directions (Kormylo and Jain, 1974). The numerator coefficients defining the filters window are often selected by trial and error, with autocorrelation and cross–correlation tests applied for validation. The filter is characterised by the coefficient vectors (numerator(s) and denominator(s)) implemented in the difference equation between forwarding and reversing the signal. To ensure an all-zero filter, the denominator coefficients of the filter are set to 1, ensuring a constant delay of 0 samples, whence zero-phase filtering (MathWorks, 2016).

Spike detection and removal from the signal is a bit more challenging, and a number of approaches have been proposed in the literature. We opt for the technique developed by Goring and Nikora (2002) which assumes that any point lying outside of a cluster of good data may be a spike, and this is more evident in phase-space where spike separation from the cluster is more evident in the derivatives of the high frequency components. Usually, this is an iterative process whereby an acceleration threshold is defined, or a wavelet thresholding technique is implemented as a universal criterion to identify locations of spikes within the time series. Goring and Nikora (2002) use a three-dimensional Poincare' map (a phase-space plot) of the variable and its derivatives; and points falling outside the ellipsoid defined by the universal criterion are designated as spikes. These are then replaced using a local, third-order (cubic) polynomial through several points at either end of the spike. Mori et al. (2007) modified the method to use the true 3D phase-space as opposed to the original 2D projection. To sum up, the modified 3D phase-space despiking method is given by the following algorithm:

a- calculate the first and second derivatives of the velocity component
b- calculate the universal threshold ($\lambda = \sqrt{2 \ln N}$) from a number of data N; and the correlation between u and its second derivative $\Delta^2 u$
c- plot the ellipsoid of $u, \Delta u$ and $\Delta^2 u$ and calculate the angle from the correlation between $u - \Delta^2 u$; identifying the major and minor axes
d- identify the points outside the ellipsoid and replace these by cubic interpolation; reiterating until no further spikes are recognised.

An example ADV measurement run from the Fast Flow Facility experiment (cf. Chapter 6) is given in Figure 4.1 whereby a series of monochromatic waves; 0.3 m high and with a peak period of 2 seconds; are super-imposed on a current opposing the direction of wave propagation. Measurements by a downward-looking ADV were collected over a period of 500 seconds at 25 Hz, at a wall-normal height of 0.181 m above the bed, in 1.05 m of (still) water. The time series of the streamwise velocity component, u, as well as its statistical and spectral properties are displayed following major data pre-processing steps leading to the de-spiked turbulence components. The boxplots show the 25th, 50th (median) and 75th percentiles of the sample in the bottom, middle and top of the box respectively, whereas the red (+) signs indicated outliers. The values of mean, skewness (skew) and kurtosis (kurt) are indicated in the histograms (the third vertical panel) and the spectral density functions (through a Fast Fourier transform using a Hanning window and 50% overlap) are also presented. The dashed, vertical red lines in the 4th vertical panel indicate spectral peaks corresponding to the peak wave period and corresponding half-cycle. The Kolmogorov-Obukohv rate of inertial dissipation (-5/3) is shown in the turbulence spectra (cf. §4.2.2.2).

The effect of the all zero FIR filter to remove the wave signal is demonstrated in Figure 4.2 with three arbitrary filter orders, defined by 3 numerator coefficient vectors used in the digital filter's difference equation between forwarding and reversing the signal through the filter. The influence of each of the tested filter coefficients on the signal is evident in the time series of the turbulence fluctuation, its statistical distribution, the prominence of peak wave periods observed in the power spectral densities and the spectral decay properties. The chosen filter (panel a) is a compromise between preserving the statistical properties of the distribution whilst attempting to remove the wave-signal aliasing without altering the spectral properties in the inertial sub-range. As such, a small wave-imprint is still observed (in minor peaks corresponding to wave and half-wave periods), and a Kolmogorov-Obukhov rate of energy transfer (-5/3) is observed within the inertial sub-range defined whose extents are calculated following Stapleton and Huntley (1995).

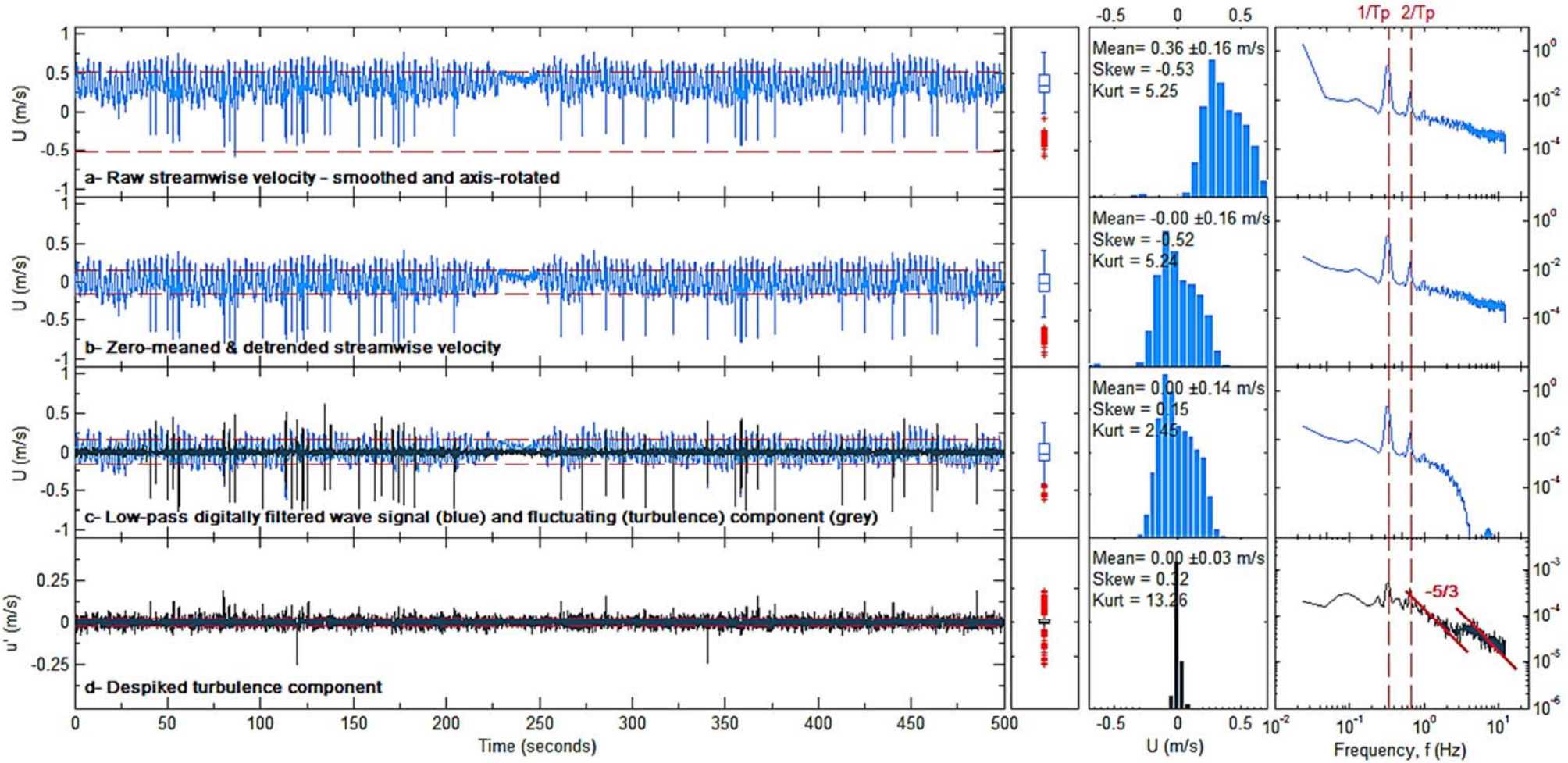

Figure 4.1 Pre-processing ADV measurements to extract de-spiked turbulence components. The horizontal lines in the time series indicate $\pm 1.0\,\sigma$ (standard deviation). Boxplots and histograms describe the statistical properties of the signal. Spectral densities are shown.

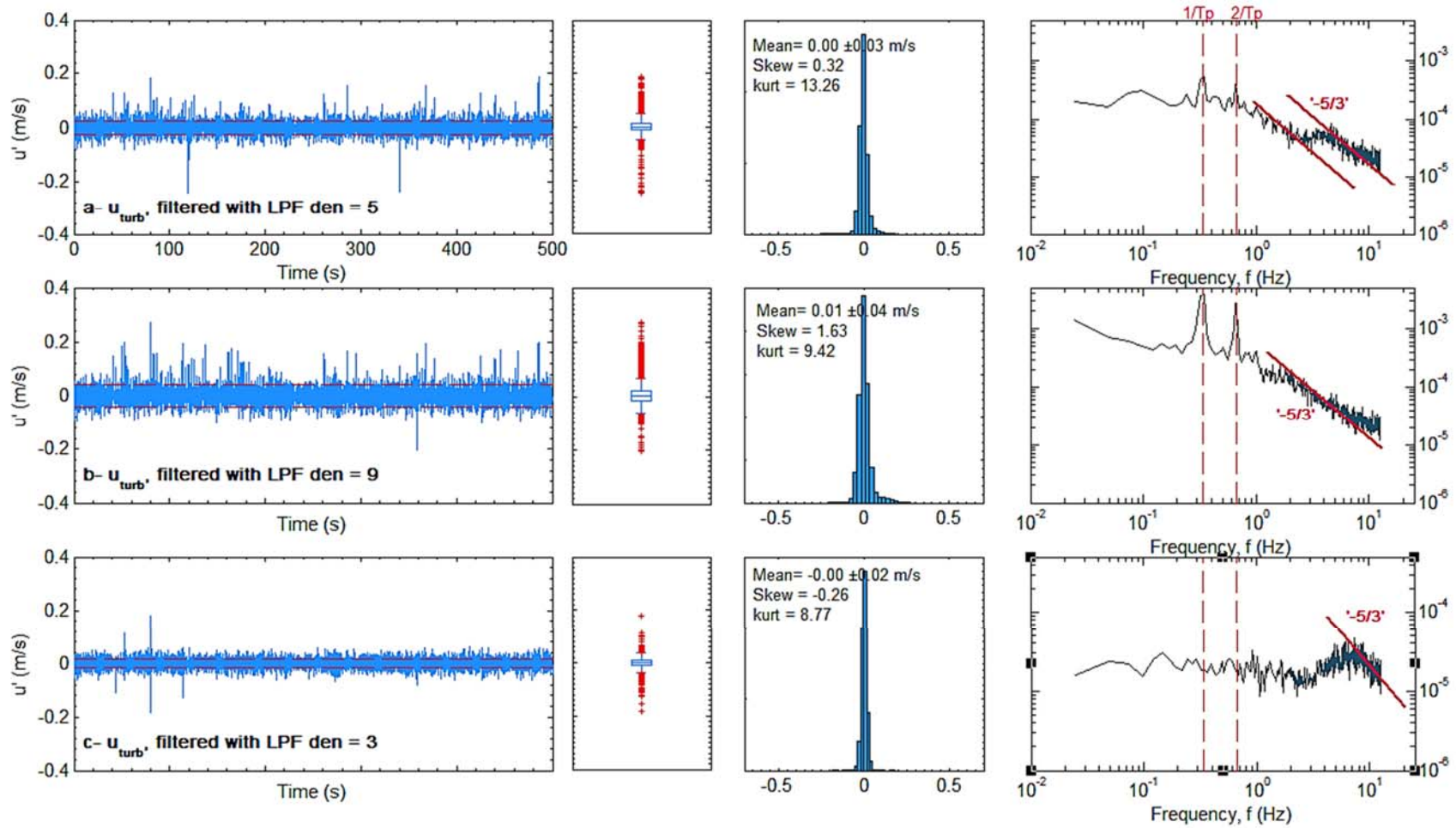

Figure 4.2 Effect of three filter orders of the low-pass filter (by varying numerator of the differencing equation in MATLAB) used to extract the wave signal from the velocity time series, on the resulting turbulence component.

4.2.2 Statistical description of turbulence

While the Navier-Stokes equations, which contain a full description of turbulence at all scales, are deterministic (conjectured to have a unique solution for all times given initial conditions); chaotic fluctuations remain the defining feature of turbulence despite the emergence of some coherent structures. If turbulent flows were set up repeatedly under the same conditions, the instantaneous values of the dynamic flow fields will inevitably be different each time (Monin and Yaglom, 1971). It follows that the velocity field of the solution to these equations can be considered a random function, depending on several space and time variables (Frisch, 1995). The randomness of the solution of such a deterministic system arises from unavoidable perturbations in initial conditions, boundary conditions and material properties, to which the flow fields are acutely sensitive (Pope, 2000). While distributions of instantaneous values of the flow fields in space are similar, they constitute a disordered set of three-dimensional fluctuations, thus lending themselves to a statistical study approach, with distinct mean values over time or spatial domain; and a prime example of that is Reynolds decomposition. Spectral estimates provide a suitable means of examining how turbulent fluctuations are distributed around an average from a statistical point of view. The time series of the fluctuating velocity (turbulence) components in three dimensions, extracted from the ADV records as described in §4.2.2 are thus used to describe mean turbulent properties, including Reynolds stresses and turbulent kinetic energy which can then be related to suspended sediment transport processes observed in the experiments reported in this thesis. These are also analysed spectrally to describe the scales of turbulent motions and their relationship to resuspension events both in space and in time.

4.2.2.1 Mean value functions

High frequency measurements of velocity provide information on the spatial structure of turbulence as it evolves in time. The application of a Reynolds decomposition to the Navier Stokes equations (hence RANS equations)

results in 'virtual' mean stresses, proportional to the coefficient of correlation between the components of turbulent velocity at a given point (Taylor, 1935). Thus, the time-averaged (denoted by ⟨ ⟩), Reynolds stresses are defined as velocity covariance, a second order tensor, whose off-diagonal components are shear stresses: $\langle u_i u_k \rangle = \overline{u'w'}$; $\langle u_i u_j \rangle = \overline{u'v'}$; $\langle u_j u_k \rangle = \overline{v'w'}$; and diagonal components are normal stresses $\langle u_i^2 \rangle = \overline{u'^2}$, $\langle u_j^2 \rangle = \overline{v'^2}$, and $\langle u_k^2 \rangle = \overline{w'^2}$ (Pope, 2000).

The mean value of a fluctuating quantity over a time, T, is by definition zero:

$$\overline{u_i'} = \lim_{T\to\infty} \frac{1}{T} \int_{t_0}^{t_0+T} (u_i - \overline{u}) dt \equiv 0 \qquad \text{(Eq. 4.5)}$$

and the product of the two fluctuating components is non-zero ($\overline{u'w'} \neq 0$) only when the two components are correlated (Tennekes and Lumley, 1972). The autocorrelation of a velocity component describes its dependence at a given time, t, on the values of another time with a time-lag, (Δt) is:

$$autoCorr\left(u'u'(t)\right) = \lim_{T\to\infty} \frac{1}{T} \int_{t_0}^{t_0+T} u'(t).u'(t+\Delta t) dt \qquad \text{(Eq. 4.6)}$$

When the time lag exceeds that required by an eddy to travel across the measuring volume, the velocity is statistically independent and the correlation tends to zero.

The fluctuation can be defined as the root mean squared (rms) velocity ($u_i' = \overline{u_i^2}^{0.5}$) at a given position across the boundary layer (Tennekes and Lumley, 1972). The turbulent kinetic energy per unit mass is defined as half the trace of the Reynolds stress tensor ($\frac{1}{2} \langle u_i . u_i \rangle$) in the fluctuating velocity field (*ibid.*), and thus the total, time-averaged kinetic energy (TKE) is given by root mean square turbulent velocities :

$$\overline{k_{TKE}} = \frac{1}{2}\left(\overline{u'^2} + \overline{v'^2} + \overline{w'^2}\right) \quad \text{(Eq. 4.7)}$$

The rate of change of the kinetic energy is due to work done by the pressure gradient, the transport by the turbulent velocity fluctuations, the transport by the viscous stresses and deformation of the fluid (rate of strain); which is evident when deriving the energy budget equation from the Navier-Stokes equations (Tennekes and Lumley, 1972).

4.2.2.2 Turbulence spectra and the integral scales of motion

The multitude of scales (both spatial and temporal) of turbulent eddies manifest in the bursting phenomenon comprise a spectrum ranging from the macroscale (long period and spatially limited only by the dimensions of the flow) to the high frequency microscale limited by viscosity, with the energy transfer being driven by vortex stretching (*ibid*.). Spectral analysis decomposes the measured turbulence data into waves of different periods (frequencies) and wavelengths, providing a suitable means of examining how these fluctuations are distributed from a statistical viewpoint (Tennekes and Lumley, 1972). The value of a spectrum at a certain frequency or wavelength equates to the mean energy of that wave, and as a result, it provides a means of assessing how eddies of different sizes exchange energy and how turbulence evolves with time. The three dimensionality of the problem necessitates construction of energy spectra in three dimensions (Cebeci and Smith, 1974). In fully developed turbulence, the rate of exchange of energy between scales must equate the rate of energy dissipation at the smallest scale. Kolmogorov (1941b) argued that the large eddies are anisotropic, and affected by the flow's boundary conditions, but as they chaotically break and transfer energy into smaller scales, they lose their directional bias and thus, the small scale motions are isotropic, and hence their statistics can be described universally. Within the inertial sub-range of scales, between large energy-containing scales and small dissipative scales, the spectrum of the turbulent kinetic energy, in wavenumber space, is given by:

$$E(k) = C_K \, \varepsilon^{\frac{2}{3}} \, k_\ell^{-\frac{5}{3}} \qquad \text{(Eq. 4.8)}$$

where C_K is the Kolmogorov constant, ε is the mean rate of energy dissipation, and $k_\ell = 2\pi/\ell$ is the wavenumber for scales of the size ℓ. The existence of this inertial sub-range depends on the full separation of scales between energy production and dissipation, which becomes more evident as the flow Reynolds number increases.

In wavenumber (k) space, the spectral energy for all eddies of size ℓ is roughly proportional to $E(k)$; the spectral energy distribution over wavenumbers, multiplied by the width of the measured spectrum, and the strain rate of an eddy of wave number k is given by (Tennekes and Lumley, 1972):

$$S(k) = \frac{(kE)^{0.5}}{2\pi/k} = \frac{(k^3E)^{0.5}}{2\pi} \qquad \text{(Eq. 4.9)}$$

The strain rate of an eddy is thus a function of its wavenumber, which is often scaled by the measuring height, z, into a non-dimensional form, $k^* = kz$. Hence, one can normalise the k^*-weighted spectra into an energy/variance preserving form, whereby an equal area under the curve represents equal energy, in the form $kE_{uu}(k)/\int_0^\infty E_{uu}(k)dk$ (Soulsby, 1977). Subsequently, it is possible to calculate the dominant (integral) eddy sizes by identifying the peak of the normalised, non-dimensional k^*-weighted spectrum, and backing out the relevant length scale, following (Soulsby, 1983; Soulsby et al., 1984). This approach can also be applied to passive scalars within the flow (*e.g.* estimating suspension cloud sizes).

In practice, nearly all turbulence measurements are collected as a time series at a fixed location. Taylor's theory of "frozen turbulence" suggests that turbulence is advected by the mean current more rapidly than it is developing temporally, and as a result, the measured turbulence fluctuations at a fixed point would correspond better to the spatial rather than temporal changes in

velocity (Taylor, 1938; Wyngaard and Clifford, 1977). Subsequently, this hypothesis is often invoked when evaluating the spatial structure of turbulence based upon time-resolved velocity measurements at a single point. Such an approximation is only valid when the turbulent fluctuations are small compared to the mean velocity (*i.e.* for small turbulent intensities) (Wilczek et al., 2014). Nonetheless, Taylor's hypothesis is limited by the fact that turbulent fluctuations also evolve in time, and this is particularly problematic when the magnitude of these fluctuations is comparable to that of the mean flow. The applicability of this hypothesis is thus strongly dependent on the scale of the structures being investigated (Higgins et al., 2012). Yet, even in the presence of large coherent structures, there is experimental evidence demonstrating the accuracy of such approximation in turbulent boundary layers, up to projections distances several times the thickness of the boundary layer thickness (Dennis and Nickels, 2008).

4.2.2.3 Estimating the rate of energy dissipation in the nearshore

Assuming turbulent diffusion to be negligible, the turbulent energy balance equation in the benthic boundary layer under non-breaking waves (seawards of the surf zone) can be represented as the balance between shear production, P, and dissipation, ε, as a steady state balance (Tennekes and Lumley, 1972; Trowbridge and Elgar, 2001; Feddersen, 2012a):

$$P = \varepsilon \qquad \text{(Eq. 4.10)}$$

For depth-limited wave breaking in the nearshore, the turbulent kinetic energy balance is between downward diffusion in the vertical due to the breaking wave, and dissipation (Feddersen, 2012b):

$$\frac{d}{dz}\left(K_s \frac{dk}{dz}\right) = \varepsilon \qquad \text{(Eq. 4.11)}$$

where z is the height above bed, K_s is eddy diffusivity, and ε is dissipation rate. The turbulence dissipation rate, ε, can be estimated from the velocity

spectrum following (Feddersen and Williams, 2007; Feddersen, 2012a; Feddersen, 2012b):

$$\varepsilon = \left\langle \left[\frac{P_{ww}(f) 2\ (2\pi)^{\frac{3}{2}}}{\alpha\ M_{ww}(f; \overline{u}, \sigma^2_{u,v,w}} \right]^{\frac{2}{3}} \right\rangle \qquad \text{(Eq. 4.12)}$$

where $\alpha = 1.4$ is Kolmogorov's constant, $\overline{u}$ is the mean horizontal current, $\sigma^2_{u,v,w}$ is the wave-dominated, three-dimensional velocity variance; M_{ww} is an integral of the 3D wave-number space converting the inertial subrange relation $k^{-5/3}$, from wavenumber to frequency domain (Trowbridge and Elgar, 2001).

4.3. Educing coherent structures and their dynamics

In the absence of quantitative means of measuring vorticity fields in three dimensions at scales encountered in the field, and thus identifying coherent structures as defined by Hussain (1983), single point measurements at high frequencies, such as those afforded by an ADV have proven to be of significant utility. A number of approaches have been proposed, including quadrant analysis, octant analysis, and pointwise Hölder exponents (Keylock, 2008). Quadrant analysis, based on cross-correlations between orthogonal velocity components, is perhaps the most common technique for structure identification, following the leading work of Wallace et al. (1972) and Willmarth and Lu (1972).

4.3.1 Structure identification using Quadrant and Octant analysis

The first quadrant analysis of the Reynolds stresses was conceived by Wallace et al. (1972) to quantify the visual observations of Corino and Brodkey (1969) in the boundary layer, based on the sign (positive or negative) of the streamwise and wall-normal velocity fluctuations. Similarly, in an attempt to measure the intermittency of the bursting processes and support the claim to their role in the production of turbulent energy and Reynolds stress,

Willmarth and Lu (1972) applied conditional sampling to the velocity field in the boundary layer of a smooth flat plate, while Papadimitrakis et al. (1986) reported similar work in water waves. The Reynolds stress in the main plane of motion is described by the inverse correlation between the time–average streamwise (u') and vertical (w') fluctuations of velocity at a point:

$$Reynolds\ Stress;\ \tau_{xz} = -\rho\ \overline{u'w'} \qquad \text{(Eq. 4.13)}$$

Quadrant analysis was employed as a technique for detecting various turbulence structures. This consisted of distributing streamwise and vertical velocity fluctuations into the four quadrants of the ($u'v'$) plane (Deleuze et al., 1994). In a quadrant plot of $u'$and w', Wallace et al. (1972) found that the second and fourth quadrants (Q1 and Q4) correspond to the ejection and sweep motions identified by Corino and Brodkey (1969); and called Q1 and Q3 motions 'outward' and 'inward interactions'. Subsequently, four types of event structures may be distinguished based on the simultaneous, instantaneous fluctuating velocity components: (a) an ejection where a low speed fluid ($u' < 0$) near the bed moves upward ($w' > 0$); (b) a sweep where a high velocity fluid ($u' > 0$) moves downwards to the bed ($w' < 0$); (c) inward interactions (II) where ($u' < 0$) an ($w' < 0$); and (d) outward interactions (OI) where ($u' > 0$) an ($w' > 0$). "Ejections/bursts" and "sweeps" are associated with a negative value of $u'w'$ and consequently a positive Reynolds stress, and the largest contributions to stress often occur in the quadrants denoting ejections and sweeps, even though these occupy shorter amounts of time (Soulsby, 1983). Wallace (2016) identifies Q2 and Q4 events as gradient-type motions whereby the vertical momentum fluxes are partially due to motion up and down the mean vertical gradient, with streamwise momentum less than and greater than the local mean streamwise momentum, respectively. Conversely, Q1 and Q3 are counter-gradient-type motions. These four event types are often associated with the passage of a coherent structure which induces velocity fluctuations (Zhou et al., 1999). For instance, a low speed near bed fluid pumped upwards between the legs of a horseshoe vortex encountering high speed streamwise fluid is manifest by a

second quadrant (Q2) ejection-type event, often associated with vertical entrainment of bed sediment. Using a vortex detection criterion for DNS results, Jeong et al. (1997) showed that spatial difference between $u'$and w'within a fully developed coherent structure dictate the dominance of a particular motion (*e.g.* Q4 over Q2 events near the bed). By examining the spatial extent of these events, they suggest that large Q2 and Q4 events typically lie on either side of the vortex (inward and outward legs of the vortex) and Q1 and Q3 regions lying below and above the vortex head, confirming earlier results by Robinson (1991). More recently,, Lozano-Duran et al. (2012) DNS results showed that Q2 and Q4 events are mostly grouped at side-by-side pairs and predominant coherent structures are formed by such a pair being embedded within the base of the Q2 motion, and underneath the Q4 motion forming wall-attached eddies. Typically, ejections (Q2 motions) are associated with entrainment of mass (sediment particles) into suspension, while sweeps (and sufficiently frequent outward interactions) are effective at transporting bedload or sediments in continuous contact with the bed (Heathershaw, 1979; Soulsby, 1983; Dyer and Soulsby, 1988; Cao, 1997; Keylock, 2007; Yuan et al., 2009).

Willmarth and Lu (1972) extended the quadrant analysis of Wallace et al. (1972) by focussing on the intense Reynolds stress events. Their approach to determining the fractional contribution of each of the four aforementioned structural features was restricted to values that lie above a critical threshold, H, which defines the hole between a set of hyperbolae defined by:

$$|u'w'| \geq H.\left|\overline{u'w'}\right| \qquad \text{(Eq. 4.14)}$$

Hence, the contributions of individual events in the (u'w') plane are the ones which occur in each quadrant outside the central "hole" region bounded by the four hyperbolae defined by the Equation 4.14. This is illustrated in Figure 4.3 where the Reynolds stress occurrences are delimited by two hole regions, based on a variation of Equation 4.14 which uses rms velocity covariance rather than averaged product of the two components. The process outlined

in Cellino and Lemmin (2004); and Longo et al. (2012) is used to calculate the concentrations within each quadrant (i) as follows:

$$C_H^i = \frac{1}{N} . \sum_{j=1}^{N} \phi_{\mathrm{H,j}}^i \qquad \text{(Eq. 4.15)}$$

$$\phi_{\mathrm{H,j}}^i = \begin{cases} 1 \text{ if } |u'w'|_j > H . u'_{rms} . w'_{rms} \text{ and belongs to } i^{th} \text{quadrant} \\ 0 \text{ otherwise} \end{cases} \qquad \text{(Eq. 4.16)}$$

There is no common definition of the threshold restricting the hole size, and its value is commonly chosen arbitrarily (Keylock, 2008). Bogard and Tiederman (1986) determined $H \cong 1.0$ to be their optimal threshold for detecting ejections and this value has been commonly used by Nagano and Tagawa (1995) to track quadrant events. Alternative definitions of the threshold detection criterion have been defined in terms of the standard deviations of the components, autocorrelation, variable interval time–averaging variance, statistical/probability distributions *etc.* (Blackwelder and Kaplan, 1976; Bogard and Tiederman, 1986; Wu and Yang, 2004; Keylock, 2007). Extending quadrant analysis into three dimensions, known as Octant analysis, is less common, given that the cross–wise flow component is often assumed less important (Gheisi et al., 2006; Ölçmen et al., 2006). In both quadrant and octant analysis, as the threshold increases, the number of exceedances decreases, biasing the stress magnitude to be mostly contributed by ejections in the second quadrant (Willmarth and Lu, 1972; Keylock, 2007).

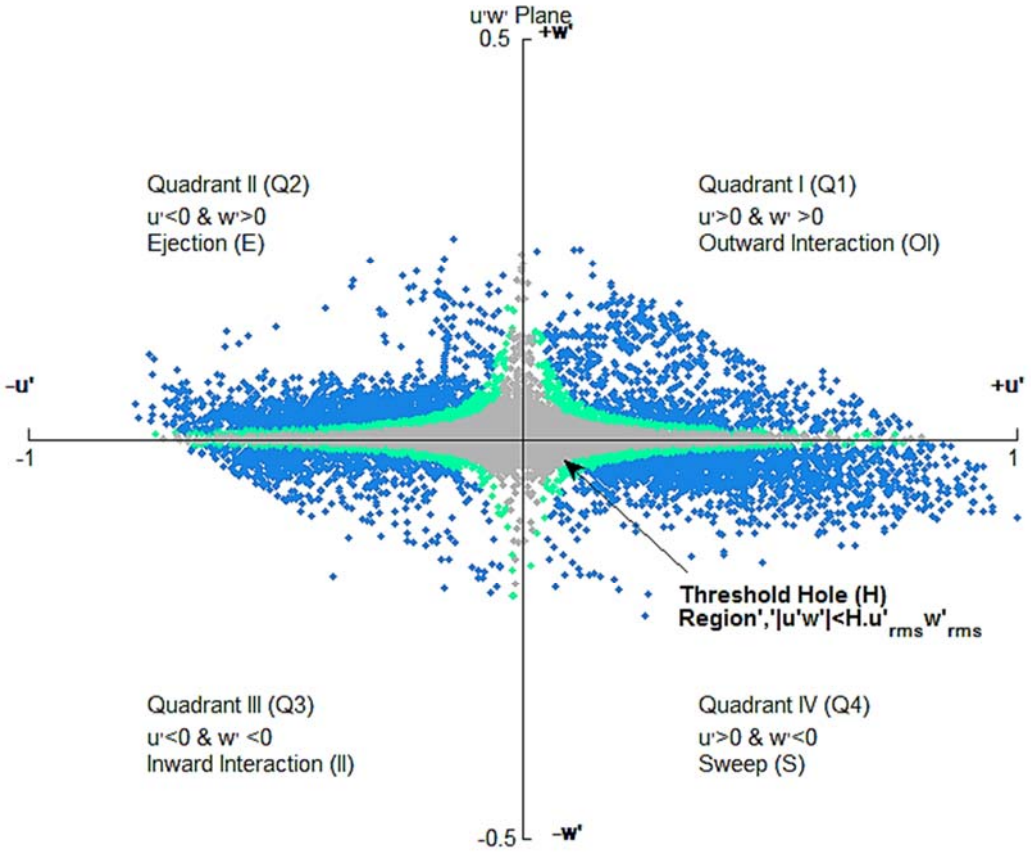

Figure 4.3 An example of quadrant analysis of the Reynolds stress in the streamwise-vertical plane (taken from Bardex II experiment, cf. Chapter 5). Areas delimited by hole sizes defined by H=1 (grey) and H =2 (green) are highlighted.

4.3.2 Space-time dynamic using wavelet transforms

Wavelets analysis has recently become one of the more lucrative mathematical tools for the evaluation of signals, time series, images, fields and patterns, and are increasingly being adopted by fluid mechanists to examine turbulent flows (Farge, 1992; Schneider and Vasilyev, 2010). Wavelets possess several attractive mathematical properties, the most important of which is their ability to perform efficient multi–scale decomposition (Kumar and Foufoula-Georgiou, 1997; De Stefano and Vasilyev, 2012), identify and isolate localised structures such as vortices in physical and wave–number spaces (Farge et al., 2001; Farge et al., 2003; Khujadze et al., 2011), and to analyse localised variations of power within a time series (Daubechies, 1990;

Torrence and Compo, 1998; Grinsted et al., 2004). In this respect, wavelet analysis conveniently lends itself to the study of turbulence, and particularly that concerned with coherent structures.

Traditionally, Fourier analysis is used to study turbulent flows and identify integral scales of motion (energy containing range), stemming from a classical understanding of the turbulent energy cascade (Frisch, 1995). This statistical view was quantified by Kolmogorov–Obukhov into the well–known $k^{-5/3}$ law in the inertial subrange, where wavenumbers are larger than those of the integral scale of motion yet smaller than the dissipative scales, with k being the wave–number for the energy spectrum in Fourier Space (Monin and Yaglom, 1971; Tennekes and Lumley, 1972; Frisch, 1995). The presence of coherent structures cannot be resolved by Fourier transforms which are inherently space–filling, and hence fail to capture their locality. Conversely, wavelets are able to expand time series into time-frequency space and thus determine localised intermittent periodicities (Farge, 1992; Grinsted et al., 2004). Using cross wavelet transforms, the causality between two time series can be scrutinized by examining whether regions in the time–frequency space with large common power have consistent phase relationships. Wavelet multi–resolution analysis is capable of detecting and tracking energetic fine–scale motions (Schneider and Vasilyev, 2010). Wavelets therefore offer a unique hierarchical framework for modelling and simulating flows, either by means of wavelet–based discretisation of the Navier–Stokes equations adapted to the local resolution of intermittent flow structures (Okamoto et al., 2007; Schneider and Vasilyev, 2010), or through coherent vortex extraction/simulation (Farge et al., 1999; 2001; Farge and Schneider, 2001).

4.3.2.1 Wavelets: properties and characteristics

Wavelet transforms (WT) originated from an industrial research need to analyse seismic reflection data resolving power, energy and frequency of quasi–periodic wave propagation (Morlet et al., 1982a; Daubechies, 1990). The method needed to separate the contributions of different frequency bands without excessive loss of resolution, and be able to reconstruct the

original function robustly (*i.e.* stable under small perturbations) with arbitrary high precision (Goupillaud et al., 1984). Morlet et al. (1982b) showed, both experimentally and theoretically, that using complex models of wave numbers and physical properties of a medium, 'wavelets' can preserve both phases and amplitudes for a large range of frequencies. These wavelets are generalised basis functions (integration kernels; with zero mean), localised in both physical and wavenumber space, owing to their rapid decay/compact support and their vanishing moments and smoothness, respectively (Grinsted et al., 2004; Schneider and Vasilyev, 2010). By comparison, a Fourier transform is based on trigonometric functions that are well–localised in wave–number space, but not physically within a series as they have global support.

A wavelet transform is in essence a linear operation which decomposes a given signal into components that appear at different scales, based on convolution of the signal with a dilated filter (Mallat, 1991). The mathematical underpinning of such a technique was provided by Grossmann and Morlet (1984), who showed that the transform satisfies energy conservation, and the signal can be reconstructed from its wavelet transform. However, the uncertainty principle (of Heisenberg) dictates that one cannot obtain arbitrary good localisation in both time and frequency, and a trade–off must exist whereby spatial resolution is bad at large scales while scale resolution is bad in the small scales (Foufoula-Georgiou and Kumar, 1994; Lau and Weng, 1995; Farge et al., 1996; Grinsted et al., 2004). Hence wavelets have the unique ability to be scaled to match most high and low frequencies with minimal number of base functions, thus permitting localisation of short–lived high–frequency signals in time, yet still resolving low–frequency variability (Lau and Weng, 1995). In Fourier space, one computes transfer between different independent wavenumber bands detecting modulations and resonances excited under the flow dynamics, while in wavelet space one computes exchanges between different locations and different scales, detecting advections and scaling instead (Farge et al., 1996). Therefore, comparing transfers calculated by means of wavelets, wavelet packets, and

Fourier modes is deceptive, and these three approaches measure different processes.

4.3.2.2 Continuous and Cross Wavelet transforms

Mathematically speaking, a wavelet transform (WT) decomposes a signal (time series) in terms of some elementary functions derived from a single 'mother' wavelet by dilation (stretching and compression) and translation (Daubechies, 1990; Lau and Weng, 1995). The analysing function has to be admissible, *i.e.* be an integrable function with a zero average, and the scale decomposition must be obtained from only one mother function through translation and dilation. Hence, all daughter wavelets are mutually similar, scale covariant with one another, and have a constant number of oscillations (Farge, 1992). The dilation process is what provides an optimal compromise in light of the uncertainty principle discussed above. In principle, two classes of wavelet transforms exist, Continuous and Discrete, the first being better for feature extraction while the latter being useful for noise reduction and data compression (Grinsted et al., 2004). The Continuous Wavelet transform (CWT) is commonly used to analyse local intermittency in a time series, and hence we only discuss the CWT here. When analysing turbulence, wavelets are also required to have vanishing high–order moments besides their admissibility (the condition that they must integrate to zero), hence allowing the study of high–order fluctuations and singularities. Because the wavelet transform measures the local scaling in the velocity field, it can interpret the power scaling of the energy spectrum relative to the geometry of coherent structures, be they dense or isolated, non–oscillating (cusp vortices) or oscillating singularities (spiral vortices), implying a multi–fractal nature of energy dissipation (Farge et al., 1996).

A continuous wavelet transform (CWT), decomposes a signal, $f(t)$, in terms of the daughter wavelets, $\psi_{b,a}(t)$, derived by stretching or compressing and shifting (translating) the mother wavelet, $\psi(t)$:

$$\psi_{b,a}(t) = \frac{1}{\sqrt{a}} . \psi\left(\frac{t-b}{a}\right) \quad \text{(Eq. 4.16)}$$

where b denotes the position (translation), and $a > 0$ defines the scale of the wavelet (dilation), with the normalisation factor $\frac{1}{\sqrt{a}} = a^{-0.5}$ ensuring daughter wavelets share the same energy as their mother. Consequently, for a real signal $f(t)$, the wavelet transform with respect to the analysing wavelet is the convolution integral:

$$CWT(b,a) = \frac{1}{\sqrt{a}} . \int_{-\infty}^{+\infty} \psi^*\left(\frac{t-b}{a}\right) . f(t) . dt \quad \text{(Eq. 4.17)}$$

where ψ^* is the complex conjugate of ψ defined on the open time and scale real (b,a) half plane (Lau and Weng, 1995). Thus, the original signal can be reconstructed from the wavelet coefficients by inverting the above formula:

$$f(t) = \frac{1}{C_\psi} . \int_a \frac{da}{a^2} . \int_b db \ . \frac{1}{\sqrt{a}} . \psi\left(\frac{t-b}{a}\right) . CWT_{b,a} \quad \text{(Eq. 4.18)}$$

whereby

$$C_\psi = \int_0^{+\infty} \frac{\left|\hat{\psi}(\omega)\right|^2}{\omega} . d\omega \ < +\infty \quad \text{(Eq. 4.19)}$$

and $\hat{\psi}$ is the Fourier transform of ψ, and ω the angular frequency.

Figure 4.4. illustrates the difference between the modes of operation of a(n) (inverse) Fourier transform and wavelet transform on a signal. In the top panel, a spectral analysis of the frequency scales is described by a Fourier transform, $X(f)$ of a continuous signal $x(t)$; given by:

$$X(f) = \int_{-\infty}^{+\infty} x(t) . e^{j2\pi ft} \, dt \quad \text{(Eq. 4.20)}$$

Thus, the inverse Fourier transform is:

$$x(t) = \int_{-\infty}^{+\infty} X(f).\, e^{j2\pi ft}\, df \qquad \text{(Eq. 4.21)}$$

The Fourier transform is thus a convolution of the time series $x(t)$ and a series of sine and cosine functions (base functions) expressing the average frequency information during the entire period of the analysed signal (Gao and Yan, 2011). In the lower panel, the operation of a wavelet transform is illustrated in the lower panel of the figure, whereby the transform allows variable window sizes (as opposed to the entire period) in analysing the different frequency components within the signal, through shifting the base function, or mother wavelet $\psi_{s,t}$, along the time axis ($t, t-\tau, \ldots, t-n\tau$); and scaling the base wavelet ($1/\sqrt{s_n}\,\psi\left(\frac{t}{s_n}\right)$) from s_1 to s_n at each instant shifted in time. Here, s stands for a; and τ for b in equations 4.16 to 4.19. Realising the localised variations in frequency components is done by comparing the time series and the scaled and shifted base wavelet.

A plethora of analysing wavelets exist (seen both as a strength and weakness of the approach), and these are classed as either orthogonal or continuous, and complex or real. As a general rule, the shape of wavelet function needs to reflect the features within the analysed time series (Torrence and Compo, 1998). The most commonly used of all is the Morlet wavelet, given by:

$$\psi(t) = e^{ik_\psi . t}.\, e^{-\frac{|t|^2}{2}} \qquad \text{(Eq. 4.22)}$$

The Morlet wavelet is a plane wave of wave vector k_ψ , modulated by a Gaussian envelope of unit width, and is practically admissible (*i.e.* has a finite Fourier transform, and hence is invertible) for $k_\psi = 6$, (Farge, 1992). The continuous and complex nature of this wavelet gives it the advantage of being able to detect both the time–dependent amplitude and phase for different frequencies in the time series (Lau and Weng, 1995). This wavelet is also

centred in time, t, and its Fourier transform is supported over almost the entire frequency spectrum (Foufoula-Georgiou and Kumar, 1994).

The wavelet coefficients for frequency or time scale, are represented by octaves, logarithms of base two which in turn may be further decomposed, hence encompassing a broad range of scales (Lau and Weng, 1995). Subsequently, a wavelet transform maps a one dimensional time series into a two–dimensional image portraying the evolution of scales and frequencies in time (linear scale on time b–axis pointing right, and logarithmic scale on the a–axis facing down with increasing scales in the octave). To resolve a localised signal, the mother wavelet is chosen such that it vanishes outside some interval (t_{min}, t_{max}), and the domain that can be influenced by a point (b_0, a_0) which lies largely within the "cone of influence" defined by $|b - b_0| = a\,\Lambda$ where a_0 is the scale at octave zero, and $\Lambda = 2^{0.5}$ for a Morlet wave. As we are dealing with a time series of finite length, errors arise towards the start and end of the wavelet power spectrum. Computationally, one may pad the end of the time series with zeroes before the transform takes place, then remove these afterwards, limiting edge effects and speeding up the transform (Torrence and Compo, 1998). However, this may present discontinuity at larger scales near the end, decreasing the amplitude where more zeroes are analysed. Therefore, the cone of influence (coi) determines the region in the spectrum where edge effects are important, and is often defined by the e-folding time for the autocorrelation of power at every single scale (*ibid*.). This highlights Heisenberg's uncertainty principle which dictates that one cannot obtain arbitrarily good localisation in both time and frequency, and as such, a trade-off must be reached whereby spatial (time) resolution is bad at the larger scales, and scale (frequency) resolution is bad at the smallest scales (Foufoula-Georgiou and Kumar, 1994; Farge et al., 1996; Grinsted et al., 2004).

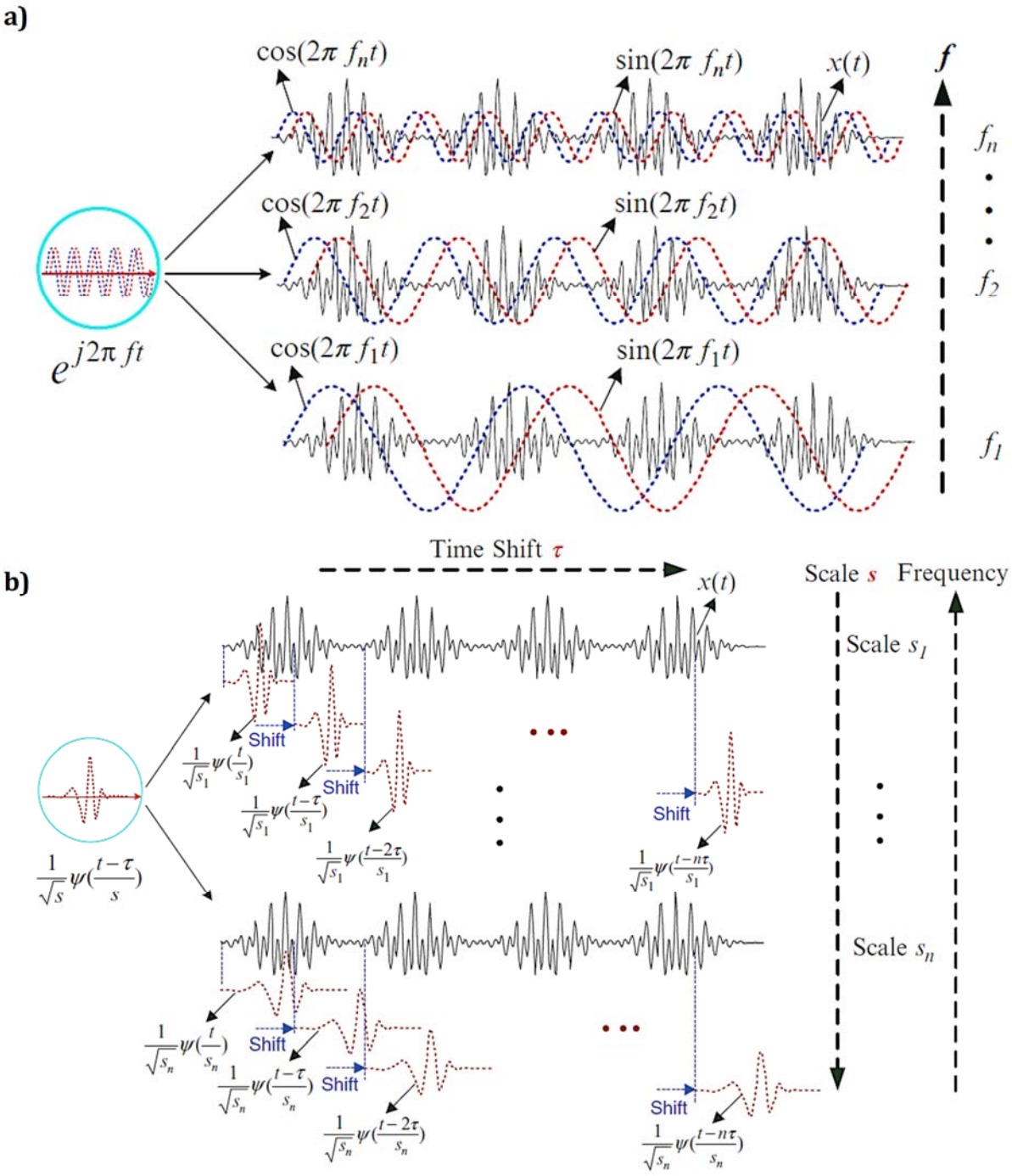

Figure 4.4 (a) Illsutration of the Fourier Transform of a continuous signal $x(t)$ as its convolution with a series of sine and cosine functions, expressing average frequency information during the entire period over which the signal is analysed. **(b)** Illustration of a wavelet transform of the signal, where variable window sizes allow analysing different frequency components within the signal through scaling and shifting a set of daughter functions of the base base (Mother) wavelet ψ. Adapted from (Gao and Yan, 2011).

In order to analyse two time series together, for example turbulent Reynolds stresses and suspended sediment concentrations, the continuous wavelet transform needs to be extended in bivariate analysis. Hudgins et al. (1993) introduced the concept of a wavelet cross spectrum to study the intermittency of turbulent fluxes in atmospheric turbulence. As with Fourier analysis of two time series, the cross-wavelet spectrum can be defined by the product of the corresponding transforms for each of the two signals (Maraun and Kurths, 2004). For two time series X and Y, with continuous wavelet transforms $W_b^X(a)$and $W_b^Y(a)$, respectively, the cross spectrum is:

$$W_b^{XY}(a) = W_b^X(a) \,.\, W_b^{Y*}(a) \qquad \text{(Eq. 4.23)}$$

whereby $W_b^{Y*}(a)$ is the complex conjugate of $W_b^Y(a)$. The cross-spectrum power is defined as $|W_b^{XY}(a)|$ (Torrence and Compo, 1998). If the two series have theoretical Fourier spectra P_k^X and P_k^Y; then the cross-wavelet distribution is:

$$D\left(\frac{|\, W_b^X(a) \,.\, W_b^{Y*}(a)\,|}{\sigma_X\, \sigma_Y} < p\right) = \frac{Z_v(p)}{v} \,.\, \sqrt{P_k^X P_k^Y} \qquad \text{(Eq. 4.23)}$$

where $Z_v(p)$ is the confidence level associated with the probability p for a probability density function with v degrees of freedom) defined by the square root of the product of two χ^2 distributions , and σ_X and σ_Y are the standard deviations (Grinsted et al., 2004). The 5% significance level for real wavelets ($v = 1$); $Z_1(95\%) = 2.182$; and for complex wavelets ($v = 2$); $Z_1(95\%) = 3.999$.

Wavelet coherence provides another useful parameter in assessing the relationship between two time series, measuring the cross-correlation between the two time-series as a function of frequency. Wavelet coherence is

defined as the square of the cross-spectrum normalised by the individual power spectra, thus ranging between 0 and 1:

$$R_b^2(a) = \frac{|S(b^{-1}\, W_a^{XY}(b))|^2}{S(b^{-1}\, |W_a^X(b)|^2).\, S(b^{-1}\, |W_a^Y(b)|^2)} \qquad \text{(Eq. 4.24)}$$

where S is a smoothing operator (Torrence and Webster, 1999); which includes smoothing along the wavelet scale axis and smoothing in time. Furthermore, if there is a causality between the two time series, their cross-wavelet spectra would be expected to be phase locked, in regions with significant common power. The phase difference between the two series can be quantified by the mean of the phase over regions with common significance (higher than 5%) outside the cone of influence. In this work, space-time dynamics of turbulent stresses and sediment resuspension are assessed. A cross–wavelet transform (XWT) analysis is used to expose regions of high common power between the two signals of Reynolds stresses and suspended sediment flux, looking into the phase relationships between the two, following Grinsted et al. (2004).

Chapter 5.

Wave-induced coherent structures and nearshore sediment resuspension[1]

> "And yet relation appears.
> A small relation expanding like a shade.
> Of cloud on sand. A shape on the side of a Hill"
> Wallace Stevens (1942) - *Connoisseur of Chaos*

5.1 Introduction

The mobilisation of sediment in the nearshore and shoreface of sandy beaches is dominated by wave-induced bed shear stresses in moderate and stormy conditions (Thompson et al., 2012). Our ability to predict sediment transport remains limited by insufficient understanding of the hydrodynamic and physical processes contributing to the mobilisation and suspension of bed material into the water column (Aagaard and Jensen, 2013). Over finite length scales, the advection-diffusion framework dictates that the concentration of suspended particles under waves depends on the balance between upward (gradient diffusion caused by small scale turbulence; and pick-up by coherent vortices) and downward (settling) directed sediment fluxes (Aagaard and Hughes, 2010). The vertical structure of the sediment flux components on the shoreface and in the inner surf zone, as well as the dynamics of sediment transport under shoaling waves in the nearshore, are both considered to be insufficiently understood (van Rijn et al., 2013). In a review of future research needs in coastal sediment dynamics, van Rijn et al. (2013) highlight a requirement for prioritising research with reference to coherent flow structures and the intermittent stirring of sediment by breaking and shoaling

[1] This chapter is based on the publication: Kassem, H., Thompson, C.E.L., Amos, C.L., and Townend, I.H. (2015), Wave-induced coherent turbulence structures and sediment resuspension in the nearshore of a prototype-scale sandy barrier beach, Continental Shelf Research, 109, 78-94, doi: 10.1016/j.csr.2015.09.007 – Appendix 3

waves; as well as the time-history effects of suspended sediments under irregular wave conditions. Understanding the spatial, temporal and frequency characteristics of sediment suspension events in relation to turbulent fluctuations, both in structural form and in temporal distribution, is an important step towards providing a more satisfactory conceptual model for describing sediment entrainment by coherent turbulence structures and subsequent accurate predictions of suspended sediment transport. The aim of this chapter is to provide insight into the temporal and spatial scale relationships between wave–generated boundary layer turbulence and event–driven sediment transport in oscillatory flow in the nearshore of a prototype sandy barrier beach. In particular, two aspects are investigated: (a) the time–frequency properties that characterise turbulent burst cycles and ensuing sediment suspension; and (b) the relationship between near–bed sediment resuspension events with wave–induced turbulent coherent structures as manifest by intermittent Reynolds stresses. The intermittency of turbulent structures, identified through traditional quadrant/octant analysis assessing covariance of stress–bearing events in three planes of motion is assessed. Fourier analysis is used to characterise the integral scales of motion and suspension events, while wavelet analysis offers the ability to investigate localised variations of power (variance) within the time series, determine localised intermittent periodicities, and hence identify time and frequency scales of turbulent bursts and suspension fluxes, and causality through phase relationships. We restrict our study to two series of irregular, erosive and accretive, wave runs on a prototype sandy barrier beach; carried out through the EU–funded Barrier Dynamics Experiments II – BARDEX II project (HYDRALAB IV Contract no. 261520 by the European Community's Seventh Framework Programme).

5.2 The Barrier Dynamics Experiment II (BARDEX II)

The Barrier Dynamics Experiment II is the second of the EU-funded experiments on barrier beach dynamics within the Hydralab framework, conducted at the Delta Flume facility, the Netherlands, following the gravel barrier experiments of Williams et al. (2012). The overall aim of BARDEX II

was to collect a near prototype-scale data set on a sandy barrier beach system subjected to energetic, erosive and accretive wave conditions, to improve quantitative understanding of, and modelling capability of shallow water sediment transport processes in the inner surf, swash and overwash zones (Masselink et al., 2013; Masselink et al., 2015). This was formulated into six work packages covering barrier hydrology, swash and berm dynamics, bar dynamics and exchanges between swash and surf zones, barrier overwash, sediment resuspension and bed morphology in the nearshore, and numerical modelling; and included 20 days of experimental runs during the period of the project (May – July 2012). The data presented in this work were collected as part of the fifth work package of the project, which aimed to observe and measure vortex resuspension processes and bedform dynamics under shoaling and breaking waves in order to quantify changes in the magnitude and direction of bedload and suspended sediment transport in the region outside the surf zone (Thompson et al., 2013).

5.2.1 Experimental set-up

A 4.5 m high, 75 m wide (cross–shore) sandy barrier beach was constructed from moderately sorted, coarse-skewed medium fluvial sand with a median grain diameter, D_{50}, of 0.42mm within the 5 m wide Delta Flume. A typical particle size distribution, calculated from repeated settling column experiments (using Soulsby (1997)) on samples collected in the nearshore of the barrier is given in Figure 5.1, showing a moderately sorted, coarsely skewed, meso-kurtic medium sand following the classifications of Folk and Ward (1957) and Tucker (1991). The sediment in the flume, with about 1% gravel, was compacted by 20% before the experiments. The barrier, backed by a lagoon and fronted by a 20 m flat section (of the same bed material, 0.5 m deep), was subjected to a JONSWAP spectrum of random waves (Hasselmann et al., 1973), generated by a single stroke wave paddle fitted with an automated reflection compensator to supress reflection and low frequency resonance, situated 49 m before the start of the 1:15 m seaward slope (Figure 5.2(a); and Figure 5.3). The entire experimental testing program is given in (Masselink et al., 2015).

The present laboratory experiment was designed to address cross-shore sand transport across a sandy barrier beach without the added complexities of alongshore (littoral) variations. In the field, the dynamics of barrier beaches represent an interplay of both cross-shore and alongshore sediment transport, and therefore present a three dimensional problem (Fredsøe and Deigaard, 1992; Roelvink et al., 2009; Masselink and van Heteren, 2014). Natural sediment was used to avoid scaling issues, and its size chosen as a compromise whereby resuspension of sediment was possible given the applied wave forcing within the nearshore region (under shoaling waves), whilst ensuring the required hydraulic conductivity for cross-barrier groundwater flow (lagoon to sea). Irregular wave forcing provided a realistic representation of the wave field in the absence of tidal forcing; and the use of active reflective compensation system eliminated 'artificially reflected waves' from the modelled barrier structure. Indeed, the use of 1:1 (prototype) scaling in wave tanks implies no significant scale effects, and is well established for accurate modelling of flow processes and responses in coastal environments without distortion (Hughes, 1993; Oumeraci, 1999; Frostick et al., 2011). The relatively shallow water depth at the seaward side of the barrier ensured wave-generated bed shear stresses which exceed the threshold for particle motion and/or suspension are attained. For the purposes of our study, the use of unidirectional waves as the hydrodynamic forcing on the barrier is a reasonable approximation to the case of swash-aligned barrier beaches, where wave crests are parallel to the shoreline and onshore-offshore sediment transport describes the morphological evolution of the beach (Bird, 2005; Masselink et al., 2011).

As part of these experiments, time–synched acoustic measurements of turbulence, suspension, and bed morphology were recorded from an instrumented frame at the nearshore position, situated just at the break of the seaward slope of the barrier; 49 m from the wave paddle (Figure 5.2 (b, c)). Turbulence estimates from velocity measurements were collected by means of two coupled, downward-looking 10MHz Nortek Vectrino Acoustic Doppler Velocimeters (ADVs) with a vertical offset of 0.26 m and an across–flume

horizontal offset of 036 m, sampling at 25 Hz. Sediment suspensions were inferred from backscatter measured with an Aquatec Aquascat Acoustic Backscatter Profiling Sensor (ABS), with 1, 2, and 4 MHz channels, measuring between 5 and 0.95 m below the instrument in 0.5 mm bins at 64 Hz (Thompson et al., 2013). Due to the internal logger's limited disk storage capacity, the burst intervals were limited during each run to 8 minutes. Unfortunately, it was not possible to directly calibrate the ABS measurements (and hence infer volume/mass concentrations) due to failure of peristaltic pump equipment, so pre-calibration procedures were used instead. Subsequently, concentrations and backscatter are used interchangeably in this work to look at relative change. Three dimensional bed morphology was inferred from a combination of a Marine Electronics 1.1 MHz dual-head sand ripple profiling system (SPRS) recording sequential cross–shore profiles and a Marine Electronics 500 kHz Sector Scanning Sonar (SSS) which provided a 360^{o} plan–view of the bedforms. The dual-head SRPS performed 4 μs, 120° sweeps at a rate of 1 Hz and a range extending from 0.5 -2.5 m. The two SRPS units were installed to face one another, providing a cross-shore sonar image of the bed close to the flume's centre and to the flume's inner wall. The SSS performed continuous 40 μs, 360° sweeps with a range of 10 m. Surface water elevation (pressure) was recorded through a 5 Hz self-logging Paraoscientific 745 pressure transducer, mounted 0.35 m above the starting bed elevation. Although turbulence and bedform data were recorded for the entire length of each wave run, memory limitations in the ABS instrument mean bursts of a maximum length of 8 minutes are presented. As such, where turbulence records are analysed in conjunction with suspension data, these are trimmed accordingly. All instruments (apart from the pressure transducer) logged live to a set of computers, time-synched to precision GPS clock-network.

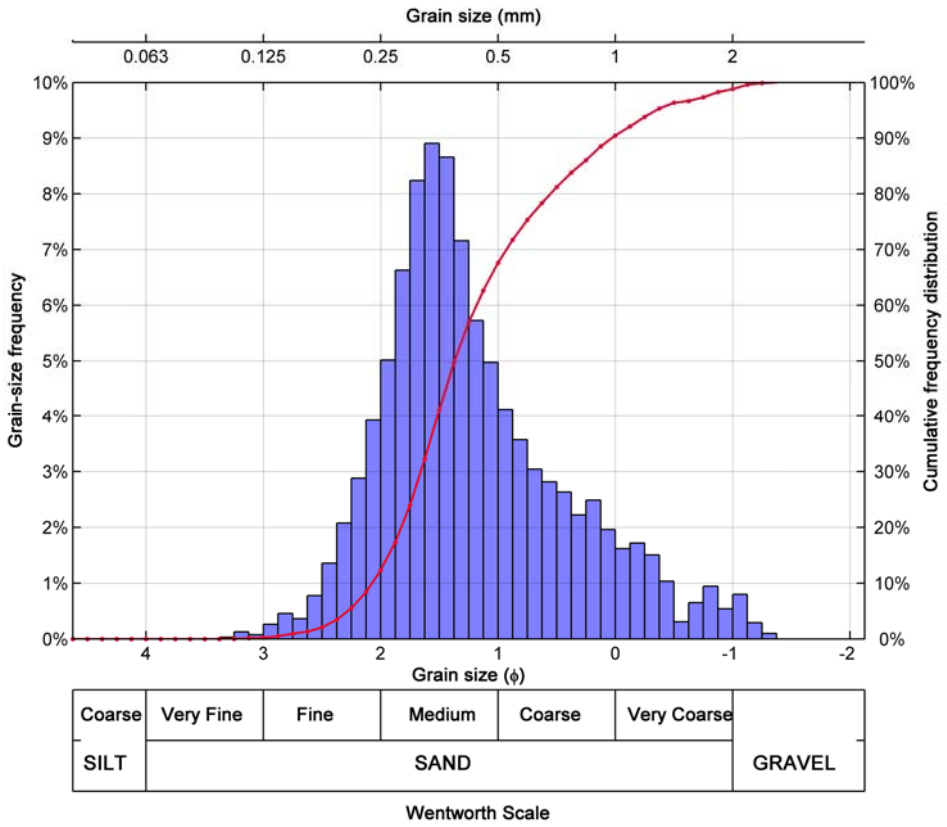

Figure 5.1 Particle size distribution in the nearshore of the barrier.

5.2.2 Data collection, quality control and pre-processing

5.2.2.1 Three-dimensional velocity field and turbulent components

The three-dimensional (3D) flow velocity field (U, V, W) representing the streamwise (along-flume), cross–wise (across-flume), and vertical components of instantaneous velocity, respectively; is given by ADVs measuring at two discrete 7mm sample volumes above the bed (Figure 5.1(c)). However, ADVs are inherently contaminated by noise due to Doppler signal aliasing, bubbles, etc. (Mori et al., 2007) and inferred stresses are susceptible to errors due to sensor misalignment (Soulsby and Humphery, 1990). For quality control purposes, a threshold of measurement correlation based on the instrument sampling frequency was used (after Elgar et al. (2005)), giving ~70% as the lower limit. A limit of 20% corrupted data per record was subsequently applied, delimiting sequences where samples fall

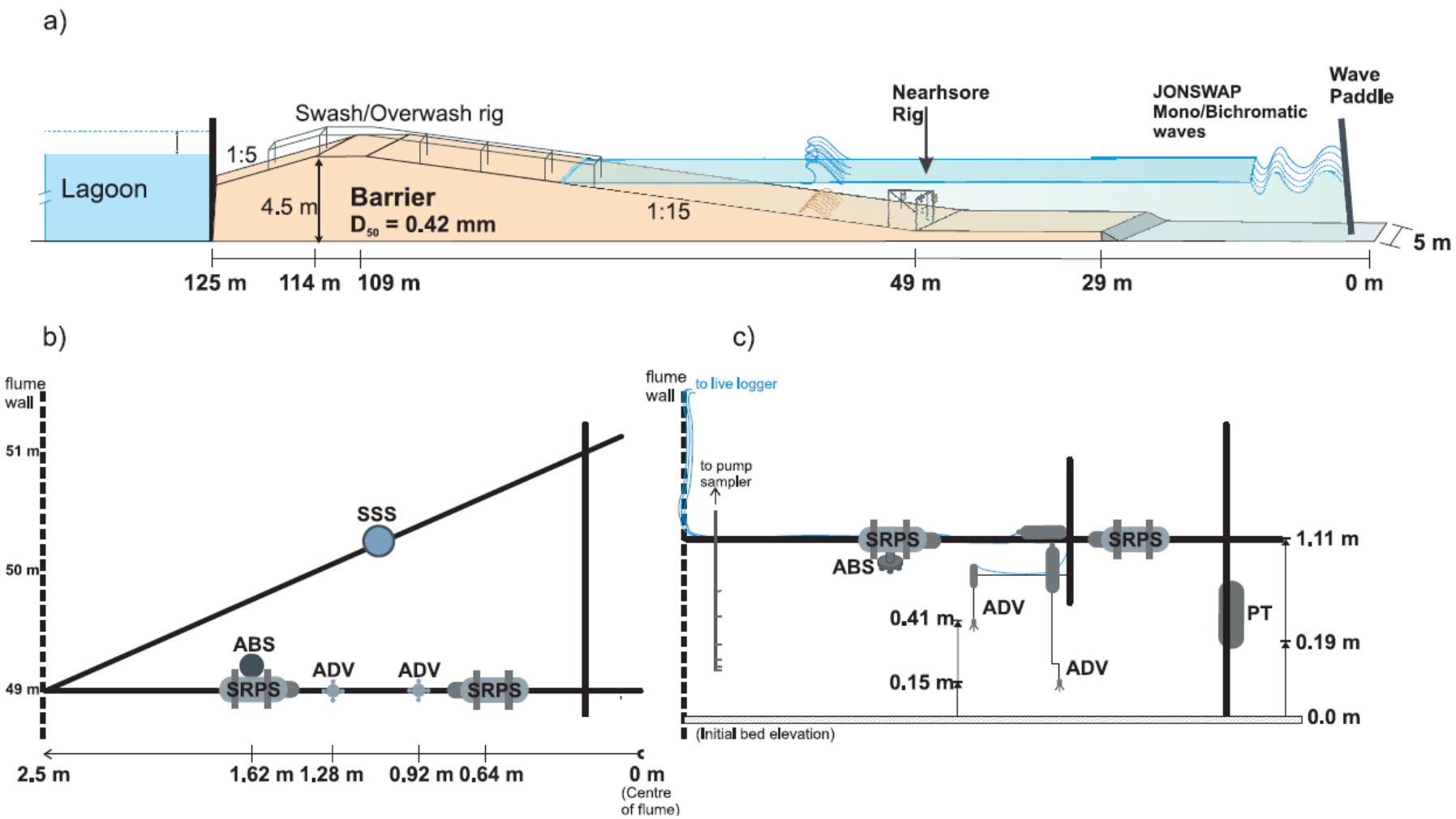

Figure 5.2 (a) Cross-sectional profile of the barrier within the Delta Flume at the start of the experiments, with location of the nearshore instrumented rig; **(b)** plan view of the instrument rig with distance from the wave paddle on left hand wall; and indicating relative location of instruments from the centre of the flume; **(c)** cross-section view of instrument rig with heights above initial bed elevation. SRPS: sand ripple profiler system; ABS: Acoustic backscatter profiler system; ADV: acoustic Doppler velocimeter; SSS: sector scanning sonar; PT: pressure transducer.

Figure 5.3 Some photos from the experiment, showing: (a) barrier setup at the start of the experiment; with the swash/over wash rig present, and bed profiling trolley (green) visible; (b) first week team photo (for scale); (c) a plunging wave breaking over the nearshore bar, followed by a shoaling wave at the location of the nearshore instrumented rig.

continuously below the accepted correlation threshold for over two consecutive seconds (Elgar et al., 2001; Feddersen, 2010). Any 8-minute-long record which failed this criterion was discarded By Comparison, time series with up to 40% bad data per record have been used in the literature (e.g. Ruessink, 2010). The records were then patched (to replace contaminated data) by applying a moving average algorithm which interpolates the missing data by averaging column–wise along with the surrounding elements that fit on the column matrix of size (2Fr+1), centred on it as well as smoothing in the edges, whereby Fr is the window semi-length in rows, following Thompson et al. (2012). Ideally, the smallest window size such that all missing values are replaced by an interpolated value is chosen for the corresponding record. Subsequently, an axis–rotation algorithm is used to eliminate the effects of sensor misalignment, following Elgar et al. (2001). This requires calculating the angle of rotation about the Y–axis, given by the gradient of a least-squares straight–line fitted through the scatter of points in the (X, Y) space. This is then used to construct a rotation matrix applied to the coordinates in the $(x-y)$ plane. A similar operation is applied to the $(y-z)$ plane before the mean values of the rotated coordinates are deducted to remove the contamination of the "*U*" data by the "*V*" data (cf. §4.2.1).

To extract the turbulence component (u'), the mean flow velocity of each component ($\overline{u}$), determined by applying a moving average, zero-phase digital filter (in forward and reverse directions to ensure no phase distortion) as a low pass filter, then subtracted from the instantaneous flow field (u), before the record is zero–meaned and de–trended (Thompson et al., 2012). The numerator coefficients defining the filter window were selected by trial and error, with autocorrelation and cross–correlation tests applied for validation. It follows that two fluctuating components are identified, a wave-induced (periodic) component (denoted by u'_{wave}) and the residual "random/high frequency" component, u'. The signals are then de-spiked using the modified "true" 3 D phase space method by (Goring and Nikora, 2002; 2003) as modified by (Mori et al., 2007). Notabely, similar power (variance) properties

and scales in the time-frequency domain were observed before and after despiking, albeit with smaller magnitude stresses.

5.2.2.2 Spectral properties of the incident wave field

The non-directional wave parameters (peak wave periods, T_p (s) and significant wave heights, $H_s = H_{m0}$ (m)) were computed by zero-crossing and spectral analysis of the pressure variations, having compensated for transducer height above the bed, and pressure attenuation with depth following Tucker and Pitt (2001). The transducer height above bed level before each experimental run (were possible) was determined from relative heights to the concurrent bed level determined prior to each test run by flume morphology surveys conducted by means of a rolling, crane-mounted mechanical profiling wheel (50 mm in diameter).

5.2.2.3 Bed morphology and bedform dynamics

Bed morphology was inferred from the backscatter intensity of the SSS and SRPS records. The SSS backscatter intensity was used in raw acoustic form (in dB) to assess ripple crest shape and orientation, providing a top view of any variations in bedforms. Mean bedform wavelengths, following slant range correction, and rotation of the image to align with the flume walls, were evaluated from the locations of the peaks in backscatter along the central line of the echograms at the start and end of each wave run. Bed location was determined using the built-in 'bed detection' function of the SRPS dual-head programmer software (Marine Electronics Ltd.) with a threshold value (20 dB) above the average backscatter intensity, having adjusted for sound attenuation. Bed level data were then detrended to remove the bed slope, and de-spiked to remove outliers pertaining to high concentration suspension events. A zero-crossing algorithm is used to determine ripple heights and wavelengths. Variations in bed morphology across the flume were examined through raw backscatter intensity given by the Sector Scan Sonar (SSS). Changes in bed morphology over time was inferred from the series of sequential scans within each run, taken approximately once a minute.

5.2.2.4 Suspended sediment concentration profiles

For the ABS records, the mean grain size and speed of sound, based on measured temperature and salinity, was used to correct backscatter for attenuation and spreading, and hence infer concentration. Thus, the one–dimensional vertical profiles of suspended sediment concentration (backscatter) and mean particle sizes could be calculated from sediment cross–section scattering of the individual sound frequencies. The attenuation coefficient for viscous dissipation due to freshwater fluid motion under the oscillating pressure, α_w , was calculated following Fisher and Simmons (1977) using the measured temperature, and SIS beam frequency. The attenuation coefficients pertaining to viscous dissipation due to the relative motion between particles and the fluid, α_{sv} , and scattering of sound by particles, α_{ss} , were estimated following Thorne and Hanes (2002), and Thosteson and Hanes (1998) as presented in the MATSCAT toolkit (Buscombe, 2012). An implicit inversion method for multi-frequency acoustic measurements of Thorne and Hanes (2002) was used to calculate suspended sediment concentration (SSC) and grain size profiles, averaging over 10 profiles to minimise noise, and using the grain-size distribution properties of the bed sediment. Subsequently, the range-corrected backscatter intensities along each beam of a given sweep were normalised against the maximum intensity of that beam, and the background noise, defined as the mean backscatter within the water column was removed. The bed was then detected as the range-corrected height at which the maximum normalised backscatter occurs.

The ADV records of the turbulence components were eventually trimmed to match the ABS records, which, in turn, are down–sampled from 64 Hz to 25 Hz only for the cross wavelet transforms of Reynolds stresses and synchronous suspended sediment fluxes. Given that the subsampled records displayed the same spatial and temporal properties as their original series through spectral and continuous wavelet analyses, this is believed to have no significant impact on the results.

5.3 Results and Discussion

5.3.1 Wave hydrodynamics

Eight records of erosive and accretive wave conditions (classified as such following Sunamura and Takeda (1993)) are analysed and presented here: four erosive sub–records taken from BARDEX II test series A301 (1st, 2nd, 3rd, 4th), and four accretive records from test series A7 (A705, A706) and A8 (A801, A802). The design wave conditions, as well as calculated and measured hydrodynamic flow properties are given in Table 5.1. The design wave forcing in each sub-run is reproduced systematically by the paddle, with measured significant wave heights (H_s ~ 0.75±0.03m in erosive, and ~0.61±0.07m in accretive runs) and peak periods (T_p ~8.12±0.5s in erosive; and 12 s in accretive runs) satisfying the erosion/accretion criteria (shoreward/seaward migration of nearshore bed material) of Sunamura and Takeda (1993) for the given beach slope and mean grain size (settling velocity). The wave Reynolds numbers indicate turbulent rough flows (Soulsby and Clarke, 2005), with estimated near-bed orbital velocities of 0.68±0.03m/s for the erosive runs (spilling and plunging breakers with surf-similarity parameter, ξ= 0.5±0.012), and 0.67±0.07m/s for the accretive runs (plunging breakers with $\xi \cong 0.62$ (Massel, 2013)). Turbulence measurements by both ADVs were confirmed to be taken within ($Z_{\mathrm{ADV1}} < \delta_w$) and outside within ($Z_{\mathrm{ADV2}} > \delta_w$) the wave benthic boundary layer.

5.3.2 Bed morphology

Within the erosive and accretive runs presented, wave-induced suborbital vortex-type ripples were observed in a bifurcating, two-dimensional configuration across and along the flume (Figure 5.4), following the classification of (Clifton and Dingler, 1984). These were characterised by ripple height: H_r = 0.098 ± 0.008 m; and wavelength, λ_r= 0.45 ± 0.09m in the erosive runs; and H_r = 0.10 ± 0.02 m; and λ_r= 0.57 ± 0.06 m in the accretive runs. While certain trends in bedform growth and relaxation were observed during entire experimental runs, only millimetric scale variations in geometry were evident within the 8-minutes long sub-records chosen for analysis of stress-suspension co-variation.

Table 5.1 Wave test conditions, and calculated/measured hydrodynamic properties/parameters

Wave Conditions	**Erosive Runs** Design characteristics: $h = 2.5\ m;\ H_s = 0.8\ m; T_p = 8s$, JONSWAP					
Run (sub-run)	**A301-1st**	**A301-2nd**	**A301-3rd**	**A301-4th**	**mean $\overline{x}$**	**St. dev. σ_x**
Water height, h (m)	2.506	2.512	2.512	2.514	**2.51**	**0.0034**
Measured Significant wave height, H_s (H_{m0}) (m)	0.779	0.761	0.734	0.710	**0.750**	**0.028**
Peak wave period, T_p (s)	8.0	8.0	8.98	7.5	**8.12**	**0.53**
Near–bed orbital amplitude, (m) $A_\delta = H_s/(2.\sinh(k.h)$	0.903	0.865	0.998	0.756	**0.88**	**0.086**
Near–bed orbital velocity, $U_{w,orb,\delta} = A_\delta.\omega$ (m/s) (van Rijn, 1993)	0.709	0.679	0.698	0.634	**0.680**	**0.029**
Wave Reynolds number, $Re_{w,\delta}$	2.53E+05	2.53E+05	2.38E+05	2.38E+05	**2.45E+05**	**0.7E+05**
Wave boundary layer thickness, δ_w (m), calculated from measured stress	0.249	0.140	0.128	0.123	**0.160**	**0.052**
Wave friction factor, $\boldsymbol{f_w}$ using TKE method (Thompson et al., 2012)	0.020	0.032	0.026	0.023	**0.025**	**0.004**

Continued …

Wave Conditions	**Accretive Runs** Design characteristics: $h = 2.5\ m;\ H_s = 0.6\ m; T_p = 12s$, JONSWAP					
Run (sub-run)	**A705**	**A706**	**A801**	**A802**	**mean $\overline{x}$**	**St. dev. σ_x**
Water height, h (m)	2.507	2.509	2.509	2.509	**2.508**	**0.0008**
Measured Significant wave height, H_s (H_{m0}) (m)	0.566	0.705	0.532	0.629	**0.608**	**0.066**
Peak wave period, T_p (s)	12.0	12.0	12.0	11.48	**12.0**	**0**
Near–bed orbital amplitude, (m) $A_\delta = H_s/(2.\sinh(k.h)$	1.065	1.363	1.363	1.363	**1.289**	**0.129**
Near–bed orbital velocity, $U_{w,orb,\delta} = A_\delta.\omega$ (m/s) (van Rijn, 1993)	0.557	0.713	0.713	0.713	**0.674**	**0.068**
Wave Reynolds number, $Re_{w,\delta}$	2.14E+05	2.26E+05	2.40E+05	2.37E+05	**2.29E+05**	**0.1E+05**
Wave boundary layer thickness, δ_w (m), calculated from measured stress	0.177	0.184	0.178	0.194	**0.183**	**0.007**
Wave friction factor, $\boldsymbol{f_w}$ using TKE method (Thompson et al., 2012)	0.024	0.024	0.024	0.023	**0.024**	**0.0**

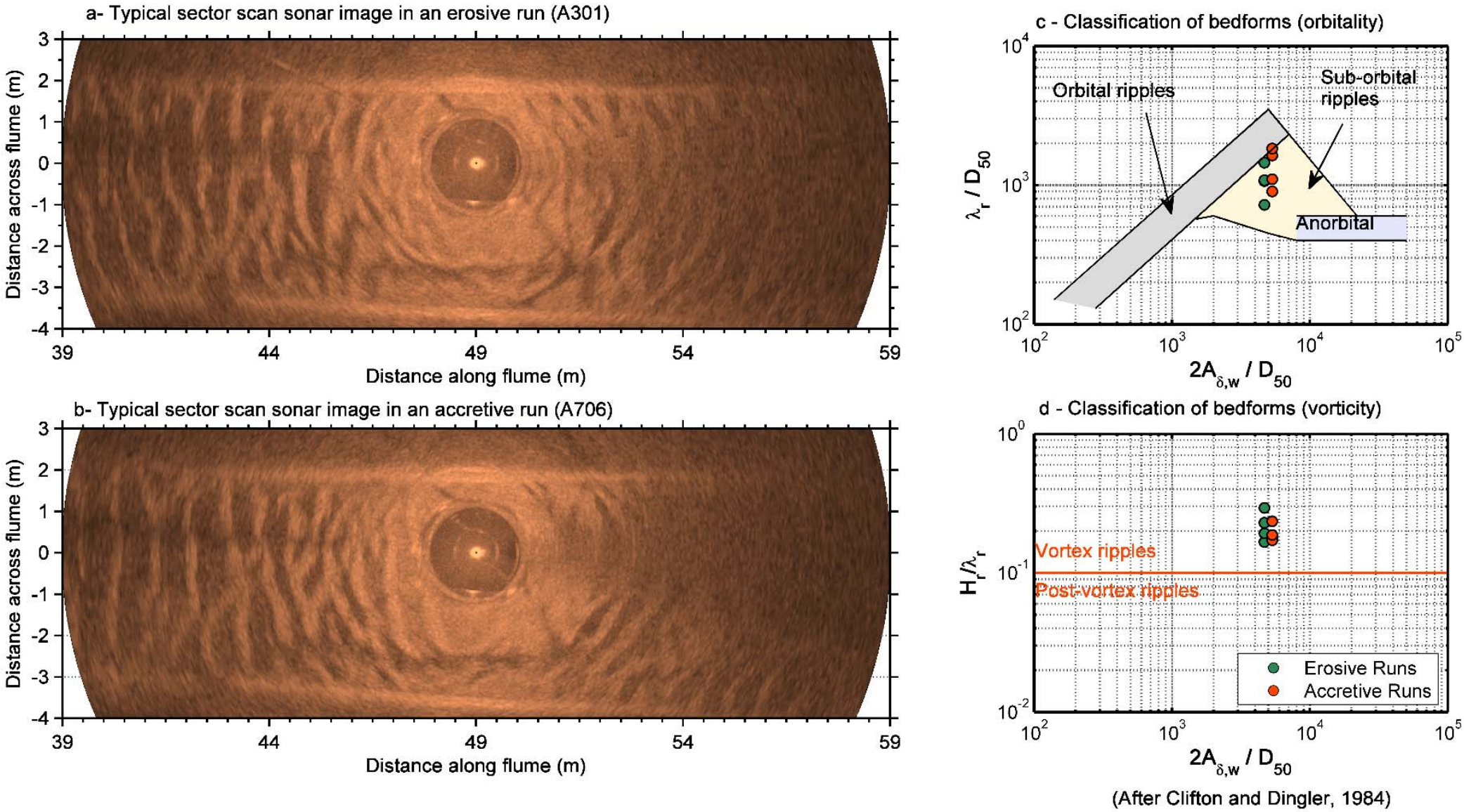

Figure 5.4 Typical 2D ripple configurations observed from backscatter intensity along and across the flume in the vicinity of the instrumented nearshore frame, for **a)** erosive, and **b)** accretive wave runs. Classification of bedform in terms of **c)** orbitality, and **d)** vorticity for the average bedform characteristic lengths is after Clifton and Dingler (1984).

5.3.3 Turbulence Intermittency and higher-order statistics

Figure 5.5 shows the time series of the three instantaneous, zero-meaned velocity (U, V, and W) and inherent turbulent (u', v', and w') fluctuations, measured within and outside of the wave boundary layer (by ADV1 and ADV2 respectively) for almost the entire length of the erosive wave run A301; together with their corresponding probability distributions. The velocities were zero-meaned to eliminate the influence of any net currents induced by the asymmetry of the propagating waves. The four erosive sub-records carried forward in the analysis are delimited by the vertical blue lines. Considering the entire length of this experimental run (180 min), the averaged statistical properties of the streamwise velocity (U) (top panel of each subplot; green) exhibit a slight deviation from a normal distribution within (subplot a) and outside (subplot c) the wave benthic boundary layers, while their corresponding turbulent fluctuations having sharply leptokurtic distributions, suggesting that while the data is heavily clustered around the mean (zero), a considerable number of fluctuations are significant statistical outliers despite the very large population (180 minutes at 25 Hz). The crosswise (second panel within each subplot, gold), and vertical (third panel of each subplot, orange) components of velocity and turbulence are both characterised by very high kurtosis, particularly in the crosswise component. The four sub-records analysed below were randomly selected throughout this time series and their statistical properties, despite much shorter lengths, exhibit similar properties. Table 5.2 summarises the corresponding averaged statistical properties for the turbulent component of the 8-minute subsampled records from both erosive and accretive wave runs. The streamwise velocity component, U, both within and outside the boundary layer, exhibits a quasi-Gaussian distribution (skewness $\sim$ 0, kurtosis $\sim$ 3) hinting at a stochastic process of independent probabilistic events; while the crosswise and vertical components are markedly non–Gaussian. The turbulence components are anisotropic in all three dimensions both within and outside the bottom boundary layer.

The crosswise component, commonly overlooked when analysing shear stresses in relation to sediment suspension, shows remarkably high amplitude spikes, comparable in magnitude to the streamwise flow and for a considerable amount of time, particularly near the bed. This, in turn, is reflected in a pronounced leptokurtic distribution for the transverse velocity fluctuation, which also appears to be asymmetric. The vertical velocity fluctuations are characterised by relatively high kurtosis for the erosive wave runs, which is even more pronounced in the accretive runs. This is generally suggestive of a high degree of intermittency in momentum exchange. Similar results have been reported (as unexpected findings) in experimental and numerical simulations of strong boundary layers and turbulent channels, particularly in wall (bed) proximity (Kim et al., 1987; Choi and Guezennec, 1990) and at high Reynolds numbers (Kuo and Corrsin, 1971); in obstructed flow (El Khoury et al., 2010); and in viscoelastic flows (Samanta et al., 2009). Asymmetry in the vertical in commonly encountered in convective boundary layers where it is associated with diffusion of passive scalars in the up-draught (bottom–up) direction (Weil, 1990; Wyngaard and Weil, 1991). The effect of the proximity of measurements to the slope of the barrier may be relevant in this case, however, given that all measurements were taken at the same distance relative to that 'obstruction', it is not possible to pursue this line of investigation with the current dataset, requiring further experimental work.

The peaked and asymmetric crosswise velocity distribution particularly near the bed has been attributed to the nearly self–similar growth and self–sustaining mechanisms of spanwise structures in close proximity to low speed regions of flow. These are often speculated to be generated by induction of the asymmetric legs of inclined, streamwise-aligned, wall-attached horseshoe vortex structures (Zhou et al., 1997; Christensen and Adrian, 2001; Panton, 2001; Tomkins and Adrian, 2003; Adrian, 2007; Lozano-Duran et al., 2012). It has also been attributed to the more frequent occurrence, and merging, of one-legged 'cane-like' elliptical vortices, at high Reynolds numbers (Tomkins and Adrian, 2003). The highly three–dimensional fluid

entrainment process cannot be studied in the streamwise-vertical plane only, where entrainment with vortex structures is not evident (Robinson, 1991). Large streamwise vortices in wall bounded channels with moveable beds appear as secondary flows in the crosswise plane perpendicular to the streamwise flow, and affect the distribution of mean velocity, turbulence intensities, and Reynolds and bed shear stresses through the channel (Adrian and Marusic, 2012). Such eddies have been observed with a spanwise width up to 1.5 times the water depth, oscillating slowly at the centre while forming stationary flows near the wall (Tamburrino and Gulliver, 2007). In the absence of practical means of visualising these structures in the field, we undertake quadrant analysis of the tangential stresses to assess the frequency of occurrence of sweep (Q4)–ejection (Q2) pairs as it may shed additional light on the three-dimensional structure of momentum transfer near the bed (Alfredsson and Johansson, 1984; Kim et al., 1987; Lozano-Duran et al., 2012). There is no consensus as to whether the succession of ejections and sweeps creates vortices, or conversely, rolling vortices give rise to the bursting sequence, and it is plausible that both mechanisms operate cooperatively (Adrian and Marusic, 2012). Furthermore, while the velocities presented earlier have been zero-meaned to eliminate the influence of any net currents induced by the asymmetry of the propagating waves; a relatively strong undertow along the flume was evident in both erosive and accretive wave runs (magnitude $\sim$ 0.2m/s). This offshore directed current would interact with the on-shore propagating waves. The interaction between waves and currents (undertow) is non-linear, and often results in enhanced momentum exchanges, the formation of paired counter-rotating vortex clusters, and may contribute to the asymmetry in the transverse plane as suggested earlier (a detailed discussion in given in §6.4). The above results emphasise the three–dimensionality of the momentum and subsequent mass exchange problem, and as such, the contributions of the three components of turbulence to momentum flux need to be considered. Quadrant analyses of the Reynolds stresses ($u'w', u'v', v'w'$) is carried out to identify active momentum exchanges and their fractional contributions to the overall stress.

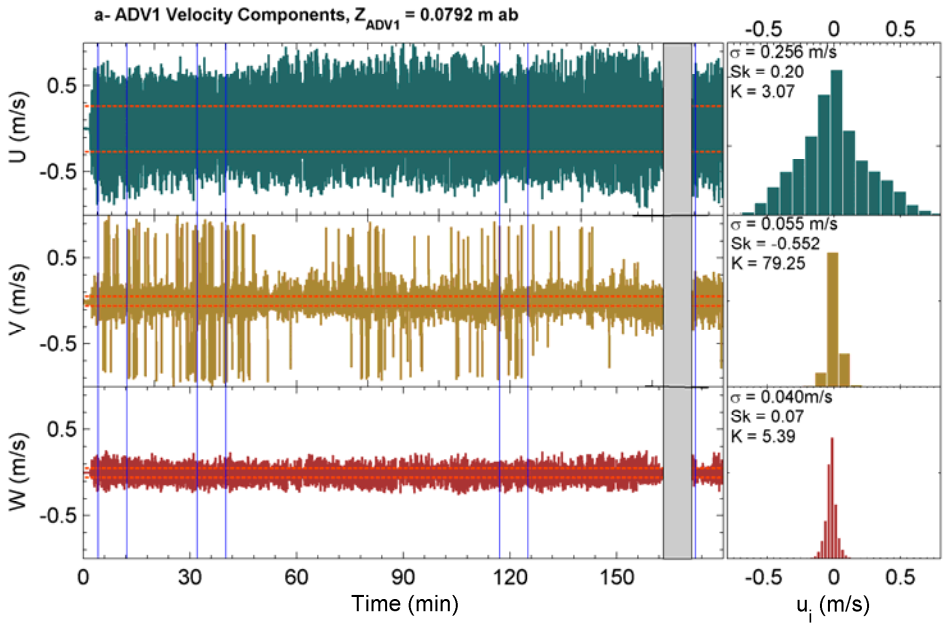
a- ADV1 Velocity Components, Z_{ADV1} = 0.0792 m ab
U (m/s)
V (m/s)
W (m/s)
σ = 0.256 m/s
Sk = 0.20
K = 3.07
σ = 0.055 m/s
Sk = -0.552
K = 79.25
σ = 0.040m/s
Sk = 0.07
K = 5.39
Time (min)
u_i (m/s)

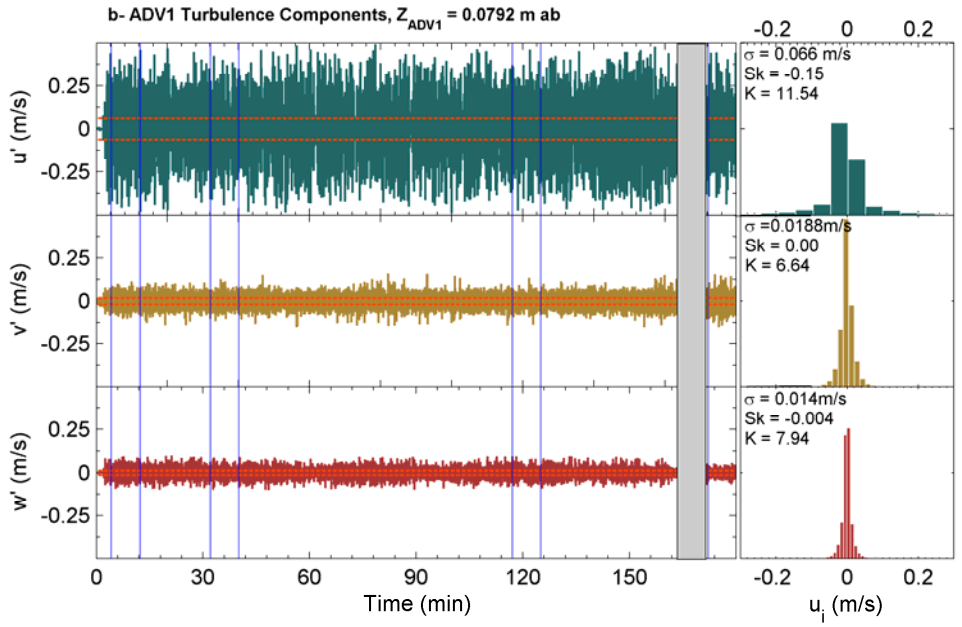
b- ADV1 Turbulence Components, Z_{ADV1} = 0.0792 m ab
u' (m/s)
v' (m/s)
w' (m/s)
σ = 0.066 m/s
Sk = -0.15
K = 11.54
σ =0.0188m/s
Sk = 0.00
K = 6.64
σ = 0.014m/s
Sk = -0.004
K = 7.94
Time (min)
u_i (m/s)

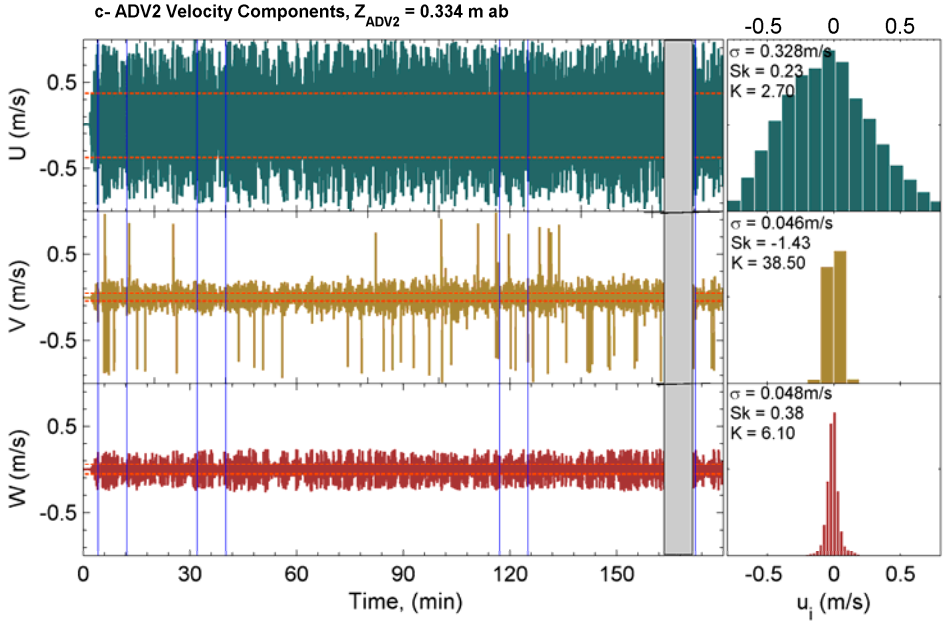
c- ADV2 Velocity Components, Z_{ADV2} = 0.334 m ab
U (m/s)
V (m/s)
W (m/s)
σ = 0.328m/s
Sk = 0.23
K = 2.70
σ = 0.046m/s
Sk = -1.43
K = 38.50
σ = 0.048m/s
Sk = 0.38
K = 6.10
Time, (min)
u_i (m/s)

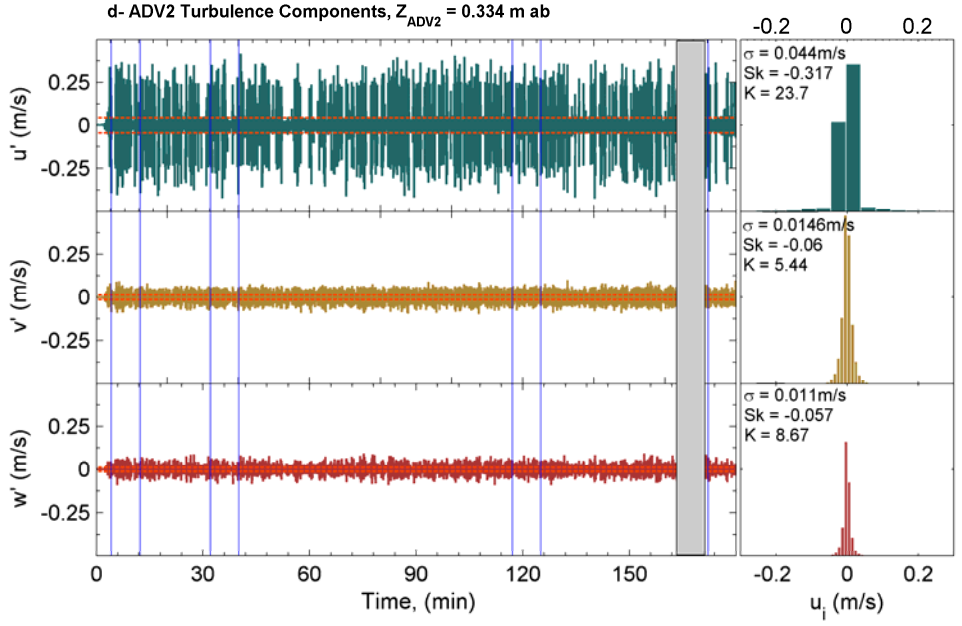
d- ADV2 Turbulence Components, Z_{ADV2} = 0.334 m ab
u' (m/s)
v' (m/s)
w' (m/s)
σ = 0.044m/s
Sk = -0.317
K = 23.7
σ = 0.0146m/s
Sk = -0.06
K = 5.44
σ = 0.011m/s
Sk = -0.057
K = 8.67
Time, (min)
u_i (m/s)

Figure 5.5 Time series and probability density functions of 3D velocity (U, V, and W) and inherent turbulence (u', v', w') components, in the streamwise/along-flume (dark green), crosswise (gold), and vertical (orange) for the entire experimental wave run A301 (Hs=0.8 m, Tp=8 s). The horizontal dashed lines (red) in the time series represent ±1 standard deviations; while the vertical blue lines delimit the 4 sub-records analysed; σ is standard deviation, Sk is skewness, and K is Kurtosis. The grey-shaded area marks no wave activity.

Table 5.2 Statistical properties of the three turbulence components measured within (ADV1) and outside (ADV2) the wave boundary layer for the two types of wave conditions. These are averages of the 4 sub-sampled records analysed for each of the erosive and accretive runs.

Wave run - subrecord	ADV	Height above bed (m)	turbulence component	Standard deviation	Variance	Skewness	Kurtosis
Erosive Runs	ADV1	0.0792	u'	0.27±0.027	0.07±0.014	0.27±0.06	2.97±0.38
			v'	0.05±0.005	0.00	-0.78±1.3	37.47±28.76
			w'	0.04±0.005	0.00	0.09±0.38	6.52±1.68
	ADV2	0.334	u'	0.33±0.015	0.11±0.01	0.26±0.08	2.61±0.07
			v'	0.09±0.004	0.00	-1.70±1.10	39.22±27.08
			w'	0.05±0.002	0.00	0.34±0.22	5.99±0.59
Accretive Runs	ADV1	0.09±00.1	u'	0.25±0.025	0.06±0.012	0.32±0.12	3.04±0.0.33
			v'	0.06±0.013	0.00	1.10±1.32	36.69±23.43
			w'	0.03±0.003	0.00	-0.18+0.54	7.94±2.03
	ADV2	0.337±0.016	u'	0.28±0.015	0.08±0.009	0.37±0.039	3.08±0.2
			v'	0.04±0.003	0.00	-0.60±0.72	22.75±22.28
			w'	0.04±0.002	0.00	0.01±0.12	7.30±1.04

5.3.4 Quadrant/Octant analysis and structural features of flow

Quadrant analysis is used to quantify the intermittency of the instantaneous Reynolds stress signals and identify turbulence structures within a turbulent bursting sequence. To stay true to the original formulation, we present the extension into 3 dimensions as three distinct, orthogonal planes of motion (Figure 5.6). These are obtained from the four 8-minute ADV1 sub-records measured near the bed, corresponding to the ABS sampling periods in each case, shown here without applying a threshold (Hole size, H=0). The scatter of $u'w'$ (in (xz) plane) highlights the dominance of the streamwise component, with the cluster of data of larger magnitude stresses generally inclined towards Q2 and Q4 type motions in the erosive runs (Figure 5.6 (a)) beside a significant proportion of Q1 type events (nearly twice as much as Q4 events). For the accretive runs (Figure 5.6 (b)), a large positive streamwise component skews the cluster towards Q1 and Q4 type motions, yet with a significant proportion of events in Q2. Hence, in the streamwise–vertical plane, fluid motions appear to be dominated by onshore directed fluctuations in the accretive runs; while prevalent Q1 and Q2 motions in erosive conditions entrain low speed near-bed fluid and particles upwards to be transported by net currents, such as the offshore-directed undertow. In the horizontal plane ($u'v'$ in (xy)), significant transverse fluctuations (comparable in magnitude to u') result in a large number of high-stress events lying outside of the zero-centred cloud of points. Q1 structures associated with shoreward–directed motions skewed to the right (of the flume) largely dominate. Again, from a 3D perspective, the dominance of shoreward directed motions (although inferred from a single point measurement and in no way descriptive of the problem) is reassuring as the wave are accretive, moving sediments from the nearshore towards the beach. In the transverse-vertical plane ($v'w'$ in $(x-y)$); the stresses are closely clustered around zero in both erosive and accretive runs, yet with notable occurrences of high-magnitude predominantly with a right-oriented transverse component. This cross-wise skewness is particularly interesting given most rectangular flume studies assume two-dimensional flow configuration, and thus highlights the three-dimensional nature of the

flow. The influence of this transverse motion could be seen higher up across the barrier, with winnowing and sorting of larger grain sediment fraction to one side of the flume.

The averaged statistical results of the quadrant analysis for the 8 erosive and accretive runs are summarised in Figure 5.7. The top panel (Figure 5.7(a)) highlights the influence of the hyperbolic hole size, H, (cf. §4.3.1) applied as a delimiting plane-specific threshold (green: H =2; grey: H=1). This is introduced to identify (and eventually disregard) small scale departures from the mean such that only strong, stress-bearing structures are considered. Notably, it was found that applying a threshold value has a far more pronounced impact in the erosive wave runs, reducing the fractional occurrence of all four types of structures by up to 80% for H=2, with the most pronounced effect on the outward (OI) and inward (II) interactions, but only up to 30% for the accretive runs. The effect of a threshold value applied to the stresses of the accretive runs reduces the accounted motions in relatively equal proportions in any given plane, with only a marginal increase in the Q1 (OI) and sweep motions at the expense of the accounted ejections. This implies that the accretive waves, characterised by plunging breakers, features much more extreme events (higher-magnitude stresses than the delimiting threshold) compared with the erosive conditions. The middle panel (Figure 5.7 (b)) presents the averaged results (of 4 sub-runs) for the erosive and accretive records, of the percentage of occurrence of each of the 4 types of bursting event structures, before and after filtering out the periodic component from the velocity fluctuations, in all three planes. The lower panel (Figure 5.7 (c)) shows the averaged percentage of contribution to stress by each of the bursting motion types, to the total Reynolds stress in the primary flow plane (uw). Filtering out the periodic component appears to have a significant impact only on the proportion of time occupied by specific motions (particularly Q2 and Q3) in the dominant flow plane (uw) of the erosive runs, and almost no effect for the accretive runs. It is also found that this has a negligible impact on the contribution to stress by each type of structure. For the erosive runs, Q2 (Ejection) and Q3- (Inward Interaction) motions

dominate the vertical motion along ($u'w'$ plane) and across ($v'w'$ plane), respectively, with the wave signal present. These events entrain low speed fluid (and particulates) near the bed upwards into the water column, and highlight a prevalence of motions are directed offshore (negative u') contributing to the erosion of the barrier face. However, when considering only the fluctuating part, Q2- and Q4- motions become relatively more frequent. For the accretive wave runs, filtering out the wave signal appears to result in nearly equal proportions for each of the 4 types of motion in all planes. In the horizontal planes ($u'v'$), Q1 and Q4 structures associated with shoreward–directed motions skewed to the right are marginally emphasised; with all motions of a bursting sequence represented relatively equally. Collectively, ejections and sweeps contribute slightly more to the total Reynolds stress (56% in erosive, 57% in accretive) than the Outward and Inward interactions (44% in erosive, and 43% in accretive). If a threshold were applied to the stresses in the erosive runs, the occurrence of Sweeps and Ejections outweighs that of the weaker interactions by a factor of 1.6 for H=2 due to the observed dominance of particular quadrant events of higher magnitude in the erosive runs, compared to the nearly equal distribution (balance) of the four quadrant event motions in the accretive tests. Remarkably, the fractional contribution of ejections and inward interactions, and hence reduced thresholds, is reportedly enhanced in sediment mixtures with high standard deviations in grain size distribution, like the coarsely skewed sediments present here; while that of the Q1 events becomes less significant (Wu and Yang, 2004; Wu and Jiang, 2007). Furthermore, it is important to note that these single point measures are limited by the frozen turbulence hypothesis in a field moving streamwise as proposed by Taylor (1938), thus showing local anisotropy induced by convective velocity fluctuations (Wyngaard and Clifford, 1977), and corresponding better to the spatial rather than the temporal changes in a given structure (Soulsby, 1983). The large vertical and horizontal separation of the two ADVs in the experimental setup (compared to boundary layer thickness) restricts our investigation in this respect.

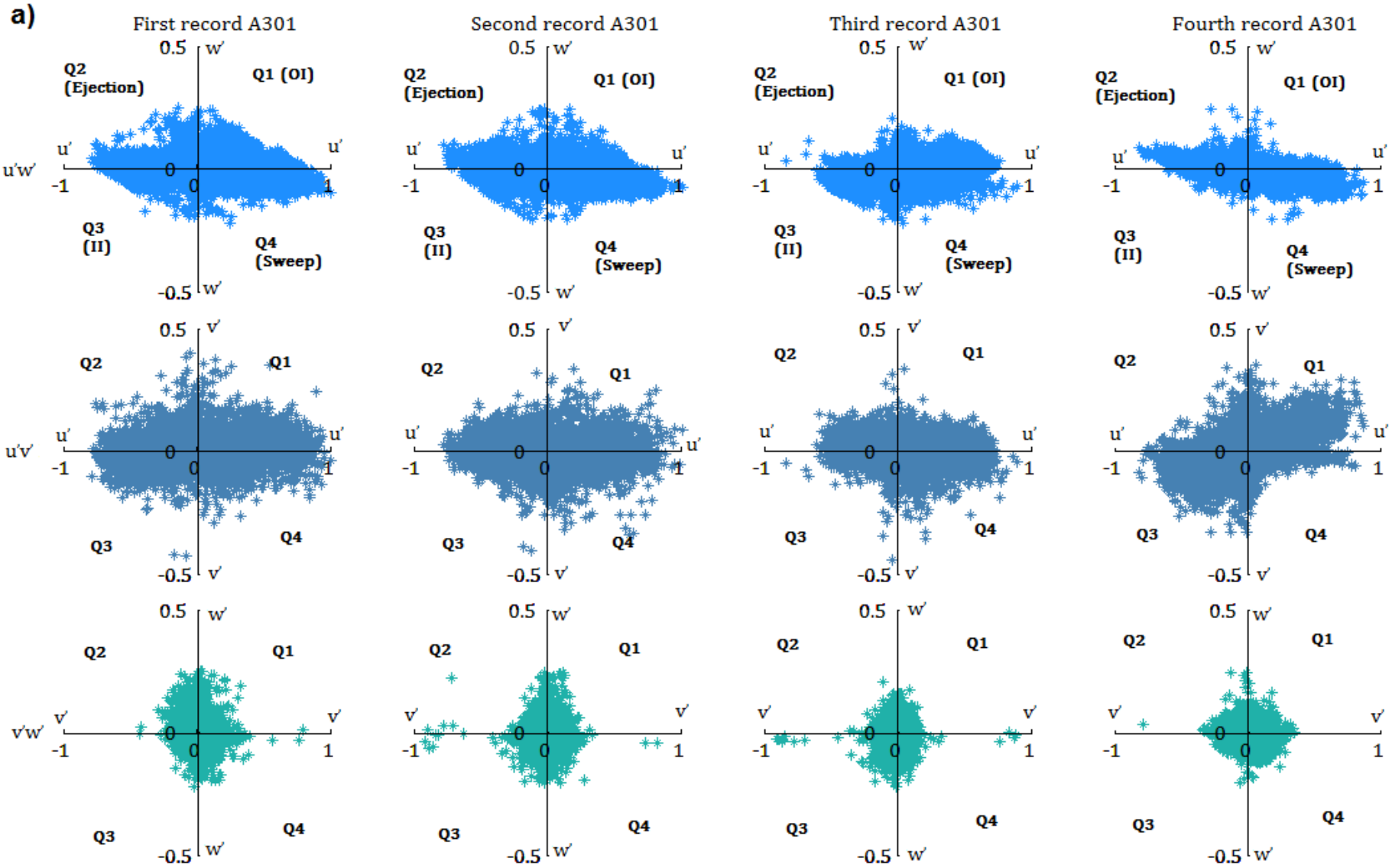
a)
First record A301
Second record A301
Third record A301
Fourth record A301
Q2 (Ejection)
Q1 (OI)
Q3 (II)
Q4 (Sweep)
u'w'
u'v'
v'w'
0.5
-0.5
-1
0
1

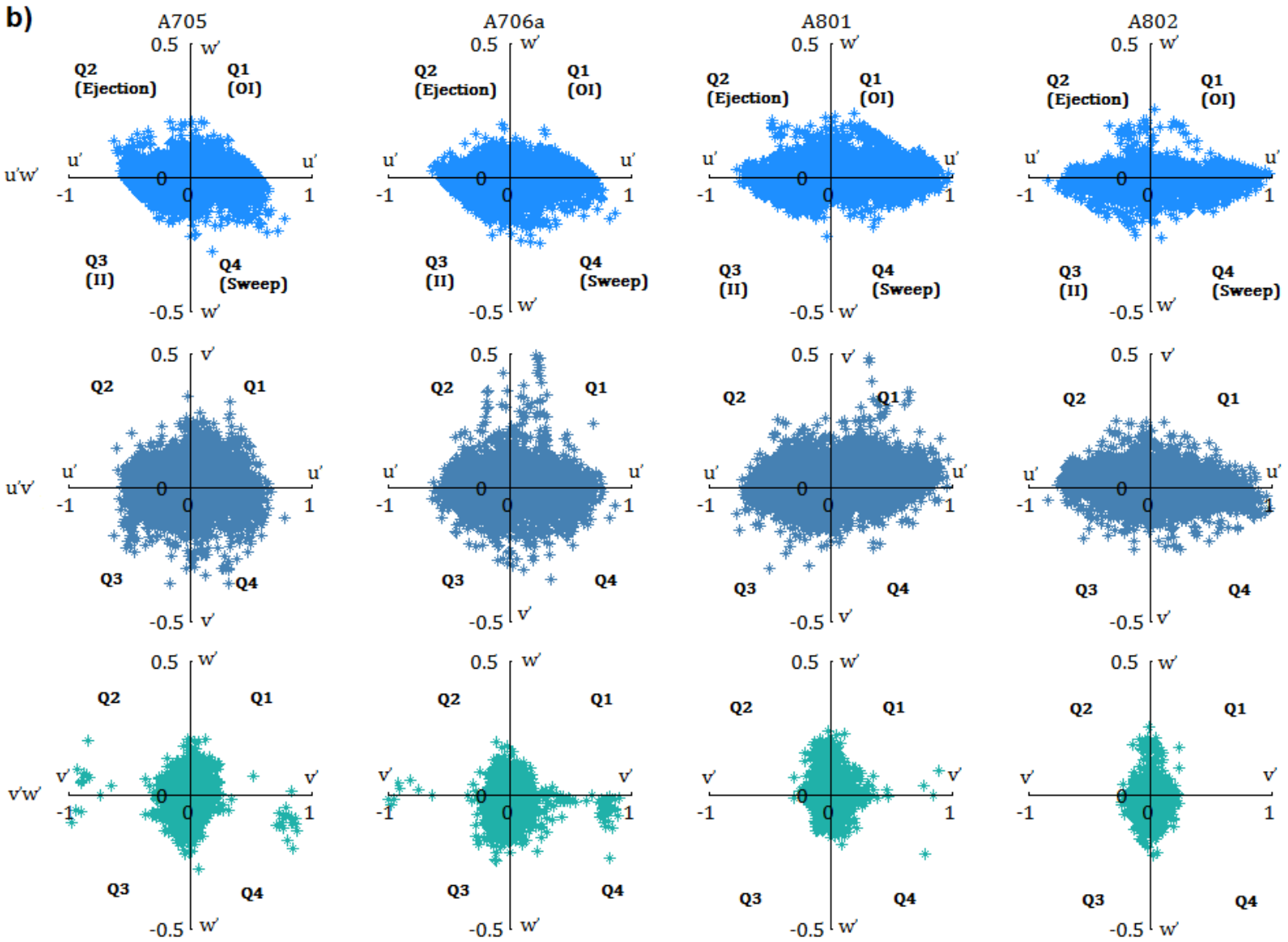

Figure 5.6 Quadrant plots of instantaneous Reynolds stresses in 3 planes for **(a)** erosive, and **(b)** accretive wave runs.

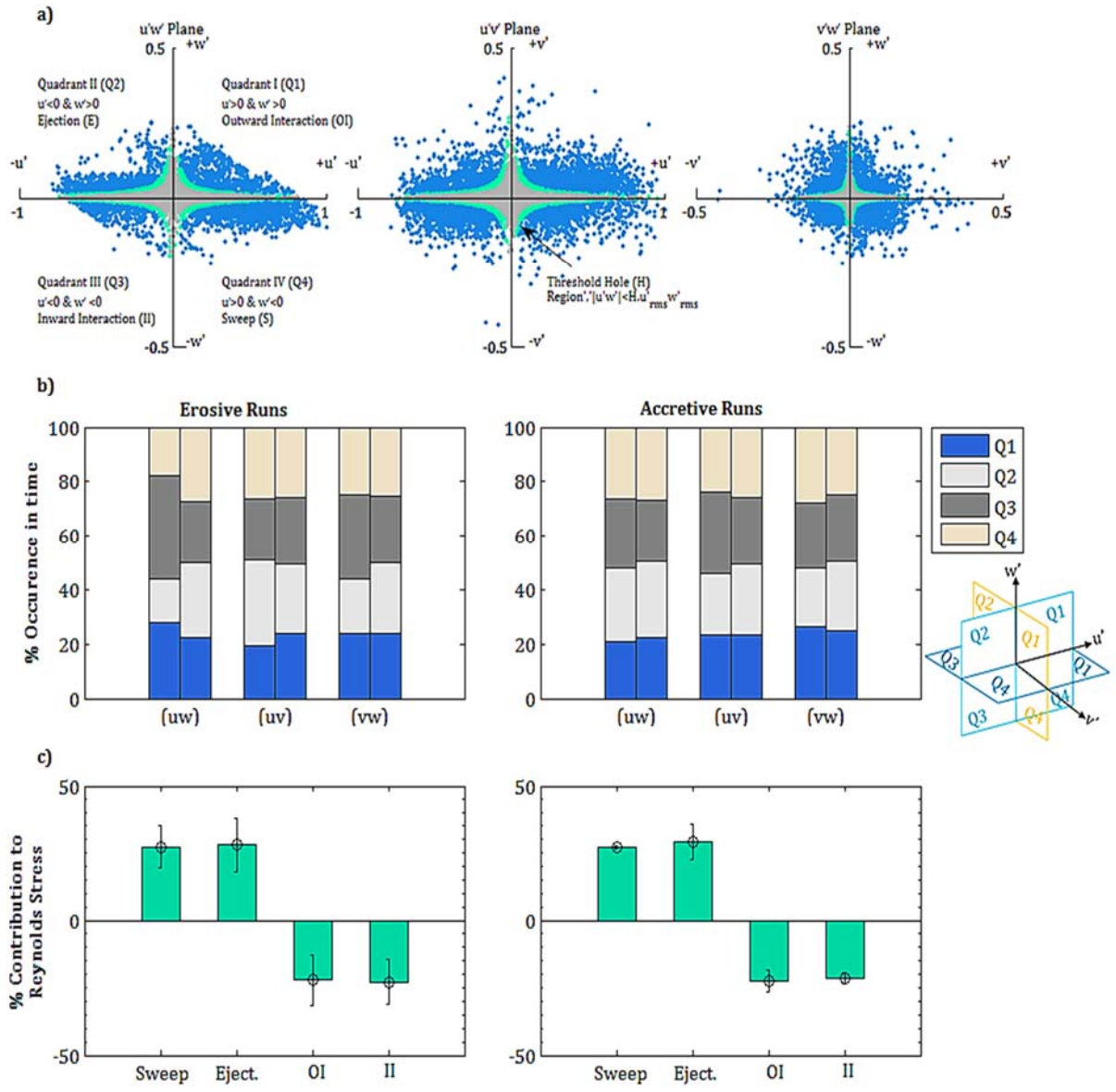

Figure 5.7 (a) Quadrant analyses of instantaneous Reynolds stresses in three planes for an 8 minute sub-record from wave series A3-01(Erosive). Areas delimited by hole sizes defined by H= 1 (grey) and H=2 (green) are highlighted. (b) average percentage of occurrence in time occupied by the 4 Quadrant-type events in each plane, in the erosive and accretive runs, before and after filtering the periodic signal, with H =0; and (c) average contribution to total, time-averaged Reynolds stress by the 4 types of motion in the primary (vertical streamwise) plane of motion (*u*'*w*').

5.3.5 Spectral properties of flow

Spectral analysis decomposes the measured turbulence data into waves of different periods (frequencies) and wavelengths, providing a suitable means of examining how these fluctuation are distributed from a statistical viewpoint (Tennekes and Lumley, 1972). The multitude of scales (both spatial and temporal) of turbulent eddies comprise a spectrum ranging from the macroscale (long period and spatially limited only by the dimensions of the flume/flow) to the high frequency microscale limited by viscosity, with the energy transfer being driven by vortex stretching (*ibid*.). The value of a spectrum at a certain frequency or wavelength equates to the mean energy of that wave, and as a result, it provides a means of assessing how eddies of different sizes exchange energy and how turbulence evolves with time. With turbulence being a largely three-dimensional problem, this necessitates construction of energy spectra in three dimensions (Cebeci and Smith, 1974). Figure 5.8 shows the power spectral densities (PSD) of the velocity components ($U = u + u' + u'_{wave}$) within and outside the boundary layer for the entire length of the erosive wave test ($\sim$ 180 minutes). These have been calculated using Welch's method with a Hann window at 50% overlap. The velocity spectra display a peak corresponding to a period of 8.19 seconds in all three components, as expected (design peak period being Tp = 8 sec). Nonetheless, a striking feature is a significant peak in the crosswise turbulence spectrum at both elevations, with a corresponding period of 2.64 seconds. This is also apparent in the accretive runs (cf. Figure 5.9), as well as what seems to be corresponding higher order harmonics. Chu et al. (1991) have reported on unstable transverse shear flows leading to large scale turbulent motions across wide and shallow open channels (horizontal length scales significantly larger than water depth), induced by the growth of small scale disturbances induced by bed friction (critical value of 0.12–0.145) or depth variation. However, neither of these appear to be applicable in this case, given the relatively uniform cross section of the flume, and the lower wave–induced bed friction factors reported in Table 5.1, and some alternative mechanism must be at work.

Standing cross-waves (transverse waves) induced by symmetric wave makers in rectangular channels have been reported to occur with excitations at nearly twice one of the natural frequencies of the paddle due to nonlinear parametric resonance (Garrett, 1970; Miles, 1988). The first mode of oscillation for a rectangular channel of width, B = 5m, and water depth hs = 2.5m occurs as half a wave with a node point at the centre of the flume, and two maxima(crests)/ minima(troughs) on either end (the rigid walls). Paterson (1983) presented the equations needed to calculate the associated wave number ($k = \pi/l$), and angular frequency $\left(\omega = \left((\pi g/B).\tanh(\pi h_s/B)\right)^{0.5}\right)$, in which case the corresponding period in our case comes to exactly 2.64 seconds, matching perfectly the peak in the spectrum, with higher order oscillations also observed in the spectra. The existence of a stable transverse standing wave may also be a contributor to the observed asymmetry and high kurtosis of the crosswise velocity fluctuation. Such transverse oscillations are documented in rectangular harbours with constant bottom slopes, and often attributed to non-linear wave transformations and harbour resonance (Wang et al., 2013). Similar cross waves have been generated in large wave basins, such as the recent edge wave experiments at IH Cantabria (Coco, pers comm.), but the existence of such waves on unconfined lengths of coast remains an open research question.

Time series and spectral analysis of 3D fluctuating velocity components, in the streamwise/along-flume (dark green), crosswise (gold), and vertical (orange) for the entire experimental wave run A301 (Hs = 0.8m, Tp = 8 s) measured (a) within; and (b) outside the oscillatory benthic boundary layer, δ_w are also undertaken to describe the dominant energy-containing structures. Power spectral densities are similarly calculated using Welch's method with a Hann window (2^11 datapoints in length) with 50% overlap, and a sampling frequency of 25 Hz. Peak wave frequencies are indicated. Thus, the power spectra of turbulence components both within and outside the boundary layer are constructed for each of the erosive and accretive sub-runs, following the same methodology (Figures 5.9 and 5.10).

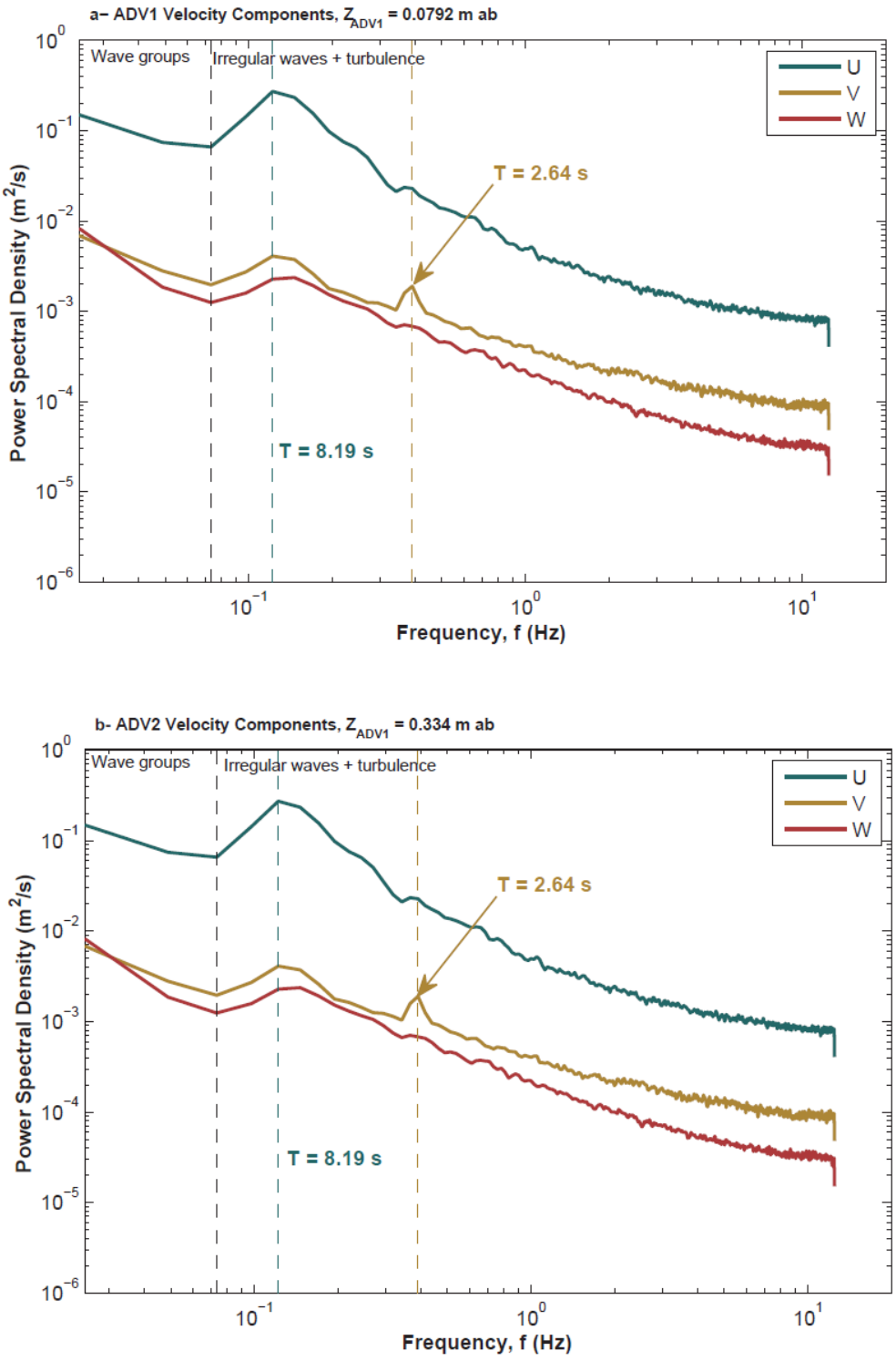

Figure 5.8 Spectral analysis of 3D fluctuating velocity components, in the streamwise/along-flume (dark green), crosswise (gold), and vertical (orange) for the entire experimental wave run A301 (H_s = 0.8m, T_p = 8 s) measured **(a)** within; and **(b)** outside the oscillatory benthic boundary layer, δ_w . Power spectral densities calculated using Welch's method with a Hann window (2^{11} length) with 50% overlap, sampling frequency 25 Hz). Peak wave frequencies are indicated.

The design peak periods (or combinations thereof used to drive the wave maker), are observed as defined peaks in the turbulence spectra in all three dimensions (prominently in the streamwise components), in both erosive and accretive wave runs. No significant peaks were apparent in the lower frequency range (periods longer than the peak wave period); suggesting limited effect of wave groups in the turbulence signal. When the wave signal is filtered out, no sharply-defined peaks could be attributed to the harmonics of the applied wave forcing (progressive waves along the channel); but the highest variances lie between the first harmonics of the progressive wave and the second harmonics of the transverse standing wave. This shows that the turbulent energy lies within the wave frequency range, as has been seen in studies of the inner surf zone (Ting and Kirby, 1996). Local peaks corresponding to the second harmonics of both could be discerned, indicating induced turbulence at flow reversal, often associated with the vortex shedding process. When shown in wave number space, these fluctuations approach the Kolmogorov–Obukhov $-5/3$ relation within the inertial sub-range (Frisch, 1995; Stapleton and Huntley, 1995). Note, however, that spectral analysis with Fourier transforms are limited by the Nyquist frequency, limiting detected frequencies to those higher than half the sampling frequency of the instruments (Glover et al., 2011), or 12.5 Hz.

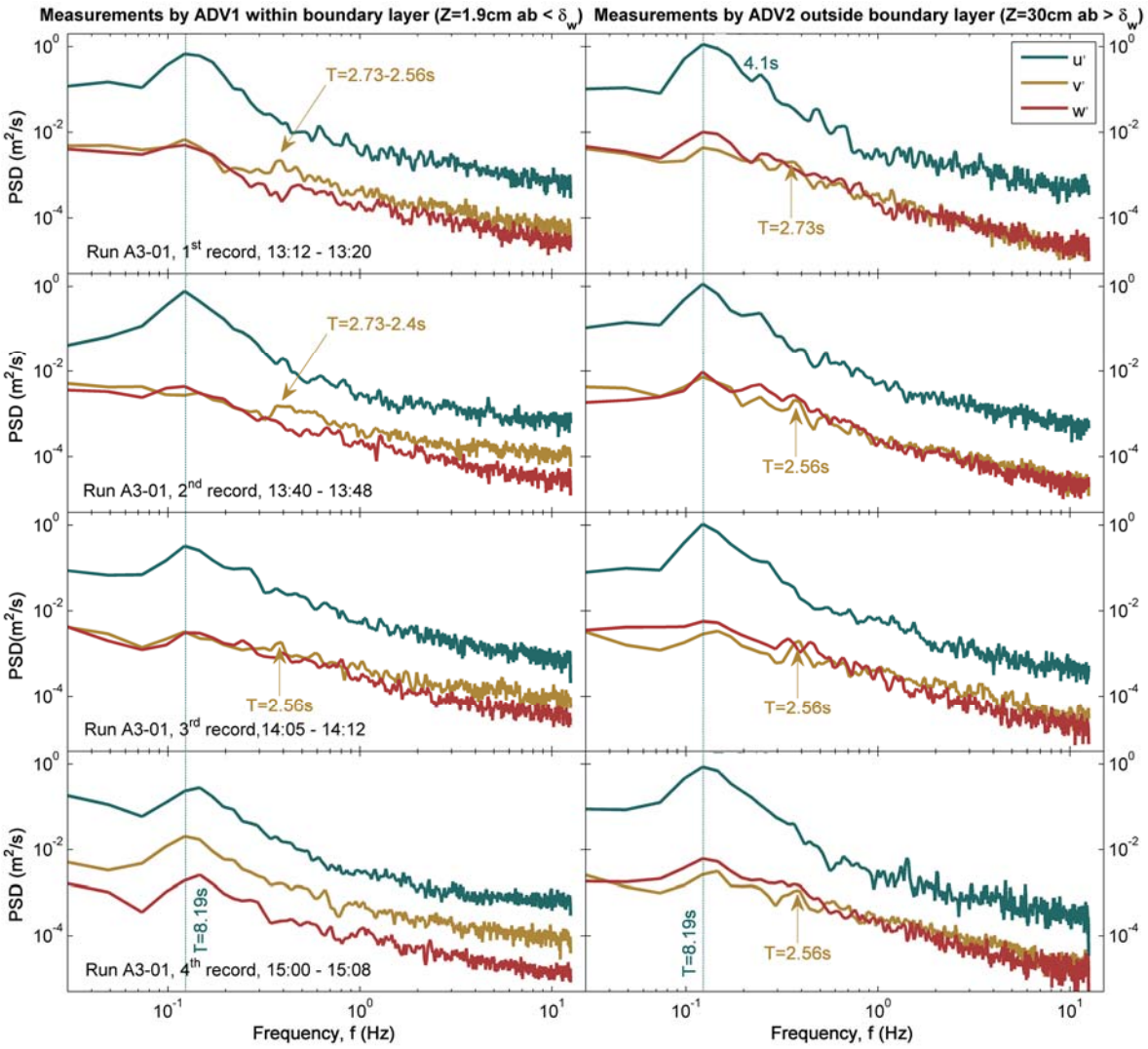

Figure 5.9 Power spectral densities (PSD) of the three turbulence components, (u', dark green), crosswise (v', gold), and vertical (w', orange) for four randomly selected sub–records of the erosive wave run A301, measured within the benthic boundary layer (left panels, 2 cm above bed) and outside the wave boundary thickness (right panel, 30 cm above bed).

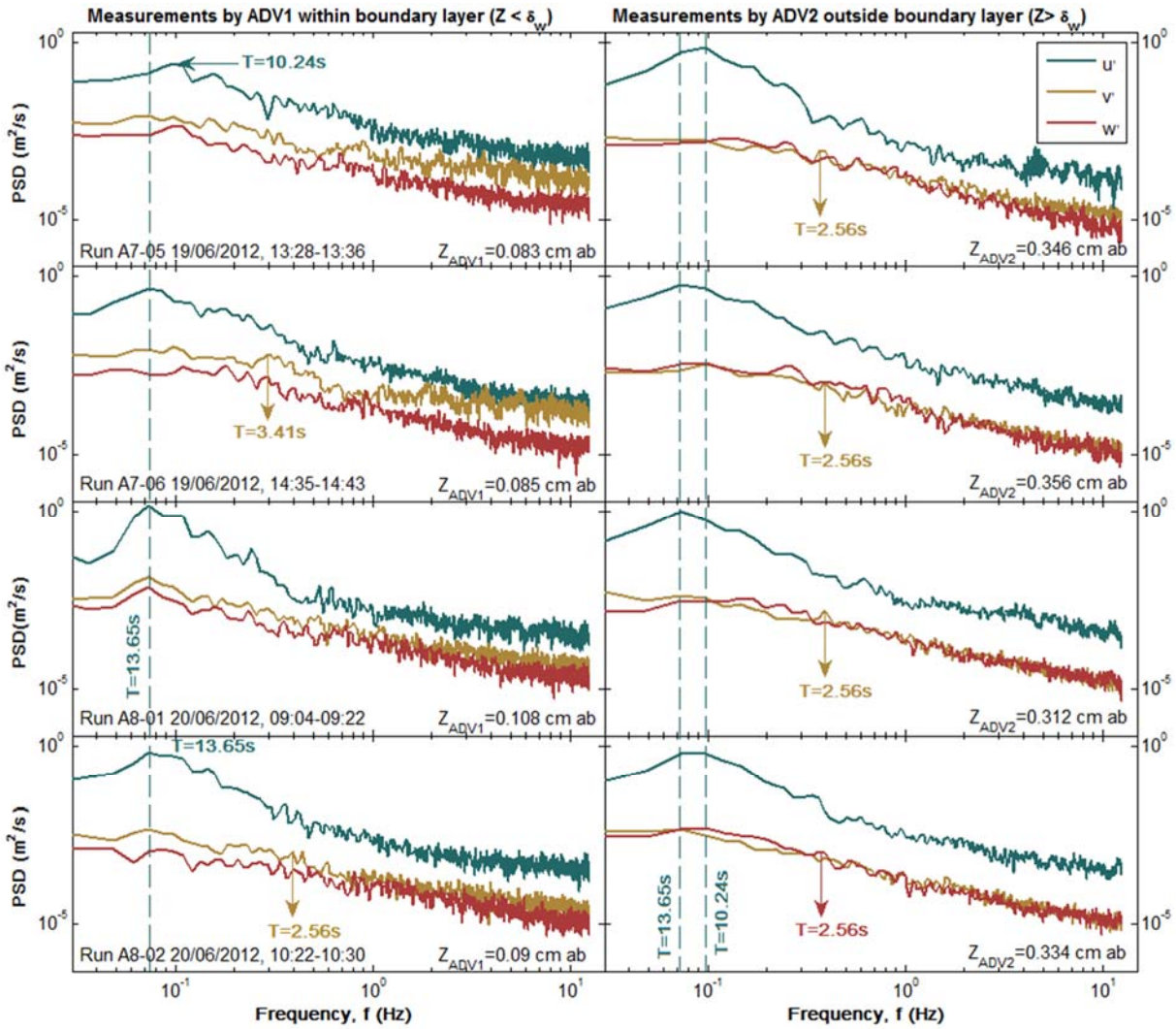

Figure 5.10 Power spectral densities (PSD) of the three turbulence components, (u', dark green), crosswise (v', gold), and vertical (w', orange) for four selected sub–records of the accretive waveruns (A705, A706, A801, and A802), measured within the benthic bounary layer (left panels, 2 cm above bed) and outside the wave boundary thickness (right panel, 30 cm above bed).

Taylor's theory of "frozen turbulence" relates the strain rate of an eddy to its wave number; and by plotting the normalised turbulence spectra in an energy preserving form in non-dimensional wave-number space, following Soulsby (1977); the dominant scales of motion can be discerned. This is shown, after smoothing with a moving-average algorithm, in Figure 5.11, where error bars represent standard deviations for the averaged four sub-runs. The peaks indicate similar scaling in the crosswise and vertical components near the bed for both erosive and accretive runs (~ 0.05 m), and slightly larger scales along the flow in the accretive runs (~0.18 m) as opposed to the erosive ones (~0.12 m). Along the direction of wave propagation, these vary over a range of scales higher in the water column (at ADV2) for the erosive runs (between 0.1 – 0.3 m), and increase substantially in the accretive ones (~1 m streamwise, 0.2 m in the crosswise and vertical). The vertical excursions scale well with the wave boundary layer thickness in both erosive and accretive runs. Overall, the wavenumbers contributing to horizontal motions are smaller than those contributing the vertical motions.

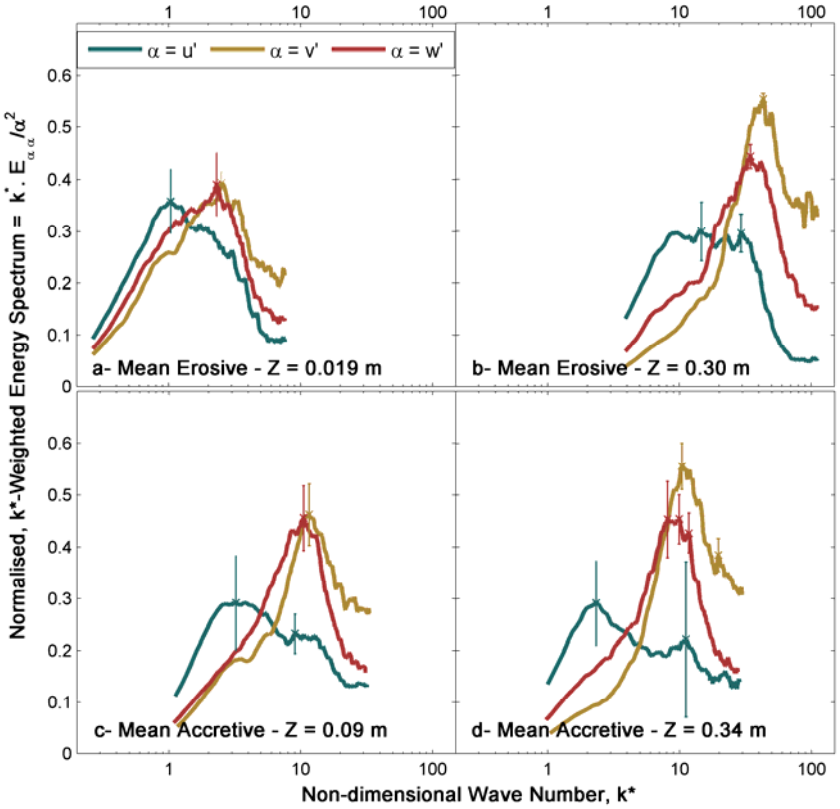

Figure 5.11 Average non-dimensional number k^*-weighted turbulent energy spectra within **(a, c)**; and outside **(b, d)** the wave boundary layer in erosive and accretive runs respectively. Colour scheme same as Figure 5.10.

The power spectral densities of sediment backscatter at 5 elevations above the bed are presented in Figure 5.12, for all of the analysed sub-runs. The suspension spectra in both erosive and accretive runs exhibit multiple or broad peaks near the bed and higher in the water column, with frequencies corresponding to the second harmonic of the progressive waves, as well as that of the transverse waves. This implies suspension of sediment is associated with the shedding of vortices from bedforms within the boundary layer (O'Hara Murray et al., 2011), and extending much higher in the water column, potentially due to pairing of vortices (Williams et al., 2007). This claim is supported by the bed morphology: stable, 2D vortex ripples with little or no migration over the duration of each 8 minute sub-run. It does not appear, however, that wave groups play a role in this case, as has been reported in irregular waves over evolving bedforms (O'Hara Murray et al., 2012). The peaks corresponding to the transverse wave properties highlight the nonlinearity and three dimensionality of the sediment suspension process, both in terms of sediment pick up and maintenance of suspension higher in the water column. While the spectra in the lower frequency range are steeper near the bed, and relatively flatter higher up, these trends reverse at the higher frequency scales. This may suggest that the stirring of sediment near the bed is driven by the mean flow properties, but the waves do not play a significant role in retaining sediment in suspension. Hence, while the immediate resuspension of sediment from the bed is controlled by mean flow properties pertaining to the prevailing wave conditions, the sustenance of suspension clouds within the water column is governed by turbulent processes, and the eventual net transport is dictated by non-linear prevailing currents resulting from non-linear interactions between the waves and beach morphology. Steeper slopes of energy spectra at higher frequencies are often associated with coherent structures (Maltrud and Vallis, 1991), and as such, higher frequency turbulence may be the dominant mechanism at work at higher elevations above the bed, and hence key to modelling suspension of sediment outside the boundary layer. A distortion of frequency response near the bed might be due to particle interference at high concentration which results in damping and hence a frequency shift. Studies of cospectra of near

bed and cross–shore velocity have shown that shoaling waves (seen in the accretive runs) produce strong onshore transport at wave frequency against weaker offshore transport at lower frequencies, both on barred and non–barred beaches, which may be attributed to low frequency modulation by wave groups (Osborne and Greenwood, 1992a; 1992b). The time dependency between the horizontal shear stress and sediment concentration also varies with elevation (Venditti and Bennett, 2000). Given the existence of an undertow in this case (~ 0.2 m/s offshore), vertical variations are expected in spilling breakers (erosive runs) as turbulence gradually spread downwards as moderate scale eddies from the surface roller, but not in plunging breakers where downward generated large scale vortices create strong vertical mixing (Ting and Kirby, 1994; 1996). Plunging breakers are dominated by orbital wave motion and turbulence is thus convected landwards, favouring accretion and indicating strong dependence on history downstream, while spilling breakers are dominated by the undertow moving sediments seaward (*ibid.*).

The erosion process, locally, is likely to be affected by the passage of large scale coherent structures with low occurrence probabilities (Adrian and Marusic, 2012). There is growing evidence that the concept of bursting as a violent ejection is replaced by the concept of "slowly evolving" fast packets of vortices creating sequences of ejecting/sweeping events each associated with one of the vortices (Christensen and Adrian, 2001; Jimenez, 2012; Jiménez, 2013). We conjecture that the succession of convected or locally generated intermittent bursting or sweeping motions would dictate whether the entrained sediment has enough time to settle, is amplified by added suspensions, or swept back to the bed. This governs the frequency response of suspension events and interference with turbulent fluctuations. Wavelet analysis may offer some clues as it provides information not only on frequency scales, but their spatial (occurrence in time) variability too. Whether erosion or accretion is observed at the barrier is then governed by the mean currents which could transport the agitated sediments above the bed. This is typical of a stochastic process where particle concentration is

closely related to that of the turbulence fluctuation arising from large eddies as shown in the work of Liu et al. (2012). Such episodic events could occur at any location of the bed, with short periods of considerable sediment movement intermingled with long periods of negligible transport (Dey et al., 2012).

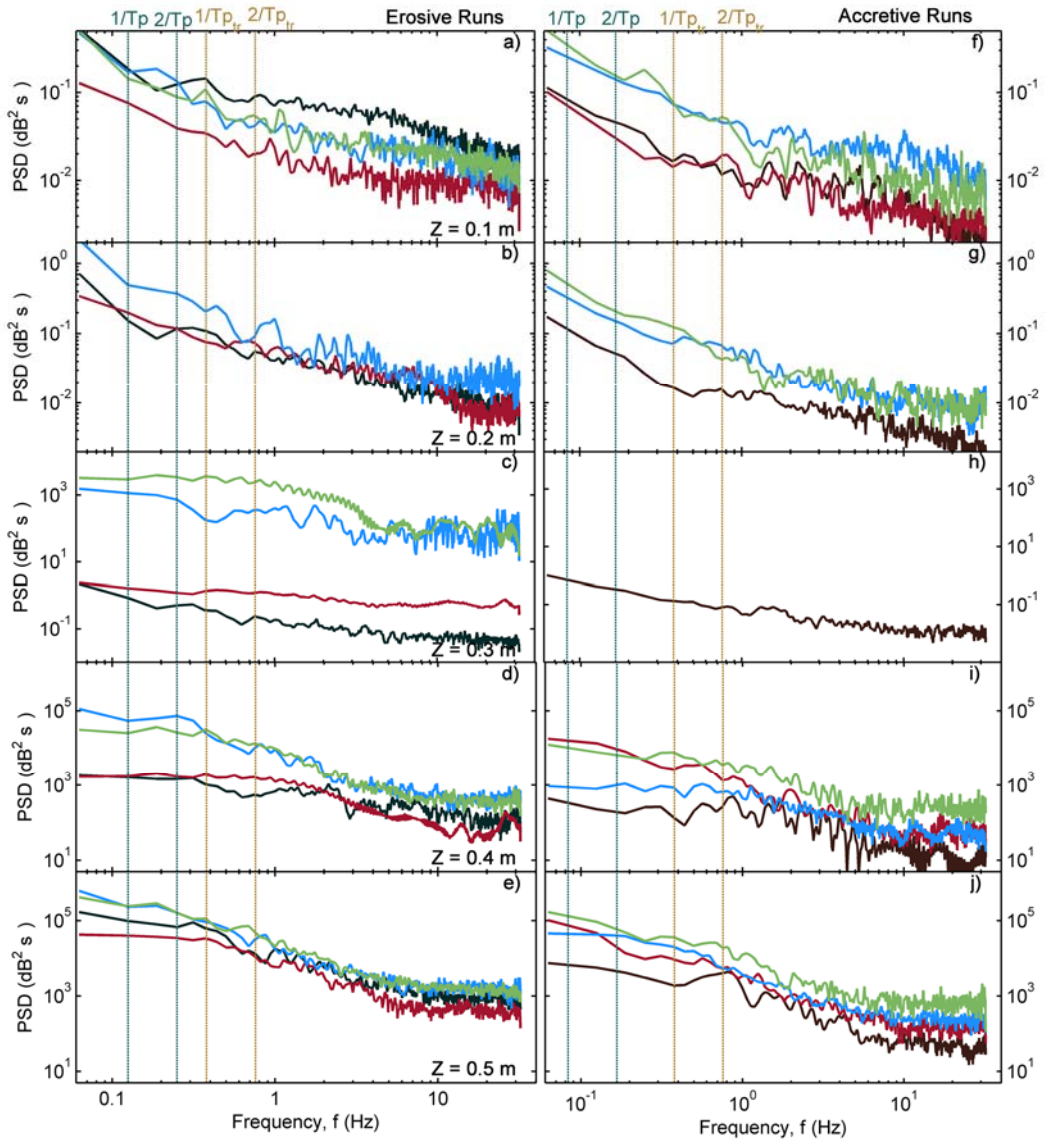

Figure 5.12 Power spectral densities (PSD) of the suspended sediment backscatter at 5 different elevations above the bed, for all the analysed erosive (left panel) and accretive (right panel) wave runs. The first ($1/T_p$) and second ($2/T_p$) harmonics of the progressive wave forcing, and the transverse standing waves are shown by the dark green and golden vertical dashed lines respectively.

5.3.6 Wavelet analysis of Reynolds stresses and sediment resuspension

Wavelet transforms are carried out to investigate the variability of high frequency turbulence structures and the ensuing suspension events, as well as their clustering (sequential occurrence) in time for each of the 8 minute records presented earlier. These structures are hereby defined in terms of the Reynolds stresses as the second moment velocity covariance (product of the turbulent components in each of the three planes). The contours of power spectra are constructed from a continuous wavelet transform of the time series of Reynolds stresses, and of the concentration time series using a Morlet wavelet (cf. §4.3.2.2 and Equation 4.22), following the methodology of Torrence and Compo (1998) and tools presented in Grinsted et al. (2004).

Figures 5.13 and 5.14 show the power spectra highlighting time-frequency characteristics of the three Reynolds' stresses and sediment suspension obtained through continuous wavelet transforms for two example sub-runs from the erosive and accretive series respectively. Similar results are evident in the other sub-runs (plots presented in Appendix 4), and the behaviour reported hereafter is true for both erosive and accretive runs. In these figures, the left panels pertain to measurements at the level of ADV1 (within the wave boundary layer), while results from measurements corresponding to ADV2 (outside the boundary layer) are displayed in the right panels. The figures show the time series of the three Reynolds' stresses in 3 orthogonal planes of motion: ($u'w'$) in the streamwise-vertical plane (bed normal along the direction of wave propagation), ($u'v'$) in the horizontal plane, and ($v'w'$) in the crosswise-vertical plane, having filtered out the wave-signal from the fluctuating turbulence components, as well as their energy spectra (obtained by Fourier transforms, as discussed in section §5.3.5). The time-series of continuous wavelet transforms (CWT) for each of the stresses in the time-frequency domain, are presented subsequently in the same order, together with their global spectral power (integrated variance). We opted to present the inverse frequencies (*i.e.* periods) on the vertical axes, to facilitate the

discussion when related to wave properties. The global power pertains to time averages, if we were to take a vertical slice through the wavelet plot, and average all the local wavelet spectra (Torrence and Compo, 1998).

Finally, the lower two panels show the time series of vertical suspension (logarithmic backscatter, higher values in warmer colours) profiles below the ABS sensor head, the power spectral densities of suspended sediment concentration at the level of the corresponding ADV (ADV1 on the left, ADV2 on the right), and the related continuous wavelet transform of the suspension time series at that elevation, together with its global spectral power. In these plots, warmer colours indicate higher power (variance), the white-shaded region represents the cone of influence where edge effects may distort the image, and the thick contours represent the 95% confidence limit (5% significance against red noise). Note that at higher periods (low frequency events), the power falls within the cone of influence, limiting our ability to investigate the temporal evolution of the particular peak frequencies reported in section §5.3.5. Therefore, we are restricted to investigating very high frequency events occurring at time scales up to 2 seconds. This limitation arises from Heisenberg's uncertainty principle, which dictates that one cannot obtain arbitrary good localisation in both time and frequency, and a trade–off must exist whereby spatial resolution is bad at large scales while scale (frequency) resolution is bad in the small scales (Foufoula-Georgiou and Kumar, 1994; Lau and Weng, 1995; Farge et al., 1996; Grinsted et al., 2004). Having said that, it is clear that most of the power (variance) in concentration lies within the lower frequency range (high period) associated with the mean flow properties for both stresses and suspensions near the bed.

The Fourier-transform-derived spectra of Reynolds stresses show that they approach the universal Kolmogorov–Obukhov -5/3 relation corresponding to the inertial decay sub-range (Frisch, 1995, Stapleton and Huntley, 1995). While this is still true for stresses measured outside the boundary layer (by ADV2), it is interesting that a secondary peak appears within the higher frequency range, suggesting enhanced turbulence with smaller scales of motion. The CWT results show that 'powerful' (*i.e.* high variance) turbulent

events occur intermittently throughout the records, in slowly evolving clusters that persist over short durations in the dominant flow direction (streamwise-vertical) near the bed, and for longer durations (significant from a turbulence perspective, up to several minutes); higher up in the water column, and at lower frequencies in the erosive runs (Figure 5.13). The larger clusters fall over short bands of frequency scales (*e.g.* specific periods, predominantly 0.5 and 2 seconds); while the fast-evolving clusters extend over a bigger range of frequency scales (primarily between ½ and 1/64 seconds) before diminishing. This may indicate breakup of the larger eddies into smaller and smaller ones within the inertial sub-range (between energy-containing scales and small dissipative scales), before the energy is consumed by viscosity, as described by the classical turbulence cascade which suggests that inertia results in stretching and rapid breakup of vortices into many smaller, excited degrees of freedom, until energy is dissipated through viscosity (Tennekes and Lumley, 1972; Kolmogorov, 1991a; Frisch, 1995; Sreenivasan and Antonia, 1997). Nonetheless, the occurrence of long-lasting events outside of the wave boundary layer and which do not correspond in time to those identified within the wave boundary layer indicates turbulence that is independent from bottom induced friction. This are likely to be the result of free-stream turbulence introduced by the spilling breakers which characterise these erosive runs; and these do not result in observed suspensions. The turbulent clusters within the streamwise-vertical plane (hereafter referred to as the dominant plane of motion) have the highest power, which appears to be uniformly distributed across the aforementioned frequency range. In the horizontal plane, such events are also considerably powerful, but tend to spike (peak sharply) closer to the lower end of the range, at periods comparable to the harmonics of the transverse standing wave. In the crosswise-vertical plane, significant clusters of turbulent stresses occur for longer times, but their power is negligible compared to those of the other two planes of motion.

In the accretive runs, (Figure 5.14), the streamwise–vertical plane is characterised by long lasting, high variance events of low frequencies near

the bed, persisting for considerable durations (several minutes), together with significant, small and rapidly evolving structures occurring intermittently within the record at much higher frequency scales. From a global (time averaged perspective), these two different structural scales contribute nearly equally to the global spectral power. Outside the boundary layer, only the smaller scale (between ½ and 1/64 seconds) events are evident. In the crosswise and horizontal planes, significant events (weaker/ of lower variance) are collocated in time with those observed in the $(x-z)$ plane suggesting they correspond to the same structural features of the flow. The imprint of the transverse standing wave is also evident in these runs, particularly in the CWT of $v'w'$ at both elevations. In contrast to the erosive runs, no free (boundary independent) turbulence is observed within the records (events which do not correspond to those seen within the boundary layer), Hence, with the plunging breakers that characterise these accretive runs, any downward injected turbulence from breaking waves is likely to extend all the way to the bottom; and whether the observed events in both records are bed-induced or surface-generated cannot be discerned in this experiment.

Under both erosive and accretive conditions, the simultaneous presence of the two scale of motions at their intensity maxima suggests a modulating effect of the larger clusters of the frequencies of smaller motion near the bed, in agreement with similar studies in wall turbulence (Ganapathisubramani et al., 2012). Similarly, the simultaneous visualisation of cross-correlations $(u'w', u'v', v'w')$ in the three planes reveals the extent of coherence of these turbulent fluctuations, and is analogous to observations of hair-pin packets dragging a forward-inclined low-speed region into the flow, as reported by Christensen and Adrian (2001) in open channels, and by Ganapathisubramani et al. (2005) in wind tunnels; and would explain the multiple large-scale ejections and sweeps noted.

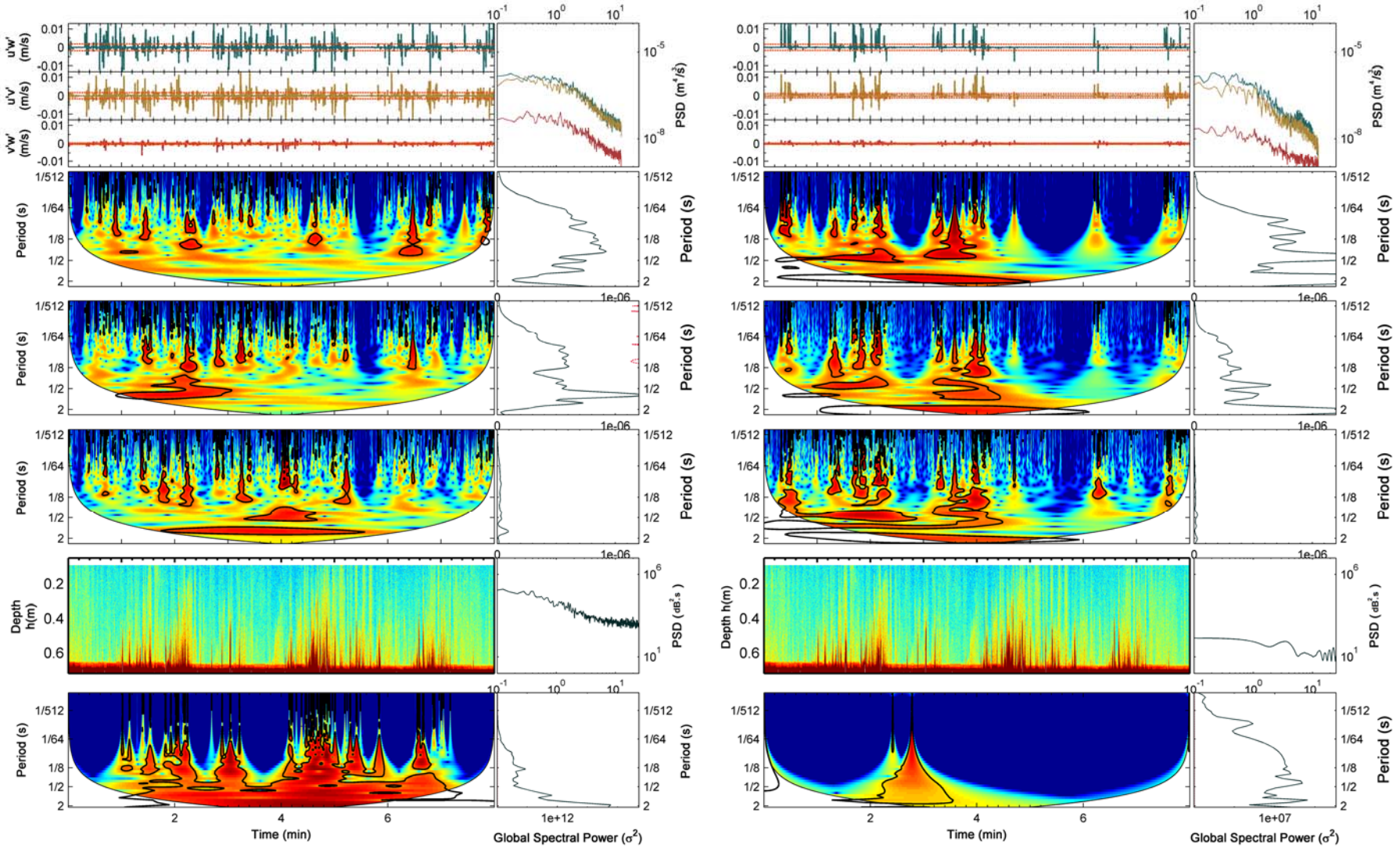
u'w' (m/s)
u'v' (m/s)
v'w' (m/s)
PSD (m⁴/s²)
Period (s)
Depth h(m)
PSD (dB².s)
Time (min)
Global Spectral Power (σ²)

Figure 5.13 Time-frequency properties of the three instantaneous Reynolds stresses ($u'w'$, $u'v'$, and $v'w'$) and suspended sediment concentrations (SSC), measured within (left hand side) and outside (right hand side) the wave-induced benthic boundary layer for Erosive waver run (A301-2nd sub record). In each panel, the top three subplots show the time series of the three aforementioned stresses , respectively; together with their frequency spectrum (through a Fourier transform). The following three sub-panels present the time series of continuous wavelet transforms (CWT) for each of the stresses in the time-frequency domain, presented in the same order, together with their global spectral power (integrated variance) across the various frequency (inverse period) scales. Subsequently, the lower two sub-panels show the time series of vertical suspension profiles (logarithmic backscatter; with higher values in warmer colours) below the ABS sensor head. The power spectral densities of SSC at the levels of the corresponding ADV (ADV1 on the left, within the boundary layer; ADV2 on the right, outside the boundary layer) are also presented, as well as the related continuous wavelet transform of the suspension time series at that elevation. In the time-frequency domains, warmer colours indicate high power (variance); the white-shaded region represents the cone of influence where edge effects may distort the image, and the thick contour lines represent the 95% confidence limit (5% significance against red noise).

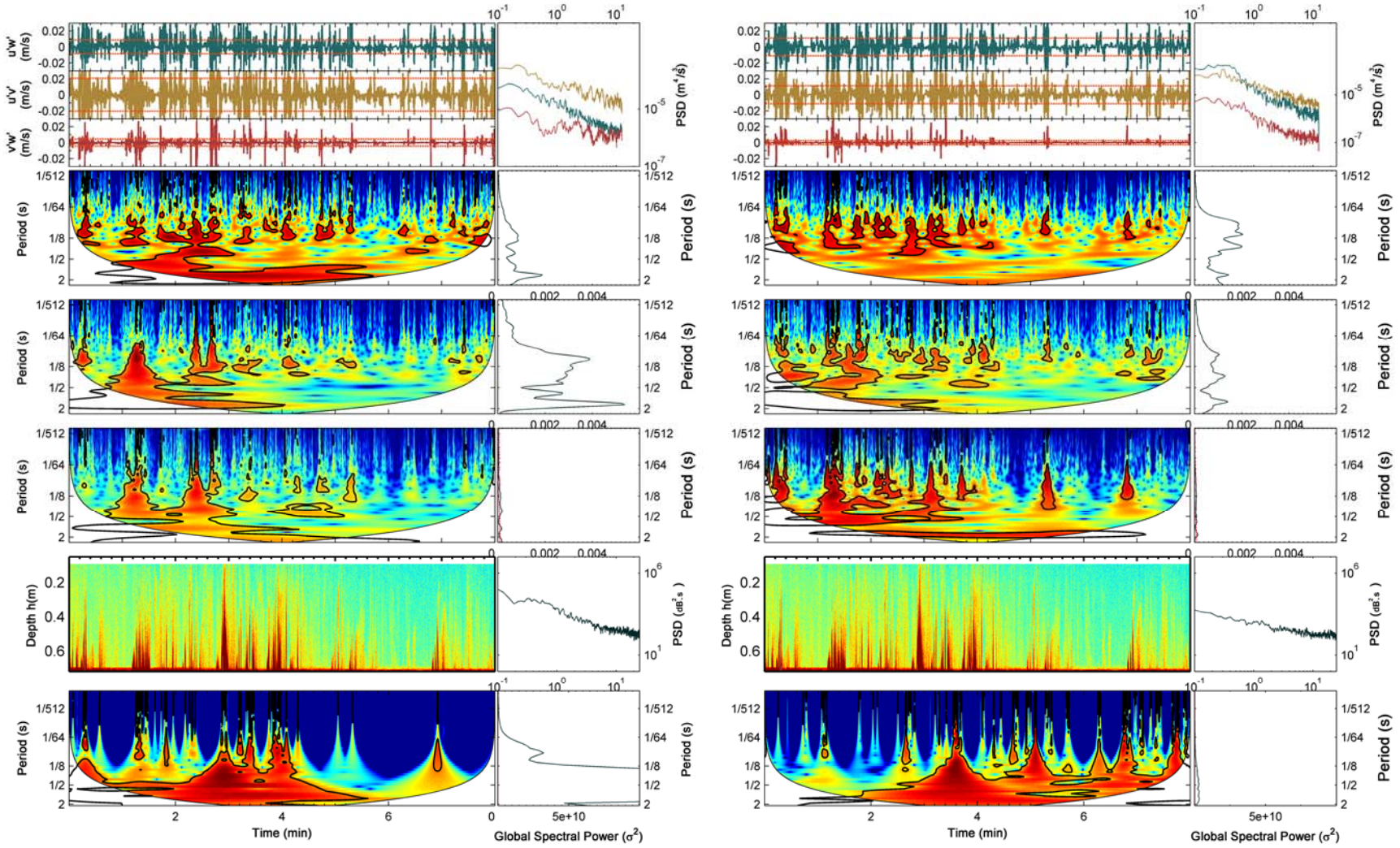
u'w' (m/s)
u'v' (m/s)
v'w' (m/s)
PSD (m²/s²)
Period (s)
Depth h(m)
PSD (dB².s)
Time (min)
Global Spectral Power (σ²)

Figure 5.14 Spectral powers of Reynolds stresses and Suspension for an accretive wave run (A706). Refer to Figure 5.13.

Periods associated with a succession of powerful turbulent events are very closely followed by periods of powerful, high frequency suspensions, extending from the larger scales observed in the low frequency range (periods up to 4 seconds/outside the cone of influence), and exponentially extending over smaller and smaller scales (higher frequencies/lower periods) before decaying as turbulence clusters cease. This may be explained as cumulative, highly-varied suspensions in response to the faster turbulent perturbations, where continuing upward diffusion exceeds the settling velocity of the entrained particles. Figures 4.13 and 4.14 both show much better correlations between identified turbulent cluster events and the intermittent, high variance occurrences within the CWT of turbidity (suspended sediment concentration) measured at the corresponding elevation within the wave boundary layer than outside of it. Hence, near-bed suspension events are directly linked to local process within the wave benthic boundary layer while those measured outside the boundary layer are controlled by non-local (advected) turbulence. Even the more sporadic suspension events of lower significance appear to conform to the aforementioned behaviour, if the wave signal is not excluded from the turbulent fluctuations (shown in Figure 5.15). Figure 5.15 shows abundant intermittent clusters of high power Reynolds stress events (oscillating and turbulent components included) with defined frequency scales persisting for different durations throughout the wave runs both within and outside the wave benthic boundary layer.

The identified periods of high power (in Reynolds stresses) and long suspension events often appear directly following significantly large amplitude variations in water surface elevation of up to 1.4 m, inferred from the pressure gauge in all erosive and accretive sub-records (Figure 4.16). This suggests that the initiation of a large suspension event beyond the mean flow frequency range is instigated by the passage of the more energetic waves within the JONSWAP spectrum, or with early wave breaking events. Its persistence in the higher frequency range is then dictated by the supply of fluid momentum; either generated through bed friction, or injected downwards by the spilling breakers of these erosive wave runs. Higher in the

water column, few suspension events are observed at the high frequencies, and where they do occur, these are characterised by a rapid expanse of the scales followed by a rapid decay (dissipation of energy). In the accretionary runs, the turbulence events span even wider scales and occur over longer durations, corresponding to significant fluctuations in the time series of the turbulence components (and water elevation). These clusters can be interpreted as large scale, uniform momentum regions convected or formed near the bed in the low frequency range. As they evolve, they cause small scales vortices that experience sudden and short lived changes in velocity, manifest by short duration events of high variance, that appear to be 'shooting out' of the larger clusters and spanning a significant extent in the high frequency range in these plots. This change can cause higher shear stresses compared with the mean flow as reported by (Hutchins et al., 2011) and Mathis et al. (2011) and, as such, are often followed by significant suspension clusters.

Collectively, Figures 5.13, 5.14 and 5.15 show that the bulk of sediment suspension events can be attributed to wave-induced turbulent fluctuations of low frequency (only higher order harmonics of the wave period (4/Tp) are visible outside the cone of influence), where most of the global power is retained. Yet, the short-lasting suspension clusters scale with the rapidly decaying high frequency turbulence. This perhaps highlights a hysteresis effect, where a dynamic lag occurs between the driving mechanism in terms of the formation, and evolution of a vortex structure and ensuing bursting sequence, and the response in terms of sediment resuspension. It also confirms the distortion and shift in frequency response of the sediment concentrations near the bed at high concentrations, reported in §5.3.5. The attenuation of turbulence by means of the suspended particles is commonly referred to as drag reduction, but its investigation is often constrained to cohesive sediments (Li and Gust, 2000; Cloutier et al., 2006; Thompson et al., 2006). Evidence of drag reduction by non-cohesive sediment is scarce, and limited experimental work focusing on spherical particles has shown that

relatively low concentrations can reduce turbulence intensity and the number of ejection events (Rashidi et al., 1990).

Dyer and Soulsby (1988) and Soulsby et al. (1994) have also attributed reductions in turbulence intensity to sand clouds suspended by ejection events in the field. Zhao et al. (2011) also observed a decrease in entrainment rate as sediment clouds are advected by the orbital motion of waves compared to quiescent periods, until the coherency of sediment-bearing vortex-cores is eventually diminished. Numerical simulations of two-way coupled spherical particle-laden flows (feedback of sediments included in numerical simulation of flow) have demonstrated pronounced modulation of the turbulence, an enhancement in turbulent anisotropy, and attenuation of Reynolds stresses typical of drag reduction (Zhao et al., 2010). Finally, transverse motion of the standing wave is likely to contribute to the observed dissipation of the motion, as spanwise motion is considered a relatively efficient reduction technique for skin-friction drag in aerodynamics (Quadrio, 2011).

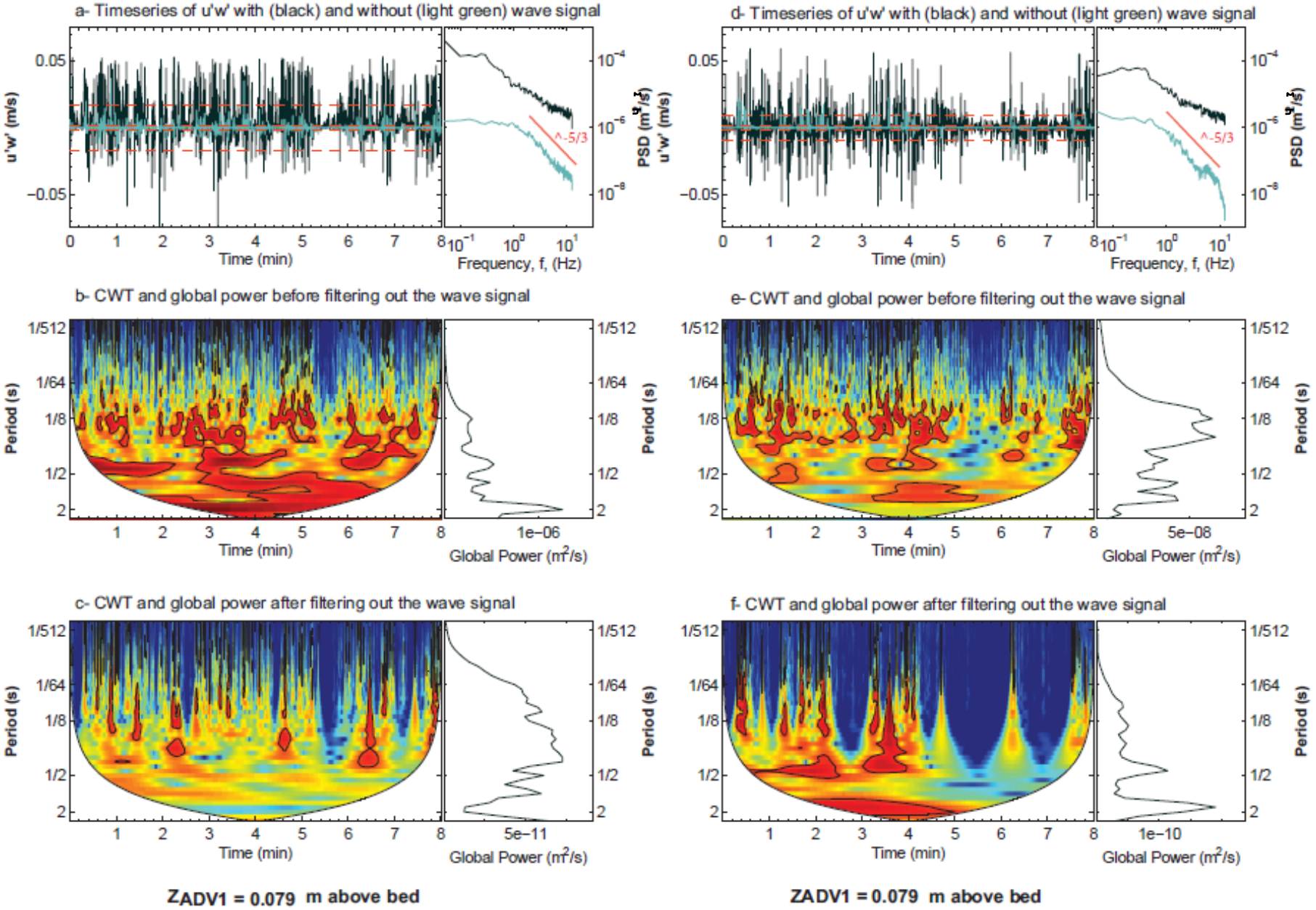
a- Timeseries of u'w' with (black) and without (light green) wave signal
u'w' (m/s)
0.05
−0.05
Time (min)
PSD (m²/s²)
^-5/3
Frequency, f, (Hz)
b- CWT and global power before filtering out the wave signal
Period (s)
1/512
1/64
1/8
1/2
2
Time (min)
1e−06
Global Power (m²/s)
c- CWT and global power after filtering out the wave signal
5e−11
ZADV1 = 0.079 m above bed
d- Timeseries of u'w' with (black) and without (light green) wave signal
e- CWT and global power before filtering out the wave signal
5e−08
f- CWT and global power after filtering out the wave signal
1e−10
ZADV1 = 0.079 m above bed

Figure 5.15 Influence of wave-signal on the time–frequency properties of Reynolds stress in the streamwise-vertical plane ($u'w'$), measured near the bed (left panel), and outside the wave boundary layer (right panel). In each panel, top sub-plots (a), and (d) show the time series of Reynolds stress (before and after filtering out the wave signal), together with its corresponding frequency spectrum (by Fourier transform). The dashed horizontal lines indicate ±1.σ (standard deviation). The rate of inertial dissipation is shown by the sloping red line in the frequency plot. The middle (b) and (e) and bottom (c) and (d) sub-panels sow the time-series of continuous wavelet transform (CWT) of the Reynolds stress before and after filtering out the wave signal, respectively, together with the corresponding global power spectrum. Refer to Figure 5.13 for legend.

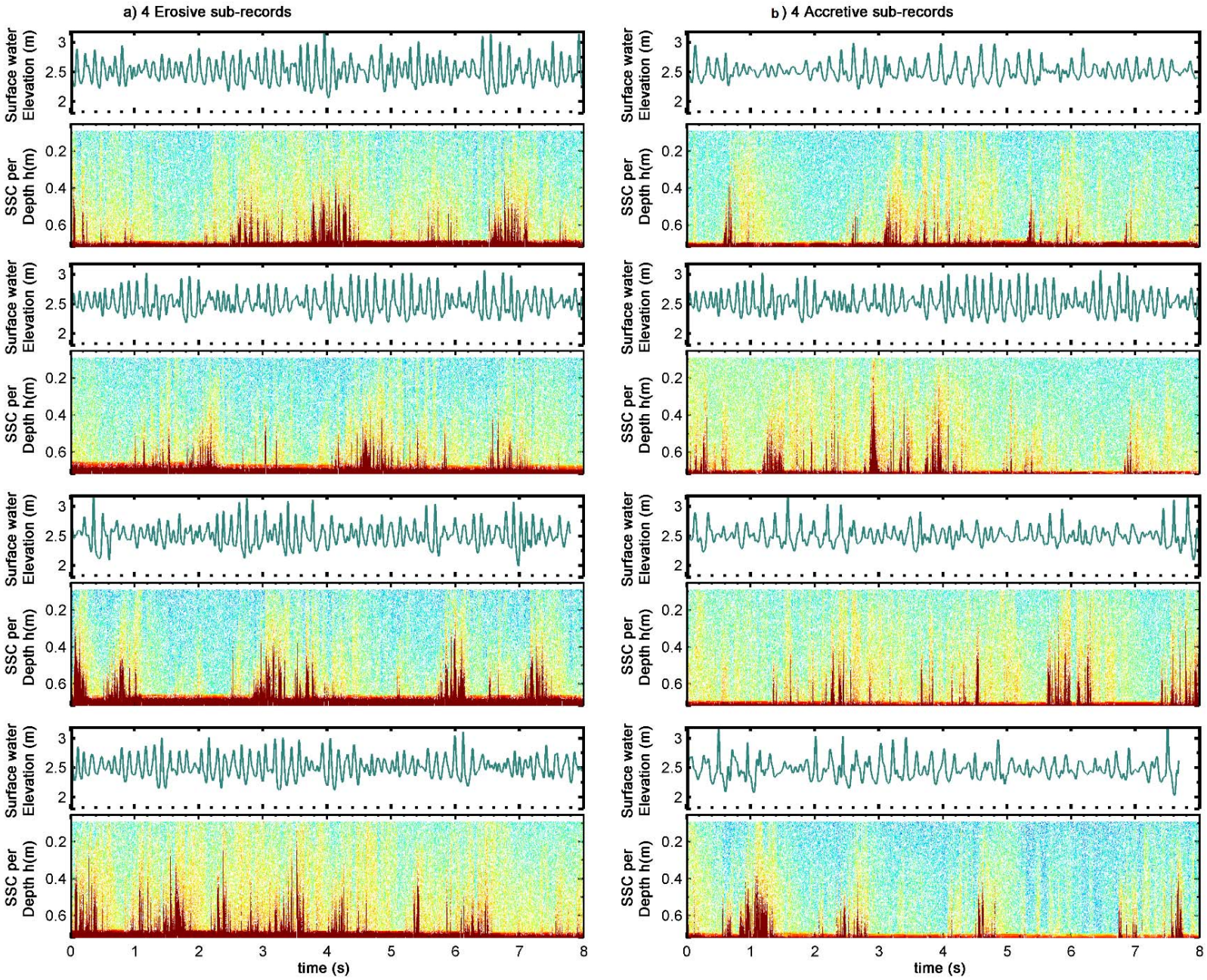
a) 4 Erosive sub-records
b) 4 Accretive sub-records
Surface water Elevation (m)
SSC per Depth h(m)
time (s)

Figure 5.16 Water surface elevations and suspended sediment concentration/ backscatter (SSC) profiles for (a) the four erosive sub-records (top to bottom, A301-1st, A301-2nd , A301-3rd ,A301-4th); and (b) the four accretive sub-records (A705, A706, A801, and A802).

To examine the hypothesis thus posited, cross-wavelet transforms (XWT) of the Reynolds stresses in three planes, and the recorded suspended sediment concentrations are presented in Figure 5.17, both within and outside the wave boundary layer (other runs are presented in Appendix 5). Note that this can only be performed after down-sampling the 64 Hz suspension record to match the sampling frequency (25 Hz) of the ADVs. The significance levels are tested against red noise generated by a first order autoregressive model following Grinsted et al. (2004), and denoted by the thick contours. The lightly shaded area represents the cone of influence. The XWT has been applied to the turbulent fluctuations before (denoted by the "wave" subscript); and after filtering out the wave signal for each of the Reynolds' stresses in every plane. The phase relationship between the two signals (stress and concentration) is shown by the arrows, whereby right arrows indicate the signals are in-phase, left-pointing arrows indicate anti-phase, and vertical arrows suggest that the Reynolds stresses lead concentration by 90 degrees phase shift, testing the coherence of the transform (Grinsted et al., 2004). Here we notice common features observed earlier where suspension events and turbulent stresses share high common power at a range of scales in both erosive (Figure 5.13) and accretive (Figure 5.14) records. At all frequency scales, these regions of significant common power occur for most of the time near the bed and in all three planes with both the oscillatory signal present (Figure 5.16 a - c) or removed to indicated fluctuating turbulence only (d - f). This indicated that both the mean flow properties and the fluctuations correlate well with the local sediment flux, and hence the suspension of sand is governed by local processes. The oscillating component seems to dominate the low frequency scales (higher periods) whereas the observed small-scale events are related to high-frequency, short lived turbulence clusters near the bed. Outside the wave boundary layer, most regions of high common power between suspension and stress appear to be dominated by the fluctuating component of the stress (j –l), with weaker fluxes attributed to the oscillating component, which seems most evident in the horizontal plane (g –i, and mostly in h). The powerful events at lower periods of 2 – 4 seconds are phase locked, implying causality between the wave-induced turbulence and the ensuing suspension,

but with no time lag. However, no robust measure of whether this may be an artefact of the dominance of one of the signals, or not, is carried out (*e.g.* combining clustered wavelet spectra with maximum covariance analysis presented by Rouyer et al. (2008)). The higher-frequency 'wave-contaminated' scales appear to be less coherent in all planes both near the bed and outside the boundary layer. However, once the wave signal is filtered out, the turbulent fluctuations outside the boundary layer appear to be predominant in driving the suspensions at this level, with the highest power, although being phase-locked in the opposite direction. This confirms that the sediment flux outside the boundary layer is governed by turbulence fluctuations, independent of the mean-flow induced turbulence at the bed, as these are not co-located in time with the measurements within the boundary layer, particularly in the (x-z) plane.

Collectively, the wavelet analyses presented collectively support the conjecture proposed, postulating a mechanism in which successive intermittent bursting motions play a significant role in moving and maintaining sediments in suspension. In time-frequency space, it is shown that most of the momentum exchange, and ensuing suspension, lies within the low frequency range (high periods) dictated by the mean flow properties. The passage of intermittent and relatively large momentum regions of uniform spectral properties at higher frequencies, plays a direct role in sediments suspensions which exhibits significant variability within the higher frequency range. As these regions, which signify the passage of a coherent structure, persist for a considerable amount of time, suspensions near the bed are amplified before decaying as the supply of momentum by these turbulent structures ceases. Within a given cluster of turbulence, both stresses and suspensions span a certain range of frequencies, which may hint at a nonlinear modulation of both the amplitude and frequency of such small structures with the larger flow structures near the bed. Such behaviour in wall turbulence has been attributed to local changes in shear but not necessarily the spatial and temporal structure of large flow events (Ganapathisubramani et al., 2012).

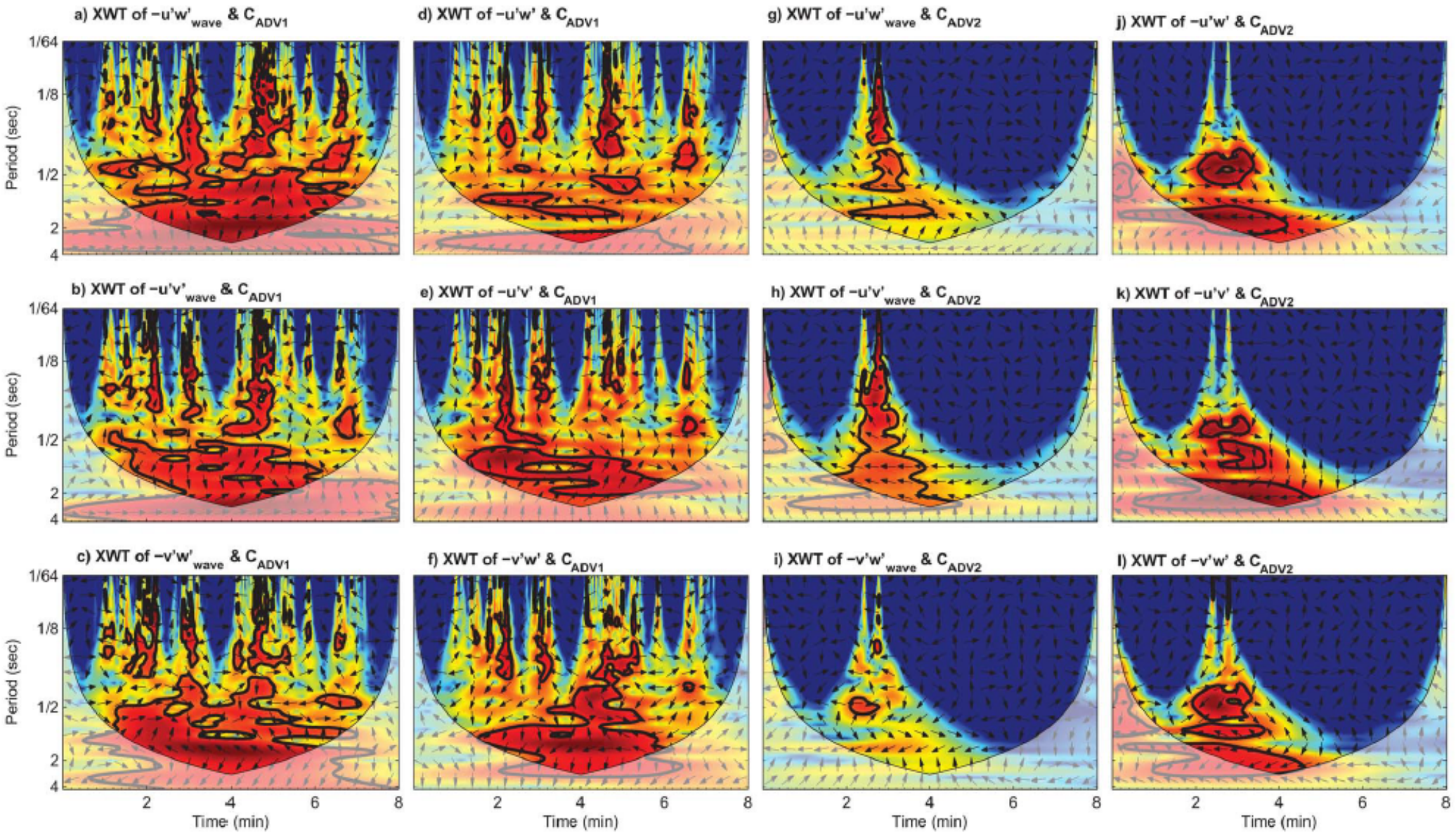
a) XWT of −u'w'wave & CADV1
d) XWT of −u'w' & CADV1
g) XWT of −u'w'wave & CADV2
j) XWT of −u'w' & CADV2
b) XWT of −u'v'wave & CADV1
e) XWT of −u'v' & CADV1
h) XWT of −u'v'wave & CADV2
k) XWT of −u'v' & CADV2
c) XWT of −v'w'wave & CADV1
f) XWT of −v'w' & CADV1
i) XWT of −v'w'wave & CADV2
l) XWT of −v'w' & CADV2
Period (sec)
1/64
1/8
1/2
2
4
Time (min)
2
4
6
8

Figure 5.17 Cross wavelet transforms of instantaneous 3 dimensional Reynolds Stresses and (downsampled) suspended sediment concentrations within (ADV1) and outside (ADV2) the bottom wave boundary layer during erosive wave run A3-01 (2nd), before and after filtering out the periodic signal from the turbulent component. The light-shaded region represents the cone of influence where edge effects may distort the image. The thick contours represent the 95% confidence limit (5% significance against red noise). The relative phase is shown in arrows (with right arrow indicating in-phase, left arrows indicating anti-phase, and vertical arrows indicate Reynolds stresses leading by 90°).

5.4 Summary, conclusions, and practical implications

The aim of this study was to provide insight into the temporal and scale relationships between wave–generated boundary layer turbulence and event–driven sediment transport in oscillatory flow. The work was carried out in the nearshore of a prototype sandy barrier beach using data collected though the BARDEX II experiments for irregular, erosive and accretive wave conditions. Statistical analysis of the time series of velocity fluctuations showed high anisotropy in the turbulence records, with strikingly peaky crosswise distributions and an intermittent nature of the momentum exchange both within and outside the wave benthic boundary layer. This is often linked to the nearly self-similar growth of spanwise structures in close proximity to low speed regions of the flow through transverse secondary flows induced by large streamwise motions, evident through counter-rotating pairs of sweeping (Q4) and ejecting (Q2) motions. Quadrant analysis was employed to quantify the intermittency of Reynolds stresses in three planes and the fractional contribution of quadrant events to stress, and to assess whether this aforementioned behaviour applied to the tested conditions. In accretive wave conditions, a dominance of streamwise-skewed motions (Q1-Q4 events) characterised the flow, with the majority of stress contributed by counter-rotating Q2-Q4 motions in the direction of wave propagation, and hence a dominance of shore-ward directed motion. Conversely, erosive conditions were dominated by upward motions (Q1 and Q2 events) lifting and sweeping the bed sediment to be transport by the undertow current offshore. The skewness in the turbulence records also resulted in an observed sorting of the sediment in across the channel. Interestingly, filtering out the oscillating component showed had a significant impact on the number of identified quadrant events beyond a delimiting threshold for the erosive runs, and a relatively limited effect in the accretionary runs; implying the latter, characterised by plunging breakers, features more extreme events (higher-magnitude stresses.). Spectral analyses further revealed a contribution to the crosswise velocity fluctuations (and hence anisotropy in the transverse plane) from a standing transverse wave across the flume, resulting from the unique

flume geometry, whose signal was reflected in the suspension records. These findings highlight the non-linear interactions within the flow and illustrate the three-dimensional nature of mass and sediment transport, even in a controlled experimental facility such as the one used. The spectral analysis further revealed independence from the effect of wave groups, with the turbulent energy and ensuing suspensions lying within the wave frequency range and through the inertial sub-range; with a significant influence of flow reversal and hence vortex shedding from the bedforms. The vertical turbulence excursions scaled with the boundary layer thickness, with similar scaling of v' and w' in the transverse plane for both wave conditions. Sediment excursions beyond the boundary layer could be attributed to the formation of jets between consecutive vortices. A reversal of steepness in the suspension spectra from near the bed to the outer flow implies that sediment stirring near the bed is controlled by mean flow properties, but waves play no role in maintaining those particles in suspension. A distortion in the frequency response could be related to particle interference, low frequency modulation and downward injected turbulence by rollers from spilling breakers, or early breaking of plunging waves. Peaks within the Reynolds stresses spectra suggested enhanced turbulence at small scales; and the sustenance of suspension governed by turbulent fluctuations through coherent structures. The entrainment and maintenance of sediments in suspension through the bursting sequence was conjectured to be associated with the passage of convected or locally formed packets of eddies which describe intermittent large coherent structures within the flow. Wavelet analysis confirmed that powerful (high variance) turbulence occurred in slowly evolving clusters over time, which were closely followed by periods of powerful suspensions near the bed, emerging from the integral (dominant, wave/mean flow related) scales at low frequencies, and decaying with memory in time, after the cessation of the turbulent perturbation. The simultaneous presence of the two scale of motions at their intensity maxima suggests a modulating effect of the larger clusters of the frequencies of smaller motion near the bed, in agreement with similar studies in wall turbulence. Similarly, distribution of a defined energetic cluster of different frequency scale suggests breaking of larger, slow-

evolving motions into smaller, high-frequency events, backing up the observed spectral scaling within inertial sub-range in the stress records. The succession and persistence of convected or locally generated intermittent clusters of energy dictates whether particles have enough time to settle before being picked up by another eddy, or whether they are retained within the suspension cloud. The larger wave-induced motions and nearbed suspensions are phase-locked in the lower frequency range, confirming that waves act to stir up and initiate entrainment of sediment in the boundary layer. Outside the boundary layer, turbulent fluctuations are dominant in driving and maintaining high frequency suspensions as long as momentum is supplied. In conclusion, the above results can be summarised as follows:

a- Turbulence in irregular oscillatory flow is highly anisotropic, and characterised by intermittent momentum exchanges, describing a spatially varied bursting sequence which may be traced in three dimensions, and the temporal variability of which dictates the net direction of sediment transport under erosive and wave accretive conditions.

b- The bursting sequence is associated with the passage of large scale slowly evolving structures, which can modulate the frequency of small scale (higher frequency) events. The persistence of such perturbations is associated with a cumulative suspension events spanning the frequency scales, which observe a hysteresis effect decaying as the motion cease. Wave motion plays a dominant role in entrainment of sediment within the boundary layer, and high frequency turbulence resulting from momentum transfer into smaller scales helps maintain particles in suspension.

Most existing models of sediment transport rely on bulk flow properties to describe sediment mobilisation and transport, such as the mean duration over which the threshold of incipient motion is exceeded, with the latter defined in terms of mean (wave-averaged) or maximum (within a wave cycle) bed shear stress. The results presented here suggest that entrainment and re-suspension of sand is an intermittent process, and the argument presented advocates that

this is dictated by coherent flow structures. Indeed, while some models acknowledge this, and calls for a stochastic description of the problem date back to the works of Einstein and Yalin (cf. 3.2.2); the problem lies in parametrising this intermittency in such models. It is demonstrated here that onshore- or offshore-directed sediment transport can be linked to quadrant-defined vortex clusters. Furthermore, the persistence is such turbulent motions defines the extent to which the wave-mobilised sediment is held in suspension, and remains available for transport but prevailing net currents. This is also shown that suspension clouds are to vortex shedding and hence depend on morphology (through vortex shedding) with modulating effects between larger scale flow structures and smaller fluctuations as well as a feedback imparted by the suspended particles on the flow itself. Modellers therefore need to provide practical and efficient means of parametrising these processes when describing entrainment, and while there is such a trend at small scales (Ji et al., 2013), scaling it up to field scales remains a promising avenue of research.

Statement of Author's Contribution to work presented in Chapter 5

The data reported in Chapter 5 were collected as part of the EU-funded Barrier Dynamics Experiment II (HYDRALAB IV Contract no. 261520 by the European Community Seventh's Framework Programme) under the fifth work package of the program, focussing on nearshore sediment resuspension and bed morphology. The design of the experimental set-up, including initial barrier morphology and sediment size and experimental program was agreed by the consortium led by Prof Gerd Masselink (University of Plymouth), and the instrumented frame was designed by Dr Charlie Thompson. The author constructed the instrument frame with Dr Thompson, and carried out all of the measurement and data collection protocols, data pre-processing, data analysis and interpretation presented in this work.

Chapter 6.

Space-time dynamics of turbulence structures in combined wave-current flows

> "Nothing puzzles me more than time and space; and yet nothing troubles me less, as I never think about them." (*Charles Lamb)*

6.1 Introduction

Fluid motion in the coastal zone is often characterised by the simultaneous presence of both waves and currents, extending towards the bed in shallow waters and resulting in complex dynamic interactions with direct implications for sediment transport studies (Grant and Madsen, 1979). Indeed, the response of the seabed to combined wave-current flows has been observed in records of highly dynamic bedforms and active sediment transport across the inner continental shelf during storm conditions (Komar et al., 1972; Li and Amos, 1998; Li and Amos, 1999b; Li and Amos, 1999a). The non-linear interactions between waves and currents in combined flows, and ensuing turbulence, result in enhanced bed shear stresses that are assumed greater than what the bed experiences through a simple, linear addition of the current-only and wave-only stress components (Soulsby and Clarke, 2005). Thus, a current below the transport threshold may move significant amounts of sediment in the presence of waves (Davies et al., 1988). The combined wave-current boundary layer is a result of complex interactions between the uniform shear due to the steady current, and the time-varying shear due to the oscillating component, as well as bed friction. Fluid and sediment entrainment very close to the bed are controlled by turbulence induced by both the (non-breaking) waves and the current, while higher in the water column, it is often assumed the only the current is at play (Yuan and Madsen, 2015). Understanding combined wave-current boundary layer processes is fundamental for accurate prediction of sediment transport in the coastal zone,

and a large number of studies has been dedicated to the problem; many of which are concerned with estimates of bed friction factors that can be implemented to determine bed shear stress for a prescribed, often time-invariant, eddy viscosity profile (cf. §2.2.4). However, the major problem in combined flows pertains to the different time scales between the steady (slowly-varying) current and the unsteady, oscillatory (short-lived) motion of the waves. Coherent flow structures, inherently intermittent and stochastic in nature, are generated within the near bed region where non-linear wave-current interactions are predominant. While these motions define momentum exchanges and shear stresses, and play a fundamental role in entrainment and transport of suspended particles, little is known about their spatial and temporal scales in combined flow, or about their interaction with bedforms and suspended sediment (Hare et al., 2014). The purpose of this chapter is to present prototype-scale measurements of the near bed flow, turbulence, and stress-bearing coherent structures over mobile bedforms under the combined effects of waves and currents. Two cases are considered: collinear currents aligned with; and opposed to the direction of wave propagation. The spatial structure and temporal scales of turbulent motions are resolved from high frequency acoustic measurements at two locations near the bed and linked to observed sediment transport processes and bed morphology.

6.2 The Fast Flow Facility Sediment Turbulence Experiment

6.2.1 Experimental setup and hydrodynamic forcing

Results are presented from an experiment conducted at HR Wallingford's Fast Flow Facility (FFF), a large, dual-channel (racecourse-shaped) flume where combined wave-current-sediment interactions can be studied (Figure 6.1a; cf. §6.2.2). A flat, sandy bed section, 0.3m thick, was constructed in the main (4 m wide) channel, starting at a distance 27 m from the wave paddle and spanning a length of ~21 m. The bed was composed of well-sorted, fine to medium fluvial silica sand, with a normal grain size distribution and a median grain diameter, D_{50}, of 0.247 ± 0.008 mm (Figure 6.2). A deeper section (1.0 m thick, 4x4 m wide) within the bed allowed the installation of an instrumented frame,

equipped to measure flow hydrodynamics and sediment motion in combined wave-current flows at high frequency.

A set of 42 experimental runs, simulating a range of hydrodynamic forcing, including waves (regular and random) only, currents only and wave-current combinations were carried out during the testing phase. Waves were generated by a 10-paddle, bottom hinged wave maker with active absorption (using measured local water levels to compensate for excessive energy). Currents were generated by two Bedford Pumps ltd SA-80.04.08 pumps, operating alternatively in forward (generating currents aligned with direction of wave propagation, counter-clockwise in flume) and reverse (opposing progressive waves, clockwise) modes. A foam baffle beach was installed at the end of the main channel at 1.05m above bed, to dissipate energy as waves enter the bend towards the minor channel. Unfortunately, only 5 test runs passed the quality control criteria for the velocimetry and suspended sediment measurements; and of these the two which were comparable in experimental layout, forcing and sampling protocols are presented here. Runs 18 and 19, undertaken in a water depth of 1.05 m above the initial, mean bed level had identical geometry and wave conditions but opposing currents. In both runs, paddle active absorption was inactive, resulting in a spectrum of waves that deviates from the assumed monochromatic distribution. The design hydrodynamic forcing and run conditions of the two tests presented are given in Table 6.1. The expected, current-only mean velocities given the flow geometry are 0.37 m/s and –0.30 m/s for Runs 18 and 19, respectively (Todd, D., 2016; *pers. comm*.).

6.2.2 Instrumentation and data acquisition

A range of instruments and sampling devices were deployed during the experiment to collectively measure the three-dimensional flow field (and turbulence); water surface elevation; temperature; bed morphology; and backscatter in the water column. A triangular frame erected in the deeper section of the bed supported multiple high frequency acoustic instruments that logged live into a suite of time-synched laptops (Figure 6.1b, c). The frame was designed to be essentially the same as that used in BARDEX II (Chapter 5)

so that measurements are consistent. The horizontal and vertical spacing between the two ADVs was reduced to ensure better correlation between the signals, a problem highlighted in the Bardex work. The frame comprised of:

- Two downward looking, Nortek acoustic Doppler Velocimeters (ADVs), offset vertically by 10 cm, and horizontally by 8 cm. The ADVs sample a cylindrical volume (7 mm in length) situated 50 mm below the probe with an acoustic frequency of 10MHz, and a sampling frequency (rate) set to 25 Hz.
- An Aquatec Aquascat 1000R Acoustic backscatter profiler (ABS) with 4 external cabled transducers of 0.5, 1, 2, and 4 MHz acoustic frequencies, flush-mounted in a circular configuration, with 10 cm radial offsets (centre to centre). These were set to profile collectively at a rate of 64 Hz averaged into 2 profiles per second, with a total of 256 bins (of equal size) and pulse lengths of 2.5 mm, storing approximately 1000 profiles upon each trigger (~08:20 minutes) with start and end bounds specified to ensure the bed is acoustically visible.
- A single-beam, horizontally-mounted Marine Electronics Sediment Image Profiling Sonar (SIS) with an acoustic frequency of 1.1 MHz, recorded sequential echograms of backscatter intensity along 1.8° pencil-beams (narrow conical beams), swept at right angles to the bed every 6 seconds. For these runs, the instrument was set so that its starting range was 0.3 m below the sonar head, and its end range at 1 m, with a 90° sweep angle, providing along-flume profiles of the bed morphology (~1.1 m long) and acoustic backscatter within the flow.
- A live-logging underwater camera recorded the migration of any bedforms and the changes in their properties and shape upstream of the ADVs' location (from a wave propagation perspective).
- A Marine Electronics Sector Scanning Sonar (SSS) with an acoustic frequency of 500 kHz, and a 4-6 m range, mounted vertically down. This provided 360° plan-view images of bedform backscatter intensity; and hence afforded a view of the three-dimensional nature of the bed morphology together with the SIS data (field of vision of 8 m).

a) Flume dimensions and layout (scale 1:267)

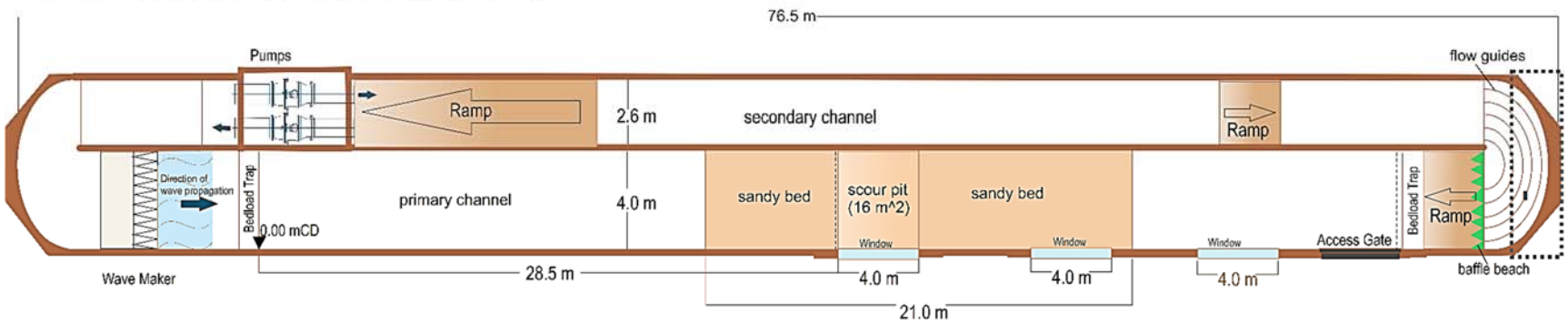

b) Front vew (facing wave paddle) of instrumented rig

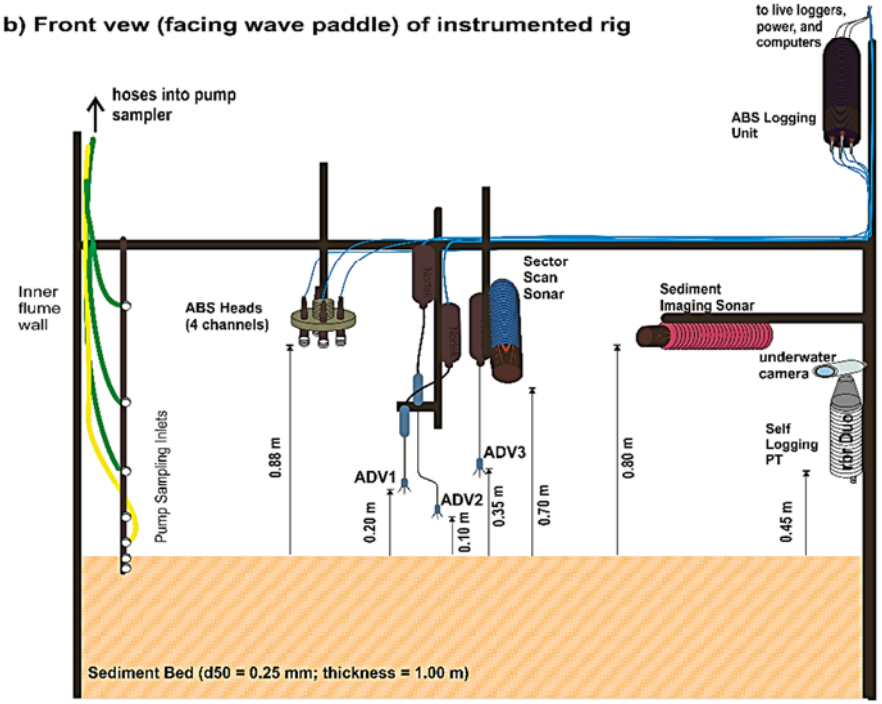

c) Top (plan) view - of instrumented rig

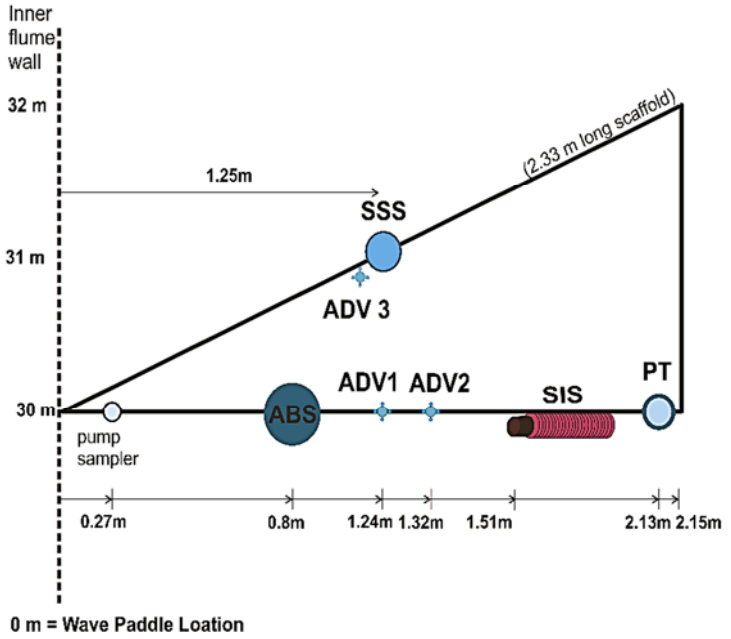

Figure 6.1 (a) Layout and dimensions of the Fast Flow Facility, showing the location of the wave paddle, the sandy bed section and the scour pit within the primary channel, and the two pumps in the secondary channel; (b) cross-sectional view of the instrumented frame during the second set of experiments (including Runs 18 and 19 presented here); (c) plan view of the instrumented frame with distances from the central flume wall. ABS: acoustic backscatter profiler system, ADV: acoustic Doppler velocimeter, SIS: sediment imaging sonar; SSS: sector scanning sonar; PT: pressure transducer.

Table 6.1. Hydrodynamic forcing during the experimental runs presented

Run	Water depth, h (m)	Design height, H (m)	Design Period, T (s)	Wave type	Pump rate (Hz)	Current direction	beach elevation h_b (m)	Paddle active absorption
Run 18; 24/11/15	1.05	0.2	3	regular (mono-chromatic)	20	forwards	1.05	off
Run 19; 25/11/15	1.05	0.2	3	regular (mono-chromatic)	20	reverse	1.05	off

- A multiple inlet sampling device was attached to the frame to collected pumped water samples for their sediment content, in order to calibrate both ABS and SIS. The nozzles faced into the flow (along direction of wave propagation). Due to technical difficulties, it was only possible to collect water samples at an elevation of 0.8 m below the ABS sensor.
- Finally, the incident wave field was measured using three HR Wallingford-built twin-wired wave probes recording immersed depth through conductivity. These were placed in the approximate distances of X= 25.3 m, 33.0 m and 46.95 m from the rest position of the wave paddle.

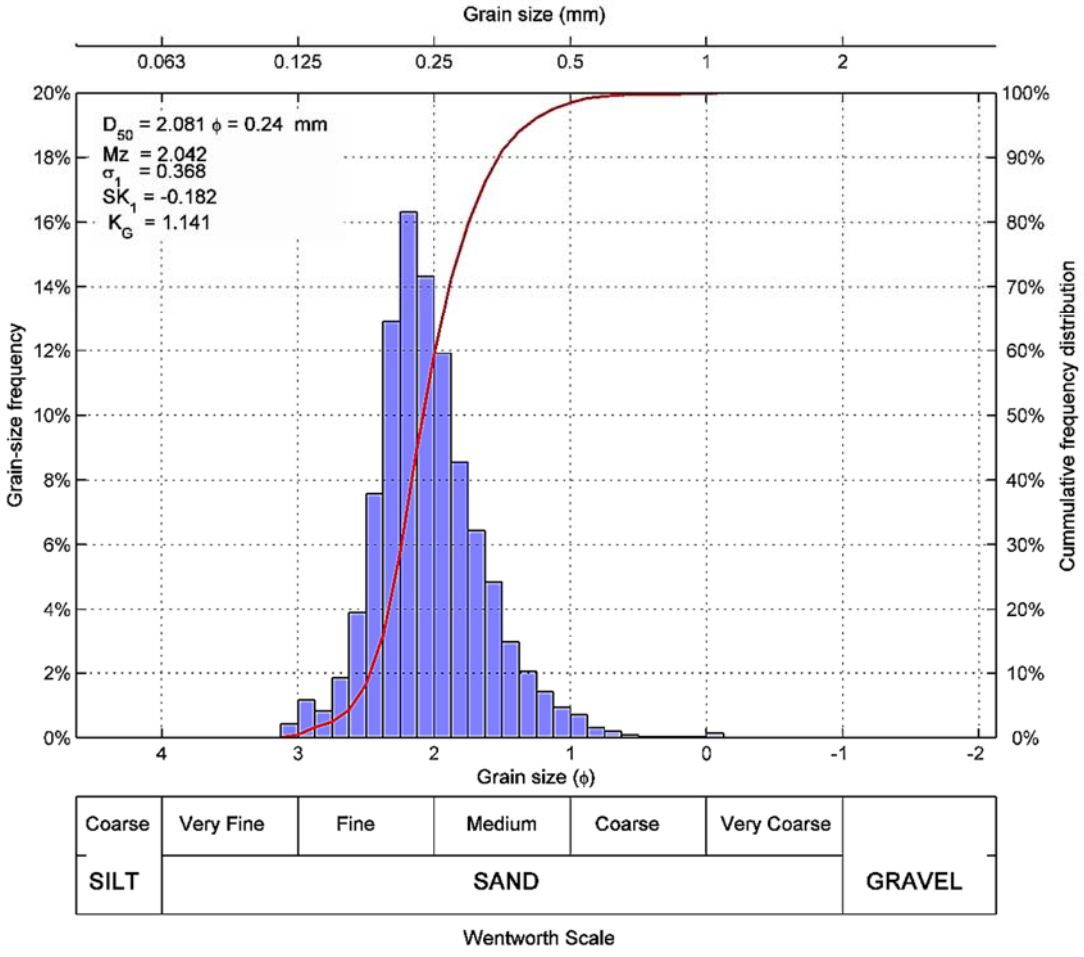

Figure 6.2 Particle size distribution of the sediment bed. D_{50}: median grain diameter; M_z: mean grain diameter (Phi units); σ_1: sorting; SK_1: skewness; K_G: kurtosis.

6.2.3 Quality control and data processing

6.2.3.1 Spectral properties of the incident wave field

The non-directional wave parameters (peak wave periods and significant wave heights, cf. §6.3.1.) were computed using zero-crossing and spectral analysis of the surface water elevation following Tucker and Pitt (2001). The wave heights were given as immersed water level variations around still water level measured at the start of each test, derived from calibrated voltage across each of the three probes (channels). Two probe channels were available for Run 18, while all three channels were available for Run 19. It is suspected, however, that these probes were not fully submerged at the troughs of waves, potentially underestimating the wave heights.

6.2.3.2 Bed morphology

The SSS backscatter intensity was used in raw acoustic form (in dB) to assess ripple crest shape and orientation, providing a plan view of any variations in bedforms. Mean bedform wavelengths, following slant range correction, and rotation of the image to align with the flume walls, were evaluated from the locations of the peaks in backscatter along the central line of the echograms at the start and end of each wave run.

The SIS backscatter intensity (given in relative integer values scaled linearly between 0 - 255) was corrected for attenuation, scattering and spreading, following Thorne and Hanes (2002). It was also adjusted to the difference, from 1500m/s, of the speed of sound evaluated for the ambient fluid properties within the flume, following Roquet et al. (2015). The attenuation coefficient for viscous dissipation due to freshwater fluid motion under the oscillating pressure, α_w , was calculated following Fisher and Simmons (1977) using the measured temperature, and the SIS beam frequency. The attenuation coefficients pertaining to viscous dissipation due to relative motion between sediment particles and the fluid, α_{sv} , and the scattering of sound by these particles, α_{ss} , were estimated following the methods outlined in Thosteson and Hanes (1998), Thorne and Hanes (2002), and Thorne and Hurther (2014) taking into account the departure from spherical spreading, ψ, within the transceiver's near field, as described by Downing et al. (1995). To simplify the

approach, an implicit method was used to solve the inverse problem with the single acoustic frequency of the SIS, using two iterations (to minimise the positive iterative feedback errors as the solution propagates down to the bed), assuming that no scattering by sediments occurs at low concentrations in the far field, and using the in-situ sediment properties to describe intrinsic scattering cross sections and form functions (Thorne and Hanes, 2002; Thorne et al., 2011). Subsequently, the range-corrected backscatter intensities along each beam of a given sweep were normalised against the maximum intensity of that beam, and the background noise, defined as the mean backscatter within the water column, was removed. The bed was then detected as the range-corrected height at which the maximum normalised backscatter occurs, following a conversion from polar to Cartesian coordinates. The bedform relief was thus inferred from SIS measurements after de-trending the bed (to remove slope), smoothing to remove small scale variability, and despiking to remove outliers resulting from high concentration suspension events. A zero-crossing algorithm was then used to determine ripple heights, and to double-check wavelengths against those inferred from the SSS, as described in Doucette and O'Donoghue (2006) and O'Donoghue et al. (2006).

6.2.3.3 Three-dimensional velocity field and turbulent characteristics

The methodology outlined in Chapters 4 (§4.2.1) and 5 (§5.2.2.1) is followed to extract turbulence from the 3 dimensional velocity field. Briefly, this encompasses a quality check such that no more than 20% of the data for a given ensemble within a time series falls below the minimal accepted correlation threshold, set at 70% following Elgar et al. (2005). This criterion was failed by 37 of the 42 tests (the data very noisy or the files corrupted). For the tests that passed the quality check, values which fall below the threshold were replaced by interpolation through a moving average algorithm, defined by Thompson et al. (2012). Subsequently, the resulting U, V, and W vectors were geometrically rotated to account for sensor misalignment (Elgar et al., 2001), then zero-meaned and detrended; and the mean velocity $\overline{U}$ was calculated from the three components, with the direction dictated by the relative angle between the two horizontal components.

The wave signal was then extracted from each of these vectors using a moving average low-pass digital filter (Thompson et al., 2012). Several filters were tested, and the best was chosen to produce the lowest wave-induced spectral peaks with minimal adverse effects on the statistical properties of the signal, and the spectral properties within the inertial subrange (cf. §4.2.1). These filtered signals were then de-spiked using the 3D phase-space method of Goring and Nikora (2002) as modified by Mori et al. (2007).

The three-dimensional turbulence components were then used to quantify energy fluxes. Measures of energetics in the flow are often confined to the variance of vertical velocity, and the rate of dissipation in turbulent kinetic energy (Gerbi et al., 2009). The vertical and horizontal offsets between the two ADVs were deemed close enough to allow estimates of structure functions (statistical moments of the flow field following Kolmogorov's 1941 theory) to describe energy dissipation. The turbulent kinetic energy, k (m^2/s^2) per unit mass, for each test run presented, is defined as:

$$k = 0.5\ \left(\overline{u'^2} + \overline{v'^2} + \overline{w'^2}\right) \quad \text{(Eq. 6.1)}$$

in which the overbar denotes the time average. The mean vertical turbulence flux is thus defined as $\overline{k'w'}$ (m^3/s^3), while the Reynolds' stress turbulent production P_{Re} (m^2/s^3), based on the vertical gradient between the two ADVs, is given by Grasso and Ruessink (2012) as:

$$P_{Re} = [-\overline{u'w'}\ \partial_z\bar{u}\ - \overline{v'w'}\ \partial_z\bar{v}] \quad \text{(Eq. 6.2)}$$

The energy advected by the wave motion and the mean current past the ADV is dissipated within the inertial sub-range (Tennekes and Lumley, 1972), whereby the angular (radian) frequency spectrum, $S_{33}(\omega)$, and dissipation rate, ε (m^2/s^3), are related (Gerbi et al., 2009):

$$S_{33}(\omega) = J_{33}.\alpha.\ \varepsilon^{\frac{2}{3}}.\omega^{-\frac{5}{3}} + n \quad \text{(Eq. 6.3)}$$

whereby $\alpha = 1.5$ is Kolmogorov's constant (Grant et al., 1962), ω is the angular frequency (rad/s); n is noise, and for unsteady wave motion, J_{33} defines the dependence of the magnitude of the inertial range upon both the mean values and the standard deviations of the three wave-contaminated

velocity components (a full description is given in Gerbi et al. (2009)). The limits of the inertial range were defined according to Stapleton and Huntley (1995) and matched those given in Gerbi et al. (2009), while the wave components were determined following Feddersen and Williams (2007), and quality controlled according to Feddersen (2010). Finally, the vertical turbulent transport, T_v (m^2/s^3) between the two vertically offset ADVs, given by Grasso and Ruessink (2012); represents the vertical gradient in turbulent kinetic energy:

$$T_v = \partial_z \overline{kw'} \qquad \text{(Eq. 6.4)}$$

6.2.3.4 Suspended sediment concentration profiles

The backscatter intensities collected along each of the 4 frequency channels of the ABS were used to infer the vertical distribution of suspended particulate matter within the water column, using the manufacturer's AQUAscat Toolkit software, implemented in Matlab™. These were range corrected for attenuance, spreading, and near-field effects using the built-in function, which follows the same methodology described earlier (Thorne and Hanes, 2002). The bed was detected using the 3rd channel (frequency of 2MHz) for the 1000 profiles measured in each run, whereby bed ranges that lie outside 5 times the standard deviation of the dataset were reset to the mean bed depth below the transducer. The second channel (frequency of 1MHz) was always heavily contaminated with noise, and thus was excluded from subsequent analysis. The built-in implicit inversion method for multi-frequency acoustic measurements of Thorne and Hanes (2002) was used to calculate suspended sediment concentration (SSC) and grain size profiles, averaging over 10 profiles to minimise noise, and using the grain-size distribution properties of the bed sediment. Although pump samples were collected at a specific range below the sensors, these were not used to directly calibrate the profiles following Thorne and Hanes (2002) explicit inversion approach as the nozzles, oriented into the waves, were likely to have under-sampled given the opposing currents, and the orbital nature of oscillatory flows.

6.3 Results and Discussion

6.3.1 Flow conditions and hydrodynamic forcing

The spectral wave characteristics for the two test runs, Run 18 with regular waves (H= 0.2 m, T = 3 s) running along a current generated by a 20Hz pump rate; and Run19 with the current opposing the direction of wave propagation are summarised in Table 6.2. These comprise the spectrally estimated significant wave height, H_{m0}, derived from the integral of variance, m_0, of the wave energy spectrum; the peak wave period, T_p, associated with the largest wave energy; as well as wave parameters computed through zero-crossing which include the significant wave height, H_s, (average height of the third-highest waves), the mean wave height H_{mean}, maximum wave height H_{max}, the mean wave period, T_{mean}, and the significant wave period, T_s (of the highest 33% of the record).

Table 6.2. Measured wave characteristics during the experimental runs

Measured wave characteristics	**Run 18; 24/11/2014 (Test 31) Series length = 1200 s** Design Characteristics: h = 1.05 m; waves: monochromatic H = 0.20 m; T = 3.00 s; current: 0.37 m/s along waves pump rate: 20 Hz			**Run 19b; 25/11/2014 Series length = 1200 s** Design Characteristics: h = 1.05 m; waves: monochromatic H = 0.20 m; T = 3.00 s; current: 0.3 m/s against waves pump rate: 20 Hz		
(by zero-crossing and spectral analysis)	**Probe 1**	**Probe 2**	**Probe 3**	Probe 1	Probe 2	Probe 3
Water level $h\ (m)$	--	1.0564	1.0551	1.0518	1.0504	1.0554
m_0	--	0.0011	1.33E-03	0.00224	0.0025	2.80E-03
$\boldsymbol{H_{m0}\ (m)}$	**--**	**0.133**	**0.146**	0.190	0.199	0.212
$\boldsymbol{T_p\ (s)}$	**--**	**3.030**	**3.030**	3.030	3.030	3.030
$\boldsymbol{H_s\ (m)}$	**--**	**0.0978**	**0.0805**	0.149	0.162	0.165
$H_{mean}\ (m)$	--	0.0521	0.056	0.135	0.130	0.071
$H_{max}\ (m)$	--	0.176	0.146	0.170	0.188	0.214
$T_{mean}\ (s)$	--	0.634	1.180	3.023	2.5821	0.935
$\boldsymbol{T_s\ (s)}$	--	1.665	1.781	3.0102	2.979	2.639

The results show that the wave paddles systematically and accurately reproduce the design wave period (estimated from the energy spectrum); with no effect from the superposition of the current on the wave whether it is aligned with or opposed to the direction of propagation. The significant wave heights, however, are significantly lower than the design heights programmed into the wave maker for Run 18; as the wave probes were intermittently emerging from the water (particularly under wave troughs), rendering these estimates inaccurate. Conversely, the design spectrally-estimated significant wave heights (H_{m0}) were reproduced experimentally in Run 19. Interestingly, the estimates of significant wave height from both statistical (zero-crossing) and spectral approaches (energy based) differ considerably. For shallow water waves, Thompson and Vincent (1985) have shown that the two significant height estimates could differ by up to 40% in some laboratory cases, and the relative change in statistical-based and energy-based parameters are often overestimated for monochromatic waves with small relative heights and low wave steepnesses. The choice of which parameter to use depends on the problem at hand (Thompson and Vincent, 1984), and as we are interested in energetic turbulence processes, the spectral estimate is used. Nonetheless, in the absence of accurate estimates of wave heights, particularly in Run 18; a reasonable approximation can be calculated from water surface elevations (η) inferred from measured streamwise flow velocities ($u(t)$) by assuming linear wave theory, whereby rearranging the dispersion equation (Svendsen, 2006):

$$\eta = \frac{u(t).\, h\, .\sinh(k\, h)}{c.\cosh(k(z+h))} \qquad \text{(Eq. 6.5)}$$

where k is the wavenumber, h is water depth, z is the elevation of measurement, and c is the wave celerity. The celerity can be obtained from direct and accurate approximation (to within 0.1%) of Hunt (1979):

$$\frac{c^2}{g\, h} = [\, y_0 + (1 + 0.6522 y_0^2 + 0.4622 y_0^4 + 0.0675 y_0^5)^{-1}]^{-1} \qquad \text{(Eq. 6.5)}$$

where $\psi_0 = 2\pi h/L_0$; $L_0 = gT^2/2\pi$; and g is gravitational acceleration.

This analysis yielded a time series of water surface elevations $\eta(t)$ for Run 18; which were then spectrally analysed to reveal an estimated significant wave height $H_{m0} = 0.188\,m$; about -6% difference from the design value. Notably, applying this approach to Run 19 yielded $H_{m0} = 0.32\,m$, about 60% higher than those recorded by the wave probes. This deviation from design value could be observed visually during the experimental run, and can be attributed to wave steepening due to the opposing current, whereby the opposing current causes the wavelengths to shorten and the wave heights to become larger in order to maintain their energy (Soulsby, 2006).

Figure 6.3 shows the measured time series of the three velocity components (U, V, W) and the mean velocity ($\overline{U}$) at two elevations for the two test runs presented (Runs 18 and 19), with identical design wave characteristics but opposing currents; together with the corresponding statistical and spectral attributes (including histograms, boxplots indicating, 25th, 50th and 75th percentiles, standard deviations and outliers; and the power spectral densities). The superposition of the current on the waves results in a mean velocity of $\sim 0.37 \pm 0.15$ m/s at a height of 0.181 m above the bed (ADV1), which reduces significantly to $\sim 0.15 \pm 0.2$ m/s closer to the bed (z = 0.11 m; ADV2) when the current is aligned with the direction of wave propagation (Run 18). This is reflected in histograms and spectral properties of the mean velocity, which reveal the dominance of the streamwise velocity component in the mean flow signal at the higher elevation (cross-correlation between U and $\overline{U}$ of 0.998); which becomes much less pronounced closer to the bed (cross-correlation of 0.22) and thus the mean velocity is governed by the considerable interaction of the three dimensional components (clearly not a two-dimensional problem). The very poor cross-correlation observed between the two ADVs (at 0.13) implies these two positions may be influenced by different processes. With currents opposing the direction of wave propagation (Run 19); the mean (time-averaged) velocity is $\sim 0.30 \pm 0.22$ m/s at a height of 0.17 m above the bed (ADV1) and $\sim 0.26 \pm 0.2$ m/s closer to the bed (z = 0.12 m; ADV2). In this run, the mean flow velocity is similarly

described predominantly by the streamwise component at the higher elevation (cross-correlation of 0.994), and the two signals share a significant cross correlation of 0.554. As a result, a higher correlation between the mean flow velocities recorded by the two ADVs is observed at 0.55 with a lag of 0.8 seconds, perhaps due to the orbital nature of the wave motion. Notably, Run 19 is also markedly characterised by considerably fewer statistical outliers at the higher ADV than Run 18.

Yuan and Madsen (2014) showed similar vertical variations in the streamwise velocity component within a periodic, turbulent oscillatory boundary layer which increases slightly below a well-defined free stream region to an overshoot, then decreasing rapidly towards the bed. The second velocity component should theoretically be zero due to the symmetric (sinusoidal) wave variations. The third velocity component has a large overshoot, and this has been shown to result from the interaction of the time-varying eddy viscosity with the time-varying velocity (Trowbridge and Madsen, 1984). The free stream region of flow constitutes, by definition, the flow lying just outside the benthic boundary layer (Davies, 1986). The measurements by the higher ADV1 in both test runs reveal a time-averaged velocity that is exactly equal to the design depth-averaged velocity expected for the current-only case given the flow geometry and pump rates (0.37m/s and 0.3m/s for Runs 18 and 19, respectively), whereas those given by the lower ADV were smaller. This indicates that while both ADVs in both runs can be confirmed to lie outside of the theoretical, combined wave-current boundary layer (cf. §6.3.2), the lower ADVs still experience some effects of drag, potentially from the shedding of vortices from bedforms. This perhaps highlights the need to move from a classical scaling of boundary layer structure based on mean flow properties (e.g. the velocity profile); towards one concerned with the exchanges of momentum governing the mean velocity (cf. §2.4.1.1).

In the power spectral density sub-plots, the (design) first and second (flow reversal) wave harmonics display obvious peaks, much larger than the residual noise, and are reproduced systematically in the velocity spectra of all components of the flow field, as well as the mean velocity. Trowbridge and

Madsen (1984) showed analytically that existing theoretical formulations of wave boundary layers, assuming time invariant eddy viscosity often reproduce the first harmonics of wave velocity accurately. They further show that temporal variations, owing to the sinusoidal nature of the waves, are not important and only a prescribed vertical structure is needed to reproduce the first wave harmonic. Higher order harmonics, however, require time-varying models of both velocity and eddy viscosity (Yuan and Madsen, 2014), are most likely generated by turbulent processes within the boundary layer, related to temporal variations in turbulent eddy viscosity. These peaks are also observed in the power spectra of the extracted turbulence components.

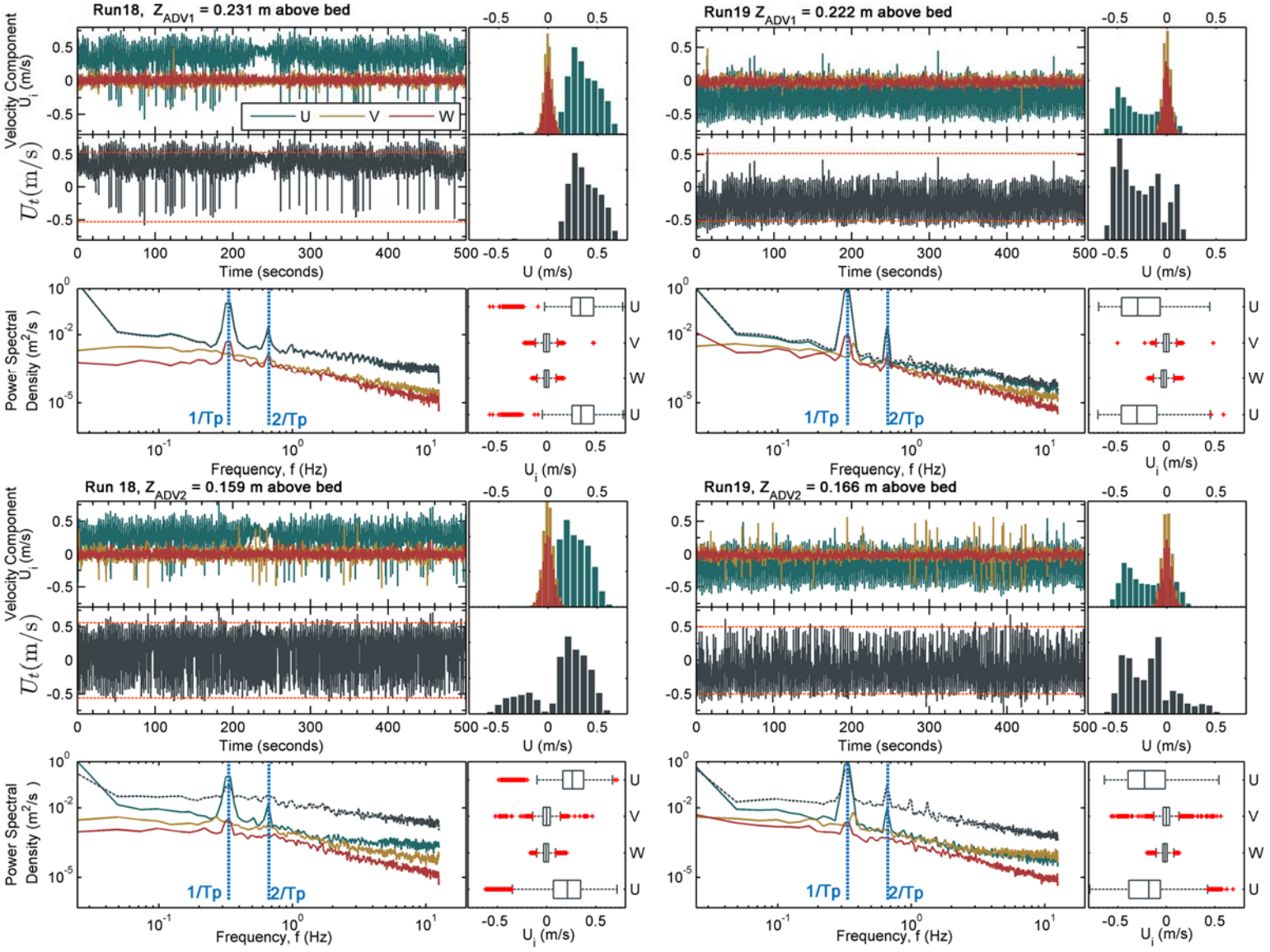
Run18, Z_{ADV1} = 0.231 m above bed
Run19 Z_{ADV1} = 0.222 m above bed
Run 18, Z_{ADV2} = 0.159 m above bed
Run19, Z_{ADV2} = 0.166 m above bed
Velocity Component U_i (m/s)
U_t(m/s)
U
V
W
Time (seconds)
U (m/s)
Power Spectral Density (m^2/s)
1/Tp
2/Tp
Frequency, f (Hz)
U_i (m/s)

Figure 6.3 Time series, probability density functions (histograms), power spectral densities and box plots of the three velocity components, U (streamwise, dark green); V (cross-wise, gold); and W (vertical, red) and the mean flow velocity $\overline{U}$ (grey) measured at two elevations above the bed during Runs 18 and 19. The peak frequency ($1/T_p$) and the second harmonic ($2/T_p$) of the progressive wave conditions are highlighted by the vertical blue lines in the power spectral density plots. The boxplots indicate the 25^{th}, 50^{th} and 75^{th} percentiles of the data (left, centre and right sides, respectively), with the whiskers indicating the standard deviation, and the red markers highlighting statistical outliers.

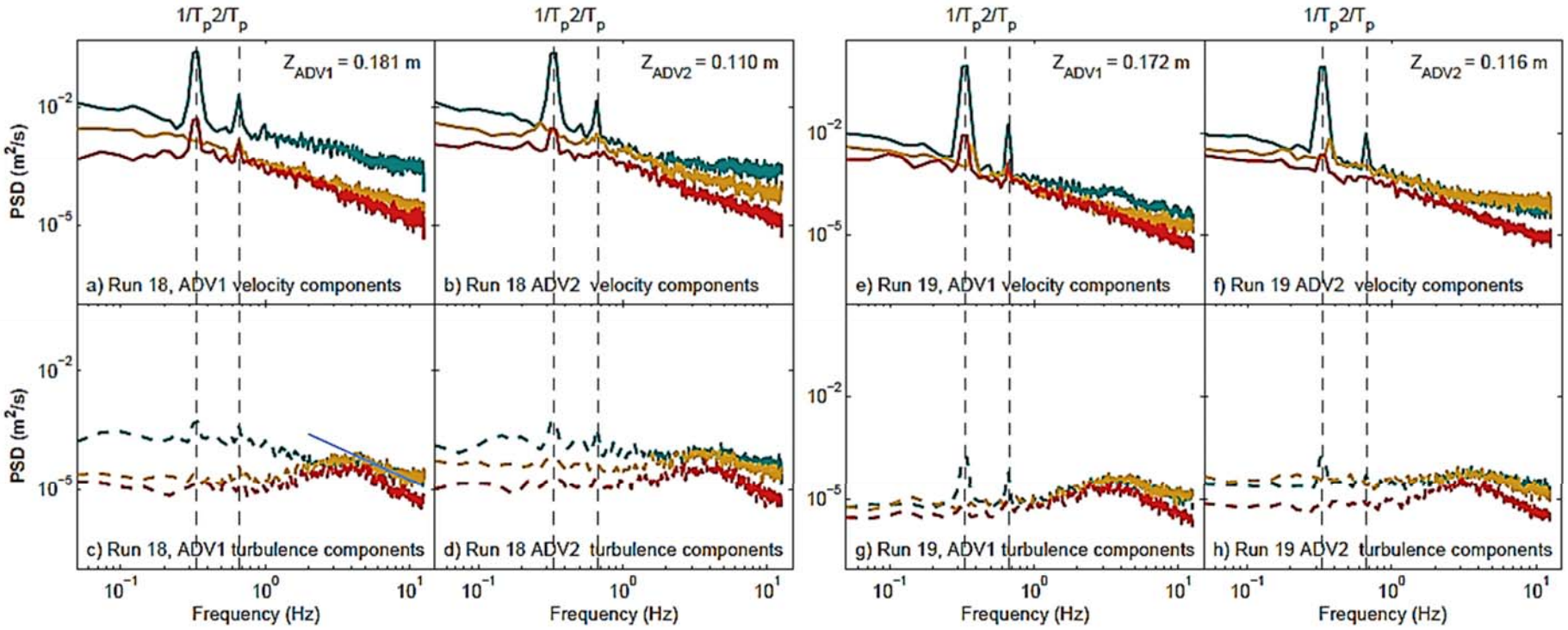

Figure 6.4 Power spectral densities of the three velocity components, U (streamwise, dark green); V (cross-wise, gold); and W (vertical, red) and their inherent turbulent fluctuations (u', v' and w', respectively) measured at two elevations above the bed during Runs 18 and 19. The peak frequency ($1/T_p$) and the second harmonic ($2/T_p$) of the progressive wave conditions are indicated by the dashed vertical lines.

6.3.2 Flow properties and combined boundary layer thickness

Estimating the thickness of the combined wave-current boundary layer in the absence of profile measurements is inaccurate, and common approaches rely upon assumed profiles of time-invariant eddy viscosity to define stress distributions (cf. §2.2.4). The boundary layer thickness in combined flows, δ_{cw}, is often assumed to depend only on the oscillatory component of the velocity (Soulsby and Clarke, 2005); and for sinusoidal waves, Yuan and Madsen (2015) suggest that the only influence of the current on the waves is a minor increase in turbulent eddy viscosity due to the current-induced bed shear stress; the waves effectively do not feel the influence of the current. The oscillating boundary layer thickness in combined flow, however, is substantially greater than with waves only; while the opposite is true for mean flow boundary layer thickness, and both increase with the increasing superimposed current (Davies et al., 1988). To estimate the thickness of the boundary layer, and the near bed orbital velocities, we need to solve the current-wave dispersion equations as a function of depth to evaluate the wave number, k, needed for calculations of near bed orbital velocities, assuming a depth uniform current speed, and hence estimating the combined wave-current bed shear stress and thus friction (shear) velocity.

In the absence of profile measurements of velocity, the mean, combined wave-current boundary layer thickness is given by Grant and Madsen (1986):

$$\delta_{cw,m} = \frac{\kappa\, u^*_{cw,m}}{\omega} \qquad \text{(Eq. 6.6)}$$

whereby $\kappa = 0.41$ is von Kármán's constant, $u^*_{cw,m}$ is the mean, combined wave-current friction velocity, and $\omega = 2\,\pi/T$ is the wave angular frequency. To estimate the theoretical bed shear stress (and hence friction velocity) under combined flow, the methods of (a) Grant and Madsen (1986) modified to include transport and ripple enhanced shear velocity after Nielsen (1986), as implemented in the Numerical Model Sedtrans05 (Neumeier et al., 2008); (b) Soulsby and Clarke (2005) including current-modified wave friction factor, and (c) the latter's technique modified by Malarkey and Davies (2012) to

account for strong wave-current interaction assuming a logarithmic velocity profile; were compared. These three methods require accurate estimate of the near bed orbital velocity, given the flow geometry and wave characteristics. To this end, an efficient Newton-Raphson numerical approximation is used to solve the simplified wave-current depth dispersion equation for the characteristic wave number, k, following Southgate and Oliver (1989), taking into account the angle ϕ between the wave and current directions, the water level, and the design current-velocity at the pumps (assumed as depth averaged velocity for a current-only flow). The protocols to estimate the wave number k and the combined bed shear stress of Soulsby and Clarke (2005), are described in Appendix A6. The near bed orbital velocity for the combined, collinear wave-current flow is estimated to within 0.1% following Soulsby (2006):

$$U_{orb,cw} = \frac{H}{2} \cdot \left(\frac{2gkh}{h \sinh(2kh)} \right)^{0.5} \qquad \text{(Eq. 6.6)}$$

and the near bed orbital amplitude for the combined flow:

$$A_{0,cw} = \frac{U_{orb,cw} T}{2\,\pi} \qquad \text{(Eq. 6.6)}$$

The mean bed shear stress is estimated from the quadratic stress law, using a combined mean wave-current drag coefficient, $C_{D,m,r}$, which incorporates the modified wave-current friction factor $f_{w,r}$ for rough turbulent flow. Note all these methods assume a two-layer, discontinuous eddy viscosity profile, accounting for near-bed modification of the wave orbital velocity by the current, but assuming the velocity outside the combined layer must equate to the current only velocity. The estimated combined wave-current flow properties are summarised in Table 6.3; which indicate rough turbulent flow conditions, and shear velocities which exceed the critical values for bedload (>0.013m/s) and nearly equal to or exceeding the critical threshold for suspension (0.022 m/s; cf. §3.2.3 and §3.3). The three approaches result in very small mean, combined boundary layer thicknesses with Sedtrans05 estimating $\delta_{cw} \cong 0.03$ m, an order of magnitude larger than the other two

($\delta_{cw} \cong 0.0026$); and similarly larger stresses. This can be attributed to the inclusion of the effect of the bedforms and the active transport modifying the skin-friction component (hence accounting for form drag); whereas the other two approaches calculate a skin-friction only stress (accounted for through a roughness, z_0, set to D50/12). These results confirm that both ADVs are located outside of the combined wave-current benthic boundary layer in both Runs 18 and 19.

Table 6.3 Estimated combined wave-current flow properties following Soulsby and Clarke (2005) and Soulsby (2006)(cf. Appendix 6). Values in parentheses are estimated after Malarkey and Davies (2012) and in squared brackets using the numerical model Sedtrans05 (Neumeier et al., 2008).

Flow property	**Run 18**	**Run 19**
ϕ; relative angle between wave and current	0°	180° (2π (rd))
$\overline{U}$ (m/s); depth averaged mean current	0.38	0.30
k ; wave number	0.6174	0.762
$U_{orb,cw}$ (m/s); near bed orbital velocity	0.268 [0.257]	0.251 [0.257]
$A_{0,cw}$ (m/s); near bed orbital amplitude	0.128 [0.123]	0.120 [0.123]
$Re_c = \overline{U}h/\nu$; Current Reynold's number	3.18×10^5	2.51×10^5
$Re_w = U_{orb,cw}A_{0,cw}/\nu$; Wave Reynold's number	2.72×10^4	2.39×10^4
Flow regime (later verified to be:)	turbulent rough	turbulent rough
$f_{wr} = 1.39\left(A_{0,cw}/z_0\right)^{-0.52}$; wave-only friction actor	0.0148	0.0153
$C_{D,m,r}$; mean drag coefficient for rough turbulent combined wave-current flow	0.005	0.006
$C_{D,max,r}$; max drag coefficient for rough turbulent combined wave-current flow	0.009	0.0103
$\tau_{m,cw,r} = \rho\, C_{D,m,r}\overline{U}^2$ (Pa) ; mean, combined wave-current bed shear stress	0.73 (0.23) [1.35]	0.54 (0.23) [1.123]
$\tau_{max,cw,r} = \rho\, C_{D,max,r}\overline{U}^2$ (Pa); max, combined wave-current bed shear stress	1.29 (0.92)	0.924 (0.91)
$u^*_{cw,m} = \sqrt{\tau_{m,cw}/\rho}$ (m/s); mean combined wave-current shear velocity	0.027 (0.048) [0.088]	0.023 (0.048) [0.078]
$u^*_{cw,max} = \sqrt{\tau_{max,cw}/\rho}$ (m/s); max combined wave-current shear velocity	0.036 (0.096)	0.03 (0.096)
$\delta_{cw,m} = \kappa\, u^*_{cw,m}/\omega$ (m); combined wave-current mean boundary layer thickness	0.005 (0.01) [0.033]	0.0044 (0.01) [0.03]

6.3.3 Sediment properties and bed morphology

6.3.3.1 Sediment properties in the top 'mobile' layer

To assess changes in sediment characteristics in the top layer of the bed, 10 cm long cores (2.7 cm diameter) were collected (when the flume was emptied); with cores collected before Run 18, and after Run 19. Vertical variations in sediment properties in the top 10% of sediment bed within the scour pit before and after the analysed wave runs are given in Figure 6.5. The cores show uniform composition in the finer fraction with little variation before and after the test runs (standard deviations: $\sigma_{D10,before} = \pm 7.8\ \mu m$ and $\sigma_{D10,after} = \pm 5.2\ \mu m$, respectively). The variance in grain diameter was reduced due to re-working of the sediments during the wave runs (with $\sigma_{D50,before} = \pm 13.7\ \mu m$ and $\sigma_{D50,after} = \pm 6.2\ \mu m$, and $\sigma_{D90,before} = \pm 22.1\ \mu m$ and $\sigma_{D90,after} = \pm 32.2\ \mu m$). Sediment sorting, calculated following Folk and Ward (1957), changed from ~0.34 to ~0.42 in the top 5 cm before and after these two runs, and was relatively more pronounced in cores taken at the crest of bedforms (~0.37) compared with the troughs (0.33) – all indicating well-sorted sand. Similarly, D_{10}, D_{50} and D_{90} were relatively finer at the ripple crests compared with ripple troughs. Similarly; the bulk sediment density in the top layer showed some variation indicating re-packing of bed material, and hence active sediment mobilisation within the top layer (hard to discern given the inherent variability within the method used for calculation).

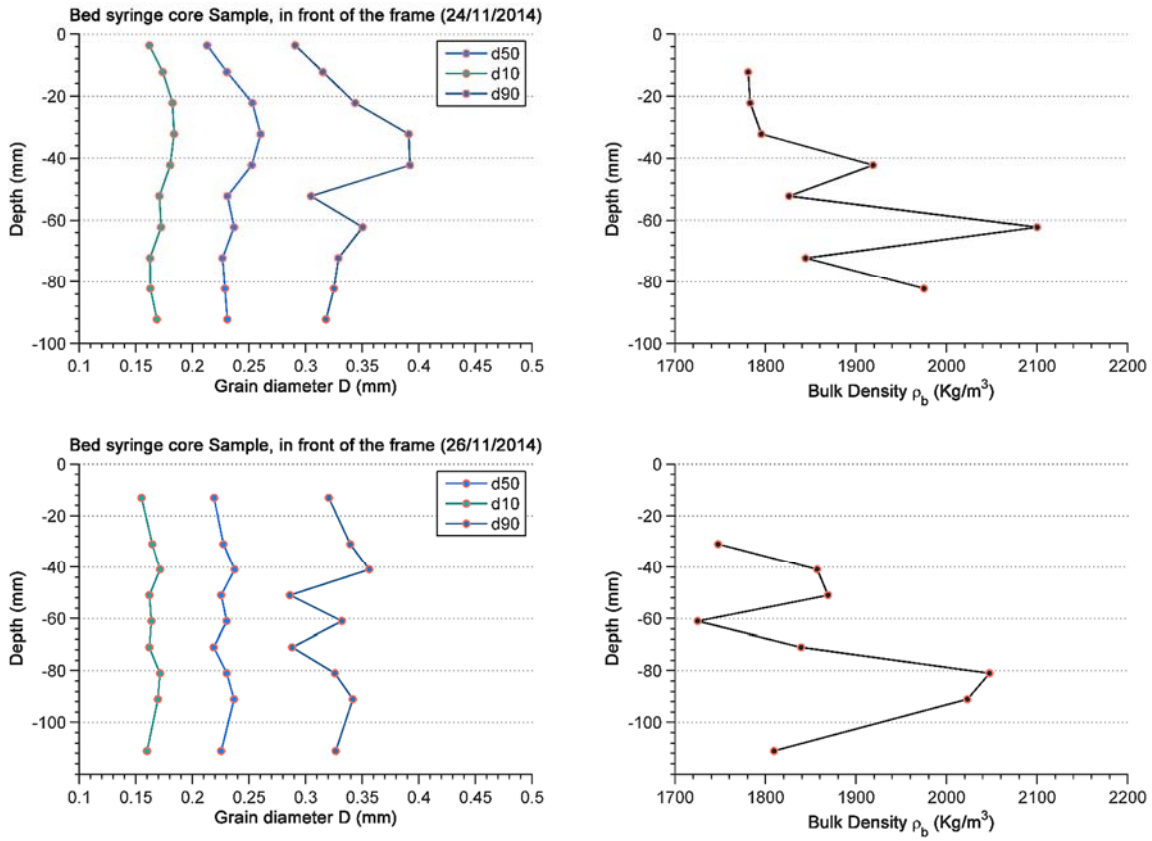

Figure 6.5 Variation in particle size distribution and bulk density of the top layer (10 cm) of the sediment bed before Run 18 and after Run 19.

6.3.2.2 Bedform geometry

The observed bed morphology in each run is both a function of the hydrodynamic forcing as well as the existing morphology from the previous runs, as the bed was not reset to a flat configuration before each wave testing sequence. Examples of the observed bed morphology (and partially-corrected suspension events) observed acoustically by the SIS for 1 minute from each of Runs 18 and 19 are shown in Appendix A6. The acoustic images (and underwater video camera) reveal highly mobile ripples and active sediment transport both as bedload, and in suspension. Large, intense sediment suspension clouds (up to 15 cm in height) were observed at flow reversal, indicating entrainment by coherent eddies through vortex shedding. Run 18 was characterised by more persistent suspension clouds, extending higher within the water column, whereas Run 19 featured more defined, and shorter-lived suspension events. During both runs, small to intermediate (wavelength ~0.1-0.25 m) and relatively symmetric, 2D combined flow ripples were observed, characterised by rounded crests and local deep scour at the lower

end of their stoss sides with discontinuous crest lines and irregular planforms, with very small, current ripples superimposed (Figure 6.6). This bedform morphology has been described for combined wave current flow experimentally (Dumas et al., 2005) and in the field (Amos et al., 1988; Li and Amos, 1998). The bedforms in Run 18, however, were observed transitioning towards (but not quite reaching) an upper-plane sheet flow, with a mobile layer of sediments (several grains deep), shallower bedform relief and bigger wavelengths. This confirms the earlier estimated results (Table 6.3) which indicated shear velocities exceeding the thresholds of motion (bedload) and suspension; with maximum shear velocity exceeding the the critical threshold of initiation of sheet flow (upper plane bed at $u^*_{cr,sheet} = 0.054\ m/s$). This is confirmed by the numerical model Sedtrans05 which predicts sediment transport ($q_{total} = 0.01$ kg/s/m) occurring for 73% of the time in Run 18 (52% of time is suspension, and 21 % as bedload); with a lower rate of transport ($q_{total} = 0.004$ kg/s/m) occurring for 79% of the time in Run 19 (34% of time as bedload and 44.5% in suspension).

The SSS scans were used to assess planform geometry along the flume, and mean bedform wavelengths were extracted through zero-crossing and wavelet decomposition of the raw acoustic signal (following slant range correction) along the centre line of the echograms. Two example echograms (taken midway through the runs) are presented in Figure 6.7, together with the corresponding continuous wavelet decomposition of the centreline backscatter signal. The wavelet transform indicates two distinct scales of bedforms, with smaller (~0.03 – 0.06 long) ripples imposed upon relatively large bedforms ($\lambda_r = \sim 0.2$ m for Run 18, and ~ 0.185 m for Run 19), while unsmoothed zero crossing identified only the small scale ripples.

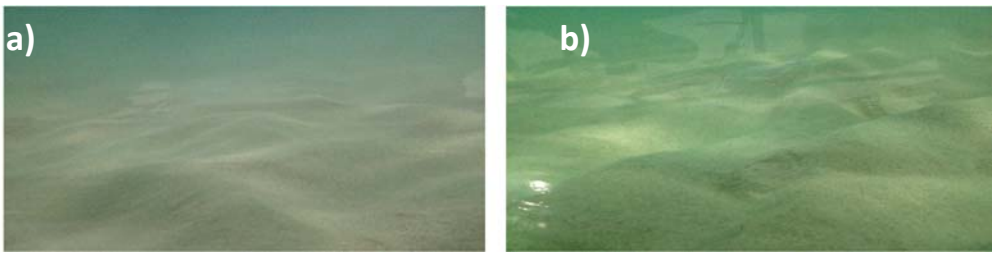

Figure 6.6 Observed bedforms in conditions similar to a) Run 18; b) Run 19.

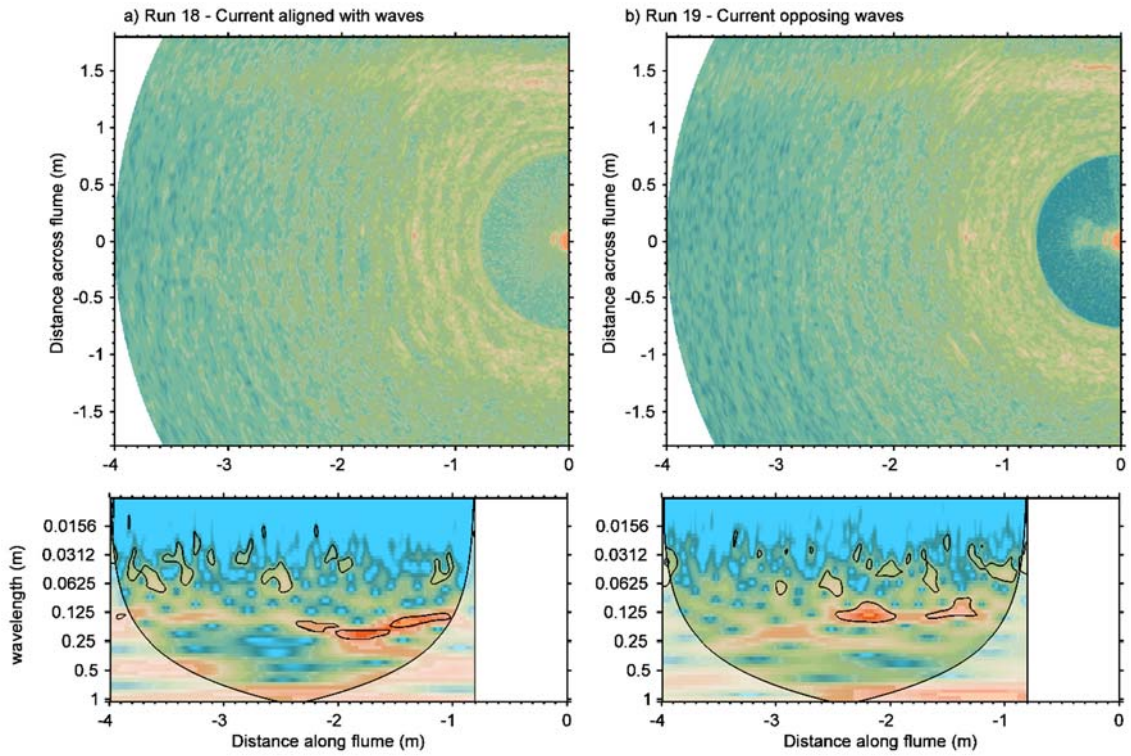

Figure 6.7 Observed bedforms in flow conditions similar to a) Run 18 and b) Run 19. The top panels shows the SSS echogram; the lower panels show the CWT of bedform wavelength along at the centreline of the echograms.

The temporal evolution and classification of bedform wavelength (λ_r), height (η_r), and bedform steepness (η_r/λ_r) for a 10 minute sub-record of each wave run, obtained from the SIS images (one profile taken every 6 seconds) are shown in Figure 6.8 (a, b and c, respectively). Notably, inferring bed relief from peak backscatter along the SIS rays was harder in the 2D echograms of Run 18 due to the mobile sediment layer, explaining the larger scatter in the results. Figure 6.8 shows larger bedforms ($\lambda_r = 0.21 \pm 0.03$ m) with smaller heights ($\eta_r = 0.055 \pm 0.005$ m) in Run 18, compared to Run 19 ($\lambda_r = 0.19 \pm 0.008$ m and $\eta_r = 0.065 \pm 0.006$ m). Both runs were characterised by similar mean ripple steepnesses (0.3 and 0.34). The non-dimensional ripple characteristics (relative to median grain diameter) were plotted against the non-dimensional near bed orbital diameter (Figure 6.8 c, d, and e) following Clifton and Dingler (1984) and Wiberg and Harris (1994), classifying the bedforms as orbital, vortex ripples for both runs.

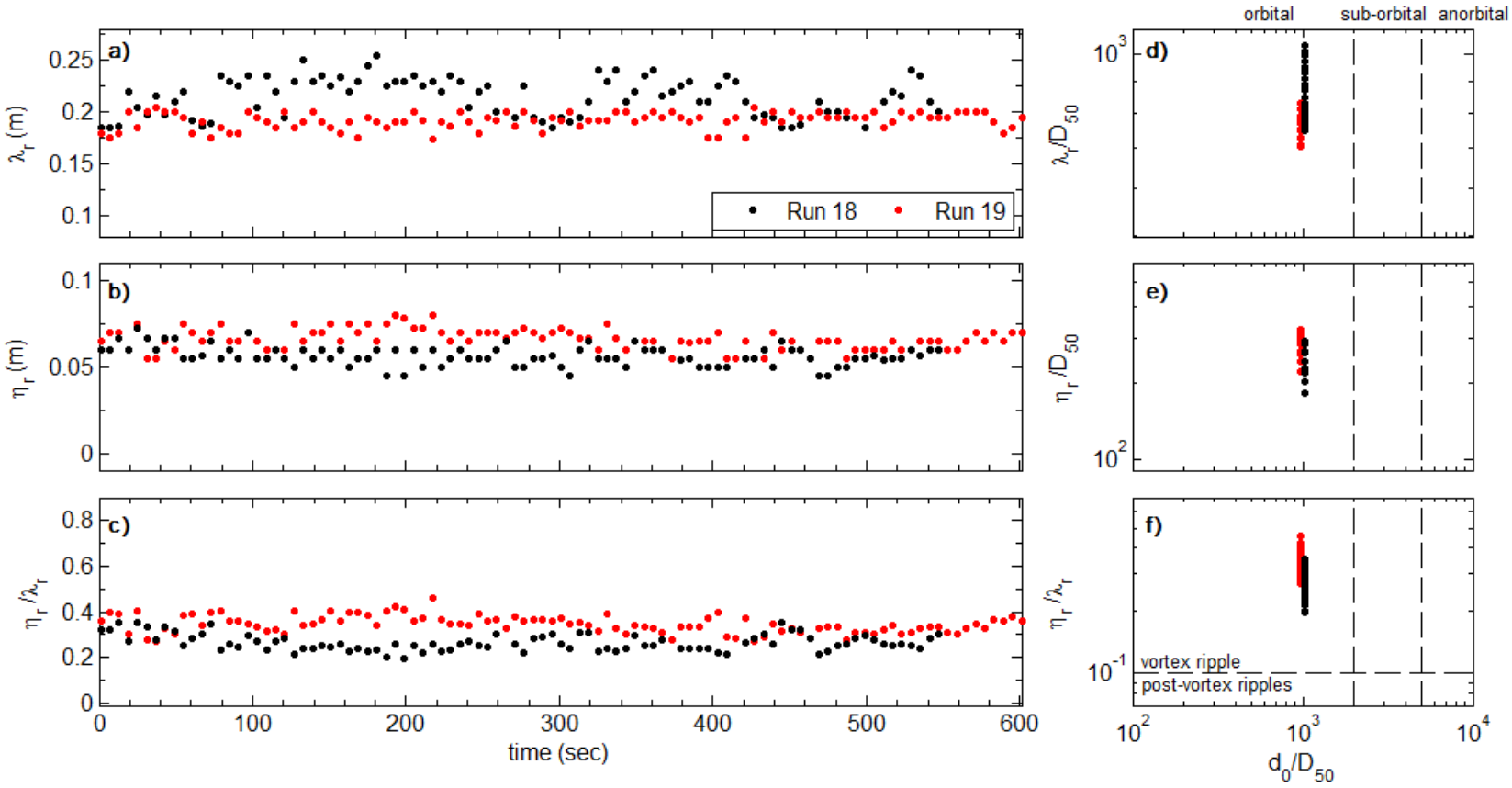

Figure 6.8 Temporal evolution of **(a)** ripple length, λ_r; **(b)** ripple height, η_r; and **(c)** ripple steepness (η_r/λ_r); and classification of bedforms based on non-dimensional **(d)** ripple length; **(e)** ripple height, and **(f)** steepness versus near bed orbital diameter, d_0 relative to median grain diameter (D_{50}), following Clifton and Dingler (1984) and Wiberg and Harris (1994). The vertical lines delimiting orbital – sub-orbital – anorbital are at d_0/D_{50} = 2000 and 5000, respectively.

6.3.4 Coherent flow structures and contribution to stress

In classic boundary layer theory, exchanges of momentum in the streamwise-vertical plane (xz), represented by the Reynolds' stress ($\tau_{xz} = -\rho u'w'$), are presumed to be the predominant turbulent flux acting on the bed material. The intermittency of these exchanges is often measured using Quadrant analysis, which distributes the momentum transport within a single plane of motion between four types of event structures in four quadrants: violent 'sweeps (S or Q4)' and 'ejections (E or Q2)', and weaker 'inward (II or Q3)' and 'outward interactions (OI or Q1)', collectively termed 'bursting' (Willmarth and Lu, 1972; Bogard and Tiederman, 1986). This does not account for the entire/mean turbulent stress as crosswise fluctuations also contribute to the mean streamwise momentum (*ibid.*). These event types are often associated with the passage of a coherent structure which induces velocity fluctuations (Zhou et al., 1999). For instance, a low speed near bed fluid pumped upwards between the legs of a horseshoe vortex encountering high speed streamwise fluid is manifest by a second quadrant (Q2) ejection-type event, often associated with vertical entrainment of bed sediment. Considering shear stresses together with their distribution between quadrants and their variability in time provides a better account of sediment entrainment and transport (Heathershaw, 1979; Keylock et al., 2014). In the absence of means for visualising these coherent turbulence structures tomographically, quadrant analysis offers a means of studying the intermittent exchanges of momentum induced by such structures, and their implications to local dynamics of sediment entrainment, resuspension and deposition. To account for the three-dimensionality of the problem, the quadrant analysis is often extended by adding the cross-wise (transverse) velocity fluctuations; and defining 8-types of motions prescribed to the 4 event structures of quadrant analysis with a sign to account for positive or negative sway in the transverse direction (Gheisi et al., 2006; Keylock et al., 2014).

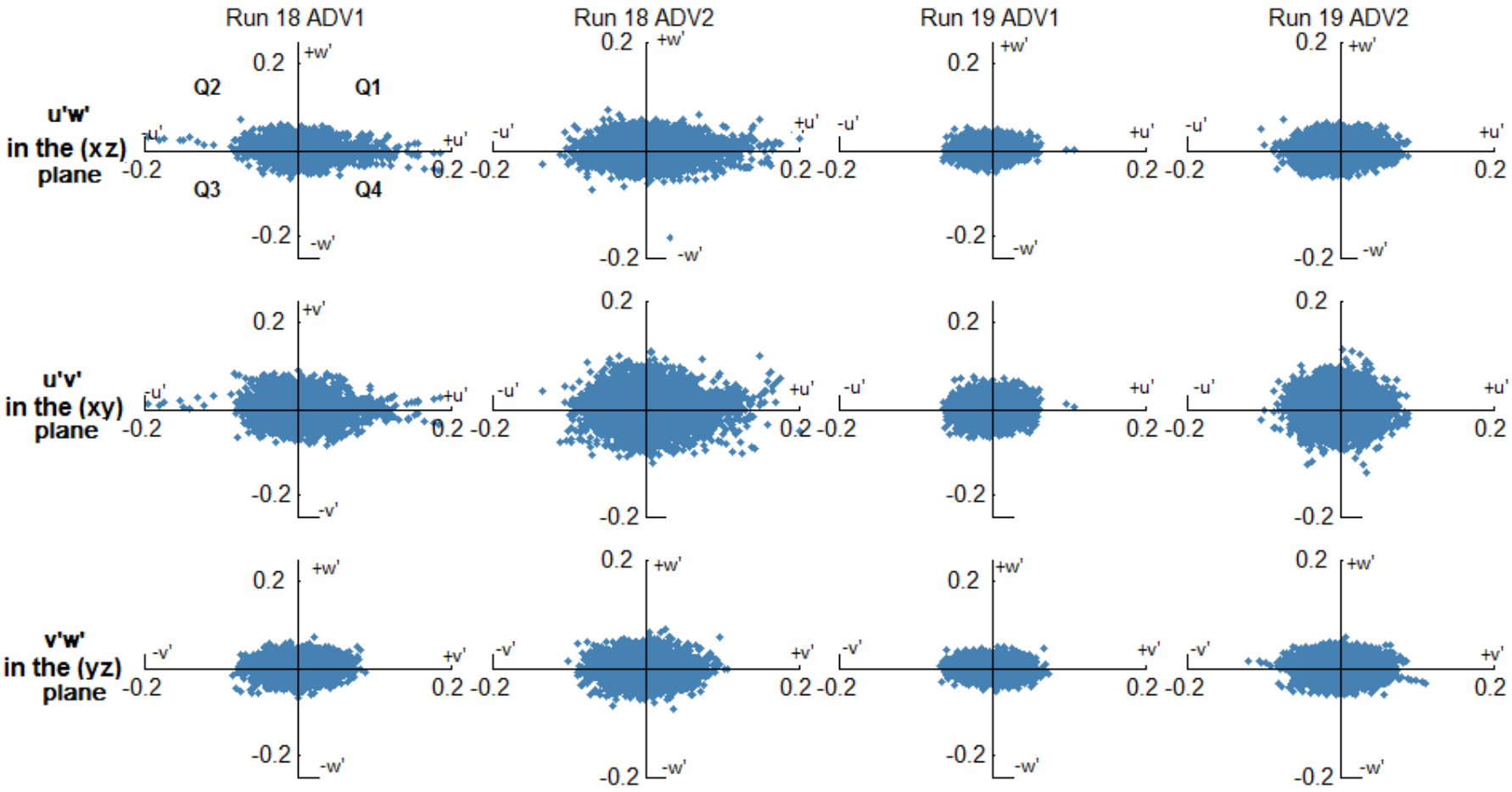

Figure 6.9 Quadrant plots of Reynolds stresses in three planes (xz, xy, yz) at two elevations (ADV1 and ADV2) for Runs 18 and 19.

To stay true to the original quadrant formulation, we present the extension into 3 dimensions as three distinct, orthogonal planes of motion. The distribution of Reynolds stress intensities $u'w'$, $v'w'$, and $u'v'$ in the streamwise-vertical (xz), horizontal (xy), and crosswise-vertical (yz) planes, respectively, across the four different types of motion (quadrant events); measured by the two ADVs during the test runs 18 and 19 are presented in Figure 6.9. For each of these quadrant plots, the shape of the scatter was assessed by approximating a least square elliptical fit (eccentricity 1 – 1.14) to the Reynolds' stress data in each plane. The inclination of these ellipses (angle between their major axis and the x-axis) was often dominated by streamwise and horizontal fluctuations (angles < 10°); and as such, the horizontal plane motions better approximated circular fits. Measurements from Run 18 featured more outliers than those of Run 19, and this was reflected in a minute shift from the centre O(0,0) of the quadrant plot for the fitted ellipses (~0.005). While it is customary to introduce a threshold Hole (H) value to delimit and ignore small-scale departures from the mean (cf. §4.3.1), no unified definition for the limiting criterion exists; and the choice is often arbitrary and these were presented without a threshold (H=0). Bogard and Tiederman (1986) suggested that the appropriate threshold is one which would yield the same number of ejections (Q2 events) as identified by flow visualisation in the streamwise-vertical plane. With no means of visualising the flow in our experiment, we apply a plane-specific universal threshold based on the cross-correlation of the root-mean-square velocity fluctuations (cf. 4.3.1). The percentage of occurrence in time, and the sensitivity of the detection technique of the various types of quadrant events to the chosen threshold Hole size (H) is demonstrated in Figure 6.10. The percentage of time spent within each quadrant as a function of the hole size (H) is normalised such that the sum of all quadrants at any H is 100%. Notably, without normalising the total sum of events to 100%; the detected events at a threshold H =4 represent only 1 – 2.5% of the all events without applying threshold, and these are the most extreme (violent) stress bearing structures. The figure shows that all types of quadrant event structures are represented in nearly equal proportion for both heights, and for both test conditions

(wave-aligned and wave-opposed currents), with no prevalence of any particular motion when no threshold is applied in any given plane. Increasing the threshold hole size, H, in the streamwise-vertical plane increases the prominence of detected sweep motions (Q4 events) for Run 18 significantly (to just under 50% of all detected motions) at both elevations, and significant decrease in detected II (Q3) motions. The opposite is observed in Run 19, whereby inward interaction (Q3) motions increase against a decrease in the number of detected sweeps (Q4). This possibly highlights the role of the superimposed current, whose mean direction governs the prevalence of a positive or negative streamwise fluctuation (with orbital motion switching signs every half cycle); in defining the predominant types of detected events. Jeong et al. (1997) have shown Q4 (sweep) events to dominate near the wall (with Q2 away from the wall) as a result of 'spatial phase difference' between streamwise and wall-normal turbulent fluctuations caused by the advection of a large coherent structure which causes counter-gradient stresses (Q1 and Q3) events above and below the structure. This causes more negative peaks in fluctuations at higher wall units than positive ones, and thus more frequent Q2 motions higher up. These Q1 and Q2 events show little effect in response to the applied Hole size, H, apart from the lower measurements (ADV2) of Run 18, where more Q1 events are observed with increasing threshold, at the expense of the Q2 motions.

The relative contribution to total Reynolds' stress of each type of the quadrant structures within each of the planes is quantified and summarised in Figure 6.11. The data are presented without applying a threshold to ensure no dynamic processes are arbitrarily removed from the analysis. In Run 18, with currents along the direction of wave propagation, the violent sweep (Q4) and ejection (Q2) motions contribute 60% of the stress in the primary plane of motion (xz) at the higher ADV, and sweeps alone contribute nearly a third of all the stress at both heights above the bed. The opposite is true for Run 19, with the current opposing progressive waves, whereby outward (Q1) and inward (Q3) interactions contribute more to the stress with the biggest contribution from inward interactions. Q4-type motions are the largest

contributor to stress in the horizontal and cross-wise vertical planes for Run 18.

Lozano-Duran et al. (2012) have shown using direct numerical simulation (DNS) that applying a higher threshold identifies structures that only fill a small fraction (by volume of flow), yet contribute significantly to stress at all wall distances. These typically correspond to larger, wall-attached events that carry most of the Reynolds' stress, compared to the background fluctuations, often regarded as imprints of detached objects which tend to be isotropic (directionally) and thus their contributions to the mean stress cancel out. Wall-attached structures tend to be formed by paired counter-rotating Q2 and Q4 events, often with an associated vortex cluster (detached and isotropically oriented) embedded in the ejection. Using tomographic PIV in a unidirectional flow, Yang and Jiang (2012) show stronger similarity of multiple structures in the vertical, compared to the other two planes (quasi-streamwise and spanwise), and a similar pair of vortices (Q2 and Q4) around a bursting event, which extends toward the wall (bed). Lozano-Durán and Jiménez (2014) measured the streamwise advection velocity of coherent structures and implied that these are deformed by the mean shear which also controls their lifetime (duration through which they persist before they are completely consumed by viscosity). Buchner et al. (2016) suggest that the mean strain rate, which depends on the type of structure considered is skewed along the positive flow direction, amplifying vorticity. We therefore suggest that within a monochromatic, orbital flow coupled with a superimposed current, the steady current will dictate the mean direction of the strain, favouring the positive streamwise motions (Q1 and Q4) in the aligned case (Run 18), and the negative streamwise events (Q2 and Q3) in the opposing current case. This agrees with the observed percentages of occurrence; and, with Q2 and Q4 motions being the most violent, these pairs provide the most significant contributions to stress in the streamwise-vertical plane for both test runs.

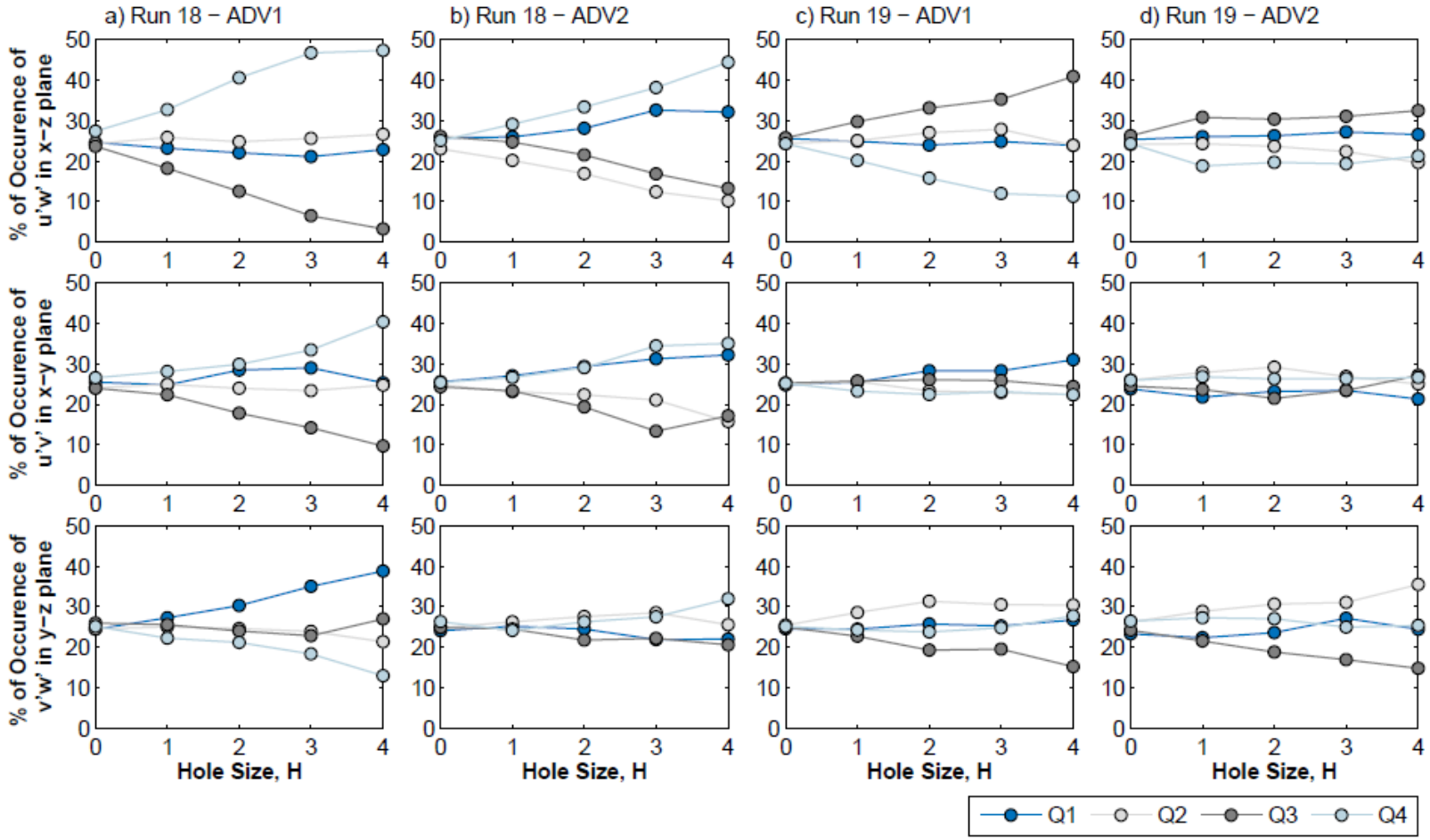

Figure 6.10 Effect of the threshold (hyperbolic Hole Size, H) on the number of detected quadrant events in the three considered planes of motion for both ADV heights for Runs 18 and 19.

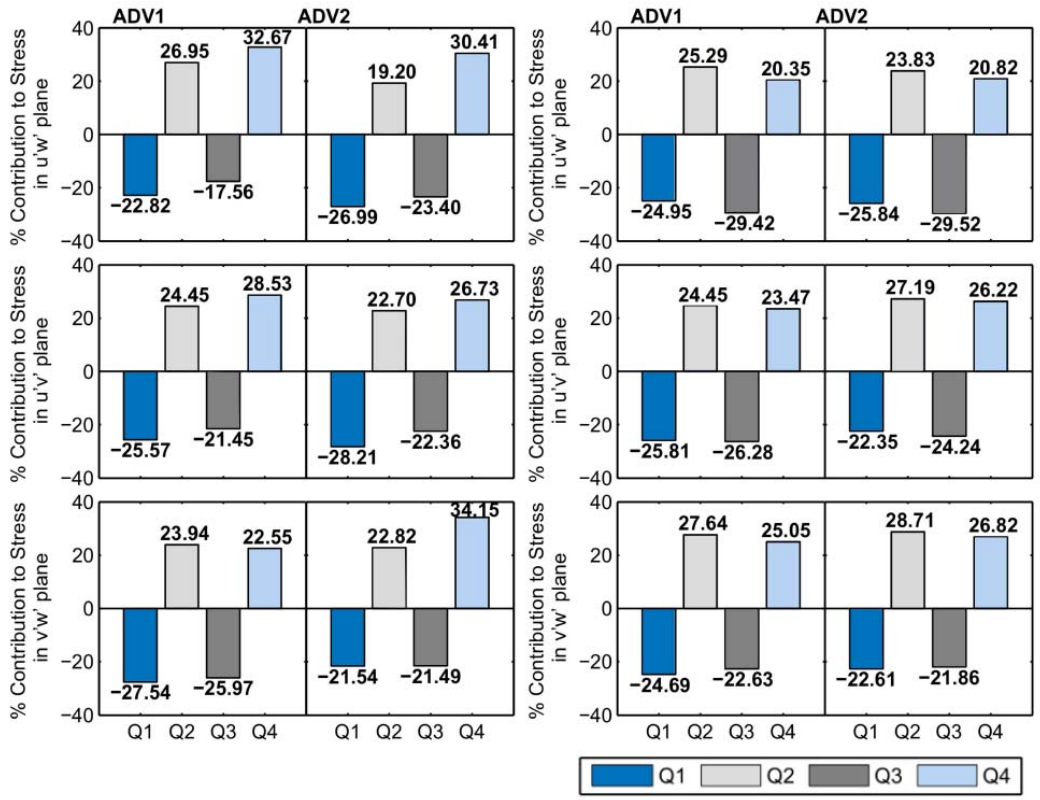

Figure 6.11 The relative contribution to Reynolds' stress of each type of quadrant structure in three planes of motion for Run 18 (left) and Run 19 (right).

6.3.5 Space-time dynamics of coherent structures

6.3.5.1 Spatial scales of turbulence

The normalised, turbulence power spectra in three dimensions are presented in non-dimensional wave-number space ($k^* = kz$, where z is the height of measurement) in Figure 6.12. The spectra were constructed in energy-preserving form such that an equal area under the curve represents equal energy (variance) following Soulsby (1977). The peaks indicate similar scaling in the streamwise, cross-wise (transverse) and vertical fluctuations with maxima correpsonding to similar wave numbers for each ADV in both test runs. As the strain rate of a particular eddy is a function of its wavenumber, then the peaks of these plots correspond to the dominant spatial scales of motions as they are advected past the fixed ADV sensor following Taylor's frozen turbulence hypothesis (cf. 4.2.2.2). The inferred spatial scales

correpsonding to the peaks in these spectra are listed in Table 6.4, which confirms scales of the order of 9-15 cm as the integral scales of motion. These fluctuations approach the near bed semi-orbital excursion (orbital amplitude, $A_{0,cw}$), calculated to be ~12.6 cm for Run 18 (aligned wave-current) and 12.1 cm for the opposing wave-current case (Run 19) just outside the thin region of combined wave-current effect in the boundary layer. Noteably, these horizontal turbulent excursions in the streamwise plane are smaller for the opposing current case. This may indicate that opposings current inhibit the growth of a flow structure induced by the oscillating motion in the streamwise direction (for half wave cycle).

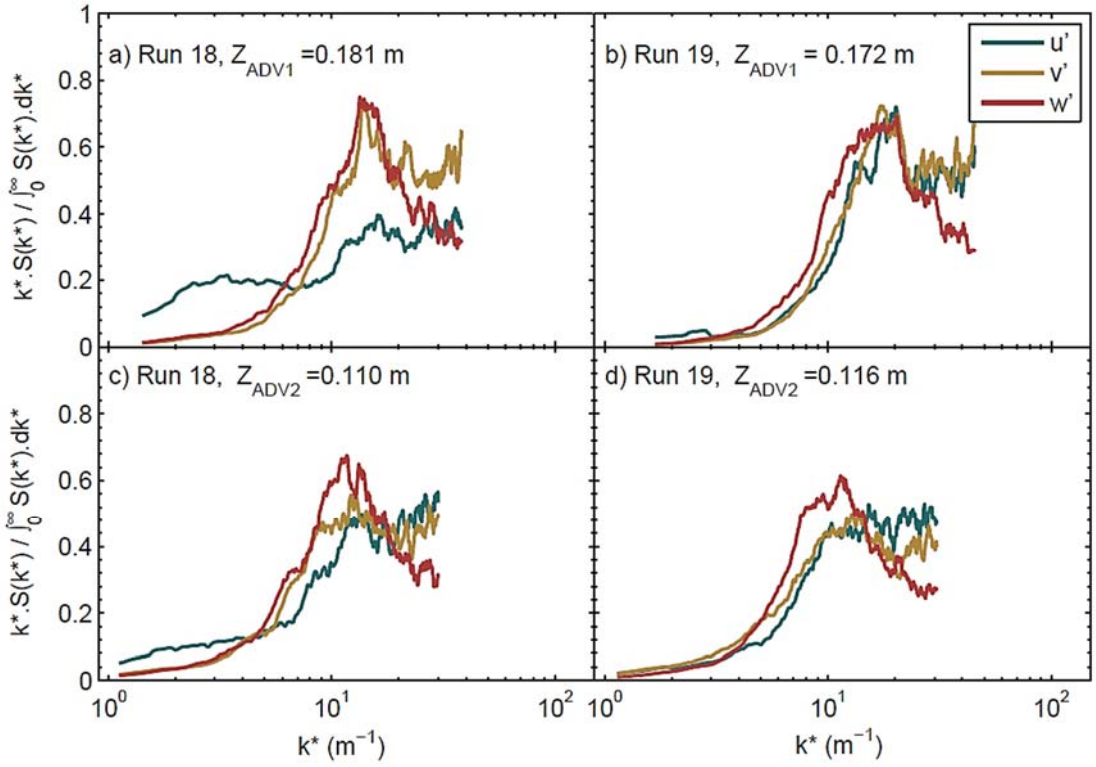

Figure 6.12 Non-dimensional wave-number k^*–weighted energy spectra

Table 6.4 Dominant spatial scales of motion through normalised energy spectra of turbulent components (parenthesis indicate second peak)

Run	ADV elevation	L(u')	L(v')	L(w')
Run 18; 24/11/2015	0.181 m ab	0.144 m (0.05 m)	0.130 m	0.137 m
	0.109 m ab	0.140 m (0.06 m)	0.100 m	0.105 m
Run 19; 25/11/2015	0.171 m ab	0.092 m	0.108 m	0.092 m
	0.116 m ab	0.106 m	0.118 m	0.142 m

6.3.5.2 Temporal/frequency scales of coherent structures

The temporal scales of turbulence can be inferred from the active periods of flow, inferred from the high variance regions within the time-frequency domain obtained through a continuous wavelet transform (CWT) decomposing the Reynolds' stress signal in three planes. Figures 6.13, 6.14, and 6.15, show the local (instantaneous) and global (over a time period) spectral properties of the $u'w'$, $u'v'$, and the $v'w'$ Reynolds' stresses, respectively; at the two measurement points (ADV1 and ADV2) for test runs 18 and 19. In these figures, the time series of the Reynolds' stresses at a given height is shown, together with its corresponding power spectral density obtained through a fast Fourier transform (FFT) using Welch's method, with a Hanning window of 2^{10} data points with 50% overlap. The horizontal dashed red lines denote the standard deviation ($\pm\ 1.\sigma$) about the mean of the time series. The power spectral densities (PSD) are presented in frequency domain rather than wavenumber space, and are expected to adhere to the same scaling laws given ADV measurements invoke Taylor's frozen turbulence theory, and thus $S_{ii}(k) = S_{ii}(f).\overline{u}\ /2\pi$ (Stapleton and Huntley, 1995). The time series of the continuous wavelet transform (CWT) of the stress signal is also computed and presented in a time-frequency domain, together with its global spectral power (integrated variance), represented for different periods (inverse frequencies) for intelligibility. The global power pertains to the time average of all local wavelet spectra (*i.e.* all the vertical slices through the wavelet plot). In the CWT time-frequency plot, warmer colours indicate high power (variance), the white shaded region represents the cone of influence whereby edge effects may distort the image (cf. §4.3.2.2), and the thicker, black contour lines delimit the 95% confidence limits (5% significance against red noise given by a Monte Carlo simulation following Torrence and Compo (1998)). The limitation given by the cone of influence is a manifestation of Heisenberg's uncertainty principle, which implies that one cannot obtain good localisation in both time and frequency, and a trade-off thus exists with bad temporal resolution at the larger scales, and bad frequency resolution at the smaller scales (Foufoula-Georgiou and Kumar, 1994; Farge et al., 1996). In

what follows, the subscripts i, j, k are used to denote a component in the x (along direction of wave propagation), y (lateral/crosswise), and z (vertical) directions.

Figure 6.13 shows the time series, power spectrum (S) and CWT of the streamwise vertical stress ($u'w'$) for Run 18, with a current aligned to the direction of wave propagation. The CWT plot for the higher ADV highlights intermittent, active regions within the flow through powerful (high variance) events that span a range of frequency (period) scales. These events are often short lived between 1 and 5 Hz (periods of 0.5 – 0.2 seconds) lasting a maximum of 9 seconds (3 times the period of the imposed wave forcing). Nonetheless, two prominent events are observed to persist noticeably over a very narrow scale distribution, with a peak global power corresponding to periods between $2.3 - 2.6\,s$ (lasting ~140 seconds); and to $1.4 - 1.8\,s$ (lasting 76 seconds). Closer to the bed, the CWT time-frequency plot of $u'w'$ is also characterised by intermittent, rapidly decaying structures (power transferred towards smaller frequencies in short time) in the range of frequencies between 1 and 5 Hz, and longer-lasting, slowly evolving structures that correspond to the forced wave frequency (peak frequency and harmonics) lasting up to 280 seconds for the peak wave frequency. Spatially, the rapidly decaying motions correspond accurately in time to those observed higher in the water column (ADV1). On the other hand, the time series of the streamwise-vertical Reynolds' stress in Run 19 displays much smaller excursions beyond the standard deviation at both elevations, resulting in a relatively flat power spectral density (PSD) distribution ($f^{-0.1}$) at the higher ADV1, and ($f^{-0.36}$) at the lower ADV2. The power spectral densities for run 19 are an order of magnitude lower than those of Run 18. The CWT plots show much weaker (low variance) clusters that are intermittent, and very short lived, across small ranges of frequencies (lifespan of ~ 3–9 sec) for fluctuations at frequencies between 1 and 5 Hz, and much weaker, longer lasting events at frequencies corresponding to the forced wave harmonics. This is true for stresses at both elevations, with events even more rapidly decaying closer to the bed (higher global variances), and no particularly dominant scales.

The CWT for the $u'v'$ time series plots shown in Figure 6.14 also display two different types of active (high variance) flows: intermittent, short lived (3 – 6 s long) events spanning several frequency scales; and, more persistent (100 – 300 seconds long) low frequency events at scales corresponding to the wave harmonics. At the lower ADV, the short-lived events are less powerful and longer events are even more acutely representative of the peak wave frequency. For the opposing current case (Run 19), intermittent high power events are also observed in the CWT plots at a variety of rapidly ceasing, small scale ranges at the higher ADV1, and even more so at the lower ADV2. No clear large-scale structures are identified. Moreover, there is no dominance of any particular scales or event types in time given the relatively constant global power distribution across frequency scales (periods) in each case. The CWT plots for the $v'w'$ time series (Figure 6.15) reveal a similar behaviour to that observed for the $u'w'$and $u'v'$ Reynolds stresses, with short lived high variance events spanning a multitude of frequency scales, and low variance, long-lived events at frequencies corresponding to the wave forcing. No active events are identified at the lower ADV location in Run 18, with most fluctuations occurring within $\pm 1.\sigma$ (standard deviation). Interestingly, Run 19 shows multiple long-lived events of low variance at wave-related frequencies, with particularly more active events closer to the bed (ADV2).

To aid the discussion of the observed behaviour, the turbulent characteristics, comprising the turbulent Kinetic energy ($TKE = \rho k$), three-dimensional Reynolds's stresses, the vertical turbulent flux, $\overline{k'w'}$, the rate of production of Reynolds' stress, P_{Rey}, the rate of dissipation of streamwise turbulence, ε_{uu}, and the rate of vertical turbulence transport, T_v are computed (cf. §6.2.3.3) and presented in Figure 6.16. The figure shows relatively similar magnitudes of turbulent kinetic energy in the aligned and opposing current-wave cases, with more variance observed in the aligned flow, particularly closer to the bed. This variance is also apparent in the wider difference between the calculated Reynolds stresses at the two elevations compared with the opposing current run, as well as the rate of production of Reynolds' stress being several times higher at the higher elevation in aligned flow. Similarly, while both runs

appear to have relatively similar rates of dissipation, the difference between both elevations is more evident under aligned flows. Moreover, the turbulent flux appears to be negligible at both elevations for the opposing current case, as well as the higher ADV in the aligned flow, and much more significant closer to the bed, resulting in significant upward-directed flux in the aligned case.

Both ADVs were measuring outside of the near-bed combined-wave current boundary layer region where kinetic energy is generated. The momentum exchanges between the combined wave-current boundary layer and the overlying flow comprise of $u'w'$ stress-bearing eddies whose energy containing scales seen at ADV2 start breaking up through inertial forces such that they fall within the inertial sub-range by the time they reach the elevation of ADV2 (Kolmogorov's cascade). This is shown by the difference in turbulence dissipation rate of the streamwise component, which is higher at the higher ADV as shown in Figure 6.16. Conversely, $u'v'$stress-bearing eddies are yet to be fully within the inertial sub-range as they progress towards ADV1.

For the opposing wave-current case, Run 19, the relatively flat spectra of the $u'w'$stresses indicate very rapid breaking of the coherent structures before they are fully formed, as shown in the CWT plots. The Reynolds' stress production rate and streamwise velocity dissipation rates vary less with elevation above bed in the opposing current case than seen in aligned flow, and the vertical turbulence transport, T_v is thus nil at both ADVs whereas the vertical flux and vertical turbulence transport are more significant closer to the bed in the aligned flow case (Figure 6.16). We suspect this to be a manifestation of the longitudinal adverse current breaking up/inhibiting the $u'w'$stress-bearing motions generated within the combined wave-current boundary layer and ejected into higher, faster fluid; whereas the lateral exchanges of momentum of bed generated motions are less affected, and thus some energy within the vortices is preserved/ forced laterally before decaying.

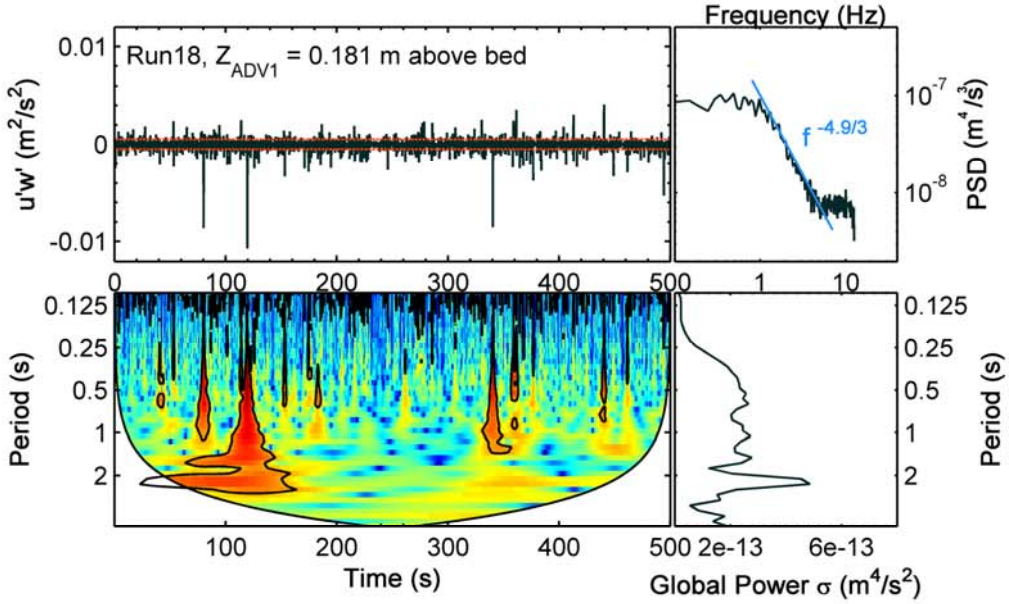
Run18, Z_{ADV1} = 0.181 m above bed
u'w' (m^2/s^2)
0.01
0
-0.01
Frequency (Hz)
$f^{-4.9/3}$
PSD (m^4/s^3)
10^{-7}
10^{-8}
0
100
200
300
400
500
1
10
Period (s)
0.125
0.25
0.5
1
2
Time (s)
2e-13
6e-13
Global Power σ (m^4/s^2)

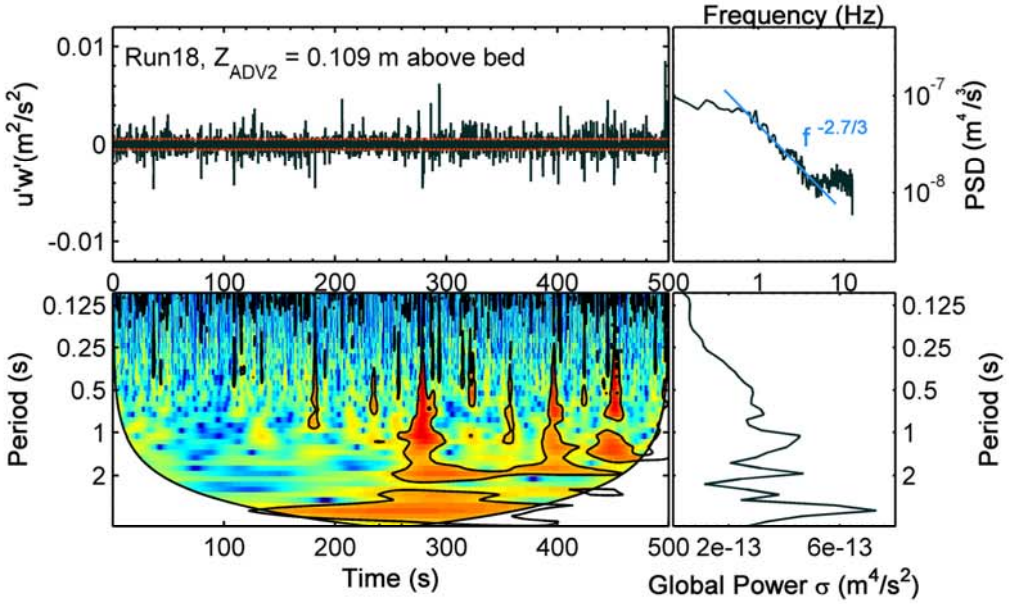
Run18, Z_{ADV2} = 0.109 m above bed
u'w'(m^2/s^2)
0.01
0
-0.01
Frequency (Hz)
$f^{-2.7/3}$
PSD (m^4/s^3)
10^{-7}
10^{-8}
0
100
200
300
400
500
1
10
Period (s)
0.125
0.25
0.5
1
2
Time (s)
2e-13
6e-13
Global Power σ (m^4/s^2)

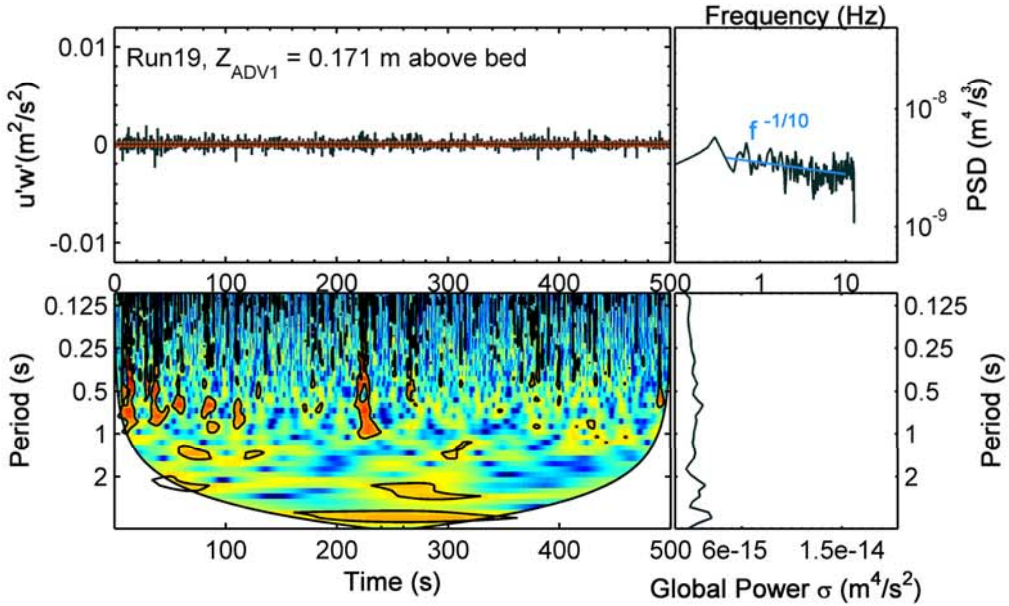
Run19, Z_{ADV1} = 0.171 m above bed
u'w'(m^2/s^2)
0.01
0
-0.01
Frequency (Hz)
$f^{-1/10}$
PSD (m^4/s^3)
10^{-8}
10^{-9}
0
100
200
300
400
500
1
10
Period (s)
0.125
0.25
0.5
1
2
Time (s)
6e-15
1.5e-14
Global Power σ (m^4/s^2)

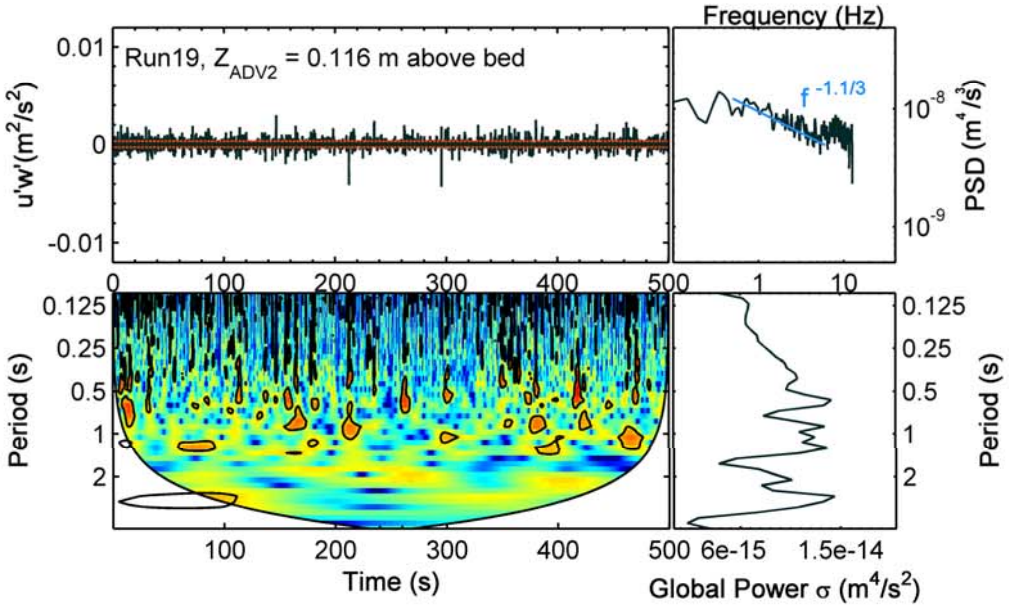
Run19, Z_{ADV2} = 0.116 m above bed
u'w'(m^2/s^2)
0.01
0
-0.01
Frequency (Hz)
$f^{-1.1/3}$
PSD (m^4/s^3)
10^{-8}
10^{-9}
0
100
200
300
400
500
1
10
Period (s)
0.125
0.25
0.5
1
2
Time (s)
6e-15
1.5e-14
Global Power σ (m^4/s^2)

Figure 6.13 Time-frequency characteristics of the instantaneous, streamwise-vertical Reynolds stress $u'w'$ measured at two elevations (ADV1 and ADV2) outside the combined wave-current boundary layer, for Run 18 (with wave-aligned current) and Run 19 (with wave-opposing current). In each of the four panels, the first subplot shows the time series of the Reynolds' stress whereby the horizontal dashed red line delimits $\pm$ 1 standard deviation about the mean; the second subplot shows the power spectral density of the time series; the third subplot shows the CWT of the signal in time-period domain, and the fourth sub-plot indicated the global spectral power of the transform at different frequency periods (frequency scales). In the CWT plot, warmer colours indicate higher variance, the white shaded region represents the cone of influence and the thicker, black contour lines delimit the 95% confidence limits (5% significance against red noise).

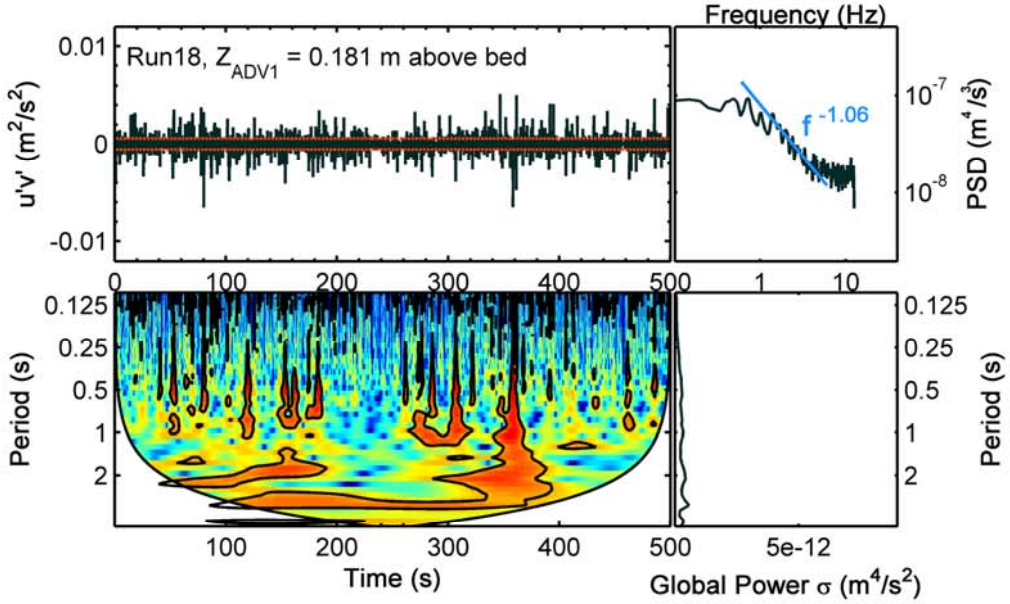
Run18, Z_{ADV1} = 0.181 m above bed
u'v' (m^2/s^2)
Frequency (Hz)
PSD (m^4/s^3)
$f^{-1.06}$
Period (s)
Time (s)
Global Power σ (m^4/s^2)

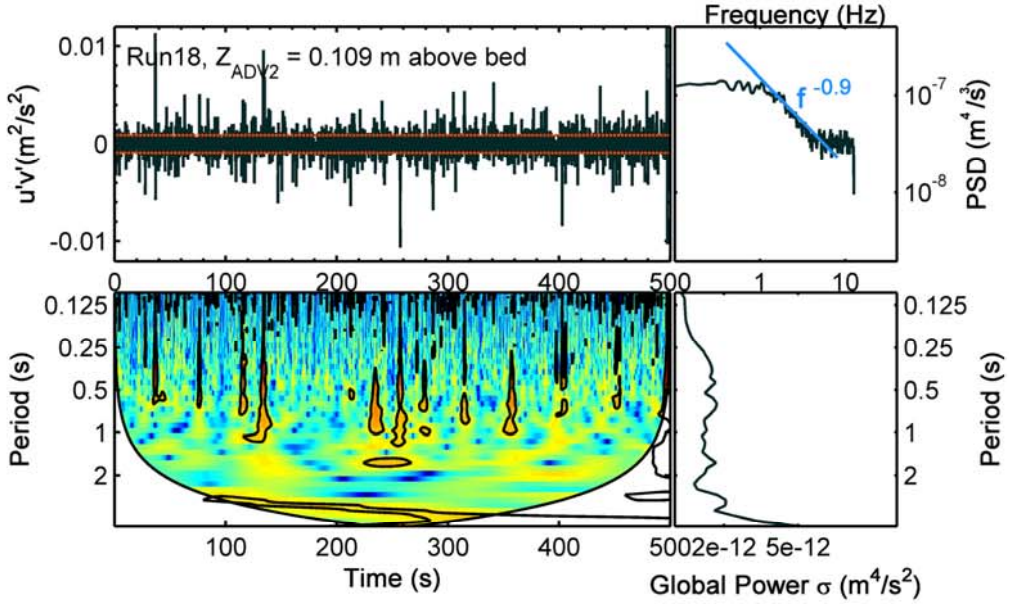
Run18, Z_{ADV2} = 0.109 m above bed
u'v'(m^2/s^2)
Frequency (Hz)
PSD (m^4/s^3)
$f^{-0.9}$
Period (s)
Time (s)
Global Power σ (m^4/s^2)

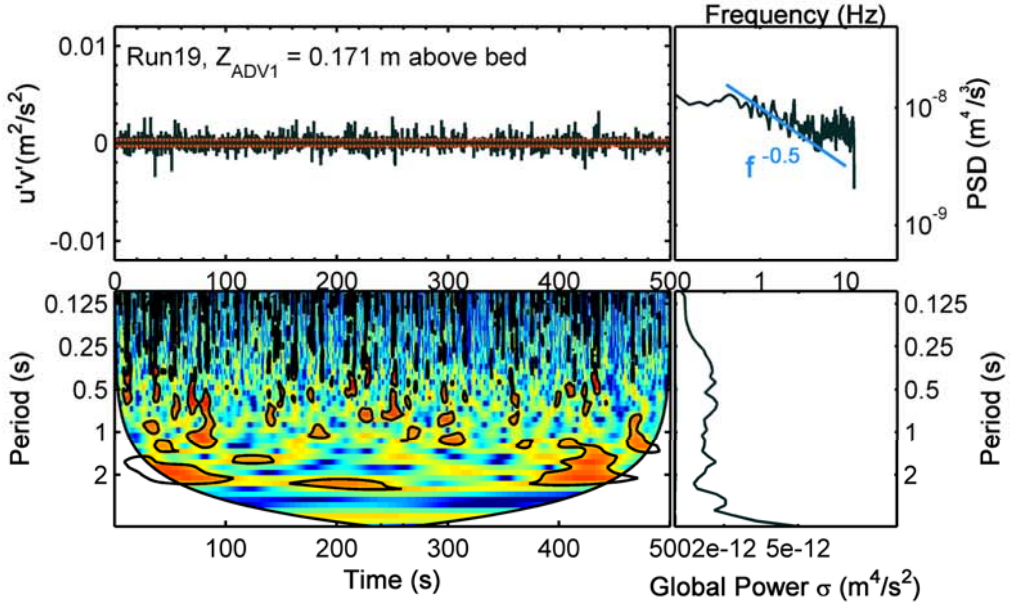
Run19, Z_{ADV1} = 0.171 m above bed
u'v'(m^2/s^2)
Frequency (Hz)
PSD (m^4/s^3)
$f^{-0.5}$
Period (s)
Time (s)
Global Power σ (m^4/s^2)

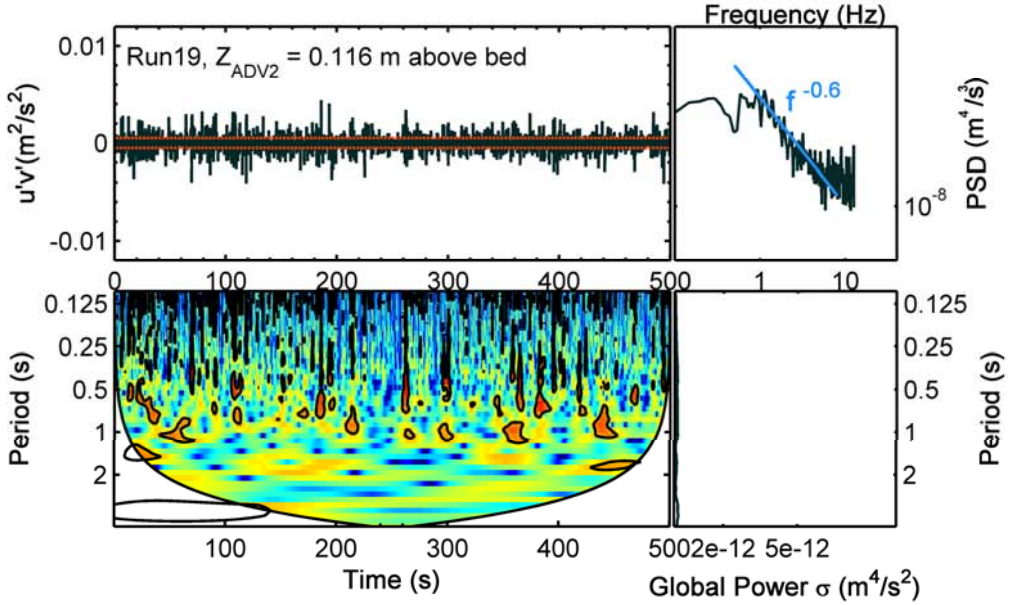
Run19, Z_{ADV2} = 0.116 m above bed
u'v'(m^2/s^2)
Frequency (Hz)
PSD (m^4/s^3)
$f^{-0.6}$
Period (s)
Time (s)
Global Power σ (m^4/s^2)

Figure 6.14 Time-frequency characteristics of the instantaneous, horizontal plane Reynolds stress $u'v'$ measured at two elevations (ADV1 and ADV2) outside the combined wave-current boundary layer, for Run 18 (with wave-aligned current) and Run 19 (with wave-opposing current). Legend same as Figure 6.13.

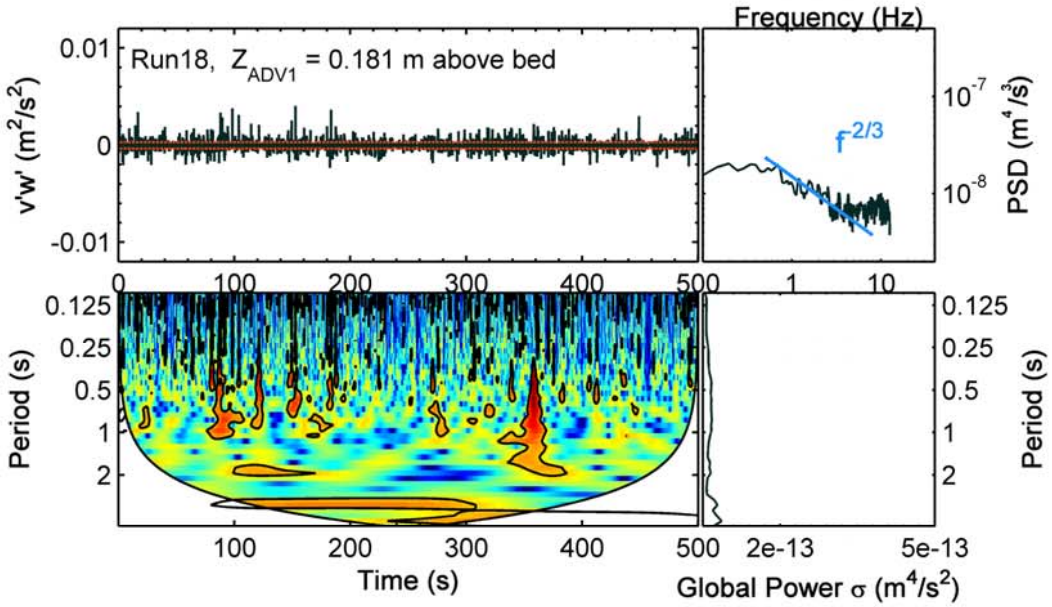
Run18, Z_{ADV1} = 0.181 m above bed
v'w' (m^2/s^2)
Frequency (Hz)
PSD (m^4/s^3)
$f^{-2/3}$
Period (s)
Time (s)
Global Power σ (m^4/s^2)
2e-13
5e-13

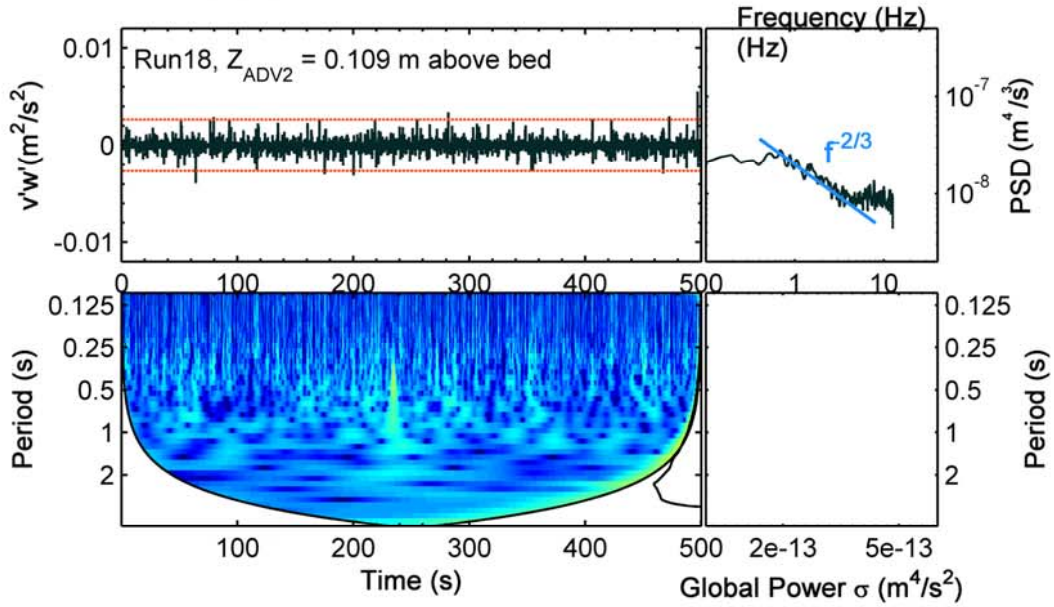
Run18, Z_{ADV2} = 0.109 m above bed
v'w'(m^2/s^2)
Frequency (Hz)
(Hz)
PSD (m^4/s^3)
$f^{-2/3}$
Period (s)
Time (s)
Global Power σ (m^4/s^2)
2e-13
5e-13

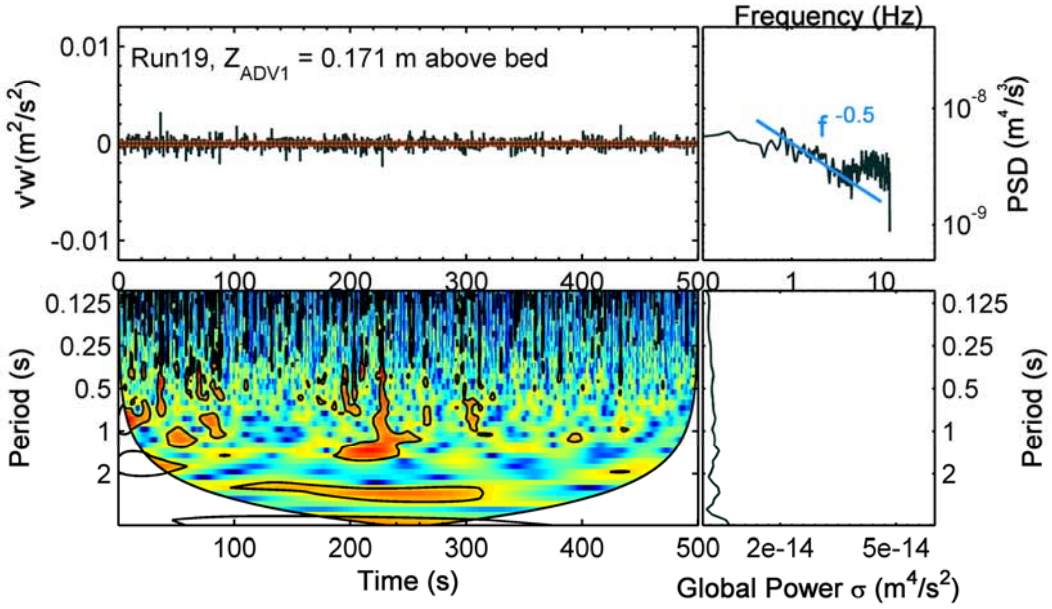
Run19, Z_{ADV1} = 0.171 m above bed
v'w'(m^2/s^2)
Frequency (Hz)
PSD (m^4/s^3)
$f^{-0.5}$
Period (s)
Time (s)
Global Power σ (m^4/s^2)
2e-14
5e-14

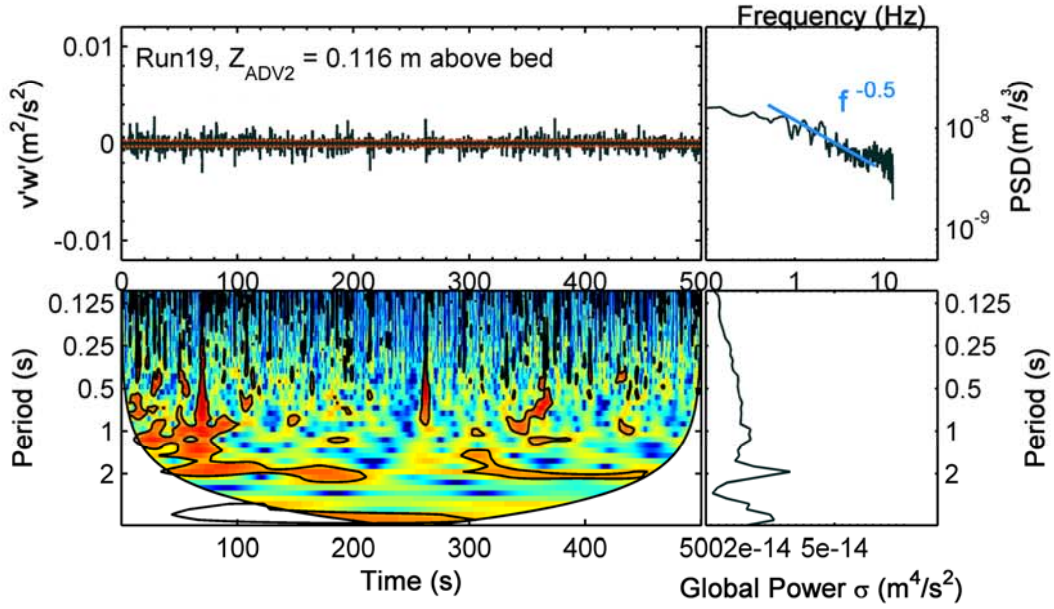
Run19, Z_{ADV2} = 0.116 m above bed
v'w'(m^2/s^2)
Frequency (Hz)
PSD (m^4/s^3)
$f^{-0.5}$
Period (s)
Time (s)
Global Power σ (m^4/s^2)
2e-14
5e-14

Figure 6.15 Time-frequency characteristics of the instantaneous, lateral-vertical Reynolds stress $v'w'$ measured at two elevations (ADV1 and ADV2) outside the combined wave-current boundary layer, for Run 18 (with wave-aligned current) and Run 19 (with wave-opposing current). Legend same as Figure 6.13.

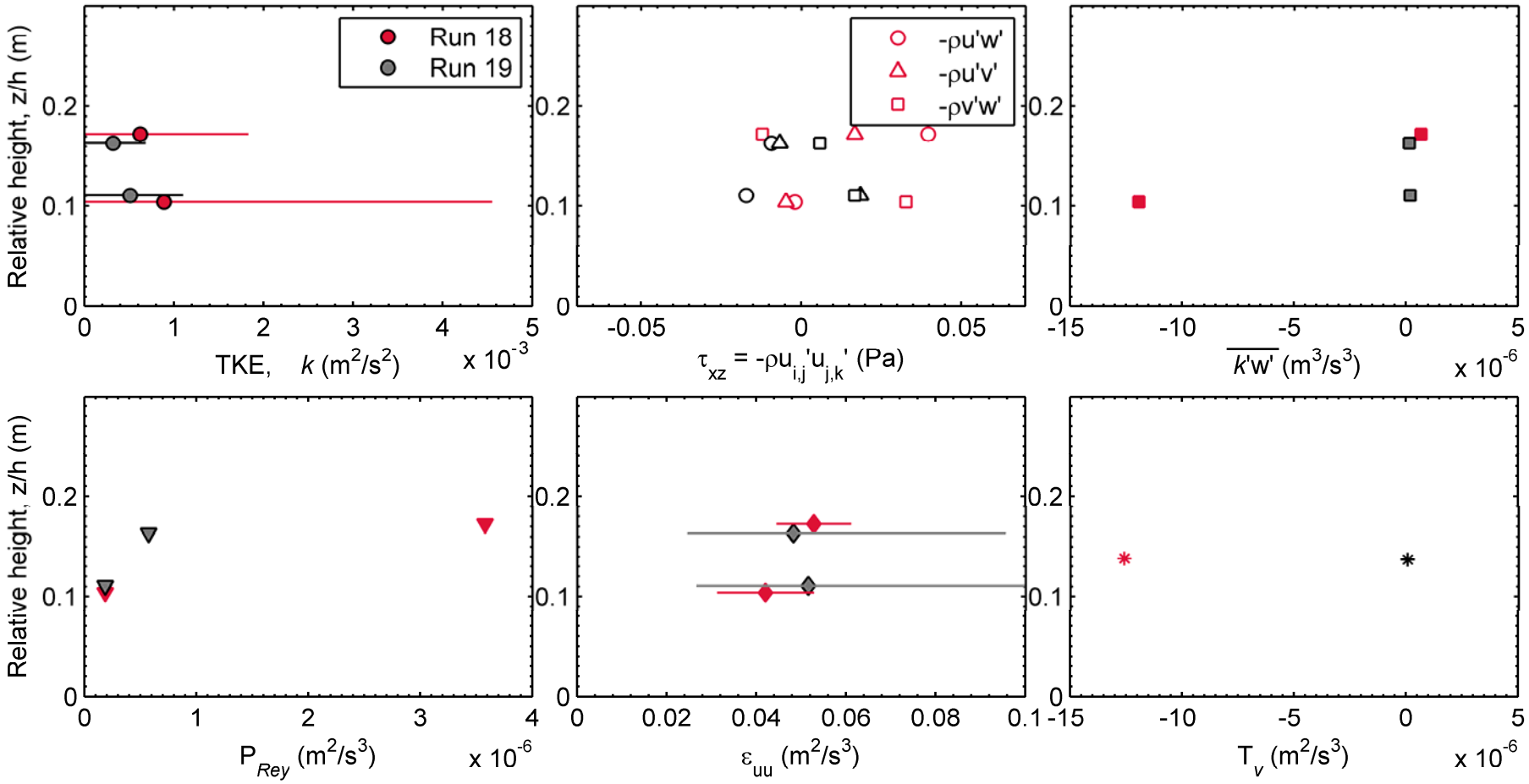

Figure 6.16 Mean turbulence properties of flow at two elevations for Runs 18 and 19; comprising: the turbulent kinetic energy per unit mass (k), three-dimensional Reynolds's stresses ($-\rho u'w'$; $-\rho u'v', -\rho v'w'$), the vertical turbulent flux, $\overline{k'w'}$, the rate of production of Reynolds' stress, P_{Rey}, the rate of dissipation of streamwise turbulence, ε_{uu}, and the rate of vertical turbulence transport, T_v.

6.4 Implications to sediment transport

To first order, regular waves do not result in net sediment transport, except for wave-induced net currents through boundary-layer streaming (Longuet-Higgins, 1953) and velocity asymmetry between wave crest and troughs as they propagate shorewards (Komar, 1976; Fredsøe and Deigaard, 1992). The oscillatory motion, nonetheless, contributes significantly to sediment pick-up, and as such, provides an effective stirring mechanism, facilitating the mass transport of locally suspended particles by relatively small steady currents (Dyer, 1986). Quantifying suspended sediment transport in combined wave-current flows requires accurate evaluation of the shear stress at the bed and within the boundary layer, which requires parametrising an eddy viscosity profile to solve the hydrodynamic equations of flow, as well as the advection-diffusion equations for sediment suspension (via sediment diffusivity). Solving the problem numerically, through algebraic eddy viscosity models and mixing length arguments (cf. §2.3 and Appendix 1), requires accurate consideration of vorticity dynamics within the core region just outside of the combined wave-current benthic boundary layer (Huang and Mei, 2003; Tambroni et al., 2015). Higher-order models (one or two-equation linear eddy viscosity models) also prescribe a boundary layer structure defined by time-varying or invariant multi-layered eddy viscosity profiles, and/or focus on the dynamics of turbulent kinetic energy production and dissipation (Davies et al., 1988; Soulsby et al., 1993; Antunes Do Carmo et al., 2003; Holmedal et al., 2003; Yuan and Madsen, 2015). For instance, Huang and Mei (2003) attributed reductions in current speed for a wave following current, as opposed to an increase in an opposing current, in addition to variations in stress all the way up to the free surface (despite no wind) to distortions in eddy viscosity. Such accounts of boundary layer structure are often bound by descriptions of vertical accelerations and pressure differentials. These are defined by coherent vortex structures which result in amplified turbulent fluctuations and shear stresses and, potentially, suspension plumes. To limit these effects to the near bed, region, models tend to impose a 'zero flux' condition on turbulent intensities and sediment concentrations at the edge of the combined boundary layer

(Holmedal et al., 2003; Holmedal et al., 2013). With sediment likely to be suspended beyond the near bed boundary layer, the interaction between flow structures induced by both waves and currents with the entrained particles needs to be accounted for throughout the flow, as is often done regarding the non-linearity imposed by the currents on the waves and vice-versa (*e.g.* apparent roughness, reduction of mean velocity, *etc.*). Furthermore, Inman and Bowen (1962) have shown that rippled beds generate vortices whose asymmetry can lead to the transport of sediment even against the mean flow. Therefore, the structural attributes and time variations of these vortex structures are important for an accurate description of sediment transport in combined flow.

In this study, field measurements of turbulent fluctuations at two elevations above the bed were collected in two flow configurations of practical relevance to sediment dynamics in coastal areas, with collinear steady currents aligned with, and opposed to the direction of wave propagation. According to Soulsby et al. (1993), the threshold of motion and entrainment of sediment is determined by the mean combined bed shear stress, while current velocity and the diffusion of suspended sediment particles into the upper part of flow are determined by the maximum combined shear stress. In calculating these combined stresses, most models employ a linear vector addition of the current and wave-induced stresses (Grant and Madsen, 1979; Grant et al., 1984; Davies et al., 1988; Fredsøe and Deigaard, 1992; Soulsby et al., 1993; Yuan and Madsen, 2015). This implies equal magnitudes of mean stress for collinear, co-directional ($\phi_{cw} = 0°$) and opposing ($\phi_{cw} = 180°$) currents to progressive waves (Li and Amos, 1995; 2001). The experiments of Kemp and Simons (1982; 1983) also showed that maximum turbulence intensities and Reynolds stresses depend on the magnitude of current and wave-induced velocities rather than the relative direction (current following or opposing the propagation of waves). They show, nonetheless, increased attenuation of wave energy in the opposing current compared with a decrease in attenuation for a following current; as well as changes in mean velocity profiles and boundary layer thickness. This is only true for rough, rippled beds where velocities are

reduced and turbulence intensities and mean stresses are enhanced by changes in vortex patterns formed between the roughness elements. In contrast, the opposite – increased attenuation in following currents and reduced attenuation in opposing currents – holds for smooth beds. Subsequently, the authors imply an increase in sediment pick-up to within 7 roughness heights (assumed 4 times for waves only), and diffusion of that sediment beyond the combined layer. They conclude, therefore, that the relative direction only influences the outer layer of flow, but not the wave-current interaction near the bed.

The results presented here, albeit from a limited dataset and range of conditions, show similar results though with pronounced vertical variations within the outer layer (no measurements were within the theoretical region of combined interaction). Whilst turbulent kinetic energy, Reynolds stresses and rates of production and dissipation of energy had similar magnitudes for currents aligned to and opposing the direction of wave propagation they varied more sharply in the opposing current case. With similar bed morphologies in the two tested cases, the streamwise-vertical stress imprints of coherent eddies at wave and half-wave frequencies (hence corresponding to vortex shedding from bedforms) in the aligned wave-current case were longer lived lower within the outer flow region, and within that frequency range, did not correspond in time to those observed higher up. Similarly, t at the lower level, their spectra indicated superposition of multiple scales of eddies within the energy cascade (k^{-1} inverse power law spectrum, cf. §6.3.5.2) compared to a well-defined Kolmogorov-Obukhov ($k^{-5/3}$) rate of inertial dissipation higher up. This implies that the core flow (outside the wave boundary layer, cf. §2.2.2) is not uniform (purely current dominated), with its lower portion comprising eddies that are both advected and locally generated; and, higher up, only advected eddies are present. The vertical excursions of turbulence (length scale of w') corresponded well with the observed vertical suspension clouds observed by the ABS (instrument fault meant data cannot be exported and hence not shown here). This is confirmed by significant vertical turbulent fluxes calculated at the lower ADV location; and implies that

active momentum exchange and sediment mobilization take place well into the outer region of the wave-aligned current flow. This warrants a re-assessment of the existing models for defining the extent of the combined wave-current boundary layer thickness, and the invalidity of the zero-flux condition commonly imposed. With opposing currents, nonetheless, the conditions presented in this study indicate very strong dissipation of these coherent eddies (within 3 waves) and, in light of the findings of chapter 5 and the proposed conceptual model in §5.4, no sustained suspension clouds within the water columns in the opposing current case will take place. Holmedal et al. (2013) have shown, numerically, that the net sediment transport is in the direction of the current, both for currents following, or opposing the direction of wave propagation; and, for linear waves, larger net transport in opposing flows. This contradicts observations presented here, with more active transport, and episodic transitions to mass layer transport (akin to sheet flow) at flow reversal in aligned flows, compared to sharply defined yet rapidly decaying suspensions by flow reversal followed by advection of these clouds by the current in the opposing flows. Nonetheless, the aforementioned study acknowledge that their findings may be tied to the imposed zero-flux conditions and linear summation of current and near-bed orbital velocities at the edge of the boundary layer which yields a more current dominated situation for opposing currents compared with aligned wave-current flow. This also raises the point that the relative magnitude of the current compared to the waves will be important in dictating the observed outcome.

Finally, the interest in structural studies focusing on statistical attributes of stress and momentum exchange by coherent structures in turbulent fluid flows is commonly questioned. Lozano-Duran et al. (2012) argued that elucidating how these structures relate to each other and how/why they evolve in time offer the most interesting results, and not the kinematic description of these motions in individual flow configurations. Three-dimensional, dynamical studies of energy or momentum transfer between different flow structures and across different scales are rather recent, limited by the need for time-resolved information in the three dimensions; and remain

constrained by the choice of the structures to track. Numerically, this is limited by the expensive computational requirements needed to resolve all scales of motion in a multi-phase fluid. In field scale studies, this level of detailed measurement is still elusive, though emerging technologies are quite promising (*e.g*. field deployable planar particle image velocimetry (Nayak et al., 2015)). Therefore, advanced computational techniques are relied upon to extract temporal and spatial information on fluid motion (Reynolds stresses and quadrant events) and suspended particles, often measured at discrete locations with the flow. This is warranted given that quadrant event motions, often considered manifestations of the passage of coherent structures, reside at the top of the turbulent energy cascade (*ibid.*), and are important for the transfer of momentum and generation of turbulent energy. An assessment of shear stress and its distribution across different quadrant events as well as its variability in time often provides a better account of sediment entrainment and transport (Heathershaw, 1979; Keylock et al., 2014). What remains to be explained is the feedback of the suspended particles, once entrained, on the vortex structure itself. Unfortunately, the limitations of this experiment meant that no joint analysis of the temporal and spatial attributes of the turbulence and suspension signals could be undertaken. Advanced visualisation studies, data analysis techniques and numerical simulations reveal complex interactions between passing coherent energy structures and sediments in suspension, such as particle response to turbulent fluctuations in the frequency domain (Liu et al., 2012), and modifications of the mean velocity profile by the dispersed sediments (Ji et al., 2013). The results of Chapter 5 suggest that the maintenance of suspension clouds within the water column is dictated by the continued supply of turbulent energy through vortex clusters. Whether similar mechanisms operated in combined flow, and what influence does the rapid dissipation in wave-opposing currents have on these clusters, remain to be ascertained. Furthermore, the role of wave frequency on the production and dissipation of energetic clusters within combined, aligned and opposing wave-current flow is also of interest, particularly where short and long periods are superimposed (*e.g.* sea and swell conditions on a beach or tidal inlet under flooding and ebbing tides.). This, in turn, raises the question

of amplitude and frequency modulation of different scale eddies, such as the superposition of multiple scales observed higher within the core flow in this study.

Chapter 7.

Summary, Conclusions and Recommendations

"When dealing with water, first experiment. Then, use judgement."
Leonardo da Vinci (Price, 1978)

7.1 Introduction

Turbulence resides at the 'noisy' end of a spectrum of drivers of morphological change, and as a sub-grid scale phenomenon presents a formidable challenge for better, robust models of sediment transport in the coastal zone. The mobilisation and transport of non-cohesive sediment in suspension in coastal benthic boundary layers, whilst having received considerable scholarly interest, is still considered to be insufficiently understood (Aagaard and Jensen, 2013). In particular, the intermittent stirring of sediment by coherent turbulence structures and the time-history effects of suspended sediments under irregular wave conditions in the shoreface are often highlighted as pressing research needs (van Rijn et al., 2013). Furthermore, complex flows in the coastal zone arise from irregular waves interacting with the bottom topography (hence shoaling and/or breaking), and non-linear interactions between oscillating motions of the waves, and steady currents (*e.g.* tidal, or net currents induced by wave asymmetry, undertow, *etc*.). The complex interactions and feedback mechanisms between the fluid motion, the seabed and the entrained particles, as well as particle-particle interactions, impede a complete mathematical description of the problem, presenting a plethora of unsettled issues including: boundary layer structure and scaling in oscillatory and combined wave-current flows (including velocity and eddy viscosity profiles); hydrodynamic and physical wall roughnesses; and momentum exchanges (Reynolds' stresses) and sediment fluxes by intermittent, orderly coherent structures within chaotic turbulent flows; alongside the feedback imparted by entrained sediment on these coherent structures. This work

addressed the complex interactions between bed-generated coherent turbulence structures and suspended non-cohesive sediment transport in (non-breaking) wave-dominated environments and under combined wave-current flows through prototype-scale experimental observations, focusing on the structural, spatial and temporal dynamics of these motions and their role in sediment entrainment. Two scenarios were considered: (a) shoaling and breaking erosive and accretive waves in the nearshore of a sandy barrier beach (spilling and plunging breakers); and (b) collinear steady currents aligned with, and opposing the direction of wave propagation over a rippled, sandy bed.

7.2 Summary of findings

7.2.1 Wave-induced coherent turbulence structures and nearshore sediment resuspension

Measurements of flow, bed morphology and suspended sediment in the nearshore of a prototype-scale sandy barrier beach collected within the Barrier Dynamics Experiment II were analysed for irregular, erosive and accretive wave conditions. Statistical analysis of the time series of velocity fluctuations showed high anisotropy in the turbulence records and an intermittent nature of the momentum exchange both within and outside the wave benthic boundary layer. Interestingly, the transverse plane of motion was markedly anisotropic in both condition. This is commonly linked to transverse secondary flows induced by large streamwise motions often attributed to counter-rotating spanwise vortex pairs near low-speed regions of the flow. Quadrant analysis was employed to quantify the intermittency of Reynolds stresses in three planes and the fractional contribution of quadrant events to stress, and to assess whether this aforementioned behaviour applied to the tested conditions. In accretive wave conditions, a dominance of streamwise-skewed motions (Q1-Q4 events) characterised the flow, with the majority of stress contributed by counter-rotating Q2-Q4 motions in the direction of wave propagation, and hence a dominance of shore-ward directed motion. Conversely, erosive conditions were dominated by upward motions (Q1 and Q2 events) lifting and sweeping the bed sediment into transport by

the undertow current in the offshore direction. The accretive conditions, characterised by plunging breakers in the surf zone, featured more extreme exchanges of momentum when the oscillatory-component was filtered out of the turbulence record, compared with the erosive conditions (characterised by spilling and plunging breakers). Secondary spanwise flows were confirmed by spectral analyses which identified a standing transverse wave across the flume, and had a visible impact on sediment transport along the beach (across flow). This highlights a three-dimensional problem, particularly applicable to conditions where transverse flows are significant, including tidal inlets and embayments. The spectral analysis of turbulence further revealed independence from the effect of wave groups, with the turbulent energy and ensuing suspensions lying within the wave frequency range and through the inertial sub-range; with a significant influence of flow reversal and hence vortex shedding from the bedforms. Sediment excursions beyond the boundary layer could be attributed to the formation of jets between consecutive vortices shed by the bedforms. Wavelet analysis confirmed that significant suspension events emerge from mean-flow-induced, near-bed clouds of stirred sediments, and are maintained within the water column (to be transported by net currents) as long as energy is supplied by convected or locally formed vortex clusters, with some delay in temporal response. The simultaneous presence of the two scales of motions suggested a modulating effect of the larger clusters on smaller motion near the bed.

7.2.2 Space-time dynamics of coherent turbulence structures in combined wave-current flows

Similar measurements of flow, bed morphology and suspended sediment were collected under combined wave-current flows in the HR Wallingford Fast Flow Facility, with currents aligned to, and opposing the direction of propagation of non-breaking regular waves. Statistical analysis of flow properties measured at two heights within the core-flow (outside the theoretical extent of the combined wave-current benthic boundary layer) indicate different mechanisms at work within the core layer, with mean flow dominating higher up, and turbulence lower, in the aligned flow case. Fewer statistical outliers

and better correlations were evident in the wave-opposing current core flow. Wave steepening and reduction in kinetic energy were also evident in the opposing current scenario. Turbulence in wave-aligned and opposing currents exhibited vertical variations, yet similar magnitudes, of mean turbulent kinetic energy, Reynolds stresses and rates of production and dissipation; with more pronounced variance in these variables in wave-opposing currents. Temporally, however, different mechanism are highlighted. With similar bed morphologies characterised by vortex type ripples in both tested cases, more active sediment mobilisation and transport were observed in the aligned current case, with more persistent sediment clouds generated through vortex shedding at flow reversal, and episodic shifts into mass layer transport (sheet flow) at flow reversal in aligned flows, compared to defined suspensions by flow reversal followed by advection and rapid dissipation of these clouds by the current in the opposing flows. Quadrant analysis showed that in a time-averaged sense, all types of event structures are equally represented for both tested conditions. Nonetheless, the most extreme stresses, which occur for a very small fraction (~2.5%) of time were dictated by the mean current direction. The majority of stress is contributed by counter-rotating vortex pairs with violent sweeps (Q4 events) lower within the core flow and ejections (Q1 events) higher up in aligned wave-current flow (a phase-difference suggests advection higher up); while counter-rotating pairs of inward and outward interactions (Q1 and Q3, respectively) are prominent in opposing flows, again a sign of the current direction dictating the prevalent motions. The existence of counter-rotating pairs often relates to wall-attached structures associated with vortex clusters. The fact that these were measured within the core flow indicates that these coherent eddies extend beyond the boundary layer. The streamwise-vertical stress imprints of coherent eddies corresponding to vortex shedding from bedforms in the aligned wave-current case were longer lived lower within the outer flow region, and within that frequency range, did not correspond in time to those observed higher up. Similarly, their spectra lower within the flow indicated superposition of multiple scales of eddies within the energy cascade (k^{-1} inverse power law spectrum) compared to a well-defined Kolmogorov-Obukhov ($k^{-5/3}$) rate of

inertial dissipation higher up. This implies that the core flow (outside the wave boundary layer) is not uniform (purely current dominated), with its lower portion comprising eddies that are both advected and locally generated; and, higher up, only advected eddies are present. This can be considered as a transition layer between the combined wave-current region and the core flow. With such differences often attributed to eddy viscosity structure and variability in time, these findings warrant a re-assessment of existing models describing combined wave-current flows, particularly with regards to imposed zero-flux conditions commonly applied at the edge of the boundary layer. This also merits a shift towards a momentum-exchange based definition of boundary layer structure, rather than classical time-invariant formulations.

7.3 Recommendations for future work

Perhaps the major limitation of the two studies presented in this body of work is the attempt to describe a complex three-dimensional, time-varying problem through discrete measurements of turbulent fluctuations at two elevations above the bed. Within this limitation, complex analyses were applied to extract temporal and frequency properties at these two elevations, but an accurate description of the problem necessitates profile or tomographic measurements of flow at high frequency, so that it is comparable with numerical studies. If correlated measurements of the three-dimensional stresses were recorded, then tools commonly applied in numerical simulations can be employed, such as using joint-probability density functions in association with percolation theory, offers a good means of assessing the spatial and temporal behaviour of quadrant-defined vortex pair clusters, and their level of connectivity, following the work of Lozano-Duran et al. (2012) and Lozano-Durán and Jiménez (2014). The local topology of these motions can be identified from invariants of velocity gradients as presented in Buchner et al. (2016). Non-intrusive techniques which can resolve turbulence and particle interactions, such as tomographic particle image velocimetry, or computed tomography are ideal to eliminate secondary effects within the flow. From a practical perspective, several variables have not been accounted for in the work presented, including the importance of wave periods in both experiments, and the relative

magnitude of wave and currents in the combined flow experiment. Concurrent, collocated measurements of suspension and turbulence have also proved problematic, and are necessary for joint analysis of turbulence and sediment fluxes.

From a theoretical perspective, the studies presented highlight the intermittent nature of momentum exchanges and sediment suspension, posing a significant challenge to classical models such as the Rouse theory. The main limitation, remains in the formulation of eddy-viscosity and the often-assumed passive standing of sediments within the flow. Scaling mean flow and Reynolds stresses remain one of the outstanding challenges in the field, and yet, a number of unresolved issues persist, including parameterising bed roughness, and the relationship between sediment diffusivity and eddy viscosity. The feedback imparted by suspended particles, once entrained, on the turbulent structures, often termed drag reduction remains poorly understood, if not altogether contested for non-cohesive sediments. Multiphase, continuum, and mixture theory models are gaining pace in this regards, yet are inherently more complex and limited by computational processing power. For the presented studies, a numerical investigation route focusing on the hydrodynamics alone may be of use, such as a large eddy simulation of flow over a rigid bedform, to compare the observed quadrant behaviour and inferred vortex clustering for both irregular waves as well as combined wave current flows. This will ultimately be limited by the parametrisation of the sub-grid scale turbulence employed, but will shed light on the production and dissipation of turbulent kinetic energy, as well as map the spatial and temporal evolution of these structures. Furthermore, the modulating effect of small energetic structures on the frequency and amplitude larger flow structures, so far limited to studies of high-speed unidirectional flows in the literature, warrants further investigation in oscillatory and combined wave current flows.

The interactions between coherent structures and bed morphology are also poorly understood. Beyond vortex shedding, little is known about the role of spatially and temporally varying bed roughness in the generation of coherent

eddies and the roles of skin friction and form drag in defining the boundary layer structure. Experiments were recently conducted at the CT Scan Lab Facility (INRS, University of Quebec) whereby near bed profiles of turbulence (using a profiling ADV), along-flow measurements of flow velocities (using planar particle image velocimetry), and high resolution (sub-millimetre scale) measurements of bed morphology (through X-Ray computed tomography) will be analysed to shed light on the interactions between flow, coherent turbulence, bed-morphology and suspended particles under laboratory conditions. The dataset collected, based on recommendations of this study, could potentially shed light on near bed sediment-turbulence interactions, including generation, evolution and dissipation of coherent structures from bedforms tracked spatially and in time; the influence of varying bed roughness, including bed permeability; and the relationship between hydrodynamic and physical roughness.

7.4 Conclusions

The main conclusions of this study can be summarised as follows:

- Turbulence under irregular waves is characterised by intermittent momentum exchanges, with large wave-induced coherent structures within the benthic boundary layer, corresponding to the mean flow properties. These structures can be described by a 3D bursting sequence which plays a significant role in moving and maintaining sediment in suspension. The temporal variability of these events dictates the net onshore and offshore transport in erosive and accretive wave conditions in the nearshore. Periods associated with a succession of powerful turbulent events cause powerful suspension clouds across multiple frequency scales, with the bulk of suspension attributed to wave-induced fluctuations of low frequencies, which modulate smaller, rapidly decaying high-frequency turbulence extending outside the boundary layer. As larger structures persist for a considerable amount of time, suspensions near the bed are amplified before decaying as the supply of momentum ceases. Outside the boundary layer, momentum transfer

via turbulent fluctuations maintains the suspensions until their energy is depleted.

- In combined wave-current flows, the current plays a significant role in dictating the prevalence of specific turbulent motions within a bursting sequence, while the regular nature of the wave implies random motions occurring equally in all directions. The current-aligned structures contribute significantly to the stress, and display characteristics of wall-attached eddies formed by paring of counter-rotating vortices with an associated detached vortex cluster. In aligned wave-current flows, the main plane of motion (streamwise-vertical) is characterised by a local balance between turbulent production and dissipation, and hence displays the 'universal' inertial cascade of energy well outside the boundary layer. Closer to the bed, however, a superposition of eddy cascades is observed, often linked to intermittent coherent turbulent structures. From a 3D perspective, there appears to be an intermediate range between energy production and dissipation, with co-existing multi-scale events. When the current opposes the direction of wave propagation, coherent turbulence structures appear to rapidly break before they are fully formed, with a high rate of energy dissipation evident within the flow. The adverse current tends to be most effective in breaking the stress-bearing structures generated within the combined boundary layer in the dominant plane of motion as they are ejected higher in the water column, with some of the energy forced laterally as they decay. Suspended clouds through vortex shedding thus cease rapidly in opposing flows, compared to more continuous sediment transport in aligned flow.
- Collectively, these results indicate that bed-induced coherent turbulence structures play a significant role in the entrainment and transport of suspended sediment in flows typically encountered in the coastal environment, with complex feedback mechanisms between fluid, bed morphology and suspended particles. This merits a re-evaluation of coastal sediment transport models, and a shift towards a stochastic description of the problem.

List of References

Aagaard, T. and Hughes, M.G., 2010. Breaker turbulence and sediment suspension in the surf zone. Marine Geology, 271(3–4): 250-259.

Aagaard, T. and Jensen, S.G., 2013. Sediment concentration and vertical mixing under breaking waves. Marine Geology, 336(0): 146-159.

Absi, R., 2010. Concentration profiles for fine and coarse sediments suspended by waves over ripples: An analytical study with the 1-dv gradient diffusion model. Advances in Water Resources, 33(4): 411-418.

Ackers, P. and White, W.R., 1973. Sediment transport: New approach and analysis. Journal of the Hydraulics Division, American Society of Civil Engineers, 99(11): 204-254.

Adrian, R.J., 2007. Hairpin vortex organization in wall turbulence. Phys Fluids, 19(4): 41301-1- 41301-16.

Adrian, R.J., 2013. Structure of turbulent boundary layers, Coherent flow structures at earth's surface. John Wiley & Sons, Ltd, pp. 17-24.

Adrian, R.J. and Marusic, I., 2012. Coherent structures in flow over hydraulic engineering surfaces. Journal of Hydraulic Research, 50(5): 451-464.

Agrawal, Y.C. and Traykovski, P., 2001. Particles in the bottom boundary layer: Concentration and size dynamics through events. Journal of Geophysical Research: Oceans, 106(C5): 9533-9542.

Alfredsson, P.H. and Johansson, A.V., 1984. On the detection of turbulence-generating events. J Fluid Mech, 139: 325-345.

Allen, J.J., Shockling, M.A., Kunkel, G.J. and Smits, A.J., 2007. Turbulent flow in smooth and rough pipes. Philosophical Transactions of the Royal Society of London A: Mathematical, Physical and Engineering Sciences, 365(1852): 699-714.

Ames, W.F., 1965. Chapter 1 the origin of nonlinear partial differential equations. In: W.F. Ames (Editor), Mathematics in science and engineering. Elsevier, pp. 1-19.

Amir, M., Nikora, V.I. and Stewart, M.T., 2014. Pressure forces on sediment particles in turbulent open-channel flow: A laboratory study. J Fluid Mech, 757: 458-497.

Amos, C.L., Bowen, A.J., Huntley, D.A. and Lewis, C.F.M., 1988. Ripple generation under the combined influences of waves and currents on the canadian continental shelf. Cont Shelf Res, 8(10): 1129-1153.

Amos, C.L. and Collins, M.B., 1978. The combined effects of wave motion and tidal currents on the morphology of intertidal ripple marks: The wash, uk. Journal of Sedimentary Research, 48(3): 849-856.

Amos, C.L. et al., 2010. The measurement of sand transport in two inlets of venice lagoon, italy. Estuar Coast Shelf S, 87(2): 225-236.

Amoudry, L., Hsu, T.J. and Liu, P.L.F., 2005. Schmidt number and near-bed boundary condition effects on a two-phase dilute sediment transport model. Journal of Geophysical Research: Oceans, 110(C9): C09003.

Amoudry, L.O., Bell, P.S., Thorne, P.D. and Souza, A.J., 2013. Toward representing wave-induced sediment suspension over sand ripples in rans models. Journal of Geophysical Research: Oceans: n/a-n/a.

Amoudry, L.O. and Liu, P.L.F., 2009. Two-dimensional, two-phase granular sediment transport model with applications to scouring downstream of an apron. Coast Eng, 56(7): 693-702.

Amoudry, L.O. and Souza, A.J., 2011. Deterministic coastal morphological and sediment transport modelling: A review and discussion. Reviews of Geophysics, 49(2): RG2002.

Anderson Jr, J.D., 2005. Ludwig prandtl's boundary layer. Physics Today, 58(12): 42-48.

Antunes do Carmo, J.S., 2012. Turbulent boundary layer models: Theory and applications. In: H.W. Oh (Editor), Advanced Fluid Dynamics. InTech, pp. 205 - 238.

Antunes Do Carmo, J.S., Temperville, A. and Seabra-Santos, F.J., 2003. Bottom friction and time-dependent shear stress for wave-current interaction. Journal of Hydraulic Research, 41(1): 27-37.

Armanini, A. and Di Silvio, G., 1988. A one-dimensional model for the transport of a sediment mixture in non-equilibrium conditions. Journal of Hydraulic Research, 26(3): 275-292.

Baeumer, B., Benson, D.A. and Meerschaert, M.M., 2005. Advection and dispersion in time and space. Physica A: Statistical Mechanics and its Applications, 350(2–4): 245-262.

Baeumer, B. and Meerschaert, M.M., 2007. Fractional diffusion with two time scales. Physica A: Statistical Mechanics and its Applications, 373(0): 237-251.

Bagnold, R.A., 1951. The movement of a cohesionless granular bed by fluid flow over it. British Journal of Applied Physics, 2(2): 29.

Bagnold, R.A., 1954. Experiments on a gravity-free dispersion of large solid spheres in a newtonian fluid under shear. Proceedings of the Royal

Society of London. Series A. Mathematical and Physical Sciences, 225(1160): 49-63.

Bagnold, R.A., 1956. The flow of cohesionless grains in fluids. Philosophical Transactions of the Royal Society of London. Series A, Mathematical and Physical Sciences, 249(964): 235-297.

Bagnold, R.A., 1966. An approach to the sediment transport problem from general physics, Physiographic and Hydraulic Studies of Rivers. USGS Professional Paper. U.S. Government Printing Office, Washington, pp. I1-I37.

Bagnold, R.A. and Taylor, G., 1946. Motion of waves in shallow water. Interaction between waves and sand bottoms. Proceedings of the Royal Society of London. Series A. Mathematical and Physical Sciences, 187(1008): 1-18.

Balachandar, S. and Eaton, J.K., 2010. Turbulent dispersed multiphase flow. Annual Review of Fluid Mechanics, 42(1): 111-133.

Barenblatt, G.I., 1993. Scaling laws for fully developed turbulent shear flows. Part 1. Basic hypotheses and analysis. J Fluid Mech, 248: 513-520.

Barenblatt, G.I. and Monin, A.S., 1979. Similarity laws for turbulent stratified shear flows. Arch. Rational Mech. Anal., 70(4): 307-317.

Bedford, K., Wai, O., Libicki, C. and Van Evra, R., 1987. Sediment entrainment and deposition measurements in long island sound. Journal of Hydraulic Engineering, 113(10): 1325-1342.

Benson, D.A., Wheatcraft, S.W. and Meerschaert, M.M., 2000. Application of a fractional advection-dispersion equation. Water Resources Research, 36(6): 1403-1412.

Bijker, E.W., 1966. The increase of bed shear in a current due to wave motion. 10th Conference Coastal Engineering, Tokyo, p.^pp. 746 - 765.

Bird, E., 2005. Drift and swash alignments. In: M.L. Schwartz (Editor), Encyclopedia of coastal science. Springer Netherlands, Dordrecht, pp. 395-397.

Blackwelder, R.F. and Kaplan, R.E., 1976. On the wall structure of the turbulent boundary layer. J Fluid Mech, 76(01): 89-112.

Bodenschatz, E. and Eckert, M., 2011. Prandtl and the göttingen school In: P.A. Davidson, Y. Kaneda, K. Moffatt and K.R. Sreenivasan (Editors), A voyage through turbulence. Cambridge University Press, Cambridge, pp. 40-100.

Bogard, D.G. and Tiederman, W.G., 1986. Burst detection with single-point velocity measurements. J Fluid Mech, 162: 389-413.

Bolaños, R., Thorne, P.D. and Wolf, J., 2012. Comparison of measurements and models of bed stress, bedforms and suspended sediments under combined currents and waves. Coast Eng, 62(0): 19-30.

Bose, S. and Dey, S., 2013. Sediment entrainment probability and threshold of sediment suspension: Exponential-based approach. Journal of Hydraulic Engineering, 139(10): 1099-1106.

Bose, S.K. and Dey, S., 2009. Suspended load in flows on erodible bed. International Journal of Sediment Research, 24(3): 315-324.

Boussinesq, J., 1877. Essai sur la théorie des eaux courantes, Mémoires présentés par divers savants à l'Académie des Sciences XXIII, Paris, pp. 1 - 680.

Bradshaw, P., 1971. An introduction to turbulence and its measurement. The commonwealth and international library thermodynamics and fluid mechanics division. Pergamon Press, Oxford, New York,, 218 pp.

Bradshaw, P., 1994. Turbulence: The chief outstanding difficulty of our subject. Experiments in Fluids, 16(3-4): 203-216.

Bradshaw, P., 2000. A note on "critical roughness height" and "transitional roughness". Phys Fluids, 12(6): 1611-1614.

Buchner, A.-J., Adrián, L.-D., Vassili, K., Callum, A. and Julio, S., 2016. Local topology via the invariants of the velocity gradient tensor within vortex clusters and intense reynolds stress structures in turbulent channel flow. Journal of Physics: Conference Series, 708(1): 012005.

Buffington, J., 1999. The legend of a. F. Shields. Journal of Hydraulic Engineering, 125(4): 376-387.

Buffington, J., 2000. Closure to "the legend of a. F. Shields" by john m. Buffington. Journal of Hydraulic Engineering, 126(9): 718-723.

Buscombe, D., 2012. Matscat version 1: Matlab toolbox for the aquascat 1000 acoustic backscatter sensor., Plymouth University.

Buscombe, D. and Conley, D., 2012. Schmidt number of sand suspensions under oscillating grid turbulence. 2012.

Cabrera, R., Deines, K., Brumley, B. and Terray, E., 1987. Development of a practical coherent acoustic doppler current profiler. OCEANS '87, p.^pp. 93-97.

Camenen, B. and Larson, M., 2008. A general formula for noncohesive suspended sediment transport. Journal of Coastal Research: 615-627.

Cantwell, B.J., 1981. Organized motion in turbulent flow. Annual Review of Fluid Mechanics, 13(1): 457-515.

Cao, Z., 1997. Turbulent bursting-based sediment entrainment function. Journal of Hydraulic Engineering, 123(3): 233-236.

Carling, P.A., Kelsey, A. and Glaister, M.S., 1992. Effect of bed roughness, particle shape and orientation on initial motion criteria. In: P. Billi, R.D. Hey, C.R. Thorne and P. Tacconi (Editors), Dynamics of gravel-bed rivers. Wiley, New York, pp. 24-39.

Carstensen, S., Sumer, B.M. and Fredsøe, J., 2010. Coherent structures in wave boundary layers. Part 1. Oscillatory motion. J Fluid Mech, 646: 169-206.

Carstensen, S., Sumer, B.M. and Fredsøe, J., 2012. A note on turbulent spots over a rough bed in wave boundary layers. Physics of Fluids (1994-present), 24(11): -.

Casey, H., 1935. Ueber geschiebebewegung. Mitteilung der Preuß. Versucjhsanstalt f. Wasserbau u. Schiffbay (VWS) Heft 19.

Castro-Orgaz, O., Giráldez, J.V., Mateos, L. and Dey, S., 2012. Is the von kármán constant affected by sediment suspension? Journal of Geophysical Research: Earth Surface, 117(F4): F04002.

Cebeci, T. and Smith, A.M.O., 1974. Analysis of turbulent boundary layers. Academic Press, New York ; London.

Cellino, M. and Lemmin, U., 2004. Influence of coherent flow structures on the dynamics of suspended sediment transport in open-channel flow. Journal of Hydraulic Engineering, 130(11): 1077-1088.

Charru, F. and Hinche, E.J., 2006. Ripple formation on a particle bed sheared by a viscous liquid. Part 1. Steady flow. J Fluid Mech, 550: 111-121.

Charru, F. and Mouilleron-Arnauld, H., 2002. Instability of a bed of particles sheared by a viscous flow. J Fluid Mech, 452: 303-323.

Chauchat, J. and Guillou, S., 2008. On turbulence closures for two-phase sediment-laden flow models. Journal of Geophysical Research: Oceans, 113(C11): C11017.

Chauchat, J., Guillou, S., Pham Van Bang, D. and Dan Nguyen, K., 2013. Modelling sedimentation–consolidation in the framework of a one-dimensional two-phase flow model. Journal of Hydraulic Research, 51(3): 293-305.

Chen, D., Sun, H. and Zhang, Y., 2013. Fractional dispersion equation for sediment suspension. Journal of Hydrology, 491(0): 13-22.

Cheng, C., Song, Z.-y., Wang, Y.-g. and Zhang, J.-s., 2013. Parameterized expressions for an improved rouse equation. International Journal of Sediment Research, 28(4): 523-534.

Choi, W.C. and Guezennec, Y.G., 1990. On the asymmetry of structures in turbulent boundary layers. Physics of Fluids A: Fluid Dynamics (1989-1993), 2(4): 628-630.

Chomaz, J.-M., 2005. Global instabilities in spatially developing flows: Non-normality and nonlinearity. Annual Review of Fluid Mechanics, 37(1): 357-392.

Chow, V.T., 1959. Open-channel hydraulics. The Blackburn Press, New Jersey, 680 pp.

Christensen, B.A., 1965. Discussion of "erosion and deposition of cohesive soils," by e. Partheniades. Journal of Hydraulic Division ASCE, 95(5): 301-208.

Christensen, K.T. and Adrian, R.J., 2001. Statistical evidence of hairpin vortex packets in wall turbulence. J Fluid Mech, 431: 433-443.

Christoffersen, J.B. and Jonsson, I.G., 1985. Bed friction and dissipation in a combined current and wave motion. Ocean Eng, 12(5): 387-423.

Chu, V., Wu, J. and Khayat, R., 1991. Stability of transverse shear flows in shallow open channels. Journal of Hydraulic Engineering, 117(10): 1370-1388.

Clauser, F.H., 1954. Turbulent boundary layers in adverse pressure gradients. Journal of the Aeronautical Sciences, 21(2): 91-108.

Clifton, H.E. and Dingler, J.R., 1984. Wave-formed structures and paleoenvironmental reconstruction. In: B. Greenwood and R.A. Davis (Editors), Developments in sedimentology. Elsevier, pp. 165-198.

Cloutier, D., LeCouturier, M., Amos, C. and Hill, P., 2006. The effects of suspended sediment concentration on turbulence in an annular flume. Aquat Ecol, 40(4): 555-565.

Coleman, G.N. and Sandberg, R.D., 2010. A primer on direct numerical simulation of turbulence - methods, procedures and guidelines. AFM 09/01a, Southampton, UK.

Coleman, S.E. and Nikora, V.I., 2008. A unifying framework for particle entrainment. Water Resources Research, 44(4): n/a-n/a.

Coles, D., 1956. The law of the wake in the turbulent boundary layer. J Fluid Mech, 1(02): 191-226.

Combest, D.P., Ramachandran, P.A. and Dudukovic, M.P., 2011. On the gradient diffusion hypothesis and passive scalar transport in turbulent flows. Industrial & Engineering Chemistry Research, 50(15): 8817-8823.

Corino, E.R. and Brodkey, R.S., 1969. A visual investigation of the wall region in turbulent flow. J Fluid Mech, 37(01): 1-30.

Cowell, P.J. et al., 2003. The coastal-tract (part 1): A conceptual approach to aggregated modeling of low-order coastal change. Journal of Coastal Research, 19(4): 812-827.

Crowe, C.T., Troutt, T.R. and Chung, J.N., 1996. Numerical models for two-phase turbulent flows. Annual Review of Fluid Mechanics, 28(1): 11-43.

Daubechies, I., 1990. The wavelet transform, time-frequency localization and signal analysis. Information Theory, IEEE Transactions on, 36(5): 961-1005.

Davidson, P.A., 2004. Turbulence : An introduction for scientists and engineers. Oxford University Press, Oxford, 657 pp.

Davidson, P.A., Kaneda, Y., Moffatt, K. and Sreenivasan, K.R., 2011. A voyage through turbulence. Cambridge University Press, Cambridge.

Davidson, P.A., Kaneda, Y. and Sreenivasan, K.R., 2013. Preface. In: P.A. Davidson, Y. Kaneda and K.R. Sreenivasan (Editors), Ten chapters in turbulence. Cambridge University Press, Cambridge, pp. ix-x.

Davies, A.G., 1986. A model of oscillatory rough turbulent boundary layer flow. Estuarine, Coastal and Shelf Science, 23(3): 353-374.

Davies, A.G., Ribberink, J.S., Temperville, A. and Zyserman, J.A., 1997. Comparisons between sediment transport models and observations made in wave and current flows above plane beds. Coast Eng, 31(1-4): 163-198.

Davies, A.G., Soulsby, R.L. and King, H.L., 1988. A numerical model of the combined wave and current bottom boundary layer. Journal of Geophysical Research: Oceans, 93(C1): 491-508.

Davies, A.G., van Rijn, L.C., Damgaard, J.S., van de Graaff, J. and Ribberink, J.S., 2002. Intercomparison of research and practical sand transport models. Coast Eng, 46(1): 1-23.

De Lemos, M.J.S., 2012. Turbulence in porous media, modelling and applications. Elsevier Sciecne Limited, London.

De Stefano, G. and Vasilyev, O.V., 2012. A fully adaptive wavelet-based approach to homogeneous turbulence simulation. J Fluid Mech, 695: 149-172.

Deleuze, J., Audiffren, N. and Elena, M., 1994. Quadrant analysis in a heated-wall supersonic boundary layer. Physics of Fluids (1994-present), 6(12): 4031-4041.

Dennis, D.J.C. and Nickels, T.B., 2008. On the limitations of taylor's hypothesis in constructing long structures in a turbulent boundary layer. J Fluid Mech, 614: 197-206.

Dey, S., 2011. Entrainment threshold of loose boundary streams. In: P. Rowiński (Editor), Experimental methods in hydraulic research. Geoplanet: Earth and planetary science. Springer-Verlag, Berlin Heidelberg, pp. 29 - 48.

Dey, S., Das, R., Gaudio, R. and Bose, S., 2012. Turbulence in mobile-bed streams. Acta Geophys., 60(6): 1547-1588.

Dey, S. and Papanicolaou, A., 2008. Sediment threshold under stream flow: A state-of-the-art review. KSCE Journal of Civil Engineering, 12(1): 45-60.

Dhawan, S. and Narasimha, R., 1958. Some properties of boundary layer flow during the transition from laminar to turbulent motion. J Fluid Mech, 3(04): 418-436.

Diplas, P. et al., 2008. The role of impulse on the initiation of particle movement under turbulent flow conditions. Science, 322(5902): 717-720.

Doucette, J.S. and O'Donoghue, T., 2006. Response of sand ripples to change in oscillatory flow. Sedimentology, 53(3): 581-596.

Downing, A., Thorne, P.D. and Vincent, C.E., 1995. Backscattering from a suspension in the near field of a piston transducer. The Journal of the Acoustical Society of America, 97(3): 1614-1620.

Drake, D.E. and Cacchione, D.A., 1989. Estimates of the suspended sediment reference concentration (ca) and resuspension coefficient (γ0) from near-bottom observations on the california shelf. Cont Shelf Res, 9(1): 51-64.

du Boys, P., 1879. Le rhône et les rivières à lit affouillable. Etude du régime du rhône et de l'action exercée par les eaux sur un lit à fond de graviers infiniment affouillable. Annales des Ponts et Chaussées, 18(5): 141-195.

Dumas, S., Arnott, R.W.C. and Southard, J.B., 2005. Experiments on oscillatory-flow and combined-flow bed forms: Implications for interpreting parts of the shallow-marine sedimentary record. Journal of Sedimentary Research, 75(3): 501-513.

Duy, N.T. and Shibayama, T., 1997. A convection-diffusion model for suspended sediment in the surf zone. Journal of Geophysical Research: Oceans, 102(C10): 23169-23186.

Dyer, K.R., 1980. Velocity profiles over a rippled bed and the threshold of movement of sand. Estuarine and Coastal Marine Science, 10(2): 181-199.

Dyer, K.R., 1986. Coastal and estuarine sediment dynamics. John Wiley and Sons

342 pp.

Dyer, K.R. and Soulsby, R.L., 1988. Sand transport on the continental shelf. Annual Review of Fluid Mechanics, 20(1): 295-324.

Einstein, H.A., 1936. Der geschiebetrieb als wahrscheinlichkeitsproblem [in english: Bedload as a probability problem], Swiss Federal Institute of Technology, Zurich, 112 pp.

Einstein, H.A., 1950. The bed-load function for sediment transportation in open channel flows, US Department of Agriculture, Soil Conservation Service, Washington DC.

Einstein, H.A. and El-Samni, E.-S.A., 1949. Hydrodynamic forces on a rough wall. Reviews of Modern Physics, 21(3): 520-524.

El Khoury, G.K., Pettersen, B., Andersson, H.I. and Barri, M., 2010. Asymmetries in an obstructed turbulent channel flow. Physics of Fluids (1994-present), 22(9): -.

Elgar, S., Raubenheimer, B. and Guza, R.T., 2001. Current meter performance in the surf zone. Journal of Atmospheric and Oceanic Technology, 18(10): 1735-1746.

Elgar, S., Raubenheimer, B. and Guza, R.T., 2005. Quality control of acoustic doppler velocimeter data in the surfzone. Measurement Science and Technology, 16(10): 1889.

Elghobashi, S., 1991. Particle-laden turbulent flows: Direct simulation and closure models. Applied Scientific Research, 48(3-4): 301-314.

Engelund, F., 1965. A criterion for the occurence of suspended load. La Houille Blanche, 8: 7.

Engelund, F. and Hansen, E., 1967. A monograph on sediment transport in alluvial streams, Technical University of Denmark, Copenhagen.

Evans, A.W. and Hardisty, J., 1989. An experimental investigation of the effect of bedslope and grain pivot angle on the threshold of marine gravel transport. Marine Geology, 89(1): 163-167.

Exner, F.M., 1920. Zur physik der dünen. Akademie der Wissenschaften in Wien Mathematisch-naturwissenschaftliche Klasse, 129(2a): 929–952.

Exner, F.M., 1925. Über die wechselwirkung zwischen wasser und geschiebe in flüssen. Akademie der Wissenschaften in Wien Mathematisch-naturwissenschaftliche Klasse, 134(2a): 356-361.

Falco, R.E., 1977. Coherent motions in the outer region of turbulent boundary layers. Phys Fluids, 20(10): S124-S132.

Farge, M., 1992. Wavelet transforms and their applications to turbulence. Annual Review of Fluid Mechanics, 24(1): 395-458.

Farge, M., Kevlahan, N., Perrier, V. and Goirand, E., 1996. Wavelets and turbulence. Proceedings of the IEEE, 84(4): 639-669.

Farge, M., Pellegrino, G. and Schneider, K., 2001. Coherent vortex extraction in 3d turbulent flows using orthogonal wavelets. Phys Rev Lett, 87(5): 054501.

Farge, M. and Schneider, K., 2001. Coherent vortex simulation (cvs), a semi-deterministic turbulence model using wavelets. Flow Turbulence Combust, 66(4): 393-426.

Farge, M., Schneider, K. and Kevlahan, N., 1999. Non-gaussianity and coherent vortex simulation for two-dimensional turbulence using an adaptive orthogonal wavelet basis. Physics of Fluids (1994-present), 11(8): 2187-2201.

Farge, M., Schneider, K., Pellegrino, G., Wray, A.A. and Rogallo, R.S., 2003. Coherent vortex extraction in three-dimensional homogeneous turbulence: Comparison between cvs-wavelet and pod-fourier decompositions. Physics of Fluids (1994-present), 15(10): 2886-2896.

Feddersen, F., 2010. Quality controlling surf zone acoustic doppler velocimeter observations to estimate the turbulent dissipation rate. Journal of Atmospheric and Oceanic Technology, 27(12): 2039-2055.

Feddersen, F., 2012a. Observations of the surf-zone turbulent dissipation rate. Journal of Physical Oceanography, 42(3): 386-399.

Feddersen, F., 2012b. Scaling surf zone turbulence. Geophys Res Lett, 39(18): L18613.

Feddersen, F. and Williams, A.J., 2007. Direct estimation of the reynolds stress vertical structure in the nearshore. Journal of Atmospheric and Oceanic Technology, 24(1): 102-116.

Fernandez Luque, R. and Van Beek, R., 1976. Erosion and transport of bed-load sediment. Journal of Hydraulic Research, 14(2): 127-144.

Fernholz, H.H. and Finleyt, P.J., 1996. The incompressible zero-pressure-gradient turbulent boundary layer: An assessment of the data. Prog. Aerosp. Sci., 32(4): 245-311.

Fiedler, H.E., 1988. Coherent structures in turbulent flows. Prog. Aerosp. Sci., 25(3): 231-269269.

Fisher, F.H. and Simmons, V.P., 1977. Sound absorption in sea water. The Journal of the Acoustical Society of America, 62(3): 558-564.

Fishler, L.S. and Brodkey, R.S., 1991. Transition, turbulence and oscillating flow in a pipe a visual study. Experiments in Fluids, 11(6): 388-398.

Folk, R.L. and Ward, W.C., 1957. Brazos river bar: A study in the significance of grain size parameters. Journal of Sedimentary Petrology, 27(1): 3-26.

Foufoula-Georgiou, E. and Kumar, P., 1994. Wavelets in geophysics. Academic Press, San Diego, CA, 373p. pp.

Franca, M.J. and Lemmin, U., 2015. Detection and reconstruction of large-scale coherent flow structures in gravel-bed rivers. Earth Surface Processes and Landforms, 40(1): 93-104.

Fransson, J.H.M., Brandt, L., Talamelli, A. and Cossu, C., 2004. Experimental and theoretical investigation of the nonmodal growth of steady streaks in a flat plate boundary layer. Phys Fluids, 16(10): 3627-3638.

Fredsøe, J., 1984. Turbulent boundary layer in wave-current motion. Journal of Hydraulic Engineering, 110(8): 1103-1120.

Fredsøe, J., Andersen, K.H. and Mutlu Sumer, B., 1999. Wave plus current over a ripple-covered bed. Coast Eng, 38(4): 177-221.

Fredsøe, J. and Deigaard, R., 1992. Mechanics of coastal sediment transport. Advanced series on ocean engineering ;. World Scientific, Singapore, xviii, 369 p. pp.

Frisch, U., 1995. Turbulence : The legacy of a.N. Kolmogorov. Cambridge University Press, Cambridge, xiii, 296 p. pp.

Frostick, L.E., McLelland, S.J. and Mercer, T.G., 2011. Users guide to physical modelling and experimentation: Experience of the hydralab network. Iahr design manual. CRC Press / Balkema Leiden, The Netherlands.

Gad-el-Hak, M. and Bandyopadhyay, P.R., 1994. Reynolds number effects in wall-bounded turbulent flows. Applied Mechanics Reviews, 47(8): 307-365.

Ganapathisubramani, B., Hutchins, N., Hambleton, W.T., Longmire, E.K. and Marusic, I., 2005. Investigation of large-scale coherence in a turbulent boundary layer using two-point correlations. J Fluid Mech, 524: 57-80.

Ganapathisubramani, B., Hutchins, N., Monty, J.P., Chung, D. and Marusic, I., 2012. Amplitude and frequency modulation in wall turbulence. J Fluid Mech, 712: 61-91.

Ganti, V., Singh, A., Passalacqua, P. and Foufoula-Georgiou, E., 2009. Subordinated brownian motion model for sediment transport. Phys Rev E, 80(1).

Ganti, V., Straub, K.M., Foufoula-Georgiou, E. and Paola, C., 2011. Space-time dynamics of depositional systems: Experimental evidence and theoretical modeling of heavy-tailed statistics. Journal of Geophysical Research: Earth Surface, 116(F2): F02011.

Gao, R. and Yan, R., 2011. From fourier transform to wavelet transform: A historical perspective, Wavelets. Springer US, pp. 17-32.

Garcia, M. and Parker, G., 1991. Entrainment of bed sediment into suspension. Journal of Hydraulic Engineering, 117(4): 414-435.

Garrett, C.J.R., 1970. On cross-waves. J Fluid Mech, 41(04): 837-849.

Gatski, T.B. and Rumsey, C.L., 2002. Linear and nonlinear eddy viscosity models. In: B.E.S. Launder, Neil D (Editor), Closure strategies for turbulent and transitional flows. Cambridge University Press, West Nyack, NY, USA, pp. 9 - 46.

Gebhardt, T. and Grossmann, S., 1994. Chaos transition despite linear stability. Phys Rev E, 50(5): 3705-3711.

George, C.B. and Sleath, J.F.A., 1979. Measurements of combined oscillatory and steady flow over a rough bed. Journal of Hydraulic Research, 17(4): 303-313.

Gerbi, G.P., Trowbridge, J.H., Terray, E.A., Plueddemann, A.J. and Kukulka, T., 2009. Observations of turbulence in the ocean surface boundary layer: Energetics and transport. Journal of Physical Oceanography, 39(5): 1077-1096.

Gheisi, A., Alavimoghaddam, M. and Dadrasmoghaddam, A., 2006. Markovian–octant analysis based stable turbulent shear stresses in near-bed bursting phenomena of vortex settling chamber. Environmental Fluid Mechanics, 6(6): 549-572.

Glover, D.M., Jenkins, W.J. and Doney, S.C., 2011. Modeling methods for marine science. Cambridge University Press ;, Cambridge, xv, 571 p. pp.

Goldenfeld, N. and Kadanoff, L.P., 1999. Simple lessons from complexity. Science, 284(5411): 87-89.

Gordon, C.M., 1975. Sediment entrainment and suspension in a turbulent tidal flow. Marine Geology, 18(1): M57-M64.

Goring, D. and Nikora, V., 2002. Despiking acoustic doppler velocimeter data. Journal of Hydraulic Engineering, 128(1): 117-126.

Goring, D. and Nikora, V., 2003. Closure to "depiking acoustic doppler velocimeter data" by derek g. Goring and vladimir i. Nikora. Journal of Hydraulic Engineering, 129(6): 487-488.

Goupillaud, P., Grossmann, A. and Morlet, J., 1984. Cycle-octave and related transforms in seismic signal analysis. Geoexploration, 23(1): 85-102.

Grant, H.L., Stewart, R.W. and Moilliet, A., 1962. Turbulence spectra from a tidal channel. J Fluid Mech, 12(02): 241-268.

Grant, W.D., III, A.J.W. and Glenn, S.M., 1984. Bottom stress estimates and their prediction on the northern california continental shelf during code-1: The importance of wave-current interaction. Journal of Physical Oceanography, 14(3): 506-527.

Grant, W.D. and Madsen, O.S., 1979. Combined wave and current interaction with a rough bottom. Journal of Geophysical Research: Oceans, 84(C4): 1797-1808.

Grant, W.D. and Madsen, O.S., 1986. The continental-shelf bottom boundary layer. Annual Review of Fluid Mechanics, 18(1): 265-305.

Grass, A.J., 1970. Initial instability of fine bed sand. Journal of the Hydraulics Division, American Society of Civil Engineers, 96(3): 619-632.

Grass, A.J., 1971. Structural features of turbulent flow over smooth and rough boundaries. J Fluid Mech, 50(Nov29): 233-&.

Grass, A.J., Stuart, R.J. and Mansour-Tehrani, M., 1991. Vortical structures and coherent motion in turbulent flow over smooth and rough boundaries, 336, 35-65 pp.

Grasso, F. and Ruessink, B.G., 2012. Turbulent viscosity in natural surf zones. Geophys Res Lett, 39(23): L23603.

Green, M.O. and Black, K.P., 1999. Suspended-sediment reference concentration under waves: Field observations and critical analysis of two predictive models. Coast Eng, 38(3): 115-141.

Greimann, B.P., Muste, M. and Holly, F.M., 1999. Two-phase formulation of suspended sediment transport. Journal of Hydraulic Research, 37(4): 479-500.

Grigoriadis, D.G.E., Balaras, E. and Dimas, A.A., 2013. Coherent structures in oscillating turbulent boundary layers over a fixed rippled bed. Flow Turbulence Combust, 91(3): 565-585.

Grinsted, A., Moore, J.C. and Jevrejeva, S., 2004. Application of the cross wavelet transform and wavelet coherence to geophysical time series. Nonlin. Processes Geophys., 11(5/6): 561-566.

Grossmann, A. and Morlet, J., 1984. Decomposition of hardy functions into square integrable wavelets of constant shape. Siam J Math Anal, 15(4): 723-736.

Grossmann, S., 2000. The onset of shear flow turbulence. Reviews of Modern Physics, 72(2): 603-618.

Gunzburger, M., Lee, E., Saka, Y., Trenchea, C. and Wang, X., 2010. Analysis of nonlinear spectral eddy-viscosity models of turbulence. J. Sci. Comput., 45(1-3): 294-332.

Gust, G., 1976. Observations on turbulent-drag reduction in a dilute suspension of clay in sea-water. J Fluid Mech, 75(01): 29-47.

Gust, G., 1984. Velocity profiles with suspended sediments. Journal of Hydraulic Research, 22(4): 263-289.

Gust, G. and Walger, E., 1976. The influence of suspended cohesive sediments on boundary-layer structure and erosive activity of turbulent seawater flow. Marine Geology, 22(3): 189-206.

Hammond, T.M. and Collins, M.B., 1979. On the threshold of transport of sand-sized sediment under the combined influence of unidirectional and oscillatory flow. Sedimentology, 26(6): 795-812.

Hanjalić, K., 1994. Advanced turbulence closure models: A view of current status and future prospects. Int. J. Heat Fluid Flow, 15(3): 178-203.

Hansen, E., Fredsøe, J. and Deigaard, R., 1994. Distribution of suspended sediment over wave-generated ripples. Journal of Waterway, Port, Coastal, and Ocean Engineering, 120(1): 37-55.

Hardy, R.J., Best, J.L., Lane, S.N. and Carbonneau, P.E., 2010. Coherent flow structures in a depth-limited flow over a gravel surface: The influence of surface roughness. Journal of Geophysical Research: Earth Surface, 115(F3): F03006.

Hardy, R.J., Best, J.L., Parsons, D.R. and Marjoribanks, T.I., 2016. On the evolution and form of coherent flow structures over a gravel bed: Insights from whole flow field visualization and measurement. Journal of Geophysical Research: Earth Surface: n/a-n/a.

Hare, J., Hay, A.E., Zedel, L. and Cheel, R., 2014. Observations of the space-time structure of flow, turbulence, and stress over orbital-scale ripples. Journal of Geophysical Research: Oceans: n/a-n/a.

Hassan, W.N.M. and Ribberink, J.S., 2010. Modelling of sand transport under wave-generated sheet flows with a rans diffusion model. Coast Eng, 57(1): 19-29.

Hasselmann, K. et al., 1973. Measurements of wind-wave growth and swell decay during the joint north sea wave project (jonswap), Deutches Hydrographisches Institut, Hamburg.

Heathershaw, A., 1974. "Bursting" phenomena in the sea. Nature, 248(5447): 394 - 395.

Heathershaw, A.D., 1979. The turbulent structure of the bottom boundary layer in a tidal current. Geophysical Journal of the Royal Astronomical Society, 58(2): 395-430.

Heathershaw, A.D., 1981. Comparisons of measured and predicted sediment transport rates in tidal currents. In: C.A. Nittrouer (Editor), Developments in sedimentology. Elsevier, pp. 75-104.

Higgins, C.W. et al., 2012. The effect of scale on the applicability of taylor's frozen turbulence hypothesis in the atmospheric boundary layer. Boundary-Layer Meteorol, 143(2): 379-391.

Hinze, J.O., 1959. Turbulence : An introduction to its mechanism and theory. Mcgraw-hill series in mechanical engineering. McGraw-Hill, New York ; London, 586 pp.

Holmedal, L.E., Johari, J. and Myrhaug, D., 2013. The seabed boundary layer beneath waves opposing and following a current. Cont Shelf Res, 65: 27-44.

Holmedal, L.E., Myrhaug, D. and Rue, H., 2003. The sea bed boundary layer under random waves plus current. Cont Shelf Res, 23(7): 717-750.

Holmes, P., Lumley, J.L. and Berkooz, G., 1996. Turbulence, coherent structures, dynamical systems and symmetry. Cambridge monographs on mechanics. Cambridge University Press, Cambridge, xviii, 420 p. pp.

Hopf, L., 1923. Die messung der hydraulischen rauhigkeit. ZAMM - Journal of Applied Mathematics and Mechanics / Zeitschrift für Angewandte Mathematik und Mechanik, 3(5): 329-339.

Hoyas, S. and Jiménez, J., 2008. Reynolds number effects on the reynolds-stress budgets in turbulent channels. Phys Fluids, 20(10): 101511.

Huang, S.-h., Sun, Z.-l., Xu, D. and Xia, S.-s., 2008. Vertical distribution of sediment concentration. J. Zhejiang Univ. Sci. A, 9(11): 1560-1566.

Huang, Z. and Mei, C.C., 2003. Effects of surface waves on a turbulent current over a smooth or rough seabed. J Fluid Mech, 497: 253-287.

Hudgins, L., Friehe, C.A. and Mayer, M.E., 1993. Wavelet transforms and atmopsheric turbulence. Phys Rev Lett, 71(20): 3279-3282.

Hughes, S.A., 1993. Physical models and laboratory techniques in coastal engineering. Advanced series on ocean engineering, 7. World Scientific, 588 pp.

Hunt, J.C.R. et al., 2010. Thin shear layers - the key to turbulence structure? J. Hydro-environ. Res., 4(2): 75-82.

Hunt, J.N., 1954. The turbulent transport of suspended sediment in open channels. Proceedings of the Royal Society of London. Series A. Mathematical and Physical Sciences, 224(1158): 322-335.

Hunt, J.N., 1979. Direct solution of wave dispersion equation. Journal of Waterway Ports Coastal and Ocean Engineering, Engineering Division ASCE, 105(WW4): 457-459.

Hussain, A., 1986. Coherent structures and turbulence. J Fluid Mech, 173: 303-356.

Hussain, A.K.M.F., 1983. Coherent structures—reality and myth. Physics of Fluids (1958-1988), 26(10): 2816-2850.

Hutchins, N. and Marusic, I., 2007. Large-scale influences in near-wall turbulence. Philos T R Soc A, 365(1852): 647-664.

Hutchins, N., Monty, J.P., Ganapathisubramani, B., NG, H.C.H. and Marusic, I., 2011. Three-dimensional conditional structure of a high-reynolds-number turbulent boundary layer. J Fluid Mech, 673: 255-285.

Hutchins, N., Nickels, T.B., Marusic, I. and Chong, M.S., 2009. Hot-wire spatial resolution issues in wall-bounded turbulence. J Fluid Mech, 635: 103-136.

Huyng-Thanh, S. and Temperville, A., 1990. A numerical model of the rough boundary layer in combined wave and current interaction Coastal Engineering Proceedings(22).

Inman, D.L. and Bowen, A.J., 1962. Flume experiments on sand transport by waves and currents. Coastal Engineering Proceedings, 1(8): 137-150.

Jackson, P.S., 1981. On the displacement height in the logarithmic velocity profile. J Fluid Mech, 111: 15-25.

Jackson, R.G., 1976. Sedimentological and fluid-dynamic implications of the turbulent bursting phenomenon in geophysical flows. J Fluid Mech, 77(03): 531-560.

Jeong, J., Hussain, F., Schoppa, W. and Kim, J., 1997. Coherent structures near the wall in a turbulent channel flow. J Fluid Mech, 332: 185-214.

Ji, C., Munjiza, A., Avital, E., Ma, J. and Williams, J.J.R., 2013. Direct numerical simulation of sediment entrainment in turbulent channel flow. Phys Fluids, 25(5): 056601-20.

Jimenez, J., 2012. Cascades in wall-bounded turbulence. In: S.H. Davis and P. Moin (Editors), Annu rev fluid mech. Annual review of fluid mechanics. Annual Reviews, Palo Alto, pp. 27-45.

Jiménez, J., 2004. Turbulent flows over rough walls. Annual Review of Fluid Mechanics, 36(1): 173-196.

Jiménez, J., 2013. Near-wall turbulence. Physics of Fluids (1994-present), 25(10): -.

Jimenez, J. and Kawahara, G., 2013. Dynamics of wall-bounded turbulence. In: P.A. Davidson, Y. Kaneda and K.R. Sreenivasan (Editors), Ten chapters in turbulence. Cambridge University Press, Cambridge, pp. 221-268.

Jonsson, I.G., 1966a. The friction factor for a current superimposed by waves, Technical University of Denmark.

Jonsson, I.G., 1966b. Wave boundary layers and friction factors. Coastal Engineering Proceedings(10).

Justesen, P., 1988. Turbulent wave boundary layers, Institute of hydrodynamics and hydraulic engineering, Lyngby.

Kajuira, K., 1968. A model of the bottom boundary layer in water waves. Bulletin of the Earthquake Research Institute, 46: 75 - 123.

Kalinske, A.A., 1947. Movement of sediment as bed load in rivers. Eos, Transactions American Geophysical Union, 28(4): 615-620.

Kamphuis, J.W., 1975. Friction factor under oscillatory waves. Journal of the Waterways Harbors and Coastal Engineering Division, 101: 135-145.

Kaneda, Y. and Morishita, K., 2013. Small-scale statistics and structure of turbulence - in the light of high resolution direct numerical simulation. In: P.A. Davidson, Y. Kaneda and K.R. Sreenivasan (Editors), Ten chapters in turbulence. Cambridge University Press, Cambridge, pp. 1 - 42.

Kawanisi, K. and Yokosi, S., 1993. Measurements of turbulence and suspended sediment in tidal river. Journal of Hydraulic Engineering, 119(6): 704-724.

Kawanisi, K. and Yokosi, S., 1997. Characteristics of suspended sediment and turbulence in a tidal boundary layer. Cont Shelf Res, 17(8): 859-875.

Kellay, H., 2011. Turbulence: Thick puddle made thin. Nat. Phys., 7(4): 279-280.

Kemp, P.H. and Simons, R.R., 1982. The interaction between waves and a turbulent current: Waves propagating with the current. J Fluid Mech, 116: 227-250.

Kemp, P.H. and Simons, R.R., 1983. The interaction of waves and a turbulent current: Waves propagating against the current. J Fluid Mech, 130: 73-89.

Keylock, C.J., 2007. The visualization of turbulence data using a wavelet-based method. Earth Surface Processes and Landforms, 32(4): 637-647.

Keylock, C.J., 2008. A criterion for delimiting active periods within turbulent flows. Geophys Res Lett, 35(11): L11804.

Keylock, C.J., Lane, S.N. and Richards, K.S., 2014. Quadrant/octant sequencing and the role of coherent structures in bed load sediment entrainment. Journal of Geophysical Research: Earth Surface, 119(2): 2012JF002698.

Khujadze, G., Nguyen van yen, R., Schneider, K., Oberlack, M. and Farge, M., 2011. Coherent vorticity extraction in turbulent boundary layers using orthogonal wavelets. Journal of Physics: Conference Series, 318(2): 022011.

Kim, H.T., Kline, S.J. and Reynolds, W.C., 1971. Production of turbulence near a smooth wall in a turbulent boundary layer. J Fluid Mech, 50(Nov15): 133-&.

Kim, J., Moin, P. and Moser, R., 1987. Turbulence statistics in fully developed channel flow at low reynolds number. J Fluid Mech, 177: 133-166.

Kline, S.J., Reynolds, W.C., Schraub, F.A. and Runstadler, P.W., 1967. The structure of turbulent boundary layers. J Fluid Mech, 30(04): 741.

Kolmogorov, A.N., 1941a. Dissipation of energy in the locally isotropic turbulence. Doklady Akademii Nauk USSR, 32(16-18).

Kolmogorov, A.N., 1941b. The local structure of turbulence in incompressible viscous fluid for very large reynolds numbers. Doklady Akademii Nauk USSR, 30: 9 -13.

Kolmogorov, A.N., 1991a. Dissipation of energy in the locally isotropic turbulence. Proceedings of the Royal Society A: Mathematical, Physical and Engineering Science, 434(1890): 15-17.

Kolmogorov, A.N., 1991b. The local structure of turbulence in incompressible viscous fluid for very large reynolds numbers. Proceedings of the Royal Society A: Mathematical, Physical and Engineering Sciences, 434(1890): 9-13.

Komar, P.D., 1976. Beach processes and sedimentation. Prentice Hall, 429 pp.

Komar, P.D. and Clemens, K.E., 1986. The relationship between a grain's settling velocity and threshold of motion under unidirectional currents. Journal of Sedimentary Petrology, 56(2): 258-266.

Komar, P.D. and Miller, M.C., 1973. The threshold of sediment movement under oscillatory water waves. Journal of Sedimentary Petrology, 43: 1101-1110.

Komar, P.D. and Miller, M.C., 1975. The initiation of oscillatory ripple marks and the development of plane-bed at high shear stresses under waves. Journal of Sedimentary Research, 45(3): 697-703.

Komar, P.D., Neudeck, R.H. and Kulm, L.D., 1972. Observations and significance of deep-water oscillation ripple marks on the oregon continental shelf. In: D.J.P. Swift, D.B. Duane and O.H. Pilkey (Editors), Shelf sediment transport. Dowden, Hutchinson and Ross, Stroudsbourg, Pa, pp. 601 - 619.

Korinna, T.A. and Bruno, E., 2012. Directed percolation model for turbulence transition in shear flows. Fluid Dynamics Research, 44(3): 031201.

Kormylo, J. and Jain, V., 1974. Two-pass recursive digital filter with zero phase shift. IEEE Transactions on Acoustics, Speech, and Signal Processing, 22(5): 384-387.

Kramer, H., 1935. Sand mixtures and sand movement in fluvial levels. Transactions of the American Society of Civil Engineers, 100: 798-838.

Kumar, P. and Foufoula-Georgiou, E., 1997. Wavelet analysis for geophysical applications. Reviews of Geophysics, 35(4): 385-412.

Kundu, P.K., Cohen, I.M., Ayyaswamy, P.S. and Hu, H.H., 2008. Fluid mechanics. Academic Press, Amsterdam ; London, xxviii, 872 p. pp.

Kuo, A.Y.-S. and Corrsin, S., 1971. Experiments on internal intermittency and fine-structure distribution functions in fully turbulent fluid. J Fluid Mech, 50(02): 285-319.

Lamb, S.H., 1932. Hydrodynamics. Cambridge University Press, 738 pp.

Lane, E.W. and Kalinske, A.A., 1941. Engineering calculations of suspended sediment. Eos, Transactions American Geophysical Union, 22(3): 603-607.

Larson, M. and Kraus, N.C., 1995. Prediction of cross-shore sediment transport at different spatial and temporal scales. Marine Geology, 126(1–4): 111-127.

Lau, K.M. and Weng, H., 1995. Climate signal detection using wavelet transform: How to make a time series sing. Bulletin of the American Meteorological Society, 76(12): 2391-2402.

Laufer, J., 1975. New trends in experimental turbulence research. Annual Review of Fluid Mechanics, 7(1): 307-326.

Lavelle, J. and Mofjeld, H., 1987. Do critical stresses for incipient motion and erosion really exist? Journal of Hydraulic Engineering, 113(3): 370-385.

Lee-Young, J. and Sleath, J., 1989. Initial motion in combined wave and current flows, Coastal engineering 1988. American Society of Civil Engineers, pp. 1140-1151.

Lee, G.-h., 2008. Sediment eddy diffusivity and selective suspension under waves and currents on the inner shelf. Geosci J, 12(4): 349-359.

Lee, G.-h., Dade, W.B., Friedrichs, C.T. and Vincent, C.E., 2004. Examination of reference concentration under waves and currents on the inner shelf. Journal of Geophysical Research: Oceans, 109(C2): C02021.

Lee, M.J., 1989. Distortion of homogeneous turbulence by axisymmetric strain and dilatation. Physics of Fluids A, 1(9): 1541-1557.

Li, M.Z. and Amos, C.L., 1995. Sedtrans92: A sediment transport model for continental shelves. Computers & Geosciences, 21(4): 533-554.

Li, M.Z. and Amos, C.L., 1998. Predicting ripple geometry and bed roughness under combined waves and currents in a continental shelf environment. Cont Shelf Res, 18(9): 941-970.

Li, M.Z. and Amos, C.L., 1999a. Field observations of bedforms and sediment transport thresholds of fine sand under combined waves and currents. Marine Geology, 158(1–4): 147-160.

Li, M.Z. and Amos, C.L., 1999b. Sheet flow and large wave ripples under combined waves and currents: Field observations, model predictions and effects on boundary layer dynamics. Cont Shelf Res, 19(5): 637-663.

Li, M.Z. and Amos, C.L., 2001. Sedtrans96: The upgraded and better calibrated sediment-transport model for continental shelves. Computers & Geosciences, 27(6): 619-645.

Li, M.Z. and Gust, 2000. Boundary layer dynamics and drag reduction in flows of high cohesive sediment suspensions. Sedimentology, 47(1): 71-86.

Li, Z. and Davies, A.G., 2001. Turbulence closure modelling of sediment transport beneath large waves. Cont Shelf Res, 21(3): 243-262.

Liu, J., Wang, Y. and Yang, B., 2012. Wavelet packet analysis of particle response to turbulent fluctuation. Advanced Powder Technology, 23(3): 305-314.

Longo, S., Chiapponi, L., Clavero, M., Makela, T. and Liang, D.F., 2012. Study of the turbulence in the air-side and water-side boundary layers in experimental laboratory wind induced surface waves. Coast Eng, 69: 67-81.

Longuet-Higgins, M.S., 1953. Mass transport in water waves, 245, 535-581 pp.

Lozano-Duran, A., Flores, O. and Jimenez, J., 2012. The three-dimensional structure of momentum transfer in turbulent channels. J Fluid Mech, 694: 100-130.

Lozano-Durán, A. and Jiménez, J., 2014. Time-resolved evolution of coherent structures in turbulent channels: Characterization of eddies and cascades. J Fluid Mech, 759: 432-471.

Lu, J., Tang, H., Wang, L. and Peng, F., 2010. A novel dynamic coherent eddy model and its application to les of a turbulent jet with free surface. Sci. China Phys. Mech. Astron., 53(9): 1671-1680.

Ludwieg, H. and Tillmann, W., 1949. Untersuchungen über die wandschubspannung in turbulenten reibungsschichten. Ingenieur-Archiv, 17(4): 288-299.

MacVicar, B.J., Beaulieu, E., Champagne, V. and Roy, A.G., 2007. Measuring water velocity in highly turbulent flows: Field tests of an electromagnetic current meter (ecm) and an acoustic doppler velocimeter (adv). Earth Surface Processes and Landforms, 32(9): 1412-1432.

Maddux, T.B., McLean, S.R. and Nelson, J.M., 2003. Turbulent flow over three-dimensional dunes: 2. Fluid and bed stresses. Journal of Geophysical Research: Earth Surface, 108(F1): n/a-n/a.

Madsen, O.S. and Grant, W.D., 1975. The threshold of sediment movement under oscillatory waves: A discussion. Journal of Sedimentary Petrology, 45 (1): 360-361.

Madsen, O.S. and Grant, W.D., 1976. Quantitative description of sediment transport by waves. Coastal Engineering Proceedings, p.^pp. 1093-1112.

Madsen, O.S. and Wood, W., 2002. Chapter iii-6, sediment transport outside the surf zone, Coastal engineering manual, part iii coastal sediment processes. U.S. Army Corps of Engineers, Washington, DC, pp. III-6-i - III-6-69.

Malarkey, J. and Davies, A.G., 1998. Modelling wave–current interactions in rough turbulent bottom boundary layers. Ocean Eng, 25(2–3): 119-141.

Malarkey, J. and Davies, A.G., 2012. A simple procedure for calculating the mean and maximum bed stress under wave and current conditions for

rough turbulent flow based on soulsby and clarke's (2005) method. Computers & Geosciences, 43: 101-107.

Mallat, S., 1991. Zero-crossings of a wavelet transform. Information Theory, IEEE Transactions on, 37(4): 1019-1033.

Maltrud, M.E. and Vallis, G.K., 1991. Energy spectra and coherent structures in forced two-dimensional and beta-plane turbulence. J Fluid Mech, 228: 321-342.

Manneville, P., 2015. On the transition to turbulence of wall-bounded flows in general, and plane couette flow in particular. European Journal of Mechanics - B/Fluids, 49, Part B: 345-362.

Maraun, D. and Kurths, J., 2004. Cross wavelet analysis: Significance testing and pitfalls. Nonlin. Processes Geophys., 11(4): 505-514.

Marusic, I. and Adrian, R.J., 2013. The eddies and scales of wall turbulence. In: P.A. Davidson, Y. Kaneda and K.R. Sreenivasan (Editors), Ten chapters in turbulence. Cambridge University Press, Cambridge, pp. 176-220.

Marusic, I., Mathis, R. and Hutchins, N., 2010a. Predictive model for wall-bounded turbulent flow. Science, 329(5988): 193-196.

Marusic, I. et al., 2010b. Wall-bounded turbulent flows at high reynolds numbers: Recent advances and key issues. Phys Fluids, 22(6).

Marusic, I., Monty, J.P., Hultmark, M. and Smits, A.J., 2013. On the logarithmic region in wall turbulence. J Fluid Mech, 716: null-null.

Massel, S.R., 2013. Ocean surface waves - their physics and prediction Advanced series on ocean engineering, 36. World Scientific, Singapore, 692 pp.

Masselink, G., Hughes, M.G. and Knight, J., 2011. Introduction to coastal processes and geomorphology. Hodder Education, London.

Masselink, G. et al., 2015. Large-scale barrier dynamics experiment ii (bardex ii): Experimental design, instrumentation, test program, and data set. Coast Eng.

Masselink, G. et al., 2013. Bardex ii: Bringing the beach to the laboratory–again! In: Conley, d.C., masselink, g., russell, p.E. And o'hare, t.J. (eds.), proceedings 12th international coastal symposium,. Journal of Coastal Research(65): 1545 - 1550.

Masselink, G. and van Heteren, S., 2014. Response of wave-dominated and mixed-energy barriers to storms. Marine Geology, 352(50th Anniversary Special Issue): 321-347.

Mathis, R., Marusic, I., Hutchins, N. and Sreenivasan, K.R., 2011. The relationship between the velocity skewness and the amplitude modulation of the small scale by the large scale in turbulent boundary layers. Physics of Fluids (1994-present), 23(12): -.

MathWorks, 2016. Singal processing toolbox™ user's guide - matlab r2016a. The MathWorks, Inc, Natick, MA, 958 pp.

McComb, W.D., 1990. The physics of fluid turbulence. Oxford engineering science series. Clarendon Press, Oxford, xxiv,572p pp.

McLean, S., Wolfe, S. and Nelson, J., 1999. Predicting boundary shear stress and sediment transport over bed forms. Journal of Hydraulic Engineering, 125(7): 725-736.

McLean, S.R., 1992. On the calculation of suspended load for noncohesive sediments. Journal of Geophysical Research: Oceans, 97(C4): 5759-5770.

Meerschaert, M.M., Benson, D.A. and Bäumer, B., 1999. Multidimensional advection and fractional dispersion. Phys Rev E, 59(5): 5026-5028.

Meerschaert, M.M., Benson, D.A., Scheffler, H.-P. and Baeumer, B., 2002. Stochastic solution of space-time fractional diffusion equations. Phys Rev E, 65(4): 041103.

Middleton, G.V. and Southard, J.B., 1984. Mechanics of sediment movement, sepm short course number 3. SEPM, Providence, Rhode Island.

Miles, J., 1988. Parametrically excited, standing cross-waves. J Fluid Mech, 186: 119-127.

Miller, M.C., McCave, I.N. and Komar, P.D., 1977. Threshold of sediment motion under unidirectional currents. Sedimentology, 24(4): 507-527.

Millikan, C.B., 1939. A critical discussion of turbulent flows in channels and circular tubes. Proceedings of the Fifth International Congress of Applied Mechanics, Cambridge, MA, p.^pp. 386–392.

Mohajeri, S.H., Righetti, M., Wharton, G. and Romano, G.P., 2016. On the structure of turbulent gravel bed flow: Implications for sediment transport. Advances in Water Resources, 92: 90-104.

Monin, A.S. and Yaglom, A.M., 1971. Statistical fluid mechanics; mechanics of turbulence, II. Dover Publications, New York, 874 pp.

Monin, A.S., Yaglom, A.M. and Lumley, J.L., 1971. Statistical fluid mechanics : Mechanics of turbulence. Dover Publications, by special arrangement with The MIT Press, Mineola, New York, 896 pp.

Monkewitz, P.A., Chauhan, K.A. and Nagib, H.M., 2008. Comparison of mean flow similarity laws in zero pressure gradient turbulent boundary layers. Phys Fluids, 20(10): 105102.

Mori, N., Suzuki, T. and Kakuno, S., 2007. Noise of acoustic doppler velocimeter data in bubbly flows. Journal of Engineering Mechanics, 133(1): 122-125.

Morlet, J., Arens, G., Fourgeau, E. and Giard, D., 1982a. Wave propagation and sampling theory; part i, complex signal and scattering in multilayered media. Geophysics, 47(2): 203-221.

Morlet, J., Arens, G., Fourgeau, E. and Giard, D., 1982b. Wave propagation and sampling theory; part ii, sampling theory and complex waves. Geophysics, 47(2): 222-236.

Moser, R.D., 2006. On the validity of the continuum approximation in high reynolds number turbulence. Phys Fluids, 18(7): 078105-3.

Mukhopadhyay, S., Usha, R. and Tulapurkara, E.G., 2009. Numerical study of concentrated fluid–particle suspension flow in a wavy channel. Int J Numer Meth Fl, 59(10): 1125-1155.

Myrhaug, D. and Slaattelid, O.H., 1989. Combined wave and current boundary layer model for fixed rough seabeds. Ocean Eng, 16(2): 119-142.

Nadaoka, K., Ueno, S. and Igarashi, T., 1988. Sediment suspension due to large scale eddies in the surf zone. Coastal Engineering Proceedings(21): 1646-1660.

Nagano, Y. and Tagawa, M., 1995. Coherent motions and heat transfer in a wall turbulent shear flow. J Fluid Mech, 305: 127-157.

Nakato, T., Kennedy, J.F., Glover, J.R. and Locher, F.A., 1977. Wave entrainment of sediment drom rippled beds. Journal of the Waterway Port Coastal and Ocean Division, 103(1): 83-99.

Nayak, A.R., Li, C., Kiani, B.T. and Katz, J., 2015. On the wave and current interaction with a rippled seabed in the coastal ocean bottom boundary layer. Journal of Geophysical Research: Oceans, 120(7): 4595-4624.

Neill, C.R. and Yalin, M.S., 1969. Quantitative definition of beginning of bed movement Journal of the Hydraulics Division, American Society of Civil Engineers, 95(1): 585-588.

Neumeier, U., Ferrarin, C., Amos, C.L., Umgiesser, G. and Li, M.Z., 2008. Sedtrans05: An improved sediment-transport model for continental shelves and coastal waters with a new algorithm for cohesive sediments. Computers & Geosciences, 34(10): 1223-1242.

Nguyen, K.D., Guillou, S., Chauchat, J. and Barbry, N., 2009. A two-phase numerical model for suspended-sediment transport in estuaries. Advances in Water Resources, 32(8): 1187-1196.

Nielsen, P., 1979. Some basic concepts of wave sediment transport, Institute of Hydrodynamics and Hydraulic Engineering, Technical University of Denmark, Lyngby.

Nielsen, P., 1986. Suspended sediment concentrations under waves. Coast Eng, 10(1): 23-31.

Nielsen, P., 1992. Coastal bottom boundary layers and sediment transport. Advanced series on ocean engineering ;. World Scientific, Singapore, 324 pp.

Nielsen, P. and Teakle, I.A.L., 2004. Turbulent diffusion of momentum and suspended particles: A finite-mixing-length theory. Phys Fluids, 16(7): 2342-2348.

Nikora, V. and Goring, D., 1998. Adv measurements of turbulence: Can we improve their interpretation? Journal of Hydraulic Engineering, 124(6): 630-634.

Nikora, V. and Goring, D., 2002. Fluctuations of suspended sediment concentration and turbulent sediment fluxes in an open-channel flow. Journal of Hydraulic Engineering, 128(2): 214-224.

Nikuradse, J., 1933. Strömungsgestze in rauhen rohren, Forschung auf dem Gebiete des Ingenieurwesens. , Forschungsheft.

NiÑo, Y., Lopez, F. and Garcia, M., 2003. Threshold for particle entrainment into suspension. Sedimentology, 50(2): 247-263.

Novak, P., Guinot, V., Jeffery, A. and Reeve, D.E., 2010. Hydraulic modelling - an introduction: Principles, methods, and applications. Spon Press, 616 pp.

O'Donoghue, T., Doucette, J.S., van der Werf, J.J. and Ribberink, J.S., 2006. The dimensions of sand ripples in full-scale oscillatory flows. Coast Eng, 53(12): 997-1012.

O'Hara Murray, R.B., Hodgson, D.M. and Thorne, P.D., 2012. Wave groups and sediment resuspension processes over evolving sandy bedforms. Cont Shelf Res, 46(0): 16-30.

O'Hara Murray, R.B., Thorne, P.D. and Hodgson, D.M., 2011. Intrawave observations of sediment entrainment processes above sand ripples under irregular waves. Journal of Geophysical Research: Oceans, 116(C1): C01001.

Obrist, D. and Schmid, P.J., 2003. On the linear stability of swept attachment-line boundary layer flow. Part 2. Non-modal effects and receptivity. J Fluid Mech, 493: 31-58.

Offen, G.R. and Kline, S.J., 1974. Combined dye-streak and hydrogen-bubble visual observations of a turbulent boundary-layer. J Fluid Mech, 62(Jan23): 223-&.

Offen, G.R. and Kline, S.J., 1975. Proposed model of bursting process in turbulent boundary-layers. J Fluid Mech, 70(Jul29): 209-228.

Okamoto, N., Yoshimatsu, K., Schneider, K., Farge, M. and Kaneda, Y., 2007. Coherent vortices in high resolution direct numerical simulation of homogeneous isotropic turbulence: A wavelet viewpoint. Physics of Fluids (1994-present), 19(11): -.

Ölçmen, S.M., Simpson, R.L. and Newby, J.W., 2006. Octant analysis based structural relations for three-dimensional turbulent boundary layers. Physics of Fluids (1994-present), 18(2): -.

Osborne, P.D. and Greenwood, B., 1992a. Frequency dependent cross-shore suspended sediment transport. 1. A non-barred shoreface. Marine Geology, 106(1–2): 1-24.

Osborne, P.D. and Greenwood, B., 1992b. Frequency dependent cross-shore suspended sediment transport. 2. A barred shoreface. Marine Geology, 106(1–2): 25-51.

Oumeraci, H., 1999. Strengths and limitations of physical modelling in coastal engineering - synergy effects with numerical modelling and field measurements. Hydralab Worskshop on Experimental Research and Synergy Effects with Mathematical Models, Hannover, Germany, p.^pp. 7-38.

Ouriemi, M., Aussillous, P. and Guazzelli, É., 2009. Sediment dynamics. Part 1. Bed-load transport by laminar shearing flows. J Fluid Mech, 636: 295-319.

Paintal, A.S., 1971. Concept of critical shear stress in loose boundary open channels. Journal of Hydraulic Research, 9(1): 91-113.

Panton, R.L., 2001. Overview of the self-sustaining mechanisms of wall turbulence. Prog. Aerosp. Sci., 37(4): 341-383.

Paola, C. and Voller, V.R., 2005. A generalized exner equation for sediment mass balance. Journal of Geophysical Research: Earth Surface, 110(F4): F04014.

Papadimitrakis, Y.A., Hsu, E.Y. and Street, R.L., 1986. The role of wave-induced pressure fluctuations in the transfer processes across an air–water interface. J Fluid Mech, 170: 113-137.

Paphitis, D., 2001. Sediment movement under unidirectional flows: An assessment of empirical threshold curves. Coast Eng, 43(3–4): 227-245.

Paphitis, D. and Collins, M.B., 2001. The 5m long recirculating flume at the school of ocean and earth sciences (soes), university of southampton. Part ii: Unidirectional flow characteristics, Southampton.

Pasquill, F., 1950. The aerodynamic drag of grassland. Proceedings of the Royal Society of London. Series A. Mathematical and Physical Sciences, 202(1068): 143-153.

Paterson, A.R., 1983. A first course in fluid dynamics. Cambridge University Press, Cambridge.

Penko, A., Slinn, D. and Calantoni, J., 2011. Model for mixture theory simulation of vortex sand ripple dynamics. Journal of Waterway, Port, Coastal, and Ocean Engineering, 137(5): 225-233.

Penko, A.M., Calantoni, J., Rodriguez-Abudo, S., Foster, D.L. and Slinn, D.N., 2013. Three-dimensional mixture simulations of flow over dynamic rippled beds. Journal of Geophysical Research: Oceans, 118(3): 1543-1555.

Perry, A.E., Schofield, W.H. and Joubert, P.N., 1969. Rough wall turbulent boundary layers. J Fluid Mech, 37(02): 383-413.

Phillips, R.J., Armstrong, R.C., Brown, R.A., Graham, A.L. and Abbott, J.R., 1992. A constitutive equation for concentrated suspensions that accounts for shear-induced particle migration. Physics of Fluids A: Fluid Dynamics (1989-1993), 4(1): 30-40.

Pope, S.B., 2000. Turbulent flows. Cambridge University Press, Cambridge, 771 pp.

Prandtl, L., 1925. Bericht über untersuchungen zur ausgebildeten turbulenz.

Prandtl, L., 1926. Bericht über neuere turbulenzforschung. , Verein Deutscher Ingenieure Verlag, Berlin.

Price, W.A., 1978. Theme speech: Models, can we learn from the past and some thoughts on the design of breakwaters 16th International Conference on Coastal Engineering, Hamburg, Germany, p.^pp. 25-36.

Quadrio, M., 2011. Drag reduction in turbulent boundary layers by in-plane wall motion. Philos T R Soc A, 369(1940): 1428-1442.

Rashidi, M., Hetsroni, G. and Banerjee, S., 1990. Particle-turbulence interaction in a boundary layer. International Journal of Multiphase Flow, 16(6): 935-949.

Raudkivi, A.J., 1976. Loose boundary hydraulics. Pergamon international library of science, technology, engineering, and social studies. Pergamon Press, Oxford ; New York, xii, 397 p. pp.

Reynolds, O., 1883. An experimental investigation of the circumstances which determine whether the motion of water shall be direct or sinuous, and of the law of resistance in parallel channels. Philosophical Transactions of the Royal Society of London, 174: 935-982.

Reynolds, O., 1895. On the dynamical theory of incompressible viscous fluids and the determination of the criterion. Philosophical Transactions of the Royal Society of London. A, 186: 123-164.

Robins, A.G. and Fackrell, J.E., 1979. Continuous plumes - their structure and prediction. In: C.J. Harris (Editor), Mathematic modelling of turbulent diffusion in the environment : Proceedings of the conference on mathematical modelling of turbulent diffusion in the environment held at liverpool university, september 12-13th, 1978, organised by the institute of mathematics and its applications. Academic Press, London, pp. 55 - 114.

Robinson, S.K., 1991. Coherent motions in the turbulent boundary layer. Annual Review of Fluid Mechanics, 23(1): 601-639.

Roelvink, D. et al., 2009. Modelling storm impacts on beaches, dunes and barrier islands. Coast Eng, 56(11–12): 1133-1152.

Rogallo, R.S. and Moin, P., 1984. Numerical simulation of turbulent flows. Annual Review of Fluid Mechanics, 16(1): 99-137.

Roquet, F., Madec, G., McDougall, T.J. and Barker, P.M., 2015. Accurate polynomial expressions for the density and specific volume of seawater using the teos-10 standard. Ocean Modelling, 90: 29-43.

Rotta, J.C., 1986. Experience of 2nd-order turbulent-flow closure models. Z Flugwiss Weltraum, 10(6): 401-407.

Rouse, H., 1937. Modern conceptions of the mechanics of fluid turbulence. Trans. Am. Soc. Civ. Eng, 102: 463 - 554.

Rouyer, T., Fromentin, J., Stenseth, N. and Cazelles, B., 2008. Analysing multiple time series and extending significance testing in wavelet analysis. Marine Ecology Progress Series, 359: 11-23.

Ruessink, B.G., 2010. Observations of turbulence within a natural surf zone. Journal of Physical Oceanography, 40(12): 2696-2712.

Saffman, P.G., 1978. Problems and progress in the theory of turbulence. In: H. Fiedler (Editor), Structure and mechanisms of turbulence ii. Lecture notes in physics. Springer Berlin Heidelberg, pp. 273-306.

Samaga, B., Ranga Raju, K. and Garde, R., 1986. Suspended load transport of sediment mixtures. Journal of Hydraulic Engineering, 112(11): 1019-1034.

Samanta, G., Housiadas, K.D., Handler, R.A. and Beris, A.N., 2009. Effects of viscoelasticity on the probability density functions in turbulent channel flow. Physics of Fluids (1994-present), 21(11): -.

Sarpkaya, T., 1993. Coherent structures in oscillatory boundary layers. J Fluid Mech, 253: 105-140.

Schlichting, H., 1936. Experimentelle untersuchungen zum rauhigkeitsproblem. Ingenieur-Archiv, 7(1): 1-34.

Schlichting, H., 1955. Boundary layer theory. Pergamon Press LTD, 535 pp.

Schmid, P.J., 2007. Nonmodal stability theory. Annual Review of Fluid Mechanics, 39(1): 129-162.

Schmitt, F.G., 2007. About boussinesq's turbulent viscosity hypothesis: Historical remarks and a direct evaluation of its validity. Cr Mecanique, 335(9-10): 617-627.

Schneider, K. and Vasilyev, O.V., 2010. Wavelet methods in computational fluid dynamics. Annual Review of Fluid Mechanics, 42(1): 473-503.

Schoppa, W. and Hussain, F., 2002. Coherent structure generation in near-wall turbulence. J Fluid Mech, 453: 57-108.

Schumer, R., Meerschaert, M.M. and Baeumer, B., 2009. Fractional advection-dispersion equations for modeling transport at the earth surface. Journal of Geophysical Research: Earth Surface, 114(F4): F00A07.

Shields, A., 1936. Application of similarity principles and turbulence research to bed-load movement [translated from german: Anwendung der aehnlichkeitsmechanik und der turbulenzforschung auf die geschiebebewegung, mitteilungen der pressichen versuchanstalt fur wasserbau nd schiffbau, berlin, by w.P.Ott and j.C. Uchelen], Soil Conservation Service, Cooperative Laboratory, California Institute of Technology , Pasadena, CA.

Shugar, D.H. et al., 2010. On the relationship between flow and suspended sediment transport over the crest of a sand dune, río paraná, argentina. Sedimentology, 57(1): 252-272.

Shvidchenko, A.B. and Pender, G., 2001. Macroturbulent structure of open-channel flow over gravel beds. Water Resources Research, 37(3): 709-719.

Singh, A. and Foufoula-Georgiou, E., 2013. Effect of migrating bed topography on flow turbulence: Implications for modelling sediment transport,

Coherent flow structures at earth's surface. John Wiley & Sons, Ltd, pp. 323-339.

Sleath, J.F.A., 1984. Sea bed mechanics. Wiley ocean engineering series. Wiley-Interscience, 335 pp.

Sleath, J.F.A., 1988. Transition in oscillatory flow over rough beds. Journal of Waterway, Port, Coastal, and Ocean Engineering, 114(1): 18-33.

Smith, C.R., 1996. Coherent flow structures in smooth-wall turbulent boundaary layers: Facts, mechnaisms and speculations. In: P.J. Ashworth, S.J. Bennett, J.L. Best and S.J. McLelland (Editors), Coherent flow structures in open channels. John Wiley & Sons, Chichester, pp. 754.

Smith, C.R., Walker, J.D.A., Haidari, A.H. and Sobrun, U., 1991. On the dynamics of near-wall turbulence. Philos T Roy Soc A, 336(1641): 131-175.

Smith, J.D. and McLean, S.R., 1977. Spatially averaged flow over a wavy surface. Journal of Geophysical Research, 82(12): 1735-1746.

Soulsby, R., 1997. Dynamics of marine sands - a manual for practical applications. Thomas Telford, 249 pp.

Soulsby, R.L., 1977. Similarity scaling of turbulence spectra in marine and atmospheric boundary layers. Journal of Physical Oceanography, 7(6): 934-937.

Soulsby, R.L., 1983. Chapter 5 the bottom boundary layer of shelf seas. In: B. Johns (Editor), Elsevier oceanography series. Elsevier, pp. 189-266.

Soulsby, R.L., 2006. Simplified calculation of wave orbital velocities. TR 155, HR Wallingford.

Soulsby, R.L., Atkins, R. and Salkield, A.P., 1994. Observations of the turbulent structure of a suspension of sand in a tidal current. Cont Shelf Res, 14(4): 429-435.

Soulsby, R.L. and Clarke, S., 2005. Bed shear stress under combined waves and currents on smooth and rough beds, HR Wallingford

Soulsby, R.L. et al., 1993. Wave-current interaction within and outside the bottom boundary layer. Coast Eng, 21(1–3): 41-69.

Soulsby, R.L. and Humphery, J.D., 1990. Field observations of wave-current interaction at the sea bed. In: A. Tørum and O.T. Gudmestad (Editors), Water wave kinematics. Nato asi series. Springer Netherlands, pp. 413-428.

Soulsby, R.L., Salkield, A.P. and Le Good, G.P., 1984. Measurements of the turbulence characteristics of sand suspended by a tidal current. Cont Shelf Res, 3(4): 439-454.

Southgate, H.N. and Oliver, N., 1989. Efficient solution to the current-depth dispersion equation. SR 181, Hydraulic Research Wallingford, Wallingford.

Spydell, M.S., Feddersen, F., Guza, R.T. and MacMahan, J., 2014. Relating lagrangian and eulerian horizontal eddy statistics in the surfzone. Journal of Geophysical Research: Oceans, 119(2): 1022-1037.

Sreenivasan, K.R., 2011. G.I. Taylor: The inspirtion behind the cambridge school. In: P.A. Davidson, Y. Kaneda, K. Moffatt and K.R. Sreenivasan (Editors), A voyage through turbulence. Cambridge University Press,, Cambridge, pp. 127-186.

Sreenivasan, K.R. and Antonia, R.A., 1997. The phenomenology of small-scale turbulence. Annual review of fluid mechanics. Vol.29. Annual Reviews, 435-472472 pp.

Sreenivasan, K.R. and Narasimha, R., 1978. Rapid distortion of axisymmetric turbulence. J Fluid Mech, 84(03): 497-516.

Stapleton, K.R. and Huntley, D.A., 1995. Seabed stress determinations using the inertial dissipation method and the turbulent kinetic energy method. Earth Surface Processes and Landforms, 20(9): 807-815.

Sternberg, R.W., 1968. Friction factors in tidal channels with differing bed roughness. Marine Geology, 6(3): 243-260.

Stokes, G.G., 1880. On the theories of the internal friction of fluids in motion, and of the equilibrium and motion of elastic solids. Mathematical and physical papers, 1. Cambridge University Press.

Sumer, B.M. and Deigaard, R., 1981. Particle motions near the bottom in turbulent flow in an open channel. Part 2. J Fluid Mech, 109: 311-337.

Sumer, B.M., Guner, H.A.A., Hansen, N.M., Fuhrman, D.R. and Fredsøe, J., 2013. Laboratory observations of flow and sediment transport induced by plunging regular waves. Journal of Geophysical Research: Oceans, 118(11): 6161-6182.

Sumer, B.M. et al., 2010. Coherent structures in wave boundary layers. Part 2. Solitary motion. J Fluid Mech, 646: 207-231.

Sumer, B.M. and Oguz, B., 1978. Particle motions near the bottom in turbulent flow in an open channel. J Fluid Mech, 86(01): 109-127.

Sunamura, T. and Takeda, I., 1993. Bar movement and shoreline change: Predictive relations. Journal of Coastal Research, 15(SI): 125-140.

Sutherland, A.J., 1967. Proposed mechanism for sediment entrainment by turbulent flows. Journal of Geophysical Research, 72(24): 6183-6194.

Svendsen, I.A., 2006. Introduction to nearshore hydrodynamics. Advanced series in ocean engineering, 24. World Scientific, 722 pp.

Swart, D.H., 1974. Offshore sediment transport and equilibrium beach profiles, Delft Hydraulics, The Netherlands.

Takeda, K., 1966. On roughness length and zero-plane displacement in the wind profile of the lowest air layer. Journal of the Meteorological Society of Japan. Ser. II, 44(2): 101-108.

Tambroni, N., Blondeaux, P. and Vittori, G., 2015. A simple model of wave–current interaction. J Fluid Mech, 775: 328-348.

Tamburrino, A. and Gulliver, J.S., 2007. Free-surface visualization of streamwise vortices in a channel flow. Water Resources Research, 43(11): W11410.

Tani, I., 1977. History of boundary layer theory. Annual Review of Fluid Mechanics, 9(1): 87-111.

Taylor, G.I., 1935. Statistical theory of turbulence. Proceedings of the Royal Society of London A: Mathematical, Physical and Engineering Sciences, 151(873): 421-444.

Taylor, G.I., 1938. The spectrum of turbulence. Proceedings of the Royal Society of London. Series A - Mathematical and Physical Sciences, 164(919): 476-490.

Tennekes, H. and Lumley, J.L., 1972. A first course in turbulence. MIT Press, Cambridge, Mass., 300 pp.

Thompson, C.E.L., Amos, C.L., Angelaki, M., Jones, T.E.R. and Binks, C.E., 2006. An evaluation of bed shear stress under turbid flows. J Geophys Res-Oceans, 111(C4).

Thompson, C.E.L. et al., 2011. In situ flume measurements of resuspension in the north sea. Estuar Coast Shelf S, 94(1): 77-88.

Thompson, C.E.L., Kassem, H. and Williams, J.J., 2013. Bardex ii: Nearshore sediment resuspension and bed morphology. 12th International Coastal Symposium Plymouth, England, p.^pp. 1593 - 1598.

Thompson, C.E.L., Williams, J.J., Metje, N., Coates, L.E. and Pacheco, A., 2012. Turbulence based measurements of wave friction factors under irregular waves on a gravel bed. Coast Eng, 63: 39-47.

Thompson, E. and Vincent, C., 1984. Shallow water wave height parameters. Journal of Waterway, Port, Coastal, and Ocean Engineering, 110(2): 293-299.

Thompson, E. and Vincent, C., 1985. Significant wave height for shallow water design. Journal of Waterway, Port, Coastal, and Ocean Engineering, 111(5): 828-842.

Thorne, P.D., Davies, A.G. and Williams, J.J., 2003. Measurements of near-bed intra-wave sediment entrainment above vortex ripples. Geophys Res Lett, 30(20): 2028.

Thorne, P.D. and Hanes, D.M., 2002. A review of acoustic measurement of small-scale sediment processes. Cont Shelf Res, 22(4): 603-632.

Thorne, P.D. and Hurther, D., 2014. An overview on the use of backscattered sound for measuring suspended particle size and concentration profiles in non-cohesive inorganic sediment transport studies. Cont Shelf Res, 73: 97-118.

Thorne, P.D., Hurther, D. and Moate, B.D., 2011. Acoustic inversions for measuring boundary layer suspended sediment processes. The Journal of the Acoustical Society of America, 130(3): 1188-1200.

Thosteson, E.D. and Hanes, D.M., 1998. A simplified method for determining sediment size and concentration from multiple frequency acoustic backscatter measurements. The Journal of the Acoustical Society of America, 104(2): 820-830.

Ting, F.C.K., 2008. Large-scale turbulence under a solitary wave: Part 2: Forms and evolution of coherent structures. Coast Eng, 55(6): 522-536.

Ting, F.C.K. and Kirby, J.T., 1994. Observation of undertow and turbulence in a laboratory surf zone. Coast Eng, 24(1–2): 51-80.

Ting, F.C.K. and Kirby, J.T., 1996. Dynamics of surf-zone turbulence in a spilling breaker. Coast Eng, 27(3–4): 131-160.

Tomkins, C.D. and Adrian, R.J., 2003. Spanwise structure and scale growth in turbulent boundary layers. J Fluid Mech, 490: 37-74.

Tomlinson, B.N., 1993. Erosion studies of mixed sand beds under the combined action of waves and currents, University of Southampton, Soutahmpton, 267 pp.

Tooby, P.F., Wick, G.L. and Isaacs, J.D., 1977. The motion of a small sphere in a rotating velocity field: A possible mechanism for suspending particles in turbulence. Journal of Geophysical Research, 82(15): 2096-2100.

Torrence, C. and Compo, G.P., 1998. A practical guide to wavelet analysis. Bulletin of the American Meteorological Society, 79(1): 61-78.

Torrence, C. and Webster, P.J., 1999. Interdecadal changes in the enso-monsoon system. International Journal of Climatology of the Royal Meteorological Society, 12: 2679-2690.

Townsend, A.A., 1951. The structure of the turbulent boundary layer. Mathematical Proceedings of the Cambridge Philosophical Society, 47(02): 375-395.

Townsend, A.A., 1956. The structure of turbulent shear flow. Cambridge monographs on mechanics and applied mathematics. Cambridge University Press, Cambridge, 315 pp.

Trowbridge, J. and Elgar, S., 2001. Turbulence measurements in the surf zone. Journal of Physical Oceanography, 31(8): 2403-2417.

Trowbridge, J. and Madsen, O.S., 1984. Turbulent wave boundary layers: 1. Model formulation and first-order solution. Journal of Geophysical Research: Oceans, 89(C5): 7989-7997.

Tucker, M.E., 1991. Sedimentary petrology: An introduction to the origin of sedimentary rocks. Blackwell Science 260 pp.

Tucker, M.J. and Pitt, E.G., 2001. Waves in ocean engineering. Elsevier ocean engineering book series, 5. Elsevier, Amsterdam.

USWES, 1933. Investigation of proposed methods of bank and embankement protection, United States Waterways Experimental Station Vicksburg.

van Kesteren, W.G.M. and Bakker, W.T., 1984. Near bottom velocities in waves with a current; analytical and numerical computations Coastal Engineering Proceedings(19).

van Rijn, L., 1982. Equivalent roughness of alluvial bed. Hydraul. Div., Am. Soc. Civ. Eng. , 108(HY10): 1215-1218.

van Rijn, L., 1984a. Sediment pick-up functions. Journal of Hydraulic Engineering, 110(10): 1494-1502.

van Rijn, L., 1984b. Sediment transport, part ii: Suspended load transport. Journal of Hydraulic Engineering, 110(11): 1613-1641.

van Rijn, L., 2007a. Unified view of sediment transport by currents and waves. I: Initiation of motion, bed roughness, and bed-load transport. Journal of Hydraulic Engineering, 133(6): 649-667.

van Rijn, L., 2007b. Unified view of sediment transport by currents and waves. Ii: Suspended transport. Journal of Hydraulic Engineering, 133(6): 668-689.

van Rijn, L., Walstra, D. and van Ormondt, M., 2007. Unified view of sediment transport by currents and waves. Iv: Application of morphodynamic model. Journal of Hydraulic Engineering, 133(7): 776-793.

van Rijn, L.C., 1993. Principles of sediment transport in rivers, estuaries and coastal seas. Aqua Publications, Amsterdam.

van Rijn, L.C., Ribberink, J.S., Werf, J.V.D. and Walstra, D.J.R., 2013. Coastal sediment dynamics: Recent advances and future research needs. Journal of Hydraulic Research, 51(5): 475-493.

Vanoni, V.A., 1964. Measurements of critical shear stress for entraining fine sediments in a boundary layer, W. M. Keck Laboratory of Hydraulics and Water Resources, California Institute of Technology, Pasadena, CA.

Venditti, J.G. and Bennett, S.J., 2000. Spectral analysis of turbulent flow and suspended sediment transport over fixed dunes. Journal of Geophysical Research: Oceans, 105(C9): 22035-22047.

Venditti, J.G., Hardy, R.J., Church, M. and Best, J.L., 2013. What is a coherent flow structure in geophysical flow?, Coherent flow structures at earth's surface. John Wiley & Sons, Ltd, pp. 1-16.

Villard, P.V. and Osborne, P.D., 2002. Visualization of wave-induced suspension patterns over two-dimensional bedforms. Sedimentology, 49(2): 363-378.

Villaret, C., Hervouet, J.-M., Kopmann, R., Merkel, U. and Davies, A.G., 2013. Morphodynamic modeling using the telemac finite-element system. Computers & Geosciences, 53: 105-113.

Vittori, G., 2003. Sediment suspension due to waves. Journal of Geophysical Research: Oceans, 108(C6): n/a-n/a.

von Kármán, T., 1930. Mechanische aenlichkeit und turbulenz. Nachrichten von der Gesellschaft der Wissenschaften zu Göttingen, Mathematisch-Physikalische Klasse: 58 -76.

Von Kármán, T., 1937. The fundamentals of the statistical theory of turbulence. Journal of the Aeronautical Sciences, 4(4): 131-138.

Vongvisessomjai, S., 1985. Regime of oscillatory flow. Journal of Waterway, Port, Coastal, and Ocean Engineering, 111(1): 96-110.

Voulgaris, G. and Trowbridge, J.H., 1998. Evaluation of the acoustic doppler velocimeter (adv) for turbulence measurements. Journal of Atmospheric and Oceanic Technology, 15(1): 272-289.

Voulgaris, G., Wallbridge, S., Tomlinson, B.N. and Collins, M.B., 1995. Laboratory investigations into wave period effects on sand bed

erodibility, under the combined action of waves and currents. Coast Eng, 26(3–4): 117-134.

Wallace, J.M., 2016. Quadrant analysis in turbulence research: History and evolution. Annual Review of Fluid Mechanics, 48(1): 131-158.

Wallace, J.M., Eckelmann, H. and Brodkey, R.S., 1972. The wall region in turbulent shear flow. J Fluid Mech, 54(01): 39-48.

Wallbridge, Voulgaris, Tomlinson and Collins, 1999. Initial motion and pivoting characteristics of sand particles in uniform and heterogeneous beds: Experiments and modelling. Sedimentology, 46(1): 17-32.

Wang, G., Zheng, J.-H., Maa, J.P.-Y., Zhang, J.-S. and Tao, A.-F., 2013. Numerical experiments on transverse oscillations induced by normal-incident waves in a rectangular harbor of constant slope. Ocean Eng, 57: 1-10.

Warhaft, Z., 2000. Passive scalars in turbulent flows. Annual Review of Fluid Mechanics, 32(1): 203-240.

Wei, T., Fife, P., Klewicki, J. and McMurtry, P., 2005. Properties of the mean momentum balance in turbulent boundary layer, pipe and channel flows. J Fluid Mech, 522: 303-327.

Wei, T. and Willmarth, W.W., 1989. Reynolds-number effects on the structure of a turbulent channel flow. J Fluid Mech, 204: 57-95.

Weil, J.C., 1990. A diagnosis of the asymmetry in top-down and bottom-up diffusion using a lagrangian stochastic model. Journal of the Atmospheric Sciences, 47(4): 501-515.

Wheatcraft, S.W. and Meerschaert, M.M., 2008. Fractional conservation of mass. Advances in Water Resources, 31(10): 1377-1381.

Wiberg, P.L. and Harris, C.K., 1994. Ripple geometry in wave-dominated environments. Journal of Geophysical Research: Oceans, 99(C1): 775-789.

Wilczek, M., Xu, H. and Narita, Y., 2014. A note on taylor's hypothesis under large-scale flow variation. Nonlin. Processes Geophys., 21(3): 645-649.

Williams, J.E.F., Rosenblat, S. and Stuart, J.T., 1969. Transition from laminar to turbulent flow. J Fluid Mech, 39(03): 547-559.

Williams, J.J., Buscombe, D., Masselink, G., Turner, I.L. and Swinkels, C., 2012. Barrier dynamics experiment (bardex): Aims, design and procedures. Coast Eng, 63(0): 3-12.

Williams, J.J., Metje, N., Coates, L.E. and Atkins, P.R., 2007. Sand suspension by vortex pairing. Geophys Res Lett, 34(15): L15603.

Willmarth, W.W., 1975. Structure of turbulence in boundary layers. In: Y. Chia-Shun (Editor), Advances in applied mechanics. Elsevier, pp. 159-254.

Willmarth, W.W. and Lu, S.S., 1972. Structure of the reynolds stress near the wall. J Fluid Mech, 55(01): 65-92.

Wosnik, M., Castillo, L. and George, W.K., 2000. A theory for turbulent pipe and channel flows. J Fluid Mech, 421: 115-145.

Wu, F. and Jiang, M., 2007. Numerical investigation of the role of turbulent bursting in sediment entrainment. Journal of Hydraulic Engineering, 133(3): 329-334.

Wu, F. and Yang, K., 2004. Entrainment probabilities of mixed-size sediment incorporating near-bed coherent flow structures. Journal of Hydraulic Engineering, 130(12): 1187-1197.

Wyngaard, J.C. and Clifford, S.F., 1977. Taylor's hypothesis and high–frequency turbulence spectra. Journal of the Atmospheric Sciences, 34(6): 922-929.

Wyngaard, J.C. and Weil, J.C., 1991. Transport asymmetry in skewed turbulence. Physics of Fluids A: Fluid Dynamics (1989-1993), 3(1): 155-162.

Yalin, M.S., 1972. Mechanics of sediment transport. Pergamon Press, 290 pp.

Yang, S. and Jiang, N., 2012. Tomographic tr-piv measurement of coherent structure spatial topology utilizing an improved quadrant splitting method. Sci. China Phys. Mech. Astron., 55(10): 1863-1872.

Yong, L. and Parker, S., 1983. Fir filter design over a discrete powers-of-two coefficient space. IEEE Transactions on Acoustics, Speech, and Signal Processing, 31(3): 583-591.

Yong, Z., Benson, D., Meerschaert, M. and Scheffler, H.-P., 2006. On using random walks to solve the space-fractional advection-dispersion equations. J Stat Phys, 123(1): 89-110.

Yuan, J. and Madsen, O.S., 2014. Experimental study of turbulent oscillatory boundary layers in an oscillating water tunnel. Coast Eng, 89(0): 63-84.

Yuan, J. and Madsen, O.S., 2015. Experimental and theoretical study of wave–current turbulent boundary layers. J Fluid Mech, 765: 480-523.

Yuan, Y., Wei, H., Zhao, L. and Cao, Y., 2009. Implications of intermittent turbulent bursts for sediment resuspension in a coastal bottom boundary layer: A field study in the western yellow sea, china. Marine Geology, 263(1–4): 87-96.

Zaki, T.A., 2013. From streaks to spots and on to turbulence: Exploring the dynamics of boundary layer transition. Flow Turbulence Combust, 91(3): 451-473.

Zhang, C. et al., 2011. Comparison of turbulence schemes for prediction of wave-induced near-bed sediment suspension above a plane bed. China Ocean Eng, 25(3): 395-412.

Zhao, B., Law, A.W.K., Huang, Z.H., Adams, E.E. and Shao, D.D., 2011. Dynamics of sediment clouds in waves. AIP Conference Proceedings, 1376(1): 245-247.

Zhao, L.H., Andersson, H.I. and Gillissen, J.J.J., 2010. Turbulence modulation and drag reduction by spherical particles. Phys Fluids, 22(8): 081702.

Zhou, J., Adrian, R.J., Balachandar, S. and Kendall, T.M., 1999. Mechanisms for generating coherent packets of hairpin vortices in channel flow. J Fluid Mech, 387: 353-396.

Zhou, J., Meinhart, C.D., Balachandar, S. and Adrian, R.J., 1997. Formation of coherent hairpin packets in wall turbulence. In: R.L. Panton (Editor), Self-sustaining mechanisms of wall turbulence, . Advances in fluid mechanics Computational Mechanics Publications, Southampton, pp. 422p.

Zhou, Z., Hsu, T.-J., Ting, F.C.K. and Liu, X., 2014. The effects of wave-breaking-induced turbulent coherent structures on bottom stress and suspended sediment transport - a 3d numerical study. 2014(34).

Zhu, H., Wang, L.-l. and Tang, H.-w., 2013. Large-eddy simulation of suspended sediment transport in turbulent channel flow. Journal of Hydrodynamics, Ser. B, 25(1): 48-55.

Appendix 1.

Eddy viscosity closures in RANS models

A1.1 Linear Eddy viscosity models

Linear eddy viscosity models close the RANS equations using a Boussinesq-type approximation between the Reynolds' stress and the mean strain rate (Equation A.1). A model as such can be extracted by analysing simple shear flows in local equilibrium (Gatski & Rumsey 2002).

$$\tau_{ij} = \frac{2}{3}\kappa\delta_{ij} - 2\nu_T S_{ij} \qquad (Eq\ A1.1)$$

In such models, the isotropic part is integrated into the pressure term (equation 2.46 in Chapter 2), and the turbulence field is coupled to the mean field through eddy viscosity, which is a component of an effective viscosity $(\nu + \nu_T)$ in the diffusive term of RANS equations (*ibid*.) This offers a numerically robust formulation compared to having an explicit expression of the stress gradient in the RANS equation, given $(\nu_T > \nu)$.

In other words, the role of turbulence is to boost the effective viscosity from ν to ν_T, where ν_T is presumed much larger than ν (Davidson 2004). Thus, combining equation A1.1 into the RANS equation gives:

$$\frac{\bar{D}U_j}{\bar{D}t} + \frac{1}{\rho}\frac{\partial \bar{p}}{\partial x_i} = \left[(\nu + \nu_T)\ \frac{\partial \bar{U}_\iota}{\partial x_j}\right] \qquad (Eq\ A1.2)$$

A multitude of linear eddy viscosity models have been proposed from the simpler algebraic models to the more complex differential models, and as such a hierarchy exists, whereby linear models are classified as zero –, half –, one – and two – equation models.

A1.1.1 Zero and half equation models

Zero equation models are algebraic models, *i.e.*, in which eddy viscosity is defined algebraically rather than differentially. The first, and arguably simplest, of these closure schemes is the mixing length theory proposed by Prandtl in 1925, which noted an analogy between Newton's law of viscosity and Reynolds' stress (the exchange of momentum) when averaged over time, for plane shear with unidirectional mean flow (Davidson 2004, Gatski & Rumsey 2002, Glover et al 2011, Pope 2000). Prandtl assumed the eddy viscosity to have the following form:

$$\nu_T = \rho l_m^2 \cdot \left|\frac{dU}{dz}\right| \qquad (Eq\ A1.3)$$

and shear stress,

$$\tau_{xz} = -\nu_T \frac{dU}{dz} \qquad (Eq\ A1.4)$$

where l_m is the mixing length, specified as a function of position for any given flow. Prandtl derived the logarithmic velocity distribution near a solid surface by using the mixing length theory and assuming the scale of velocity fluctuations near the boundary approximates the shear velocity, u^*. In the logarithmic region of the boundary layer, he argued that the mixing length must be proportional to distance, hence: $\boldsymbol{l_m = \kappa z}$, but given $\boldsymbol{\nu_T \sim u' l_m}$, it follows that $\boldsymbol{\nu_T = u^* \kappa z}$ (Kundu et al 2008), with $\boldsymbol{\kappa}$ being von Karman's constant .

Despite the simplicity of these relationships, they provide useful insight into the structure of turbulent flows. The problem, however, lies in specifying the length scale, which depends on flow geometry, as an alternative to specifying the eddy viscosity. This merely replaces one problem with another. The mixing-length theory only works for single – length and single – time scales and thus another flaw lays in the intrinsic assumption that linear momentum is retained as the fluid moves and is suddenly given up upon arrival to the new layer. In turbulent flows, there is no clear separation between scales and so the analogy between turbulent transport and molecular transport, which undermines the theory, is unrealistic (Speziale 1991). It is widely accepted that the mixing – length theory

derives its validity solely on the grounds of dimensional necessity (Kundu et al 2008), and as such has fallen into disfavour (Tennekes & Lumley 1972).

Nonetheless, the mixing-length theory is useful for estimating the order of magnitude of eddy viscosity, especially where the flow geometry is well defined, (*e.g.* in simple one-dimensional shear flows); hence its popularity in aeronautical and other technological flows. Two famous derivatives of the mixing length theory applied to compressible flows are Cebeci-Smith (Cebeci & Smith 1974) and Baldwin-Lomax (Baldwin & Lomax 1978). Both models have two-layers of eddy viscosity, and inner and outer layer, where the outer layer mixing length scale is described based upon displacement thickness from the edge in the former model, and upon vorticity in the latter; with extensions to account for pressure gradients, intermittency, and wakes (Gatski & Rumsey 2002, Pope 2000). However, this leads to an innate dependency on grid structure; and in their original form, the models are restricted to attached flows. However, this has not affected popularity of a modified version of the Baldwin-Smith approach in modelling three-dimensional vorticity (*ibid*.).

Another two-layer model was developed by Johnson and King (Johnson & King 1985) specifically for strong adverse pressure gradients (hence not proposed as a universal model). This model, so-called half-equation as it solves ordinary (rather than partial) differential equations, emphasises advection effects whereas turbulent transport and diffusion are deemed less significant and solves for the maximum shear stress.

A1.1.2 One – equation models

One–equation turbulence closure models solve one transport equation, generally the turbulent kinetic energy, $k = \frac{1}{2}\, q^2 = \overline{u_i u_i}$, as suggested by both Kolmogorov and Prandtl, with the length scale, l_m, specified algebraically to define the turbulent viscosity:

$$\nu_T = c\, k^{\frac{1}{2}}\, l_m \qquad (Eq\ A1.5)$$

where c is a constant (Pope 2000). Subsequently, Reynolds stresses can be obtained from the turbulent-viscosity hypothesis (equation 1.9), and the RANS equations are solved for time average velocity and pressure fields. Recent one-equation models such as Spalart–

Allmaras (Spalart & Allmaras 1994), derived empirically using dimensional analysis and invariance, solve a partial differential equation of transport for eddy viscosity itself. The advantage of this model is being local, and hence independent of grid structure and with low numerical costs, making it popular in industrial applications. The major drawback is that the length scale, l_m, must be specified (generally by guesswork), and it tends to yield excessive diffusivity (Pope 2000).

A1.1.3 Two–equation models

In contrast to previous closures which specify a mixing-length to solve for the kinetic energy of the flow, two-equation models attempt to solve two additional (partial-differential) equations for two turbulence quantities pertaining to the velocity and length scales. Most often, these are the turbulent kinetic energy, k, equation in association with an equation for the turbulent dissipation rate, ε, or the specific dissipation rate (per unit k), ω; from which length ($L = k^{\frac{3}{2}}/\varepsilon$) and time ($\tau = k/\varepsilon$) scales can be inferred (Pope 2000). It follows that this approach to closure forms a complete system; with no need to specify flow–dependent properties such as the mixing-length. As such, two-equation models ($k-\varepsilon$ *or* $k-\omega$ and variations thereof, including realisable models and renormalisation group RNG models) have become the standard models used in science and industry to solve/simulate engineering flow problems. Nonetheless, the founding cornerstone of two – equation models remains the eddy-viscosity hypothesis as proposed by Boussinesq. Thus, eddy viscosity is specified as:

$$\nu_T = C_\mu . \frac{k^2}{\varepsilon} = C_\mu k \tau \qquad (Eq\ A1.6)$$

where $\tau = k/\varepsilon$ and C_μ is just one of a multitude of model constants ; or, alternatively:

$$\nu_T = \frac{k}{\omega} \qquad (Eq\ A1.7)$$

with $\varepsilon = C_\mu k \omega$ in the $k-\omega$ formulation.

In $k-\varepsilon$ models, the turbulent kinetic energy is derived from the momentum equation as:

$$\frac{Dk}{dt} = P - \varepsilon + D \qquad (Eq\ A1.8)$$

where ε is the "isotropic" turbulent dissipation rate; and D account for the combined effects of turbulent transport and viscous diffusion, and P stands for the turbulence production, given by:

$$P = -\tau_{ij}.\frac{\partial U_i}{\partial x_j} \qquad (Eq\ A1.9)$$

or, as they appear in their original form, in three dimensions (Launder et al 1975):

$$P_{ij} = -\left[\overline{u_\iota u_k}.\frac{\partial U_i}{\partial x_k} + \overline{u_\jmath u_k}.\frac{\partial U_i}{\partial x_k}\right] \qquad (Eq\ A1.10)$$

With Boussinesq's assumption of isotropic eddy viscosity (isotropic partitioning of stress components), the production rate can be written as:

$$P = 2\nu_T(S_{ik}S_{ki}) = 2\nu_T.\eta^2 \qquad (Eq\ A1.11)$$

(whence, the scalar invariance of strain, $\eta = \sqrt{S_{ik}S_{ki}}$).

Similarly, the exact equation for the dissipation rate can be derived, but the issue here lies within the fact this represents a cascade of energy flow from large scale motions to the dissipative range. The diffusion term, on the other hand, can be defined using a gradient-diffusion hypothesis. Therefore the standard approach is to derive an expression for dissipation empirically and a multitude of model coefficients have been proposed, but the general expression was described by Jones and Launder (Jones & Launder 1972), and can be written (using above notation) as:

$$\frac{D\varepsilon}{Dt} = \nabla.\left(\frac{\nu_T}{\sigma_\varepsilon}.\nabla\varepsilon\right) + C_{\varepsilon 1}.\frac{P\varepsilon}{k} - C_{\varepsilon 2}.\frac{\varepsilon^2}{k} \qquad (Eq\ A1.12)$$

where σ_ε, $C_{\varepsilon 1}$, and $C_{\varepsilon 2}$ are all model constants. This expression provides satisfactory predictions for a diversity of high Reynolds number flows both near and away from the wall, and can be simplified for homogeneous shear flows, or modified for decaying turbulence, the destruction of dissipation, and viscosity (damping) effects near the wall (Gatski & Rumsey 2002, Goto & Vassilicos 2009, Jones & Launder 1972, Launder et al 1975, Pope 1975, Pope 2000, Smith & Yakhot 1993, Speziale 1991, Speziale et al 1991, Yakhot et al 1989, Yakhot & Orszag 1986, Yoshizawa 1984).

A1.2 Non-linear and other eddy viscosity models

Inherent in all linear eddy viscosity models is Boussinesq's hypothesis which assumes the turbulent Reynolds' stress proportional to the mean rate of strain in the flow. Consequently, all such models suffer an intrinsic deficiency in assuming an isotropic eddy viscosity and this has led to a new class of models attempting to tackle this inadequacy, and these are collectively referred to as non-linear eddy viscosity models (NLEVM). These models extend the one-term tensor representation of stress in terms of strain rate (Equation 2.1) into a more general form:

$$\tau_{ij} = \frac{2}{3}\kappa\delta_{ij} + \sum_{n=1}^{N} \alpha'_n . T_{ij}^{(n)} \qquad (Eq\ A1.13)$$

where α'_n is a tensorial expansion coefficient (Gatski & Rumsey 2002). The advantage is that the anisotropy in stress can thus be captured, and one needs to determine the tensor base, $T_{ij}^{(n)}$, and its expansion coefficient α'_n to define this anisotropy, b_{ij} :

$$b_{ij} = \frac{\tau_{ij}}{2k} - \frac{\delta_{ij}}{3} \qquad (Eq\ A1.14)$$

$$b_{ij} = \sum_{n=1}^{N} \alpha'_n . T_{ij}^{(n)} \qquad (Eq\ A1.15)$$

This representation is the same as its linear counterpart for n =1. However, complexity arises when coupling this with the RANS equations, especially in terms of the diffusive term. In addition, b_{ij} is considered to have a functional dependency of the turbulent

kinetic energy (corresponding to the velocity scale) and the isotropic turbulent dissipation rate (corresponding to the length scale), as well as the tensors representing the mean rate of strain (S) and mean rotation (W); [$b = b\ (k, \varepsilon, S, W)$]. Associated with this, the expansion coefficient is dependent on the four former parameters as well as the turbulent Reynolds' number. Therefore, in this class of models, the approach is to determine the expansion coefficient, either assuming a polynomial expansion based on calibration with experimental data (*e.g.* quadratic model assessed in Speziale (1991) or the cubic model of Craft et al (1996)), or using an explicit algebraic stress models. In the latter category, transport equations are solved for individual Reynold stresses, $\langle u_i u_j \rangle$, and dissipation without the need for Boussinesq's assumption:

$$\frac{\overline{D}}{\overline{D}t}\langle u_i u_j \rangle + \frac{\partial}{\partial x_k}.T_{kij} = P_{ij} + R_{ij} - \varepsilon_{ij} \qquad (Eq\ A1.16)$$

Here, knowing $\langle U \rangle, \langle p \rangle$, $\langle u_i u_j \rangle$, and ε in the Navier-Stokes equation, both mean-flow convection $\frac{\overline{D}}{\overline{D}t}\langle u_i u_j \rangle$, and the production tensor, P_{ij} form a closed system, and there remains a requirement for modelling the dissipation tensor ε_{ij}, the pressure rate-of-strain tensor, R_{ij}, and the Reynolds stress flux, T_{kij}. For a full treatment of how this is done, including the underlying mathematical theories, the reader is referred to (Launder et al 2002, Pope 2000, Wilcox 2006). Basically speaking, R_{ij} is derived from arguments on isotropy and rapid-distortion (such as elliptic relaxation models (Durbin & Pettersen-Reif 2002)), T_{kij} from gradient-diffusion models, k and ε (or ω) from modified formulations of equation (1.25) above, with wall-function treatments and redistribution terms applied to the ensuing partial differential equations. Each of the equations represents a balance between stress generation, transport, destruction and redistribution (return to isotropy). By introducing approximations to the transport terms, these models are reduced into algebraic equations, hence forming algebraic stress models (ASM) which determine local Reynolds stresses as function of k, ε, and the mean velocity gradient.

Another approach to closure, namely differential second-moment (Reynolds' stress) models (DSM), has been proposed as fundamentally superior to any eddy viscosity model (Launder 1989, Leschziner & Lien 2002). DSM models provide the extra turbulent

momentum fluxes from the solution of the full transport equations derived from the Navier-Stokes equations, where history and local effects are accounted for (Gatski & Speziale 1993). Besides solving explicitly for each Reynolds stress component, this requires a length-scale supplying equation, for which the sweeping majority of models employ the rate of dissipation (Pope 2000). However, since near the wall, $\overline{uv}/k$ and $\bar{v}^2/k$ tend to zero, rather than a wall function, damping is obtained by blocking energy redistribution via pressure fluctuations, and the wall normal component, $\bar{v}^2$ is only sustained by pressure-terms that are severely damped as one approached the wall (Laurence et al 2005). In the $\bar{v}^2 - f$ models, $\bar{v}^2$ and its source term, f, are retained as variables in addition to the traditional k and ε.

DMS models describe both convection and diffusion in differential form, and comply with mathematical formalism, that is, they are dimensionally coherent, consistent in terms of tensorial order, indifferent to coordinate or material frames, and satisfy realizability conditions and the limiting properties of 2D turbulence (Hanjalić 1994). The models are also physically coherent in that turbulent correlations are modelled in terms of turbulent parameters instead of mean flow, and because higher-order moments have a decreasing effect of mean flow properties (*ibid.*). Nonetheless, the greatest weakness of such models is that all length scales are proportional to each other, and there is an inherent uncertainty in the equations for turbulent diffusion (they hardly distinguish velocity and pressure diffusion for mathematical reasoning), and so simplifications or higher order terms are added (Mellor & Yamada 1982). Yet, these models are yet to realize their potential due to persisting numerical difficulties, as well as the need for modifications to resolve, at fine resolutions, thin viscous flows near the wall and at low Reynolds' numbers (Hanjalic' & Jakirlic' 2002, Launder 1989, Lien & Leschziner 1994).

A1.3 Discussion of eddy viscosity closures used in RANS models

The above 'brief' review of linear and non-linear eddy viscosity models highlights the plethora of approaches to close the Reynolds averaged Navier Stokes equations (RANS) in hydrodynamic or Computational Fluid Dynamics (CFD) applications. Perhaps from a modelling perspective, the choice of closure scheme will depend on the level of description each available model affords, its cost and ease of use, its applicability and accuracy provided.

Mixing length and one-equation models merely determine the turbulent viscosity, providing very little information about the turbulence. On the contrary, two-equation models, provide quantitative description of the turbulent scales of velocity (turbulent kinetic energy), length and time (in one-equation models, length scale is specified not calculated). These models do not directly represent the Reynolds stress tensor, but model it as a local function of the turbulent kinetic energy k, the dissipation rate, ε, and the mean velocity gradient $\partial\langle U_i\rangle/\partial x_j$, either using Boussinesq assumption (isotropic eddy viscosity), non-linearly, or explicitly. Thus, they all intrinsically assume that the time-averaged stress is determined by a local velocity gradient. Conversely, Reynolds stress model avoid this, and consider the mean convection to be balanced by four processes, production, dissipation, redistribution, and turbulent transport (the latter of minor significance than the rest). At this level of closure, both production and isotropic dissipation are closed, and the principal quantity to be modelled is the redistribution due to the fluctuating pressure field (Pope 2000). Near a boundary, the assumption that this is locally governed by mean stress, dissipation and velocity gradient is questionable due to the strong inhomogeneity. Apart from the mixing-length and one-equation models, all the others are complete as they do not require a prior specification of the mixing length.

The $k-\varepsilon$ model is the most commercially used (implemented in CFD codes) given it is relatively easy to implement and computationally inexpensive when wall-functions are employed. Comparatively, Reynolds' stress models are more difficult and much more costly as there are seven turbulence equation to be solved (6 complex Reynolds stress equations and dissipation rate), hence requiring longer computational time. Algebraic stress models are equally as expensive to solve due to coupled non-linear equations. In terms of applicability, $k-\varepsilon$ and Reynolds stress models can be applied to any turbulent flow, providing information on both time and length scales. Both model classes are commonly used in reactive and multiphase flow problems but DSM closures extend to atmospheric flows as they account for buoyancy.

A1.4 Simulating turbulence and further closures: LES, DNS, two-point closures and hybrid approaches

Despite the important achievements in mathematical modelling of turbulence, and the practical utility of such models, there remains a variety of issues yet to be resolved, simply

due to lack of understanding of the underlying physics and the need to employ far more complicated formulations and numerical schemes (Hanjalić 1994). Factors complicating include, but are not restricted to, three-dimensionality of the velocity field, its time dependence and randomness, unsteadiness and periodicity, multiplicity of time and length scales which is directly dependent on the Reynolds number and boundary geometry, straining of eddies (Kolmogorov's kinetic energy cascade) viscosity in wall proximity, nonlinearity and non-locality of the convective term and more so in the pressure-gradient term, as well as other specific issues such as flow separation and reversal, buoyancy and rotation, etc. (Coleman & Sandberg 2010, Hanjalić 1994, Pope 2000, Rogallo & Moin 1984).

The challenge presented by the turbulent closure problem is such that Rotta expressly warned "a really universal turbulence model is a dream and will be a dream possibly for ever" (Rotta 1986); while Bradshaw famously noted that turbulence was "probably the invention of the Devil on the seventh day of creation (when the Good Lord wasn't looking)" in his article titled: The chief outstanding difficulty of our subject (Bradshaw 1994). Progress in experimental study of turbulence has proven to be less difficult, however, and numerical simulations have proven a valuable means of providing insight into the problem. In simulating turbulent flows, the time-dependent velocity field (representing approximately the velocity field $U(x,t)$, is solved for; as opposed to solving for some mean quantity such as $\langle U \rangle$; $\langle u_i u_j \rangle$ or ε. The common approaches include Large Eddy Simulation (LES), Direct Numerical Simulation, and more recently, Detached Eddy Simulation (DES).

Direct numerical simulations (DNS) attempt to solve the Navier-Stokes equations to determine the velocity field for a particular flow realisation (given initial and boundary conditions), resolving all time and space scales. This obviously entails a huge computational cost and memory storage, which increase at a cubic rate to the Reynolds number; hence despite today's high performance computing prowess, DNS is still limited to simple geometries and low to moderate Reynolds numbers (Coleman & Sandberg 2010, Pope 2000). Thus, there is a need for DNS codes to be efficient, and this is implemented via spatial (finite volume, finite element, discrete vortex, spectral schemes, etc.) and temporal discretisation schemes (explicit versus implicit)(Moin & Mahesh 1998, Rogallo & Moin 1984). DNS are commonly employed to gain insight into physical

mechanisms such as homogeneous versus inhomogeneous turbulence, transitional flows, and hydrodynamic instabilities; as well as for developing, validating and improving analytical models, especially in the aeronautic industry.

Large eddy simulations (LES) bridge the gap between Reynolds stress models and DNS, aiming to represent the larger three-dimensional unsteady motions directly, while modelling the effects of smaller scale motions. Assuming Kolmogorov's universality law at the smaller scales (Frisch 1995, Yakhot et al 1989), LES explicitly compute the dynamics of the larger-scale motions which predominantly contain the energy and anisotropy (and are defined by the flow geometry) and use "simple" models to represent sub-scale motions (Pope 2000). This philosophy has its origins in meteorological applications, such as the famous and widely-used Smagorinsky model (Smagorinsky 1963). Commonly, this involves application of an appropriately chosen low-pass filter to eliminate fluctuations at sub-grid scale (SGS, scales with wavelength smaller than the grid mesh) (Lesieur & Metais 1996). The evolution of the filtered 3D and time-dependent velocity field is described by equations derived from the Navier-Stokes, with momentum containing an SGS residual stress tensor closed by a simple eddy viscosity model. A numerical solution to the filtered equation provides an approximation to the large scale motion (Fröhlich & Rodi 2002, Pope 2000).

A very recent development in numerical simulation of turbulent flows is Detached Eddy Simulation (DES) which came to address the challenge of high-Reynolds number and massively separated flows such as those encountered in aerospace and ground transportation problems and atmospheric studies (Spalart 2009). This combines LES with RANS, whereby the boundary layer is treated by RANS equations (originally using the Spalart-Allmaras model; (Spalart & Allmaras 1994)) and the regions of massive separation are treated with LES, often with problems in describing the space between these two. There are several recent proposal suggested and concise review is given in (Fröhlich & von Terzi 2008, Spalart 2009). Several other "hybrid models" also couple RANS with LES, owing to their structural similarities, with transitions achieved by "blending", "interfacing", and/or "segregating" the eddy-resolving models (Fröhlich & von Terzi 2008).

Moreover, a further class of closure schemes comprises two-point statistical closures, such as Direct Interaction Approximation (DIA), Eddy damped quasi-normal Markovian (EDQNM), and Test Field models (TFM), developed mainly for homogeneous isotropic turbulence but recently extended into some anisotropic and even inhomogeous flows (Cambon 2002, Cambon & Scott 1999). All other schemes described previously (in this respect referred to as single-point closures) reduce the degrees of freedom of the spectral tensor to just k and ε; or k and R_{ij}; with a large number of adjustable model constants and heuristic assumptions. These in fact can be explicitly derived by integration from two-point closures, which are aimed at strongly non-linear turbulence with mathematical structures similar closely related to the theory of weak turbulence which has applications in geophysics (Godeferd et al 2001). They account for inhomogeneity using stochastic and rational approaches, and Langragian statistics with regards to the dispersion of particles, with spectral correlations to describe distortion of eddy structures by stratification large-scale strains, and rotation, especially though the cascade process upon which production and dissipation depend (*ibid.*). Early comparisons of DNS of two-dimensional turbulence with two-point closures highlight the effects of intermittency of convected passive scalars in a Gaussian velocity field, as reported in section §1.3 earlier (Herring & Kerr 1982, Herring & McWilliams 1985).

Finally, it is worthwhile noting that yet more closure approaches, and hybrids thereof, have been presented in an ever growing body of literature. These include, but not restricted to, statistical cross-independence closures (Tatsumi 2011) probability density function methods used particularly for reacting flows (Dopazo 1975, Dopazo 1994, Kollmann 1990, Pope 2000, Roekaerts 2002), including Langragian PDF (Pope 1994) and Monte Carlo methods (Dreeben & Pope 1998, Li & Modest 2001, Pope 1985, Xu & Pope 1999) and simulations using smoothed particle hydrodynamics (Mallouppas & van Wachem 2013, Monaghan 2012, Welton & Pope 1997). On a note more cheerful than Bradshaw's (at the start of this section), Jimenez and Moser believe that with increasing computational power in the coming decades, a dynamical theory for some parts of turbulent flows, particularly at the range of scales in the momentum cascade, may emerge from such simulations (Jimenez & Moser 2007).

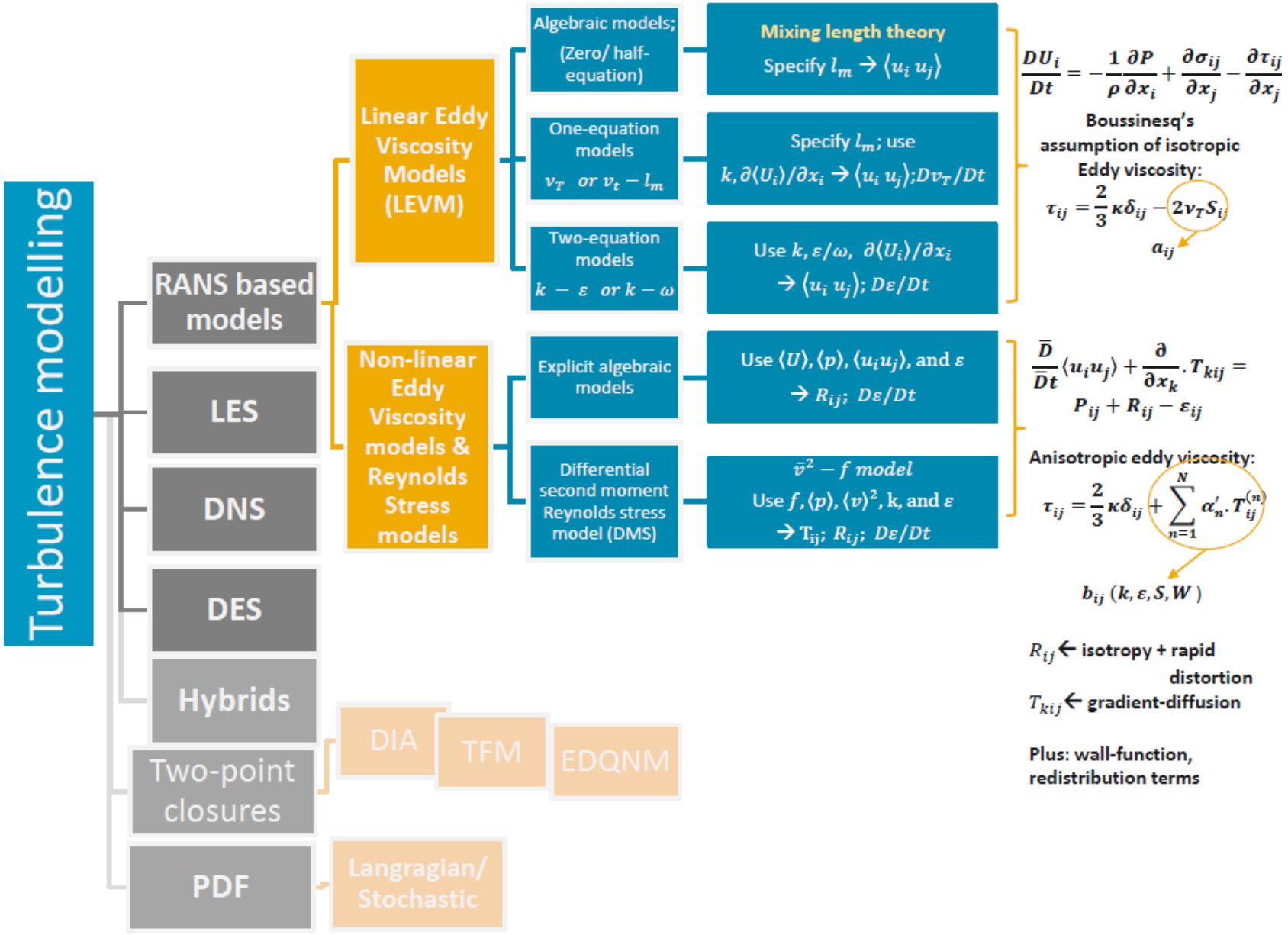

Figure A1.1 Schematic summary of numerical approaches for modelling turbulence

A1.5 Appendix A1 – List of References

Baldwin B, Lomax H. 1978. Thin-layer approximation and algebraic model for separated turbulentflows In *16th Aerospace Sciences Meeting*: American Institute of Aeronautics and Astronautics

Bradshaw P. 1994. Turbulence: the chief outstanding difficulty of our subject. *Experiments in Fluids* 16: 203-16

Cambon C. 2002. Introduction to two-point closures In *Closure Strategies for Turbulent and Transitional Flows*, ed. BES Launder, Neil D, pp. 299 - 327. West Nyack, NY, USA: Cambridge University Press

Cambon C, Scott JF. 1999. LINEAR AND NONLINEAR MODELS OF ANISOTROPIC TURBULENCE. *Annual Review of Fluid Mechanics* 31: 1-53

Cebeci T, Smith AMO. 1974. *Analysis of turbulent boundary layers*. New York ; London: Academic Press.

Coleman GN, Sandberg RD. 2010. A primer on direct numerical simulation of turbulence - methods, procedures and guidelines*. Technical Report Rep. AFM 09/01a*, Southampton, UK

Craft TJ, Launder BE, Suga K. 1996. Development and application of a cubic eddy-viscosity model of turbulence. *Int. J. Heat Fluid Flow* 17: 108-15

Davidson PA. 2004. *Turbulence : an introduction for scientists and engineers*. Oxford: Oxford University Press. 657 pp.

Dopazo C. 1975. Probability density function approach for a turbulent axisymmetric heated jet. Centerline evolution. *Physics of Fluids (1958-1988)* 18: 397-404

Dopazo C. 1994. Recent developments in pdf methods. *Turbulent reacting flows*: 375-474

Dreeben TD, Pope SB. 1998. Probability density function/Monte Carlo simulation of near-wall turbulent flows. *J Fluid Mech* 357: 141-66

Durbin PA, Pettersen-Reif BA. 2002. The elliptic relaxation method In *Closure Strategies for Turbulent and Transitional Flows*, ed. BES Launder, Neil D, pp. 127 - 52. West Nyack, NY, USA: Cambridge University Press

Frisch U. 1995. *Turbulence : the legacy of A.N. Kolmogorov*. Cambridge: Cambridge University Press. xiii, 296 p. pp.

Fröhlich J, Rodi R. 2002. Introduction to Large Eddy Simulation of Turbulent Flows In *Closure Strategies for Turbulent and Transitional Flows*, ed. BES Launder, Neil D, pp. 267 - 98. West Nyack, NY, USA: Cambridge University Press

Fröhlich J, von Terzi D. 2008. Hybrid LES/RANS methods for the simulation of turbulent flows. *Prog. Aerosp. Sci.* 44: 349-77

Gatski TB, Rumsey CL. 2002. Linear and Nonlinear Eddy Viscosity Models In *Closure Strategies for Turbulent and Transitional Flows*, ed. BES Launder, Neil D, pp. 9 - 46. West Nyack, NY, USA: Cambridge University Press

Gatski TB, Speziale CG. 1993. On explicit algebraic stress models for complex turbulent flows. *J Fluid Mech* 254: 59-78

Glover DM, Jenkins WJ, Doney SC. 2011. *Modeling methods for marine science*. Cambridge: Cambridge University Press ;. xv, 571 p. pp.

Godeferd FS, Cambon C, Scott JF. 2001. Two-point closures and their applications: report on a workshop. *J Fluid Mech* 436: 393-407

Goto S, Vassilicos JC. 2009. The dissipation rate coefficient of turbulence is not universal and depends on the internal stagnation point structure. *Physics of Fluids (1994-present)* 21: -

Hanjalic' K, Jakirlic' S. 2002. Second-moment turbulence closure modelling In *Closure Strategies for Turbulent and Transitional Flows*, ed. BES Launder, Neil D, pp. 47- 101. West Nyack, NY, USA: Cambridge University Press

Hanjalić K. 1994. Advanced turbulence closure models: a view of current status and future prospects. *Int. J. Heat Fluid Flow* 15: 178-203

Herring JR, Kerr RM. 1982. Comparison of direct numerical simulations with predictions of two-point closures for isotropic turbulence convecting a passive scalar. *J Fluid Mech* 118: 205-19

Herring JR, McWilliams JC. 1985. Comparison of direct numerical simulation of two-dimensional turbulence with two-point closure: the effects of intermittency. *J Fluid Mech* 153: 229-42

Jimenez J, Moser RD. 2007. What are we learning from simulating wall turbulence? *Philos T R Soc A* 365: 715-32

Johnson DA, King LS. 1985. A mathematically simple turbulence closure model for attached and separated turbulent boundary layers. *Aiaa J* 23: 1684-92

Jones WP, Launder BE. 1972. The prediction of laminarization with a two-equation model of turbulence. *Int. J. Heat Mass Transf.* 15: 301-14

Kollmann W. 1990. The pdf approach to turbulent flow. *Theoret Comput Fluid Dynamics* 1: 249-85

Kundu PK, Cohen IM, Ayyaswamy PS, Hu HH. 2008. *Fluid mechanics*. Amsterdam ; London: Academic Press. xxviii, 872 p. pp.

Launder BE. 1989. Second-moment closure: present… and future? *Int. J. Heat Fluid Flow* 10: 282-300

Launder BE, Reece GJ, Rodi W. 1975. Progress in the development of a Reynolds-stress turbulence closure. *J Fluid Mech* 68: 537-66

Launder BE, Sandham ND, Isaac Newton Institute for Mathematical Sciences. 2002. *Closure strategies for turbulent and transitional flows*. Cambridge: Cambridge University Press. xiii, 754 p. pp.

Laurence DR, Uribe JC, Utyuzhnikov SV. 2005. A robust formulation of the v2−f model. *Flow Turbulence Combust* 73: 169-85

Leschziner MA, Lien FS. 2002. Numerical aspects of applying scond-moment closure to complex flows In *Closure Strategies for Turbulent and Transitional Flows*, ed. BES Launder, Neil D, pp. 153 - 87. West Nyack, NY, USA: Cambridge University Press

Lesieur M, Metais O. 1996. New Trends in Large-Eddy Simulations of Turbulence. *Annual Review of Fluid Mechanics* 28: 45-82

Li G, Modest MF. 2001. An Effective Particle Tracing Scheme on Structured/Unstructured Grids in Hybrid Finite Volume/PDF Monte Carlo Methods. *Journal of Computational Physics* 173: 187-207

Lien FS, Leschziner MA. 1994. Assessment of Turbulence-Transport Models Including Nonlinear Rng Eddy-Viscosity Formulation and 2nd-Moment Closure for Flow over a Backward-Facing Step. *Comput Fluids* 23: 983-1004

Mallouppas G, van Wachem B. 2013. Large Eddy Simulations of turbulent particle-laden channel flow. *International Journal of Multiphase Flow* 54: 65-75

Mellor GL, Yamada T. 1982. Development of a turbulence closure model for geophysical fluid problems. *Reviews of Geophysics* 20: 851-75

Moin P, Mahesh K. 1998. DIRECT NUMERICAL SIMULATION: A Tool in Turbulence Research. *Annual Review of Fluid Mechanics* 30: 539-78

Monaghan JJ. 2012. Smoothed Particle Hydrodynamics and Its Diverse Applications In *Annu Rev Fluid Mech*, ed. SH Davis, P Moin, pp. 323-46. Palo Alto: Annual Reviews

Pope SB. 1975. More General Effective-Viscosity Hypothesis. *J Fluid Mech* 72: 331-40

Pope SB. 1985. PDF methods for turbulent reactive flows. *Progress in Energy and Combustion Science* 11: 119-92

Pope SB. 1994. Lagrangian PDF Methods for Turbulent Flows. *Annual Review of Fluid Mechanics* 26: 23-63

Pope SB. 2000. *Turbulent flows*. Cambridge: Cambridge University Press. 771 pp.

Roekaerts D. 2002. Reacting flows and Porbability Density Function Methods In *Closure Strategies for Turbulent and Transitional Flows*, ed. BES Launder, Neil D, pp. 328 - 37. West Nyack, NY, USA: Cambridge University Press

Rogallo RS, Moin P. 1984. Numerical Simulation of Turbulent Flows. *Annual Review of Fluid Mechanics* 16: 99-137

Rotta JC. 1986. Experience of 2nd-Order Turbulent-Flow Closure Models. *Z Flugwiss Weltraum* 10: 401-07

Smagorinsky J. 1963. GENERAL CIRCULATION EXPERIMENTS WITH THE PRIMITIVE EQUATIONS. *Monthly Weather Review* 91: 99-164

Smith LM, Yakhot V. 1993. Short- and long-time behavior of eddy-viscosity models. *Theoret Comput Fluid Dynamics* 4: 197-207

Spalart PR. 2009. Detached-Eddy Simulation. *Annual Review of Fluid Mechanics* 41: 181-202

Spalart PR, Allmaras SR. 1994. A One-Equation Turbulence Model for Aerodynamic Flows. *Rech Aerospatiale*: 5-21

Speziale CG. 1991. Analytical Methods for the Development of Reynolds-Stress Closures in Turbulence. *Annual Review of Fluid Mechanics* 23: 107-57

Speziale CG, Gatski TB, Fitzmaurice N. 1991. An Analysis of Rng-Based Turbulence Models for Homogeneous Shear-Flow. *Phys Fluids a-Fluid* 3: 2278-81

Tatsumi T. 2011. Cross-independence closure for statistical mechanics of fluid turbulence. *J Fluid Mech* 670: 365-403

Tennekes H, Lumley JL. 1972. *A first course in turbulence*. pp. xii, 300 p. Cambridge, Mass.: MIT Press. 300 pp.

Welton WC, Pope SB. 1997. PDF Model Calculations of Compressible Turbulent Flows Using Smoothed Particle Hydrodynamics. *Journal of Computational Physics* 134: 150-68

Wilcox DC. 2006. *Turbulence modeling for CFD*. La Cãnada, Calif.: DCW Industries. xxii, 522 p. pp.

Xu J, Pope SB. 1999. Assessment of Numerical Accuracy of PDF/Monte Carlo Methods for Turbulent Reacting Flows. *Journal of Computational Physics* 152: 192-230

Yakhot A, Orszag SA, Yakhot V, Israeli M. 1989. Renormalization group formulation of large-eddy simulations. *J. Sci. Comput.* 4: 139-158158

Yakhot V, Orszag SA. 1986. Renormalization-group analysis of turbulence. *Phys Rev Lett* 57: 1722-24

Yoshizawa A. 1984. Statistical analysis of the deviation of the Reynolds stress from its eddy-viscosity representation. *Phys Fluids* 27: 1377-87

Appendix 2.

Derivation of the Rouse Model for sediment suspension

A.2 Modelling sediment suspension

The traditional approach to modelling the suspension of sediments is founded upon the passive scalar hypothesis, whereby no or little interaction between sediment particles and fluid flow is assumed (Chauchat and Guillou, 2008). The implication of this is that the horizontal velocity of the sediment (u_s) is equal to that of the fluid (u), and the difference in true density between solid particles and surrounding fluids is accounted for only in the vertical via a settling velocity term (w_s). In other words, sediment transport in suspension is described by the balance between the downward settling of sediment particle due to gravity versus the upward mixing of sediment by turbulent motions, as per the advection-diffusion theory (ADE; Equation 3.13, §3.5.2). This assumption was also applied by Nakato et al. (1977) to homogenous oscillatory flows too.

$$u_s = u_{fluid} + w_s \qquad (Eq\ A2.1)$$

A.2.1 The Rouse Profile

The most classical model describing the vertical distribution of sediment transport within the ADE framework was proposed by Hunter Rouse (1937). Rouse argued that if the mean components of streamwise, crosswise and vertical velocity (following a Reynolds decomposition) do not vary in either space or time, then the turbulent flow may be considered steady and uniform (Rouse, 1937). Substituting these in the original Navier Stokes equations leads to an expression equivalent to the Newtonian equilibrium of force by mass-acceleration. By introducing "Boussinesq's turbulent coefficient, v_T", Rouse describes the effective shear of momentum transport (the stress) in a form similar to equation A1.4. Rouse then assumes a mixing length, l, to denote the average transverse

distance in the region of flow over which a small fluid mass is carried by the turbulent mixing process (as per Prandtl's definition), such that:

$$\tau = \rho l^2 . \left(\frac{dw}{d_z}\right)^2 \qquad (Eq\ A2.1)$$

The mixing length, is classically defined by von Kármán as:

$$l = \kappa, \frac{\frac{dw}{dz}}{\frac{d^2w}{dz^2}} \qquad (Eq\ A2.2)$$

Arguing that the difference between the original average velocity of the particle and that of the region into which it comes must be proportional to the magnitude of the velocity fluctuations involved in the transverse motion (*ibid.*), Rouse postulates:

$$|w_x'| = l . \frac{d\overline{w}}{dz} \qquad (Eq\ A2.3)$$

Hence, he defines the effective shearing stress (ignoring molecular viscosity in turbulent flow) as:

$$\bar{\tau} = \rho |w'|\ l . \frac{d\overline{w}}{dz} \qquad (Eq\ A2.4)$$

By comparison, Rouse defines the "kinematic turbulence factor", (*i.e.* the turbulent eddy viscosity), as:

$$\nu_T = |w_z'| . l \qquad (Eq\ A2.5)$$

Rouse suggested that the problem of suspended load (or temperature, or salinity) in a stream can be tackled similarly, in a convective manner. Using the settling velocity of a given particle size, w_s, the temporal rate of transport, N, of concentration per unit area must equate the number of particles, n, per unit volume multiplied by their rate of fall.

$$N = w_s n = -|w_z'| l . \frac{dn}{dz} \qquad (Eq\ A2.6)$$

This can be integrated into:

$$\ln\frac{n}{n_a} = -w_s.\int_a^z \frac{dz}{|w_z'|.l} \qquad (Eq\ A2.7)$$

in which n/n_a is the relative concentration at any point, referred to some arbitrary elevation, a, above the bottom. If follows that knowledge of the variation of the eddy viscosity with depth becomes a requirement to evaluate the last term in Equation A2.6, and hence to describe the concentration profile. From the equation A2.3, Rouse then quotes von Kármán as having presented, in a discussion of the same transaction, the integrable expression (this was originally derived for a pipeline by Rouse assuming static pressure variation balanced by non-viscous shear):

$$\frac{dz}{|w_z'|l} = \frac{dz}{\frac{\tau}{\rho.\frac{d\,\overline{w}}{dz}}} = \frac{\rho.\frac{d\,\overline{w}}{dz}}{\tau}.dz = \frac{\rho.\frac{d\,\overline{w}}{dz}}{\tau_0\left(1-\frac{z}{d}\right)}\,dz \qquad (Eq\ A2.8)$$

This relationship can be verified by simplifying the RANS equation for two-dimensional uniform flow, and applying boundary conditions whereby shear stress at bed is given by the energy slope equation, and zero stress at the water surface (Raudkivi, 1976). Subsequently, by using von Kármán's law of the wall, the logarithmic profile of the mean velocity gradient for rough conditions is:

$$\frac{d\,\overline{w}}{dz} = \frac{1}{\kappa}.\sqrt{\frac{\tau_0}{\rho}}.\frac{1}{z} \qquad (Eq\ A2.9)$$

Therefore, assuming a parabolic distribution of eddy viscosity in the vertical, in line with the logarithmic velocity distribution, equation A2.7 becomes:

$$\ln\frac{n}{n_a} = -w_s.\int_a^z \frac{\rho.\frac{d\overline{w}}{dz}}{\tau_0\left(1-\frac{z}{d}\right)}.dz \qquad (Eq\ A2.10)$$

By considering the settling velocity of sediment, w_s, the fluid density ρ, and the bed shear stress, $\tau_0 = \rho.u^{*2}$, are constants, then the profile for suspended sediments can be shown to vary in a parabolic fashion in the water column, extending from a near bed reference height, a, to the full water depth, d, as follows:

$$\frac{n}{n_a} = \left[\frac{1-\frac{z}{d}}{\frac{z}{d}} \times \frac{\frac{a}{d}}{1-\frac{a}{d}}\right]^R = \left[\frac{a(d-z)}{z(d-a)}\right]^R = \left[\frac{1-\frac{z'}{d'}}{1+\frac{z'}{a}}\right]^R \qquad (Eq\ A2.11)$$

in which the power, R, is what is commonly now called the Rouse Exponent, defined as:

$$R = \frac{w_s}{\kappa.\sqrt{\frac{\tau_0}{\rho}}} = \frac{w_s}{\kappa.u^*} \qquad (Eq\ A2.12)$$

and where $d' = d - a;$ with d being the total water depth, and a the reference height. Replacing n with concentration, C, this is the Rouse model for sediments in suspension:

$$C = C_a.\left[\frac{a}{z}.\frac{(d-z)}{(d-a)}\right]^R = C_a.\left[\frac{1-\frac{z'}{d'}}{1+\frac{z'}{a}}\right]^R \qquad (Eq\ A2.13)$$

The above relation indicates that the relative sediment distribution (for a given particle size and hence a particular settling velocity) is a function of relative depth only, and can only extend to a given arbitrary depth, *d*', such that the concentration at that depth does not affect the fluid-mixture density nor the velocity distribution (hence the notion of a reference concentration, C_a at the reference height).

The integrity of the Rouse profile can be scrutinised as it seems that the validity of nearly all of its underlying assumptions has been questioned in the literature. For instance, (Bagnold, 1966)first assumption that $w_s = w'_{up}$ for deriving the suspension threshold has been contested by field measurements (Al-Ragum et al., 2014; Amos et al., 2010*)*. This would require a new definition of the "pick up" function used in modelling. Moreover, the form of the Rouse profile depends on the chosen model for representing the vertical distribution of eddy viscosity. The latter may take on any form in a plethora of realisations (from negative and infinity constant values, to linearly increasing models, parabolic profiles, *etc*…); and it is crucial to consider its time-dependent variability as well (Fredsøe and Deigaard, 1992; Grant and Madsen, 1986). Alternative solutions of the steady one dimensional and two-dimensional SSC profiles for arbitrary velocity and eddy viscosity distributions are given in Liu and Nayamatullah (2014) and Liu (2016), respectively.

Appendix A2 – List of References

Al-Ragum, A., Monge-Ganuzas, M., Amos, C.L., Cearreta, A., Townend, I., Manca, E., 2014. An evaluation of the Rouse theory for sand transport in the Oka estuary, Spain. Cont Shelf Res 78, 39-50.

Amos, C.L., Villatoro, M., Helsby, R., Thompson, C.E.L., Zaggia, L., Umgiesser, G., Venturini, V., Are, D., Sutherland, T.F., Mazzoldi, A., Rizzetto, F., 2010. The measurement of sand transport in two inlets of Venice lagoon, Italy. Estuar Coast Shelf S 87, 225-236.

Bagnold, R.A., 1966. An approach to the sediment transport problem from general physics, Physiographic and Hydraulic Studies of Rivers, - ed. U.S. Government Printing Office, Washington, pp. I1-I37.

Chauchat, J., Guillou, S., 2008. On turbulence closures for two-phase sediment-laden flow models. Journal of Geophysical Research: Oceans 113, C11017.

Fredsøe, J., Deigaard, R., 1992. Mechanics of coastal sediment transport. World Scientific, Singapore.

Grant, W.D., Madsen, O.S., 1986. The Continental-Shelf Bottom Boundary Layer. Annual Review of Fluid Mechanics 18, 265-305.

Liu, X., 2016. Analytical solutions for steady two-dimensional suspended sediment transport in channels with arbitrary advection velocity and eddy diffusivity distributions. Journal of Hydraulic Research 54, 389-398.

Liu, X., Nayamatullah, M., 2014. Semianalytical Solutions for One-Dimensional Unsteady Nonequilibrium Suspended Sediment Transport in Channels with Arbitrary Eddy Viscosity Distributions and Realistic Boundary Conditions. Journal of Hydraulic Engineering 140, 04014011.

Nakato, T., Kennedy, J.F., Glover, J.R., Locher, F.A., 1977. Wave entrainment of sediment drom rippled beds. Journal of the Waterway Port Coastal and Ocean Division 103, 83-99.

Raudkivi, A.J., 1976. Loose boundary hydraulics, 2d ed. Pergamon Press, Oxford ; New York.

Rouse, H., 1937. Modern conceptions of the mechanics of fluid turbulence. Trans. Am. Soc. Civ. Eng 102, 463 - 554.

Appendix 3.

Barrier Dynamics Experiment II

Paper based on Chapter 5

Kassem, H., Thompson, C.E.L. , Amos, C.L. , and Townend, I.H. (2015), Wave-induced coherent turbulence structures and sediment resuspension in the nearshore of a prototype-scale sandy barrier beach, *Cont Shelf Res*, *109*, 78-94, doi:http://dx.doi.org/10.1016/j.csr.2015.09.007.

Continental Shelf Research 109 (2015) 78–94

Contents lists available at ScienceDirect

Continental Shelf Research

journal homepage: www.elsevier.com/locate/csr

Research papers

Wave-induced coherent turbulence structures and sediment resuspension in the nearshore of a prototype-scale sandy barrier beach

Hachem Kassem *, Charlotte E.L. Thompson, Carl L. Amos, Ian H. Townend

Ocean and Earth Science, National Oceanography Centre Southampton, University of Southampton Waterfront Campus, European Way, Southampton SO14 3ZH, United Kingdom

ARTICLE INFO

Article history:
Received 15 May 2015
Accepted 10 September 2015
Available online 15 September 2015

Keywords:
Coherent turbulence structures
Sediment resuspension
Wavelets

ABSTRACT

The suspension of sediments by oscillatory flows is a complex case of fluid–particle interaction. The aim of this study is to provide insight into the spatial (time) and scale (frequency) relationships between wave-generated boundary layer turbulence and event-driven sediment transport beneath irregular shoaling and breaking waves in the nearshore of a prototype sandy barrier beach, using data collected through the Barrier Dynamics Experiment II (BARDEX II). Statistical, quadrant and spectral analyses reveal the anisotropic and intermittent nature of Reynolds' stresses (momentum exchange) in the wave boundary layer, in all three orthogonal planes of motion. The fractional contribution of coherent turbulence structures appears to be dictated by the structural form of eddies beneath plunging and spilling breakers, which in turn define the net sediment mobilisation towards or away from the barrier, and hence ensuing erosion and accretion trends. A standing transverse wave is also observed in the flume, contributing to the substantial skewness of spanwise turbulence. Observed low frequency suspensions are closely linked to the mean flow (wave) properties. Wavelet analysis reveals that the entrainment and maintenance of sediment in suspension through a cluster of bursting sequence is associated with the passage of intermittent slowly-evolving large structures, which can modulate the frequency of smaller motions. Outside the boundary layer, small scale, higher frequency turbulence drives the suspension. The extent to which these spatially varied perturbation clusters persist is associated with suspension events in the high frequency scales, decaying as the turbulent motion ceases to supply momentum, with an observed hysteresis effect.

1. Introduction

The suspension of sediment in turbulent flows is a complex case of fluid–particle interaction, governed by shear stresses (momentum exchanges) at the bed and within the benthic boundary layer (BBL). Defining the physical processes which dictate the resuspension of sediments in coastal and estuarine settings is fundamental for accurate predictions of bed morphology evolution (van Rijn et al., 2007), and has profound implications for the biogeochemical processes that shape their local ecology (Thompson et al., 2011). It is also a prerequisite to quantifying erosion and deposition trends, and hence guiding engineering applications such as beach nourishment, defence schemes against erosion and flooding, maintenance of marine infrastructure and waterways, and aggregate dredging. There is a genuine need for better, robust models of suspended sediment transport in the coastal zone (Aagaard and Jensen, 2013). In a vision paper on future research needs in coastal dynamics, van Rijn et al., (2013) highlighted the pressing need for research to support such models, focusing in particular on sand transport in the shoreface (non-breaking waves), surf and swash zones; employing field and controlled laboratory experiments.

The mobilisation of sediments in the nearshore and shoreface is dominated by wave-induced bed shear stresses in moderate and stormy conditions (Thompson et al., 2012). The vertical structure of sediment flux components on the shoreface and in the inner surf zone, as well as the dynamics of sediment transport under shoaling waves in the nearshore, are both considered to be insufficiently understood (van Rijn et al., 2013). This requires prioritising research with reference to coherent flow structures and the intermittent stirring of sediments by breaking and shoaling waves, and the time-history effects of suspended sediments under irregular wave conditions [*ibid.*]. Understanding the spatial, temporal,

* Corresponding author.
E-mail addresses: Hachem.kassem@soton.ac.uk (H. Kassem), celt1@noc.soton.ac.uk (C.E.L. Thompson), cla8@noc.soton.ac.uk (C.L. Amos), I.Townend@soton.ac.uk (I.H. Townend).

http://dx.doi.org/10.1016/j.csr.2015.09.007
0278-4343/

and frequency characteristics of sediment suspension events in relation to turbulent fluctuations, both in structural form and in temporal distribution, is an important step towards providing a more satisfactory conceptual model for describing suspended sediment transport.

The role played by bed-generated coherent eddy structures in entraining and transporting sediment particles is widely acknowledged, yet the exact mechanism is still unclear (Dey et al., 2012; Ji et al., 2013). Coherent turbulence structures have been defined, albeit reluctantly, as "connected turbulent fluid masses with instantaneously phase-correlated vorticity over their spatial extent" (Hussain, 1983, 1986). Fiedler (1988) added several criteria to the definition, namely; composite scales, recurrent patterns (lifespan longer than the passage time of the structure), high organisation and quasi-periodic appearance. Besides the "conventional" bursting events which describe the intermittent, energetic process resulting from the passage of near-wall vortices as perceived by passive markers and/or visualisation studies (Schoppa and Hussain, 2002); one may identify vortices induced by wave breaking (Aagaard and Hughes, 2010), or by flow separation from vortex ripples upon reversal in an oscillatory flow, *i.e.* vortex entrainment/shedding (Amoudry et al., 2013). Vortex shedding from bedforms in wave dominated flows was first reported by Bagnold and Taylor (1946). As flow reverses over steep two-dimensional bedforms, the benthic boundary layer can separate from the bed, trapping sediments and ejecting them higher into the flow (O'Hara Murray et al., 2011). This is in essence a repeatable and hence coherent convective entrainment process (Nielsen, 1992) that is observed in both regular (at half cycle) and irregular wave conditions (O'Hara Murray et al., 2012; O'Hara Murray et al., 2011; Thorne et al., 2003). Where vortex pairs may develop, sediments may be violently ejected much higher (several orders of a ripple height) than classically described (Williams et al., 2007).

The intermittent transfer of momentum by coherent structures of turbulence is manifest by velocity fluctuations, and is linked to short-term variations in near-bed stresses (Heathershaw, 1974; Laufer, 1975). This is evident in the turbulent "bursting" process (Kline et al., 1967; Offen and Kline, 1974, 1975), which is a critical mechanism for production of turbulent kinetic energy (Dey et al., 2012; Schoppa and Hussain, 2002). Turbulent bursting may be explained by the advection of spatially distributed vortices and structural features past a fixed point of measurement (Robinson, 1991), although this may not detect how such vortices evolve in time (Schoppa and Hussain, 2002). The largest contributions to stress often occur through ejecting or sweeping motions (Soulsby, 1983). Typically, ejections are associated with entrainment of mass (sediment particles) into suspension, while sweeps are effective at transporting bedload (Cao, 1997; Dyer and Soulsby, 1988; Heathershaw, 1979; Keylock, 2007; Soulsby, 1983; Yuan et al., 2009). While ejections and sweeps reportedly occur in relatively equal proportions near the bed, the former type dominates higher in the water column (Cellino and Lemmin, 2004). Suspension of sediments is often related to large scale turbulence structures associated with clusters of ejections (Bennett et al., 1998; Kawanisi and Yokosi, 1993).

Recent sediment suspension models attempt to account for turbulent bursting by implementing entrainment functions that theoretically account for the average time and space scales of these motions (e.g. Cao, 1997; Wu and Yang, 2004; Wu and Jiang, 2007). Considerable recent work therefore focusses on the structural form of these features of flow, their role in fluid and sediment entrainment, bed shear stress generation, energy transfer and velocity asymmetry; and the influence of the space-time structure of the flow, with emphasis on oscillatory flows, and different bed roughnesses (Adrian and Marusic, 2012; Carstensen et al., 2010, 2012; Grigoriadis et al., 2013; Hardy et al., 2010; Hare et al., 2014; Okamoto et al., 2007). Advanced visualisation and data analysis techniques reveal complex interactions between passing coherent energetic structures and sediments in suspension, such as particle response to turbulent fluctuations in the frequency domain (e.g. Liu et al., 2012), and modifications of the mean velocity profile by the dispersed sediments (e.g. Ji et al., 2013). The aim of this study is to describe the temporal and scale relationships between wave-generated boundary layer turbulence and event-driven sediment suspension in oscillatory flow in the nearshore of a prototype sandy barrier beach. In particular, two aspects are investigated: (a) the time–frequency characteristics that describe the relationship between turbulent burst cycles and ensuing sediment suspension; and (b) the scale of covariance of near-bed sediment resuspension events with wave-induced turbulent coherent structures as manifest by the intermittent Reynolds' Stresses.

2. Methodology

2.1. Experimental setup and wave conditions

The results presented here arise from the analysis of two wave data sets collected within the European HYDRALAB IV **Bar**rier **D**ynamics **Ex**periment **II** (**BARDEX II**) carried out at the Delta Flume facility/Deltares, the Netherlands, between June and July 2012 (Masselink et al., 2013). A barrier beach, 75 m wide (cross-shore), 5 m alongshore, was constructed from moderately sorted, medium fluvial sand with a median grain diameter, D_{50}, of 0.42 mm. The barrier, backed by a lagoon and fronted by a 20 m flat section (of same bed material, 0.5 m deep), was subjected to a JONSWAP spectrum of waves, generated by a single-stroke wave paddle fitted with an automated reflection compensator to supress reflection and low frequency resonance, situated 49 m before the start of the 1:15 m seaward slope.

As part of these experiments, time-synched acoustic measurements of turbulence, suspension, and bed morphology were recorded from an instrumented frame at the nearshore position, situated just at the break of the seaward slope of the barrier (49 m from wave paddle). A schematic sketch of the frame and the barrier design is given in Fig. 1. Turbulence data were collected by means of two coupled, downward-looking Nortek Vectrino Acoustic Doppler Velocimeters (ADVs) with a vertical offset of 26 cm and an across-flume horizontal offset of 36 cm, sampling at 25 Hz. Sediment suspensions were inferred from backscatter measured with an Aquatec Aquascat Acoustic Backscatter Profiling Sensor (ABS), with 1, 2, and 4 MHz channels, measuring between 5 and 95 cm below the instrument in 0.5 mm bins at 64 Hz (Thompson et al., 2013). Unfortunately, it was not possible to calibrate the ABS measurements (and hence infer volume/mass concentrations) due to failure of pump equipment. Subsequently, concentrations and backscatter are used interchangeably in this work. Three dimensional bed morphology was inferred from a combination of a Marine Electronics 1.1 MHz dual sand ripple profiling system (SPRS) recording sequential cross-shore profiles and a 500 kHz Sector Scanning Sonar (SSS) which provided a 360° plan-view of the bedforms. Surface water elevation (pressure) was recorded through a 5 Hz self-logging Paraoscientific 745 pressure transducer, mounted 0.35 m above the bed. Although turbulence and bedform data were recorded for the entire length of each wave run, memory limitations in the ABS instrument mean bursts of a maximum length of 8 min are presented. As such, where turbulence records are analysed in conjunction with suspension data, these are trimmed accordingly.

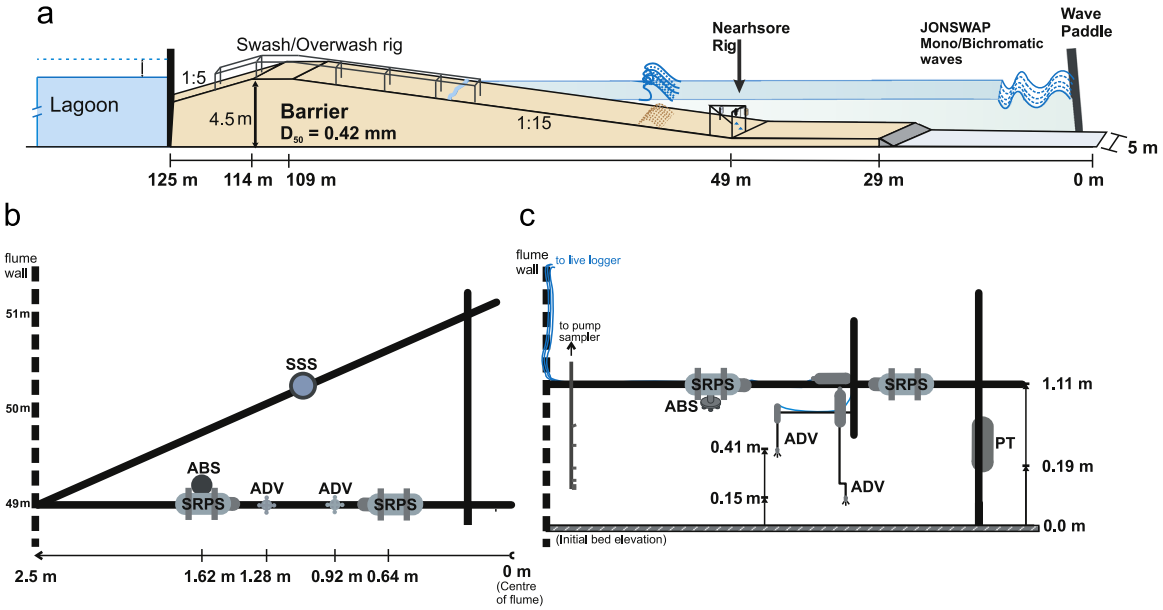

Fig. 1. (a) Cross-sectional profile of the barrier within the Delta Flume at the start of the BARDEX II experiments, with location of the nearshore instrument frame; (b) plan view of instrument rig with distance from the wave paddle on left hand wall, and indicating relative location of instruments from the centre of the flume; and (c) cross-section view of instrument rig with heights above initial bed elevation. SRPS: sand ripple profiler system; ABS: acoustic backscatter profiler system, ADV: acoustic Doppler velocimetre, SSS: sector scanning sonar, PT: pressure transducer.

2.2. Data collection, quality and pre-processing

The 3D instantaneous flow velocity field (U, V, W) representing the streamwise (along-flume), cross-wise (across-flume); and vertical components of instantaneous velocity, respectively; is given by ADVs measuring at two discrete 7 mm sample volumes above the bed (Fig. 1c). However, ADVs are inherently contaminated by noise due to Doppler signal aliasing, bubbles, etc. (Mori et al., 2007) and inferred stresses are susceptible to errors due to sensor misalignment (Soulsby and Humphery, 1990). For quality control purposes, a threshold of measurement correlation based on the instrument sampling frequency was used (after Elgar et al., 2005), giving ~70% as the lower limit. A limit of 20% corrupted data per record was subsequently applied, delimiting sequences where samples fall continuously below the accepted correlation threshold for >2 s (Elgar et al., 2001; Feddersen, 2010). The records were then patched by applying a moving average algorithm interpolating the missing data, following Thompson et al. (2012). Subsequently, an axis-rotation algorithm is used to eliminate effects of sensor misalignment, following Elgar et al. (2001). A similar operation is applied to the y–z plane before the mean values of the rotated coordinates are deducted to remove the contamination of the "U" data by the "V" data.

To extract the turbulence component (u'), the mean flow velocity of each component ($\bar{u}$), determined by applying a moving average as a low pass filter, is subtracted from the instantaneous flow field (u), before the record is zero-meaned and de-trended (Thompson et al., 2012). The numerator coefficients defining the filter window were selected by trial and error, with autocorrelation and cross-correlation tests applied for validation. It follows that two fluctuating components are identified, a wave-induced (periodic) component (denoted by u'_{wave}) and the residual "random/high frequency" component, u'. The signals are then despiked using the modified "true" 3 D phase space method by (Goring and Nikora, 2002, 2003) as modified by (Mori et al., 2007). It is to be noted that similar power (variance) properties and scales in the time–frequency domain were observed before and after despiking, albeit with smaller magnitude stresses.

The non-directional wave parameters (peak wave periods and significant wave heights) were computed by zero-crossing and spectral analysis of the pressure variations, having compensated for transducer height above bed, and pressure attenuation with depth following Tucker and Pitt (2001). Bed morphology was inferred from the backscatter intensity of the SSS and SRPS records. Bed location was determined using the built-in 'bed detection' function of the SRPS dual-head programmer software (Marine Electronics Ltd.) with a threshold value (20 dB) above the average backscatter intensity, having adjusted for sound attenuation. Bed level data were then detrended to remove the bed slope, and despiked to remove outliers pertaining to high concentration suspension events. A zero-crossing algorithm is used to determine ripple heights and wavelengths. Variations in bed morphology across the flume was examined through raw backscatter intensity given by the Sector Scan Sonar (SSS). Changes in bed morphology over time was inferred from the series of sequential scans within each run, taken approximately once a minute.

For the ABS records, the mean grain size and speed of sound, based on measured temperature and salinity, was used to correct backscatter for attenuation and spreading, and hence infer concentration. Thus, the one-dimensional vertical profiles of suspended sediment concentration (backscatter) and mean particle sizes could be calculated from sediment cross-section scattering of the individual sound frequencies following the methodology of (and Thorne and Hanes, 2002; Thosteson and Hanes, 1998), as presented in the MATSCAT toolkit (Buscombe, 2012). The ADV records of the turbulence components are sub-sampled to match the ABS records, which, in turn, are down-sampled from 64 Hz to 25 Hz only for the cross wavelet transforms of Reynolds' stresses and synchronous suspended sediment fluxes. Given that the sub-sampled records displayed the same spatial and temporal properties as their original series through spectral and continuous wavelet analyses, this is believed to have no significant impact on the results.

2.3. Quadrant analysis

In a three-dimensional orthogonal system (x, y, z) [where $x_1 = x_i = x$: along flow; $x_2 = x_j = y$: across flow; $x_3 = x_k = z$: vertical], a Reynolds'

decomposition of the instantaneous velocities (U_i) is given by:

$$U_i = \overline{u_i} + u_i' + u_{wave}' \quad (1)$$

whereby the over-bar denotes a time-average, the prime indicates a fluctuation about the mean, and the 'wave' subscript refers to the periodic/oscillatory (wave) component. The Reynolds' stress is described by the inverse correlation between the time-average fluctuations of streamwise (u') and vertical (w') velocity components at a point:

$$\text{Reynolds Stress;}\ \ \tau_{xz} = -\rho\overline{u'w'} \quad (2)$$

Quadrant analysis, a technique for detecting various turbulence structures, consists of distributing streamwise and vertical velocity fluctuations into the four quadrants of the plane (Deleuze et al., 1994). Four types of structures may be distinguished: (a) an ejection/burst (E, Quadrant 2) where a low speed fluid ($u'<0$) near the bed moves upward ($w' > 0$); (b) a sweep (S, Quadrant 4) where a high velocity fluid ($u' > 0$) moves downwards to the bed ($w' < 0$); (c) inward interactions (II, Quadrant 3) where an ; and (d) outward interactions (OI, Quadrant I) where an . Determining the fractional contribution of each of these structural features is commonly restricted to values that lie above a critical threshold, H, whereby:

$$|u'w'| > H.\ u_{rms}'.\ w_{rms}' \quad (3)$$

Hence, the contributions of individual events in the ($u'w'$) plane are the ones which occur in each quadrant outside the central "hole" region bounded by the four hyperbolae defined by the above inequality. However, there is no agreed definition for the threshold criterion (Blackwelder and Kaplan, 1976; Bogard and Tiederman, 1986; Keylock, 2007; Wu and Yang, 2004), and its value is chosen arbitrarily (Keylock, 2008) or ignored altogether (Keylock et al., 2014). As the threshold increases, the number of exceedances decreases, biasing the stress magnitude to be mostly contributed by ejections within the second quadrant (Keylock, 2007; Willmarth and Lu, 1972). The process outlined in Cellino and Lemmin (2004), Longo et al. (2012), Lu and Willmarth (1973) is used to calculate the concentrations within each quadrant. Extending quadrant analysis into three dimensions, known as Octant analysis, is less common, given that the cross-wise flow component is often assumed less important in classical flows (Gheisi et al., 2006; Keylock et al., 2014; Ölçmen et al., 2006). Quadrant/octant analysis provide a relatively simple means of characterising dominant flow structures, which can be linked to the entrainment of sediment from the bed and into suspension, and whose frequencies would dominate the velocity spectra and contribute the majority of the total shear stress (Keylock et al., 2014).

2.4. Spectral properties: Fourier and wavelet transforms

Fourier analysis is used to study turbulent flows and identify integral scales of motion, stemming from a classical understanding of the turbulent energy cascade. This statistical view was quantified by Kolmogorov–Obukhov into the well-known $k^{\frac{-5}{3}}$ law in the inertial subrange, with k denoting the wave-number for the energy spectrum in Fourier Space (Frisch, 1995; Monin and Yaglom, 1971; Tennekes and Lumley, 1972). However, the existence of organised yet stochastically intermittent eddy structures of multiple scales, varying in space and time, cannot be resolved by Fourier transforms as these transforms are inherently space-filling (Berry and Greenwood, 1975). Wavelets, on the other hand, are able to expand a time series into time–frequency space and thus determine localised intermittent periodicities (Farge, 1992; Grinsted et al., 2004), and are capable of performing efficient multi-scale decomposition (De Stefano and Vasilyev, 2012; Kumar and Foufoula-Georgiou, 1997), identifying and isolating localised structures such as vortices in physical and wave-number spaces (Farge et al., 2001, 2003; Khujadze et al., 2011), as well as analysing localised variations of power within a time series (Daubechies, 1990; Grinsted et al., 2004; Torrence and Compo, 1998).

A wavelet transform is in essence a linear operation which decomposes a given signal into components that appear at different scales, based on convolution of the signal with a dilated filter (Mallat, 1991). A continuous wavelet transform (CWT) decomposes a signal, $f(t)$, in terms of the 'daughter' wavelets, $\psi_{b,a}(t)$, derived by stretching or compressing and shifting (translating) the 'mother' wavelet, $\psi(t)$ function (Lau and Weng, 1995; Torrence and Compo, 1998). The most common mother function is the Morlet wavelet (Morlet, 1983; Morlet et al., 1982a, b), of wave vector, k_ψ=6, used in this work, and defined by

$$\psi(t) = e^{ik_\psi.t}.\ e^{-\frac{|t|^2}{2}} \quad (4)$$

The continuous and complex nature of this wavelet gives it the advantage of being able to detect both the time-dependant amplitude and phase for different frequencies in the time series (Lau and Weng, 1995). The transform maps a one dimensional time series into a two-dimensional image portraying the evolution of scales and frequencies in time (linear scale on time b-axis, and logarithmic scale on the a-axis). To speed up the transform and limit edge effects, we pad the time series with zeros, then remove these afterwards, and represent the region of spectrum where the effects may be important (near large scales) by a 'cone of influence' following (Torrence and Compo, 1998). Wavelet transforms are carried out to investigate the variability of high frequency turbulence structures and the ensuing suspension events, as well as their clustering (sequential occurrence) in time. These structures are hereby defined in terms of the Reynolds stresses as the second moment velocity covariance (product of the turbulent components in each of the three planes). The contours of power spectra are constructed from a continuous wavelet transform of the time series of Reynolds stresses, and of the concentration time series, following the methodology of Torrence and Compo (1998) and tools presented in Grinsted et al. (2004). Finally, using cross wavelet transforms, the causality between two time-series can be scrutinised by examining whether regions in the time–frequency space with large common power have consistent phase relationships. Wavelet multi-resolution analysis is capable of detecting and tracking energetic fine-scale motions (Schneider and Vasilyev, 2010). A cross-wavelet transform (XWT) is therefore used to expose regions of high common power between the two signals of Reynolds' stresses and suspended sediment flux, looking into the phase relationships between the two (Grinsted et al., 2004).

3. Results and discussions

3.1. Wave hydrodynamics and bed morphology

Eight records of erosive and accretive wave conditions (from the barrier's perspective) are analysed and presented here (four erosive sub-records taken from BARDEX II test series A3, and four accretive records from series A7 and A8). The design wave conditions, as well as calculated and measured hydrodynamic flow properties are given in Table 1. The design wave forcing in each sub-run is reproduced systematically by the paddle, with measured significant wave heights (Hs~0.75 $\pm$0.03 m in erosive, and ~0.61 $\pm$0.07 m in accretive runs) and peak periods (Tp ~8.12 $\pm$0.5 s in erosive; and 12 s in accretive runs) satisfying the erosion/accretion criteria (shoreward/seaward migration of nearshore bed material) of Sunamura and Takeda (1993) for the given beach slope and mean grain size. The wave Reynolds numbers

Table 1
Wave test conditions, and calculated/measured hydrodynamic properties/parameters.

Wave conditions	**Erosive runs** design characteristics: $h = 2.5$ m; $H_s = 0.8$ m; T_p=8s,JONSWAP						**Accretive runs** design characteristics: $h = 2.5$ m; $H_s = 0.6$ m; $T_p = 12$ s, JONSWAP					
Run (sub-run)	**A301- 1st**	**A301- 2nd**	**A301- 3rd**	**A301- 4th**	**mean $\bar{x}$**	**St. dev. σ_x**	**A705-**	**A706**	**A801-**	**A802-**	**mean ($\bar{x}$)**	**St. dev. σ_x**
Water height, h(m)	2.506	2.512	2.512	2.514	**2.51**	**0.0034**	2.507	2.509	2.509	2.509	**2.508**	**0.0008**
Measured Significant wave height, H_s (H_{m0}) (m)	0.779	0.761	0.734	0.710	**0.750**	**0.028**	0.566	0.705	0.532	0.629	**0.608**	**0.066**
Peak wave period, T_p (s)	8.0	8.0	8.98	7.5	**8.12**	**0.53**	12.0	12.0	12.0	11.48	**12.0**	**0**
Near–bed orbital amplitude, (m) $A_\delta = H_s/(2.\sin h(k.h)$	0.903	0.865	0.998	0.756	**0.88**	**0.086**	1.065	1.363	1.363	1.363	**1.289**	**0.129**
Near–bed orbital velocity, $U_{w,orb,\delta} = A_\delta.\omega$ (m/s) (van Rijn, 1993)	0.709	0.679	0.698	0.634	**0.680**	**0.029**	0.557	0.713	0.713	0.713	**0.674**	**0.068**
Wave Reynolds number, $Re_{w,\delta}$ (Soulsby and Clarke, 2005a)	2.53E+05	2.53E+05	2.38E+05	2.38E+05	**2.45E+05**	**0.7E+05**	2.14E+05	2.26E+05	2.40E+05	2.37E+05	**2.29E+05**	**0.1E+05**
Wave boundary layer thickness, δ_w (m), calculated from measured stress	0.249	0.140	0.128	0.123	**0.160**	**0.052**	0.177	0.184	0.178	0.194	**0.183**	**0.007**
Wave friction factor, f_w using TKE method (Thompson et al., 2012)	0.020	0.032	0.026	0.023	**0.025**	**0.004**	0.024	0.024	0.024	0.023	**0.024**	**0.0**

indicate turbulent rough flows (Soulsby and Clarke, 2005b), with estimated near-bed orbital velocities of 0.68 ± 0.03 m/s for the erosive runs (spilling and plunging breakers with surf-similarity parameter, $\xi = 0.5 \pm , \ 0.012$), and 0.67 ± 0.07 m/s for the accretive runs (plunging breakers with $\xi \cong 0.62$ (Massel, 2013)). Turbulence measurements by the two ADV's were confirmed to be taken within and outside the wave benthic boundary layer.

Within the erosive and accretive runs presented, wave-induced suborbital vortex-type ripples were observed in a bifurcating, two-dimensional configuration across and along the flume (Fig. 2), following the classification of (Clifton and Dingler, 1984). These were characterised by ripple height: $H_r = 0.098 \pm 0.008$ m; and wavelength, $\lambda_r = 0.45 \pm 0.09$ m in the erosive runs; and $H_r = 0.10 \pm 0.02$ m; and $\lambda_r = 0.57 \pm 0.06$ m in the accretive runs. While certain trends in bedform growth and relaxation were observed during entire experimental runs, only millimetric scale variations in geometry were evident within the 8-minutes long sub-records chosen for analysis of stress-suspension co-variation.

3.2. Turbulence intermittency and Higher order statistics

Fig. 3 shows the time series of the three instantaneous, zero-meaned velocity (U, V, and W) and inherent turbulent (u', v', and w') fluctuations, measured within and outside of the wave boundary layer (by ADV1 and ADV2 respectively) for almost the entire length of the erosive wave run A301; together with their corresponding probability distributions. The four erosive sub-records carried forward in the analysis are delimited by the vertical blue lines. Table 2 summarises the corresponding averaged statistical properties for the turbulent component of the 8-minute subsampled records from both erosive and accretive wave runs. The streamwise velocity component, U, both within and outside the boundary layer, exhibits a quasi-Gaussian distribution (skewness~0, kurtosis~3) hinting at a stochastic process of independent probabilistic events; while the crosswise and vertical components are markedly non-Gaussian. The turbulence components are anisotropic in all three dimensions both within and outside the bottom boundary layer.

The crosswise component, commonly overlooked when analysing shear stresses in relation to sediment suspension, shows remarkably high amplitude spikes, comparable in magnitude to the streamwise flow and for a considerable amount of time, particularly near the bed. This, in turn, is reflected in a pronounced leptokurtic distribution for the transverse velocity fluctuation, which also appears to be asymmetric. The vertical velocity fluctuations are characterised by relatively high kurtosis for the erosive wave runs, and even more pronounced in the accretive runs. The is generally suggestive of a high degree of intermittency in momentum exchange. Similar results have been reported (as unexpected findings) in experimental and numerical simulations of strong boundary layers and turbulent channels, particularly in wall (bed) proximity (Choi and Guezennec, 1990; Kim et al., 1987) and at high Reynolds numbers (Kuo and Corrsin, 1971); in obstructed flow (El Khoury et al., 2010), and in viscoelastic flows (Samanta et al., 2009).

The peaked and asymmetric crosswise velocity distribution particularly near the bed has been attributed to the nearly self-similar growth and self-sustaining mechanisms of spanwise structures in close proximity to low speed regions of flow. These are often speculated to be generated by induction of the asymmetric legs of an inclined, streamwise-aligned, wall-attached horseshoe vortex structures (Adrian, 2007; Christensen and Adrian, 2001; Lozano-Duran et al., 2012; Panton, 2001; Tomkins and Adrian, 2003; Zhou et al., 1997). It has also been attributed to the more frequent occurrence, and merging, of one-legged 'cane-like' elliptical vortices, at high Reynolds numbers (Tomkins and Adrian, 2003). The highly three-dimensional fluid entrainment process cannot be studied in the streamwise-vertical plane only, where entrainment with vortex

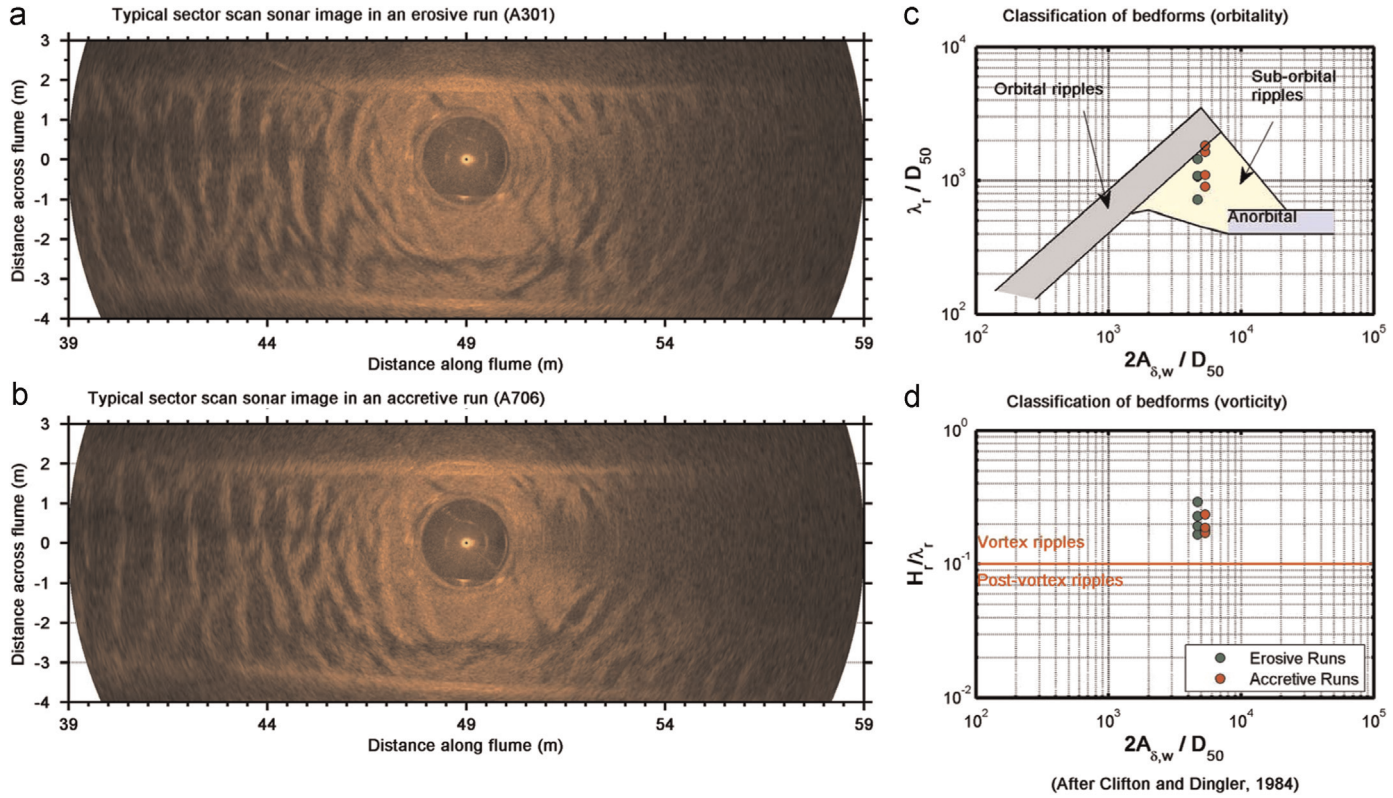

Fig. 2. Typical 2D ripple configurations observed via backscatter intensity along and across the flume in the vicinity of the instrumented offshore frame, for (a) erosive, and (b) accretive wave runs. Classification of bedform in terms of (c) orbitality, and (d) vorticity for the average bedform characteristic lengths is after Clifton and Dingler (1984).

structures is not evident (Robinson, 1991). Large streamwise vortices in wall bounded channels with moveable beds appear as secondary flows in the crosswise plane perpendicular to the streamwise flow, and affect the distribution of mean velocity, turbulence intensities, and Reynolds and bed shear stresses through the channel (Adrian and Marusic, 2012). Such eddies have been observed with a spanwise width up to 1.5 times the water depth, which oscillate slowly at the centre while forming stationary flows near the wall (Tamburrino and Gulliver, 2007). In the absence of practical means of visualising these structures in the field, we undertake quadrant analysis of the tangential stresses to assess the frequency of occurrence of sweep (Q4)-ejection (Q2) pairs as it may shed additional light on the three dimensional structure of momentum transfer near the bed (Alfredsson and Johansson, 1984; Kim et al., 1987; Lozano-Duran et al., 2012). Notably, there is no consensus as to whether the succession of ejections and sweeps creates vortices, or conversely, rolling vortices give rise to the bursting sequence, and it is plausible that both mechanisms operate cooperatively (Adrian and Marusic, 2012).

The above results emphasise the three-dimensionality of the momentum and subsequent mass exchange problem, and as such, the contributions of the three components of turbulence to momentum flux need to be considered. Subsequently, octant analyses of the three dimensional Reynolds stresses ($u'w'$, $u'v'$,$v'w'$) is carried out to identify the 'active' times where momentum exchanges occur, and their fractional contributions to the overall stress. However, to remain true to the original formulation, we have opted to perform this in three distinct orthogonal planes.

3.3. Quadrant/octant analysis and dominant structural features of flow

Quadrant analysis is used to quantify the intermittency of the instantaneous Reynolds stress signals and identify turbulence structures within a turbulent bursting sequence. Fig. 4 summarises the averaged results of the quadrant analysis, performed in three planes of motion (streamwise-vertical plane (uw), crosswise-vertical (vw), horizontal (uv)) for the erosive and accretive runs analysed. These are obtained from the four 8 min ADV1 sub-records measured near the bed, corresponding to the ABS sampling periods in each case, without applying a threshold (Hole size, $H=0$). The top panel (Fig. 4.a); highlights the influence of the hyperbolic hole size, H, applied as a delimiting threshold (green: $H=2$; grey: $H=1$). Notably, it was found that applying a threshold value has a far more pronounced impact in the erosive wave runs, reducing the fractional occurrence of all four types of structures by up to 80% for $H=2$ (most pronounced effect is on the outward (OI) and inward (II) interactions), but only up to 30% for the accretive runs. The effect of a threshold value applied to the stresses of the accretive runs reduces the accounted motions in relatively equal proportions in any given plane (only marginal increase in the Q1 OI and sweep motions at the expense of the accounted ejections). The middle panel (Fig. 4.b) presents the averaged results (of 4 sub-runs) for the erosive and accretive records, of the percentage of occurrence of each of the 4 types of bursting event structures, before and after filtering out the periodic component from the velocity fluctuations, in all three planes. The lower panel (Fig. 4.c) shows the averaged percentage of contribution to stress by each of the bursting motion types, to the total Reynolds stress in the primary flow plane (uw). Filtering out the periodic component appears to have a significant impact only on the proportion of time occupied by specific motions (particularly Q2 and Q3) in the dominant flow plane (uw) of the erosive runs, and almost no effect in the accretive runs. It is also found that this has a negligible impact on the contribution to stress by each type of structure. For the erosive runs, Q2 (Ejection) and Q3- (Inward Interaction) motions dominate the vertical motion along ($u'w'$ plane) and across ($v'w'$ plane), respectively, with the wave signal present. These events entrain low speed fluid (and particulates) near the bed

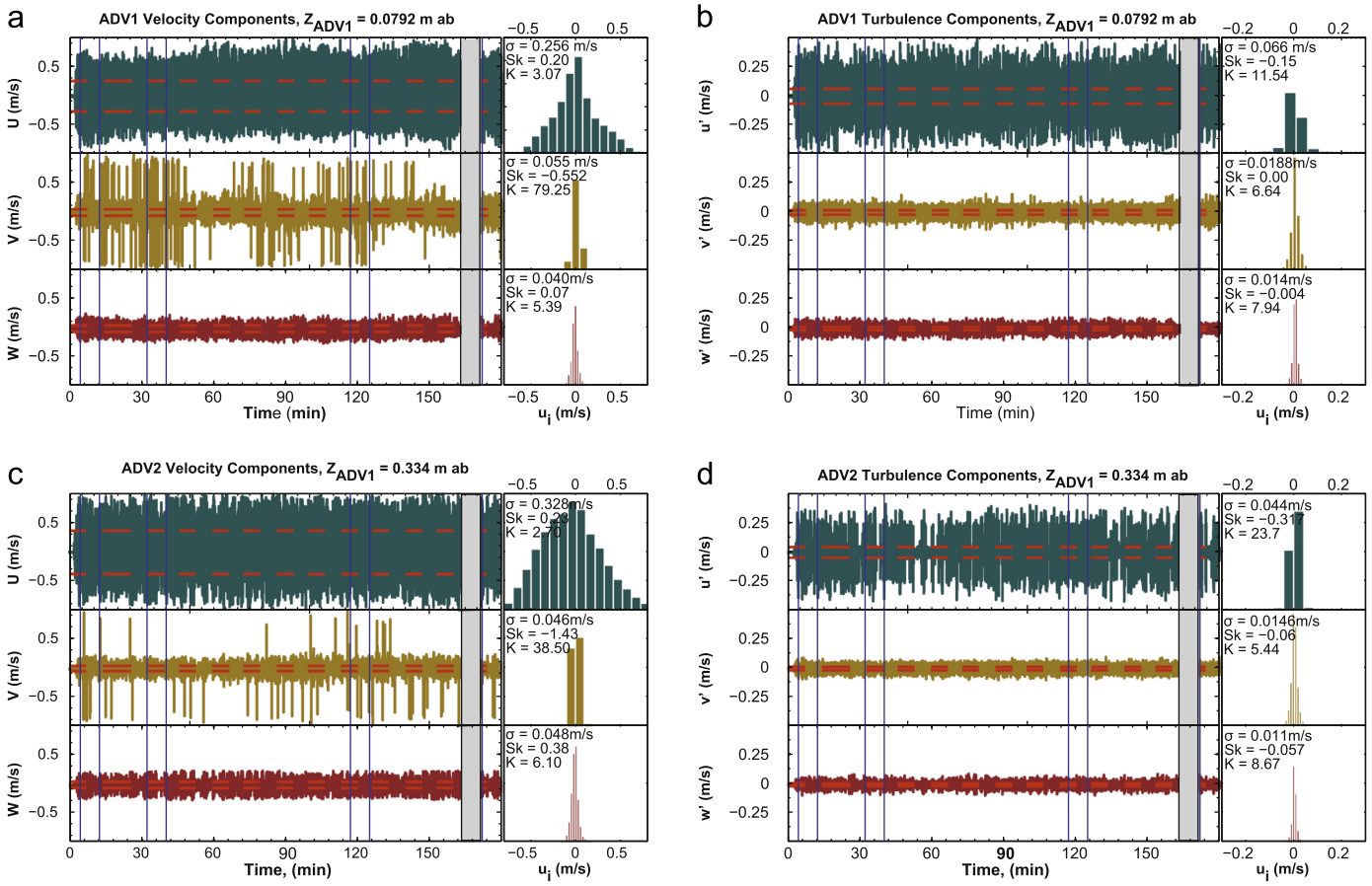

Fig. 3. Time series and probability density functions of 3D velocity (U, V, and W) and inherent turbulence (u', v', w') components, in the streamwise/along-flume (dark green), crosswise (gold), and vertical (orange) for the entire experimental wave run A301 (Hs=0.8 m, Tp=8 s). The horizontal dashed lines (red) in the time series represent ± 1 standard deviations; while the vertical blue lines delimit the 4 sub-records analysed; σ is standard deviation, Sk is skewness, and K is Kurtosis (For interpretation of the references to colour in this figure legend, the reader is referred to the web version of this article.).

Table 2
Statistical properties of the three turbulence components measured within (ADV1) and outside (ADV2) the wave boundary layer for the two types of wave conditions. These are averages of the 4 sub-sampled records analysed for each of the erosive and accretive runs.

Wave run-subrecord	ADV	Height above bed (m)	Turbulence component	Standard deviation	Variance	Skewness	Kurtosis
Erosive runs	ADV1	0.0792	u'	0.27 ± 0.027	0.07 ± 0.014	0.27 ± 0.06	2.97 ± 0.38
			v'	0.05 ± 0.005	0.00	−0.78 ± 1.3	37.47 ± 28.76
			w'	0.04 ± 0.005	0.00	0.09 ± 0.38	6.52 ± 1.68
	ADV2	0.334	u'	0.33 ± 0.015	0.11 ± 0.01	0.26 ± 0.08	2.61 ± 0.07
			v'	0.09 ± 0.004	0.00	−1.70 ± 1.10	39.22 ± 27.08
			w'	0.05 ± 0.002	0.00	0.34 ± 0.22	5.99 ± 0.59
Erosive runs	ADV1	0.09 ± 00.1	u'	0.25 ± 0.025	0.06 ± 0.012	0.32 ± 0.12	3.04 ± 0.0.33
			v'	0.06 ± 0.013	0.00	1.10 ± 1.32	36.69 ± 23.43
			w'	0.03 ± 0.003	0.00	−0.18 ± 0.54	7.94 ± 2.03
	ADV2	0.337 ± 0.016	u'	0.28 ± 0.015	0.08 ± 0.009	0.37 ± 0.039	3.08 ± 0.2
			v'	0.04 ± 0.003	0.00	−0.60 ± 0.72	22.75 ± 22.28
			w'	0.04 ± 0.002	0.00	0.01 ± 0.12	7.30 ± 1.04

upwards into the water column, and highlight a prevalence of motions are directed offshore (negative u') contributing to the erosion of the barrier face. However, when considering only the fluctuating part, Q2- and Q4- motions become relatively more frequent. For the accretive wave runs, filtering out the wave signal appears to result in nearly equal proportions for each of the 4 types of motion in all planes. In the horizontal planes ($u'v'$), Q1 and Q4 structures associated with shoreward-directed motions skewed to the right are marginally emphasised; with all motions of a bursting sequence represented relatively equally. Collectively, ejections and sweeps contribute slightly more to the total Reynolds stress (56% in erosive, 57% in accretive) than the Outward and Inward interactions. If a threshold were applied to the stresses in the erosive runs, the occurrence of Sweeps and Ejections outweighs that of the weaker interactions by a factor of 1.6 for $H=2$ due to the observed dominance of particular quadrant events of higher magnitude in the erosive runs, compared to the nearly equal distribution (balance) of the four quadrant event motion in the accretive tests. Remarkably, the fractional contribution of ejections and inward interactions, and hence reduced thresholds,

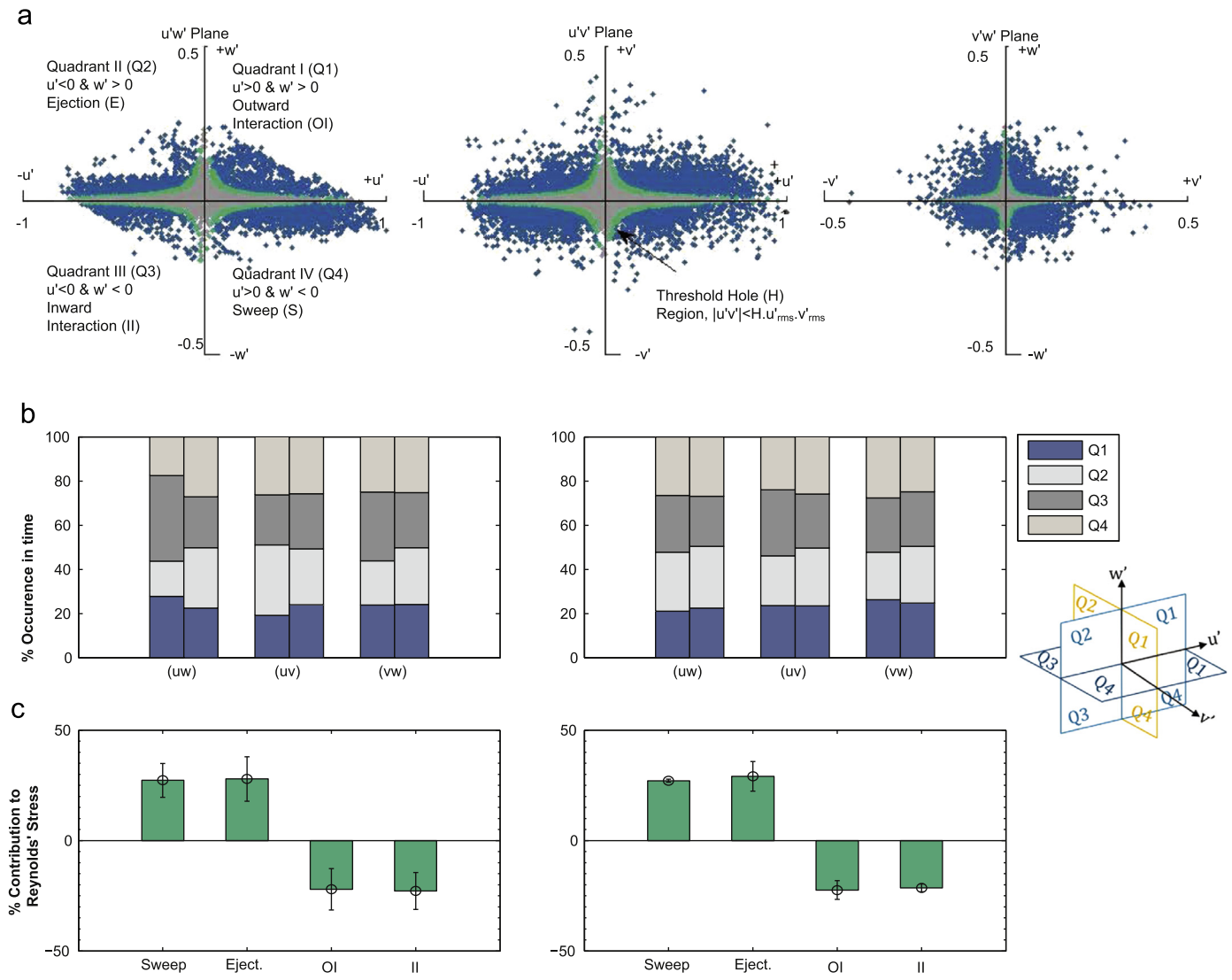

Fig. 4. (a) Quadrant analyses of instantaneous Reynolds' stresses in three planes for an example 8 min sub-record from wave series A3-01(Erosive). Areas delimited by hole sizes defined by $H=1$ (grey) and $H=2$ (green) are highlighted. (b) Average percentage of occurrence in time occupied by the 4 Quadrant-type events in each plane, in the erosive and accretive runs, before and after filtering the periodic signal, with $H=0$; and (c) average contribution to Reynolds' stress by the 4 types of motion in $(u'w')$ (For interpretation of the references to colour in this figure legend, the reader is referred to the web version of this article.).

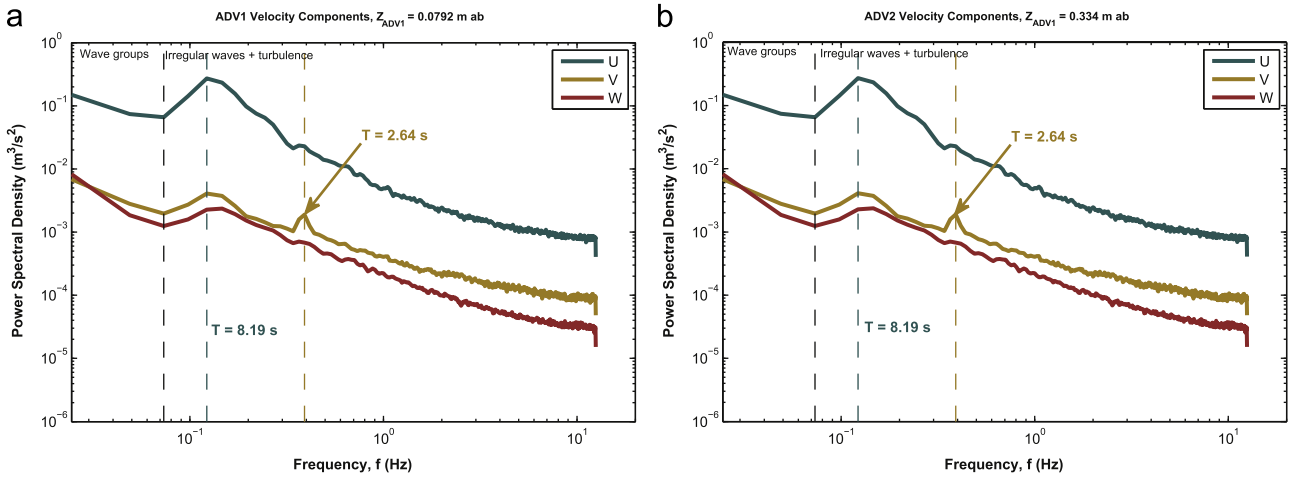

Fig. 5. Time series and spectral analysis of 3D fluctuating velocity components, in the streamwise/along-flume (dark green), crosswise (gold), and vertical (orange) for the entire experimental wave run A301 (Hs=0.8 m, Tp=8 s) measured (a) within; and (b) outside the oscillatory benthic boundary layer, δ_w. Power spectral densities calculated using Welch's method with a Hann window (2^{11} length) with 50% overlap, sampling frequency 25 Hz). Peak wave frequencies are indicated (For interpretation of the references to colour in this figure legend, the reader is referred to the web version of this article.).

is reportedly enhanced in sediment mixtures with high standard deviations in grain size distribution, like the coarsely skewed sediments present here; while that of the Q1 events becomes less significant (Wu and Jiang, 2007; Wu and Yang, 2004).

3.4. Spectral analysis of turbulence and suspension

Spectral analysis decomposes the measured turbulence data into waves of different periods (frequencies) and wavelengths, providing a suitable means of examining how these fluctuation are distributed from a statistical viewpoint (Tennekes and Lumley, 1972). The multitude of scales (both spatial and temporal) of turbulent eddies comprise a spectrum ranging from the macroscale (long period and spatially limited only by the dimensions of the flume/flow) to the high frequency microscale limited by viscosity, with the energy transfer being driven by vortex stretching (*ibid.*). The value of a spectrum at a certain frequency or wavelength equates to the mean energy of that wave, and as a result, it provides a means of assessing how eddies of different sizes exchange energy and how turbulence evolves with time. With turbulence being a largely three-dimensional problem, this necessitates construction of energy spectra in three dimensions (Cebeci and Smith, 1974). Fig. 5 shows the power spectral densities (PSD) of the three fluctuating velocity components (u'_{wave}) within and outside the boundary layer for the entire length of the erosive wave test (~ 180 min). These have been calculated using Welch's method with a Hann window with 50% overlap. The velocity spectra display a peak corresponding to a period of 8.19 s in all three components, as expected (design peak period being Tp=8 s). Nonetheless, a striking feature is a significant peak in the crosswise turbulence spectrum at both elevations, with a corresponding period of 2.64 s. This is also apparent in the accretive runs, as well as what seems to be higher order harmonics. Chu et al. (1991) have reported on unstable transverse shear flows leading to large scale turbulent motions across wide and shallow open channels (horizontal length scales significantly larger than water depth), induced by the growth of small scale disturbances induced by bed friction (critical value of 0.12–0.145) or depth variation. However, neither of these appear to be applicable in this case, given the relatively uniform cross section of the flume, and the lower wave-induced bed friction factors reported in Table 1, and some alternative mechanism must be at work.

Standing cross-waves (transverse waves) induced by symmetric wave makers in rectangular channels have been reported to occur with excitations at nearly twice one of the natural frequencies of the paddle due to nonlinear parametric resonance (Garrett, 1970; Miles, 1988). The first mode of oscillation for a rectangular channel of width, B=5 m, and water depth hs=2.5 m, occurs as half a wave with a node point at the centre of the flume, and two maxima(crests)/ minima(troughs) on either end (the rigid walls). Paterson (1983) presented the equations needed to calculate the associated wave number ($k = \pi/l$), and angular frequency ($\omega = ((\frac{\pi g}{B}).\tan h(\frac{\pi h_s}{B}))^{0.5}$), in which case the corresponding period in our case comes to exactly 2.64 s, matching perfectly the peak in the spectrum, with higher order oscillations also observed in the spectra. The existence of a stable transverse standing wave may also be a contributor to the observed asymmetry and high kurtosis of the crosswise velocity fluctuation. Similar cross waves have been generated in much larger wave basins, such as the recent edge wave experiments at IH Cantabria (Coco, per comm.), but the existence of such waves on unconfined lengths of coast remains an open research question.

The spectra of turbulence components both within and outside the boundary layer were also constructed for each of the erosive and accretive sub-runs, following the same methodology. No significant peaks were apparent in the lower frequency range (periods longer than the peak wave period); suggesting limited effect of wave groups in the turbulence signal. When the wave signal is filtered out, no sharply-defined peaks could be attributed to the harmonics of the applied wave forcing (progressive waves along the channel); but the highest variances lie between the first harmonics of the progressive wave and the second harmonics of the transverse standing wave. This shows that the turbulent energy lies within the wave frequency range, as has been seen in studies of the inner surf zone (Ting and Kirby, 1996). Local peaks corresponding to the second harmonics of both could be discerned, indicating induced turbulence at flow reversal, often associated with the vortex shedding process. When shown in wave number space, these fluctuations approach the Kolmogorov–Obukhov $-5/3$ relation within the inertial dissipation sub-range (Frisch, 1995; Stapleton and Huntley, 1995). Note, however, that spectral analysis with Fourier transforms are limited by the Nyquist frequency, limiting detected frequencies to those higher than half the sampling frequency of the instruments (Glover et al., 2011), in this case, 12.5 Hz.

Taylor's theory of "frozen turbulence" suggests that turbulence is advected by the mean current more rapidly than it is developing temporally, and as a result, the measured turbulence fluctuations at a fixed point would correspond better to the spatial rather than temporal changes in velocity (Taylor, 1938; Wyngaard and Clifford, 1977). In wavenumber (k) space, where $k = 2\pi f/\bar{U}$, the spectral energy for all eddies of size $\frac{2\pi}{k}$ is roughly proportional to $E(k)$ times the width of the spectrum (Tennekes and Lumley, 1972). The strain rate of an eddy is thus a function of its wavenumber, which is often scaled by the measuring height, z, into a non-dimensional form, k^*. Hence, by normalising the k^*-weighted spectra into an energy/variance preserving form, whereby an equal area under the curve=equal energy, it is possible to calculate the dominant eddy sizes, following (Soulsby, 1977, 1983; Soulsby et al., 1984).This was applied to the turbulence spectra, before smoothing with a moving-average algorithm, as shown in Fig. 6, where error bars represent standard deviation for the averaged sub-runs. The peaks indicate similar scaling in the crosswise and vertical components near the bed for both erosive and accretive runs (~0.05 m), and slightly larger scales along the flow in the accretive runs (~0.18 m) as opposed to the erosive ones (~0.12 m). Along the direction of wave propagation, these vary over a range of scales higher in the water column (at ADV2) for the erosive runs (between 0.1–0.3 m), and increase substantially in the accretive ones (~1 m streamwise, 0.2 m in the crosswise and vertical). The vertical excursions scale well with the wave boundary layer thickness in both erosive and accretive runs. Overall, the wavenumbers contributing to horizontal motions are smaller than those contributing the vertical motions.

The power spectral densities of sediment backscatter at 5 elevations above the bed are presented in Fig. 7, for all of the analysed sub-runs. The suspension spectra in both erosive and accretive runs exhibit multiple or broad peaks near the bed and higher in the water column, with frequencies corresponding to the second harmonics of the progressive waves, as well those of the transverse waves. This implies suspension of sediment is associated with the shedding of vortices from bedforms within the boundary layer (O'Hara Murray et al., 2011), and extending much higher in the water column, potentially due to pairing of vortices (Williams et al., 2007). This claim is supported by the bed morphology, stable, 2D vortex ripples with no considerable migration over the duration of each 8 min sub-run. It does not appear, however, that wave groups play a role in this case, as has been reported in irregular waves over evolving bedforms (O'Hara Murray et al., 2012). The peaks corresponding to the transverse wave properties

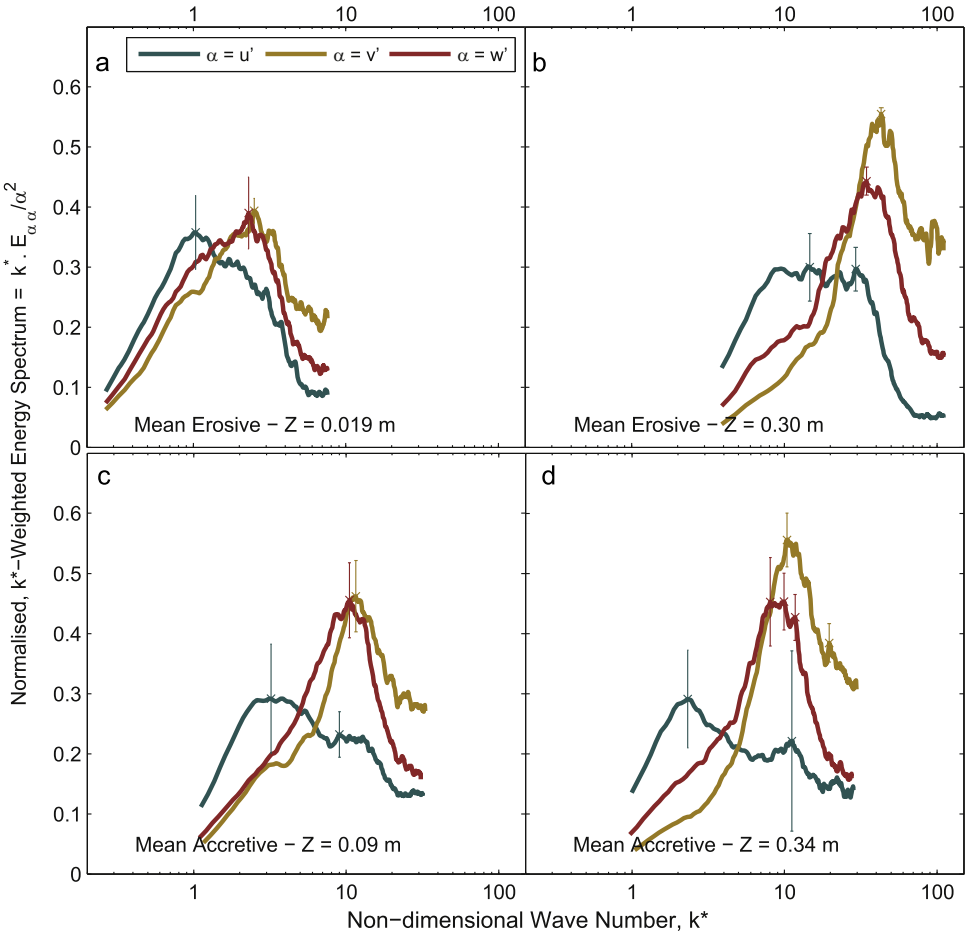

Fig. 6. Average normalised non-dimensional wavenumber (K*)-weighted turbulent energy spectra of the three turbulence components, (u', dark green), crosswise (v', gold), and vertical (w', orange) turbulence components; measured within the benthic boundary layer (a), and (c) and outside the wave boundary (b), and (e), for the erosive and accretive wave runs, respectively (For interpretation of the references to colour in this figure legend, the reader is referred to the web version of this article.).

highlight the nonlinearity and three dimensionality of the sediment suspension process, both in terms of sediment pick up and maintenance of suspension higher in the water column. While the spectra in the lower frequency range are steeper near the bed, and relatively flatter higher up, these trends reverse at the higher frequency scales. This may suggest that the stirring of sediment near the bed is driven by the mean flow properties, but the waves do not play a significant role in retaining sediment in suspension. Steeper slopes of energy spectra at higher frequencies are often associated with coherent structures (Maltrud and Vallis, 1991), and as such, higher frequency turbulence may be the dominant mechanism at work at higher elevations above the bed, and hence key to modelling suspension of sediment outside the boundary layer.

The time dependency between the horizontal shear stress and sediment concentration also varies with elevation (Venditti and Bennett, 2000). Given the existence of an undertow in this case (~ 0.2 m/s offshore), vertical variations are expected in spilling breakers (erosive runs) as turbulence gradually spread downwards by moderate scale eddies from the surface roller, but not in plunging breakers where downward generated large scale vortices create strong vertical mixing (Ting and Kirby, 1994, 1996). Plunging breakers are dominated by orbital wave motion and turbulence is thus convected landwards, favouring accretion and indicating strong dependence on history downstream, while spilling breakers are dominated by the undertow moving sediments seaward (*ibid.*).

The erosion process, locally, is likely to be affected by the passage of large scale coherent structures with low occurrence probability (Adrian and Marusic, 2012), and there is growing evidence that the concept of bursting as a violent ejection is replaced by the concept of "slowly evolving" fast packets of vortices creating sequences of ejecting/sweeping events each associated with one of the vortices (Christensen and Adrian, 2001; Jimenez, 2012; Jiménez, 2013). We conjecture that the succession of convected or locally generated intermittent bursting or sweeping motions would dictate whether the entrained sediment has enough time to settle, is amplified by added suspensions, or swept back to the bed. This governs the frequency response of suspension events and how they interfere with turbulent fluctuations. Wavelet analysis may offer some clues as it provides information not only on frequency scales, but their spatial (occurrence in time) variability too. Whether erosion or accretion is observed at the barrier is then governed by the mean currents which could transport the agitated sediments above the bed. This is typical of a stochastic process where particle concentration is closely related to that of the turbulence fluctuation arising from large eddies as shown in the work of (Liu et al., 2012). Such episodic events could occur at any location of the bed, with short periods of considerable sediment movement intermingled with long periods of negligible transport (Dey et al., 2012).

3.5. *Wavelet analysis of Reynolds' stresses and sediment resuspension*

Fig. 8 shows the power spectra highlighting time–frequency

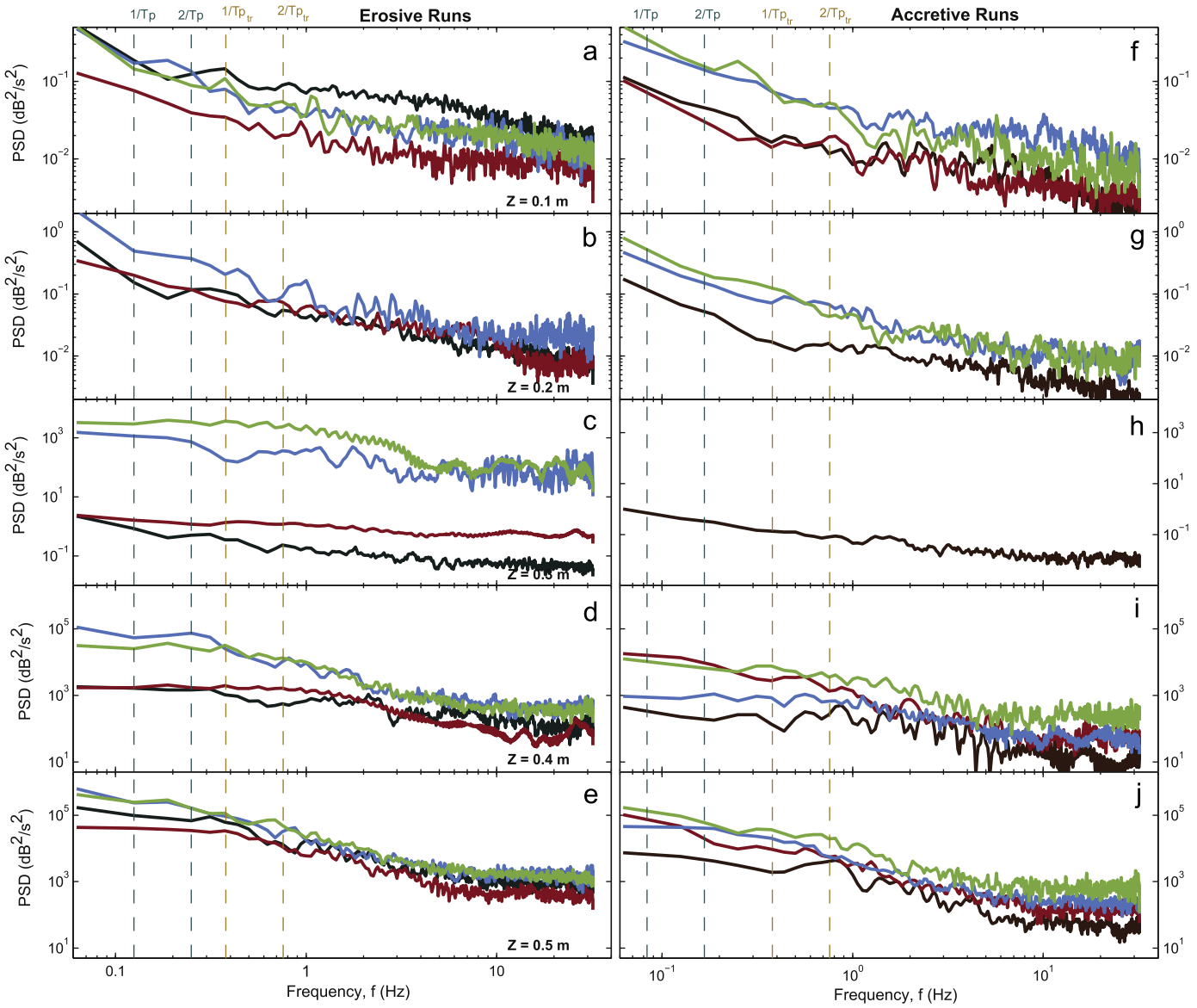

Fig. 7. Power spectral densities (PSD) of the suspended sediment backscatter at 5 different elevations above the bed, for all the analysed erosive (left panel), and accretive (right panel) wave runs. The first (1/Tp) and second (2/Tp) harmonics of the progressive wave forcing, and the transverse standing waves are shown by the green and golden dashed lines, respectively (For interpretation of the references to colour in this figure legend, the reader is referred to the web version of this article.).

characteristics of the three Reynolds' stresses and sediment suspension obtained through continuous wavelet transforms for an example sub-run from the erosive series. Matching results are evident in the other runs (not shown for brevity), and the behaviour reported hereafter is true for both erosive and accretive runs. In this figure, the left panels pertain to measurements at the level of ADV1 (within the wave boundary layer), while results from measurements corresponding to ADV2 (outside the boundary layer) are displayed on the right panels. The figure shows the time series of the three Reynolds' stresses in 3 orthogonal planes of motion: ($u'w'$) in the streamwise-vertical plane (bed normal along the direction of wave propagation), ($u'v'$) in the horizontal plane, and ($v'w'$) in the crosswise-vertical plane, having filtered out the wave-signal from the fluctuating turbulence components, as well as their energy spectra (obtained by Fourier transforms, as discussed in Section 2.4. The time-series of continuous wavelet transforms (CWT) for each of the stresses in the time–frequency domain, are presented subsequently in the same order, together with their global spectral power (integrated variance). We opted to present the inverse frequencies (i.e. periods) on the vertical axes, to facilitate the discussion when related to wave properties. The global power pertains to time averages, if we were to take a vertical slice through the wavelet plot, and average all the local wavelet spectra (Torrence and Compo, 1998).

Finally, the lower two panels show the time series of vertical suspension (logarithmic backscatter, higher values in warmer colours) profiles below the ABS sensor head, the power spectral densities of suspended sediment concentration at the level of the corresponding ADV (ADV1 on the left, ADV2 on the right), and the related continuous wavelet transform of the suspension time series at that elevation, together with its global spectral power. In these plots, warmer colours indicate higher power (variance), the white-shaded region represents the cone of influence where edge effects may distort the image, and the thick contours represent the 95% confidence limit (5% significance against red noise). Note that at higher periods (low frequency events), the power falls within the cone of influence, limiting our ability to investigate the temporal evolution of the particular peak frequencies reported in Section 2.4. Therefore, we are restricted to investigating very high frequency events occurring at time scales up to 2 s. This limitation

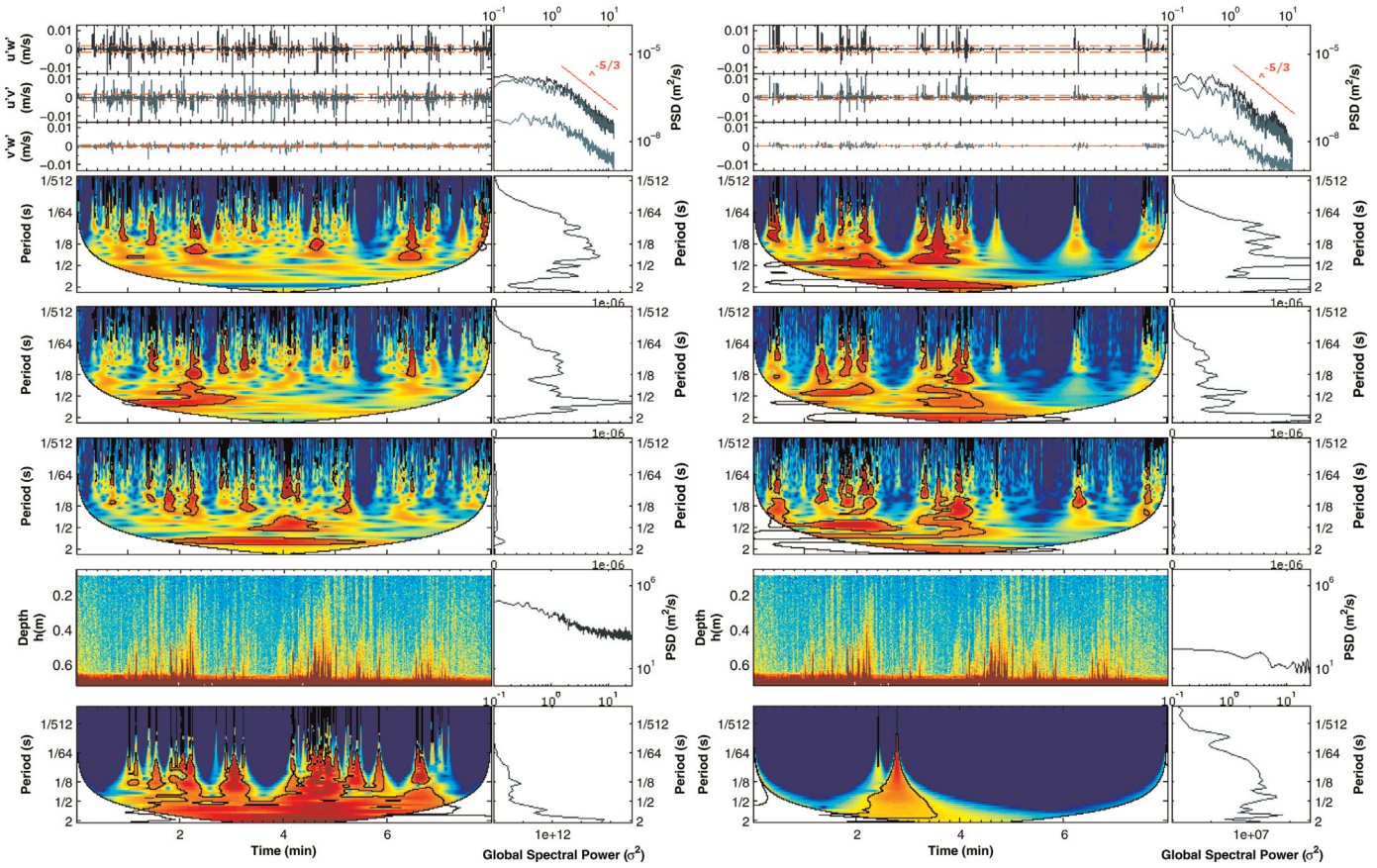

Fig. 8. Time–frequency properties of the three instantaneous Reynolds stresses ($u`w`$, $u`v`$, and $v`w`$) and suspended sediment concetrations, measured within (left handside), and outside (right handside) the benthic wave boudnary layer. In each panel, the top three subplots show the time series of the three aforementioned stresses, respectively, together with their frequency spectrum (through a Fourier transform) in which universal Kolmogorov–Obukhov rate of inertial dissipation (-5/3) is represented by the red line. The following three sub-panels present the time-series of continuous wavelet transforms (CWT) for each of the stresses in the time–frequency domain, presented in the same order, together with their global spectral power (integrated variance) across the various frequency scales (inverse period). Subsequently, the lower two sub-panels show the time series of vertical suspension (logarithmic backscatter, higher values in warmer colours) profiles below the ABS sensor head, the power spectral densities of suspended sediment concentration at the level of the corresponding ADV (ADV1 on the left, ADV2 on the right), and the related continuous wavelet transform of the suspension time series at that elevation, together with its global spectral power. In the time–frequency domains, warmer colours indicate higher power (variance), the white-shaded region represents the cone of influence where edge effects may distort the image, and the thick contours represent the 95% confidence limit (5% significance against red noise) (For interpretation of the references to colour in this figure legend, the reader is referred to the web version of this article.).

arises from Heisenberg's uncertainty principle, which dictates that one cannot obtain arbitrary good localisation in both time and frequency, and a trade–off must exist whereby spatial resolution is bad at large scales while scale (frequency) resolution is bad in the small scales (Farge et al., 1996; Foufoula-Georgiou and Kumar, 1994; Grinsted et al., 2004; Lau and Weng, 1995). Having said that, it is clear that most of the power (variance) in concentration lies within the lower frequency range (high period) associated with the mean flow properties for both stresses and suspensions near the bed.

The Fourier-transform-derived spectra of Reynolds stresses show that they approach the universal Kolmogorov–Obukhov -5/3 relation corresponding to the inertial dissipation sub-range (Frisch, 1995, Stapleton and Huntley, 1995). While this is still true for stresses measured outside the boundary layer (by ADV2), it is interesting that a secondary peak appears within the higher frequency range, suggesting enhanced turbulence with smaller scales of motion. The CWT results show that 'powerful' (*i.e.* high variance) turbulent events occur intermittently throughout the records, in slowly evolving clusters that persist over short times in the dominant flow direction (streamwise-vertical) near the bed, and for longer times (significant from a turbulence perspective, up to several minutes), higher up in the water column, and at lower frequencies. The larger clusters fall over short bands of frequency scales (specific periods, predominantly 0.5 and 2 s); while the fast-evolving clusters extend over a bigger range of frequency scales (primarily between 1/2 and 1/64 s) before diminishing. This may indicate breakup of the larger eddies into smaller and smaller ones within the inertial dissipation range, before the energy is consumed by viscosity, as described by the classical turbulence cascade which suggests that inertia results in stretching and rapid breakup of vortices into many smaller, excited degrees of freedom, until energy is dissipated through viscosity (Frisch, 1995; Kolmogorov, 1991; Sreenivasan and Antonia, 1997; Tennekes and Lumley, 1972). The turbulent clusters within the streamwise-vertical plane (hereafter referred to as the dominant plane of motion) have the highest power, which appears to be uniformly distributed across the aforementioned frequency range. In the horizontal plane, such events are also considerably powerful, but tend to spike closer to the lower end of the range, at periods comparable to the harmonics of the transverse standing wave. In the crosswise-vertical plane, significant clusters of turbulent stresses occur for longer times, but their power is negligible compared to those of the other two planes of motion.

Periods associated with a succession of powerful turbulent events are very closely followed by periods of powerful, high frequency suspensions, extending from the larger scales observed in the low frequency range (periods up to 4 s/outside the cone of influence), and exponentially extending over smaller and smaller scales (higher frequencies/lower periods) before decaying as

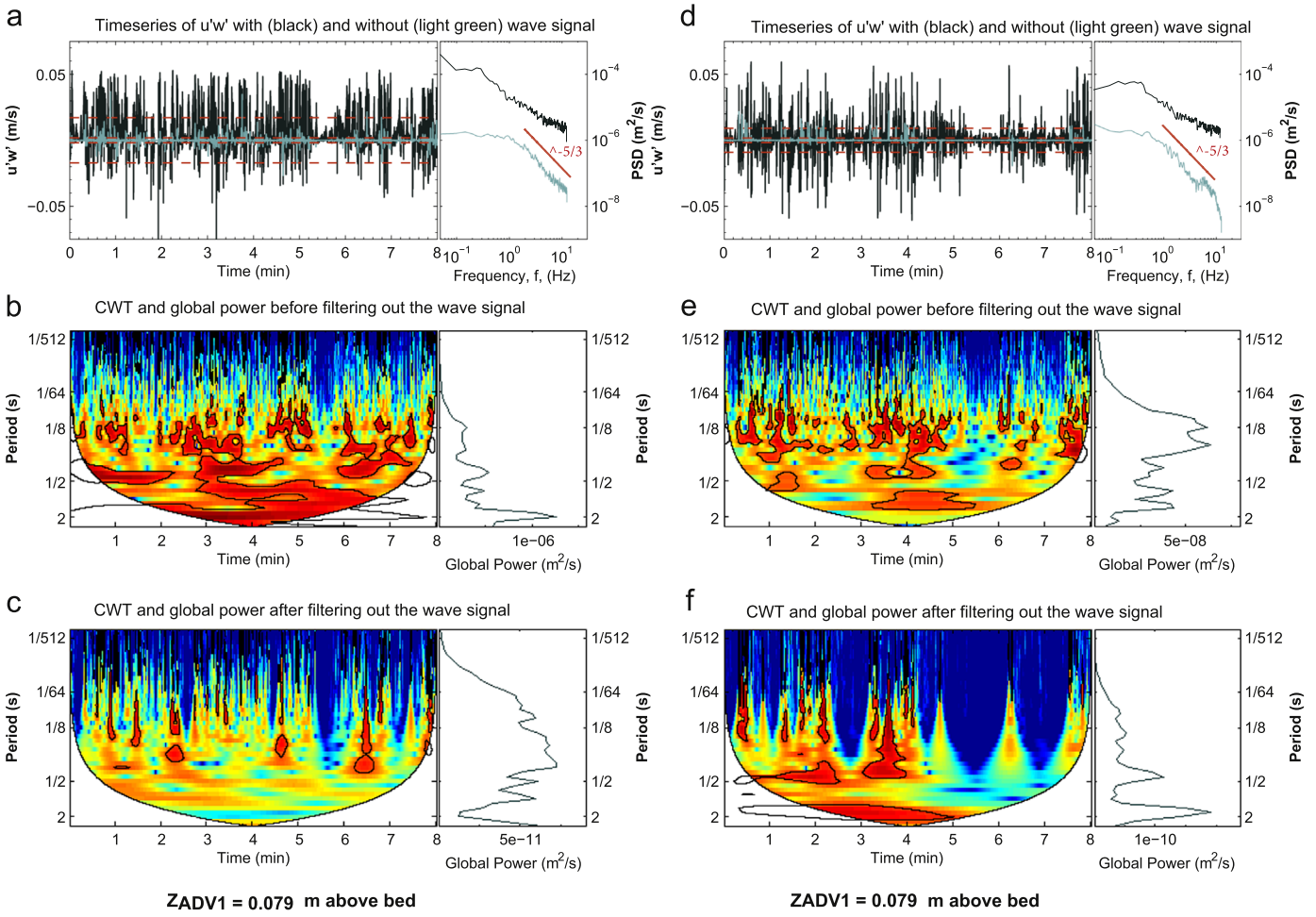

Fig. 9. Influence of wave-signal on the time–frequency properties of Reynolds stress in the streamwise-vertical plane ($u'w'$), measured near the bed (left panel), and putside the wave boundary layer (right panel). In each panel, top sub-plots (a), and (d) show the time series of Reynolds stress (before and after filtering out the wave signal), together with its corresponding frequency spectrum (by Fourier transform). The dashed horizontal lines indicate $\pm 1.\sigma$ (standard deviation). The rate of inertial dissipation is shown by the sloping red line in the frequency plot. The middle (b) and (e) and bottom (c) and (d) sub-panels sow the time-series of continuous wavelet transform (CWT) of the Reynolds stress before and after filtering out the wave signal, respectively, together with the corresponding global power spectrum. In the time–frequency domains, warmer colours indicate higher power (variance), the white-shaded region represents the cone of influence where edge effects may distort the image, and the thick contours represent the 95% confidence limit (5% significance against red noise).

turbulence clusters cease. This may be explained as cumulative, highly-varied suspensions in response to the faster turbulent perturbations, where continuing upward diffusions exceeds the settling velocity of the entrained particles. Even the more sporadic suspension events of lower significance appear to conform to the aforementioned behaviour, if the wave signal is not excluded from the turbulent fluctuation (shown in Fig. 9). Comparing the two figures shows that the bulk of sediment suspension events can be attributed to wave-induced turbulent fluctuations of low frequency (only higher order harmonics of the wave period (4/Tp) are visible outside the cone), where most of the global power is retained. Yet, the short-lasting suspension clusters scale with the rapidly decaying high frequency turbulence. This perhaps highlights a hysteresis effect, where a dynamic lag occurs between the driving mechanism in terms of the formation, and evolution of a vortex structure and ensuing bursting sequence, and the response in terms of sediment resuspension. These periods of high power and long suspension events often appear directly following significantly large amplitude variations in water surface elevation of up to 1.4 m, inferred from the pressure gauge (not shown here). This suggests that the initiation of a large suspension event beyond the mean flow frequency range is instigated by the passage of the more energetic waves within the JONSWAP spectrum, or with early wave breaking events. Its persistence in the higher frequency range is then dictated by the supply of fluid momentum; either generated through bed friction, or injected downwards by the spilling breakers of these erosive wave runs. Higher in the water column, few suspension events are observed at the high frequencies, and where they do occur, these are characterised by a rapid expanse of the scales followed by rapid decay (dissipation of energy). In the accretionary runs, the turbulence events span even wider scales and occur over longer times, corresponding to significant fluctuations in the time series of the turbulence components (and water elevation). These clusters can be interpreted as large scale, uniform momentum regions convected or formed near the bed in the low frequency range. As they evolve, they cause small scales vortices that experience sudden and short lived changes in velocity, manifest by short duration events of high variance, that appear to be 'shooting out' of the larger clusters and spanning a significant extent in the high frequency range in these plots. This change can cause higher shear stresses compared with the mean flow, as reported by (Hutchins et al., 2011; Mathis et al., 2011), and as such, are often followed by significant suspension clusters.

To examine the hypothesis thus posited, cross-wavelet transforms (XWT) of the Reynolds stresses in three planes, and the recorded suspended sediment concentrations are presented in Fig. 10, both within and outside the wave boundary layer. Note that

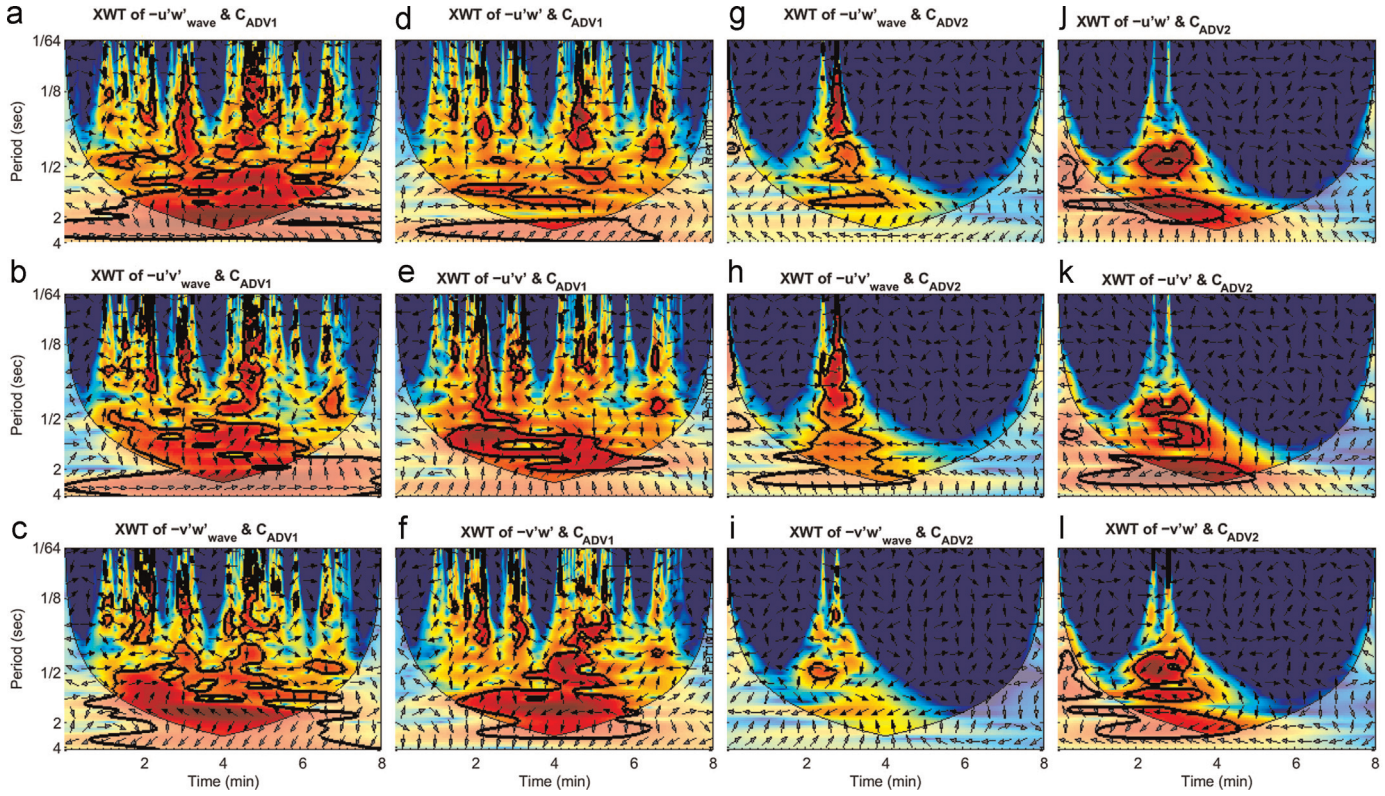

Fig. 10. Cross wavelet transforms of instantaneous 3 dimensional Reynolds Stresses and (downsampled) Sediment Concentrations within (ADV1) and outside (ADV2) the bottom wave boundary layer during erosive wave run A3-01 (2nd), before and after filtering out the periodic signal from the turbulent component. The light-shaded region represents the cone of influence where edge effects may distort the image. The thick contours represent the 95% confidence limit (5% significance against red noise). The relative phase is shown in arrows (with right arrow indicating inphase, left arrows indicating anti-phase, and vertical arrows indicate Reynolds stresses leading by 90°.

this can only be done after down-sampling the 64 Hz suspension record to match the sampling frequency (25 Hz) of the ADVs. The significance levels are tested against red noise generated by a first order autoregressive model following Grinsted et al. (2004), and denoted by the thick contours. The lightly shaded area represents the cone of influence. The XWT has been applied to the turbulent fluctuations before (denoted by the "wave" subscript); and after filtering out the wave signal for each of the Reynolds' stresses in every plane. The phase relationship between the two signals (stress and concentration) is shown by the arrows, whereby right arrows indicate signals are in-phase, left-pointing arrows indicate anti-phase, and vertical arrows suggest that the Reynolds stresses lead concentration by 90 degrees phase shift, testing the coherence of the transform (Grinsted et al., 2004). Here we notice common features as observed in Figs. 8 and 9, where suspension events and turbulent stresses share high common power at a range of scales. At the smaller frequency scales, these regions of significant common power occur for most of the time near the bed and in all three planes, particularly when the wave signal is present, albeit falling within the cone of influence. The powerful events at lower periods of 2–4 s are phase locked, implying causality between the wave-induced turbulence and the ensuing suspension, but with no notion of time lag. However, no robust measure of whether this may be an artefact of the dominance of one of the signals, or not, is carried out (e.g. combining clustered wavelet spectra with maximum covariance analysis presented by Rouyer et al. (2008)). The higher-frequency 'wave-contaminated' scales appear to be less coherent in all planes both near the bed and outside the boundary layer. However, once the wave signal is filtered out, the turbulent fluctuations outside the boundary layer appear to be predominant in driving the suspensions at this level, with the highest power, although being phase-locked in the opposite direction.

Nonetheless, the wavelet analyses presented collectively support the conjecture proposed, postulating a mechanism in which successive intermittent bursting motions play a significant role in moving and maintaining sediments in suspension. In time–frequency space, it is shown how most of the momentum exchange, and ensuing suspension, lies within the low frequency range (high periods) dictated by the mean flow properties. The passage of intermittent and relatively large momentum regions of uniform spectral properties at higher frequencies, plays a direct role in sediments suspensions which exhibit significant variability within the higher frequency range. As these regions, which signify the passage of a coherent structures, persist for a considerable amount of time, suspensions near the bed are amplified before decaying as the supply of momentum by these turbulent structures ceases. Within a given cluster of turbulence, both stresses and suspensions span a certain range of frequencies, which may hint at a nonlinear modulation of both the amplitude and frequency of such small structures with the larger flow structures near the bed. Such behaviour in wall turbulence has been attributed to local changes in shear but not necessarily the spatial and temporal structure of large flow events (Ganapathisubramani et al., 2012).

4. Conclusions

The aim of this study was to provide insight into the temporal and scale relationships between wave-generated boundary layer turbulence and event-driven sediment transport in oscillatory flow. The work was carried out in the nearshore of a prototype sandy barrier beach using data collected though the BARDEX II experiments for irregular erosive and accretive wave conditions.

Statistical analysis of the time series of velocity fluctuations show high anisotropy in the turbulence records, with strikingly peaky crosswise distributions and an intermittent nature of the momentum exchange. Quadrant analysis quantified the intermittency of Reynolds stresses in three planes. The fractional contribution to stress in terms of occurrence times reveal the dominance of shoreward directed motions in accretionary waves, and sweeping motion seawards under erosive conditions; as well as a tendency to move sediments to one side of the channel, as observed in the skewness in the turbulence records. Spectral analysis further reveal a contribution to the crosswise velocity fluctuations from a standing transverse waves across the flume, resulting from the unique flume geometry, whose signal was reflected in the suspension records. The entrainment and maintenance of sediments in suspension through the bursting sequence is conjectured to be associated with the passage of convected or locally formed packets of eddies which describe intermittent large coherent structures within the flow. Wavelet analysis further confirmed that powerful (high variance) turbulence occurred in slowly evolving clusters over time, which were closely followed by periods of powerful suspensions near the bed, emerging from the integral (dominant) scales at low frequencies, and decaying with memory in time, after the cessation of the turbulent perturbation. The larger wave-induced motions and nearbed suspension are phase-locked in the lower frequency range, suggesting that waves acts to stir up and initiate entrainment of sediment in the boundary layer. Outside the boundary layer, turbulent fluctuations are dominant in driving and maintaining high frequency suspensions as long as momentum is supplied. In summary:

(a) Turbulence in irregular oscillatory flow is highly anisotropic, and characterised by intermittent momentum exchanges, describing a spatially varied bursting sequence which may be traced in three dimensions, and the temporal variability of which dictates the net direction of sediment transport in erosive and accretive runs.
(b) The bursting sequence is associated with the passage of large scale slowly evolving structures, which can modulate the frequency of small scale (higher frequency) events. The persistence of such perturbations is associated with a cumulative suspension events spanning the frequency scales, which observe a hysteresis effect decaying as the motion cease. Wave motion plays a dominant role in entrainment of sediment within the boundary layer, and high frequency turbulence resulting from momentum transfer into smaller scales helps maintain particles in suspension.
(c) Flume studies of turbulence and sediment transport must consider the effect of flow geometry which may induce artefact hydrodynamics that can significantly have an influence on the processes being investigated. The transverse standing wave reported in this study is a case in point, whereby a secondary process at work was evident in the statistical and spectral properties of turbulence and suspension events observed.

Acknowledgements

The data reported here were collected in the Delta Flume, Deltares (The Netherlands) as part of the EU-funded Barrier Dynamics Experiments II – BARDEX II project (HYDRALAB IV Contract no. 261520 by the European Community's Seventh Framework Programme). Special thanks are due to Dr. Gerald Muller for information on transverse standing waves. The work reported here forms part of the first author's PhD research, jointly funded by the Graduate School at National Oceanography Centre, Southampton; Faculty of Engineering and the Environment; University of Southampton; Southampton Marine and Maritime Institute; and HR Wallingford Ltd.

References

Aagaard, T., Hughes, M.G., 2010. Breaker turbulence and sediment suspension in the surf zone. Mar. Geol. 271, 250–259.
Aagaard, T., Jensen, S.G., 2013. Sediment concentration and vertical mixing under breaking waves. Mar. Geol. 336, 146–159.
Adrian, R.J., 2007. Hairpin vortex organization in wall turbulence. Phys. Fluids 19, 41301–41316.
Adrian, R.J., Marusic, I., 2012. Coherent structures in flow over hydraulic engineering surfaces. J. Hydraul. Res. 50, 451–464.
Alfredsson, P.H., Johansson, A.V., 1984. On the detection of turbulence-generating events. J. Fluid Mech. 139, 325–345.
Amoudry, L.O., Bell, P.S., Thorne, P.D., Souza, A.J., 2013. Toward representing wave-induced sediment suspension over sand ripples in RANS models. J. Geophys. Res.: Oceans.
Bagnold, R.A., Taylor, G., 1946. Motion of waves in shallow water. Interaction between waves and sand bottoms. Proc. R. Soc. Lond. Ser. A. Math. Phys. Sci. 187, 1–18.
Bennett, S.J., Bridge, J.S., Best, J.L., 1998. Fluid and sediment dynamics of upper stage plane beds. J. Geophys. Res.: Oceans 103, 1239–1274.
Berry, M.V., Greenwood, D.A., 1975. On the ubiquity of the sine wave. Am. J. Phys. 43, 91.
Blackwelder, R.F., Kaplan, R.E., 1976. On the wall structure of the turbulent boundary layer. J. Fluid Mech. 76, 89–112.
Bogard, D.G., Tiederman, W.G., 1986. Burst detection with single-point velocity measurements. J. Fluid Mech. 162, 389–413.
Buscombe, D., 2012. MATSCAT version 1: MATLAB toolbox for the aquascat 1000 acoustic backscatter sensor. Technical Report for the School of Marine Science and Engineering. Plymouth University, p. 6.
Cao, Z., 1997. Turbulent bursting-based sediment entrainment function. J. Hydraul. Eng. 123, 233–236.
Carstensen, S., Sumer, B.M., Fredsoe, J., 2010. Coherent structures in wave boundary layers. Part 1. Oscillatory motion. J. Fluid Mech. 646, 169–206.
Carstensen, S., Sumer, B.M., Fredsøe, J., 2012. A note on turbulent spots over a rough bed in wave boundary layers. Phys. Fluids (1994-present) 24, 115104.
Cebeci, T., Smith, A.M.O., 1974. Analysis of Turbulent Boundary Layers. Academic Press, New York; London.
Cellino, M., Lemmin, U., 2004. Influence of coherent flow structures on the dynamics of suspended sediment transport in open-channel flow. J. Hydraul. Eng. 130, 1077–1088.
Choi, W.C., Guezennec, Y.G., 1990. On the asymmetry of structures in turbulent boundary layers. Phys. Fluids A: Fluid Dyn. (1989–1993) 2, 628–630.
Christensen, K.T., Adrian, R.J., 2001. Statistical evidence of hairpin vortex packets in wall turbulence. J. Fluid Mech. 431, 433–443.
Chu, V., Wu, J., Khayat, R., 1991. Stability of transverse shear flows in shallow open channels. J. Hydraul. Eng. 117, 1370–1388.
Clifton, H.E., Dingler, J.R., 1984. Wave-formed structures and paleoenvironmental reconstruction. In: Greenwood, B., Davis, R.A. (Eds.), Developments in Sedimentology. Elsevier, pp. 165–198.
Daubechies, I., 1990. The wavelet transform, time–frequency localization and signal analysis. IEEE Trans. Inf. Theory 36, 961–1005.
De Stefano, G., Vasilyev, O.V., 2012. A fully adaptive wavelet-based approach to homogeneous turbulence simulation. J. Fluid Mech. 695, 149–172.
Deleuze, J., Audiffren, N., Elena, M., 1994. Quadrant analysis in a heated-wall supersonic boundary layer. Phys. Fluids (1994-present) 6, 4031–4041.
Dey, S., Das, R., Gaudio, R., Bose, S., 2012. Turbulence in mobile-bed streams. Acta Geophys. 60, 1547–1588.
Dyer, K.R., Soulsby, R.L., 1988. Sand transport on the continental shelf. Annu. Rev. Fluid Mech. 20, 295–324.
El Khoury, G.K., Pettersen, B., Andersson, H.I., Barri, M., 2010. Asymmetries in an obstructed turbulent channel flow. Phys. Fluids (1994-present) 22, 095103–095113.
Elgar, S., Raubenheimer, B., Guza, R.T., 2001. Current meter performance in the surf zone*. J. Atmos. Oceanic Technol. 18, 1735–1746.
Elgar, S., Raubenheimer, B., Guza, R.T., 2005. Quality control of acoustic Doppler velocimeter data in the surfzone. Meas. Sci. Technol. 16, 1889.
Farge, M., 1992. Wavelet transforms and their applications to turbulence. Annu. Rev. Fluid Mech. 24, 395–458.
Farge, M., Kevlahan, N., Perrier, V., Goirand, E., 1996. Wavelets and turbulence. Proc. IEEE 84, 639–669.
Farge, M., Pellegrino, G., Schneider, K., 2001. Coherent vortex extraction in 3D turbulent flows using orthogonal wavelets. Phys. Rev. Lett. 87, 054501.
Farge, M., Schneider, K., Pellegrino, G., Wray, A.A., Rogallo, R.S., 2003. Coherent vortex extraction in three-dimensional homogeneous turbulence: comparison between CVS-wavelet and POD-Fourier decompositions. Phys. Fluids (1994-present) 15, 2886–2896.
Feddersen, F., 2010. Quality controlling surf zone acoustic doppler velocimeter

observations to estimate the turbulent dissipation rate. J. Atmos. Ocean. Technol. 27, 2039–2055.
Fiedler, H.E., 1988. Coherent structures in turbulent flows. Prog. Aerosp. Sci. 25, 231–269269.
Foufoula-Georgiou, E., Kumar, P., 1994. Wavelets in Geophysics. Academic Press, San Diego, CA.
Frisch, U., 1995. Turbulence: the legacy of A.N. Kolmogorov. Cambridge University Press, Cambridge.
Ganapathisubramani, B., Hutchins, N., Monty, J.P., Chung, D., Marusic, I., 2012. Amplitude and frequency modulation in wall turbulence. J. Fluid Mech. 712, 61–91.
Garrett, C.J.R., 1970. On cross-waves. J. Fluid Mech. 41, 837–849.
Gheisi, A., Alavimoghaddam, M., Dadrasmoghaddam, A., 2006. Markovian–Octant analysis based stable turbulent shear stresses in near-bed bursting phenomena of vortex settling chamber. Environ. Fluid Mech. 6, 549–572.
Glover, D.M., Jenkins, W.J., Doney, S.C., 2011. Modeling Methods for Marine Science. Cambridge University Press, Cambridge.
Goring, D., Nikora, V., 2002. Despiking acoustic doppler velocimeter data. J. Hydraul. Eng. 128, 117–126.
Goring, D., Nikora, V., 2003. Closure to "Depiking Acoustic Doppler Velocimeter Data" by Derek G. Goring and Vladimir I. Nikora. J. Hydraul. Eng. 129, 487–488.
Grigoriadis, D.G.E., Balaras, E., Dimas, A.A., 2013. Coherent structures in oscillating turbulent boundary layers over a fixed rippled bed. Flow Turbul. Combust. 91, 565–585.
Grinsted, A., Moore, J.C., Jevrejeva, S., 2004. Application of the cross wavelet transform and wavelet coherence to geophysical time series. Nonlin. Process. Geophys. 11, 561–566.
Hardy, R.J., Best, J.L., Lane, S.N., Carbonneau, P.E., 2010. Coherent flow structures in a depth-limited flow over a gravel surface: the influence of surface roughness. J. Geophys. Res.: Earth Surf. 115, F03006.
Hare, J., Hay, A.E., Zedel, L., Cheel, R., 2014. Observations of the space-time structure of flow, turbulence, and stress over orbital-scale ripples. J. Geophys. Res.: Oceans.
Heathershaw, A., 1974. "Bursting" phenomena in the sea. Nature 248, 394–395.
Heathershaw, A.D., 1979. The turbulent structure of the bottom boundary layer in a tidal current. Geophys. J. R. Astron. Soc. 58, 395–430.
Hussain, A., 1986. Coherent structures and turbulence. J. Fluid Mech. 173, 303–356.
Hussain, A.K.M.F., 1983. Coherent structures—reality and myth. Phys. Fluids (1958–1988) 26, 2816–2850.
Hutchins, N., Monty, J.P., Ganapathisubramani, B., NG, H.C.H., Marusic, I., 2011. Three-dimensional conditional structure of a high-Reynolds-number turbulent boundary layer. J. Fluid Mech. 673, 255–285.
Ji, C., Munjiza, A., Avital, E., Ma, J., Williams, J.J.R., 2013. Direct numerical simulation of sediment entrainment in turbulent channel flow. Phys. Fluids 25, 056601–056620.
Jimenez, J., 2012. Cascades in wall-bounded turbulence. In: Davis, S.H., Moin, P. (Eds.), Annual Review Fluid Mechanics. Annu. Rev., Palo Alto, pp. 27–45.
Jiménez, J., 2013. Near-wall turbulence. Phys. Fluids (1994-present) 25.
Kawanisi, K., Yokosi, S., 1993. Measurements of turbulence and suspended sediment in tidal river. J. Hydraul. Eng. 119, 704–724.
Keylock, C.J., 2007. The visualization of turbulence data using a wavelet-based method. Earth Surf. Process. Landforms 32, 637–647.
Keylock, C.J., 2008. A criterion for delimiting active periods within turbulent flows. Geophys. Res. Lett. 35, L11804.
Keylock, C.J., Lane, S.N., Richards, K.S., 2014. Quadrant/octant sequencing and the role of coherent structures in bed load sediment entrainment. J. Geophys. Res.: Earth Surf. 119 2012JF002698.
Khujadze, G., Nguyen van yen, R., Schneider, K., Oberlack, M., Farge, M., 2011. Coherent vorticity extraction in turbulent boundary layers using orthogonal wavelets. J. Phys.: Conf. Ser. 318, 022011.
Kim, J., Moin, P., Moser, R., 1987. Turbulence statistics in fully developed channel flow at low Reynolds number. J. Fluid Mech. 177, 133–166.
Kline, S.J., Reynolds, W.C., Schraub, F.A., Runstadler, P.W., 1967. The structure of turbulent boundary layers. J. Fluid Mech. 30, 741.
Kolmogorov, A.N., 1991. Dissipation of energy in the locally isotropic turbulence. Proc. R. Soc. Math. Phys. Eng. Sci. 434, 15–17.
Kumar, P., Foufoula-Georgiou, E., 1997. Wavelet analysis for geophysical applications. Rev. Geophys. 35, 385–412.
Kuo, A.Y.-S., Corrsin, S., 1971. Experiments on internal intermittency and fine-structure distribution functions in fully turbulent fluid. J. Fluid Mech. 50, 285–319.
Lau, K.M., Weng, H., 1995. Climate signal detection using wavelet transform: how to make a time series sing. Bull. Am. Meteorol. Soc. 76, 2391–2402.
Laufer, J., 1975. New trends in experimental turbulence research. Annu. Rev. Fluid Mech. 7, 307–326.
Liu, J., Wang, Y., Yang, B., 2012. Wavelet packet analysis of particle response to turbulent fluctuation. Adv. Powder Technol. 23, 305–314.
Longo, S., Chiapponi, L., Clavero, M., Makela, T., Liang, D.F., 2012. Study of the turbulence in the air-side and water-side boundary layers in experimental laboratory wind induced surface waves. Coast. Eng. 69, 67–81.
Lozano-Duran, A., Flores, O., Jimenez, J., 2012. The three-dimensional structure of momentum transfer in turbulent channels. J. Fluid Mech. 694, 100–130.
Lu, S.S., Willmarth, W.W., 1973. Measurements of the structure of the Reynolds stress in a turbulent boundary layer. J. Fluid Mech. 60, 481–511.
Mallat, S., 1991. Zero-crossings of a wavelet transform. IEEE Trans. Inf. Theory 37, 1019–1033.
Maltrud, M.E., Vallis, G.K., 1991. Energy spectra and coherent structures in forced two-dimensional and beta-plane turbulence. J. Fluid Mech. 228, 321–342.
Massel, S.R., 2013. Ocean Surface Waves-Their Physics and Prediction, Second ed. World Scientific, Singapore.
Masselink Il Turner, G., Conley, D.C., Ruessink, G., Matias, A., Thompson, C., Castelle, B., Wolters, G., 2013. BARDEX II: Bringing the beach to the laboratory–again! In: Conley, D.C., Masselink, G., Russell, P.E., O'Hare, T.J. (Eds.), Proceedings of the 12th International Coastal Symposium. Journal of Coastal Research, pp. 1545–1550.
Mathis, R., Marusic, I., Hutchins, N., Sreenivasan, K.R., 2011. The relationship between the velocity skewness and the amplitude modulation of the small scale by the large scale in turbulent boundary layers. Phys. Fluids (1994-present) 23.
Miles, J., 1988. Parametrically excited, standing cross-waves. J. Fluid Mech. 186, 119–127.
Monin, A.S., Yaglom, A.M., 1971. Statistical Fluid Mechanics; Mechanics Of Turbulence. In: English (Ed.), 1971. MIT Press, Cambridge, Mass.
Mori, N., Suzuki, T., Kakuno, S., 2007. Noise of Acoustic Doppler Velocimeter Data in Bubbly Flows. J. Eng. Mech. 133, 122–125.
Morlet, J., 1983. Sampling theory and wave propagation. In: Chen, C.H. (Ed.), Issues in Acoustic Signal—Image Processing and Recognition. Springer, Berlin Heidelberg, pp. 233–261.
Morlet, J., Arens, G., Fourgeau, E., Giard, D., 1982a. Wave propagation and sampling theory; Part I, Complex signal and scattering in multilayered media. Geophysics 47, 203–221.
Morlet, J., Arens, G., Fourgeau, E., Giard, D., 1982b. Wave propagation and sampling theory; Part II, Sampling theory and complex waves. Geophysics 47, 222–236.
Nielsen, P., 1992. Coastal Bottom Boundary Layers and Sediment Transport. World Scientific, Singapore.
O'Hara Murray, R.B., Hodgson, D.M., Thorne, P.D., 2012. Wave groups and sediment resuspension processes over evolving sandy bedforms. Cont. Shelf Res. 46, 16–30.
O'Hara Murray, R.B., Thorne, P.D., Hodgson, D.M., 2011. Intrawave observations of sediment entrainment processes above sand ripples under irregular waves. J. Geophys. Res.: Oceans 116, C01001.
Offen, G.R., Kline, S.J., 1974. Combined dye-streak and hydrogen-bubble visual observations of a turbulent boundary-layer. J. Fluid Mech. 62.
Offen, G.R., Kline, S.J., 1975. Proposed model of bursting process in turbulent boundary-layers. J. Fluid Mech. 70, 209–228.
Okamoto, N., Yoshimatsu, K., Schneider, K., Farge, M., Kaneda, Y., 2007. Coherent vortices in high resolution direct numerical simulation of homogeneous isotropic turbulence: a wavelet viewpoint. Phys. Fluids (1994-present) 19.
Ölçmen, S.M., Simpson, R.L., Newby, J.W., 2006. Octant analysis based structural relations for three-dimensional turbulent boundary layers. Phys. Fluids (1994-present) 18.
Panton, R.L., 2001. Overview of the self-sustaining mechanisms of wall turbulence. Prog. Aerosp. Sci. 37, 341–383.
Paterson, A.R., 1983. A First Course in Fluid Dynamics. Cambridge University Press, Cambridge.
Robinson, S.K., 1991. Coherent motions in the turbulent boundary layer. Annu. Rev. Fluid Mech. 23, 601–639.
Rouyer, T., Fromentin, J., Stenseth, N., Cazelles, B., 2008. Analysing multiple time series and extending significance testing in wavelet analysis. Mar. Ecol. Prog. Ser. 359, 11–23.
Samanta, G., Housiadas, K.D., Handler, R.A., Beris, A.N., 2009. Effects of viscoelasticity on the probability density functions in turbulent channel flow. Phys. Fluids (1994-present) 21.
Schneider, K., Vasilyev, O.V., 2010. Wavelet methods in computational fluid dynamics. Annu. Rev. Fluid Mech. 42, 473–503.
Schoppa, W., Hussain, F., 2002. Coherent structure generation in near-wall turbulence. J. Fluid Mech. 453, 57–108.
Soulsby, R.L., 1977. Similarity scaling of turbulence spectra in marine and atmospheric boundary layers. J. Phys. Oceanogr. 7, 934–937.
Soulsby, R.L., 1983. Chapter 5 The Bottom Boundary Layer of Shelf Seas. In: Johns, B. (Ed.), Elsevier Oceanography Series. Elsevier, pp. 189–266.
Soulsby, R.L., Clarke, S., 2005a. Bed Shear-Stresses Under Combined Waves and Currents on Smooth and Rough Beds. HR Wallingford, Wallingford, UK, p. 22.
Souls, R.L., Clarke, S., 2005b. Bed Shear Stress Under Combined Waves and Currents on Smooth and Rough Beds.
Soulsby, R.L., Humphery, J.D., 1990. Field Observations of Wave-Current Interaction at the Sea Bed. In: Tørum, A., Gudmestad, O.T. (Eds.), Water Wave Kinematics. Springer, Netherlands, pp. 413–428.
Soulsby, R.L., Salkield, A.P., Le Good, G.P., 1984. Measurements of the turbulence characteristics of sand suspended by a tidal current. Cont. Shelf Res. 3, 439–454.
Sreenivasan, K.R., Antonia, R.A., 1997. The phenomenology of small-scale turbulence. Annual Reviews.
Stapleton, K.R., Huntley, D.A., 1995. Seabed stress determinations using the inertial dissipation method and the turbulent kinetic energy method. Earth Surf. Process. Landforms 20, 807–815.
Sunamura, T., Takeda, I., 1993. Bar movement and shoreline change: predictive relations. J. Coast. Res. 15, 125–140.
Tamburrino, A., Gulliver, J.S., 2007. Free-surface visualization of streamwise vortices in a channel flow. Water Resour. Res. 43, W11410.
Taylor, G.I., 1938. The spectrum of turbulence. Proc. R. Soc. Lond. Ser. A—Math. Phys. Sci. 164, 476–490.
Tennekes, H., Lumley, J.L., 1972. A First Course in Turbulence. MIT Press, Cambridge, Mass.

Thompson, C.E.L., Couceiro, F., Fones, G.R., Helsby, R., Amos, C.L., Black, K., Parker, E. R., Greenwood, N., Statham, P.J., Kelly-Gerreyn, B.A., 2011. In situ flume measurements of resuspension in the North Sea. Estuar. Coast. Shelf Sci. 94, 77–88.
Thompson, C.E.L., Kassem, H., Williams, J.J., 2013. BARDEX II: Nearshore sediment resuspension and bed morphology. In: Conley, D.C., Masselink, G., Russell, P.E., O'Hare, T.J. (Eds.), Proceedings of the 12th International Coastal Symposium. Journal of Coastal Research. Plymouth, England, pp. 1593–1598.
Thompson, C.E.L., Williams, J.J., Metje, N., Coates, L.E., Pacheco, A., 2012. Turbulence based measurements of wave friction factors under irregular waves on a gravel bed. Coast. Eng. 63, 39–47.
Thorne, P.D., Davies, A.G., Williams, J.J., 2003. Measurements of near-bed intra-wave sediment entrainment above vortex ripples. Geophys. Res. Lett. 30, 2028.
Thorne, P.D., Hanes, D.M., 2002. A review of acoustic measurement of small-scale sediment processes. Cont. Shelf Res. 22, 603–632.
Thosteson, E.D., Hanes, D.M., 1998. A simplified method for determining sediment size and concentration from multiple frequency acoustic backscatter measurements. J. Acoust. Soc. Am. 104, 820–830.
Ting, F.C.K., Kirby, J.T., 1994. Observation of undertow and turbulence in a laboratory surf zone. Coast. Eng. 24, 51–80.
Ting, F.C.K., Kirby, J.T., 1996. Dynamics of surf-zone turbulence in a spilling breaker. Coast. Eng. 27, 131–160.
Tomkins, C.D., Adrian, R.J., 2003. Spanwise structure and scale growth in turbulent boundary layers. J. Fluid Mech. 490, 37–74.
Torrence, C., Compo, G.P., 1998. A practical guide to wavelet analysis. Bull. Am. Meteorol. Soc. 79, 61–78.
Tucker, M.J., Pitt, E.G., 2001. Waves in Ocean Engineering. Elsevier, Amsterdam.
van Rijn, L., Walstra, D., van Ormondt, M., 2007. Unified view of sediment transport by currents and waves. IV: application of morphodynamic model. J. Hydraul. Eng. 133, 776–793.
van Rijn, L.C., 1993. Principles of Sediment Transport in Rivers, Estuaries and Coastal Seas. Aqua Publications, Amsterdam.
van Rijn, L.C., Ribberink, J.S., Werf, J.V.D., Walstra, D.J.R., 2013. Coastal sediment dynamics: recent advances and future research needs. J. Hydraul. Res. 51, 475–493.
Venditti, J.G., Bennett, S.J., 2000. Spectral analysis of turbulent flow and suspended sediment transport over fixed dunes. J. Geophys. Res.: Oceans 105, 22035–22047.
Williams, J.J., Metje, N., Coates, L.E., Atkins, P.R., 2007. Sand suspension by vortex pairing. Geophys. Res. Lett. 34, L15603.
Willmarth, W.W., Lu, S.S., 1972. Structure of the Reynolds stress near the wall. J. Fluid Mech. 55, 65–92.
Wu, F., Jiang, M., 2007. Numerical investigation of the role of turbulent bursting in sediment entrainment. J. Hydraul. Eng. 133, 329–334.
Wu, F., Yang, K., 2004. Entrainment probabilities of mixed-size sediment incorporating near-bed coherent flow structures. J. Hydraul. Eng. 130, 1187–1197.
Wyngaard, J.C., Clifford, S.F., 1977. Taylor's hypothesis and high–frequency turbulence spectra. J. Atmos. Sci. 34, 922–929.
Yuan, Y., Wei, H., Zhao, L., Cao, Y., 2009. Implications of intermittent turbulent bursts for sediment resuspension in a coastal bottom boundary layer: a field study in the western Yellow Sea, China. Mar. Geol. 263, 87–96.
Zhou, J., Meinhart, C.D., Balachandar, S., Adrian, R.J., 1997. Formation of coherent hairpin packets in wall turbulence. In: Panton, R.L. (Ed.), Self-Sustaining Mechanisms Of Wall Turbulence. Computational Mechanics Publications, Southampton, p. 422p.

Appendix 4.

Continuous Wavelet transforms of 3D Reynolds stresses and Sediment resuspension

The following images present the time-frequency properties of the three instantaneous Reynolds stresses ($u'w'$, $u'v'$, and $v'w'$) and suspended sediment concentrations (SSC), measured within (left hand side) and outside (right hand side) the wave-induced benthic boundary layer for the corresponding wave run turbulence records, from the Barrier Dynamics Experiment. In each panel, the top three subplots show the time series of the three aforementioned stresses , respectively; together with their frequency spectrum (through a Fourier transform) in which the "universal" Kolmogorov-Obukhov rate of inertial dissipation ($k^{-\frac{5}{3}}$) is displayed by the red line. The following three sub-panels present the time series of continuous wavelet transforms (CWT) for each of the stresses in the time-frequency domain, presented in the same order, together with their global spectral power (integrated variance) across the various frequency (inverse period) scales. Subsequently, the lower two sub-panels show the time series of vertical suspension profiles (logarithmic backscatter; with higher values in warmer colours) below the ABS sensor head. The power spectral densities of SSC at the levels of the corresponding ADV (ADV1 on the left, within the boundary layer; ADV2 on the right, outside the boundary layer) are also presented, as well as the related continuous wavelet transform of the suspension time series at that elevation. In the time-frequency domains, warmer colours indicate high power (variance); the white- shaded region represents the cone of influence where edge effects may distort the image, and the thick contour lines represent the 95% confidence limit (5% significance against red noise).

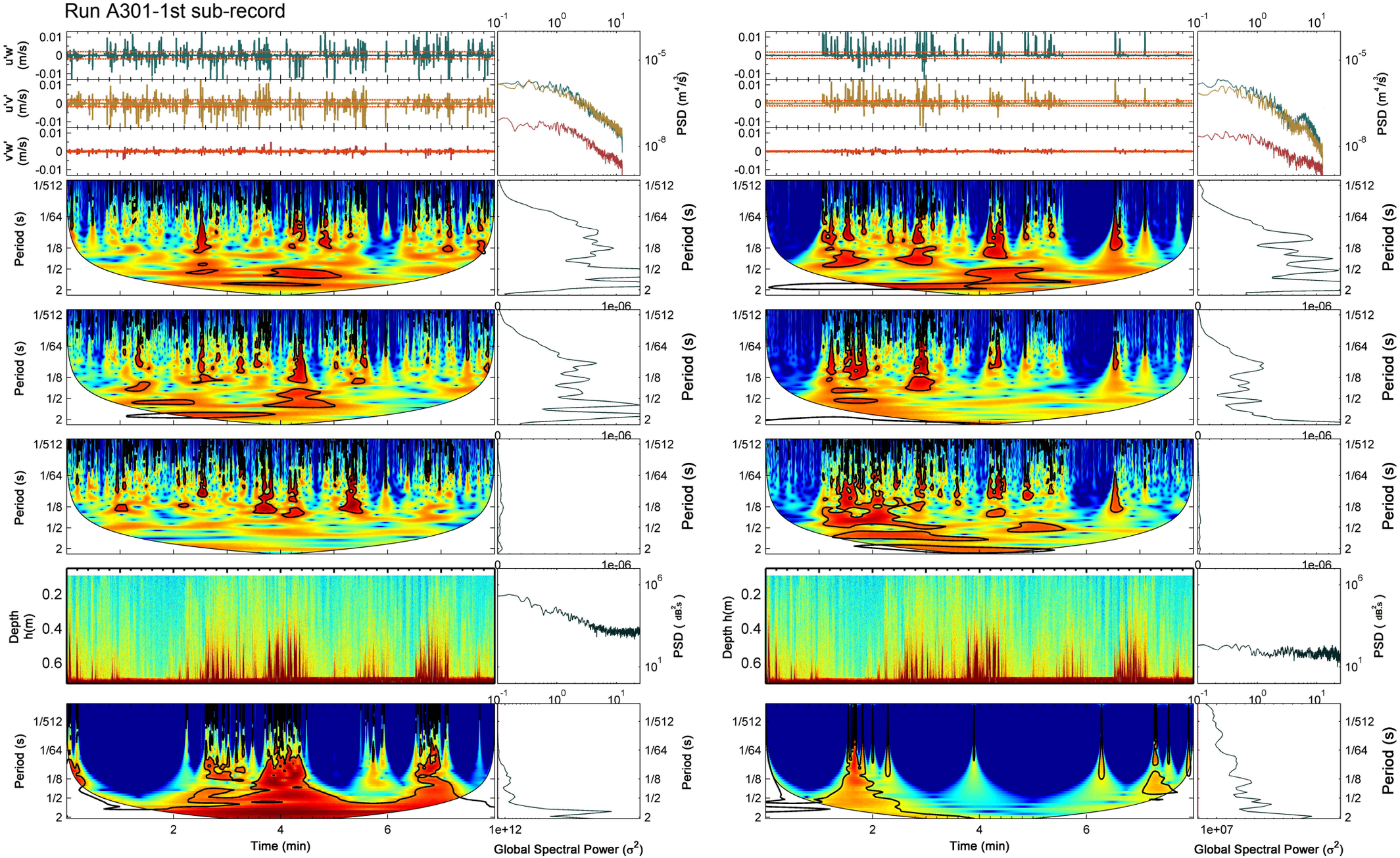
Run A301-1st sub-record
u'w' (m/s)
u'v' (m/s)
v'w' (m/s)
PSD (m⁴/s³)
Period (s)
Depth h(m)
PSD (dB².s)
Time (min)
Global Spectral Power (σ²)

Run A301-2nd sub-record

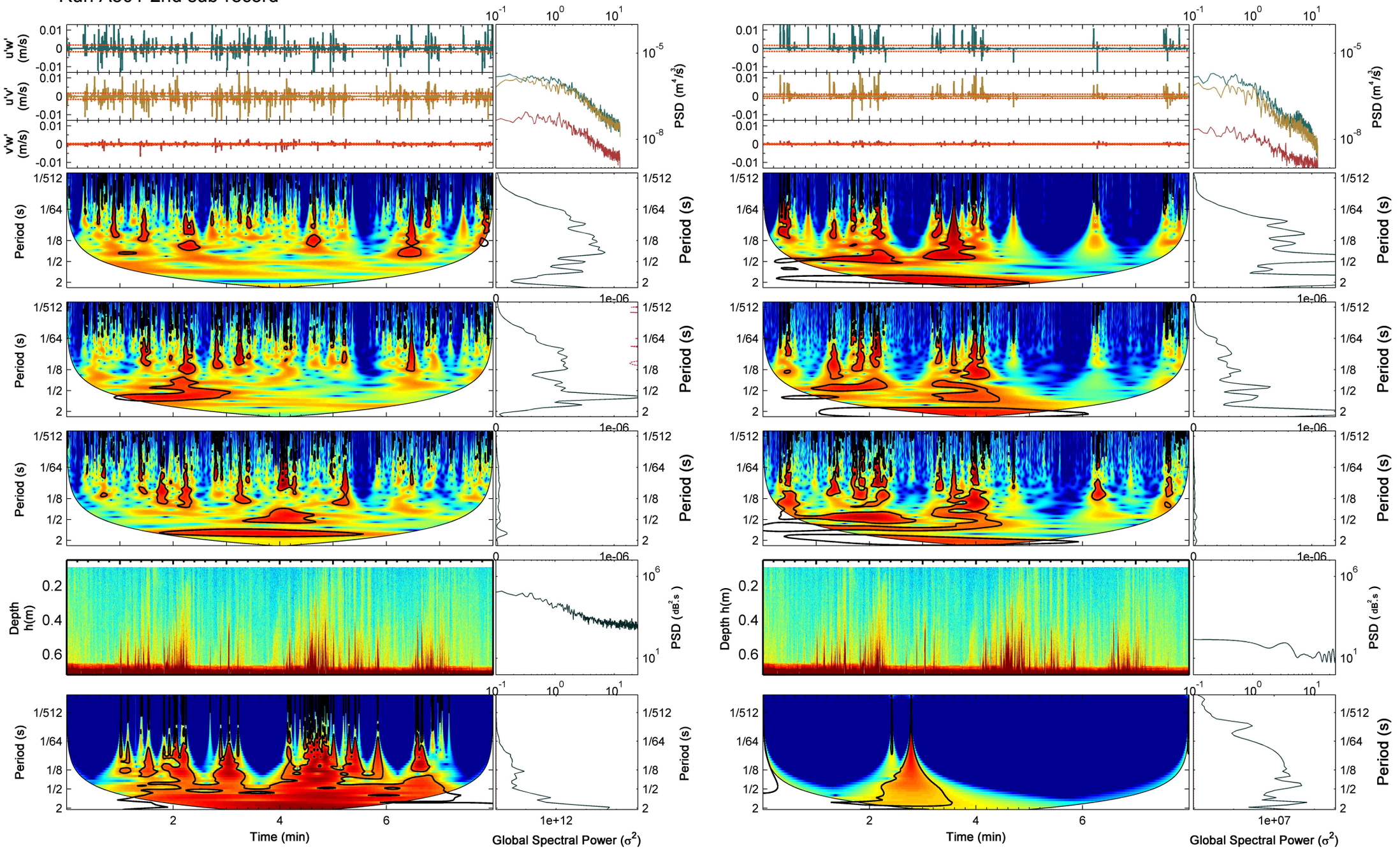

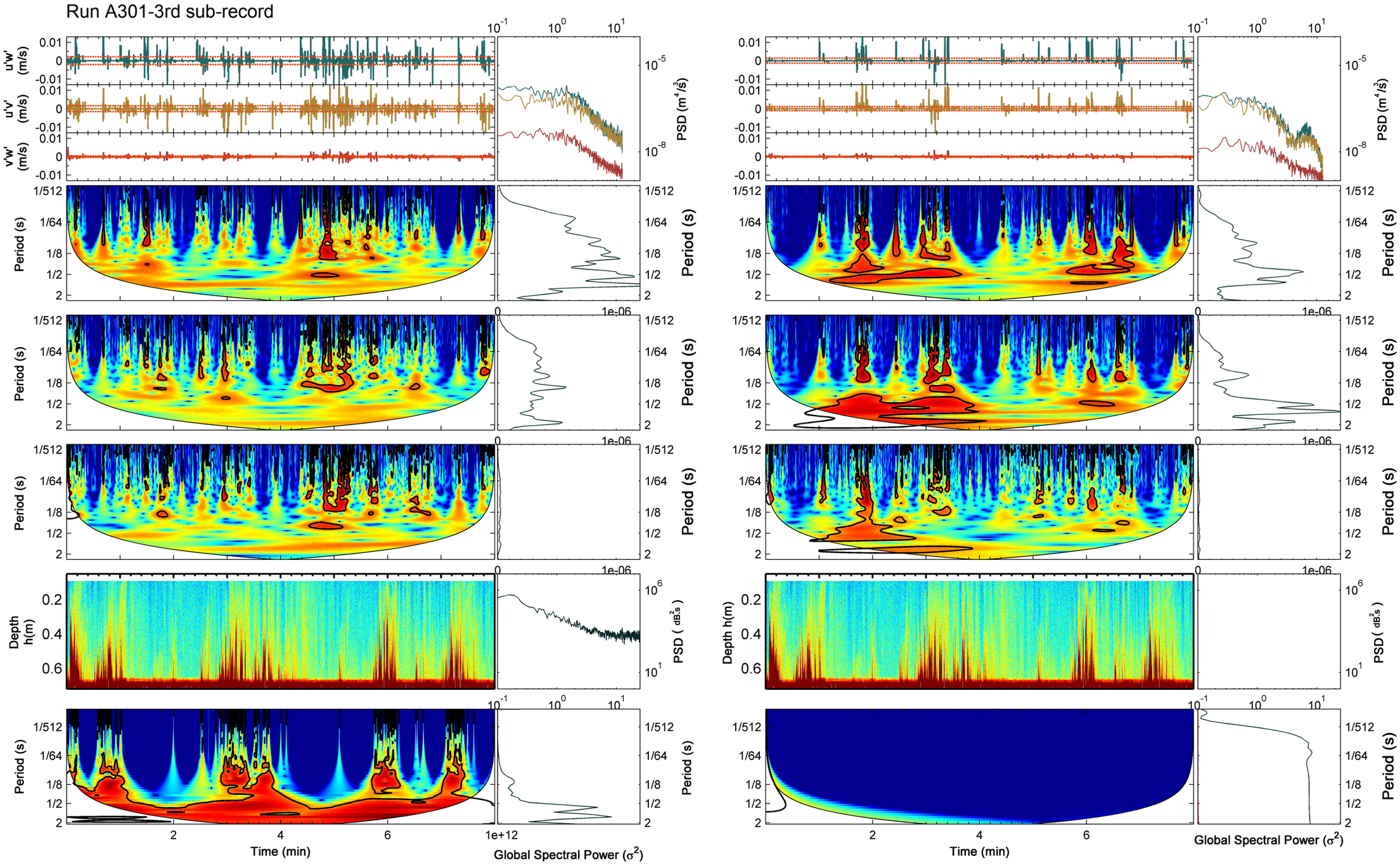
Run A301-3rd sub-record
u'w' (m/s)
u'v' (m/s)
v'w' (m/s)
PSD (m⁴/s³)
Period (s)
Depth h(m)
PSD (dB.s²)
Time (min)
Global Spectral Power (σ²)

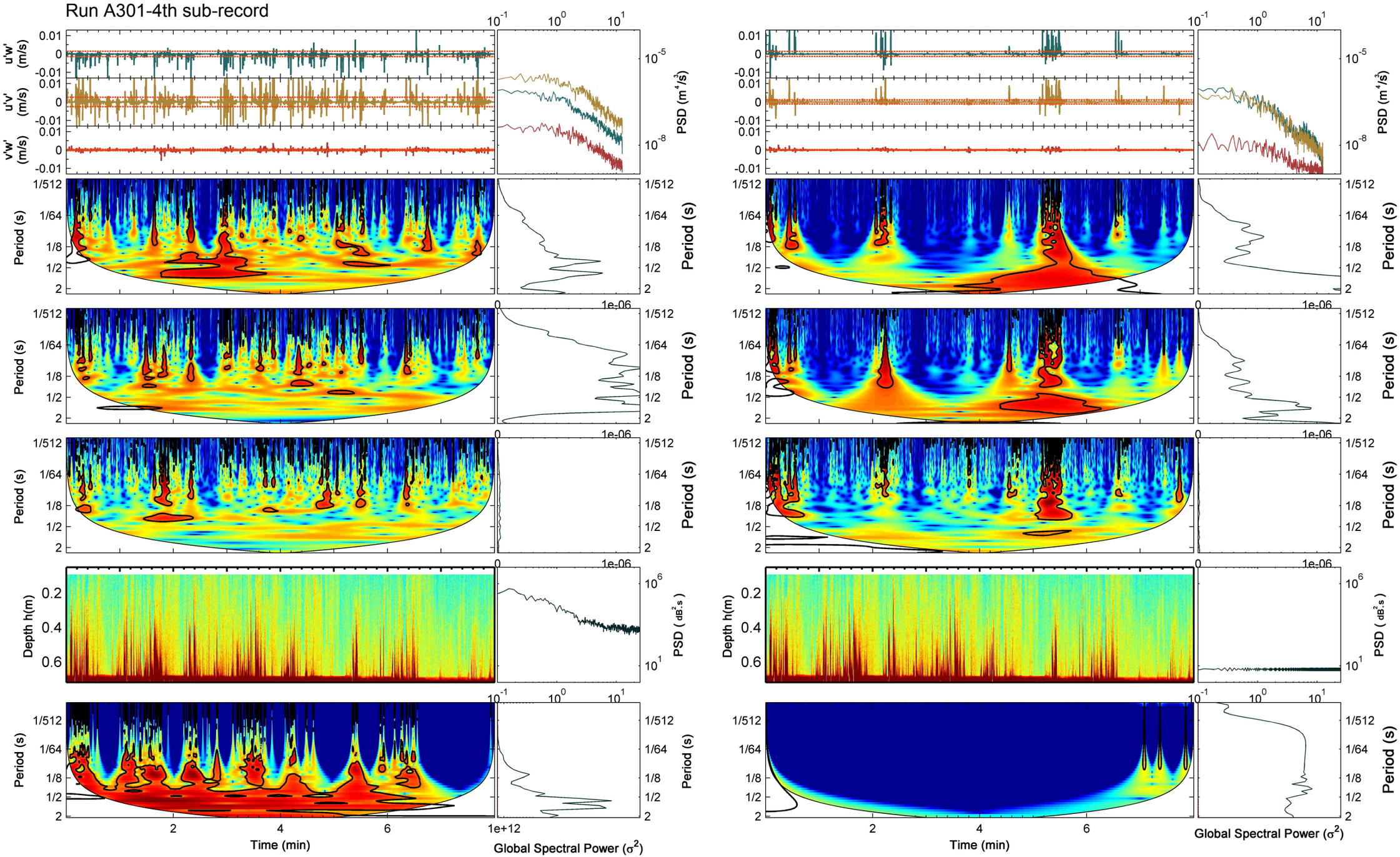
Run A301-4th sub-record
u'w' (m/s)
u'v' (m/s)
v'w' (m/s)
PSD (m²/s³)
Period (s)
Depth h(m)
PSD (dB².s)
Time (min)
Global Spectral Power (σ²)

Run A705- sub-record

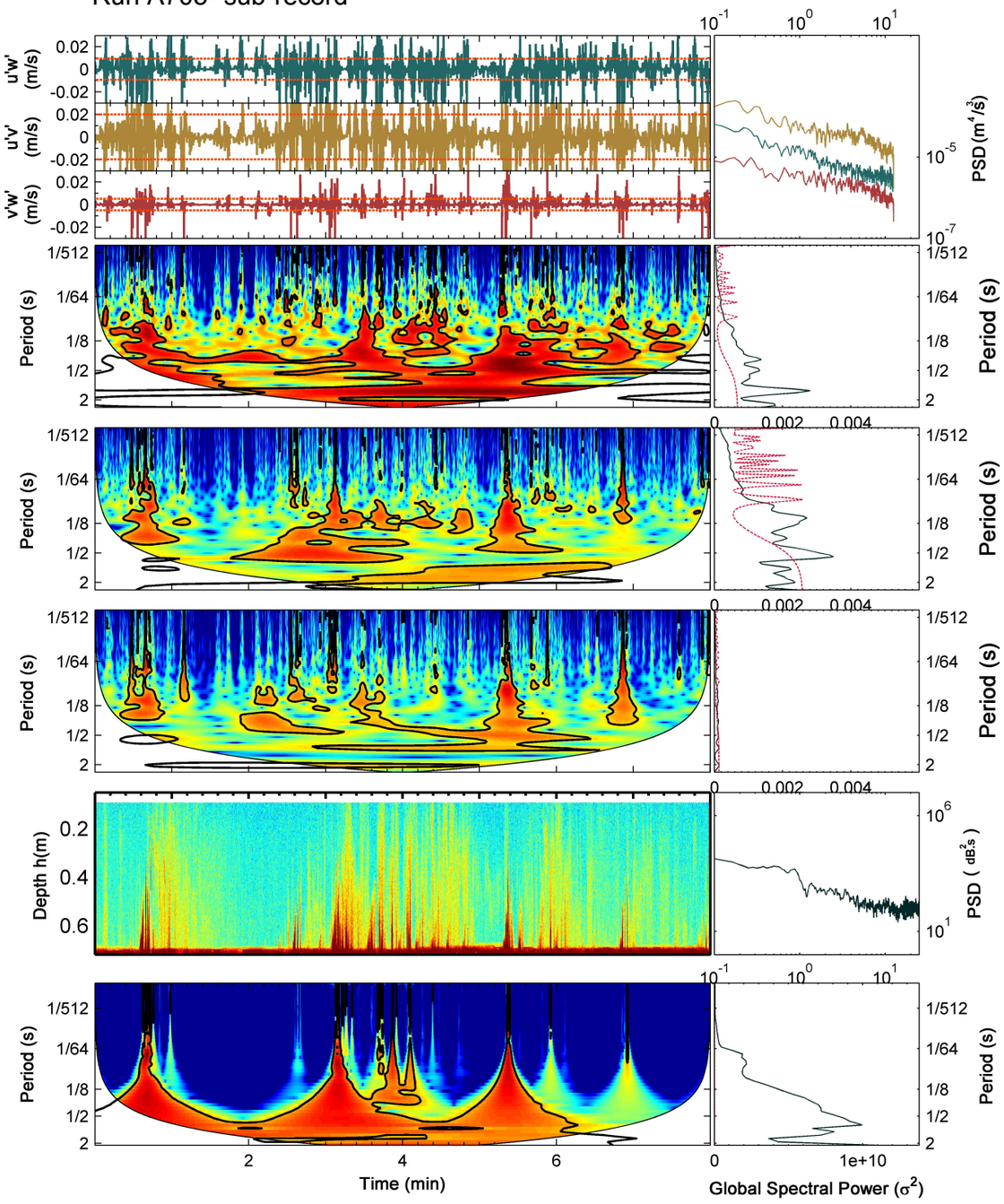

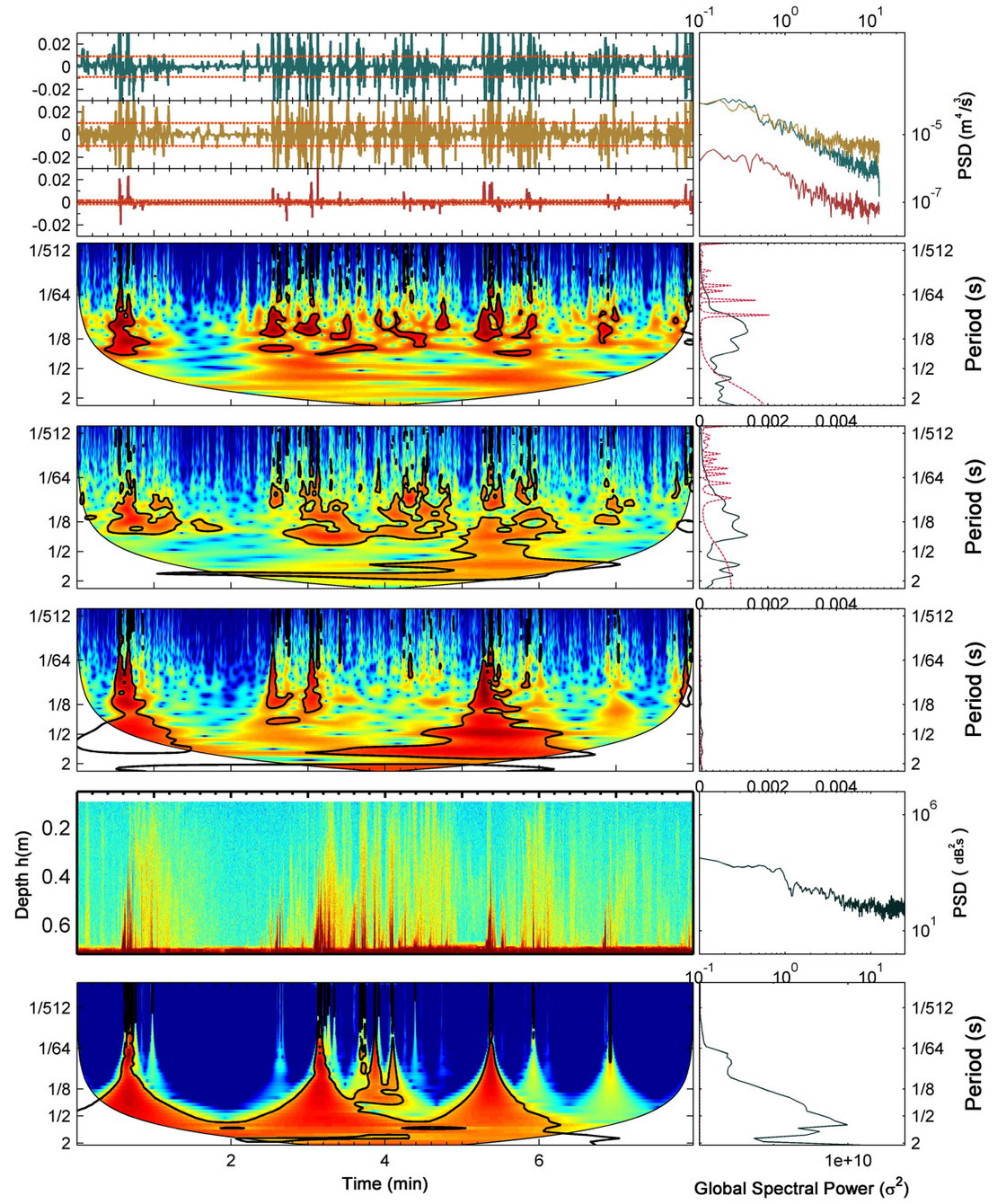

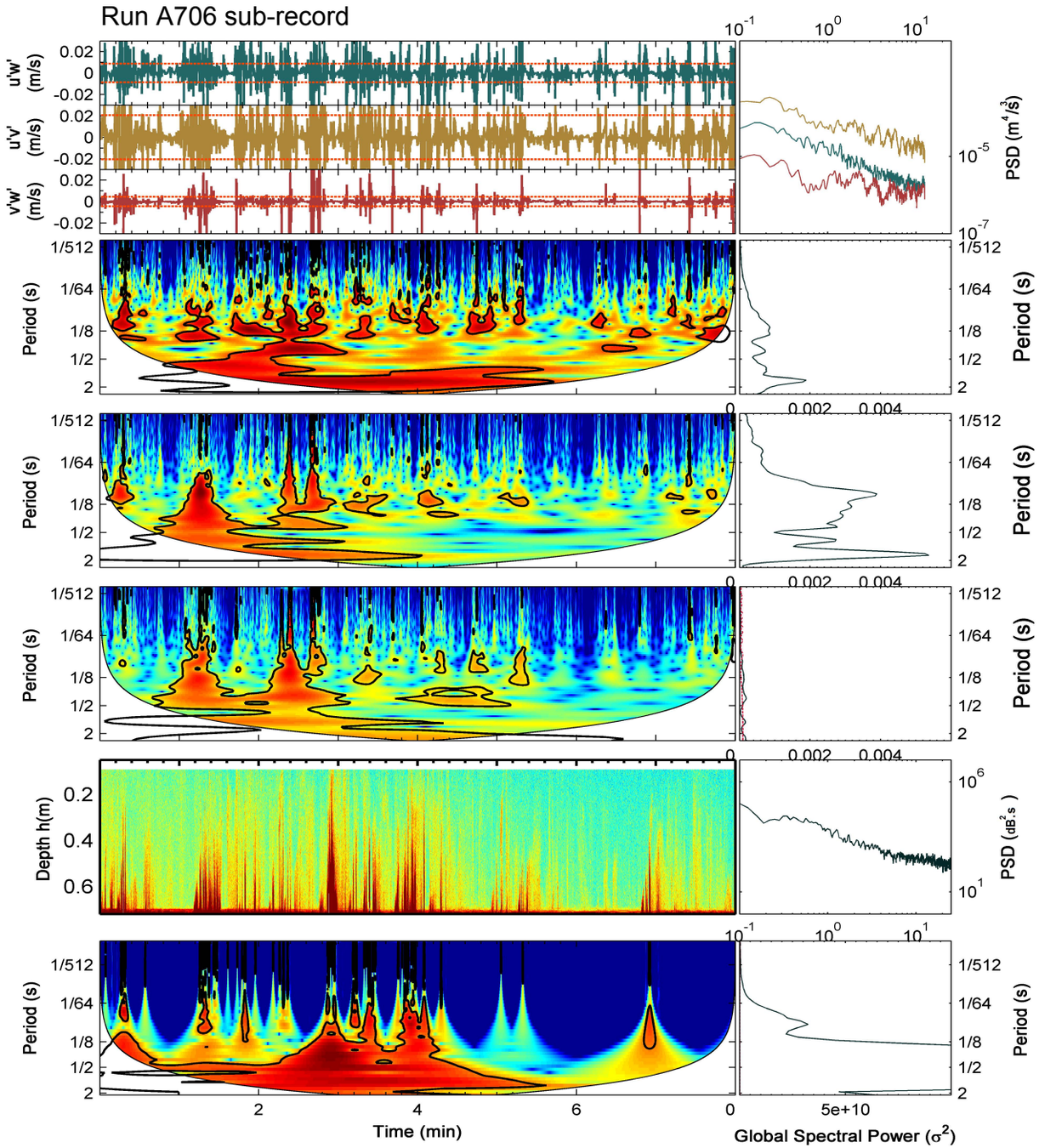
Run A706 sub-record
u'w' (m/s)
u'v' (m/s)
v'w' (m/s)
PSD (m²/s³)
Period (s)
Depth h(m)
PSD (dB².s)
Time (min)
Global Spectral Power (σ²)

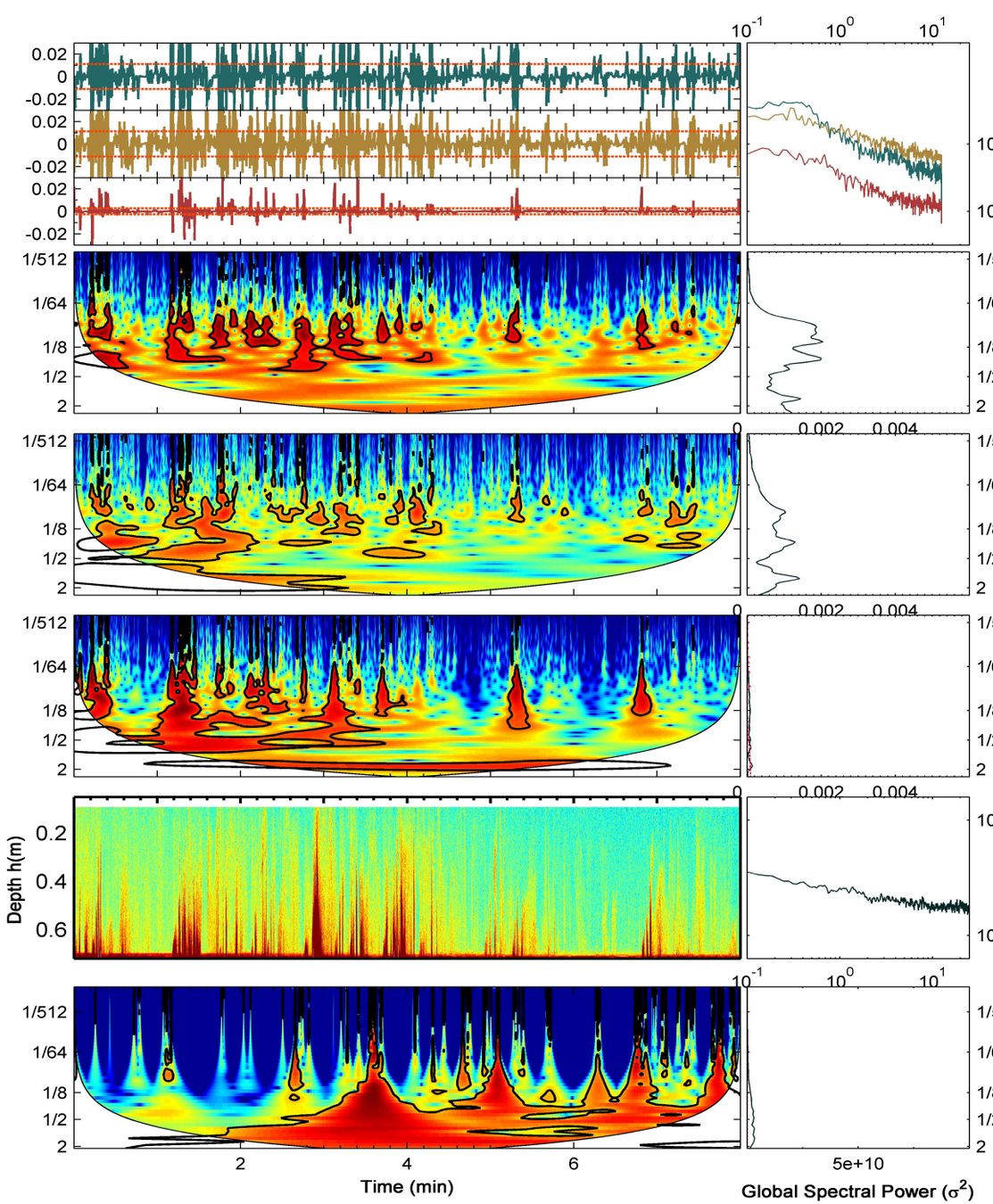
Time (min)
Global Spectral Power (σ²)

Appendix 5.

Continuous Wavelet transforms of 3D Reynolds stresses and Sediment resuspension

The following images present the Cross wavelet transforms of instantaneous 3 dimensional Reynolds Stresses and (downsampled) suspended sediment concentrations within (ADV1) and outside (ADV2) the bottom wave boundary layer for the corresponding wave test run. The light-shaded region represents the cone of influence where edge effects may distort the image. The thick contours represent the 95% confidence limit (5% significance against red noise). The relative phase is shown in arrows (with right arrow indicating in-phase, left arrows indicating anti-phase, and vertical arrows indicate Reynolds stresses leading by 90°).

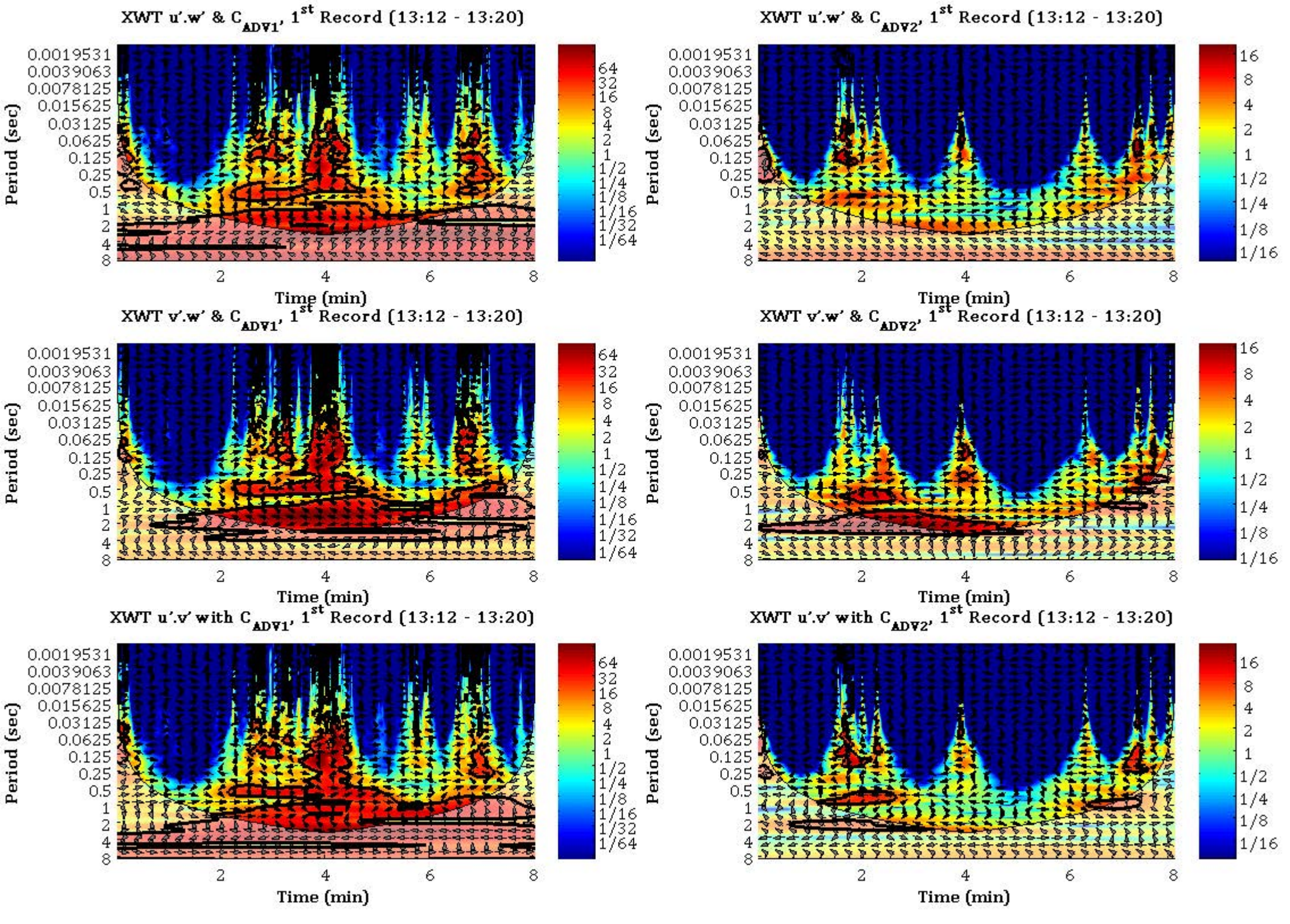
XWT u'.w' & C ADV1, 1st Record (13:12 - 13:20)
XWT u'.w' & C ADV2, 1st Record (13:12 - 13:20)
XWT v'.w' & C ADV1, 1st Record (13:12 - 13:20)
XWT v'.w' & C ADV2, 1st Record (13:12 - 13:20)
XWT u'.v' with C ADV1, 1st Record (13:12 - 13:20)
XWT u'.v' with C ADV2, 1st Record (13:12 - 13:20)
Period (sec)
0.0019531
0.0039063
0.0078125
0.015625
0.03125
0.0625
0.125
0.25
0.5
1
2
4
8
Time (min)
2
4
6
8
64
32
16
8
4
2
1
1/2
1/4
1/8
1/16
1/32
1/64

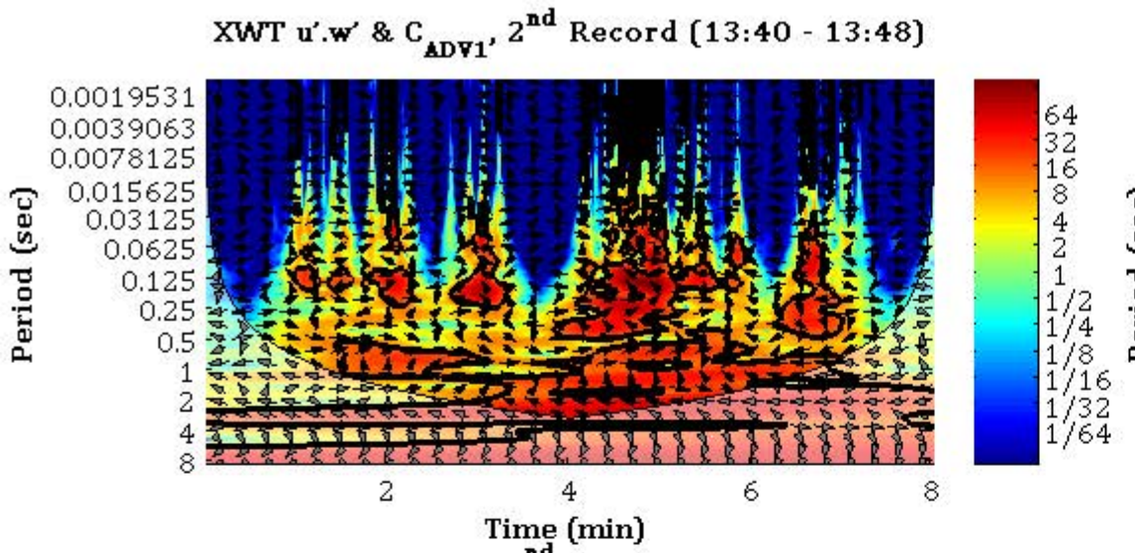
XWT u'.w' & C ADV1, 2nd Record (13:40 - 13:48)
Period (sec)
0.0019531
0.0039063
0.0078125
0.015625
0.03125
0.0625
0.125
0.25
0.5
1
2
4
8
Time (min)
2
4
6
8
64
32
16
8
4
2
1
1/2
1/4
1/8
1/16
1/32
1/64

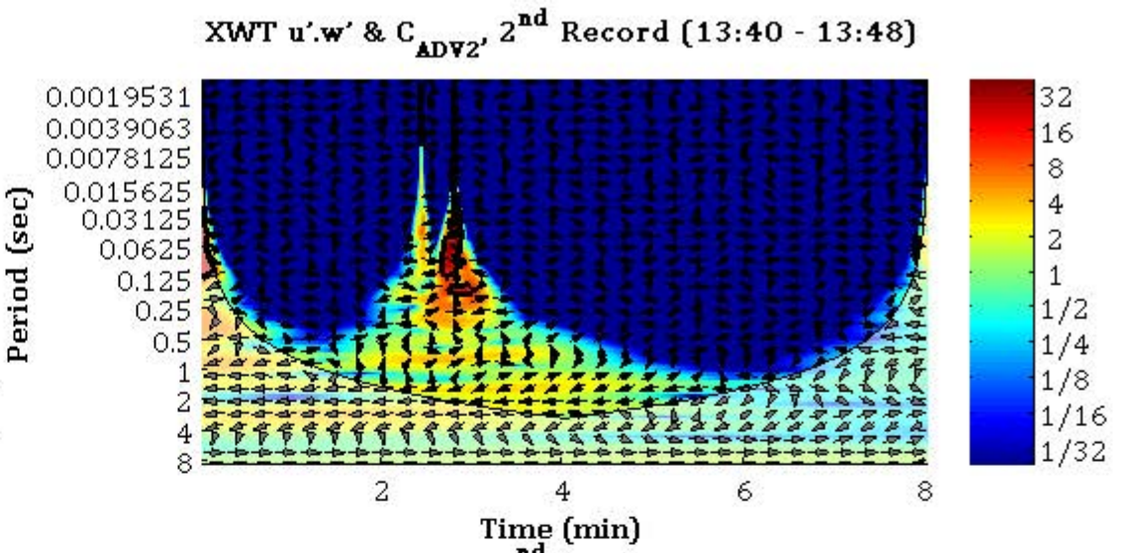
XWT u'.w' & C ADV2, 2nd Record (13:40 - 13:48)
Period (sec)
0.0019531
0.0039063
0.0078125
0.015625
0.03125
0.0625
0.125
0.25
0.5
1
2
4
8
Time (min)
2
4
6
8
32
16
8
4
2
1
1/2
1/4
1/8
1/16
1/32

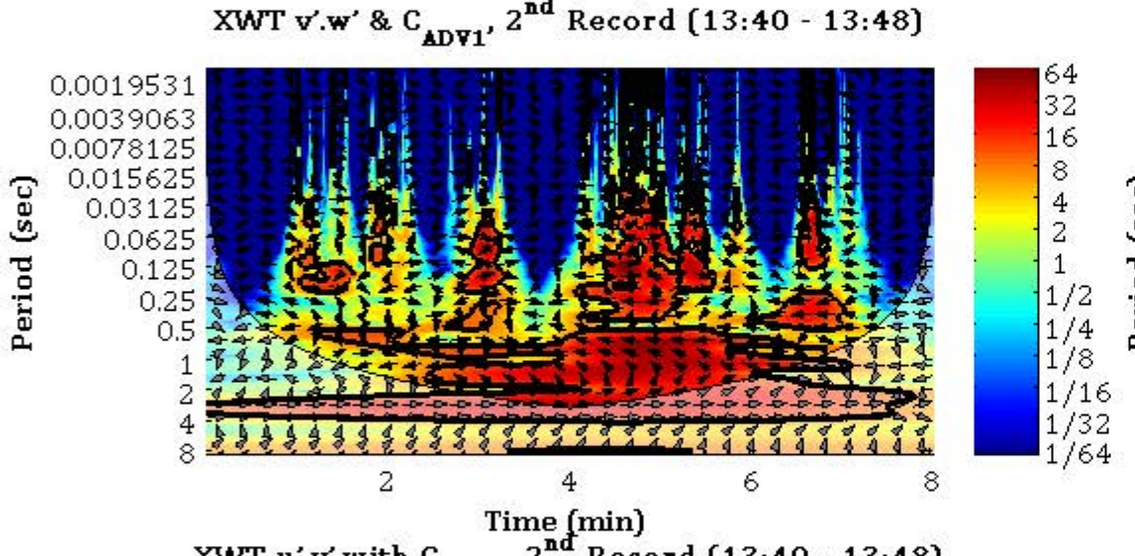
XWT v'.w' & C ADV1, 2nd Record (13:40 - 13:48)
Period (sec)
0.0019531
0.0039063
0.0078125
0.015625
0.03125
0.0625
0.125
0.25
0.5
1
2
4
8
Time (min)
2
4
6
8
64
32
16
8
4
2
1
1/2
1/4
1/8
1/16
1/32
1/64

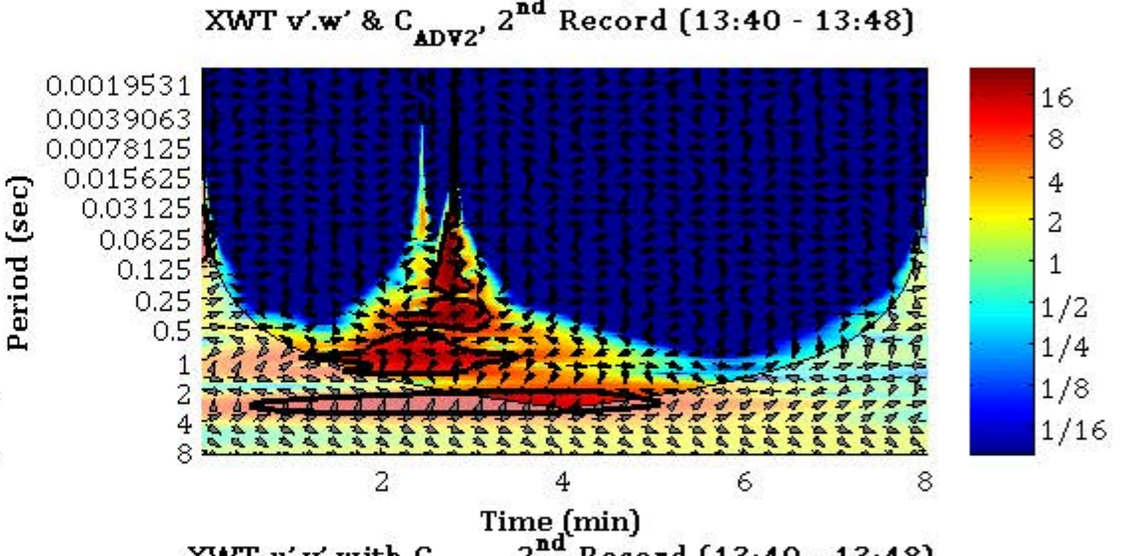
XWT v'.w' & C ADV2, 2nd Record (13:40 - 13:48)
Period (sec)
0.0019531
0.0039063
0.0078125
0.015625
0.03125
0.0625
0.125
0.25
0.5
1
2
4
8
Time (min)
2
4
6
8
16
8
4
2
1
1/2
1/4
1/8
1/16

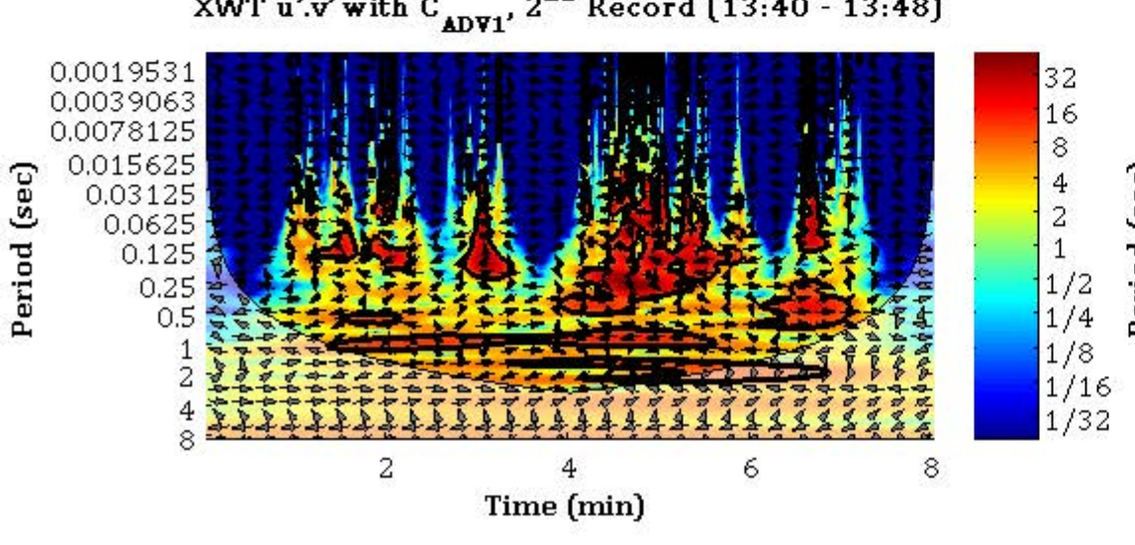
XWT u'.v' with C ADV1, 2nd Record (13:40 - 13:48)
Period (sec)
0.0019531
0.0039063
0.0078125
0.015625
0.03125
0.0625
0.125
0.25
0.5
1
2
4
8
Time (min)
2
4
6
8
32
16
8
4
2
1
1/2
1/4
1/8
1/16
1/32

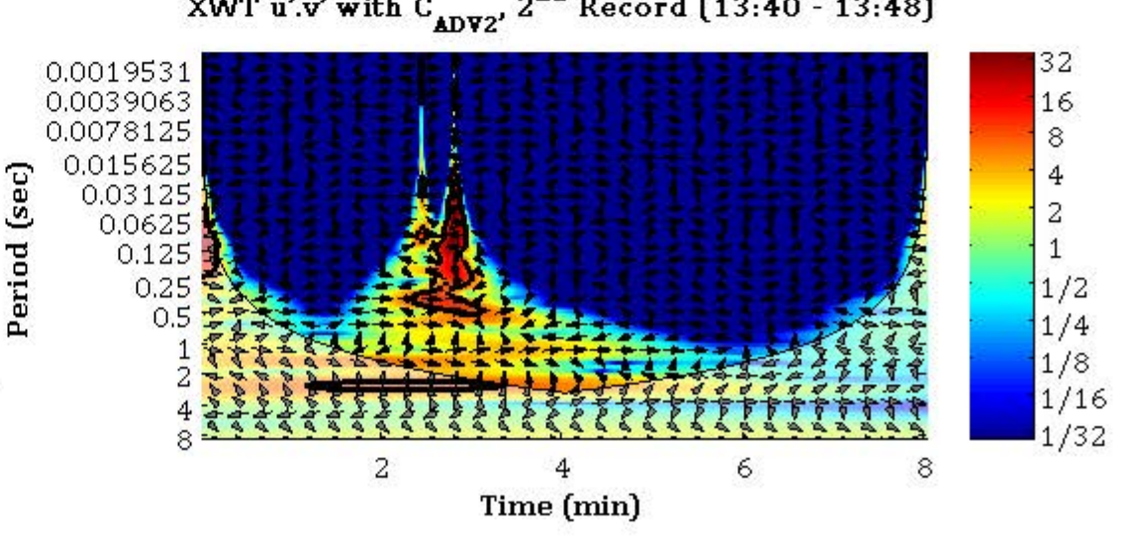
XWT u'.v' with C ADV2, 2nd Record (13:40 - 13:48)
Period (sec)
0.0019531
0.0039063
0.0078125
0.015625
0.03125
0.0625
0.125
0.25
0.5
1
2
4
8
Time (min)
2
4
6
8
32
16
8
4
2
1
1/2
1/4
1/8
1/16
1/32

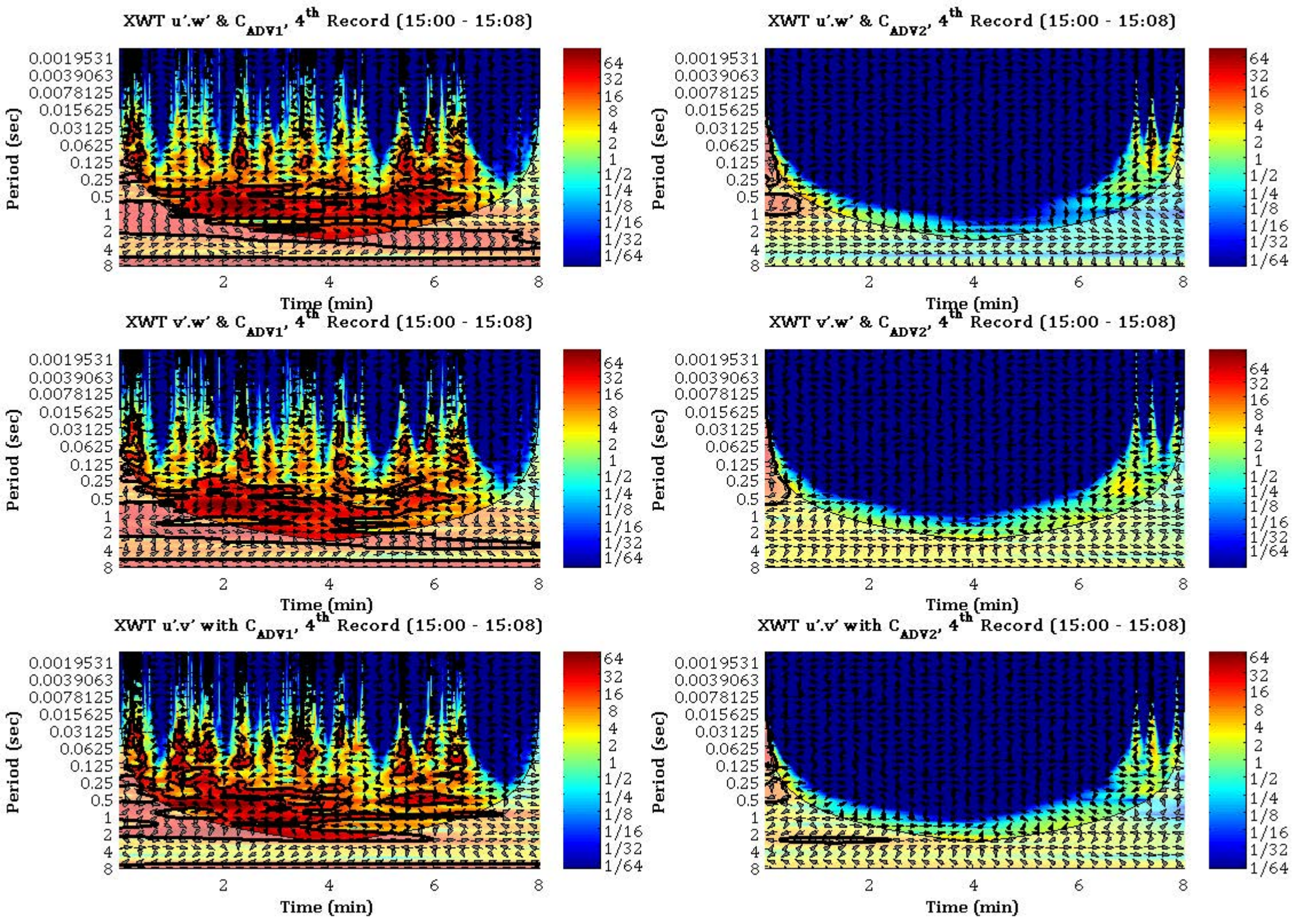
XWT u'.w' & C_ADV1', 4th Record (15:00 - 15:08)
XWT u'.w' & C_ADV2', 4th Record (15:00 - 15:08)
XWT v'.w' & C_ADV1', 4th Record (15:00 - 15:08)
XWT v'.w' & C_ADV2', 4th Record (15:00 - 15:08)
XWT u'.v' with C_ADV1', 4th Record (15:00 - 15:08)
XWT u'.v' with C_ADV2', 4th Record (15:00 - 15:08)
Period (sec)
0.0019531
0.0039063
0.0078125
0.015625
0.03125
0.0625
0.125
0.25
0.5
1
2
4
8
Time (min)
2
4
6
8
64
32
16
8
4
2
1
1/2
1/4
1/8
1/16
1/32
1/64

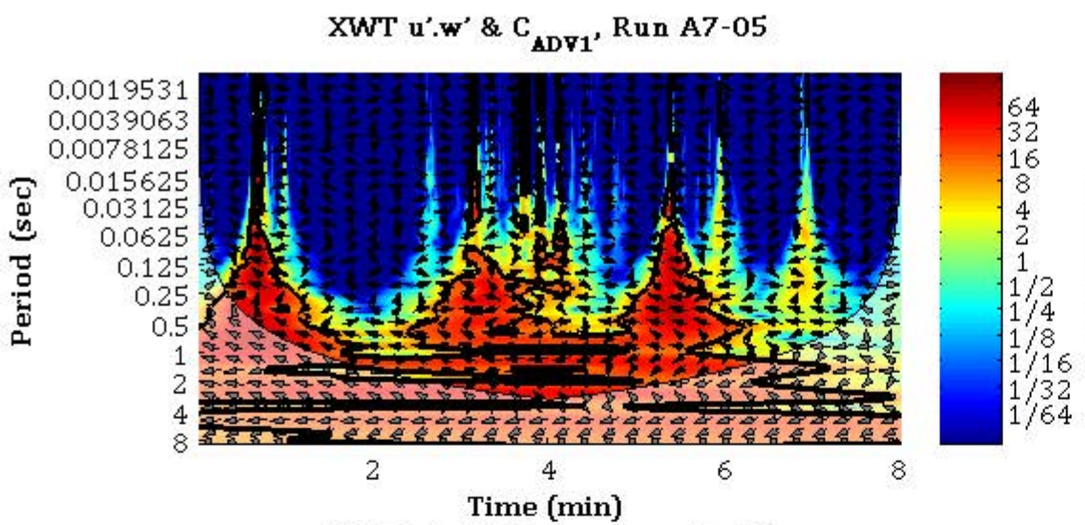

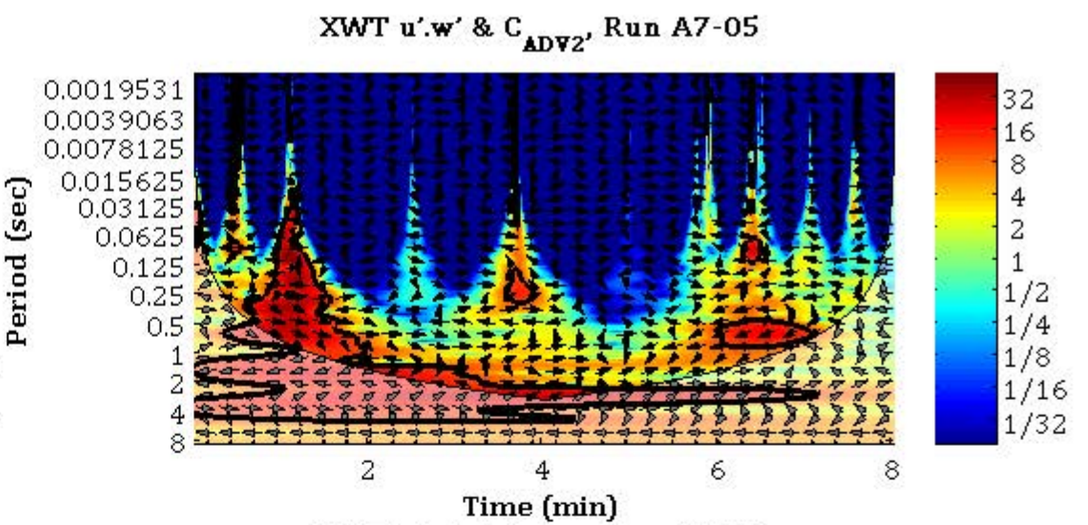

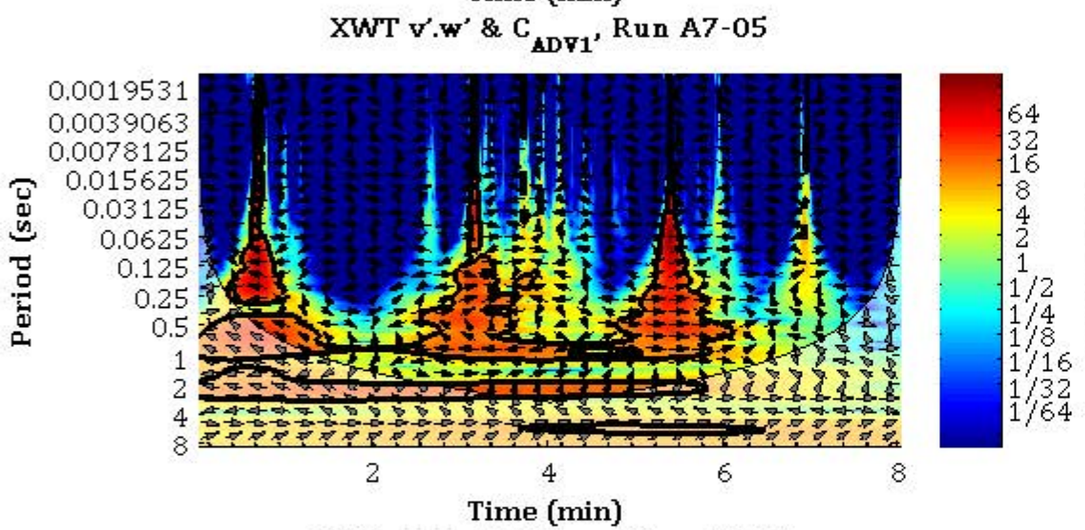

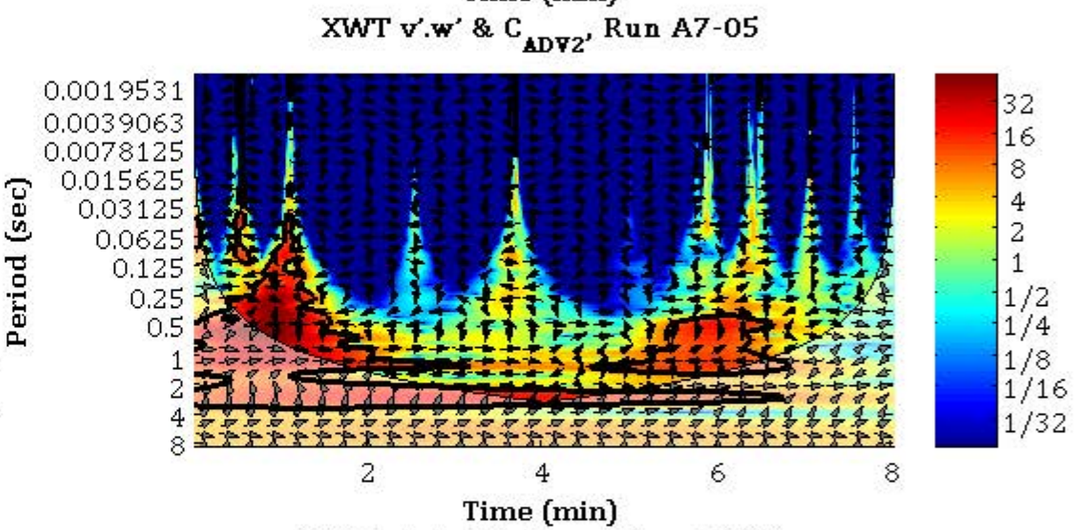

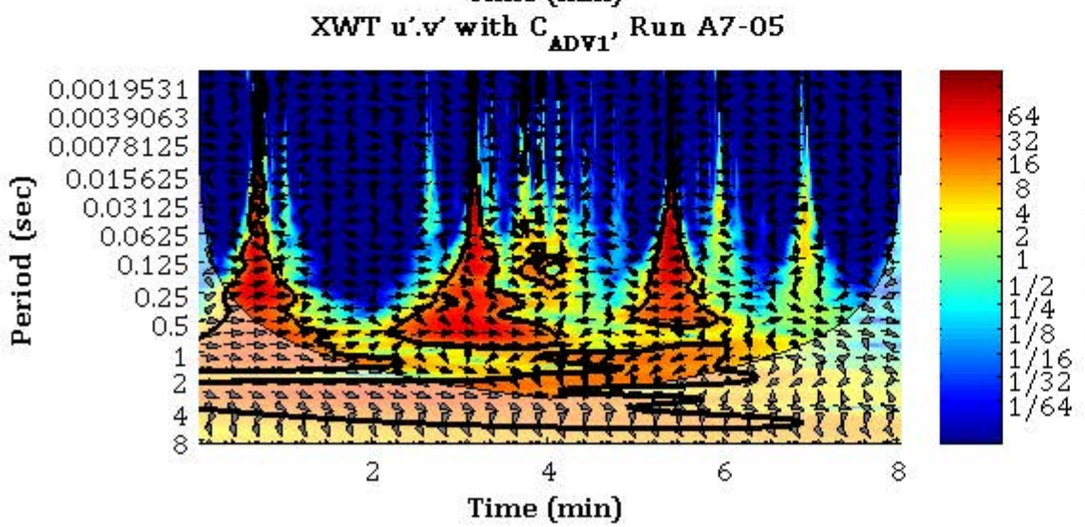

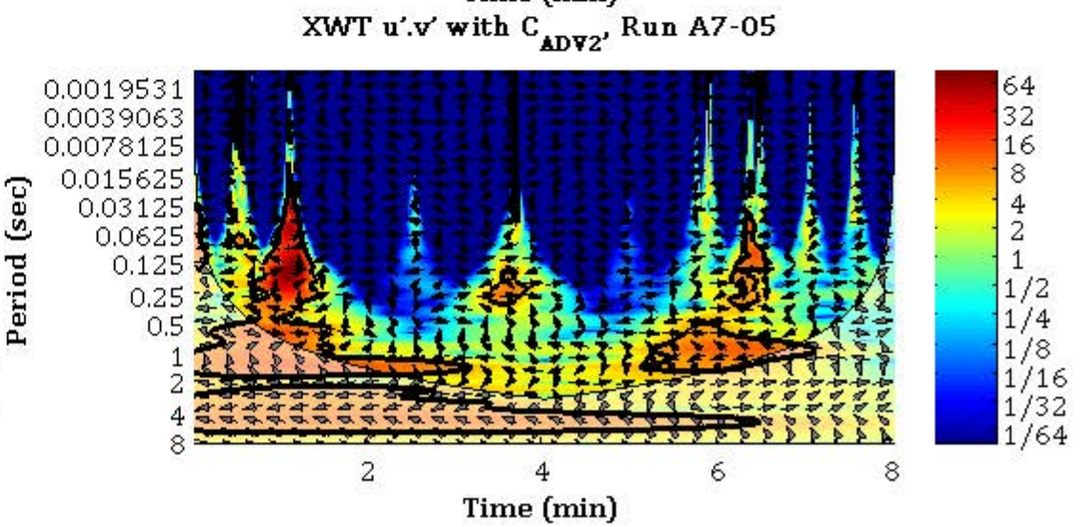

Cross wavelet transforms (XWT) or Reynsolds Stress and instantaneous Concentrations; Hs = 0.6m; Tp = 12 s (Accretive), Run A7-05
19/06/2013 13:28-13:36, Z_{ADV1} = 0.0831m; Z_{ADV2} = 0.3462m

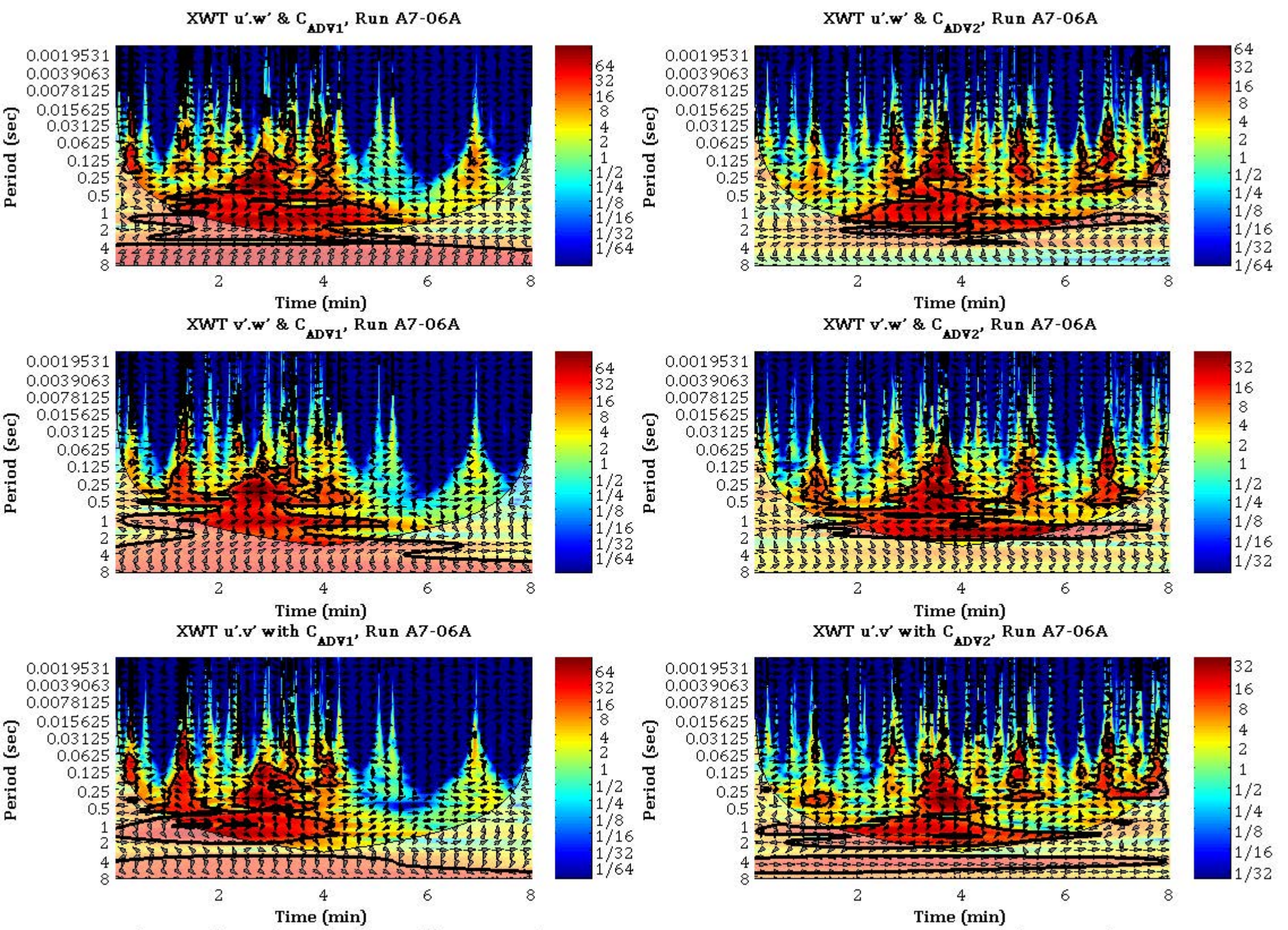

Cross wavelet transforms (XWT) or Reynsolds Stress and instantaneous Concentrations; Hs = 0.6m; Tp = 12 s (Accretive), Run A7-06A 19/06/2013 14:35-14:43, Z_{ADV1} = 0.085m; Z_{ADV2} = 0.3562m

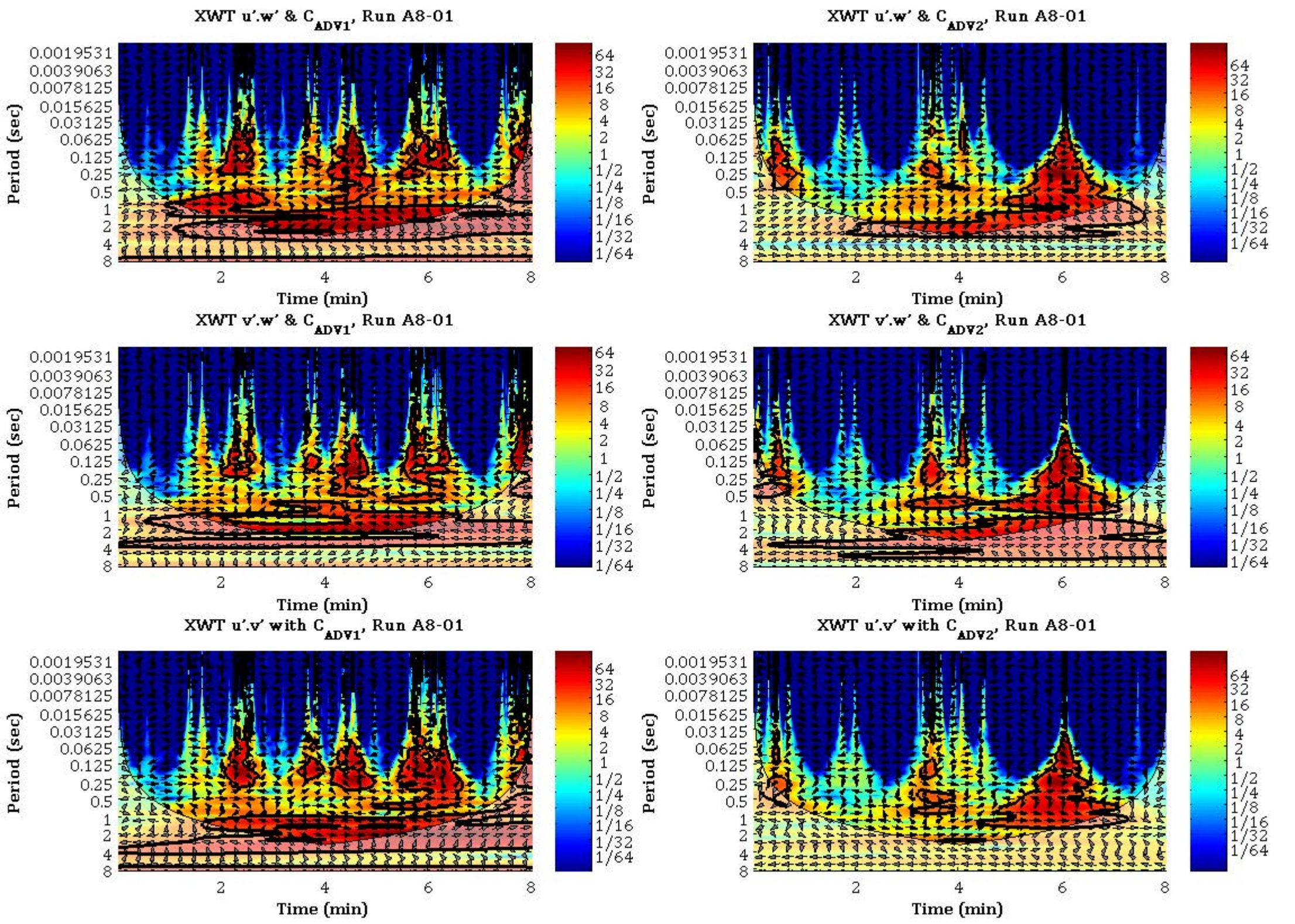

Cross wavelet transforms (XWT) or Reynsolds Stress and instantaneous Concentrations; Hs = 0.6m; Tp = 12 s (Accretive), Run A8-01
20/06/2013 10:22-10:30, Z_{ADV1} = 0.1082m; Z_{ADV2} = 0.312m

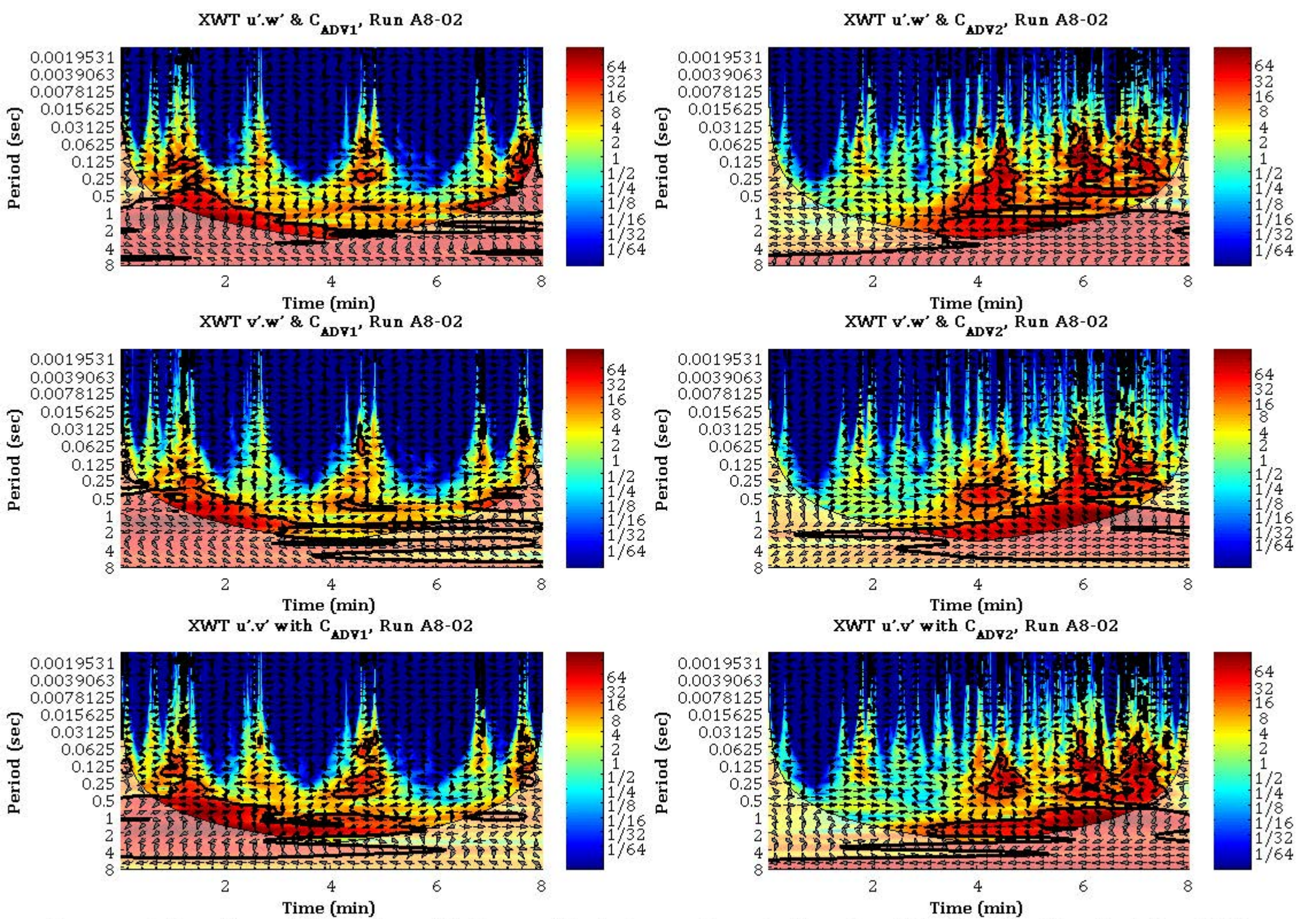

Cross wavelet transforms (XWT) or Reynsolds Stress and instantaneous Concentrations; Hs = 0.6m; Tp = 12 s (Accretive), Run A8-02
20/06/2013 10:22-10:30, Z_{ADV1} = 0.0898m; Z_{ADV2} = 0.334m

Appendix 6.

SIS scans for 1 minute of the aligned and opposing wave-current cases

The following images present 1 minute scans of the SIS showing acoustic backscatter and bed morphology measured every 6 seconds for a duration of 1 minute within the sediment-turbulent experiment conducted at the HR Wallingford Fast Flow Facility; with collinear currents aligned with, and opposing the direction of wave propagation, respectively.

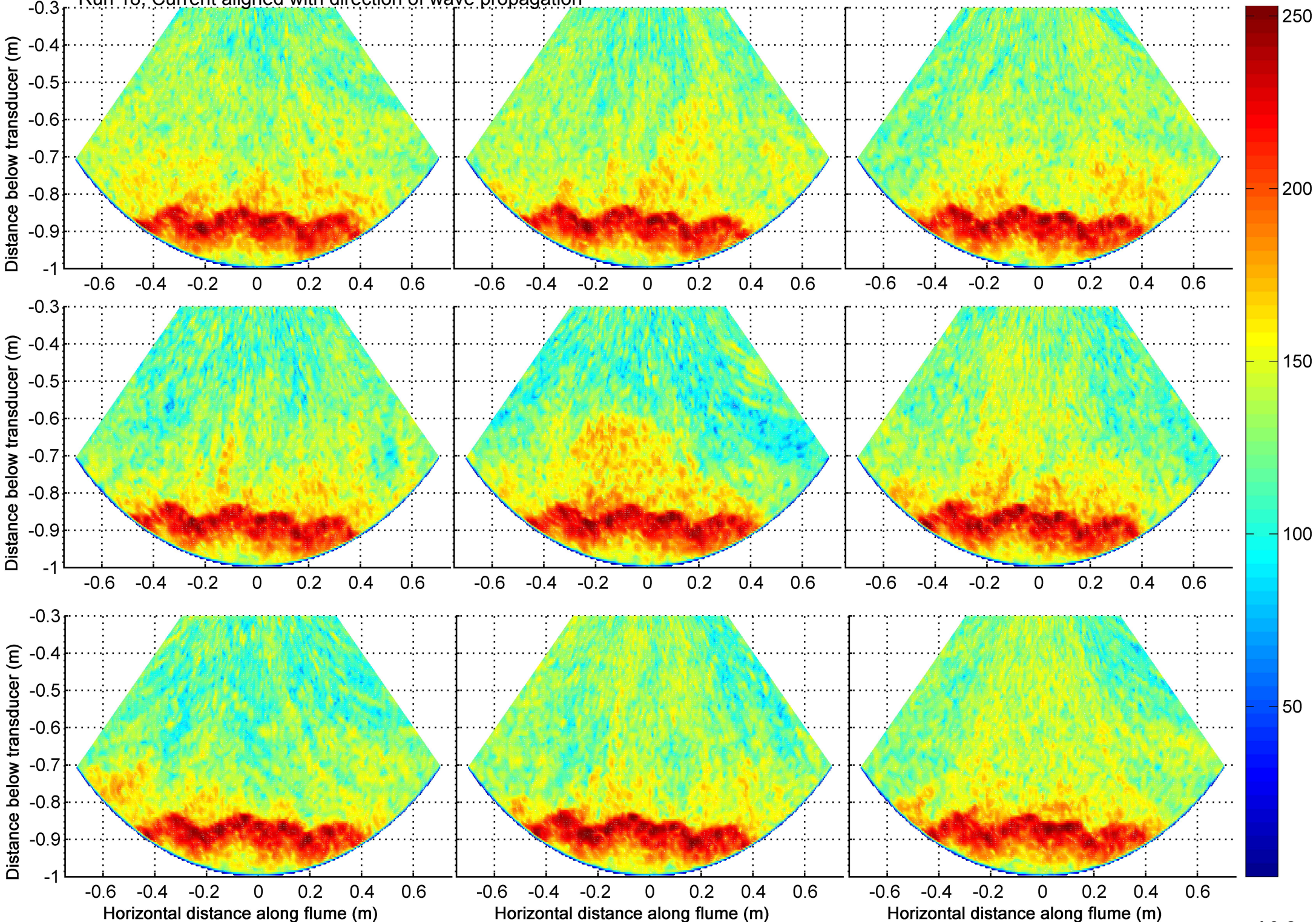
Run 18, Current aligned with direction of wave propagation
Distance below transducer (m)
-0.3
-0.4
-0.5
-0.6
-0.7
-0.8
-0.9
-1
-0.6 -0.4 -0.2 0 0.2 0.4 0.6
Horizontal distance along flume (m)
250
200
150
100
50

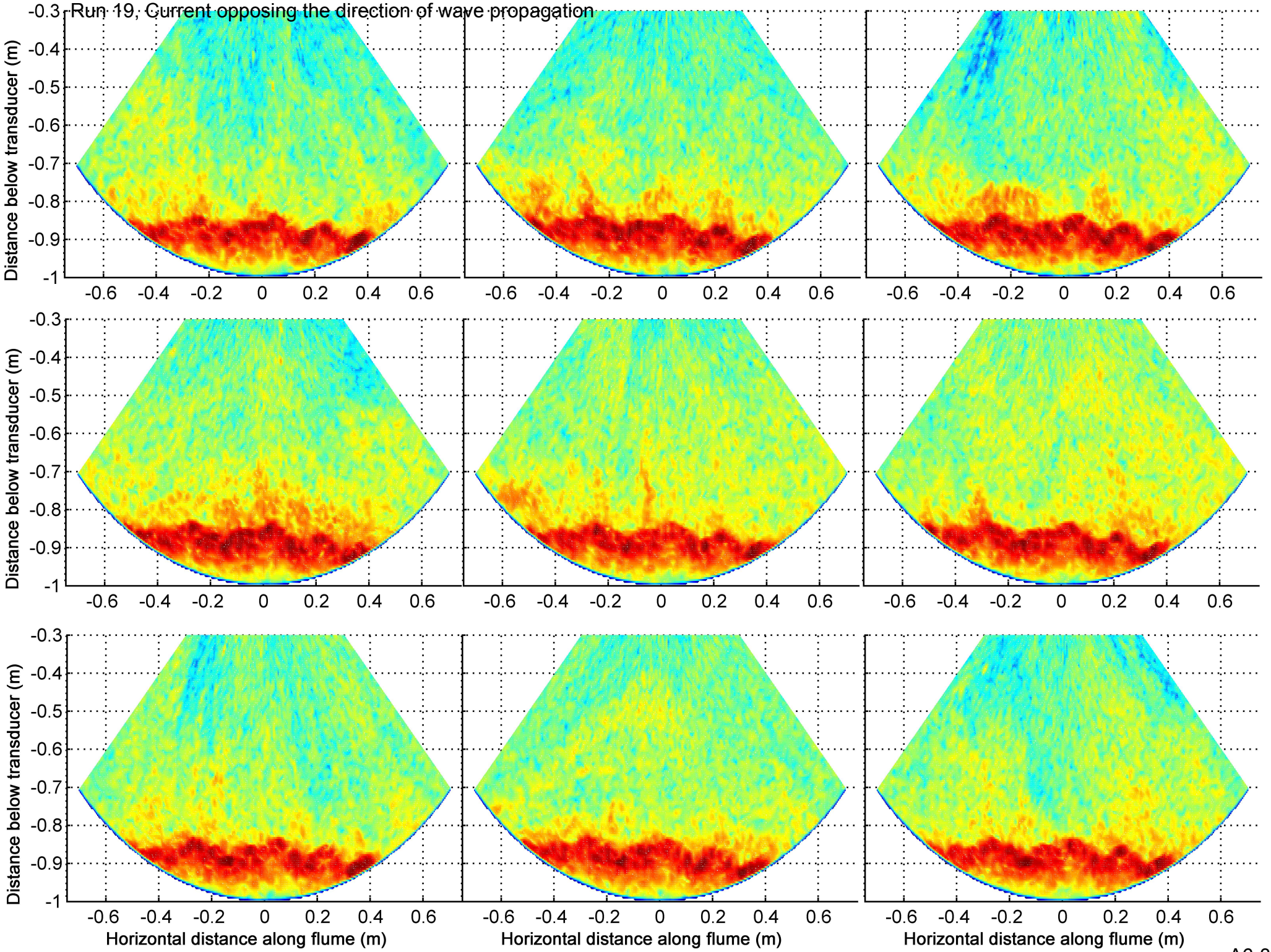
Run 19, Current opposing the direction of wave propagation
Distance below transducer (m)
-0.3
-0.4
-0.5
-0.6
-0.7
-0.8
-0.9
-1
-0.6 -0.4 -0.2 0 0.2 0.4 0.6
Horizontal distance along flume (m)